



A11104 463276

NIST
PUBLICATIONSUnited States Department of Commerce
Technology Administration
National Institute of Standards and Technology*NISTIR 5025***IRRADIATION DAMAGE IN INORGANIC
INSULATION MATERIALS FOR ITER MAGNETS:
A REVIEW**

N.J. Simon

QC
100
.U56
NO. 5025
1994

NISTIR 5025

IRRADIATION DAMAGE IN INORGANIC INSULATION MATERIALS FOR ITER MAGNETS: A REVIEW

N.J. Simon

Materials Reliability Division
Materials Science and Engineering Laboratory
National Institute of Standards and Technology
Boulder, Colorado 80303

Sponsored by
Department of Energy
Office of Fusion Energy
Washington, DC 20545

September 1994



U.S. DEPARTMENT OF COMMERCE, Ronald H. Brown, Secretary
TECHNOLOGY ADMINISTRATION, Mary L. Good, Under Secretary for Technology
NATIONAL INSTITUTE OF STANDARDS AND TECHNOLOGY, Arati Prabhakar, Director

IRRADIATION DAMAGE IN INORGANIC INSULATION MATERIALS
FOR ITER MAGNETS: A REVIEW

N.J. Simon*

National Institute of Standards and Technology
Boulder, Colorado 80303

A literature search on the irradiation resistance of inorganic insulators for the ITER TF[†] magnets is reported. The materials included Al₂O₃, AlN, MgO, porcelain, SiO₂, MgAl₂O₄, ZrO₂, and mica. No in situ measurements of the 4-K compressive, shear, and electrical breakdown strengths after 4-K neutron irradiation were retrieved. Limited optical and thermal property measurements made on these insulators after cryogenic irradiations indicate that recovery occurs in ceramic oxides at ambient temperatures. Host atom amorphization has been demonstrated in Al₂O₃ at 77 K, but was not successful at 300 K. Apparently, host ion amorphization does not occur in most ceramic oxides at 300 K. Amorphization has evidently not been attempted in AlN, MgO, or MgAl₂O₄ at 77 K. Silicate-bonded structures, such as mica, porcelain, and silica, do amorphize at ambient temperature and are, at present, considered unacceptable unless proven otherwise by in situ electrical and mechanical property testing after 4-K irradiation. Zirconia, even if stabilized, will probably transform under neutron irradiation and is, therefore, considered unsuitable. Mica layers delaminated under low energy electron bombardment. Natural mica layers are porous, owing to spontaneous and induced tracks from U impurities. Tracks caused a decrease in electrical breakdown strength. Simulation of neutron irradiation by other radiation species is also reviewed in this report.

Key words: cryogenic; ceramic oxide; inorganic insulation; irradiation; ITER; magnet insulation; mica; radiation damage; superconducting magnet

*Materials Reliability Division, Materials Science and Engineering Laboratory.

[†]ITER = International Thermonuclear Experimental Reactor; TF = toroidal field.

EXECUTIVE SUMMARY

Results of a literature search on the irradiation resistance of candidate inorganic insulators for the ITER TF magnets are reported. The materials investigated include: Al_2O_3 , AlN , MgO , porcelain, SiO_2 , MgAl_2O_4 , ZrO_2 , and mica. A companion report* reviews the low temperature mechanical, thermal, and electrical properties of these materials.

For material downselection and design, data are required on the 4-K compressive and shear strengths and the electrical breakdown strength after a fusion fast neutron fluence of $10^{22}/\text{m}^2$ ($E > 0.1$ MeV). However, no in situ measurements of these or other properties after 4-K irradiation were retrieved in the literature search. Only limited optical and thermal property measurements have been made on these insulators after cryogenic irradiations. Therefore, this report provides guidance in material selection based upon data obtained at the lowest available irradiation temperatures. The lack of 4-K irradiation data is a very serious limitation. Because much of the radiation damage in organic insulators is chemical and results from the ionizing component of the radiation, there may be some correspondence, at least at low fluences, between 4-K mechanical strengths after irradiation at either 300, 77, or 4 K. Some preliminary results on organics indicate that 4-K mechanical strength values may correspond within about a factor of 2 or 3, despite different temperatures of irradiation, because ambient-temperature annealing is apparently limited.[†] However, the radiation damage to the ceramic oxides reviewed here is primarily displacive. Studies on copper reported recovery of 64% of displacive defects induced by deuteron radiation at 10 K by annealing to 70 K; between 70 and 300 K, a further recovery of 32% was observed, so at 300 K, only 4% of the defects remained. The available evidence indicates that similar recovery occurs in ceramic oxides; for example, the number of defects retained after a given irradiation fluence at 77 to 91 K in BeO and Al_2O_3 has

*Simon, N. J. 1994 (In press). Cryogenic Properties of Inorganic Insulation Materials for ITER Magnets: A Review. NISTIR 5030, National Institute of Standards and Technology, Boulder, CO.

[†]Simon, N.J. 1993. A Review of Irradiation Effects on Organic-Matrix Insulation. NISTIR 3999, National Institute of Standards and Technology, Boulder, CO.

been measured to be 10, 16, and 30 times the number retained at 300 K, in various different experiments. The foreign-ion irradiation fluence necessary to induce amorphization in Al_2O_3 at 300 K was 200 times that required at 77 K. For screening purposes only, it is proposed to account for ambient-temperature recovery by examining data at fast neutron fluences about 100 times those expected at 4 K. Currently, this gives an ambient-temperature screening fluence of $100 \times 10^{22}/\text{m}^2$, or $10^{24}/\text{m}^2$. (Of course, available data at other fluences are also reviewed here, since this screening strategy is very approximate, and the expected magnet fluence could change as the ITER design progresses, and will differ with location within the TF magnets.)

The ambient-temperature irradiation data base consists mainly of data on the number of defects, the extent of swelling, and the tendency to amorphize. Limited thermal conductivity and mechanical property data are available. Some of the best mechanical property data, recently obtained by Dienst and Zimmermann at KfK,* ranks $\text{MgAl}_2\text{O}_4 > \text{Al}_2\text{O}_3 > \text{AlN}$ from strength retention in three-point bending tests. MgO would probably rank lower, owing to brittleness in compressive testing of single crystals after a fast neutron fluence of $\sim 2 \times 10^{22}/\text{m}^2$ ($\sim 3 \times 10^{-5}$ dpa[†]), but the other ceramic oxides have not been similarly tested. Because silicate-bonded structures usually amorphize at fluences near $10^{24}/\text{m}^2$, silica and mica have low radiation resistance, and are at present considered unacceptable unless proven otherwise by in situ tests of electrical and mechanical properties after 4-K irradiation. Porcelain has an even lower reported fluence of amorphization and is difficult to evaluate, owing to very limited testing. Zirconia, even if stabilized, will probably transform under neutron irradiation and is therefore considered unsuitable on the basis of present information.

Mica has the added problem of a layered structure that is known to delaminate under low energy electron irradiation in TEM.[‡] Individual natural mica layers are porous, owing to the spontaneous fission and decay of the impurity, ^{238}U , through geological times periods in which "fossil" fission-fragment and

*KfK = Kernforschungszentrum Karlsruhe.

†dpa = displacements per atom.

‡TEM = transmission electron microscope or microscopy.

recoil nuclei tracks are formed to a density that varies approximately from 10^3 to $10^8/\text{cm}^2$. Even though U is present as an impurity in natural micas only in the range of 10^8 to 10^{12} parts per atom, the amount of ^{235}U in a phlogopite mica was sufficient to allow an induced fission-fragment track density of $4 \times 10^5/\text{cm}^2$ after a thermal neutron fluence of $10^{21}/\text{m}^2$. Comparable measurements of induced tracks for muscovite mica, the form commonly used in commercial mica insulation, are not available. The induced track density is expected to vary with the mica source and with processing techniques. Tracks lower the electrical breakdown strength; the delamination of mica from displacement of the interlaminar-bonding K atom in neutron cascades is expected to link both pre-existing and induced porosity, and may result in unacceptable electrical properties.

Any other insulation with impurities that are natural or arise from production methods is potentially subject to similar problems if used in a subdivided state. For example, non-cubic polycrystalline materials may exhibit a lack of grain boundary cohesion, owing to anisotropic expansion under neutron irradiation. If the currently accepted thermal spike mechanism of track formation is correct, the track size is inversely proportional to a power of the specific heat. Because the specific heat is often 3 orders of magnitude smaller at 4 K, even α particles may cause tracking in insulators at 4 K, although this is not observed at 300 K (except in organics). Owing to the high percentage, ~7%, of the neutron spectrum in the very high energy range ($E > 5 \text{ MeV}$), where (n, α) reactions are possible for atoms of low atomic number, α emission is expected to be a factor in 4-K electrical breakdown strength. In situ data are not currently available. (In situ measurements are necessary, owing to the possible recovery of track defects at 77 or 300 K, as well as the diffusion of displaced interlayer cations in mica, at 77 or 300 K, since diffusion allows rebonding between layers and closure of fissures.)

Because in situ testing after 4-K irradiation is urgently needed, although sources of 4-K neutron irradiation are very limited, the problem of simulation of neutron irradiation by other radiation species is also reviewed in this report. An evaluation of simulation is required in any event, because much of the data base on inorganic insulation was obtained with other radiation sources. Since an incident neutron displaces a primary ion and initiates a

cascade of displacement damage, ion irradiation offers the most accurate simulation, especially if an ion of similar atomic number, or better, a host ion is used, to avoid chemical and size effects. However, since the mean free path of neutrons is of the order of centimeters, whereas that of ions is of the order of tens of micrometers, specimen size is extremely limited. Electron irradiation also offers both displacement damage, and, because the mean free path is of the order of millimeters, also a less limited specimen size. However, each incident electron usually displaces only one host atom, so the electron displacement damage is randomly scattered throughout the specimens, rather than localized in dense clusters as neutron damage is.* Also, the ratio of ionizing to displacive absorbed dose for electrons (~10 000) is very much higher than for ions (~100) or neutrons (~100). Gamma irradiation is also an unacceptable substitute for neutron irradiation because of its predominant ionizing dose. However, the silicate bonds in SiO_2 (and, probably, in mica) have low ionizing-radiation resistance and are susceptible to some displacive damage from γ rays.

In situ electrical and mechanical measurements after 4-K fast neutron or host ion irradiation of the most promising inorganic insulation candidates, MgAl_2O_4 , Al_2O_3 , AlN , and, perhaps, MgO , are urgently needed. It is disconcerting that host atom amorphization has been demonstrated in Al_2O_3 at 77 K, but was not successful at 300 K. Host atom amorphization is roughly equivalent to neutron amorphization, since it is the host PKAs[†] that do the damage in neutron irradiation. Apparently, host ion amorphization does not occur in most ceramic oxides at 300 K. Amorphization has evidently not been attempted in AlN , MgO , or MgAl_2O_4 at 77 K. The observation of a pronounced temperature dependence of amorphization raises a cautionary signal against proceeding with the design of ITER TF magnets under the present assumptions, without 4-K irradiation and in situ test measurements of all critical properties, as soon as possible.

*Cluster damage should occur if the electron energy is above ~25 MeV, but detailed experiments to compare this cluster damage with that of neutron cascades have not yet been performed for ceramic oxides.

[†]PKA = primary knocked-on atom.

ACKNOWLEDGMENTS

The author is indebted to R. P. Reed for numerous discussions of the issues raised in this report and for encouragement to undertake the task of compiling and evaluating the data. R. J. Deal has extracted data from the references with care and has expertly and accurately prepared the large number of graphs in this publication. A number of readers have assisted in removing errors and omissions from the text: C. W. Bushnell, D. R. Smith, M. Young, and M. E. DeWeese. Of course, the author is responsible for the imperfections that remain. Finally, the author is grateful to M. M. Cohen of the Office of Fusion Energy for sponsoring this work.

Trade names are used in this report solely to provide complete identification of specimens for scientific purposes. Such identification of products neither constitutes nor implies endorsement of the products by NIST or the author.

CONTENTS

EXECUTIVE SUMMARY	iv
ACKNOWLEDGMENTS	vii
CONTENTS	ix
LIST OF FIGURES	xiii
LIST OF TABLES	xxix
1. ASSESSMENT OF THE IRRADIATION DATA BASE ON INORGANIC INSULATORS	1
1.1. COMPARISON OF THE EXISTING DATA BASE WITH ITER REQUIREMENTS . . .	2
1.2. IRRADIATION SPECIES	7
1.2.1. Damage Production by Neutrons: Theory	8
1.2.2. Damage Production by Electrons: Theory	19
1.2.3. Experimental Comparisons of Neutron and Electron Damage	26
1.2.4. Damage Production by γ Rays: Theory	34
1.2.5. Experimental Comparisons of Neutron and γ -Ray Damage . .	38
1.2.6. Damage Production by Ions: Theory	44
1.2.7. Experimental Comparisons of Neutron and Ion Damage . . .	50
1.3. EFFECT OF IRRADIATION TEMPERATURE UPON RADIATION DAMAGE . . .	53
1.4. DAMAGE FROM VERY HIGH ENERGY NEUTRONS ($E \geq 5$ MEV)	70
1.4.1. General Principles	70
1.4.2. Neutron Damage from Collisions	73
1.4.3. Production of α Particles and H Atoms	78
1.5. WARM-UP: RECOVERY AND ANNEALING	84
1.6. PRINCIPLES OF MATERIAL SELECTION	91
2. LOW TEMPERATURE IRRADIATION OF ALUMINA	103
2.1. DEFECT DENSITY	103
2.1.1. Frenkel Defects	103
2.1.2. Dislocation Loops; Defect Aggregates	115
2.2. CHANGE IN VOLUME	118
2.3. AMORPHIZATION	131
2.4. MECHANICAL PROPERTIES	134
2.5. THERMAL PROPERTIES	143
2.5.1. Thermal Conductivity	143
2.5.2. Thermal Expansion	149
3. LOW TEMPERATURE IRRADIATION OF ALUMINUM NITRIDE	155
3.1. DEFECT DENSITY	155
3.2. CHANGE IN VOLUME	155
3.3. AMORPHIZATION	159
3.4. MECHANICAL PROPERTIES	160
3.5. THERMAL PROPERTIES	161

4.	LOW TEMPERATURE IRRADIATION OF MAGNESIA	167
4.1.	DEFECT DENSITY	167
4.1.1.	Frenkel Defects	167
4.1.2.	Dislocation Loops; Defect Aggregates	175
4.2.	CHANGE IN VOLUME	177
4.3.	AMORPHIZATION	182
4.4.	MECHANICAL PROPERTIES	184
4.5.	THERMAL PROPERTIES	194
5.	LOW TEMPERATURE IRRADIATION OF PORCELAIN	201
5.1.	DEFECT DENSITY	201
5.2.	CHANGE IN VOLUME	201
5.3.	AMORPHIZATION	203
5.4.	MECHANICAL PROPERTIES	204
5.5.	THERMAL PROPERTIES	206
6.	LOW TEMPERATURE IRRADIATION OF VITREOUS SILICA AND QUARTZ	207
6.1.	DEFECT PRODUCTION AND DENSITY	207
6.1.1.	Displacement Threshold Energy	207
6.1.2.	Defect Density	213
6.2.	CHANGE IN VOLUME	213
6.3.	AMORPHIZATION	225
6.4.	MECHANICAL PROPERTIES	230
6.4.1.	Flexural Strength	230
6.4.2.	Elastic Moduli	232
6.5.	THERMAL PROPERTIES	232
6.5.1.	Specific Heat	232
6.5.2.	Thermal Conductivity	240
6.5.3.	Thermal Expansion	251
7.	LOW TEMPERATURE IRRADIATION OF SPINEL	255
7.1.	DEFECT DENSITY	255
7.1.1.	Frenkel Defects	255
7.1.2.	Dislocation Loops; Defect Aggregates	258
7.2.	CHANGE IN VOLUME	261
7.3.	AMORPHIZATION	265
7.4.	MECHANICAL PROPERTIES	267
7.5.	THERMAL PROPERTIES	272
8.	LOW TEMPERATURE IRRADIATION OF ZIRCONIA	277
8.1.	DEFECT DENSITY	278
8.2.	CHANGE IN VOLUME	278
8.3.	AMORPHIZATION AND TRANSFORMATION	279
8.4.	MECHANICAL PROPERTIES	282
8.5.	THERMAL PROPERTIES	282

9.	MICA: RADIATION PROBLEMS OF A LAYERED STRUCTURE	285
9.1.	STRUCTURE OF MICA	285
9.2.	DIRECT OBSERVATIONS OF RADIATION DAMAGE	287
9.3.	ELECTRON MICROSCOPY	293
9.4.	ION-IRRADIATION ENHANCED SOLUBILITY	299
9.5.	FORMATION OF ETCHABLE TRACKS IN MICA	300
9.5.1.	Critical Dose	300
9.5.2.	Mica Tracks from U Fission	305
9.5.3.	Temperature Effect upon Track Recovery and Formation	313
9.5.4.	Electric-Field Enhancement of Tracks	319
9.6.	AMORPHIZATION	319
10.	RADIATION RESISTANCE OF HYBRID INSULATION	323
10.1.	LOW TEMPERATURE IRRADIATION OF A MICA-GLASS CERAMIC	323
10.1.1.	Defect Density	323
10.1.2.	Change in Volume	323
10.1.3.	Microstructural Changes; Amorphization	324
10.1.4.	Mechanical Properties	328
10.1.5.	Thermal Properties	328
10.2.	IRRADIATION OF HYBRID MICA INSULATION	330
10.3.	IRRADIATION OF DUPLEX STRUCTURES	332
11.	RADIATION-INDUCED ELECTRICAL DEGRADATION (ELECTRIC FIELD EFFECT) . .	335
11.1.	ELECTRICAL CONDUCTIVITY IN INSULATORS	335
11.2.	INVESTIGATIONS OF RADIATION-INDUCED CONDUCTIVITY	339
11.3.	INVESTIGATIONS OF FIELD-INDUCED DEGRADATION	350
12.	COMPARATIVE EVALUATION OF INSULATORS; CONCLUSIONS	365
12.1.	COMPARISON OF DEFECT DENSITIES	365
12.2.	COMPARISON OF VOLUME CHANGES	367
12.3.	COMPARISON OF FLUENCES REQUIRED FOR AMORPHIZATION	369
12.4.	COMPARISON OF MECHANICAL PROPERTIES; COMPRESSIVE FAILURE . .	371
12.4.1.	Mechanical-Property Measurements	371
12.4.2.	Critical Strain for Compressive Failure	373
12.5.	CONCLUSIONS: MATERIAL SELECTION	375
12.6.	CONCLUSIONS: FURTHER RESEARCH	376
12.7.	HYBRID INSULATION SUMMARY	377
12.8.	ELECTRICAL DEGRADATION BY RADIATION AND FIELD: SUMMARY . . .	378
13.	REFERENCES	379

LIST OF FIGURES

	Page
Figure 1.1.1. Concept sketch of the TF magnet shear plates and conductor-in-cable configuration: "solid" rib option. From Reed [1993].	4
Figure 1.1.2. Concept sketch of the TF magnet shear plates and conductor-in-cable configuration: "bonded" rib option. From Reed [1993].	5
Figure 1.2.1. Computer simulation of a cascade in Fe from a 5-keV Fe ion, planar projection. Reprinted with permission from Displacement Spikes in Cubic Metals. I. α -Iron, Copper, and Tungsten by J.R. Beeler, Jr., in <i>Physical Review</i> 150, p. 470 (1966). Copyright 1966 The American Physical Society	10
Figure 1.2.2. Damage energy $T(E_p)$ and number of Frenkel pairs produced as a function of PKA energy, E_p (for Fe, $E_d = 40$ eV). The curve is not linear because the energy expended in electron excitation and ionization increases with the ion energy, E_p . This ionization energy is not available for displacements. Data from Norgett et al. [1975].	12
Figure 1.2.3. Comparison of the calculations of the N_d generated in bcc Fe by a PKA: for (1) Kinchin-Pease model with $E_d = 40$ eV, $E_1 = 56$ keV (Eqn. 1.3); (2) the Norgett-Robinson-Torrens [1975] model (Eqn. 1.4). Data from Norgett et al. [1975].	13
Figure 1.2.4. Neutron spectra used in calculation of displacement cross sections in Table 1.2.3. Data from Dell and Goland [1981].	15
Figure 1.2.5. Average number of displaced atoms produced over the entire range of an electron as a function of initial electron energy. Data from Oen and Holmes [1959].	20
Figure 1.2.6. The specific ionization for electrons, illustrating the sizeable decrease in ionization at ~ 1 MeV. Data from Lapp and Andrews [1954].	22
Figure 1.2.7. Effective range of ionization of electrons of increasing energy, corresponding to regions A, B, and C in Figure 1.2.6.	23
Figure 1.2.8. Development of an electromagnetic shower from very high energy electrons. Dashed lines represent electrons and wavy lines represent γ radiation. Transverse spreading is exaggerated in this schematic diagram. B indicates bremsstrahlung and P indicates pair production. A (γ, n) reaction is illustrated at N. From Fassó et al. [1984].	24

Figure 1.2.9. Comparison of optical spectra of MgO crystal irradiated with electrons or neutrons. Data from Chen et al. [1969].	27
Figure 1.2.10. Comparison of swelling of Al_2O_3 from 1-MeV electron and fast neutron irradiation after 20 dpa. Citations in Hughes [1986].	29
Figure 1.2.11. Comparison of swelling of Al_2O_3 from electron and neutron irradiation as a function of fluence or dpa. Citations in Hughes [1986].	30
Figure 1.2.12. Comparison of cryogenic thermal conductivity of quartz after electron and neutron irradiation. Data and citations from Laermans and Daudin [1980].	32
Figure 1.2.13. Interaction mechanisms of γ rays with matter, illustrating the dependence on the atomic number, Z , of the absorber. The Compton effect will dominate for the energy range of γ rays expected at the TF magnet in the ITER reactor. Data from Kircher [1964].	35
Figure 1.2.14. Schematic diagram of the Compton process, illustrating the scattered γ ray and the recoil electron.	36
Figure 1.2.15. Atomic cross sections for the production of primary displacements of lattice atoms by γ rays through the Compton process vs. energy of the incident γ ray. $Z = 4$ is the atomic number and E_d is as indicated beside the curve. Data from Oen and Holmes [1959].	37
Figure 1.2.16. Surface microstructure of quartz irradiated as follows: (a) none; (b) X-ray; (c) γ , 800 Gy; (d) γ , 6000 Gy; (e) γ , 10^4 Gy; (f) 1.4×10^{15} fast neutrons/ m^2 (~ 0.8 Gy). From Bahadur, H.; Parshad, R. 1980 Radiation Induced Damage on Quartz Crystal Surfaces Detected by Scanning Electron Microscope. <i>Physica Status Solidi (a)</i> 59. pp. K13-K16. Reprinted with permission from Akademie Verlag GmbH.	39
Figure 1.2.17. Dependence of induced optical attenuation of vitreous SiO_2 on radiation dose from neutron and γ irradiation. Data from Tanaka et al. [1982].	41
Figure 1.2.18. Increase in dc conductivity of polycrystalline Al_2O_3 after 20-MeV proton and X-ray irradiation. Data from Pells [1986].	42
Figure 1.2.19. The dose rate exponent, δ , for proton and x-ray irradiation of polycrystalline Al_2O_3 . Data from Pells [1986].	43

Figure 1.2.20. Volume concentration of O defects (250-nm band) in MgO from both fast neutron and MeV Ne ion irradiation, detected by optical absorption. The "equivalent" fast neutron fluence is about 10^5 times the Ne fluence. The defect identity of the 574-nm band was not known. Data from Evans et al. [1972].	46
Figure 1.2.21. The PKA spectra of an Au crystal irradiated with charged particles, 4-MeV α particles, and fast neutrons (fission spectrum). Data from Agranovich and Kirsanov [1986].	49
Figure 1.3.1. Absorption coefficient vs. wavelength for 2-MeV electron irradiation of vitreous silica at 77 and 295 K. Data from Arnold and Compton [1959].	56
Figure 1.3.2. Comparison of ~ 77 -K thermal conductivity in BeO after irradiation (without warm-up) at 91 K (McDonald [1963]) and irradiation at $\sim 75^\circ\text{C}$ (Pryor et al. [1964]).	57
Figure 1.3.3. Recovery of thermal conductivity above 100 K during 15-min. annealing periods. Data from McDonald [1963].	58
Figure 1.3.4. Thermal conductivity of SiC above 300 K after neutron irradiation at 353 and 600 K. Data from Rohde [1991].	60
Figure 1.3.5. Increase in length of polycrystalline Al_2O_3 after neutron irradiation at 523 and 973 K. Data from Thorne and Howard [1967].	61
Figure 1.3.6. Temperature dependence of induced optical attenuation in vitreous SiO_2 after γ irradiation at the indicated temperature. Data from Tanaka et al. [1982].	62
Figure 1.3.7. Oxygen vacancies produced in MgO as a function of Ne-ion fluence at 80 and 300 K, compared with the Lindhard, Scharff, and Schiøtt theory. Data from Evans [1974].	64
Figure 1.3.8. Increase in swelling of polycrystalline Al_2O_3 as Ar-ion irradiation temperature is varied from 890 to 200 K. Data from Pells and Murphy [1992].	65
Figure 1.3.9. The optical density at the peak of the Al_2O_3 F-center (O vacancy with 2 trapped electrons) absorption band after irradiation with 3-MeV N ions. The nominal dpa scale includes both Al and O displacements. Optical measurements were made at the irradiation temperature. Data from Pells and Murphy [1992].	66
Figure 1.3.10. Comparison of the O vacancy concentration measured at ambient temperature after irradiations of single-crystal Al_2O_3 at 15 and 360 K. Data from Atobe and Nakagawa [1987].	68

Figure 1.3.11. Annealing behavior at 670 K of defects created at 15 and 360 K in single-crystal Al_2O_3 . Data from Atobe and Nakagawa [1987].	69
Figure 1.4.1. The neutron cross section for SiO_2 between 0.01 and 1000 MeV. Data from Primak [1980].	71
Figure 1.4.2. The potential energy function of a proton and a neutron near a nucleus.	72
Figure 1.4.3. He production cross sections. Data from Kulcinski [1979].	74
Figure 1.4.4. The relative dilation rate in vitreous SiO_2 exposed to a high energy spallation source of neutrons. Data from Primak [1980].	76
Figure 1.4.5. Oxygen vacancy concentration (F and F^+ centers) in Al_2O_3 produced by 14-MeV neutrons and fission neutrons. Data from Evans and Stapelbroek [1979].	77
Figure 1.4.6. Swelling of polycrystalline Al_2O_3 after Ar irradiation at 535 K, with and without preimplantation of H and He. Data from Pells and Murphy [1991].	81
Figure 1.4.7. Swelling of polycrystalline MgAl_2O_4 after Ar irradiation at 535 K, with and without preimplantation of H and He. Data from Pells and Murphy [1991].	82
Figure 1.4.8. Cross sections for n, α production for N, O, Mg, Al, and Si. Very sharp resonance spikes and other fine structure in the curves are not shown. Data from McLane et al. [1988].	83
Figure 1.5.1. The increase in thermal resistivity of sintered BeO vs. irradiation time. Both irradiation and measurement at -91 K. Data from McDonald [1963].	85
Figure 1.5.2. Decay of the optical absorption band indicating the presence of O vacancies in single-crystal Al_2O_3 after neutron irradiation at 23 K. Optical measurements were made at ambient temperature. Data from Atobe et al. [1985].	87
Figure 1.5.3. Isotherms of length recovery of Al_2O_3 irradiated to $1.5 \times 10^{24}/\text{m}^2$. Separate specimens were used at each temperature. Data from Stevanovic and Elston [1967].	88
Figure 1.5.4. Isotherms of length recovery of MgO irradiated to $8 \times 10^{23}/\text{m}^2$. All measurements were made on the same specimen. Data from Stevanovic and Elston [1967].	89
Figure 1.5.5. Isotherms of the recovery of density in vitreous SiO_2 irradiated to $\sim 5.9 \times 10^{23}/\text{m}^2$. The increase in density after irradiation was about 2.7%. Data from Primak and Szymanski [1956].	90

Figure 1.6.1. Thermal criterion for the occurrence of amorphization. Cubic structures are underlined. Data from Naguib and Kelly [1975] and Matzke [1982].	93
Figure 1.6.2. The bond-type criterion for the occurrence of amorphization. Cubic structures are underlined. Data from Naguib and Kelly [1975] and Matzke [1982].	95
Figure 1.6.3. Relationship between energy density for amorphization and the bonding (ionicity) for several materials. The data fall between the dotted curves, as shown. Data from Burnett and Page [1986]. . .	97
Figure 1.6.4. Thermal conductivity vs. critical energy for track formation in insulators used as nuclear track detectors. Data from Matzke [1982].	98
Figure 2.1.1. Optical absorption of single-crystal Al_2O_3 irradiated by 14-MeV neutrons and fission neutrons. Data from Bunch and Clinard [1974].	104
Figure 2.1.2. Oxygen vacancy concentration (F and F^+ centers) of single-crystal Al_2O_3 for 14-MeV neutrons and fission neutrons. Data from Evans and Stapelbroek [1979].	105
Figure 2.1.3. Optical absorption of single-crystal Al_2O_3 irradiated at 360 K, measured at ambient temperature. Data from Atobe and Nakagawa [1987].	107
Figure 2.1.4. Optical absorption of single-crystal Al_2O_3 irradiated at 15 K, measured at ambient temperature. Data from Atobe and Nakagawa [1987].	108
Figure 2.1.5. Comparison of the O vacancy concentration measured at ambient temperature after irradiations of single-crystal Al_2O_3 at 15 and 360 K. Data from Atobe and Nakagawa [1987].	109
Figure 2.1.6. Comparison of the Atobe and Nakagawa [1987] results with earlier investigations. From Atobe and Nakagawa [1987]. . .	110
Figure 2.1.7. Annealing behavior at 670 K of defects created at 15 and 360 K in single-crystal Al_2O_3 . Data from Atobe and Nakagawa [1987].	112
Figure 2.1.8. Threshold energy vs. temperature; derivation of displacement energy for Al and O in Al_2O_3 . Data from Pells and Phillips [1979a].	114
Figure 2.1.9. Dislocation loop density vs. dose, dpa in Al_2O_3 . Data from Lee et al. [1985].	117
Figure 2.2.1. Log/log dependence of volume swelling upon Ar-ion fluence. The nominal dpa is calculated. Data from Pells and Murphy [1992].	119

Figure 2.2.2. Linear expansion, $\Delta L/L$, of Al_2O_3 and $MgAl_2O_4$. Data from Tanimura et al. [1987].	120
Figure 2.2.3. Linear expansion, $\Delta L/L$, of Al_2O_3 single crystals. Data from Martin [1959].	122
Figure 2.2.4. Linear expansion, $\Delta L/L$, of Al_2O_3 single crystals during neutron irradiation at 423 K. Data from Wilks et al. [1967]. . .	123
Figure 2.2.5. Linear expansion, $\Delta L/L$, of Al_2O_3 single crystals. A few higher irradiation temperatures are indicated on the graph. Data and citations from Wilks [1968].	124
Figure 2.2.6. Density changes of both single and polycrystalline Al_2O_3 . Data and citations from Wilks [1968].	126
Figure 2.2.7. Volume increase, $\Delta V/V$, showing some grain boundary separation in Al_2O_3 . Data from Keilholtz et al. [1971].	127
Figure 2.2.8. Comparison of data from the six preceding figures and additional data from Keilholtz et al. [1971].	129
Figure 2.3.1. Disorder of the Al sublattice measured by RBS after Cr-ion implantation of Al_2O_3 at the indicated temperatures. Data from McHargue et al. [1986].	132
Figure 2.4.1. Critical peeling load of Zr film on Al_2O_3 with 0.1-mm radius diamond stylus and scratching speed of 50 mm/min. Data from Noda et al. [1985].	135
Figure 2.4.2. Critical cracking load of Ti film on Al_2O_3 with 0.1-mm radius diamond stylus and scratching speed of 50 mm/min. Data from Noda et al. [1985].	137
Figure 2.4.3. Decrease of four-point bending strength in Al_2O_3 and AlN with irradiation at ~ 400 – $600^\circ C$. Data from Dienst [1992].	138
Figure 2.4.4. Broadening of the strength distribution in Al_2O_3 and AlN, represented by the decrease of the Weibull modulus under neutron irradiation. Data from Dienst [1992].	139
Figure 2.4.5. Volume change in Al_2O_3 and AlN after neutron irradiation at the indicated temperatures. Data from Dienst [1992]. . .	140
Figure 2.4.6. Decrease in the fracture strength of Al_2O_3 and AlN with volume increase. Data from Dienst [1992]. (No citation was given for the additional curve labeled as CEA.)	141
Figure 2.4.7. Decrease in minimum and 1% failure bending strength of Al_2O_3 with volume increase. Data from Dienst [1992].	142
Figure 2.5.1. Thermal conductivity of single-crystal Al_2O_3 after γ and neutron irradiation. Data from Berman et al. [1960b]. . . .	144

Figure 2.5.2. Thermal conductivity of single-crystal and sintered Al_2O_3 after γ irradiation. Data from Berman et al. [1960b].	145
Figure 2.5.3. Increase in thermal resistivity of Al_2O_3 after neutron irradiation. Data from Berman et al. [1955].	147
Figure 2.5.4. Fractional change of thermal conductivity, K , of Al_2O_3 after 523-K irradiation (K_0 = Initial Conductivity). Data from Thorne and Howard [1967].	148
Figure 2.5.5. Thermal conductivity of single-crystal Al_2O_3 after high temperature irradiation at several facilities. Data from Rohde and Schulz [1992].	150
Figure 2.5.6. Thermal conductivity of polycrystalline Al_2O_3 after high temperature irradiation at several facilities. Data from Rohde and Schulz [1992].	151
Figure 2.5.7. Thermal contraction, $\Delta L/L$, of single-crystal Al_2O_3 . Data from Brown and Brown [1981].	152
Figure 2.5.8. Thermal expansion coefficient, $\Delta L/L$, of single-crystal Al_2O_3 . Data from Brown and Brown [1981].	153
Figure 3.2.1. Arrangement of three unit cells in the wurtzite structure of AlN	156
Figure 3.2.2. Increase of the a and c lattice parameters and total volume of AlN under neutron irradiation. Data from Hickman and Jostsons [1969].	157
Figure 3.2.3. Increase of the a and c lattice parameters and total volume of AlN under neutron irradiation. Data from Billy et al. [1984].	158
Figure 3.4.1. Four-point bending strength of AlN as a function of volume swelling (see text). Data from Yano and Iseki [1991].	162
Figure 3.4.2. Increase of Vickers hardness and fracture toughness of AlN as a function of volume swelling (see text). Data from Yano and Iseki [1991].	163
Figure 3.5.1. Decrease of high temperature thermal conductivity of AlN after neutron irradiation at high temperatures. Data from Rohde and Schulz [1992].	164
Figure 3.5.2. Decrease of thermal conductivity and thermal diffusivity of AlN after neutron irradiation at various temperatures. Data from Yano and Iseki [1991].	166
Figure 4.1.1. Fractional change of lattice parameter and number of F^+ centers created in MgO after irradiation. Data from Henderson and Bowen [1971].	168

Figure 4.1.2. Absorption coefficient and defect-center concentration of MgO after electron irradiation. See text for sample differences. Data from Sibley and Chen [1967].	169
Figure 4.1.3. Absorption coefficient and defect-center concentration of MgO after neutron irradiation. See text for sample differences. Data from Sibley and Chen [1967].	170
Figure 4.1.4. Absorption coefficient and defect-center concentration after neutron irradiation of MgO at different energies. Data from Chen et al. [1975].	172
Figure 4.1.5. Effect of electron radiation energy on production of defects in MgO. See text for sample differences. Data from Sibley and Chen [1967].	173
Figure 4.1.6. Ambient temperature decay rates of V_i centers (Mg^{2+} vacancies plus holes) produced after saturation γ irradiation (2.3-eV absorption). Data from Chen and Sibley [1967].	176
Figure 4.2.1. The change of lattice parameter ($\Delta a/a$) and crystal density ($\Delta \rho/\rho$) with neutron irradiation of MgO at 318 K. Data from Henderson and Bowen [1971].	178
Figure 4.2.2. The change of lattice parameter ($\Delta a/a$) and crystal density ($\Delta \rho/\rho$) with neutron irradiation of MgO at 318 K. Data at higher fluence. From Henderson and Bowen [1971].	179
Figure 4.2.3. Compilation of data on the change in lattice parameter with neutron irradiation of MgO. Data and citations from Wilks [1968].	180
Figure 4.2.4. Density change of MgO with neutron irradiation. Data and citations from Wilks [1968].	181
Figure 4.2.5. Compilation of volume swelling data on MgO.	183
Figure 4.4.1. Critical resolved shear stress (see text) of single-crystal MgO after neutron irradiation. Data from Davidge [1968].	185
Figure 4.4.2. Increase in compressive flow strength of single-crystal MgO after neutron irradiation. The arrow indicates that only one sample was useable at this fluence; the others underwent brittle fracture before yielding. Data from McGowan and Sibley [1969].	187
Figure 4.4.3. Incremental increase of compressive flow strength of single-crystal MgO for (a) electron and (b) neutron irradiation. The error bars represent only statistical, not systematic, errors. The arrow indicates that only one sample was useable at this fluence; the others underwent brittle fracture before yielding. Data from McGowan and Sibley [1969].	188

Figure 4.4.4. The compressive flow strength of single-crystal MgO plotted as a function of fluence, for comparison with Figure 4.4.1. Data from McGowan and Sibley [1969].	190
Figure 4.4.5. Four-point bending strength vs. reciprocal square root of grain size before and after irradiation for two types of surface finish. Data from Evans and Davidge [1969] on polycrystalline MgO.	192
Figure 4.4.6. Diametral compressive strength of polycrystalline MgO specimens after neutron irradiation. Data from Hurley et al. [1981]. . .	193
Figure 4.5.1. Thermal conductivity of single-crystal MgO after ambient γ irradiation. Data from Abramishvili et al. [1981].	195
Figure 4.5.2. Thermal conductivity of single-crystal MgO after ambient neutron irradiation. Data from Gardner and Anderson [1981b]. . .	196
Figure 4.5.3. Change in specific heat of single-crystal MgO after ambient neutron irradiation. Data from Gardner and Anderson [1981b]. . .	197
Figure 4.5.4. Thermal conductivity of single-crystal MgO after ambient neutron irradiation. Data from Kupperman et al. [1973].	199
Figure 5.5.1. Flexural strength vs. fast neutron fluence for Al_2O_3 , ultraporcelain, and steatite. Data from Kostyukov et al. [1981].	205
Figure 6.1.1. Enhancement of defect density of amorphous SiO_2 with compaction. Data from Devine [1990].	208
Figure 6.1.2. Optical absorption of vitreous SiO_2 from reactor and γ irradiation. Spectra were normalized to the same height at points of maximum absorbance. Data from Levy [1960].	209
Figure 6.1.3. Optical absorption of vitreous SiO_2 and quartz after neutron irradiation to $2.9 \times 10^{24}/\text{m}^2$. Data from Nelson [1957]. . .	210
Figure 6.1.4. Electron fluence required to amorphize quartz as a function of increasing electron energy. Data from Das and Mitchell [1974].	212
Figure 6.2.1. Dimensional change of vitreous SiO_2 and in quartz after neutron irradiation. The irradiation temperature for the highest fluence was estimated as $\sim 250\text{-}300^\circ\text{C}$. Data from Primak et al. [1955]. . .	214
Figure 6.2.2. Density change of vitreous SiO_2 after neutron irradiation. The fluence at (a) is estimated at 2.5 to $4.0 \times 10^{24}/\text{m}^2$. Data from Primak [1958].	216
Figure 6.2.3. Density change of quartz after neutron irradiation. The fluence at (a) is estimated at 2.5 to $4.0 \times 10^{24}/\text{m}^2$. Data from Primak [1958].	217

Figure 6.2.4. Comparison of density change of vitreous SiO ₂ and quartz after neutron irradiation. Data from Lell et al. [1966].	218
Figure 6.2.5. Correlation of density change of quartz after neutron irradiation with formation of clusters of interstitial Si atoms, detected by electron microscopy. Data from Weissman and Nakajima [1963].	219
Figure 6.2.6. Volume compaction of vitreous SiO ₂ after 18-keV electron irradiation. Data from Norris and EerNisse [1974].	221
Figure 6.2.7. Volume compaction after γ irradiation of SiO ₂ and various commercial borosilicate glasses. Data from Shelby [1980]. . . .	222
Figure 6.2.8. Increase of refractive index after neutron and electron irradiation of SiO ₂ . Data from Shelby [1980].	223
Figure 6.2.9. Decrease of relative thermal expansion (between 173 and 273 K) after γ irradiation in various commercial borosilicate glasses. Data from Shelby [1980].	224
Figure 6.3.1. Degree of disorder of ion-irradiated quartz. Data from Fischer et al. [1983a].	228
Figure 6.4.1. Flexural strength of vitreous SiO ₂ at 77 K after neutron irradiation at ambient and 77-K temperatures. Data from Thompson [1957].	231
Figure 6.4.2. Effect of neutron irradiation upon the cryogenic shear modulus of vitreous SiO ₂ . Data from Strakna et al. [1963].	233
Figure 6.4.3. Effect of neutron irradiation upon the compressibility of vitreous SiO ₂ . Data from Strakna et al. [1963].	234
Figure 6.5.1. Cryogenic specific heat/T ³ of vitreous SiO ₂ after neutron irradiation. Higher fluence data omitted for clarity. Solid lines indicate calculations from model. Data from Smith et al. [1978].	236
Figure 6.5.2. Specific heat of quartz after neutron irradiation and thermal annealing, compared to specific heat of unirradiated vitreous silica. Data from Saint-Paul and Lasjaunias [1981].	237
Figure 6.5.3. Specific heat/T ³ of quartz after neutron irradiation, compared to that of unirradiated vitreous silica and a theoretical calculation. Data from Gardner and Anderson [1981a].	238
Figure 6.5.4. Specific heat of quartz after γ irradiation. Data from Chaussy et al. [1979].	239
Figure 6.5.5. Specific heat of quartz after electron irradiation. Data and citation from Hofacker and Löhneysen [1981].	241

Figure 6.5.6. Thermal conductivity of quartz after neutron irradiation, compared with vitreous SiO ₂ . Data from Berman [1951, 1952] and Berman et al. [1950].	242
Figure 6.5.7. Thermal conductivity of neutron- and electron-irradiated quartz, compared with that of vitreous SiO ₂ . Only a portion of the original data points is shown. Data from Laermans et al. [1980].	243
Figure 6.5.8. Thermal conductivity of quartz after electron irradiation. Data from Hofacker and Löhneysen [1981].	244
Figure 6.5.9. Thermal conductivity of quartz after neutron irradiation, compared with that of vitreous SiO ₂ . Data from Gardner and Anderson [1981a].	245
Figure 6.5.10. Thermal conductivity of vitreous SiO ₂ after neutron irradiation. Solid lines are calculated from the tunneling states model. Data from Smith et al. [1978].	247
Figure 6.5.11. Thermal conductivity of vitreous SiO ₂ after neutron irradiation. Data from Raychaudhuri and Pohl [1982].	248
Figure 6.5.12. Relative change of density and thermal resistivity of vitreous SiO ₂ with increasing neutron fluence. Data from Raychaudhuri and Pohl [1982].	249
Figure 6.5.13. Thermal conductivity of vitreous SiO ₂ after neutron irradiation. Data from Cohen [1958].	250
Figure 6.5.14. Linear thermal expansion per unit length of quartz, before and after an ambient-temperature neutron fluence of 10 ²³ /m ² . The cylinder axis was normal to the optic axis. Data from White and Birch [1965].	252
Figure 6.5.15. Thermal expansion coefficient of vitreous SiO ₂ , before and after an ambient-temperature neutron fluence of 5 × 10 ²³ /m ² . Data from White and Birch [1965].	253
Figure 7.1.1. Optical density at the 5.3-eV (235-nm) absorption peak as a function of incident electron energy measured at ~300 K, after (a) 77-K or (b) ~300-K irradiation of MgAl ₂ O ₄ . Corrected for thickness losses. Data from Summers et al. [1980].	256
Figure 7.1.2. The magnitude of the peak optical absorption coefficient of the F center (at 5.3 eV) after cryogenic neutron irradiation of MgAl ₂ O ₄ . Data from Cain et al. [1988].	259
Figure 7.2.1. Swelling of single-crystal MgAl ₂ O ₄ after neutron irradiation. Data from Coghlan et al. [1986].	262

Figure 7.2.2. Swelling of single-crystal MgAl_2O_4 , as a function of storage time, after neutron irradiation. Data from Coghlan et al. [1986].	264
Figure 7.3.1. Percentage of crystalline X-ray diffraction peak intensity for MgAl_2O_4 and pollucite ($\text{CsAlSi}_2\text{O}_6$) vs. ion fluence. Data from Vance et al. [1983].	268
Figure 7.4.1. Tensile strength of polycrystalline Al_2O_3 and MgAl_2O_4 as measured in the diametral compression test after neutron irradiation at 660 K. Data from Tucker et al. [1986].	270
Figure 7.4.2. Tensile strength of polycrystalline MgAl_2O_4 as measured in the diametral compression test after neutron irradiation. Data from Hurley et al. [1981].	271
Figure 7.4.3. Hardness of MgAl_2O_4 as a function of depth after Mg-ion irradiation. Data from Zinkle [1989].	273
Figure 7.5.1. Reduction of high temperature thermal conductivity of MgAl_2O_4 after irradiation at 600 K. Data from Rohde and Schulz [1992].	275
Figure 8.3.1. Plot of lattice parameters of cubic phase and new phase induced by N ion irradiation vs. diffraction angle, 2θ . Lattice parameters of new phase calculated on assumption of face-centered cubic structure. Data on 10-mol% Y_2O_3 - ZrO_2 from Hasegawa et al. [1986].	281
Figure 8.4.1. Surface-fracture strain of 640-nm (6400-Å) anodic film on Zr vs. neutron fluence. Data from Harrop et al. [1967].	283
Figure 9.1.1. Schematic of structure of mica. Data from Brindley [1981].	286
Figure 9.2.1. Expansion in the c-axis direction of mica after neutron irradiation. Data from Klein [1955].	289
Figure 9.2.2. Density change of mica after neutron irradiation; the average energy of the neutrons in the MTR reactor is greater than that in the OGR reactor, which accounts for the greater degree of damage per indicated total fluence. Data from Bopp et al. [1960].	290
Figure 9.2.3. Creeping flashover voltage characteristics in hybrid mica insulation under γ irradiation. Data from Aki et al. [1983].	292
Figure 9.3.1. Image of electron-beam damaged paragonite showing lenticular fissures along layers. From Ahn, J.H.; Peacor, D.R.; Essene, E.J. 1986. Cation-Diffusion-Induced Characteristic Beam Damage in Transmission Electron Microscope Images of Micaceous Minerals. <i>Ultramicroscopy</i> 19. pp. 375-382. Reprinted with permission from Elsevier Science.	294

- Figure 9.3.2. Electron microscope image (100 keV) of phlogopite mica showing ordered, undamaged 1 nm (10 Å) stacking sequence. From Yau, Y.; Anovitz, L.M.; Essene, E.J.; Peacor, D.R. 1984. *Phlogopite-Chlorite Reaction Mechanisms and Physical Conditions during Retrograde Reactions in the Marble Formation, Franklin, New Jersey. Contributions to Mineralogy and Petrology* 88. p. 302. Figure 2. Copyright by Springer-Verlag. Reprinted with permission. 296
- Figure 9.3.3. Electron microscope image of muscovite mica (on the left) and biotite mica showing fissures between the layers, probably from the 200-keV electron beam. From Iijima, S.; Zhu, J. 1982. *Electron Microscopy of a Muscovite-Biotite Interface. American Mineralogist* 67. pp. 1195-1205. Figure 7. Copyright by the Mineralogical Society of America. Reprinted with permission. 298
- Figure 9.5.1. Calculated dose of ionization energy in cellulose nitrate at 1.5 nm (15 Å) as a function of the ion type and energy. Solid symbols indicate formation of etchable tracks; open symbols otherwise. Squares: Fleischer et al. [1967]; circles: Benton [1967]; triangles: overlapped points. Partial track formation (not plotted) is observed along the dividing line of critical dose. Shading along y-axis gives response to γ irradiation: X = severe damage; / = moderate damage; open = negligible damage. Data and citations from Katz and Kobetich [1968]. 301
- Figure 9.5.2. Calculated dose of ionization energy in cellulose nitrate at 1.9 nm (19 Å) as a function of the ion type and energy. Solid circles indicate formation of etchable tracks; open circles otherwise. Partial track formation (not plotted) is observed along the dividing line of critical dose. Data from Katz and Kobetich [1968]. 302
- Figure 9.5.3. Model coil insulation characteristics of hybrid mica/organic insulators after 10^6 Gy of γ irradiation at 3 kV/mm and 155°C. Data from Aki et al. [1983]. 303
- Figure 9.5.4. Electrical breakdown voltage vs. coil bending fatigue cycles of hybrid mica/organic insulation with and without 2×10^6 Gy of γ irradiation. Data from Aki et al. [1983]. 304
- Figure 9.5.5. "Fossil" tracks in Madagascar phlogopite from ^{238}U spontaneous fission fragments after visualization by etching for 1 min. in 15% HF at 50°C. Track density is $\sim 5 \times 10^4/\text{cm}^2$. From Price, P.B.; Walker, R.M. *Fossil Tracks of Charged Particles in Mica and the Age of Minerals. Journal of Geophysical Research* 68. pp. 4847-4862. 1963. Copyright by the American Geophysical Union. Reprinted with permission. 306

Figure 9.5.6. Induced tracks in Madagascar phlogopite from ^{238}U fission after thermal-neutron fluence of $10^{21}/\text{m}^2$. New track density is $\sim 4 \times 10^5/\text{cm}^2$. Same specimen as shown in Figure 9.5.5 before activation. From Price, P.B.; Walker, R.M. Fossil Tracks of Charged Particles in Mica and the Age of Minerals. <i>Journal of Geophysical Research</i> 68. pp. 4847-4862. 1963. Copyright by the American Geophysical Union. Reprinted with permission.	307
Figure 9.5.7. Fission fragment tracks in synthetic mica, observed by TEM. The material was irradiated with fission fragments from ^{235}U . From Price, P.B.; Walker, R.M. Fossil Tracks of Charged Particles in Mica and the Age of Minerals. <i>Journal of Geophysical Research</i> 68. pp. 4847-4862. 1963. Copyright by the American Geophysical Union. Reprinted with permission.	308
Figure 9.5.8. Conductance as a function of time for 7.1- μm thick mica of track density $4 \times 10^5/\text{cm}^2$. Etched in 35.7% HF at 25°C. Arrow indicates addition of acid. Data from Bean et al. [1970].	309
Figure 9.5.9. Etching rates of tracks in several types of mica. From Price and Walker [1962b].	311
Figure 9.5.10. Electron micrograph of electrical breakdown sites in muscovite mica after irradiation with fission fragments. Track density: $10^{11}/\text{cm}^2$. From Davidson, A.T.; Yoffe, A.D. 1965. Dielectric Breakdown in Thin Mica Crystals. <i>Nature</i> 206. pp. 1247-1248. Reprinted with permission from <i>Nature</i> ; copyright 1965; MacMillan Magazines, Ltd..	312
Figure 9.5.11. Annealing of ^{238}U -ion tracks (3.9-GeV) in mica, as determined by the track etching velocity. Data from Khan et al. [1984].	314
Figure 10.1.1. Experimental values for the swelling of Macor as a function of the 14-MeV neutron fluence. Data from Coghlan and Clinard [1991]. The value of zero for the swelling at a fluence of $10^{22}/\text{m}^2$ is roughly consistent with the increase of +0.05 to +0.1% in the density observed by Fowler et al. [1981], which would require initial compaction ($-\Delta V/V$).	325
Figure 10.1.2. Calculated density of Macor and its two constituent phases, as a function of the 14-MeV neutron fluence. Data from Coghlan and Clinard [1991].	326
Figure 10.1.3. Calculated swelling of Macor, following the procedures described in the text, as a function of the 14-MeV neutron fluence. Data from Coghlan and Clinard [1991].	327
Figure 10.1.4. Change in Vickers hardness of Macor as a function of 14-MeV neutron fluence. Data from Coghlan and Clinard [1991].	329

Figure 10.2.1. Deterioration of electrical breakdown strength of mica-paper and mica-flake layered insulation under static bending load, with respect to performance of polyimide film. Data from Aki et al. [1983].	331
Figure 11.1.1. Schematic occupancy by electrons of allowed energy bands in an insulator and a metal.	336
Figure 11.1.2. The RIC of single-crystal Al_2O_3 for electron and neutron irradiation. Data from Klaffky et al. [citation in Clinard, 1979].. . . .	337
Figure 11.2.1. Increase of DC conductivity of polycrystalline Al_2O_3 after 20-MeV proton and X-ray irradiation. Data from Pells [1986].	340
Figure 11.2.2. The dose rate exponent, δ , for proton and X-ray irradiation of polycrystalline Al_2O_3 . Data from Pells [1986].	341
Figure 11.2.3. The RIC vs. ionization dose rate for γ (^{60}Co) and reactor irradiation of single-crystal Al_2O_3 . Data from Shikama et al. [1992a].	342
Figure 11.2.4. The constant, K , for RIC of polycrystalline Al_2O_3 vs. temperature. Data from Pells [1986].	343
Figure 11.2.5. Increase in base conductivity, I_0 , in single-crystal Al_2O_3 for different electron-irradiation conditions. Data from Hodgson [1991].	344
Figure 11.2.6. SiO_2 cable insulation resistivity vs. temperature before and during a γ flux of 2.6×10^6 R/h. (Converted to $\Omega\cdot\text{m}$ from $\Omega\cdot\text{ft}$, assuming $\Omega\cdot\text{mil}\cdot\text{ft}$ was not the intended unit). Data from Cannon [1982].	346
Figure 11.2.7. MgO cable insulation resistivity vs. temperature before and during a γ flux of 2.6×10^6 R/h. (Converted to $\Omega\cdot\text{m}$ from $\Omega\cdot\text{ft}$, assuming $\Omega\cdot\text{mil}\cdot\text{ft}$ was not the intended unit). Data from Cannon [1982].	347
Figure 11.2.8. DC electrical conductivity of 10 mol% Y_2O_3 - ZrO_2 vs. temperature before and after a γ dose of 5.3×10^5 Gy. Data from Abou Sekkina et al. [1987].	348
Figure 11.2.9. DC electrical conductivity of monoclinic, unstabilized ZrO_2 vs. temperature before and after several γ radiation doses. Data from Tawfik et al. [1985].	349
Figure 11.3.1. Base conductivity, σ_0 , in Al_2O_3 for 773-K electron irradiation, indicating change in activation energy, E_A . Data from Hodgson [1991].	351

Figure 11.3.2. Increase of electrical conductivity of Al_2O_3 and MgAl_2O_4 under neutron irradiation and electric field. Data from Ivanov et al. [1981].	352
Figure 11.3.3. The RIC and onset of electrical breakdown for Al_2O_3 and MgO at 723 K. Data from Hodgson [1989].	353
Figure 11.3.4. Change of δ with temperature and impurity level in MgO . Data from Hodgson and Clement [1988].	355
Figure 11.3.5. Electrical conductivity of Al_2O_3 vs. reactor time, with and without an electric field (500 V/mm). Data from Shikama et al. [1992b].	356
Figure 11.3.6. The RIC at 287 K in single-crystal MgO . Data from Hodgson and Clement [1988].	358
Figure 11.3.7. DC base conductivity of Al_2O_3 after electron irradiation of 2×10^7 Gy at 723 K, vs. field. Data from Hodgson [1992b].	360
Figure 11.3.8. Electrical degradation of Al_2O_3 , as indicated by sample current, following electron irradiation for times and voltages indicated. The highest field corresponds to 133 V/mm. Data from Hodgson [1992a].	361
Figure 11.3.9. The intrinsic electrical conductivity of MgAl_2O_4 vs. ionization dose from 18-MeV protons, after irradiation at indicated temperatures. Data from Pells [1990].	362
Figure 11.3.10. The intrinsic electrical conductivity of Al_2O_3 vs. ionization dose from 18-MeV protons, after irradiation at indicated temperatures. Data from Pells [1990].	363

LIST OF TABLES

	Page
Table 1.1.1. ITER Concept Insulation Parameters for TF Magnets and CS (Central Solenoid). (April 1994).	3
Table 1.2.1. Maximum Energy (MeV) Imparted to Common Insulator Atoms by an Incident Neutron. Calculated from Equation (1.1).	9
Table 1.2.2. Values of the Threshold Displacement Energy, E_d , for Several Insulators. See Pells [1988] for Citations.	9
Table 1.2.3. Spectrum-Averaged Damage Cross Sections for Al_2O_3 and $MgAl_2O_4$. See Figure 1.2.4 for Spectra. Calculations from Dell and Goland [1981]. Recalculations of σ_{dis} in parentheses for $MgAl_2O_4$ are based upon the E_d values suggested in Table 1.2.3. . . .	16
Table 1.2.4. Maximum Energy Imparted to Common Insulator Atoms by an Incident Electron. Calculated from Equation (1.5).	18
Table 1.2.5. Displacements per Atom (dpa) for Neutron and Electron Irradiation of Al_2O_3 . Calculations from Pells and Phillips [1979b]. . .	28
Table 1.2.6. Calculated Ranges for Noble-Gas Ions in Vitreous SiO_2 . Calculations from Schroeder and Dieselman [1969].	47
Table 1.2.7. Ionizing and Displacive Radiation in Al_2O_3 in Various Irradiation Sources. Calculated by Zinkle and Greenwood [1993] using Experimental Results for Al and Correcting for the Density Difference. .	51
Table 1.4.1. Calculated Transmutation Product Yields per Unit dpa for Low Z Insulator Atoms. Calculations from Pells [1988].	84
Table 1.6.1. Response of Nonmetallic Solids to Ion Irradiation. See Naguib and Kelly [1975] for Discussion and Citations.	92
Table 2.2.1. Characteristics of Commercial Alumina Products. Data from Keilholtz et al. [1971].	130
Table 5.2.1. Effect of Radiation upon Thermal Conductivity and Density of Insulators. Data from Sisman et al. [1957].	202
Table 9.2.1. Results of X-Ray Examination of Ceramics. Data from Klein [1955].	288
Table 12.1.1. Comparison of Defect Densities after Ambient Fast Neutron Fluence of $10^{24}/m^2$	366
Table 12.2.1. Comparison of Volume Changes after Ambient Irradiation to a Fast Neutron Fluence of $10^{24}/m^2$	368

Table 12.3.1. Comparison of Fluences Required for Amorphization (Ambient Temperature).	370
Table 12.4.1. The Change in the Mean Ultimate Bending Strength (with statistical standard deviation for 13 specimens, each value) of Several Ceramic Insulators after a Fast Neutron Fluence of $2.0 \pm 0.2 \times 10^{25}/\text{m}^2$ ($E > 0.1$ MeV) at 110 to 115°C. Data from Dienst and Zimmermann [1994].. . . .	372
Table 12.4.2. The Compressive Strength at 295 K of Several Polycrystalline Oxides and a Nitride, and Quartz, Porcelain, Mica, and Glass-Mica Composites.	374
Table 12.4.3. Comparison of $(\Delta V/V)_{\text{crit}}$ with Experimental Swelling. . . .	375

1. ASSESSMENT OF THE IRRADIATION DATA BASE ON INORGANIC INSULATORS

This report presents the results of a literature search on radiation damage of inorganic insulators that are candidates for use in the ITER TF superconducting magnets. The insulators included are: alumina (Al_2O_3), aluminum nitride (AlN), magnesia (MgO), mica, porcelain, vitreous silica and quartz (SiO_2), spinel (MgAl_2O_4), and zirconia (ZrO_2). A companion report will review the available data on the low temperature mechanical, thermal, and electrical properties of these insulators [Simon, 1994]. (Only the α - Al_2O_3 structure is included in these reviews, unless otherwise noted.)

Often, an irradiation data base will include information in which the irradiation spectrum or even the irradiating species is different from that expected in a fusion device. Dose rate and gaseous and other environmental conditions also are often different. In the case of inorganic insulation, an environmental condition of primary importance, the operating temperature of 4 K, is almost never found in the existing data base. This introductory section on data base assessment is intended to assist the reader in evaluating the available information. It is also intended to set forth guidelines for future research, because, owing to the lack of 4-K neutron sources, some screening and perhaps even design data may have to be obtained by simulation techniques with other radiation species.

Although data on compressive strength and electrical breakdown strength are needed for material downselection and design, the available radiation data base comprises mostly information on the number of defects produced and the extent of swelling and amorphization. Limited mechanical and thermal property information is available. No cryogenic-temperature electrical breakdown information was found in the radiation literature. For each of the materials listed above (except mica), the topics considered in §§2 through 8 are: (1) defect production; (2) volume change (swelling); (3) amorphization; (4) mechanical properties; and (5) thermal properties. Early screening tests at ORNL (Oak Ridge National Laboratory) in the 1950s showed very unfavorable radiation properties for mica relative to other insulators; probably this explains the lack of conventional radiation studies on this material. The available radiation-damage information on mica is evaluated in §9. Since

hybrid insulations are under consideration for ITER, the few studies on hybrid radiation damage are summarized in §10. Radiation studies on the glass-mica ceramic, Macor, are also reviewed in §10. Electrical breakdown, especially under conditions in which the material is irradiated while an electric field is simultaneously applied, are reviewed in §11. Section 12 presents a comparative evaluation of all of the insulators reviewed, as well as the conclusions of this report.

This literature review was undertaken to assist in materials research for ITER magnets, not to provide an exhaustive survey of the field and its development. Consequently, no attempts could be made to give proper historical credit for precedence in research, nor to cite all those who contributed in a particular area.

1.1 COMPARISON OF THE EXISTING DATA BASE WITH ITER REQUIREMENTS

At this writing, the most severe requirements for magnet insulation are those for the TF magnets. Table 1.1.1 presents some of these requirements, and Figures 1.1.1 and 1.1.2 show possible configurations for the TF magnet insulation. Maximum compressive stresses will be about 200 to 250 MPa; although information is not included in the table, these compressive stresses may be accompanied by much smaller shear stresses. Shear stresses up to about 30 MPa are present, associated with unspecified compressive stresses, but the magnitudes of such unsupported stresses are very dependent upon both the magnet design and the details of the stress analysis. The expected number of fatigue cycles is 8×10^4 for the central solenoid (CS) coils and 400 (in compression) for the TF coils, but the TF coils will also experience $\sim 4 \times 10^4$ cycles of pulsed operation [Bushnell, 1994]. The maximum operating-voltage-to-thickness ratios are about 0.8 to 1.2 kV/mm. Operation is at 4 K in a vacuum. The total fast neutron fluence ($E \geq 0.1$ MeV) will be $10^{22}/\text{m}^2$, and the associated γ radiation dose will be 10^7 Gy. About 7% of the total neutron fluence will have an energy, $E > 5$ MeV [Sawan, 1993]. (A factor of about 0.75 should be applied to a fission fast neutron fluence to equate it to this fusion fast neutron fluence of $10^{22}/\text{m}^2$.) These values are representative of the EDA (Engineering Design Activity) in April 1994, and of course, are subject to change. The current draft of the design criteria document specifies that the

Table 1.1.1. ITER Concept Insulation Parameters for TF Magnets and CS (Central Solenoid). (April 1994)

	TF Coils ⁽²⁾				CS ⁽³⁾		
	Turn To Plate	Plate To Plate	Gnd.	Key	Turn To Turn	Layer (Incl. Turn)	Gnd. (Incl. Turn)
Thickness (mm)	2.5	2	8	8	3	6	11.5
Operating ⁽¹⁾ Voltage (kV)	1.5	1.5	10	10	1	5	15
Operating ⁽⁴⁾ Stress (MPa - compression)	100	250	200	250	250	250	200

- (1) "Operating" is normal operation plus the inclusion of limited fault conditions for one breaker failure or a single ground fault.
- (2) The TF coil insulation must be capable of experiencing fast (> 0.1 MeV) neutron fluence of 1×10^{22} n/m² and the associated gamma radiation will be up to 1×10^7 Gy.
- (3) The CS coil insulation must be capable of experiencing fast (> 0.1 MeV) neutron fluence of 1×10^{20} n/m² and the associated gamma radiation will be about 1×10^4 Gy.
- (4) Operation is at 4K in vacuum. CS total operation cycles = 8×10^4 . TF compression cycles = 400; cool down cycles = 40

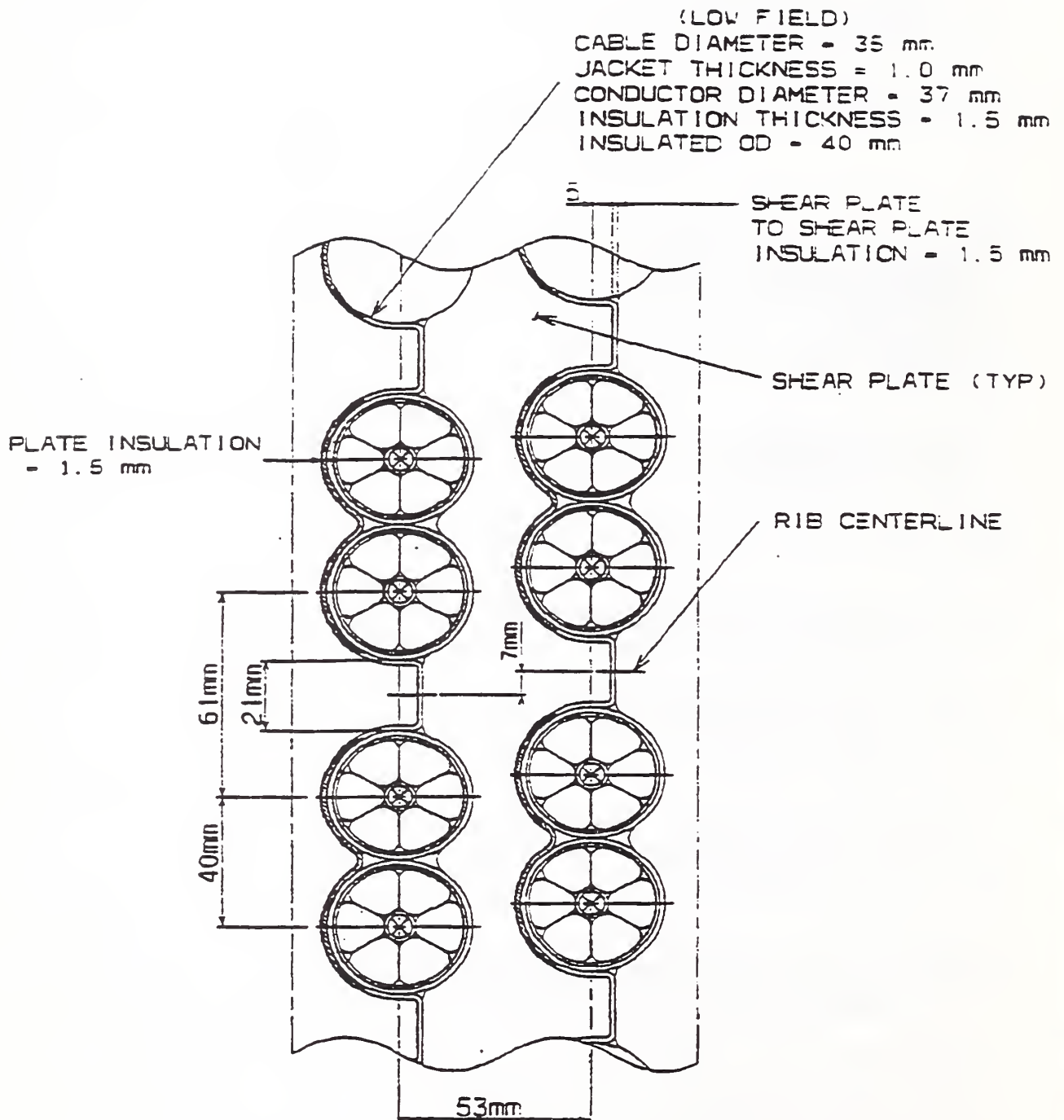


Figure 1.1.1. Concept sketch of the TF magnet shear plates and conductor-in-cable configuration: "solid" rib option. From Reed [1993].

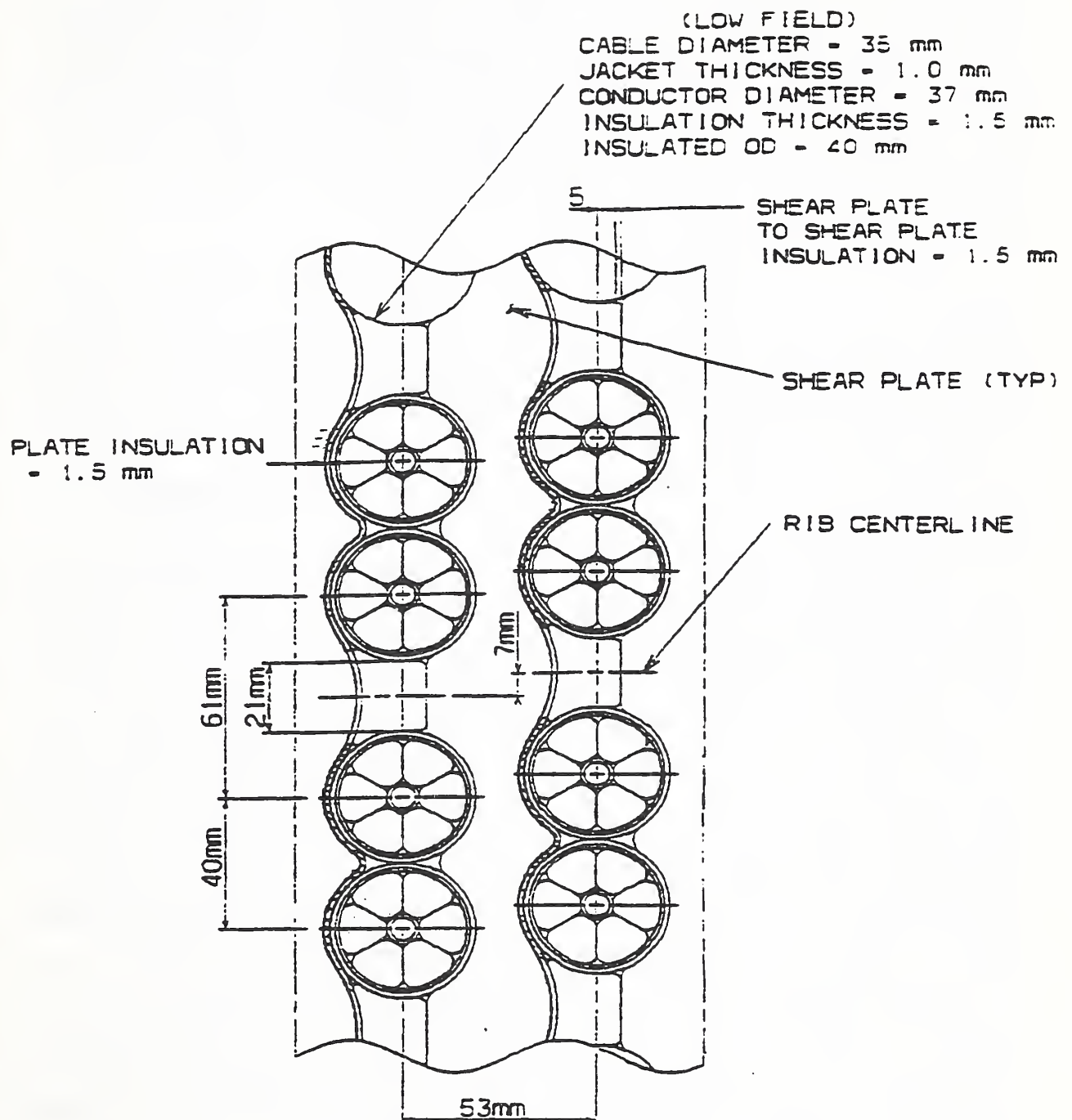


Figure 1.1.2. Concept sketch of the TF magnet shear plates and conductor-in-cable configuration: "bonded" rib option. From Reed [1993].

material must withstand, after irradiation, twice the operating stress and 20 (possibly, 10) times the expected number of fatigue cycles. The electrical breakdown strengths must be several times those of operating voltages/insulation thickness (Table 1.1.1). Thus, an insulator is needed that has the following properties after a fast-neutron fluence of $10^{22}/\text{m}^2$ at 4 K: a breakdown strength of about 2.5 to 5 kV/mm, a compressive strength of about 400 to 500 MPa, and a shear strength of about 40 MPa, associated with an unspecified compressive stress. The material should also withstand about 8×10^5 fatigue cycles after irradiation.

Unfortunately, the available data base on inorganic insulation does not correspond to these requirements in any way. There is almost a complete lack of 4-K irradiation data, even on swelling, from which the stress for compressive failure might be estimated under some conditions (§12.4.2). Data on electrical breakdown, especially, should be obtained in situ, while irradiation is proceeding [e.g., Zinkle, 1993a]. Direct measurements of mechanical properties of inorganics after irradiation are very rare, even at ambient temperatures. Such measurements should be made in situ at 4 K, before higher temperature recovery processes can occur. However, measurements of mechanical properties on ceramics are difficult and subject to large scatter. A companion report on properties of inorganic insulations from 4 to 300 K will show that few data are available on mechanical properties below 300 K even for unirradiated ceramics. The low temperature data on irradiated ceramics often pertain only to optical properties, from which the defect density is sometimes calculated. Much of the irradiation data below 300 K were obtained with other radiation species, rather than with neutrons. Section 1.2 considers the applicability of these data to ITER requirements. Section 1.3 discusses the possible extrapolation of ambient-temperature irradiation data to 4 K. ("Ambient temperature" usually includes temperatures up to $\sim 100^\circ\text{C}$ in this report.) An additional problem is that even when neutron irradiation was used, the spectrum usually did not include a significant component above 5 MeV, and the issues of greater damage and α -particle generation at 4 K have not yet been addressed. Section 1.4 surveys these issues.

One advantage of the mostly high temperature data base on inorganics is that the extent of the damage recovery during warm-up can sometimes be estimated.

Section 1.5 discusses this possibility. Since most inorganic insulation is thought to sustain a lower degree of permanent chemical change after irradiation than organic insulations do, significant recovery may occur during warm-up, except, perhaps, for mica, porcelain, and SiO_2 . However, permanent damage to electrical properties of insulators, including increased conductivity and degradation of electrical breakdown strength has recently been reported above -200°C (§11). This degradation requires the application of a threshold electric field of only 19 V/mm, well below the turn-to-plate operating fields of 0.83 kV/mm (Table 1.1.1). Therefore, recovery of electrical properties after irradiation at 4 K accompanied by an electric field cannot be assumed at present.

Finally, principles that may be applied to selection of inorganic insulation, especially in the absence of an adequate data base, are discussed in §1.6.

1.2. IRRADIATION SPECIES

When radiation of any species type interacts with a solid, the energy of the incident particles is transferred both to the constituent atoms, which are knocked out of their normal positions, and to the electrons, which are removed from their ground-state orbits. The result of the first type of energy transfer is called displacement or displacive damage; the second type is known as ionization or electronic excitation. Displacive processes produce Frenkel pairs that consist of an interstitial ion and a vacancy; ionization processes normally cause emission of photons and phonons from de-excitation of electronically excited states. Although a small portion of the ionization energy does result in atomic displacement, as discussed further below (and by Itoh and Tanimura [1986]), the most serious radiation damage to ceramic oxides usually arises from direct displacive energy transfer. Therefore, in comparing radiation damage from different species, the extent of displacive damage is normally the most important consideration. Heat or thermal energy is generally an insignificant component of the total energy deposited from ion or neutron radiation, except for irradiation with massive ions with energies below 200 keV [Zinkle and Greenwood, 1993]. However, thermal energy deposition can be significant in γ and electron irradiation.

1.2.1. Damage Production by Neutrons: Theory

Fast neutrons have relatively large mean free paths, ~ 1 cm, because they are uncharged particles. When a neutron collides with a lattice atom, in an elastic collision in which energy and momentum are conserved, the maximum energy transferred (in a head-on collision) is

$$E_p(\text{max}) = 4E(\text{inc})Mm/(M + m)^2, \quad (1.1)$$

where $E(\text{inc})$ is the energy of the incident neutron, m is the neutron mass, and M is the mass of the struck atom. Table 1.2.1 shows the maximum energy that neutrons of various energies can impart to the more common constituent atoms of inorganic insulators. Since the energy, E_d , required to displace a constituent atom is typically 20 to 60 eV (Table 1.2.2), fast neutrons of energy, $E \geq 0.1$ MeV, will always displace one of these atoms in an elastic interaction. Furthermore, the energy of the lattice atom displaced in this primary process is considerably in excess of E_d ; hence, the primary becomes a projectile and causes secondary displacements, and the secondaries produce tertiaries, and so on, until the energy of each displaced particle has dropped so low that E_d cannot be transferred. This process is known as the displacement cascade. Figure 1.2.1 shows a computer simulation of a cascade, projected onto a plane. Observation of single-crystal Al_2O_3 by electron microscopy after neutron irradiation ($\leq 150^\circ\text{C}$) revealed a high density of defect clusters; the size of each defect clusters was about 4 nm (40 Å) [Barber and Tighe, 1968]. Modern theories of defect production in a cascade, including the time periods for the various processes and the thermal spike phenomenon were discussed (for metals) by Heinisch [1993].

After the production of the primary ion in the cascade, with energy $E_p \leq E_p(\text{max})$, determined by Equation (1.1), the subsequent collisions are governed by the same formula, with m referring to the incident ion's mass. To a first approximation [Kinchin and Pease, 1955], the number of subsequent displacements, N_d , produced by the primary knocked-on atom (PKA) is

$$N_d(E_p) \approx E_p/2E_d. \quad (1.2)$$

Table 1.2.1. Maximum Energy (MeV) Imparted to Common Insulator Atoms by an Incident Neutron. Calculated from Equation (1.1).

ATOM	INCIDENT NEUTRON ENERGY, MeV				
	0.01	0.1	1	5	14
N	0.0025	0.025	0.25	1.24	3.48
K	0.0022	0.022	0.22	1.11	3.10
Mg	0.0015	0.015	0.15	0.76	2.13
Al	0.0014	0.014	0.14	0.66	1.93
Si	0.0013	0.013	0.13	0.66	1.36
K	0.00097	0.0097	0.097	0.66	1.36
Zr	0.00043	0.0043	0.043	0.21	0.60

Table 1.2.2. Values of the Threshold Displacement Energy, E_d , for Several Insulators. See Pells [1988] for Citations.

MATERIAL	ELEMENT AND ORIENTATION		E_d (eV)	AVERAGE E_d (eV)
MgO	Mg	<001>	60±3	56
		<011>	60±3	
		<111>	60±3	
	O	<001>	44±3	
		<011>	64±3	
		<111>	46±3	
Al ₂ O ₃	Al	random	18±3	50
	O	random	76±3	
		random	90	
		<0001>	53	
		<1120>	41	
MgAl ₂ O ₄	Mg	<001>	20	45
			30	
	Al		30	
	O		59	
AlN				~50

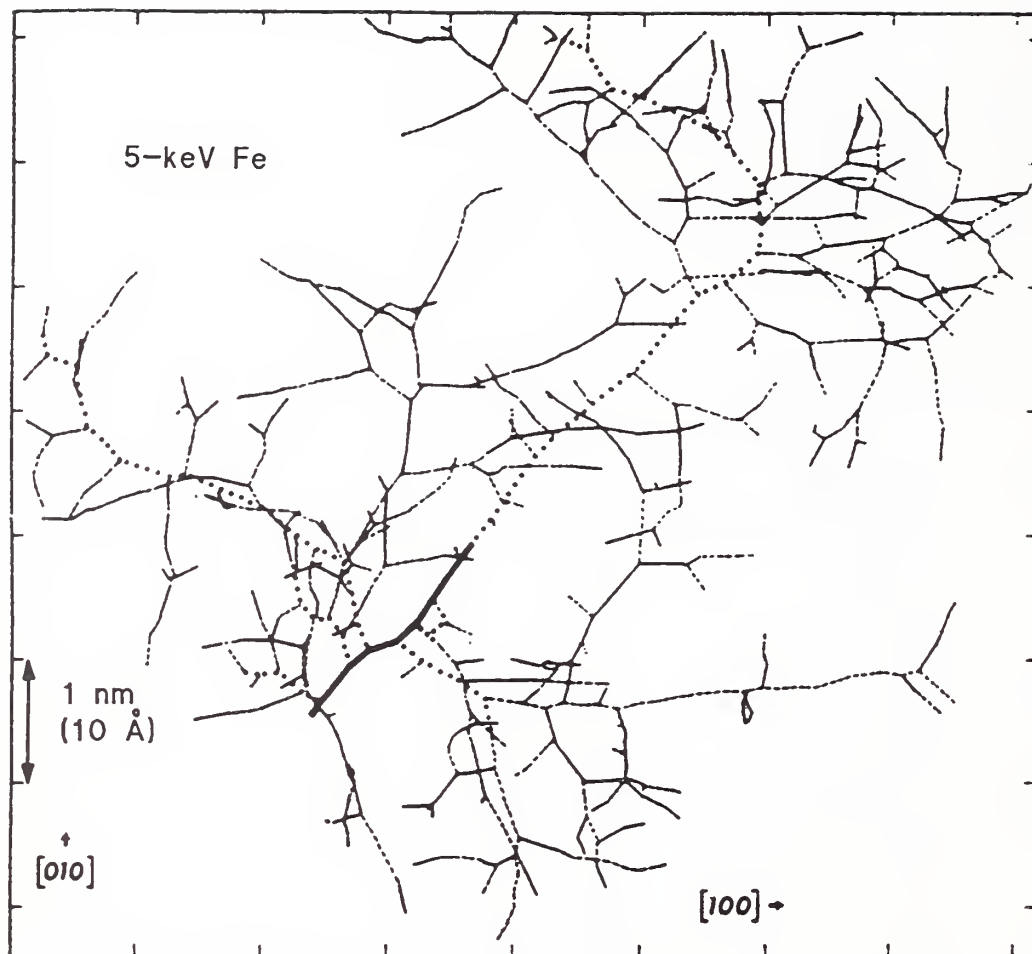


Figure 1.2.1. Computer simulation of a cascade in Fe from a 5-keV Fe ion, planar projection. Reprinted with permission from Displacement Spikes in Cubic Metals. I. α -Iron, Copper, and Tungsten by J.R. Beeler, Jr., in *Physical Review* Vol. 150, p. 470 (1966). Copyright 1966 The American Physical Society.

The factor of 2 occurs in the denominator because the incident particle must have an energy of at least $2E_d$ so that both the incident and struck atoms have an energy of at least E_d to escape from a lattice site. Since N_d is typically of the order of 1000 for a fast neutron collision with the relatively light atoms of common inorganic insulators, a high defect density is produced around the site of the primary fast neutron-lattice atom collision. Some athermal recombination of these lattice defects can occur even at 4 K if both the vacancy and interstitial remain within a critical volume.

Kinchin and Pease proposed the approximation of Equation (1.2) only for a region below a critical energy E_1 in which the PKA loses energy by hard-core elastic scattering. Energy above E_1 , again in approximation, goes into electron excitation (ionization processes) rather into elastic scattering. Thus the Kinchin-Pease model is:

$$N_d = \begin{cases} 0 & 0 < E_p < E_d, \\ 1 & E_d < E_p < 2E_d, \\ E_p/2E_d & 2E_d < E_p < E_1, \\ E_1/2E_d & E_1 < E_p. \end{cases} \quad (1.3)$$

Norgett et al. [1975] proposed a widely used modification of this model, called the modified Kinchin-Pease formula, in which the stopping power theory of Lindhard et al. [1963] was used to calculate the electronic energy losses. In this formulation,

$$N_d(E_p) = \kappa(E_p - Q)/2E_d, \quad E_p > 2E_d/\kappa, \quad (1.4)$$

where Q is the total energy lost in the cascade by electron excitation and $E_p - Q = T(E_p)$ is the damage energy or the energy available for atomic displacement. The factor κ is a constant called the displacement efficiency that is approximately equal to 0.8 for most materials. (It is a correction to the original hard-core scattering model used by Kinchin and Pease that accounts for the effects of a more realistic scattering potential.) Figure 1.2.2 is a plot of a calculation by Norgett et al. for bcc Fe that shows both the damage energy and the number of displacements as a function of the PKA energy. Figure 1.2.3 compares the number of displacements in both the Kinchin-Pease and modified Kinchin-Pease models. The important distinction is that for the

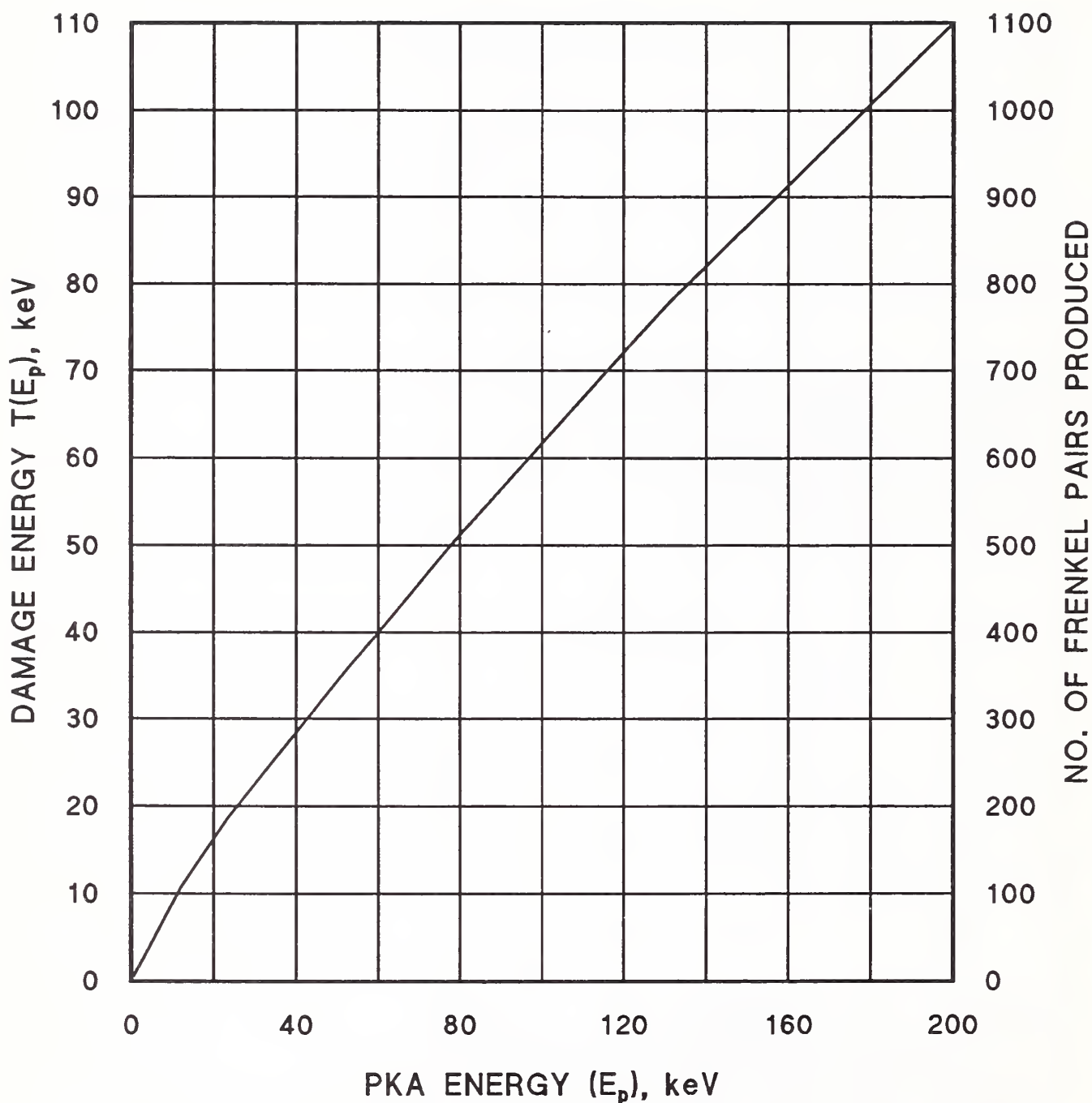


Figure 1.2.2. Damage energy $T(E_p)$ and number of Frenkel pairs produced as a function of PKA energy, E_p (for Fe, $E_d = 40$ eV). The curve is not linear because the energy expended in electron excitation and ionization increases with the ion energy, E_p . This ionization energy is not available for displacements. Data from Norgett et al. [1975].

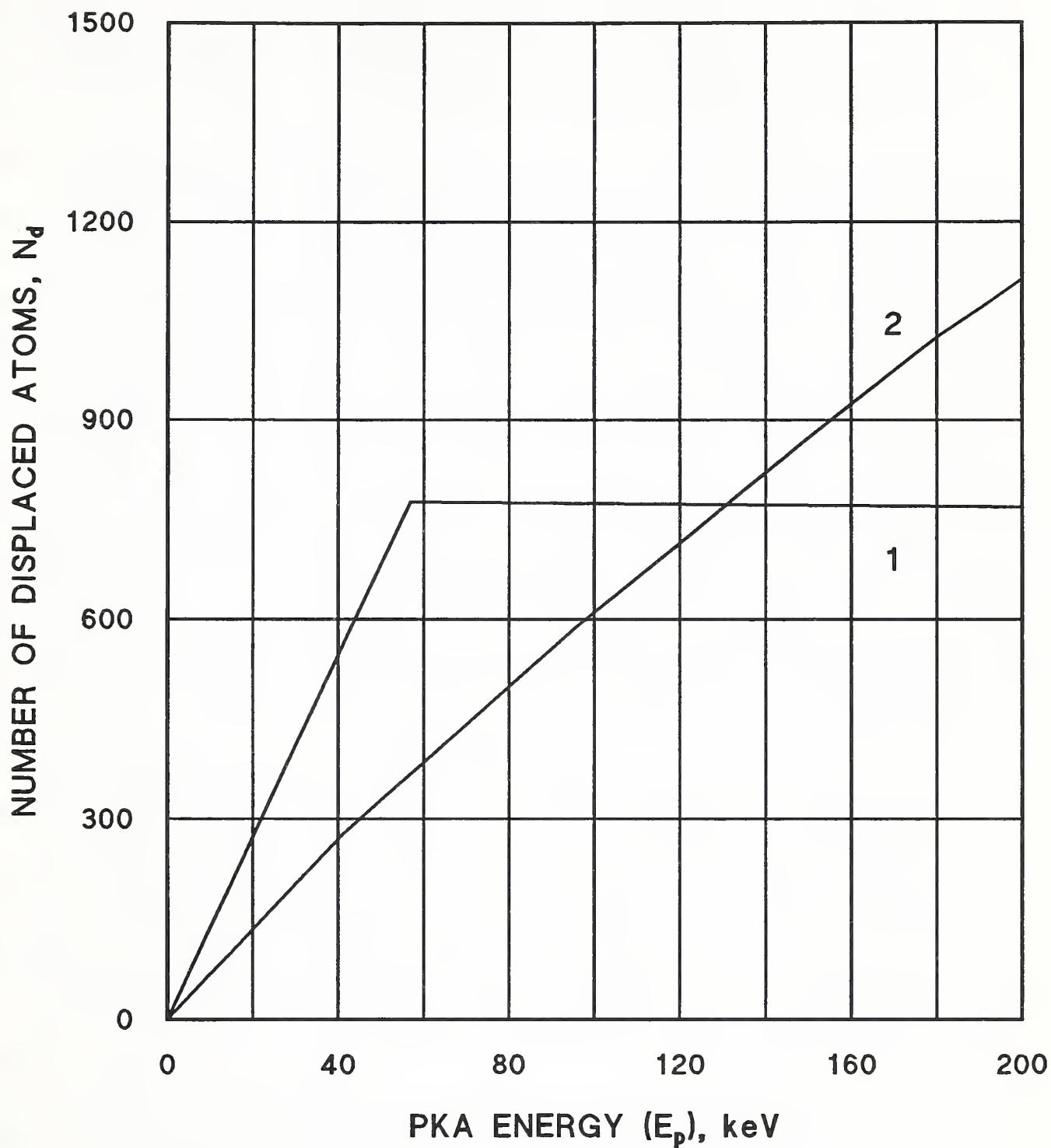


Figure 1.2.3. Comparison of the calculations of the N_d generated in bcc Fe by a PKA: for (1) Kinchin-Pease model with $E_d = 40$ eV, $E_1 = 56$ keV (Eqn. 1.3); (2) the Norgett-Robinson-Torrens [1975] model (Eqn. 1.4). Data from Norgett et al. [1975].

modified model, the number of displacements continues to rise with the energy of the PKA. This increases the significance of the high energy part of the neutron spectrum in producing displacive damage.

Displacement-damage theory was extended to multicomponent or polyatomic non-metals by Coulter and Parkin [1980], who generated damage energy functions, $T(E_p)$ for Al_2O_3 , SiN_4 , and $MgAl_2O_4$. Dell and Goland [1981] used these functions to calculate the number of displacements for each type of atom and then obtained total spectrum-averaged displacement cross sections, σ_{dis} , for several neutron spectra that are shown in Figure 1.2.4. The reader is referred to the paper by Dell and Goland for details of the calculation. Table 1.2.3 gives their cross sections for Al_2O_3 and $MgAl_2O_4$. The E_d values used for Al_2O_3 were given in Table 1.2.2; however, higher E_d values were chosen for $MgAl_2O_4$. The σ_{dis} can be scaled if different values for E_d are validated, since the dependence of σ_{dis} on E_d is that shown in Equation (1.4). The σ_{dis} results for $MgAl_2O_4$ scaled from alternate E_d values suggested by Zinkle are in parenthesis (see §7.1.1). Recently, more accurate techniques for determining E_d s from individual ionic displacements have become available (§4.1.1), but these techniques have not yet been applied to most materials in this survey.

Table 1.2.3 also shows the ionization-assisted σ_{dis} that arises from processes other than elastic displacement collisions. Again, the reader is referred to the original paper for details of the calculation, which was based on work by Yarlagadda and Robinson [citation, Dell and Goland, 1981] suggesting that the Coulomb repulsion between a recoil atom (PKA or higher-order) and an atom it has ionized may be sufficient to produce displacements in nonmetals. Dell and Goland found that L-shell ionization could contribute significantly to additional displacement damage, as indicated in Table 1.2.3.

Merkle [1974] had used the previously measured total and elastic cross sections for Au to show that when displacement cascades from 14-MeV neutron irradiation of Au were visualized with transmission electron microscopy, recoils from elastic neutron scattering events could account for <20% of the visible cascades. The size of the cascade clusters was used to indicate the number of displacements (vacancies) contained in each. At 14 MeV, one or two neutrons or a charged particle is emitted in a nonelastic process (kinetic

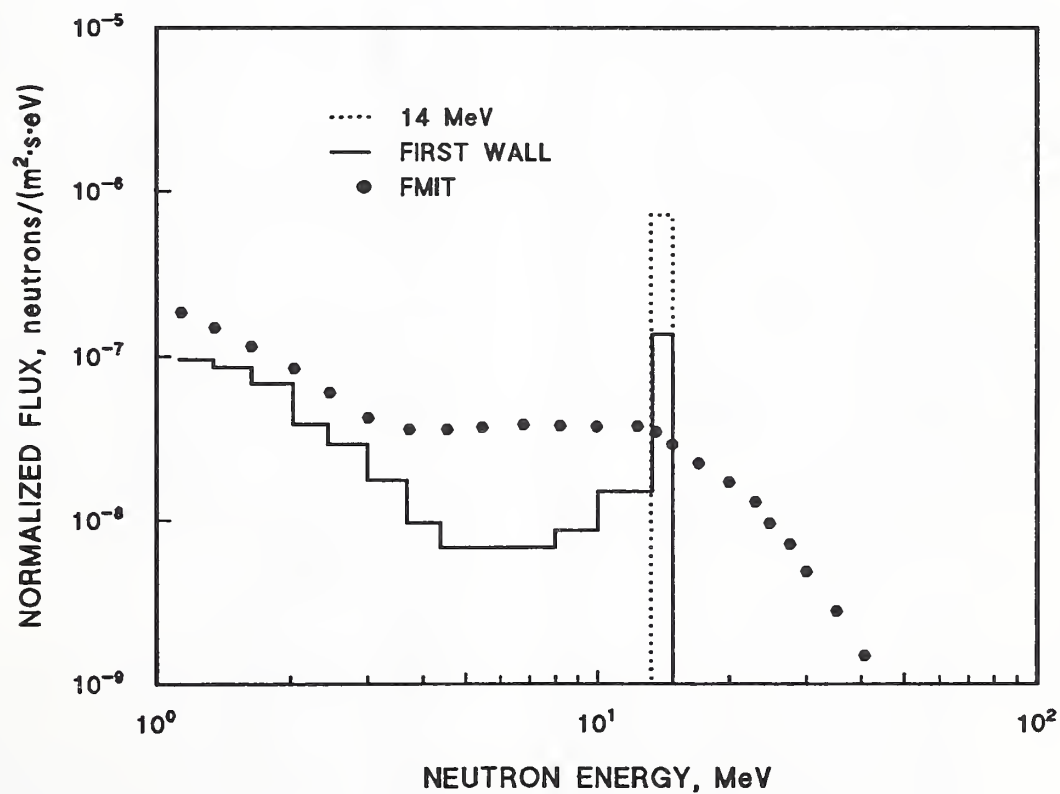
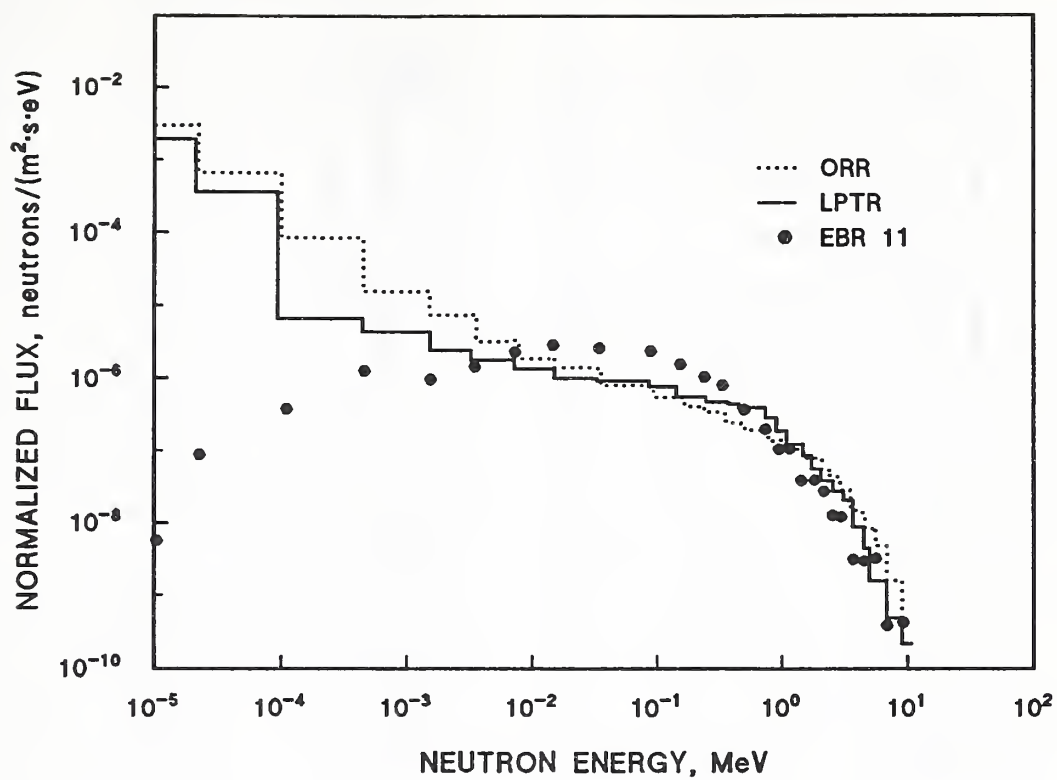


Figure 1.2.4. Neutron spectra used in calculation of displacement cross sections in Table 1.2.3. Data from Dell and Goland [1981].

Table 1.2.3. Spectrum-Averaged Damage Cross Sections for Al_2O_3 and MgAl_2O_4 . See Figure 1.2.4 for Spectra. Calculations from Dell and Goland [1981]. Recalculations of σ_{dis} in parentheses for MgAl_2O_4 are based upon the E_d values suggested in Table 1.2.3.

Al_2O_3

NEUTRON SPECTRA	FMIT	FIRST WALL	14 MeV	EBR-II	ORR	LPTR
E_n (MeV)	10.87	3.96	14.2	0.482	0.631	0.535
Displacement cross sections						
CP displacement fcns.						
$\sigma_{\text{dis}}(\text{Al})(\text{b/atom})^*$	982.1	657.4	1084.0	527.2	348.6	419.4
$\sigma_{\text{dis}}(\text{O})(\text{b/atom})$	366.3	246.8	403.2	199.6	131.4	158.4
Ionization-assisted fcns.						
$\sigma_{\text{dis}}(\text{Al})(\text{b/atom})$	71.0	35.8	83.6	16.6	16.7	17.4
$\sigma_{\text{dis}}(\text{O})(\text{b/atom})$	180.0	90.5	213.2	41.4	41.6	43.3

MgAl_2O_4

NEUTRON SPECTRA	FMIT	FIRST WALL	14 MeV	EBR-II	ORR	LPTR
E_n (MeV)	10.87	3.96	14.2	0.482	0.631	0.535
Displacement cross sections						
CP displacement fcns.						
$\sigma_{\text{dis}}(\text{Mg})(\text{b/atom})^*$	77.7 (111.4)	53.3 (76.4)	86.2 (123.6)	43.8 (62.8)	28.2 (40.4)	34.0 (48.7)
$\sigma_{\text{dis}}(\text{Al})(\text{b/atom})$	177.1 (681.8)	121.2 (466.6)	196.3 (755.8)	99.5 (383.1)	64.6 (248.7)	77.4 (298.0)
$\sigma_{\text{dis}}(\text{O})(\text{b/atom})$	184.7 (407.0)	217.9 (480.1)	203.2 (447.7)	106.7 (235.1)	68.8 (151.6)	82.8 (182.0)
Ionization-assisted fcns.						
$\sigma_{\text{dis}}(\text{Mg})(\text{b/atom})$	25.7 (36.8)	12.9 (18.5)	30.5 (43.7)	5.9 (8.5)	6.0 (8.6)	6.1 (8.7)
$\sigma_{\text{dis}}(\text{Al})(\text{b/atom})$	48.2 (185.6)	24.3 (93.6)	57.0 (219.5)	11.2 (43.1)	11.3 (43.5)	11.7 (45.0)
$\sigma_{\text{dis}}(\text{O})(\text{b/atom})$	167.0 (368.0)	84.1 (185.3)	198.0 (436.3)	38.4 (84.6)	38.8 (85.5)	40.2 (88.6)

* $b = 10^{-28} \text{m}^2$

energy is not conserved). Since the average recoil energy of the residual nucleus is about 70 keV, whereas the PKA energy from elastic collisions is 281 keV, it is probable that a significant amount of displacement damage can occur from high energy reactions such as (n,2n). Merkle concluded that non-elastic neutron scattering accounted for most of the displacement damage. Therefore, both ionization-assisted and high-energy transmutation reactions may increase the displacement cross section above what would be calculated from the modified Kinchin-Pease function and the cross section for elastic scattering events. The dpa (displaced atoms per atoms of the target) is determined by multiplying a calculated σ_{dis} by the neutron fluence. Since the σ_{dis} are usually calculated by methods similar to those described by Dell and Goland, the estimated dpa could be low by a factor of 2 or 3 in some cases, especially if the spectrum includes a strong high-energy component. Zinkle and Greenwood [1993] suggested that nonelastic processes are important contributors to displacement only for neutron energies above 10 MeV. Using an average σ_{dis} for the atoms in Al_2O_3 of 500 barns ($500 \times 10^{-28} \text{ m}^2$) from Table 1.2.3 gives a dpa of 5×10^{-4} for the ITER fluence of $10^{22}/\text{m}^2$. More recently, computer codes using all neutron reaction channels have been developed, and results are available for Al_2O_3 , using $E_d(\text{O}) = 30 \text{ eV}$ and $E_d(\text{Al}) = 27 \text{ eV}$ [Greenwood, 1990]. More information on the threshold energy, E_d , is still needed for many compounds, and some authors have proposed values of E_d for Al_2O_3 that are different from those used in this code (§2.1).

The morphology and stoichiometry of displacement cascades has not been studied in polyatomic ceramic materials as much as in metallic structural alloys. Ghoniem and Chou [1988] simulated cascade behavior in Monte Carlo binary collision approximation calculations for MgAl_2O_4 . The dimensions of the simulated cascade were found to be large, of the order of 100 to 200 nm (1000 to 2000 Å). A tree-like morphology was found, with more instantaneous recombination occurring in the trunk portion. The results for PKA energy less than about 1 keV also showed that the atoms were displaced in nonstoichiometric ratios, i.e., not in the ratio of 1:2:4 for Mg, Al, and O, respectively. Displacements from PKAs of higher energy resulted in stoichiometry. A species-independent E_d of 56 eV was used for each atom type in the initial calculation. However, when $E_d = 56 \text{ eV}$ was used for O and $E_d = 18 \text{ eV}$ was used for Al and Mg, an increased O vacancy deficiency in the cascade was observed,

as might be expected. Using similar methods of calculation, Parkin [1990] also found that the heavy-metal atom would be preferentially displaced relative to the lighter O atom in all ceramic oxides, and that local non-stoichiometry would occur in the cascade damage region. Ghoniem and Chou stated that if it were experimentally confirmed that the displacement threshold for O were higher than that for Al and Mg, the experimental simulation of fusion neutrons by ions, electrons, or fission neutrons would produce inaccurate representations of fusion neutron cascades. While this may be true for ion simulation if, for example, host ions of a particular energy are used in stoichiometric ratio, significant nonstoichiometry has also been shown to arise from heavy-ion irradiation in quartz [Macaulay-Newcombe and Thompson, 1984; Macaulay-Newcombe et al., 1990].

Table 1.2.4. Maximum Energy Imparted to Common Insulator Atoms by an Incident Electron. Calculated from Equation (1.5)

ATOM	INCIDENT ELECTRON ENERGY, MeV			
	0.1	1	10	100
O	14.9 eV	270 eV	1.47×10^4 eV	1.34×10^6 eV
Mg	9.8 eV	180 eV	0.97×10^4 eV	0.89×10^6 eV
Al	9.8 eV	160 eV	0.97×10^4 eV	0.89×10^6 eV
Si	8.5 eV	150 eV	0.84×10^4 eV	0.77×10^6 eV

1.2.2. Damage Production by Electrons: Theory

Because electrons have a very small mass (m_e) relative to the masses of lattice atoms, the energies required to displace atoms are a significant fraction of $m_e c^2$. Therefore, instead of Equation (1.1), a relativistic equation for energy transfer must be used to give the maximum energy that can be transferred to a lattice atom when the incident electron energy is E_e :

$$E_{\max} = 2(E_e + 2m_e c^2)E_e/Mc^2. \quad (1.5)$$

In units of MeV, this equation may be written as

$$E_{\max}(\text{MeV}) = 2(E_e + 1.022)E_e/938.9A, \quad (1.6)$$

where A is the atomic mass (in u) and the masses of protons and neutrons in the lattice atom nucleus are assumed equal to the average nuclear mass. Table 1.2.4 shows the maximum energy of the PKA in O, Al, Mg, and Si for electron energies of 0.1, 1, 10, and 100 MeV. Often, the energy of the PKA will be too low to cause secondary displacements. Figure 1.2.5 from Oen and Holmes [1959] gives the number of displaced atoms as a function of electron energy and E_d . For the electron energies usually employed in irradiation studies, this number is of the order of 1. Therefore, complex localized regions of displacement damage similar to those found in neutron displacement cascades (Figure 1.2.1) will not occur. Rather, Frenkel defects will be randomly distributed throughout the region of the specimen within the penetration range of the electrons. This range is 10 to 1000 μm in most materials for electrons of energy of about 0.3 to 1.0 MeV [Billington and Crawford, 1961]. A random, nonclustered distribution of defects is particularly expected for studies using high voltage electron microscopy (HVEM) irradiation, since the machines typically furnish beams in the 100 to 1000 keV range.

Most of the energy that electrons of energy up to about 1 or 2 MeV lose as they traverse matter goes into ionization. The energy loss per ion pair formed is about 30 eV in gases and is assumed to be about the same in condensed matter [Kircher, 1964]. The number of ion pairs formed per unit path length is called the specific ionization. As the energy of the primary electron increases, the specific ionization decreases, as shown in Figure

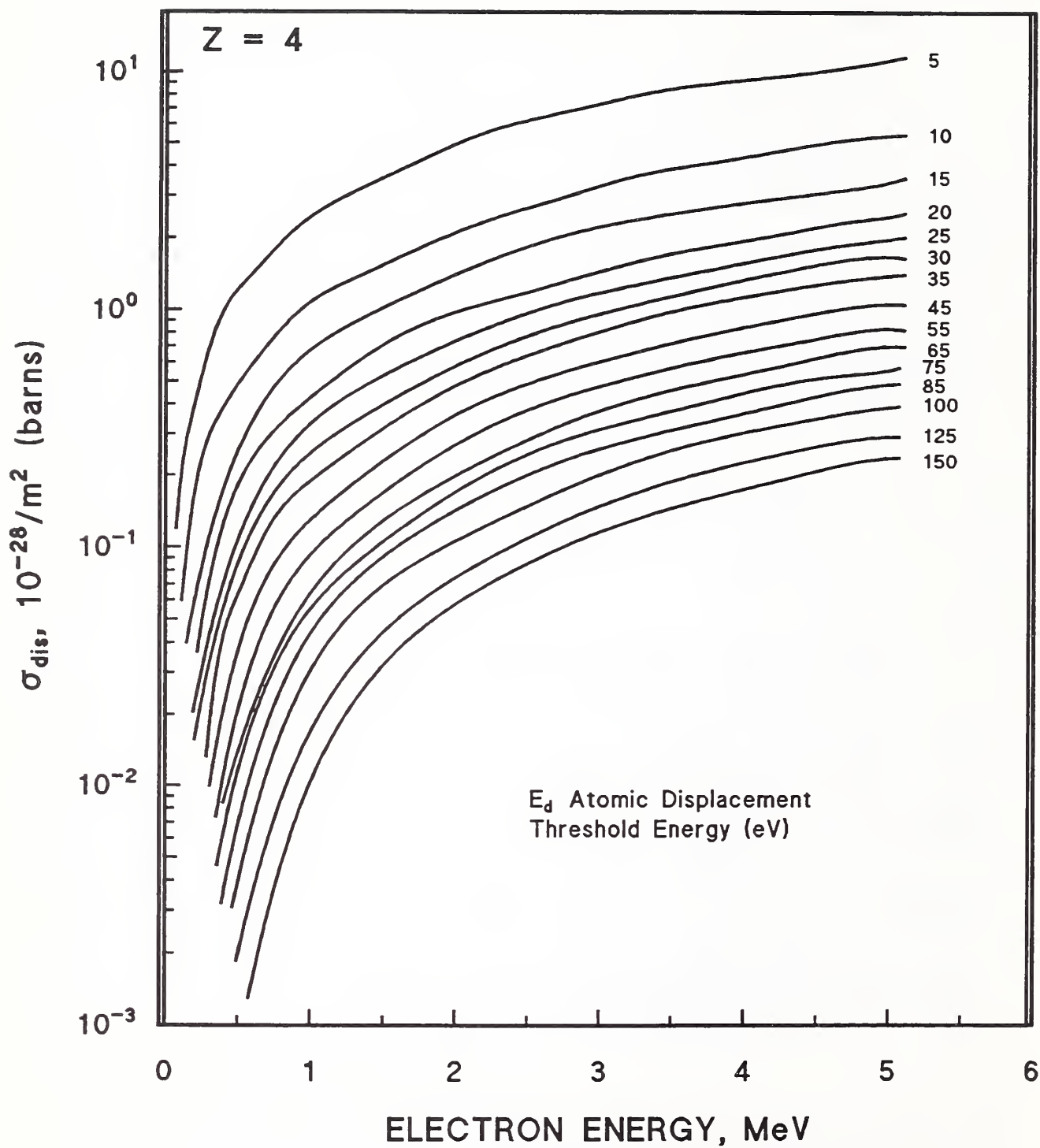


Figure 1.2.5. Average number of displaced atoms produced over the entire range of an electron as a function of initial electron energy. Data from Oen and Holmes [1959].

1.2.6 (region A to region B), because there is less time for interaction between the electron and a given atom. Some of the electrons ejected during ionization have enough energy to cause further ionization. These energetic secondaries are called δ rays. The fraction of the ionization due to δ rays increases as the atomic number, Z , of the irradiated atom increases. For O , about two thirds of the ionization arises from these secondary δ rays. Because there is a large amount of secondary ionization, the electron sweeps out a cylinder of interaction along its path in condensed matter. As noted above, the specific ionization is lower at higher incident electron energies. Hence, the radius of the cylinder of interaction decreases, as shown in Figure 1.2.7. The figure also indicates an increase in the effective interaction range for very fast electrons. Relativistic considerations show that very high energy electrons have an associated electric field that is condensed into a plane normal to its path, instead of being radially distributed. This intensified field sweeps out to a great distance and blocks out a cylinder of somewhat larger radius, but it is not as large as that of the slower electrons. This explains the slow rise in specific ionization at higher energies (Figure 1.2.6, region C) [Lapp and Andrews, 1954].

At energies above a few MeV, the relativistic electron starts to lose a greater proportion of energy through radiation ("bremsstrahlung") than through ionization. The ratio of bremsstrahlung to ionization is given approximately by

$$E \cdot Z / 800, \quad (1.7)$$

where E is the electron energy in MeV. Thus, at very high electron energies, ≥ 25 MeV, new phenomena, such as (γ, n) transmutations and pair production (electron-positron), arise from the high energy γ radiation. In this energy regime, clusters of defects will be generated, and damage may become similar to that from neutron and heavy-ion irradiation. A schematic illustration of these processes [Fassó et al., 1984] is given in Figure 1.2.8. The radiation length, X_0 , in this figure is the average length of travel of an electron before it loses $1/e$ of its energy:

$$X_0(\text{g/cm}^2) \sim 716A[Z(Z+1)\ln(183Z^{-1/3})]^{-1}. \quad (1.8)$$

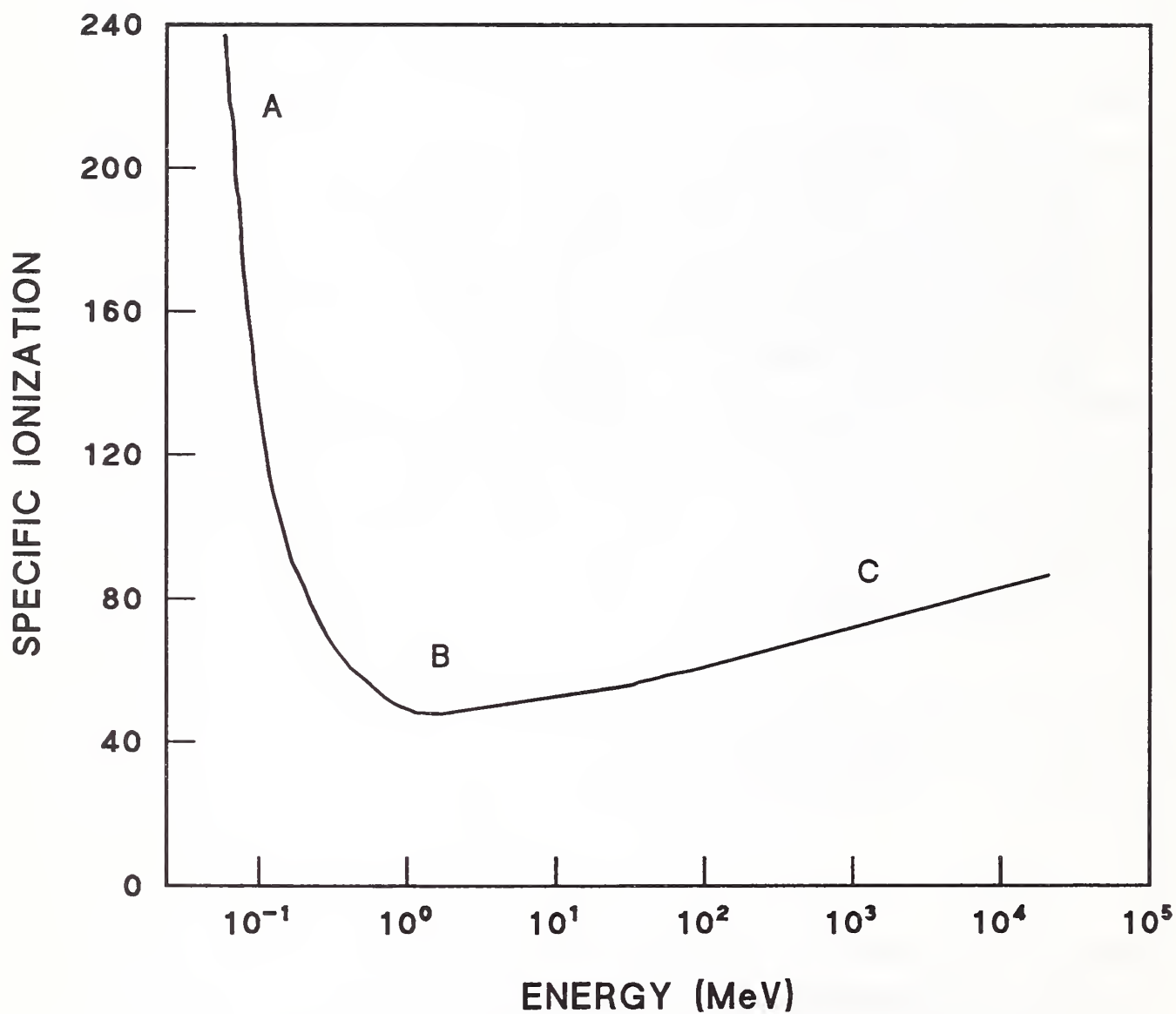
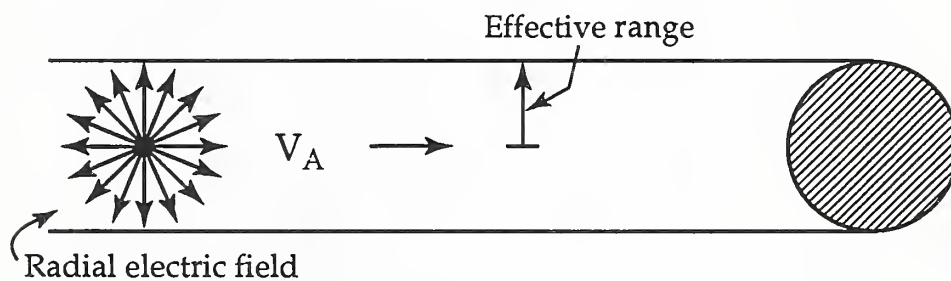
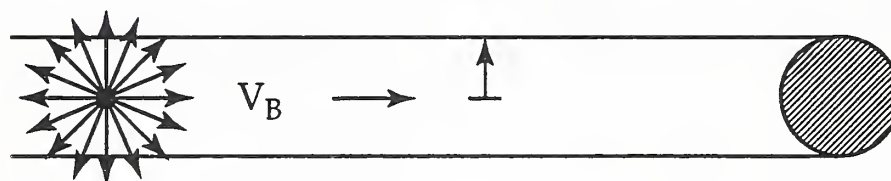


Figure 1.2.6. The specific ionization for electrons, illustrating the sizeable decrease in ionization at ~1 MeV. Data from Lapp and Andrews [1954].

A - SLOW ELECTRON



B - FAST ELECTRON



C - VERY FAST ELECTRON

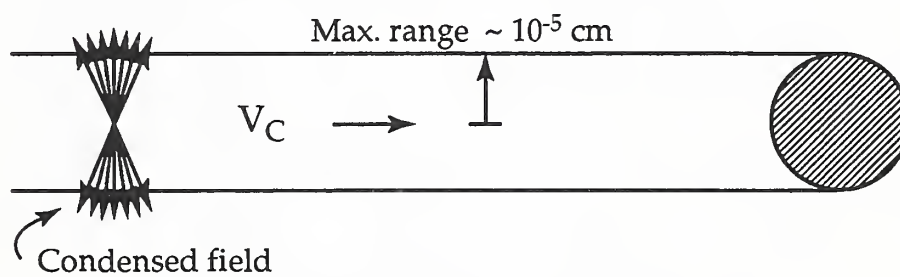


Figure 1.2.7. Effective range of ionization of electrons of increasing energy, corresponding to regions A, B, and C in Figure 1.2.6.

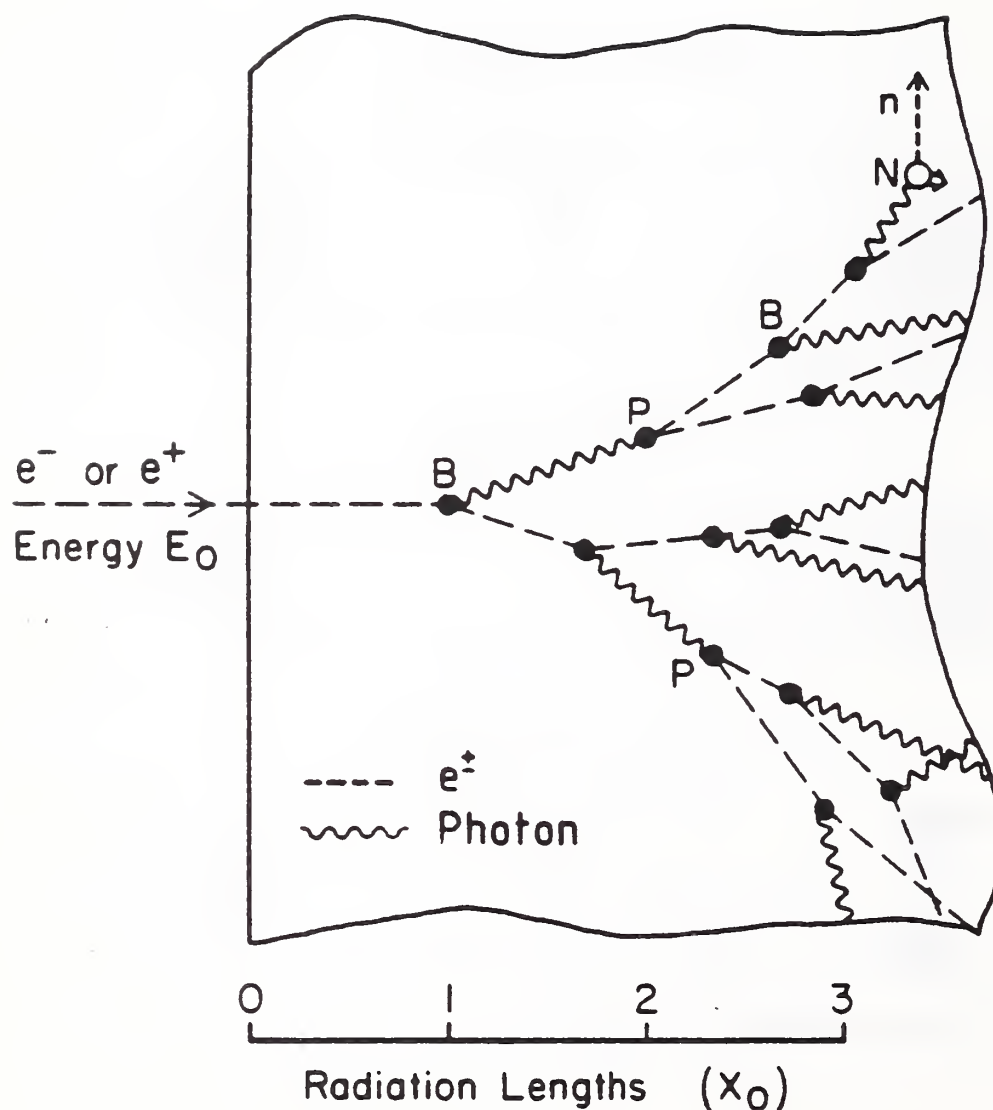


Figure 1.2.8. Development of an electromagnetic shower from very high energy electrons. Dashed lines represent electrons and wavy lines represent γ radiation. Transverse spreading is exaggerated in this schematic diagram. B indicates bremsstrahlung and P indicates pair production. A (γ, n) reaction is illustrated at N. From Fassó et al. [1984].

Most of the electron irradiation data in the literature do not pertain to this energy regime. However, screening tests could be carried out in this energy range to simulate fusion neutron damage to some extent. The size and distribution of cluster damage should be compared with that of neutrons to validate this screening procedure, however. This will be difficult to do in situ, at 4 K.

Although there is an advantage in studying radiation damage with a HVEM, in that the effect of a random distribution of defects on physical properties of the material investigated may be elucidated, such studies may be of greater academic interest than of practical utility in simulating fusion neutron damage. However, by systematically varying electron beam voltage, Das and Mitchell [1974] separated displacement damage from ionization damage in quartz. With increasing voltage, the rate of formation of displacement damage increased, as indicated in the TEM by an increasing density of black spots. However, the rate of amorphization decreased with increasing voltage, in accord with results on polymers, where the decrease was attributed to a lower cross section for ionization damage at higher electron energies. (These results of Das and Mitchell on quartz are shown below, in Figure 6.1.4.) Therefore, Das and Mitchell attributed amorphization in quartz to ionization radiation. This result, which applies only to quartz (and, possibly, to the silicate bonds in mica), is applicable to radiation damage in a fusion reactor because the neutron fluence is accompanied by a significant γ dose, and γ rays produce chiefly ionization damage. Also, it is important to distinguish ionizing from displacive damage for surrogate radiation sources because the ratio of ionizing-to-displacive absorbed radiation dose will differ significantly with radiation species, as discussed below (see Table 1.2.7 in §1.2.6).

Although the absence of localized displacement damage clusters suggests that electron-beam irradiation would overestimate fusion-neutron radiation resistance, Buckley [1984] conducted a study that reached the opposite conclusion, for a special case. He irradiated MgAl_2O_4 with 1-MeV electrons at high temperatures from 870 to 1120 K and found small precipitates of metal within the bulk, large precipitates on external surfaces, O bubbles, microcracks, and Mg segregation. He attributed these phenomena to a solid-state electrolysis induced by electric fields arising from charge separation associated with the

recoiling secondary electrons and δ rays that occur during the ionization process discussed above. Since Buckley used a focussed electron beam, the radial electric field increased at a large rate, estimated at approximately 10^{12} V/(m·s), so that after about a microsecond, the field was large enough to drive a balancing current of charge carriers in the opposite direction. The charge carriers included ions, if they were mobile; hence, the material was severely damaged by an irradiation-induced electrolysis. Presumably, this mechanism could also operate to some extent at 4 K, since the ions are driven by the electric field, not by thermal activation. However, ion mobility is reduced at 4 K.

1.2.3. Experimental Comparisons of Neutron and Electron Damage

From the basic theoretical considerations presented above, electron irradiation, at least in the energy range up to 1 or 2 MeV, should not be expected to simulate many of the features of neutron irradiation, although scattered displacement damage is produced. For the most part, experimental investigations have substantiated this premise. Evidence of the effects of very high energy electrons ($E > 25$ MeV) on the materials covered in this survey has not been found in the literature search.

Crawford [1984] reviewed evidence from optical spectra of both electron- and neutron-irradiated Al_2O_3 and MgAl_2O_4 . Color center behavior indicated that high defect densities were present around the collision site of a primary fast neutron and a lattice atom, but absent after electron irradiation. The effective radius of the disordered region around such a collision was ~ 10 nm (100 Å). Figure 1.2.9 from Chen et al. [1969] shows that for the single O vacancy defect at 250 nm in MgO, electron and neutron irradiation at ambient temperature produced similar optical absorption spectra. However, the figure also shows that neutron irradiation produced three additional absorption bands (in linear proportion to the 250-nm band) that were not observed after electron irradiation. These additional bands were ascribed to more complex aggregates of O vacancies found in thermal-spike or cascade-damage regions only.

Pells and Phillips [1979b] found that void features they saw after 1-MeV electron irradiation of Al_2O_3 appeared to differ from those reported by others

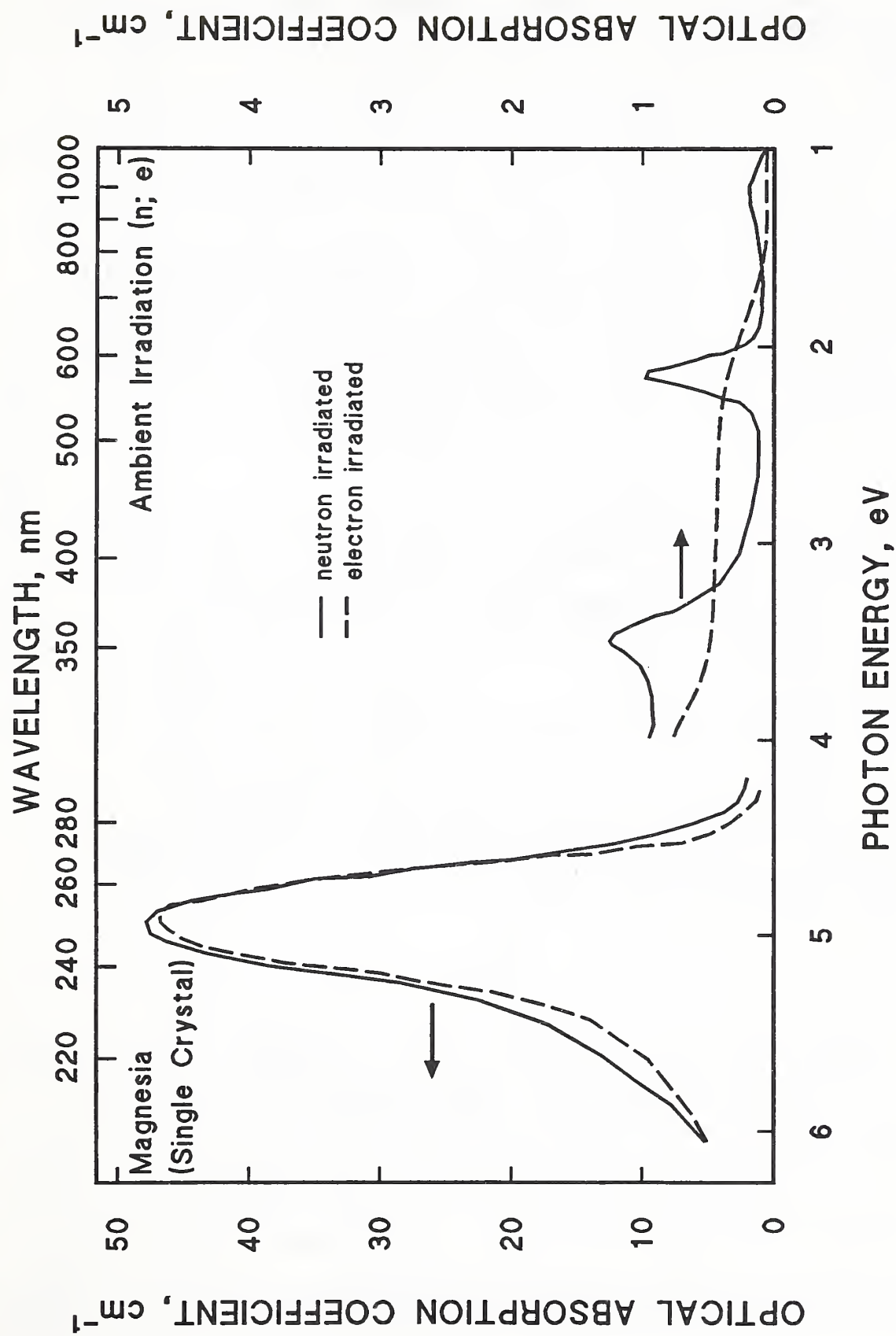


Figure 1.2.9. Comparison of optical spectra of MgO crystal irradiated with electrons or neutrons. Data from Chen et al. [1969].

after neutron irradiation. For example, equivalent dislocation densities at about 900 to 1300 K required ~ 0.1 dpa for neutron irradiation, but several dpa in the HVEM. For ~ 2 vol.% of voids from a fast neutron dose of ~ 1 dpa, ~ 10 dpa was required to give the same volume fraction of Al precipitates at 1070 K in the HVEM. Electron irradiation appeared to produce Al colloids, but neutron irradiation produced true voids. Since the displacement threshold, E_d , for Al was found to be much lower than that for O, Table 1.2.5 shows that the ratio of Al to O atoms displaced is much greater under 1-MeV electron irradiation than under 1-MeV neutron irradiation. In both types of irradiation, more Al than O atoms will be displaced, but, because energy transfer from electrons is limited [Equation (1.5)], the discrepancy is much greater for electron irradiation.

Table 1.2.5. Displacements per Atom (dpa) for Neutron and Electron Irradiation of Al_2O_3 . Calculations from Pells and Phillips [1979b].

		dpa
10^{25} neutrons/ m^2	Al	2.3
	O	0.5
2 h electron irradiation	Al	40.8
	O	2.9

The table is calculated for a neutron fluence of $10^{25}/\text{m}^2$ (1 MeV) and an electron fluence of $10^{28}/\text{m}^2$ (1 MeV), assuming values of $E_d(\text{Al}) = 18$ eV and $E_d(\text{O}) = 75$ eV.

Hughes [1986] also compared electron and neutron irradiation of Al_2O_3 at high temperatures and doses. Figure 1.2.10 shows that swelling after electron irradiation occurs at a much higher irradiation temperature than that for comparable swelling after neutron irradiation. These results are for a dose of 20 dpa for both electrons and neutrons. The difference between neutron and electron effects was ascribed to the dose rate by Hughes. Figure 1.2.11 compares swelling for electron and neutron irradiation as a function of dose. In this case, results are comparable for the two species.

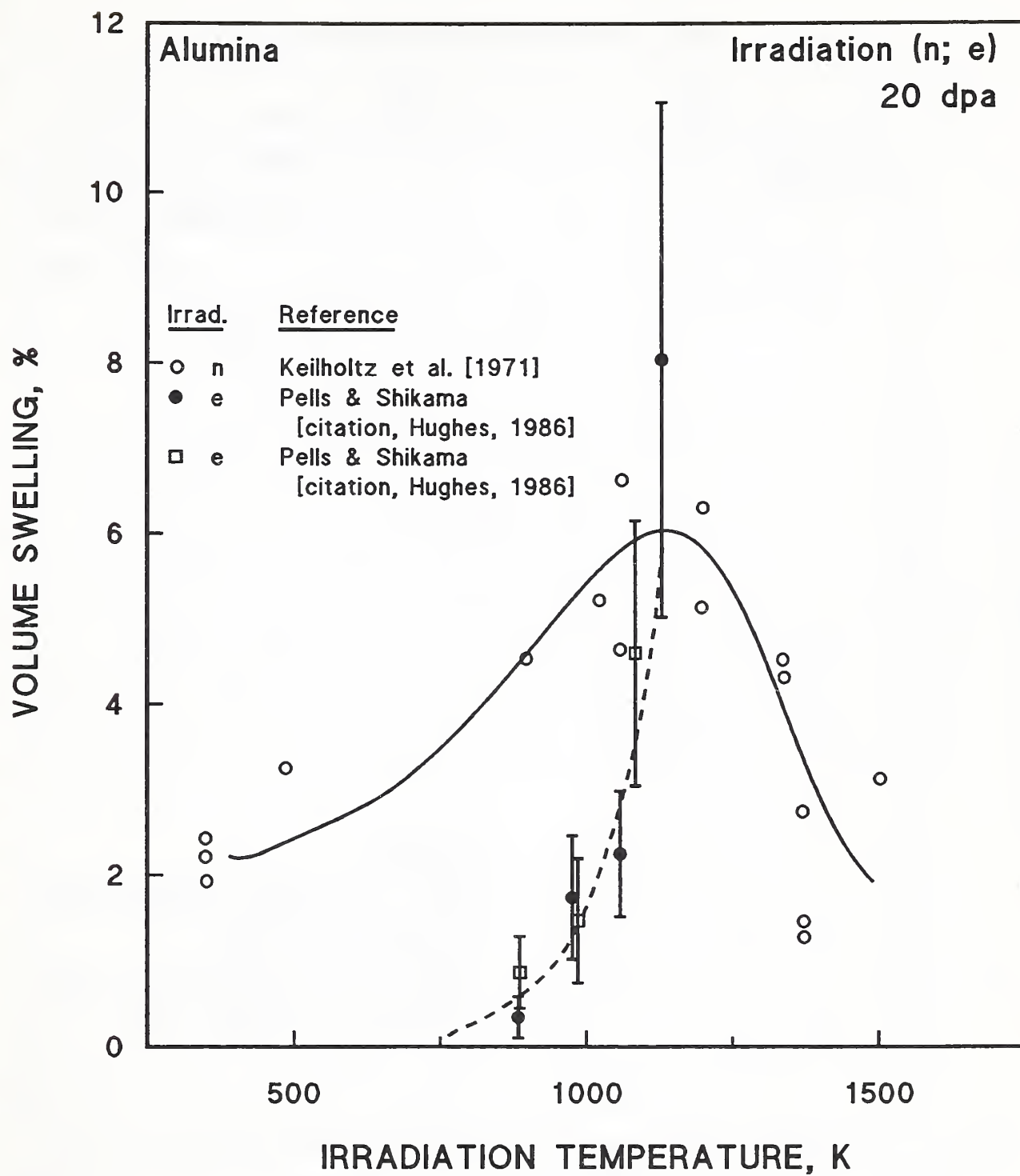


Figure 1.2.10. Comparison of swelling of Al_2O_3 from 1-MeV electron and fast neutron irradiation after 20 dpa. Citations in Hughes [1986].

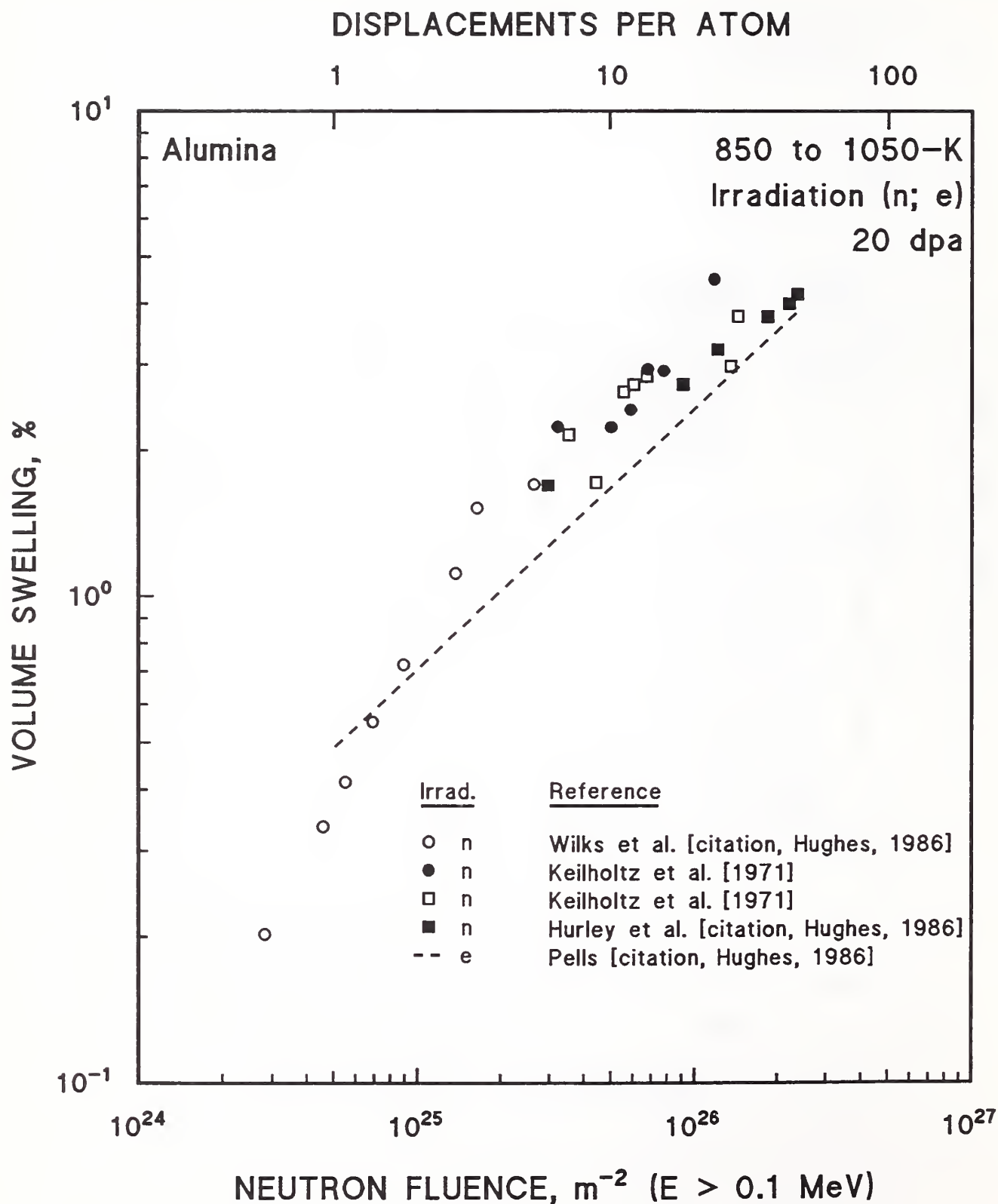


Figure 1.2.11. Comparison of swelling of Al_2O_3 from electron and neutron irradiation as a function of fluence or dpa. Citations in Hughes [1986].

Fowler et al. [1981] irradiated the glass-ceramic Macor, which consists of mica crystals embedded in a borosilicate glass matrix. Ionizing doses from 14-MeV neutron irradiation of up to $\sim 6 \times 10^6$ Gy ($10^{22}/\text{m}^2$) were compared to ionization doses of 10^{10} to 10^{11} Gy from 200-keV electron irradiation. Mica was about 4 orders of magnitude more sensitive to the neutron doses than to the much higher doses from electrons. From the literature on crystalline SiO_2 , Fowler et al. noted that a fast neutron fluence of $\sim 10^{24}/\text{m}^2$, equivalent to $\sim 4 \times 10^7$ Gy, caused amorphization, while $\sim 10^{12}$ Gy was required to attain the same level of damage in the electron microscope.

Figure 1.2.12, from Laermans and Daudin [1980], shows the decrease in low temperature thermal conductivity of quartz after ambient neutron and electron irradiation; the thermal conductivity of the neutron-irradiated material fell far below the conductivity of the electron-irradiated material and approached that of the more disordered glass. The electron irradiation was carried out with 2-MeV electrons up to a fluence of $3 \times 10^{23}/\text{m}^2$. The fast neutron fluence was $6 \times 10^{22}/\text{m}^2$. Baeta and Ashbee [1975] also achieved amorphization of quartz with a lower electron beam energy of 200 keV. The required electron fluence was not reported, but evidently was significantly greater than the fluence of $\sim 3.6 \times 10^{24}/\text{m}^2$ needed for the appearance of initial displacement damage.

Löhneysen and Platte [1979] measured the low temperature specific heat and thermal conductivity of vitreous SiO_2 after ambient 3-MeV electron irradiation. At their highest dose of about 2×10^8 Gy, no significant changes were observed. In contrast, significant changes in specific heat were reported by Smith et al. [1978] after a neutron fluence of $5 \times 10^{23}/\text{m}^2$ or less. This would be equivalent to about 2×10^7 Gy, according to Fowler et al. [1981]. The effects observed were attributed to thermal spikes produced by the neutron irradiation but absent after electron irradiation. The compaction observed by Löhneysen and Platte was also much smaller than that observed after neutron irradiation.

Buckley [1986] irradiated polycrystalline MgAl_2O_4 from ambient temperature to 1320 K with electrons of energy from 0.1 to 1.13 MeV at peak fluxes from $5 \times 10^{22}/(\text{m}^2 \cdot \text{s})$ to $1.4 \times 10^{24}/(\text{m}^2 \cdot \text{s})$. The material was irradiated with and without

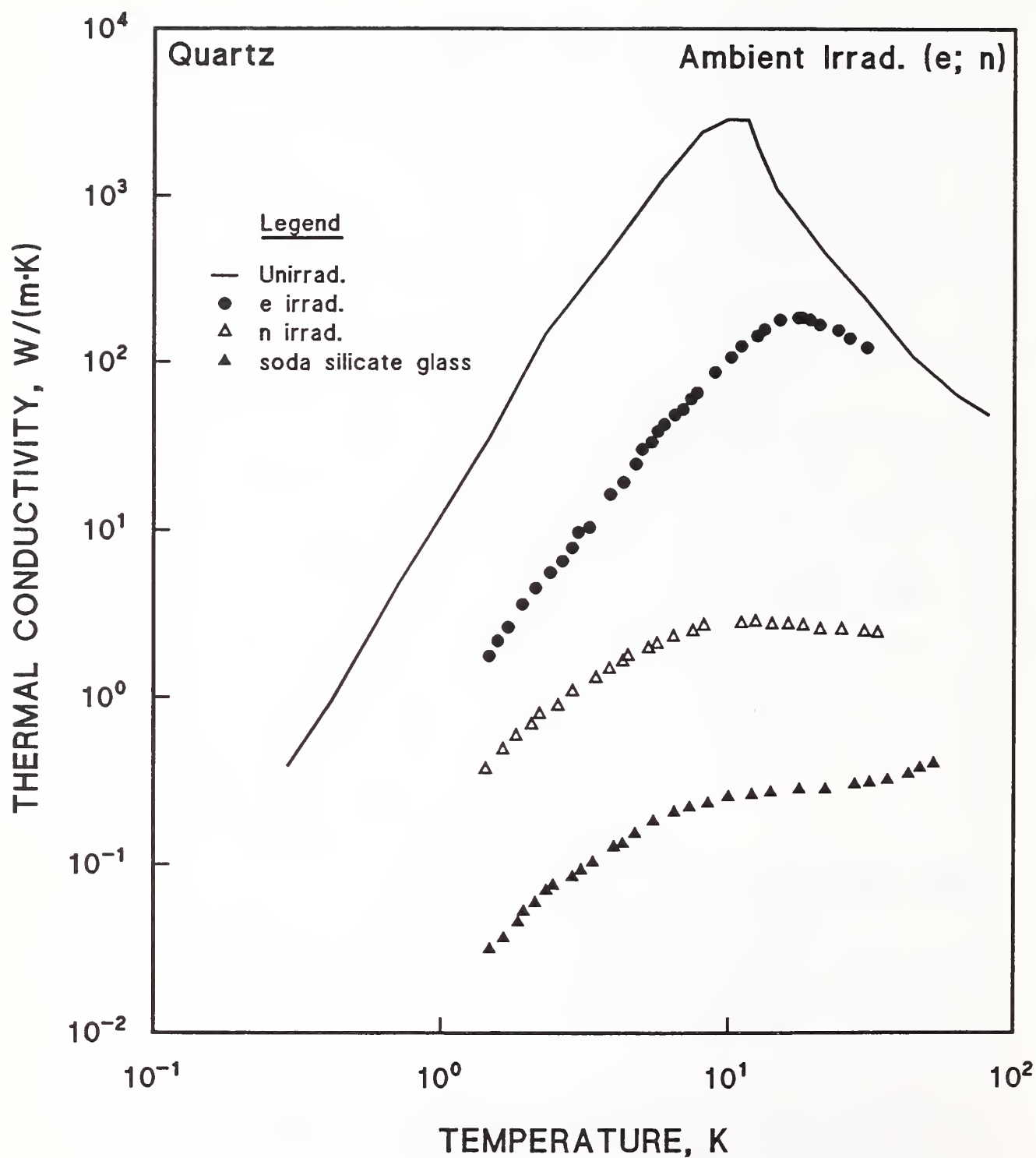


Figure 1.2.12. Comparison of cryogenic thermal conductivity of quartz after electron and neutron irradiation. Data and citations from Laermans and Daudin [1980].

implanted He, in order to simulate the effects of gas production in a fusion environment, to determine whether He stimulates nucleation of voids in the crystal matrix. However, no dislocation loop structures were generated, and since these are the usual precursors of voids, it was not surprising that no differences were detected in gas-free materials and those implanted with 1000 ppm of He. However, neutron irradiation was known to generate dislocation loops. Buckley surmised that the chaos generated in neutron-irradiated displacement cascades generated a more favorable environment for dislocation loop formation, since other investigations [citations, Buckley, 1986] indicated that electron irradiation could generate loops only in non-stoichiometric MgAl_2O_4 . Buckley concluded that the influence of He void formation in bulk MgAl_2O_4 during fast neutron irradiation could not be assessed by simulating the neutrons with electron beams of energy up to 1.13 MeV. It is possible that electron beams of much higher energy could simulate neutron irradiation, since cascade formation occurs at higher energies, as discussed in §1.2.2.

Buckley did, however, report serious degradation in MgAl_2O_4 from low-energy electron irradiation. The significant microstructural effects that Buckley observed at electron energies up to 1.13 MeV appeared to be side effects derived from the inhomogeneity of the electron beam which induced internal electric fields. These fields electrolyzed the material into its component elements, leaving Mg-deficient spinel compositions that decomposed into corundum (Al_2O_3). The source of the internal electric fields was hypothesized to be the ballistic recoil of secondary electrons, as discussed in §1.2.2. If this interpretation of the damage is correct, this is an ionization-related phenomenon, that presumably would be less important at higher electron energies [Equation (1.7)].

In contrast to most reports indicating a lack of equivalence of neutron and electron irradiations, Comer [1972] reported that enough thermal excitation was generated with high fluence, 100-keV electron irradiation of quartz to produce the Dauphiné twins that Comes et al. had proposed to explain results of their neutron irradiation to 10^{23} to $10^{24}/\text{m}^2$ [citation, Comer, 1972]. A typical electron fluence for the generation of twins was $5 \times 10^{24}/\text{m}^2$. In this case, the microstructure after relatively low-energy electron irradiation appeared similar to that obtained from neutron irradiation. However, in

contrast to ceramic oxides, quartz undergoes some displacement damage from ionizing radiation. Comes et al. suggested that the Dauphiné twins were formed after rotation of SiO_4 tetrahedra, a type of damage hypothesized to occur during ionizing radiation (see §6.1).

1.2.4. Damage Production by γ Rays: Theory

The basic processes by which γ rays or photons interact with matter are described well by Kircher [1964]. As Figure 1.2.13 illustrates, for atomic numbers in the range of about 6 to 30, which includes most inorganic insulations, the Compton effect is expected to predominate. In this process, schematically illustrated in Figure 1.2.14, the γ ray undergoes an elastic collision with an orbital electron. Part of the γ -ray energy is transferred to the electron, and the γ ray is scattered with reduced energy. (The kinetic energy of the ion is nearly unchanged.) Thus, energetic electrons are produced from the Compton effect, and it is these electrons which actually cause most of the damage produced in a material irradiated by γ rays. Hence, much of the damage arises from ionization processes, and since the energy of available radioactive γ isotopes is of the order of 1 MeV, Table 1.2.4 demonstrates that individual displacements, rather than cascades, will result. However, owing to the longer penetration distance, or range, of γ rays than of electrons (cm instead of mm), the damage can be more widely distributed within the irradiated material, and problems of specimen size do not usually occur. The Compton absorption is essentially independent of the Z of the irradiated material, since the electron binding energy is very low compared to the incident γ -ray energy.

Several authors have calculated the cross sections for atomic displacement in solids by γ rays. Oen and Holmes [1959] calculated the atomic cross sections for displacements through the Compton effect. An example of their results is given as a function of the threshold displacement energy, E_d , in Figure 1.2.15. As noted by Dell et al. [1979], for elements with $Z < 50$, the Compton displacement cross section is less than 3 barns ($3 \times 10^{-28} \text{ m}^2$). This contrasts with the much higher values for neutrons given in Table 1.2.3. Dell and Goland [1981] have calculated γ -ray displacement cross sections of 0.5 and 0.18 barn/atom for Al and O in Al_2O_3 and values of 0.016, 0.050, and

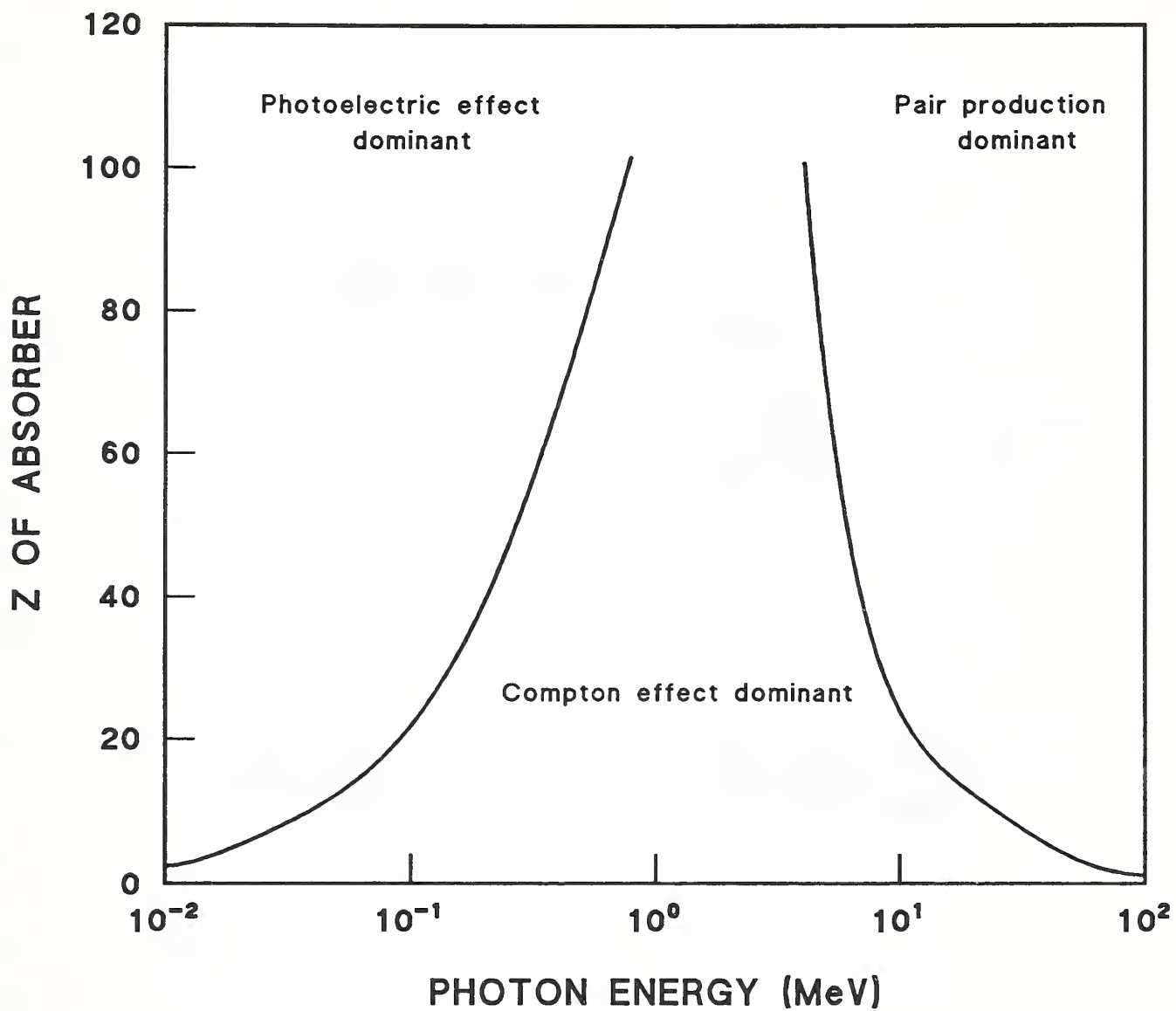
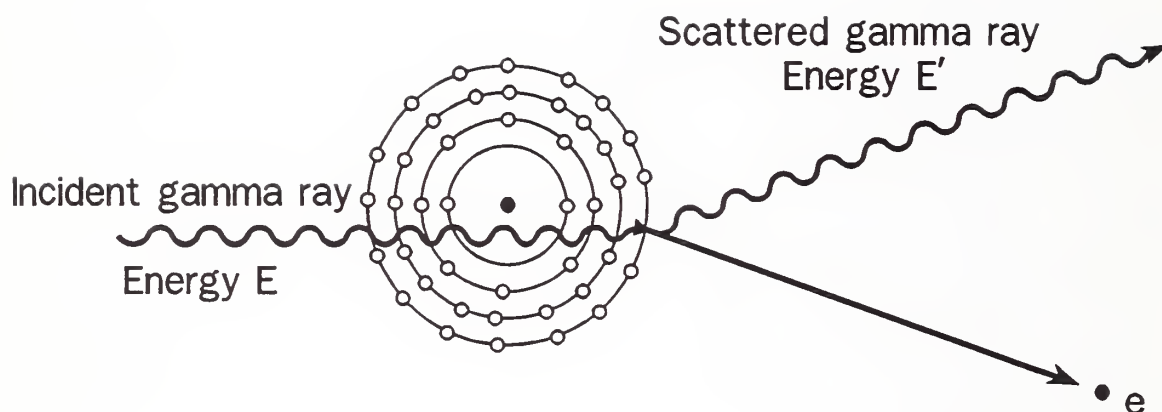


Figure 1.2.13. Interaction mechanisms of γ rays with matter, illustrating the dependence on the atomic number, Z , of the absorber. The Compton effect will dominate for the energy range of γ rays expected at the TF magnet in the ITER reactor. Data from Kircher [1964].



***Ion Kinetic Energy
~ Unchanged***

***Recoil
Electron***

Figure 1.2.14. Schematic diagram of the Compton process, illustrating the scattered γ ray and the recoil electron.

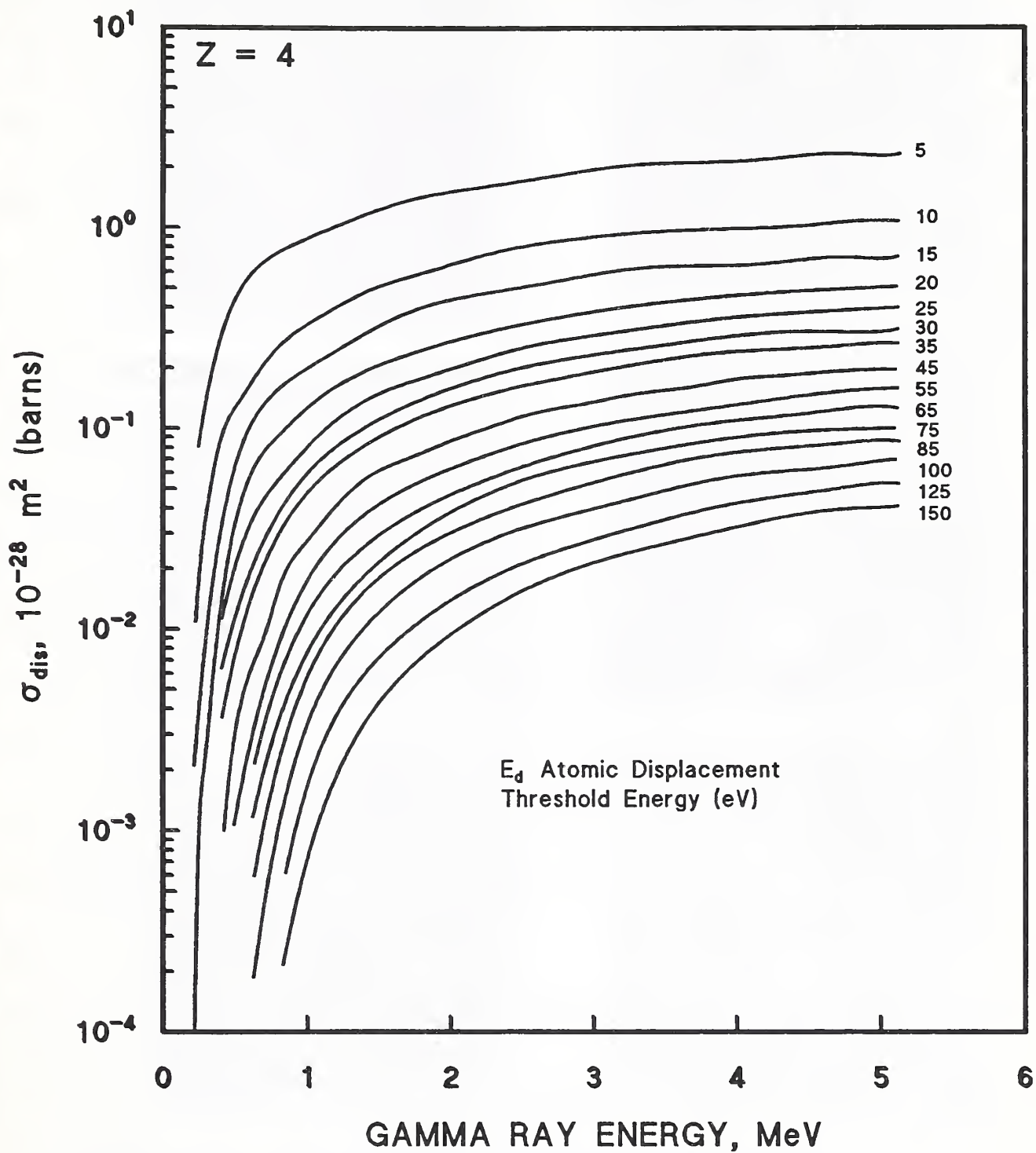


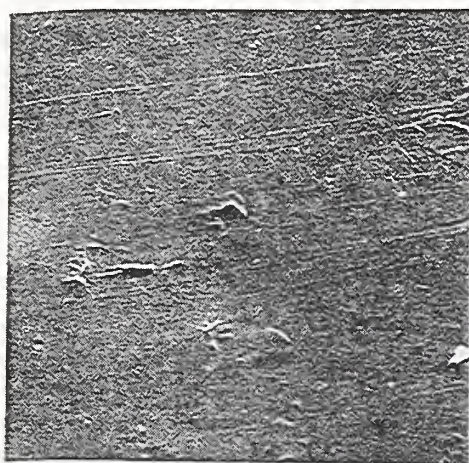
Figure 1.2.15. Atomic cross sections for the production of primary displacements of lattice atoms by γ rays through the Compton process vs. energy of the incident γ ray. $Z = 4$ is the atomic number and E_d is as indicated beside the curve. Data from Oen and Holmes [1959].

0.041 barn/atom for Mg, Al, and O in MgAl_2O_4 . Although small in comparison with neutron cross sections, these displacement cross sections are large enough to allow observation of vacancies by optical and electron spin resonance (ESR) techniques after relatively low doses of γ radiation. For example, Weeks [1963] reported ESR observations of O ion displacements in quartz after about 2×10^7 Gy of γ irradiation from a ^{60}Co source. The number of O ions displaced was calculated to be $\sim 5 \times 10^{16}/\text{cm}^3$. This corresponds to about 6×10^{-7} dpa (§6.1.2). If the conversion factor of 10^{17} neutrons/ $\text{m}^2 \approx 4$ Gy suggested by Fowler et al [1981] for SiO_2 is used, then a neutron ionization dose of 2×10^7 Gy results from a fast neutron fluence of $5 \times 10^{23}/\text{m}^2$. A typical neutron displacement cross section would be about 1000 barns/atom (e.g., Table 1.2.3, allowing for a lower E_d , §6.1). This would result in $\sim 5 \times 10^{-2}$ dpa. Thus, for inorganic insulation, there is no question that γ -ray doses cannot substitute for neutron doses in simulating damage. (Since a large part of the damage in organic insulation is chemical in nature, attempts have been made to substitute neutron dose with γ dose in testing radiation resistance of organics. However, this procedure may lead to a serious underestimate of damage, even in organics [e.g., Simon, 1993; Abe et al., 1987]). Even if dpa equivalents are used instead of ionization dose equivalents for inorganic insulators, the same problems encountered by Buckley [1986] with electrons should be expected (§1.2.3). Since the pattern of displacement distribution within the material is different and stoichiometry and microstructural features may also be dissimilar, simulation of fusion neutron irradiation damage in inorganic insulations by γ radiation should be expected to be problematic. Experimental observations are discussed in the following section.

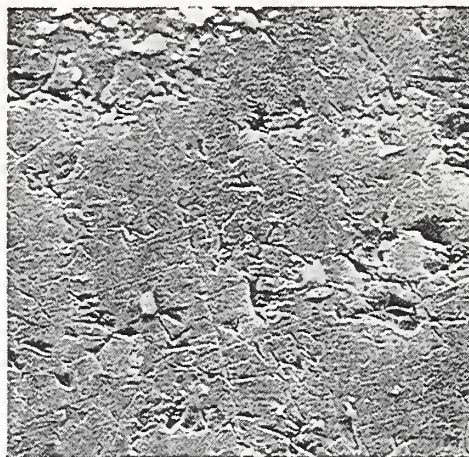
1.2.5. Experimental Comparisons of Neutron and γ -Ray Damage

A qualitative examination by SEM (scanning electron microscopy) of the difference in surface microstructure of quartz plates irradiated by γ rays from ^{60}Co and fast neutrons from ^{241}Am -Be was made by Bahadur and Parshad [1980]. The γ rays had energies of 1.17 and 1.33 MeV. Figure 1.2.16 shows the SEM surface patterns obtained, as well as the dose. As the γ -ray dose increased, both the density and size of the damage sites increased. The estimated dpa from γ radiation in Figure 1.2.16d ($\sim 3 \times 10^{-10}$) corresponds most

a



d



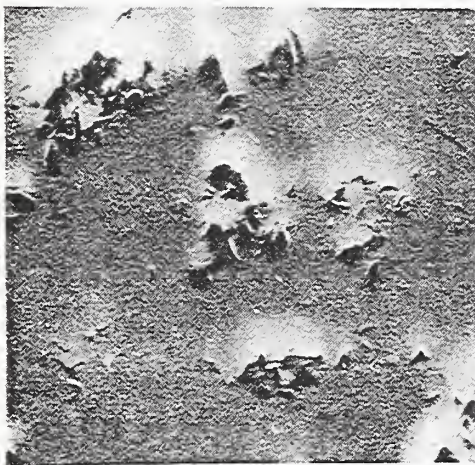
b



e



c



f

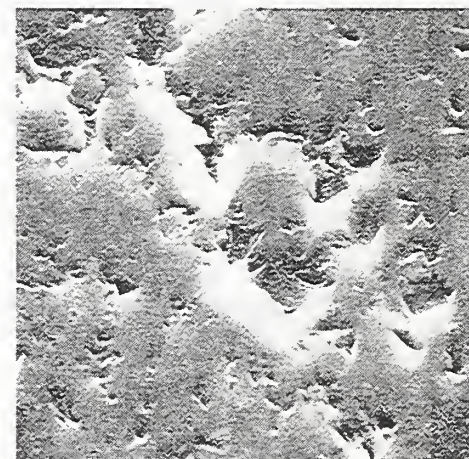


Figure 1.2.16. Surface microstructure of quartz irradiated as follows: (a) none; (b) X-ray; (c) γ , 800 Gy; (d) γ , 6000 Gy; (e) γ , 10^4 Gy; (f) 1.4×10^{15} fast neutrons/m² (~ 0.8 Gy). From Bahadur, H.; Parshad, R. 1980 Radiation Induced Damage on Quartz Crystal Surfaces Detected by Scanning Electron Microscope. *Physica Status Solidi (a)* 59. pp. K13-K16. Reprinted with permission from Akademie Verlag GmbH.

closely to the neutron irradiation dpa of part f of that figure ($\sim 1 \times 10^{-10}$). However, the two surfaces appear quite different. No additional information or analysis was supplied in this publication.

Figure 1.2.17 from Tanaka et al. [1982] on optical properties of pure (synthetic) vitreous SiO_2 fiber again indicates the increased damage from neutrons after equivalent ionization doses of fast neutrons and γ rays. (The conversion factors suggested by Fowler et al. were used to convert fluence to dose.) The γ irradiation source was ^{60}Co ; the fast neutron source was a reactor. The attenuation of light of $0.88\text{-}\mu\text{m}$ wavelength was measured in situ. Recovery of the optical attenuation to near-initial values occurred after irradiation was stopped. (Tanaka et al. also reported permanent changes in optical attenuation after extended periods of irradiation to γ doses of 10^3 to 10^6 Gy.)

The increase of DC conductivity of polycrystalline, sintered Al_2O_3 during 20-MeV proton and γ (actually, X-ray) irradiation is shown in Figure 1.2.18 from Pells [1986]. Since neutron irradiation results in a PKA ion, proton irradiation simulates neutron irradiation to some degree (but, see §1.2.6 below). Unfortunately, the highest X-ray dose rate was not as high as the proton dose rate, so the curves in Figure 1.2.18 are not completely comparable. However, the increase in conductivity under irradiation is usually described by a power law of the form

$$\sigma = KR^\delta + \sigma_0, \quad (1.8)$$

where R is the dose rate, σ_0 is the initial conductivity, and δ is obtained from a log/log plot of the conductivity against dose rate. When these data are analyzed in this way, a considerable difference between the proton and X-ray radiation as a function of temperature is evident, as Figure 1.2.19 indicates. Of course, the applicability of these data to 4-K irradiation is unknown. Since the proton energy was 20 MeV and the X-ray peak energy was 60 kV, the latter form of irradiation supplied only an ionizing dose. Pells suggested that the fall in the value of δ above 500°C could be explained by the annealing of Al vacancies, which the author has shown to begin above 400°C . The exponent δ rises again to superlinear values at higher temperatures, perhaps owing to the formation of dislocation loops. The main feature of Figure 1.2.19 that may be of some consequence for 4-K irradiation

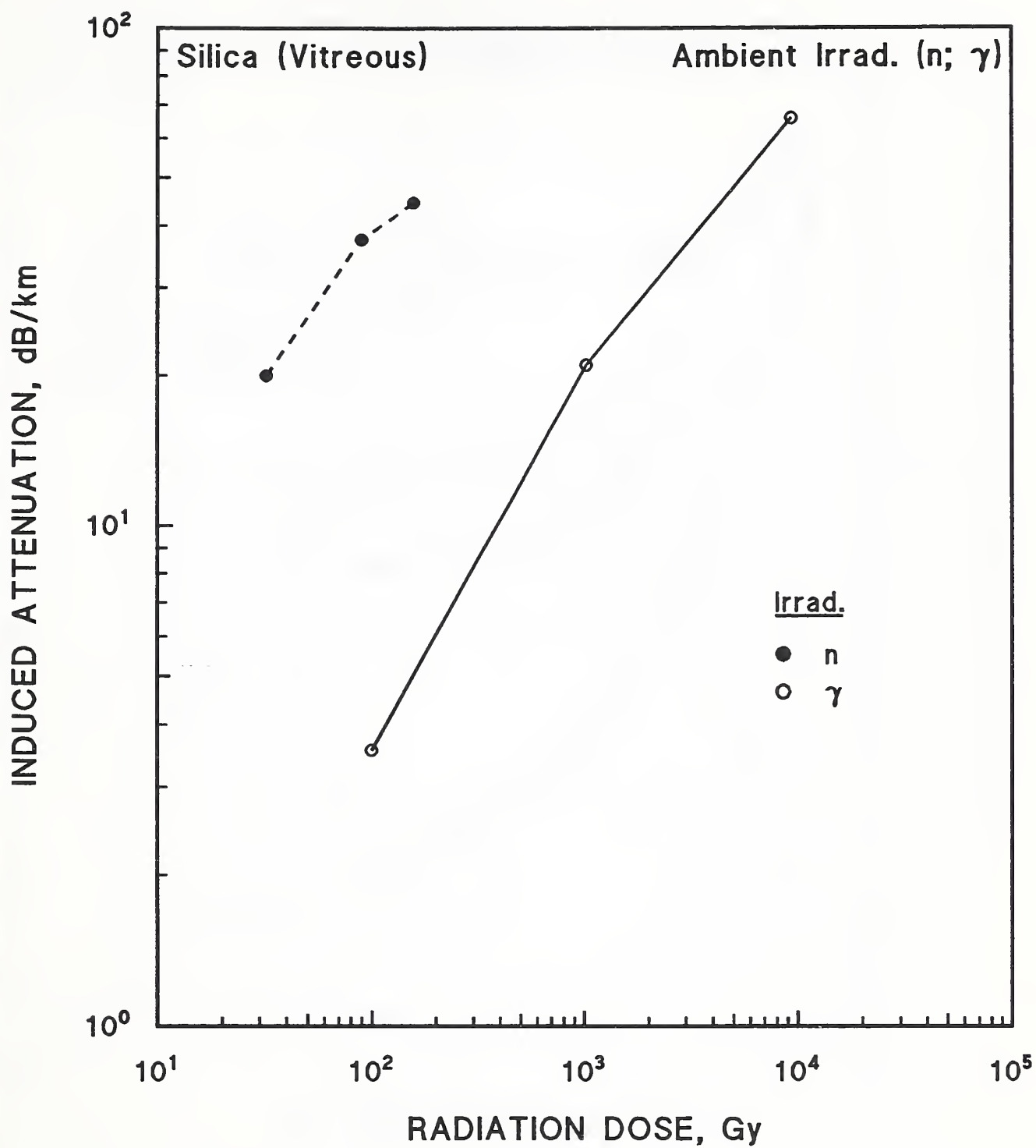


Figure 1.2.17. Dependence of induced optical attenuation of vitreous SiO_2 on radiation dose from neutron and γ irradiation. Data from Tanaka et al. [1982].

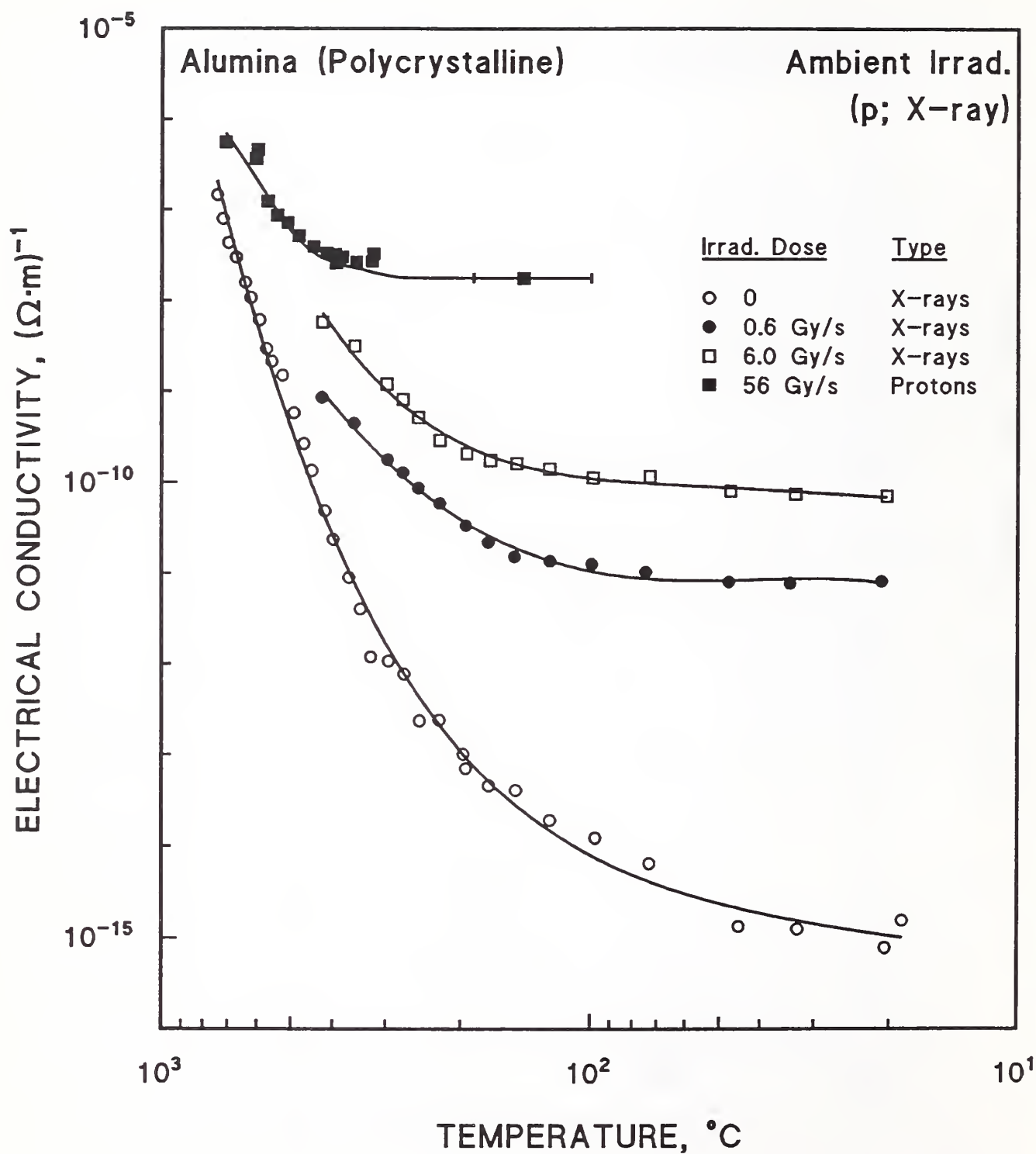


Figure 1.2.18. Increase in dc conductivity of polycrystalline Al_2O_3 after 20-MeV proton and X-ray irradiation. Data from Pells [1986].

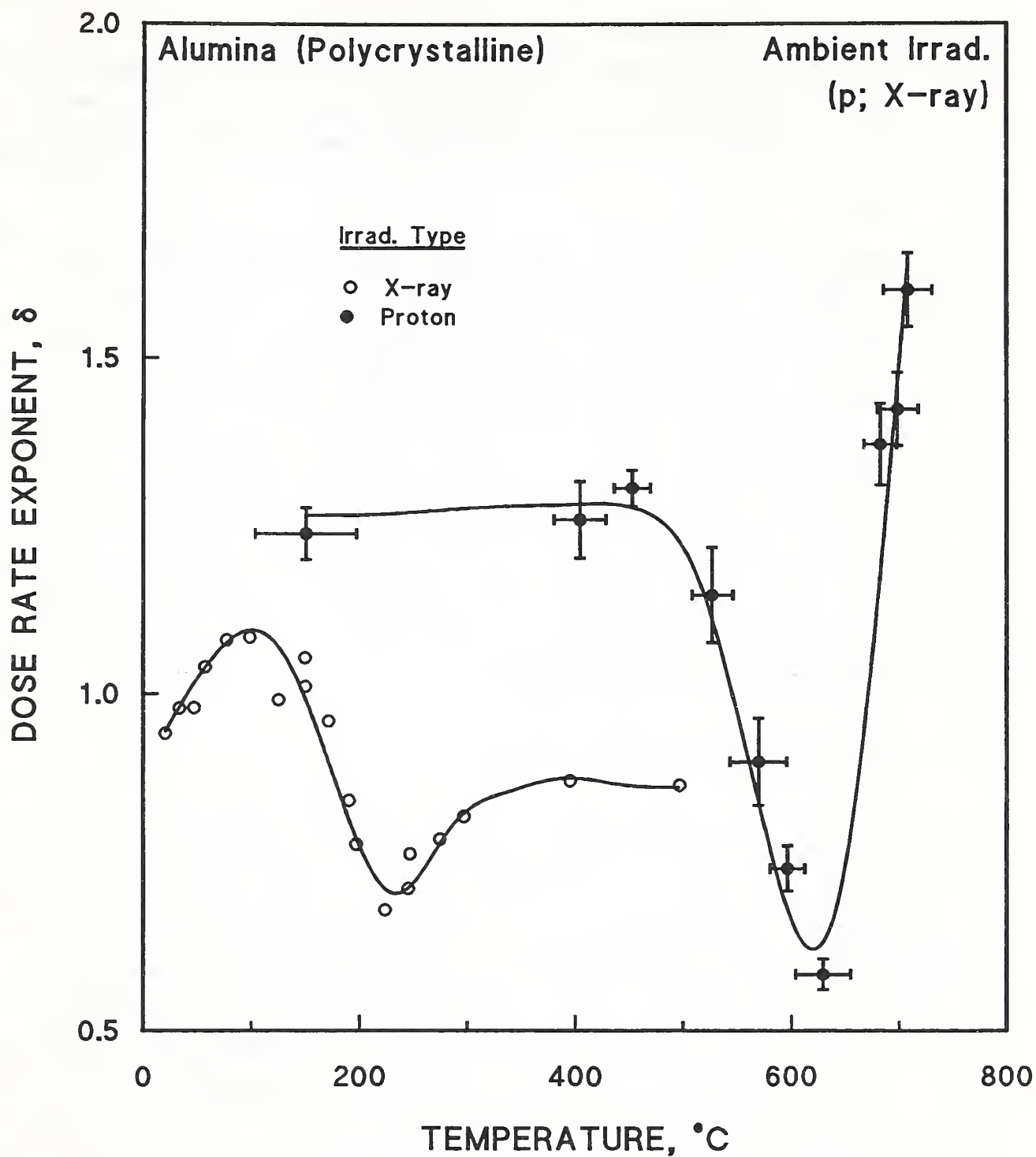


Figure 1.2.19. The dose rate exponent, δ , for proton and x-ray irradiation of polycrystalline Al_2O_3 . Data from Pells [1986].

conditions is the superlinear value of δ which appears to level off, but not disappear, at lower temperatures. If an increase in conductivity extends to temperatures far below 300 K, then radiation-induced conductivity (RIC) could conceivably be a factor at 4 K. This subject is discussed in more detail in §11 below.

Positron annihilation was used to study quartz single crystals that had been irradiated with both γ rays and fast neutrons [van den Bosch et al., 1983]. The positron annihilation lifetime spectra provide indications of the amorphization process. These spectra were unchanged up to a γ dose of 10^9 Gy. In neutron-irradiated quartz, the spectra evolved with increasing fluence, but appeared to saturate at $8 \times 10^{23}/\text{m}^2$, indicating that the amorphization process was also saturated at that fluence. According to the conversion factor used above [Fowler et al., 1981], this fluence would correspond to an ionization dose of about 3×10^7 Gy. This again indicates that dose equivalence cannot be used for inorganic insulation in efforts to simulate fast neutron irradiation with γ irradiation. (Actually, a γ dose of 10^8 Gy was also received by the specimens during the reactor irradiation.)

1.2.6. Damage Production by Ions: Theory

Except for the initial displacement of the PKA by an incident neutron, the actual transfer of energy from the neutron to the lattice atoms occurs through the interactions of the PKA ion and the secondary, tertiary, and higher-order ions. Therefore, ion irradiation might simulate neutron irradiation damage well. Ion beams can be well-defined, monoenergetic, and of high intensity, so that many dpa can be attained. Matzke [1982] reviewed investigations that showed that at low doses in Al_2O_3 , up to 160 atoms were displaced per 40-keV Kr ion or up to 500 atoms per 100-keV Pb ion; at high doses, $\geq 10^{19}$ ions/ m^2 , reordering and defect recombination became obvious, so that only about 40 atoms were displaced per 40-keV Pt or Xe ion in MgO or Al_2O_3 , with only 10 to 20 atoms per ion being permanently displaced for doses $\geq 2 \times 10^{20}$ ions/ m^2 . An approximation of the dpa can be obtained with the use of Equation (1.2) for N_d .

Evans et al. [1972] calculated that a given fluence of 3-MeV Ne ions in MgO would give the same average dpa as a fluence of fast neutrons that was a factor of 10^5 higher. To check this calculation experimentally, optical absorption at 250 nm (§§2.1, 4.1) was used to determine the number of O defects from both neutron and ion irradiation, as shown in Figure 1.2.20 (on the left axis). (Additional data at another absorption wavelength, from an unidentified defect type, are also shown in Figure 1.2.20.) Evans et al. cautioned that their factor of 10^5 was an approximate result, probably good to within an order of magnitude. Harrop et al. [1967] found a factor of $\sim 10^3$ for Ne ions of lower energy, 65 keV, by comparing the onset of electrical conductivity changes of neutron- and ion-irradiated ZrO_2 films (see §8.1).

Evans et al. used calculated values of the nuclear stopping power to determine the factor of $\sim 10^5$ to apply to MeV Ne ion fluences to convert them to fast fission fluences. When the universal nuclear stopping power curve for ions presented by Ziegler et al. [1985] is evaluated for Ne, the stopping power, dE/dx , does not vary greatly over the range from tens of keV to several MeV. Therefore, this factor is probably a reasonable estimator to apply to other ion fluences in insulators of similar atomic number. Since the nuclear stopping power cannot be experimentally separated from the much larger electronic stopping power, one must realize that most conversions of ion fluence to equivalent neutron fluence are based upon calculations that cannot be easily verified experimentally. The experiments of Evans et al. and Harrop et al. noted above furnish two examples of experimental checks. Another example of a calculation that gives a similar conversion factor is that of Pells and Murphy [1992]. Using the dpa calculated for a 4-MeV Ar-ion fluence for Al_2O_3 with a computer program, TRIM (see Figure 2.2.1, below), and an average fission cross section of 330 barns for Al and O in Al_2O_3 from Table 1.2.3, a factor of about 4×10^5 is obtained for the ratio of equivalent fast neutron fluence to ion fluence.

Although it is relatively easy to obtain sufficient dpa, as Figure 1.2.20 shows, a number of difficulties arise with ion simulation and the type of property change that can be measured is very limited [Billington and Crawford, 1961]. The ranges for suitable ion energies are usually too low to obtain appreciable penetration of a sample. Table 1.2.6 gives the calculated ranges

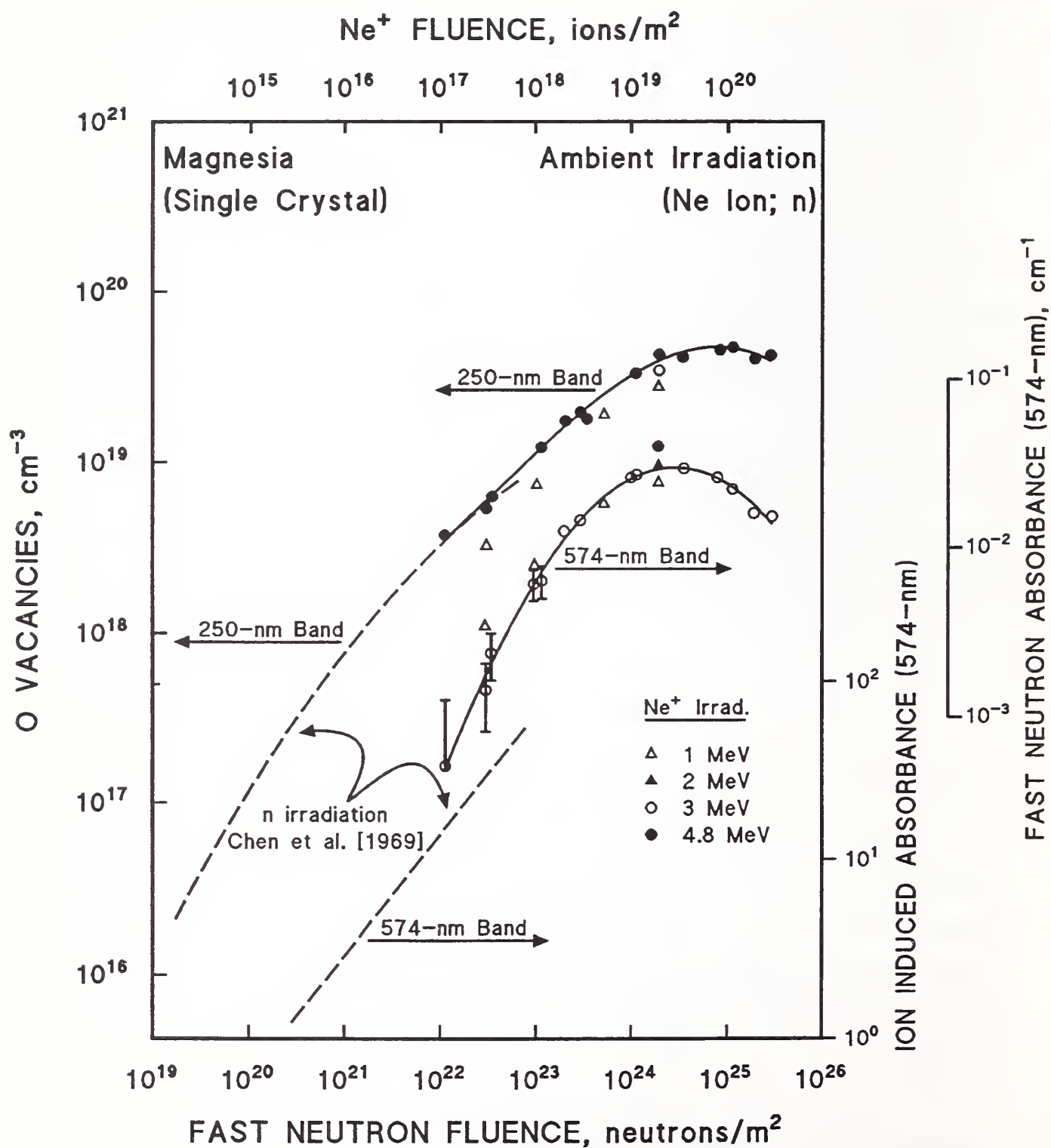


Figure 1.2.20. Volume concentration of O defects (250-nm band) in MgO from both fast neutron and MeV Ne ion bombardment, detected by optical absorption. The "equivalent" fast neutron fluence is about 10⁵ times the Ne fluence. The defect identity of the 574-nm band was not known. Data from Evans et al. [1972].

for typical ions of varying energy in vitreous SiO_2 . Because it is desirable that the bombarding ion not be trapped in the specimen, since it may be of different species and lead to spurious results, specimen thicknesses are sometimes limited to tens of micrometers (or, a few mils). Because the maximum damage rate occurs near the end of the range of the particle, it is not easy to arrange both for maximum damage and lack of contamination. Sometimes, ions of the host species can be used to avoid this problem, but the depth of damage in a specimen is still limited. Since neutrons have a mean free path of the order of centimeters, the PKA ion damage clusters are distributed over a considerable depth in neutron-irradiated specimens. Because the average energy transfer per ion collision is usually considerably less than that for neutrons, the local damaged regions would be expected to be much smaller than those produced in neutron cascades [Billington and Crawford, 1961]. However, the damaged regions should still be much larger than those obtained with electrons. Monte Carlo calculation for 14-MeV neutron cascades indicated that simulations with ions would be especially inaccurate for clusters produced by very high energy neutrons, owing to lack of reproducibility of such features as nonstoichiometry [Ghoniem and Chou, 1988].

Table 1.2.6. Calculated Ranges for Noble-Gas Ions in Vitreous SiO_2 . Calculations from Schroeder and Dieselman [1969].

ENERGY, keV	DEPTH, nm (\AA)			
	ION			
	Ne ⁺	Ar ⁺	Kr ⁺	Xe ⁺
50	120 (1200)	58 (580)	34.5 (345)	30 (300)
100	295 (2950)	118 (1180)	63.2 (632)	49.5 (495)
100	386 (3860)	204 (2040)	89 (890)	68.5 (6850)
200	480 (4800)	275 (2750)	117 (1170)	88 (880)
250	678 (6780)	428 (4280)	175 (1750)	124 (1240)

Another difference between neutron irradiation and ion simulation is illustrated in Figure 1.2.21, which shows the distribution in energy of the PKAs resulting from fast neutrons, compared to monochromatic ions (protons and α particles). The number of displacements per PKA is a function of the PKA energy, as indicated in Figure 1.2.2. Therefore, although the same dpa can be attained with a monoenergetic ion beam as with neutron irradiation, the distribution in size and extent of the clusters will not be the same. The importance of the PKA-energy spectrum for simulation of radiation damage has been investigated by Dierckx [1987]. Calculations on the Fe lattice showed that radiation damage should depend on the PKA spectrum, except for very high PKA energies above 0.4 MeV. Some authors have suggested that instead of calculating equivalent dpa to compare ion and neutron fluences, the energy deposited per unit volume should be compared instead. A review of this and other fundamental aspects of ion beam simulation has been given by Mazey [1990].

Cooling problems also may arise, owing to a high dose rate, although irradiations were obtained by J. S. Koehler's group at the University of Illinois in the 1950s at 15 K or lower (in metals) at damage rates exceeding those attained in a nuclear reactor at that time or even later. However, the ion flux must be high enough to allow for absorption in the vacuum jacketing or shielding of cryogenic apparatus.

Because the velocities of the incident ions are high, much of the energy of an incident ion beam is lost in ionization and is not used for displacement. Crawford [1984] noted that the ionization intensity was of great importance in determining the final damage configuration obtained in ion-implanted crystals. For example, a bond-strain mechanism has been suggested as a cause of displacement damage in SiO_2 from ionizing radiation, since displacement damage (in SiO_2) has been observed to arise from ionizing radiation (see §6.1). Also, ionization has been shown to enhance the amount of point-defect diffusion. In addition to changes in the microstructure that may affect mechanical properties, insulators are particularly susceptible (in comparison to metals) to degradation of electrical properties by ionizing radiation. This occurs because the concentration of valence electrons in the conduction band in polymers and ceramics is low, owing to their high band energy gaps. Ionizing

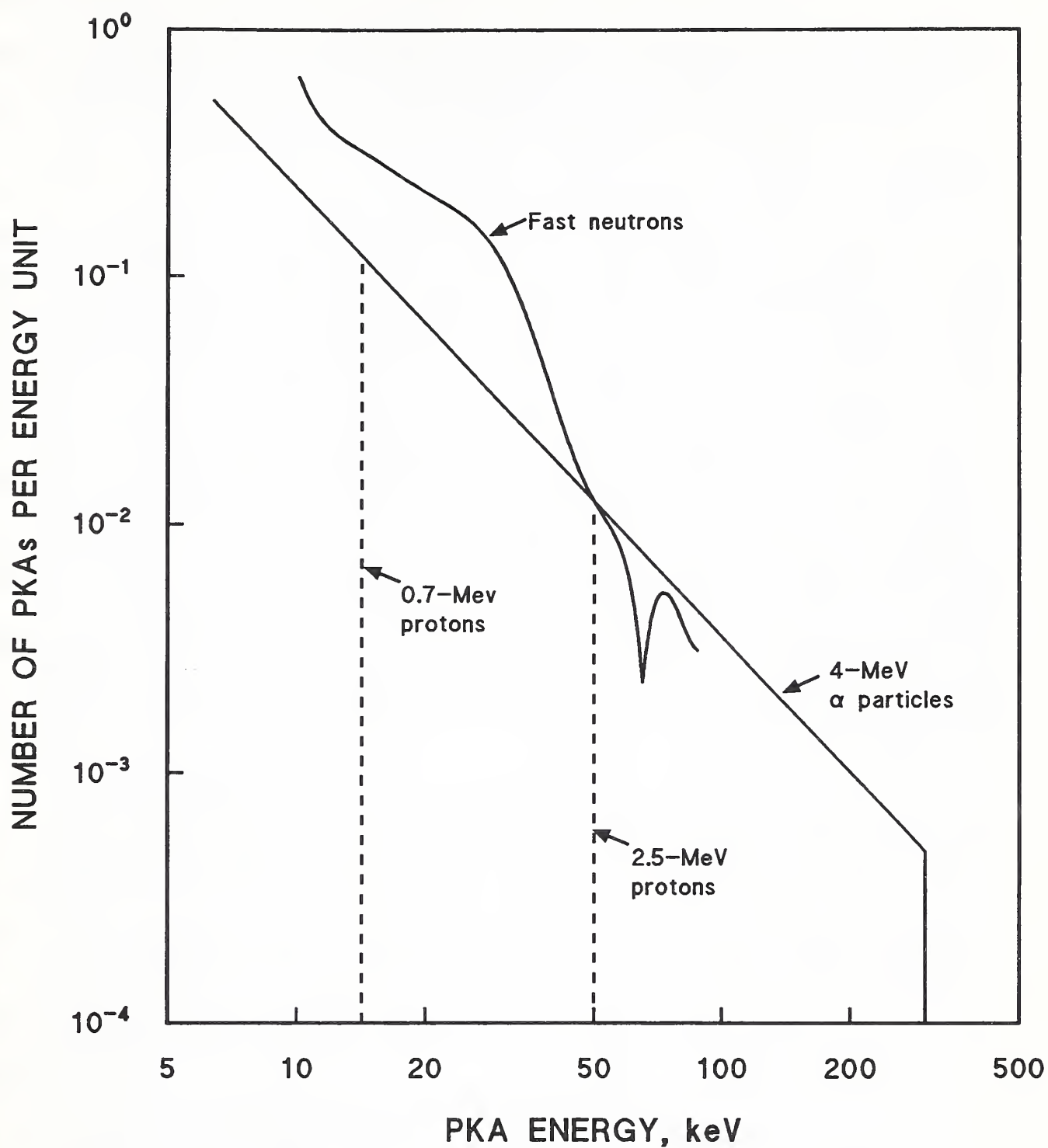


Figure 1.2.21. The PKA spectra of an Au crystal irradiated with charged particles, 4-MeV α particles, and fast neutrons (fission spectrum). Data from Agranovich and Kirsanov [1986].

radiation can excite substantial concentrations of these valence electrons into the conduction band, altering electrical properties significantly (see §11, below). Thus, if ions or other species are to simulate neutron damage, the ratio of ionization dose to displacement absorbed energy should be similar.

Zinkle and Greenwood [1993] have drawn attention to the factors discussed above and calculated estimated ratios of ionizing to displacive radiation absorbed dose (IDAD) that occur in ceramics during irradiation in accelerators and in fission and fusion reactors. For ions, the calculated IDAD ratio is the spectrum-averaged ratio of the electronic stopping power to the nuclear stopping power, assuming an electron binding energy of 2 eV and a nucleus displacement energy of 40 eV. The calculated IDAD ratios for Al_2O_3 are given in Table 1.2.7. Electrons, protons, and α particles are especially poor simulators of neutrons in fusion reactor magnets, but that ions of similar atomic number are more satisfactory. The paper should be consulted for further details of the calculation, including a discussion of even smaller IDAD ratios for neutrons obtained by Dell and Goland [1981] (§1.2.1). If Dell and Goland are correct, the discrepancy between electron and neutron irradiation becomes even greater.

A standard treatise on calculating ion ranges, ion damage distribution, and dpas in solids is that of Ziegler et al. [1985]. In addition to thorough explanations of the electronic and nuclear stopping power expressions used by Zinkle and Greenwood and other authors, this book presents the Monte Carlo computer program, TRIM (Transport of Ions in Matter). When comparing their theoretical calculations to experimental results, Ziegler et al. noted that the nuclear stopping power cannot be experimentally separated from the much larger electronic stopping power.

1.2.7. Experimental Comparisons of Neutron and Ion Damage

Rechtin [1979] used TEM to study the defect microstructure induced in single-crystal Al_2O_3 by irradiation with several species of high energy ions. Specimens of about 50- μm thickness were irradiated at temperatures ranging from 500 to 1250 K. Energies of the He, O, C, and Ne ions were 0.6 or 2 MeV. Rechtin

Table 1.2.7. Ionizing and Displacive Radiation in Al₂O₃ in Various Irradiation Sources. Calculated by Zinkle and Greenwood [1993] using Experimental Results for Al and Correcting for the Density Difference.

Irradiation Source	Ion Range	Gamma/ Neutron Absorbed Dose	Ionization/ Displacements Absorbed Dose	Damage Rate (dpa/s)	Ionizing Dose Rate (Gy/s)
1.8 MeV electrons	2.1 mm	—	~10,000	—	—
20 MeV protons	1.3 mm	—	3800♦	1.2 x 10 ^{-8**}	2.2 x 10 ^{4**}
10 MeV protons	0.39 mm	—	4400♦	1.8 x 10 ^{-8**}	3.8 x 10 ^{4**}
1 MeV protons	8.7 µm	—	1900	2.1 x 10 ^{-7**}	2.0 x 10 ^{5**}
28 MeV He ⁺ ions	0.21 mm	—	3400♦	1.2 x 10 ^{-7**}	2.0 x 10 ^{5**}
1 MeV He ⁺ ions	2.0 µm	—	820	3.8 x 10 ^{-6**}	1.5 x 10 ^{6**}
3 MeV C ⁺ ions	1.8 µm	—	280	4.3 x 10 ^{-5**}	5.7 x 10 ^{6**}
2 MeV Al ⁺ ions	1.2 µm	—	33	4.1 x 10 ^{-4**}	6.3 x 10 ^{6**}
4 MeV Fe ⁺ ions	1.5 µm	—	15	1.4 x 10 ^{-3**}	1.0 x 10 ^{7**}
4 MeV Zr ⁺ ions	1.1 µm	—	3.9	4.0 x 10 ^{-3**}	7.5 x 10 ^{6**}
Mixed spectrum fission reactor (HFIR RB*)	—	23	107	3.2 x 10 ⁻⁷	1.6 x 10 ⁴
Fast fission reactor (FFTF MOTA)	—	1.0	4.4	3.8 x 10 ⁻⁶	8000
Fusion Reactor					
- 1st wall	—	0.14	13	1.5 x 10 ⁻⁶	9300
- magnet coils	—	0.7 to 210	40 to 330	<2 x 10 ⁻⁹	<300
14 MeV neutrons (RTNS-II)	—	0.01	35	6.8 x 10 ⁻⁹	110

♦ These calculations neglect displacements due to nuclear reactions, which can be significant for light ion energies >10 MeV (see D. W. Muir and J. M. Bunch, in Radiation Effects and Tritium Technology for Fusion Reactors, p. II-517).

**Displacive and ionizing dose rates calculated for a beam current of 1 µA/cm² of singly charged ions.

reported that the basic nature of defect structures found, such as dislocation loops after He^+ irradiation, were similar to damage microstructures obtained from fast neutrons. The extrinsic effects of the implanted ions were very important in several cases. For example, implanted O interstitials caused preferred nucleation and growth of dislocation loops on certain planes. These extrinsic effects could be distinguished from the desired displacement damage production only because TEM was used in the investigation. This is another indication that it is preferable to use host ions if possible.

Since high temperatures of irradiation and annealing were used to obtain the effects observed by Reichtin, their applicability to 4-K irradiation is uncertain. However, McHargue et al. [1986] made very important observations on the effect of cryogenic temperature damage dependent upon ion species. At 300 K, they found that recovery processes were so highly dominant, that only Zr and Zn ions could produce amorphization in Al_2O_3 . Amorphization apparently could not be achieved with the host cation, Al; some degree of foreign-atom implantation was evidently necessary to stabilize the damage. Burnett and Page [citation, McHargue et al., 1986] had previously found that Cr ions could also produce amorphization in Al_2O_3 , but only at a very high dpa, >600. However, at 77 K, McHargue et al. found that a Cr fluence ~200 times lower produced amorphization, and that other ions, including host ions, also produced amorphization at this temperature, since recovery was suppressed. These experiments are also discussed in §§1.3 and 2.3, below. Since host-ion irradiation is a fairly good simulator of neutron irradiation, which damages the material through the host PKAs, these results indicate that materials that cannot be amorphized at ambient temperature by neutrons or host atoms (e.g., Al_2O_3 , MgAl_2O_4) may amorphize at 4 K after a similar fluence.

Hines and Arndt [1960] found that the absolute change in refractive index, n , of quartz produced by ion irradiation with various species (H, D, He, Ne, A, Kr, Xe) was $\Delta n = 0.067 \pm 0.002$. The change in refractive index never attained the magnitude reported for neutron irradiation, $\Delta n = 0.077$. This was attributed by Hines and Arndt to the ordering effect of the undamaged quartz substrate present in the ion irradiation specimens. But the phenomenon may also indicate the degree of recovery with ion irradiation at ambient temperature, as found by McHargue et al. Perhaps the somewhat different distribution of

the cascade damage from neutrons makes recovery at ambient temperatures somewhat more difficult than for ion irradiation.

If single crystals are used in ion irradiation studies, the effect of channeling must be considered. When the ions are incident along the most closely packed atomic row, the damage rate is decreased by a factor of ~ 2 to ~ 20 , depending upon the ion, ion energy, and target, as demonstrated by Bøgh et al. [1969]. Ions of higher energy and lighter mass, such as protons and α particles exhibited this effect to a greater degree. This can be qualitatively understood by noting that a slow, heavy ion can transfer large energies to atoms in distant collisions, whereas a fast, light ion must come very close to an atom to transfer its energy. Usually, single crystals are tilted during ion irradiation to avoid channeling effects.

Finally, the results of Macauley-Newcombe and Thompson [1984] and Macaulay-Newcombe et al. [1990] on ion irradiation of quartz should be mentioned. They found much more damage than would be predicted from the modified Kinchin-Pease formula. It is unclear whether part of the explanation for the up to 20 times higher damage is that the experiments were carried out at 50 K, where recovery would be inhibited, since the authors did not appear to recognize the possible role of temperature and recovery. They stated that "no significant difference" was observed with similar experiments conducted at 300 K, but none of the 300-K data was published. The excess damage was attributed to electronic energy losses, and other investigators have also presented evidence to indicate that displacement damage in quartz arises from ionization (§6.1).

1.3. EFFECT OF IRRADIATION TEMPERATURE UPON RADIATION DAMAGE

The effects of irradiation and holding temperature upon retained radiation damage in metals and semiconductors are well-known from early studies. For example, Simmons and Balluffi [1958] and Vook and Wert [1958] used X-ray techniques to measure the lattice expansion of high-purity Cu at about 10 and 17 K during deuteron irradiation. They found a specific length change, $\Delta L/L$, of about 4×10^{-21} for each 7-MeV deuteron/cm². This length change was attributed to Frenkel defects (lattice-vacancy-interstitial pairs). When recovery of this effect was studied, it was found that only about a 3 to 4% residual

effect remained at 300 K. (Actually, since an effect of 3 to 4% was equal to the experimental error, complete recovery could have occurred at 300 K.) At intermediate temperatures, if the stages of thermal recovery are designated as Stage I (to 70 K), Stage II (70 to 180 K), and Stage III (180 to 300 K), then the amounts of recovery per stage were 64%, 6%, and 26%, respectively. A 55% recovery was reported between 10 and 42 K.

Germanium exposed to a fast neutron fluence of $4 \times 10^{21}/\text{m}^2$ at 16 K was reported to experience large-scale annealing of defects at 100 K, and the loss of crystallinity observed in intermetallics and Ge was recovered between 77 and 300 K [Crawford and Wittels, 1958]. Diamond and graphite have much higher melting points. Diamond may not exhibit appreciable recovery from lower temperature irradiation until 100°C [Crawford and Wittels, 1958]. However, Primak [1956] cites results of Keating on graphite that showed an increase in the c-axis lattice spacing of about 6 pm (0.06 \AA) for a neutron fluence of $2 \times 10^{23}/\text{m}^2$ at $\sim 77 \text{ K} + <40 \text{ K}$. This corresponds to $0.06 \times 10^{-24} \text{ nm}$ for each damaging neutron/ m^2 . Keating stated that 41% of the damage annealed when the samples were warmed to a little above room temperature. This figure agrees fairly well with the size of the recovery effect in Cu, but the agreement may be fortuitous. When Primak irradiated vitreous SiO_2 in the same liquid nitrogen facility (at Brookhaven National Laboratory), he found that the density change would have required a 20% higher dose in the cool-test-hole facility where temperatures ranged from 35 to 60°C. Since the density change was not measured until the specimens had been warmed to ambient temperature, the actual degree of recovery was probably larger than 20%.

These data indicate the risks of applying even 77-K results to 4-K conditions, or of storing specimens at 77 K (before testing) after irradiation at 4 K. Application of results at ambient temperature and above to 4-K conditions is even more uncertain. Ambient temperatures of reactor irradiation are often 40 to 100°C or 313 to 373 K.

Temperature-effect studies of comparable precision on ceramics are almost nonexistent. Optical absorption coefficients furnish a direct estimate of the number of defects of a particular type (see §2.1, below). Arnold and Compton

[1959] showed that the efficiency of production of a defect in vitreous SiO_2 by 2-MeV electrons was about 10 times greater at 77 K than at ambient temperature. Figure 1.3.1 shows these results; optical measurements were made at 77 K in both cases. The defects had the same absorption wavelengths as displacement defects found in fast-neutron irradiation. Arnold and Compton noted that when the specimen was warmed to ~ 295 K and then immediately remeasured at 77 K, the absorption bands at 215 and 257 nm were reduced to about half their original magnitude. Further loss in absorption took place slowly at ~ 295 K, and the absorption curve approached the value obtained when the irradiation was initially made at ~ 295 K. Compton and Arnold [1961] also reported comparative X-ray irradiation of vitreous SiO_2 at 77 and 4 K. Although recovery from 4-K damage apparently was not studied, the absorption coefficient peak measured at 4 K was twice that measured at 77 K, after comparable irradiations at each temperature.

When ion irradiation was carried out to the degree that amorphization was produced in Al_2O_3 , McHargue et al. [1986] reported that the critical fluence for amorphization at 77 K was 200 times less than that at 300 K. Chromium ions were used in these experiments, but, when host ions, Al and O, were used, amorphization could only be achieved at 77 K, owing to the ease of recovery of host-ion damage at ambient temperature. (See also §1.2.7, above.)

The defect density after irradiation can also be estimated from the low temperature thermal conductivity since the defect contribution to the thermal resistivity is additive, to a first approximation. Pryor et al. [1964] determined the defect resistivity at 77 K of polycrystalline BeO irradiated in a reactor at about 75°C . Figure 1.3.2 compares these thermal conductivity results with those of McDonald [1963], who irradiated and tested specimens in situ at 91 K. This comparison indicates that the number of defects retained was about 16 times larger at 91 K, and that about 90% of the 77-K damage would anneal at 350 K, during the course of a month-long irradiation. McDonald showed that about 25% of the 91-K damage he measured had annealed at 310 K, after a series of brief, 15-min intermediate anneals and remeasurement at 91 K (Figure 1.3.3). Since specimens were often irradiated above 310 K ($\sim 100^\circ\text{C}$ or ~ 375 K is common) for long periods in other investigations, and sometimes stored before 300-K measurements, the 25% value probably understates the

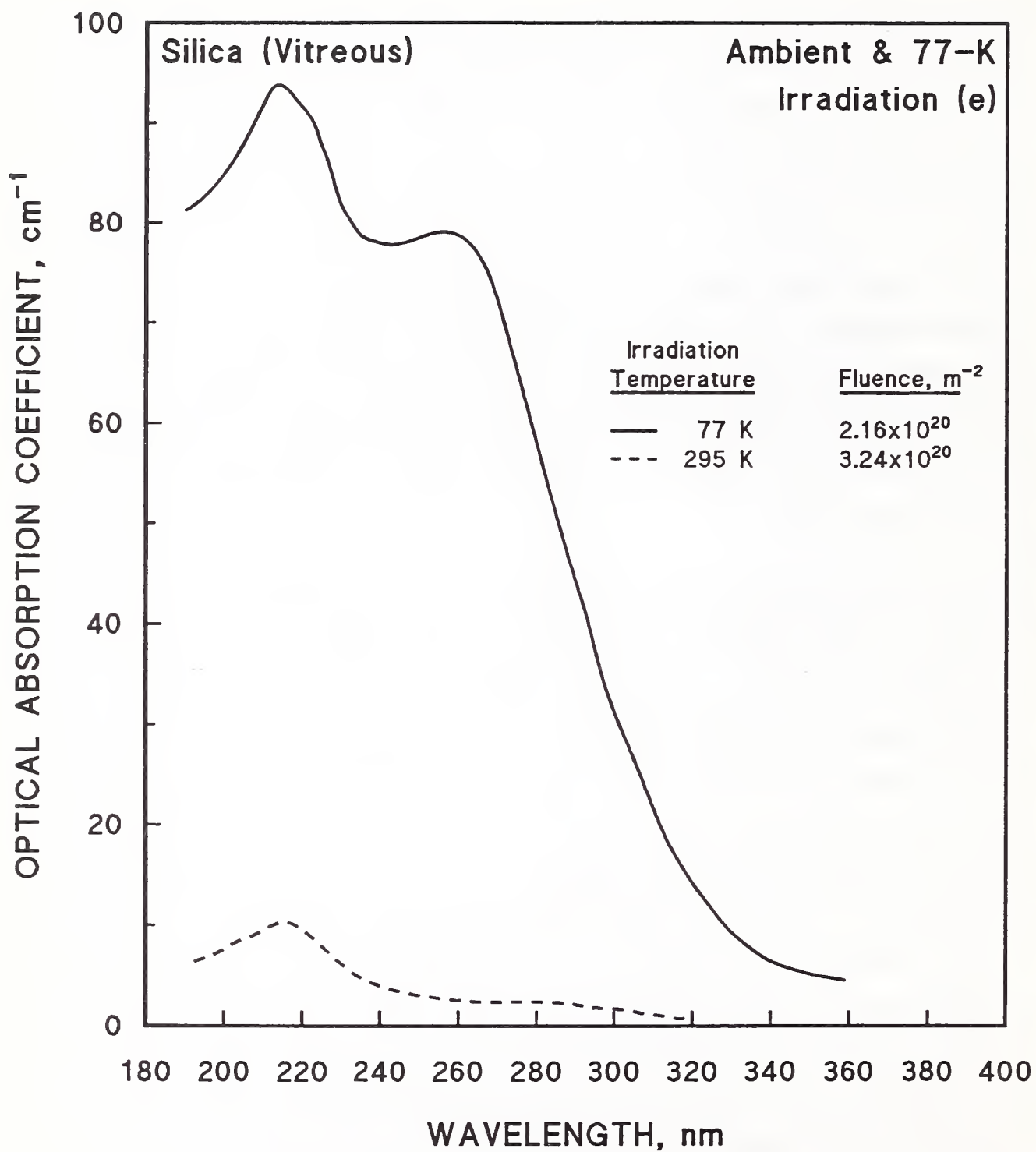


Figure 1.3.1. Absorption coefficient vs. wavelength for 2-MeV electron irradiation of vitreous silica at 77 and 295 K. Data from Arnold and Compton [1959].

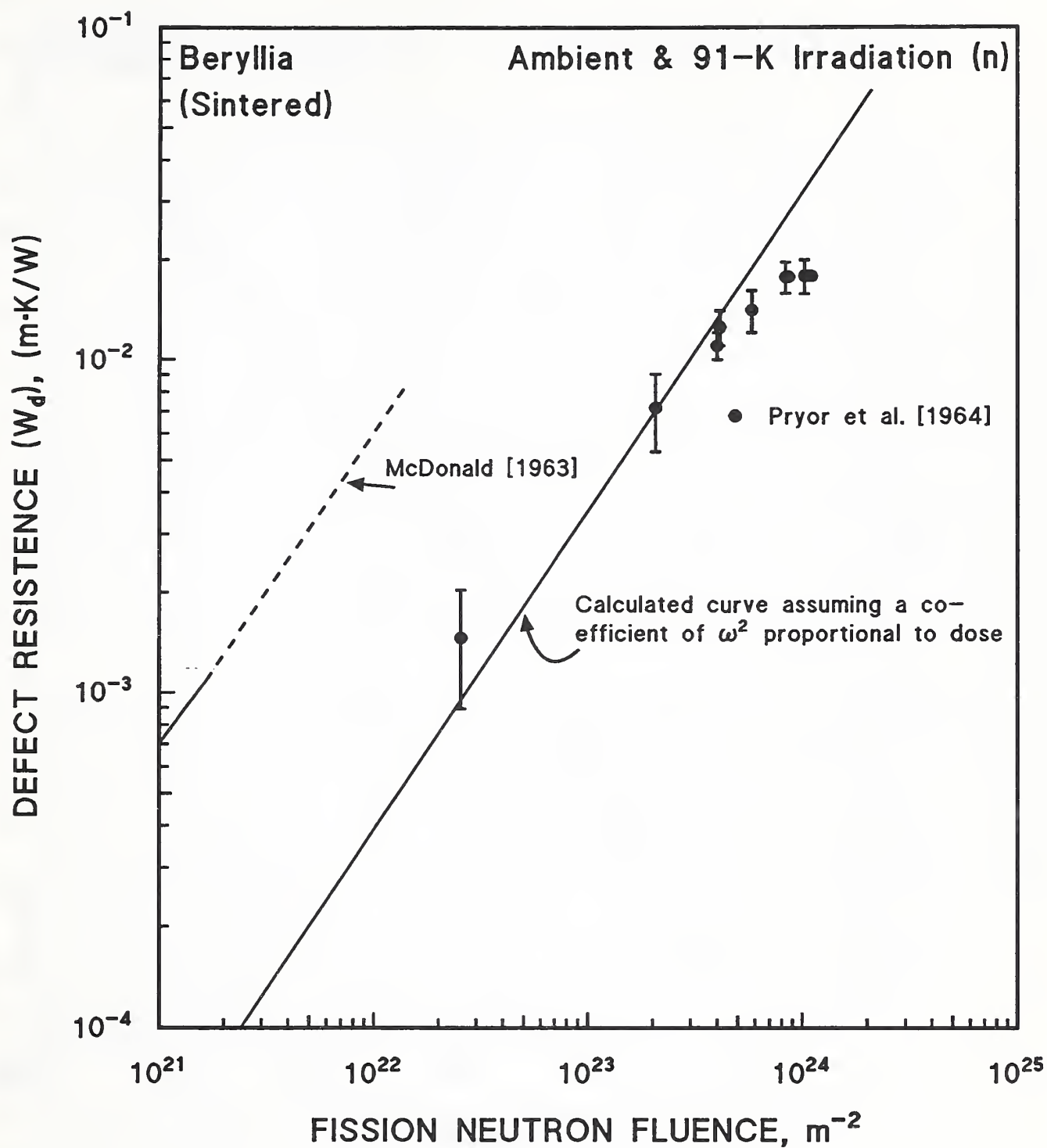


Figure 1.3.2. Comparison of ~ 77 -K thermal conductivity in BeO after irradiation (without warm-up) at 91 K (McDonald [1963]) and irradiation at $\sim 75^\circ\text{C}$ (Pryor et al. [1964]).

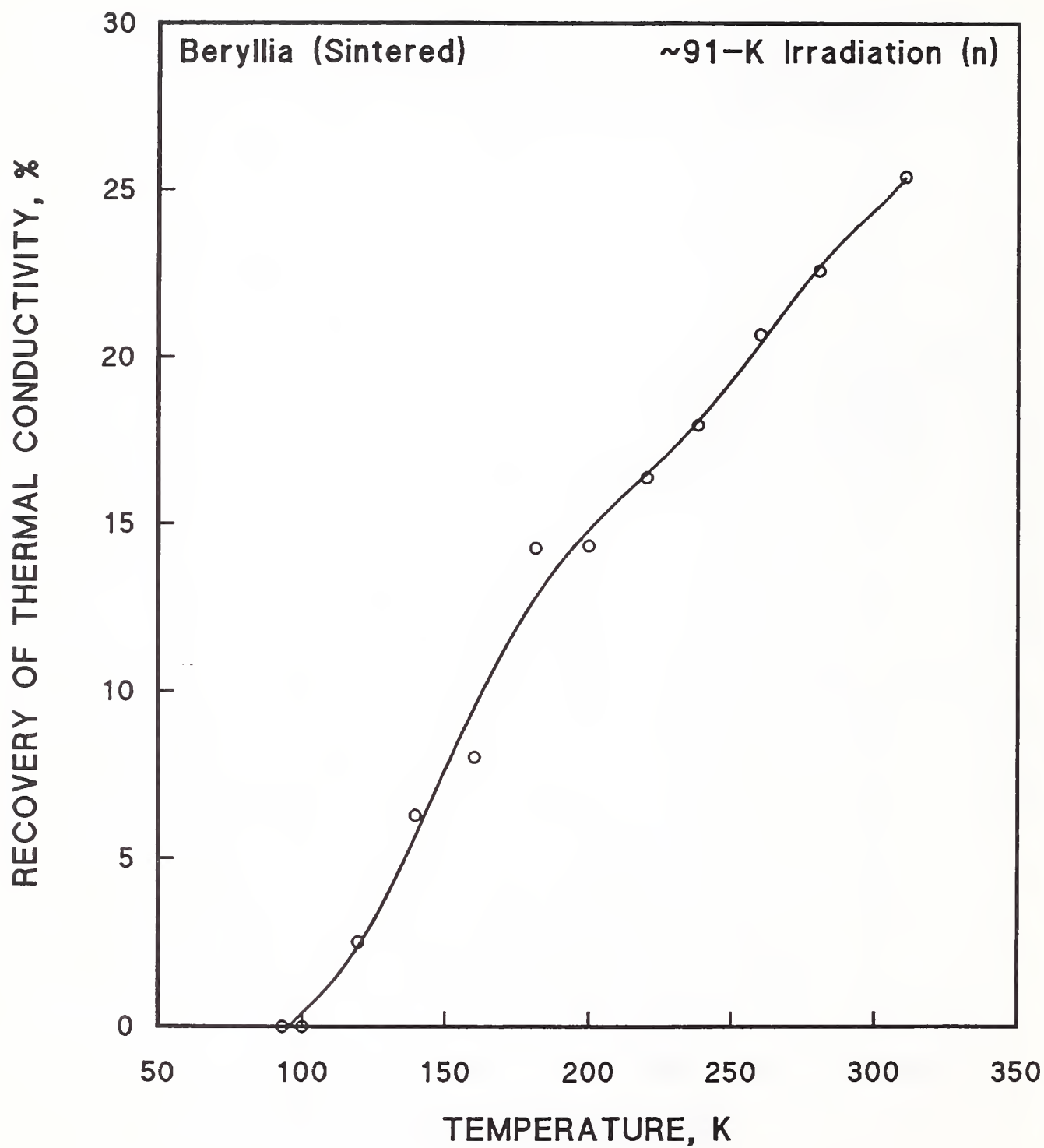


Figure 1.3.3. Recovery of thermal conductivity above 100 K during 15-min. annealing periods. Data from McDonald [1963].

actual annealing in most experiments, and the 90% value found by Pryor et al. may be more representative.

Above ambient temperature, the damage produced by irradiation is also often strongly dependent upon the temperature of irradiation. In most cases, the damage anneals more as the temperature increases; this effect is shown in Figure 1.3.4 for the thermal conductivity of SiC, since the neutron fluence of the LAMPF (Los Alamos Meson Physics Physics Facility) irradiation was 10 times higher than that in the Geesthacht facility, but the irradiation temperatures were 600 and 353 K, respectively [Rohde, 1991]. Another example is given by the radiation-induced dimensional changes of different forms of polycrystalline Al_2O_3 measured by Thorne and Howard [1967]. Figure 1.3.5 shows that the length changes from the 250°C irradiation are much larger than those from the 700°C irradiation. Keilholtz et al. [1964] also found that volume expansion decreased with increasing irradiation temperature, which was varied from 583 to 1100°C. The fracture damage in the polycrystalline BeO this group examined also decreased with increasing irradiation temperature.

Tanaka et al. [1982] showed that the in situ response of pure, vitreous SiO_2 -core fibers to γ -radiation decreased as the irradiation temperature increased from near 20 to 120°C. Radiation-induced optical attenuation at 0.88 μm was smaller as the temperature of irradiation increased (Figure 1.3.6). The authors explained their results by recombination theory: trapped electrons generated by irradiation are excited to the conduction band and become free electrons. These electrons can then move freely in the vitreous SiO_2 matrix, and recombine with positive holes. The probability of the recombination of electrons and holes increases at higher temperatures. Fiber heating was described as an effective way to improve radiation resistance.

As these examples show, higher irradiation temperatures generally produce less damage, as many of the defects produced can anneal. However, in some cases where thermal activation of diffusion or other processes is necessary for the production of a damage microstructure, a higher or different degree of damage is produced at higher temperatures. For example, Frenkel defects seem to migrate to form dislocation loops in Al_2O_3 at high temperatures.

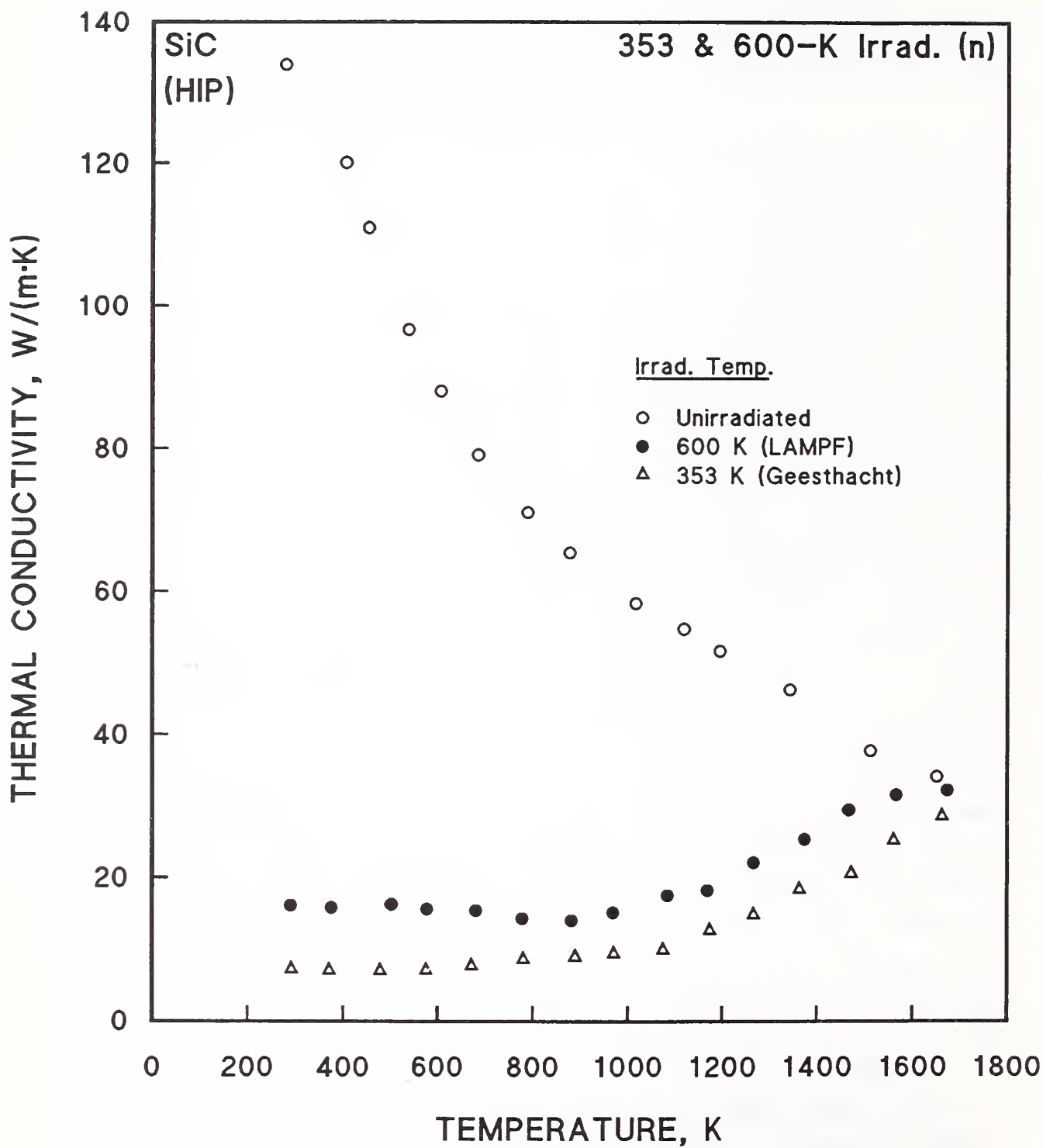


Figure 1.3.4. Thermal conductivity of SiC above 300 K after neutron irradiation at 353 and 600 K. Data from Rohde [1991].

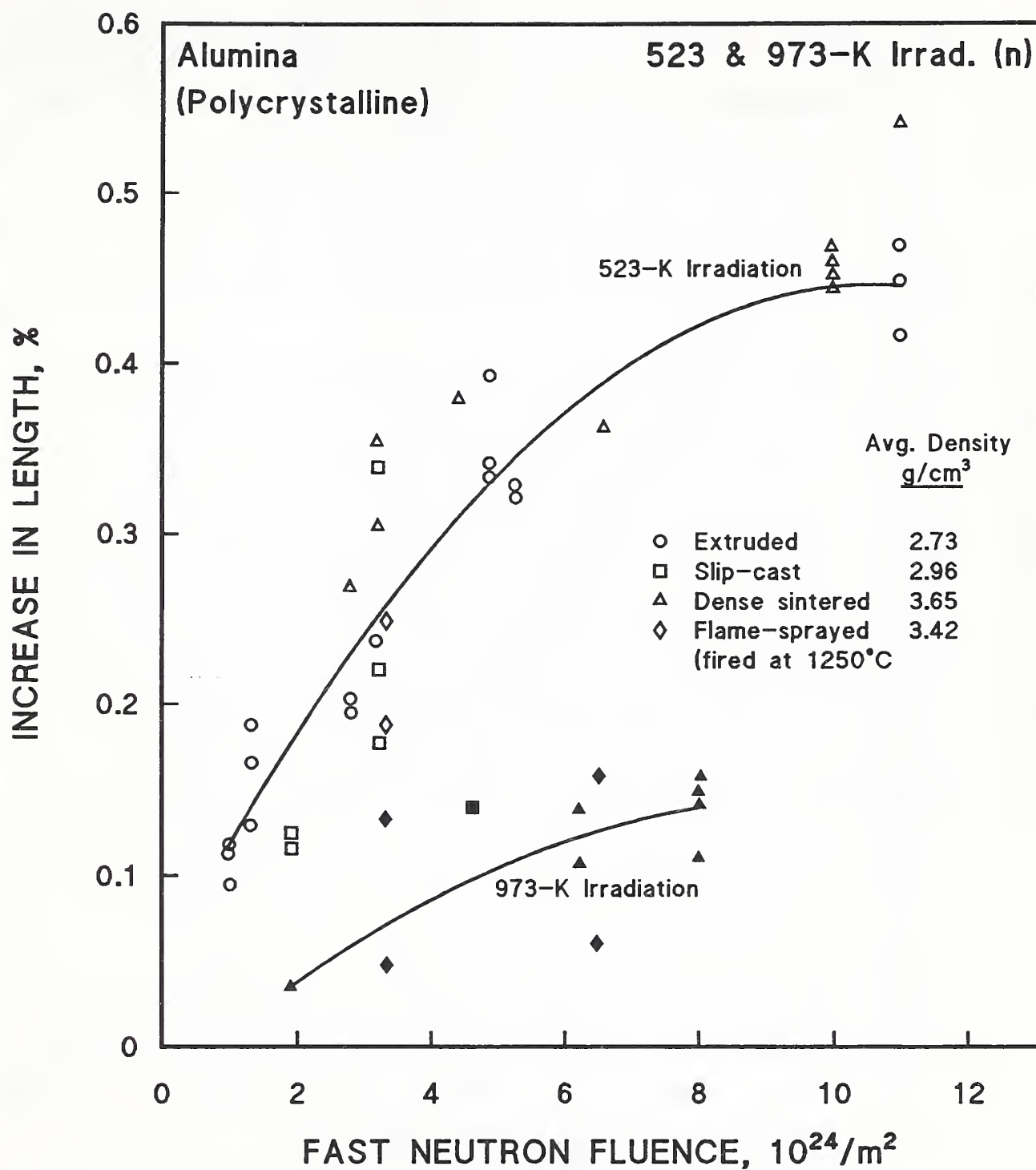


Figure 1.3.5. Increase in length of polycrystalline Al_2O_3 after neutron irradiation at 523 and 973 K. Data from Thorne and Howard [1967].

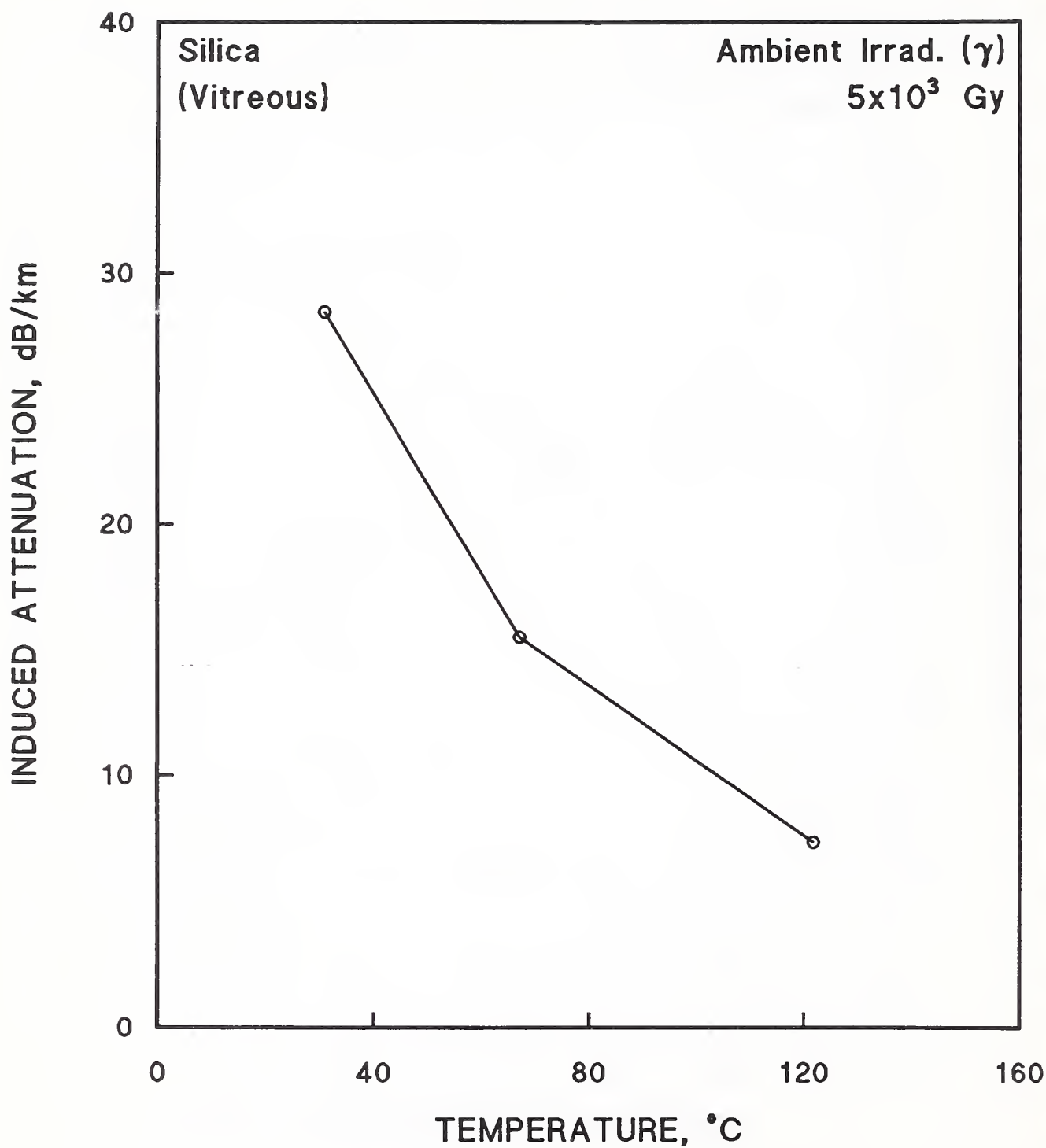


Figure 1.3.6. Temperature dependence of induced optical attenuation in vitreous SiO_2 after γ irradiation at the indicated temperature. Data from Tanaka et al. [1982].

Since the damage microstructure, as well as the density of Frenkel defects, can vary with temperature, it is not possible to use the results of irradiations at higher temperatures to validate inorganic insulation for service at 4 K. However, since so few data are available at 4 K, results of irradiations at ambient temperature and other cryogenic temperatures will be used in this report to rank, or screen, potential inorganics for use in ITER TF magnets, and to estimate swelling at 4 K. (Unless specifically noted in a figure, the irradiation temperature for data presented in this report is not cryogenic.)

One way to derive a predictive factor to estimate 4-K swelling is to compare the predicted, theoretical number of defects (a temperature-independent result) with those actually observed, since these two numbers should be approximately equal only near 4 K, where thermal recombination is very much inhibited. Figure 1.3.7 shows this comparison with theory for single-crystal MgO under 3-MeV Ne-ion irradiation [Evans, 1974]. The F^+ centers, which represent O vacancies, can be detected by optical methods. The Lindhard, Scharff, and Schiøtt [1963] theory was used to determine the portion of the incident energy used in ionization (§1.2.1). By subtracting this ionization energy, the amount of energy available for defect production was found. At an ion fluence of about $10^{16}/\text{m}^2$, before the decrease in efficiency owing to saturation-induced recombination (and, the possible onset of amorphization [Krefft and EerNisse, 1978]), the difference between theory and experiment is slightly less than a factor of 10. The results for 80-K irradiations approach theory more closely, but are still considerably below it.

Figure 1.3.8 shows the increase in swelling of Al_2O_3 under 4-MeV Ar ion irradiation as the temperature is lowered [Pells and Murphy, 1992]. The actual increase in swelling produced at high fluences, rather than the defect density, is shown to be higher by at most a factor of 5/3, taking into account the estimated error of the measurement. However, the swelling was measured at ambient temperature, which permitted recovery. Figure 1.3.9 shows the density of defects from N ion irradiation, as measured by the optical absorption. Before saturation, the defect density was about a factor of 30 higher after 77-K irradiation than after 300-K irradiation. The defect density was measured at 77 K, without warming up the specimens. When a similar experiment on Al_2O_3 was conducted by Atobe and Nakagawa [1987], the defects produced by

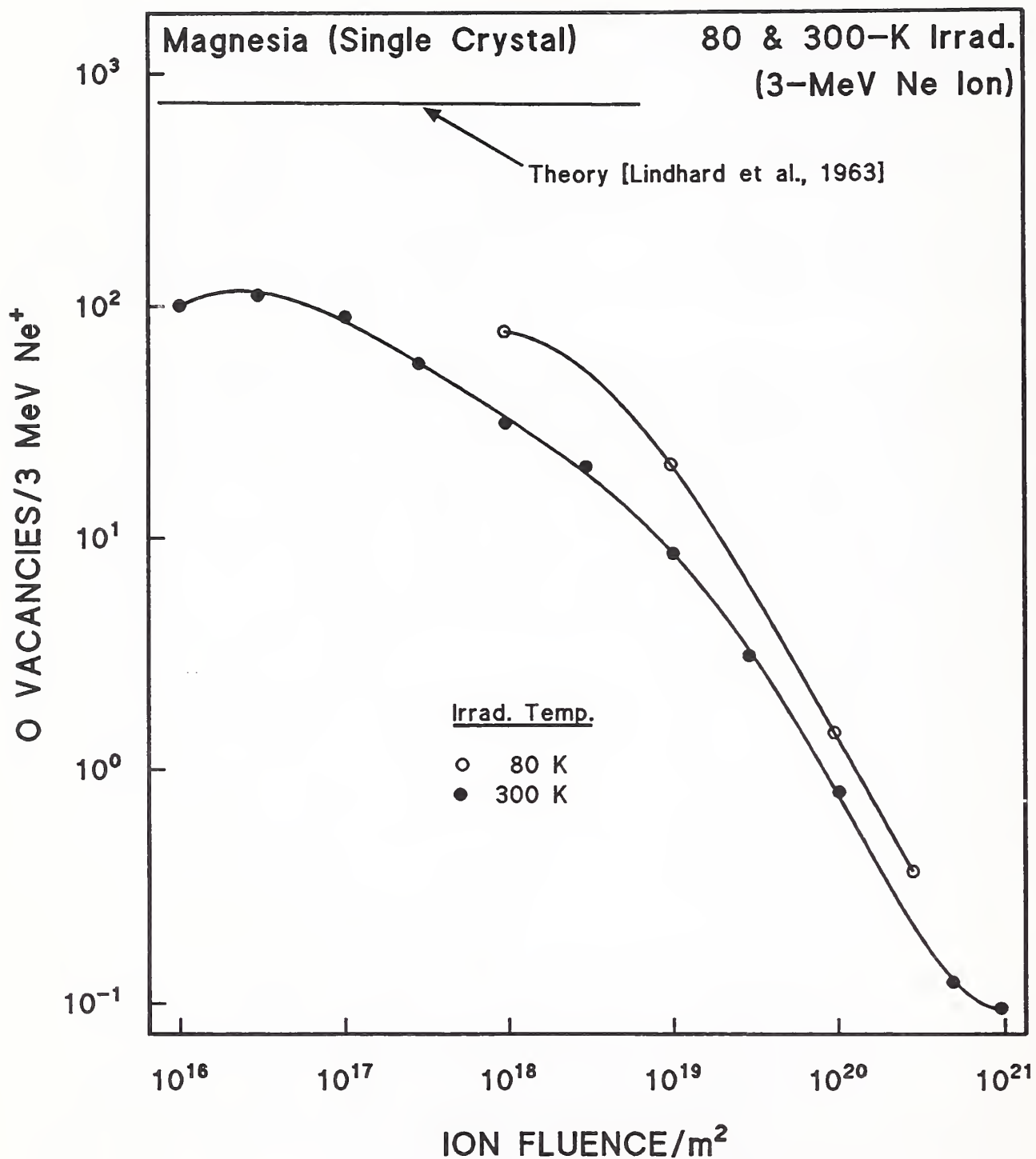


Figure 1.3.7. Oxygen vacancies produced in MgO as a function of Ne-ion fluence at 80 and 300 K, compared with the Lindhard, Scharff, and Schiøtt theory. Data from Evans [1974].

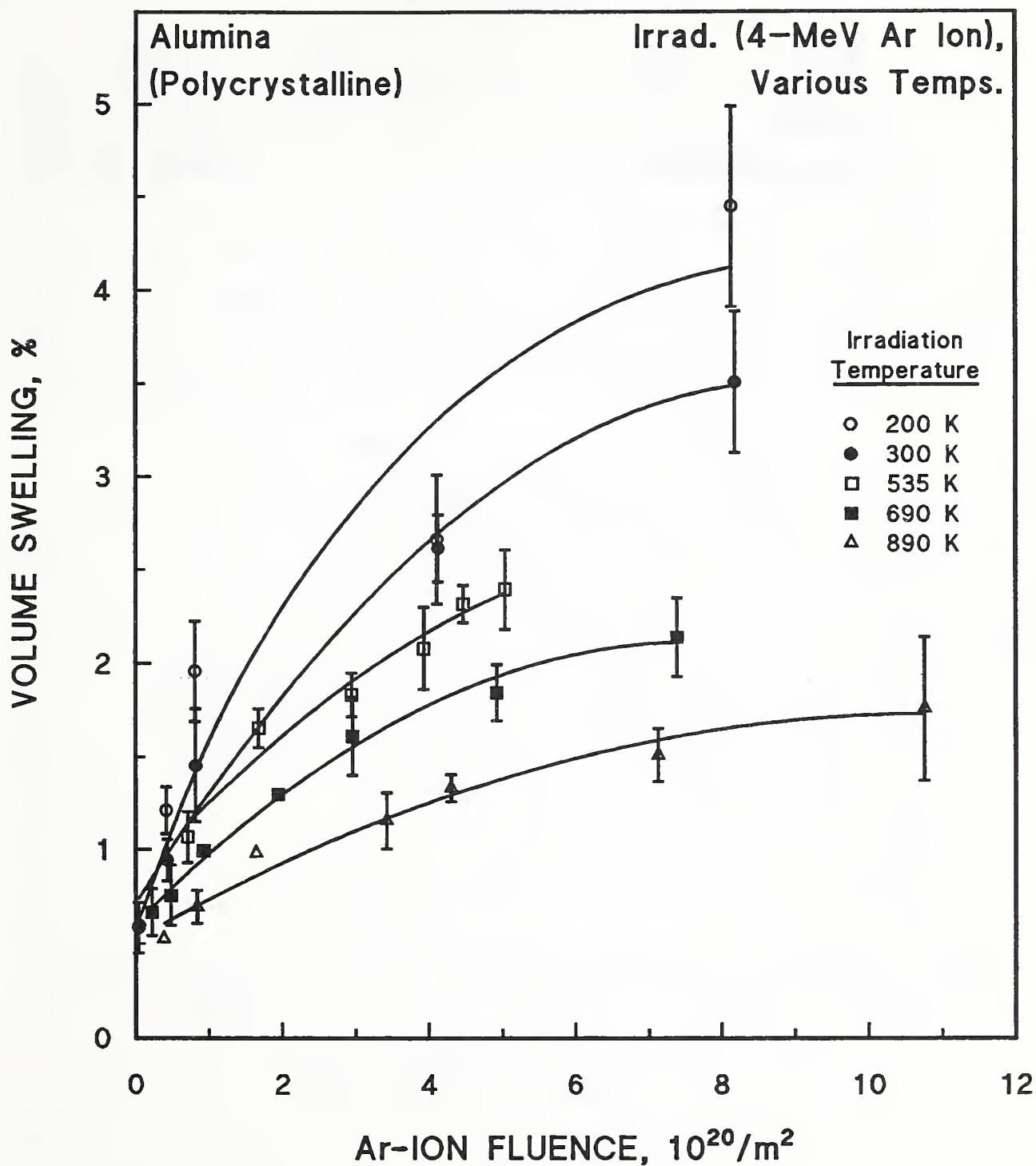


Figure 1.3.8. Increase in swelling of polycrystalline Al_2O_3 as Ar-ion irradiation temperature is varied from 890 to 200 K. Data from Pells and Murphy [1992].

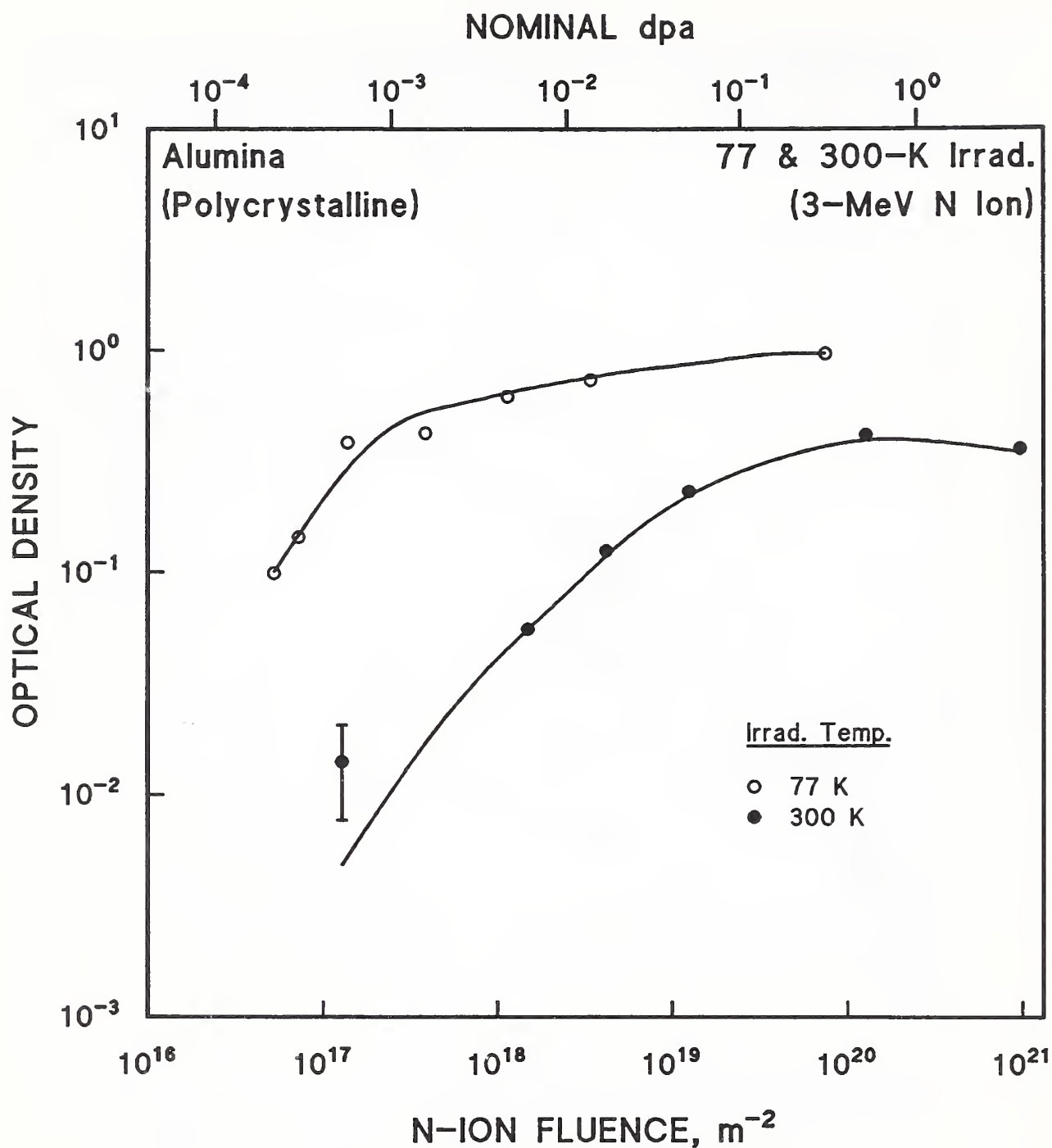


Figure 1.3.9. The optical density at the peak of the Al₂O₃ F-center (O vacancy with 2 trapped electrons) absorption band after irradiation with 3-MeV N ions. The nominal dpa scale includes both Al and O displacements. Optical measurements were made at the irradiation temperature. Data from Pells and Murphy [1992].

neutron irradiation at 15 K were measured at ambient temperature. As Figure 1.3.10 indicates, the difference in defect concentration between irradiation at 15 K and 360 K was not so large as that determined by Pells and Murphy. Presumably, this occurred, despite the lower irradiation temperature, because specimens were warmed up before measurement of the optical density. The surviving defects from the 15-K irradiation were found to have a different (higher) dose dependence, as Figure 1.3.10 indicates. They also had a different thermal behavior, as indicated by the annealing curve (Figure 1.3.11). Whether these differences can be accounted for by partial annealing at ambient temperature before measurement, or indicate real differences in damage microstructure, is unclear.

The largest differences found between defect production at 77 K and 300 K was the factor of about 31 obtained by Pells and Murphy for Al_2O_3 . Comparable figures between 4 and 77 K do not exist for insulators, but Vook and Wert [1958] found a 64% recovery between 17 and 70 K in Cu, giving a factor of about 2.8. (A factor of about 2 may also be derived from the γ irradiation of SiO_2 at 4 and 77 K by Compton and Arnold [1961].) Since the product of 2.8 and 31 is 86, it appears conservative to estimate a difference of about 100 between irradiation defect production at 4 K and reactor temperatures near ambient (~ 40 to 60°C). It is unfortunate that more direct evidence is not available, and a more conservative factor could be as high as 500, based on the 77-K fluence of amorphization reported by McHargue et al., especially since some irradiation temperatures and fluences from early work are uncertain [Garner et al., 1990]. In discussing the results for individual inorganic insulators in §§2 to 10, the screening factor of 100 will be used, where feasible, to estimate their relative performance at 4 K. Since defect production is expected to be approximately linear with dose below a neutron fluence of $10^{22}/\text{m}^2$, ambient effects at $10^{24}/\text{m}^2$ may correspond roughly to effects from $10^{22}/\text{m}^2$ at 4 K. This approximation is intended only to screen candidate insulators, and not to substitute for 4-K, in situ testing to obtain design data after 4-K irradiation with a fusion-equivalent, fast neutron fluence of $10^{22}/\text{m}^2$.

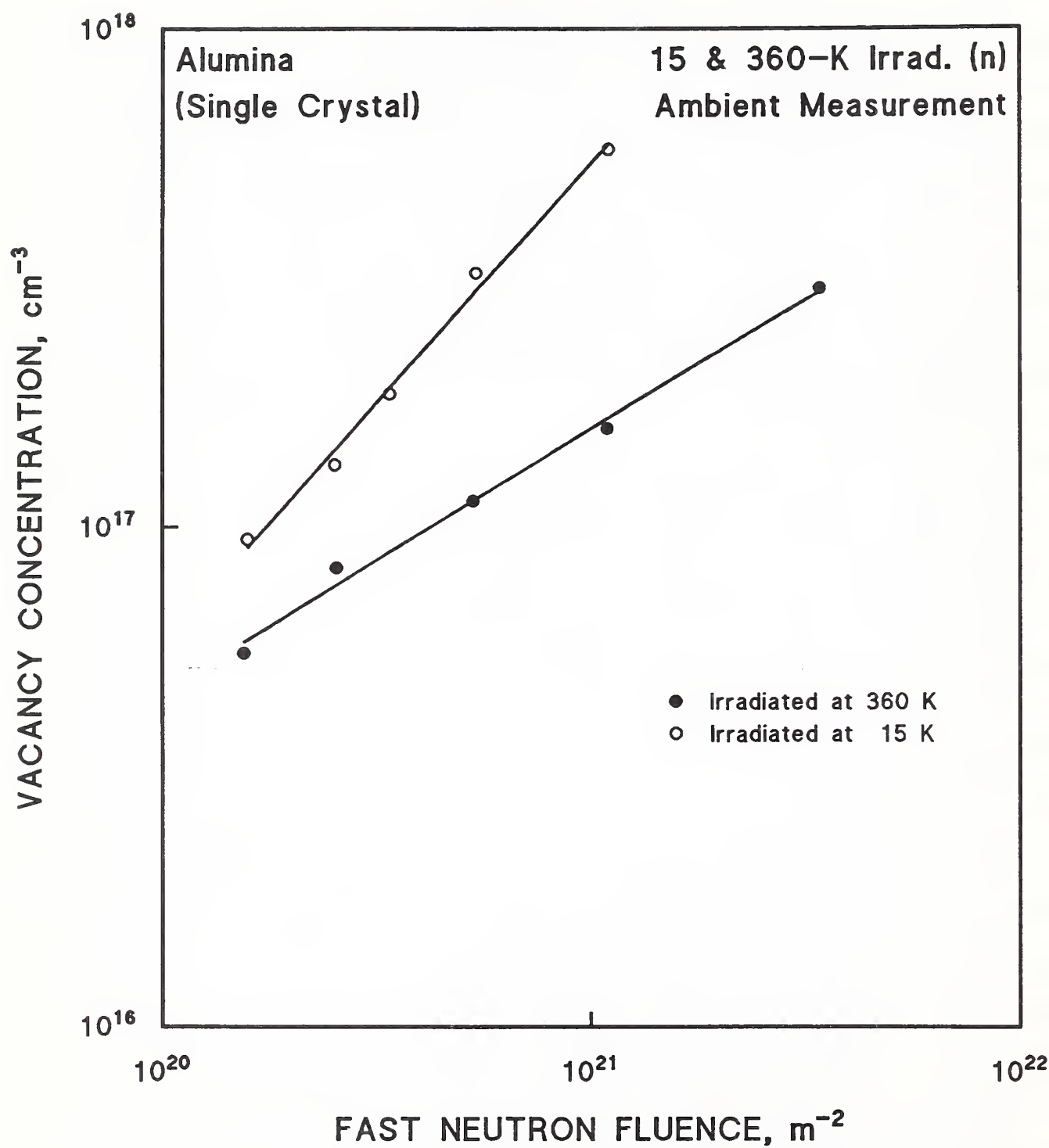


Figure 1.3.10. Comparison of the O vacancy concentration measured at ambient temperature after irradiations of single-crystal Al_2O_3 at 15 and 360 K. Data from Atobe and Nakagawa [1987].

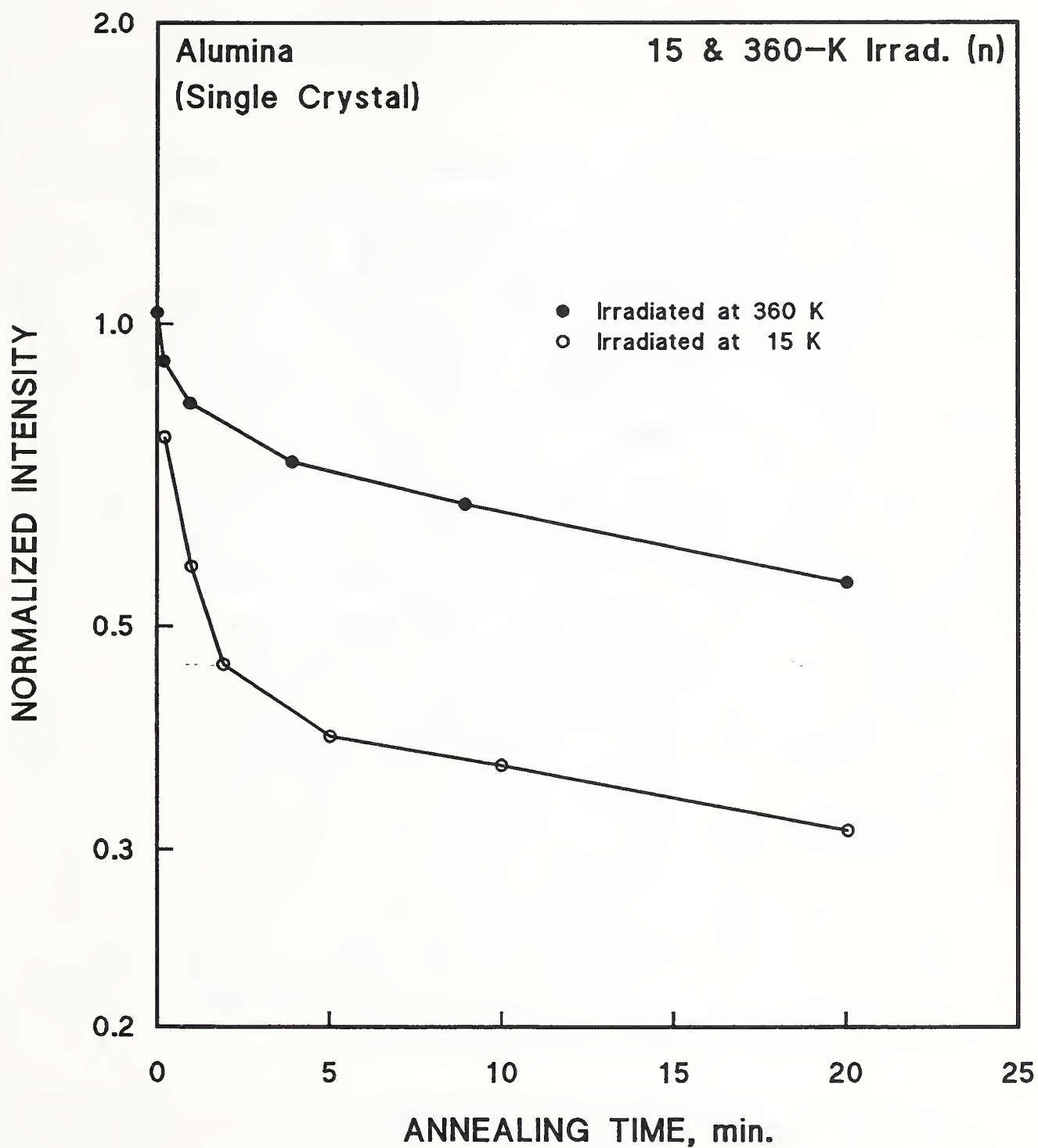


Figure 1.3.11. Annealing behavior at 670 K of defects created at 15 and 360 K in single-crystal Al_2O_3 . Data from Atobe and Nakagawa [1987].

1.4. DAMAGE FROM VERY HIGH ENERGY NEUTRONS ($E \geq 5$ MeV)

1.4.1. General Principles

With changes in shielding design from the CDA to the EDA, the very high energy component ($E \geq 5$ MeV) of the neutron spectrum increased from about 1.7 to about 7% of the total neutron fluence. Consequently, the effects of this part of the spectrum are now of greater importance. First, an increase in displacement damage is expected from an extension of Figure 1.2.2 from Norgett et al. [1975] to somewhat higher energies. Norgett et al. used energy partition functions expected to be valid below PKA energies of $25Z^{4/3}$ keV. For O this limit is about 6.4 MeV. Since the maximum O PKA energy is 0.22 times the incident neutron energy, even for a 10-MeV neutron, the PKA energy of ~2.2 MeV would be well below the limit. Constituent PKA energies of atoms of higher mass, such as Al, Mg, and Si, will also be below this limit. Using the simpler approximation of Equation (1.2), rather than the more elaborate energy partition formulas given by Norgett et al., an oxygen PKA that received 2.2 MeV from a 10-MeV neutron (if $E_d \approx 60$ eV), could generate, at most, $\sim 2.2 \text{ MeV} / 120 \text{ eV} \approx 18,000$ displacements. Owing to the energy lost in ionization, the actual damage energy for displacement will be lower than 2.2 MeV by a factor of about 3 or 4, but even a yield of 4000 to 6000 displacements is a significant increase over the yield, or number of displacements, from an incident neutron of ~0.1-MeV energy. The total number of displacements is determined by the integration of the yield, cross section and flux spectrum. The cross section for elastic collisions for O remains at or above a range of 2 to $1 \times 10^{-28} \text{ m}^2$ (barns) as the neutron energy varies from 0.8 to 14 MeV [McLane et al., 1988]; Figure 1.4.1 shows that the cross section of SiO_2 does not decline significantly between 0.01 and 14 MeV [Primak, 1980].

The second significant effect of neutrons with $E \geq 5$ MeV is that transmutation reactions begin to occur in this energy range. The occurrence of transmutation reactions in this energy range may be understood by reference to the schematic diagram, Figure 1.4.2, which indicates the potential energy function of a charged particle (proton) and a neutron near a nucleus. Although a neutron can approach the nucleus and literally "fall in," a charged particle approaching the nucleus must have enough kinetic energy (classically) to

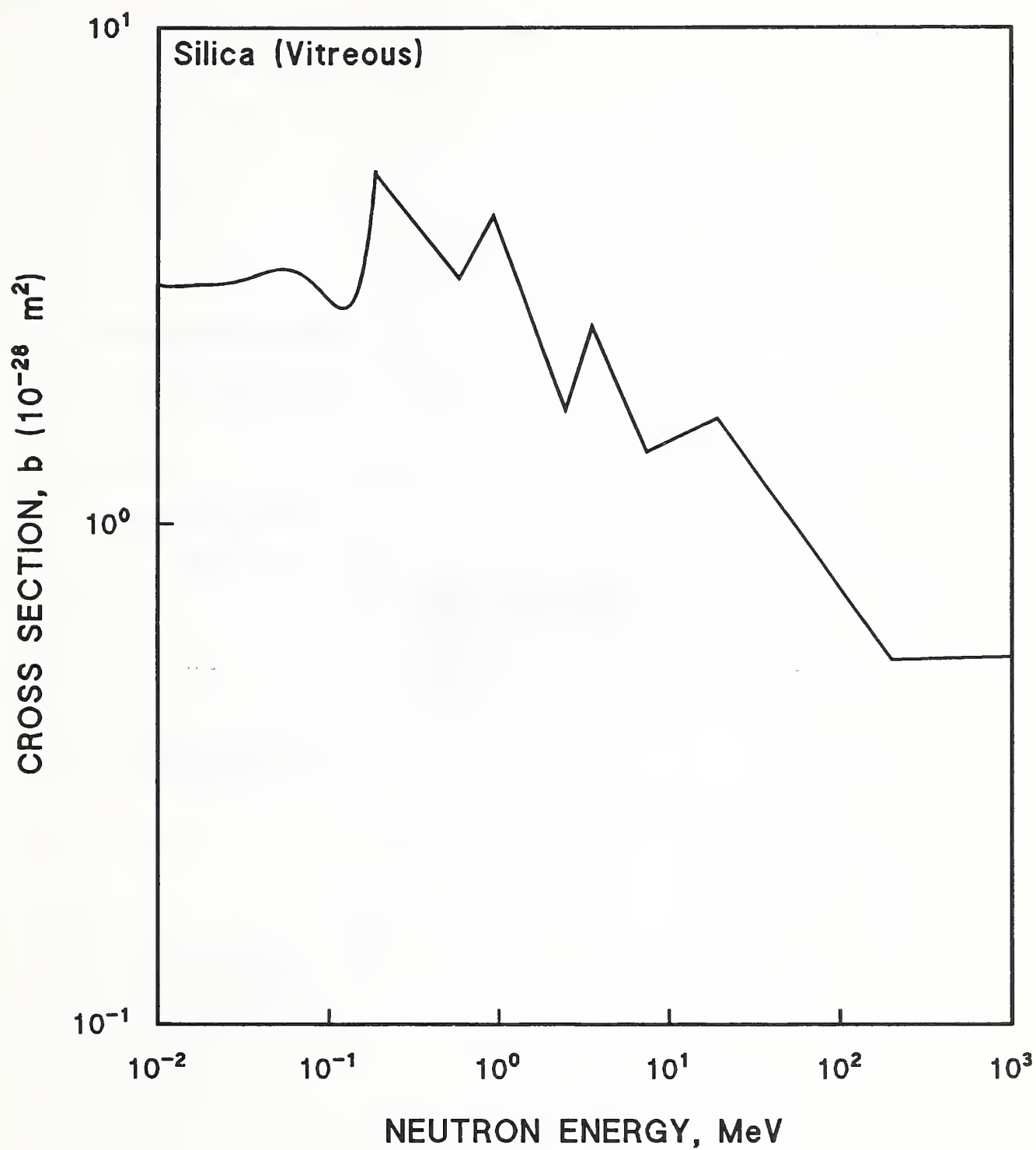


Figure 1.4.1. The neutron cross section for SiO₂ between 0.01 and 1000 MeV. Data from Primak [1980].

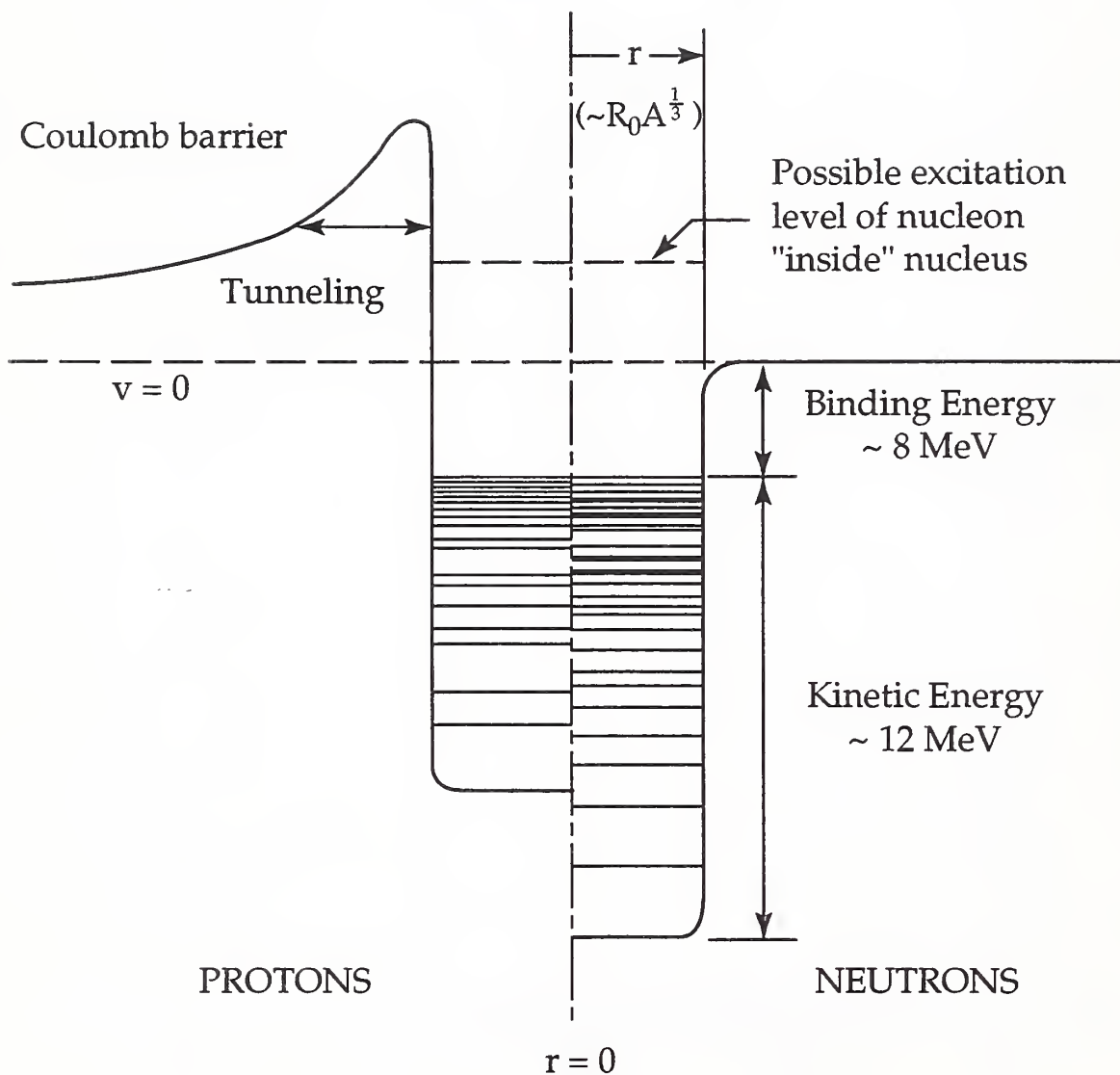


Figure 1.4.2. The potential energy function of a proton and a neutron near a nucleus.

overcome the Coulomb barrier. (Of course, the principles of quantum mechanics allow some penetration of the barrier.) It is also clear from the figure that the Coulomb barrier must be overcome by a charged particle that is emitted by the nucleus. Since it is only in the very high energy range that enough energy is available to surmount the barrier, transmutation reactions such as (n,p) and (n,α) tend to occur only in this region of the spectrum. (There are only a few exceptions to the rule that thermal neutrons induce solely (n,n') and (n,γ) reactions, notably the $^{10}\text{B}(n,\alpha)^7\text{Li}$ reaction.) Because the radius of a nucleus is approximately proportional to $A^{1/3}$, the Coulomb potential is proportional to $A^{2/3}$. In MeV, for α particles, the Coulomb barrier energy is equal to $1.16A^{2/3}$ [Leighton, 1959]. Thus, the cross section for (n,α) reactions should be shifted to a lower energy range for particles of lower atomic mass; Figure 1.4.3 shows this for several elements. To calculate the number of transmutation events in a target, note that the product of the cross section (for a given process and isotope) and the neutron fluence equals the probability at which that nuclear process occurs, per nucleus of that isotope in the target. The estimated fluence ($E > 5$ MeV) is $1.5 \times 10^{21}/\text{m}^2$, using the fast neutron fluence of $10^{22}/\text{m}^2$ in Table 1.1.1, and scaling the fluence of $5.3 \times 10^{21}/\text{m}^2$ for $E > 5$ MeV given by Sawan [1993] for a fast neutron fluence of $3.6 \times 10^{22}/\text{m}^2$ ($E > 0.1$ MeV) at the front layer of ITER TF magnet insulation.

1.4.2. Neutron Damage from Collisions

Merkle [1974] carried out calculations for Au irradiated by 14-MeV neutrons and found that elastic scattering events accounted for less than 20% of the cascade damage observed by TEM. He concluded that nonelastic events in Au were responsible for the rest of the damage. (The formulation by Norgett et al. encompasses only elastic scattering, but the authors suggested that their calculation should be extended to cover all appropriate nuclear reactions.) In Au, these nonelastic events are mainly due to the $(n,2n)$ reaction, in which the nucleus receives a recoil energy somewhat above 70 keV, on average. This recoil energy is large enough for the formation of energetic displacement cascades. Since the formula for the recoil energy, E_r , is approximately $E_r = E_n/M$, where M is the target mass, the effect of displacements produced by recoil atoms would be larger for the high-energy part of the neutron spectrum.

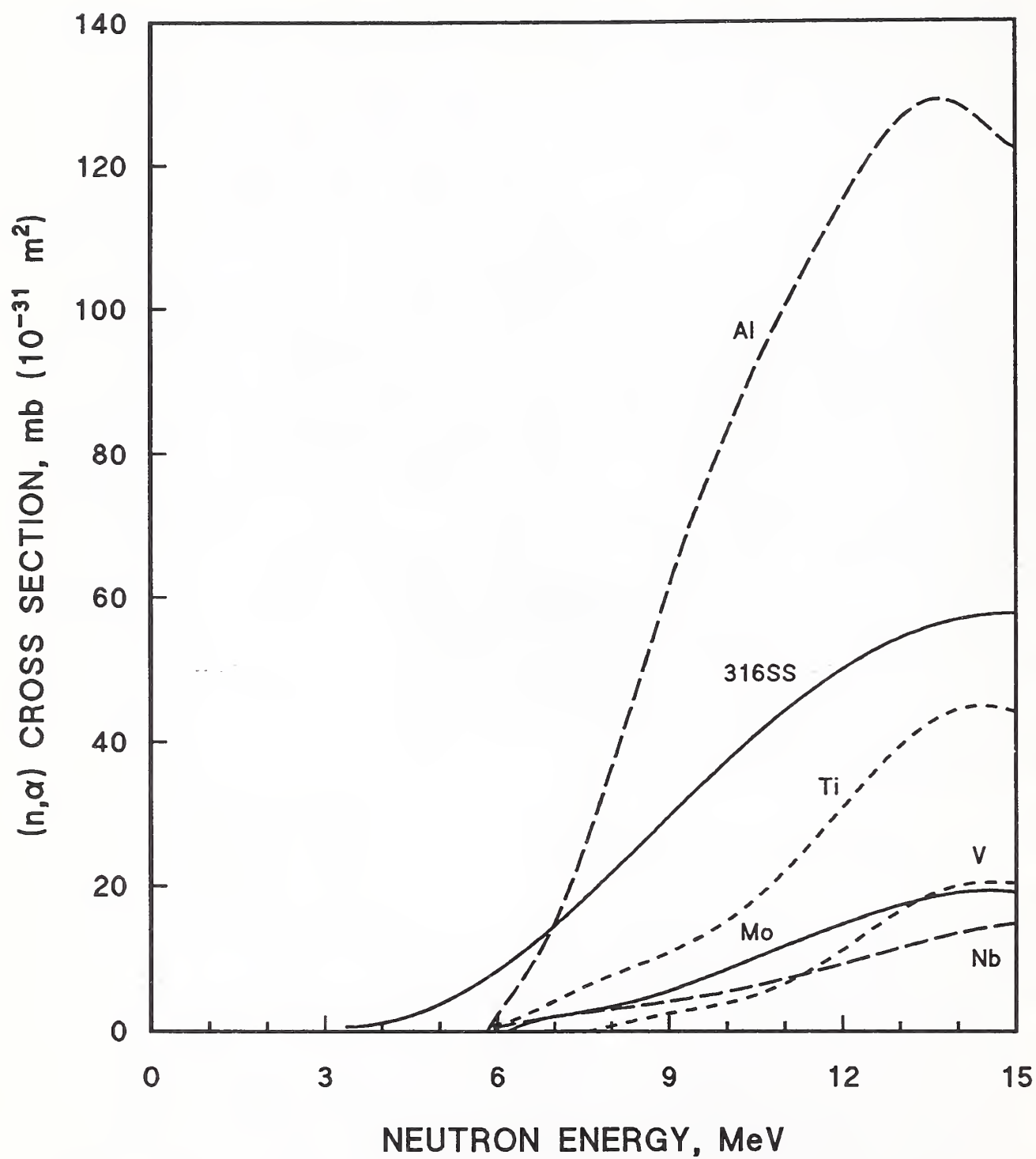


Figure 1.4.3. He production cross sections. Data from Kulcinski [1979].

Cascades of energy below ~30 keV were not observable with the TEM techniques Merkle used for Au; this observational barrier varies for different elements, so it is unclear whether or not there is an enhancement of displacement damage in the region of very high energies due to recoil damage in inorganic insulators. No relevant investigations on this point were found in this literature search.

Primak [1980] used a spallation source to obtain a high energy neutron spectrum from about 0.1 to 500 MeV. This source was used to irradiate vitreous SiO₂ at ambient temperature, and the results were used to verify the calculations shown in Figure 1.4.4. (The calculations are based on an integral of the yield function, cross section, and neutron energy spectrum.) The figure indicates an enhancement of the volume change in vitreous SiO₂ in the part of the neutron spectrum from about 1 to 100 MeV, compared to values at lower energies. The compaction of vitreous SiO₂ should therefore be increased over that measured with a fission spectrum. Primak verified this result, comparing this with the results for radiation damage to graphite from the spallation source with that from a fission reactor.

Tanimura et al. [1987] attempted to compare swelling observed in ambient-temperature, 14-MeV neutron irradiation in MgAl₂O₄ with that obtained from fission irradiation [Coghlan et al., 1986; §§2,7]. For the linear portion of the curves of expansion vs. fluence, they obtained a fractional volume change per unit fluence of neutrons of $3 \times 10^{-23} \text{ cm}^2$ for 14-MeV neutrons, whereas $2 \times 10^{-22} \text{ cm}^2$ had been reported for fission neutrons. However, other work on Al₂O₃ [Evans and Stapelbroek, 1979] and MgO [Chen et al., 1975] showed that twice as many vacancies were created by 14-MeV neutrons compared with fission neutrons of the same fluence. Bunch and Clinard [1974] obtained a factor of 4 difference in defects created by 14-MeV neutrons compared to those created by fission neutrons. The results obtained by Evans and Stapelbroek on Al₂O₃ are shown in Figure 1.4.5. The reasons for the disagreement in the results by Tanimura et al. and the earlier work are not known, but the authors noted that Coghlan et al. observed an increase in swelling of MgAl₂O₄ over several months after the fission reactor irradiation, whereas the fusion-neutron swelling measurements were obtained during irradiation (see §7.2). Also, significant swelling was caused in MgAl₂O₄ by γ irradiation, so the presence of γ rays in

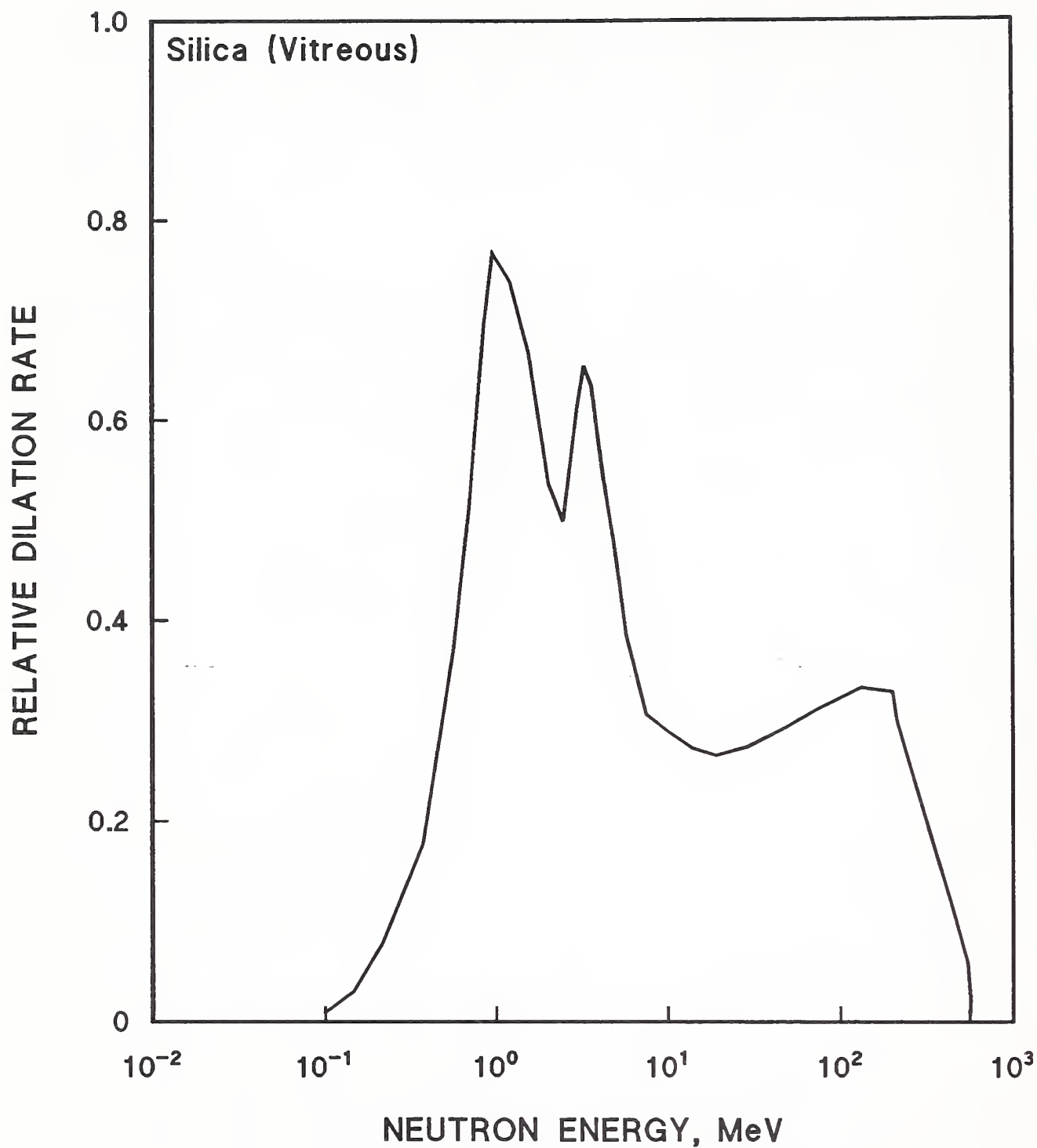


Figure 1.4.4. The relative dilation rate in vitreous SiO_2 exposed to a high energy spallation source of neutrons. Data from Primak [1980].

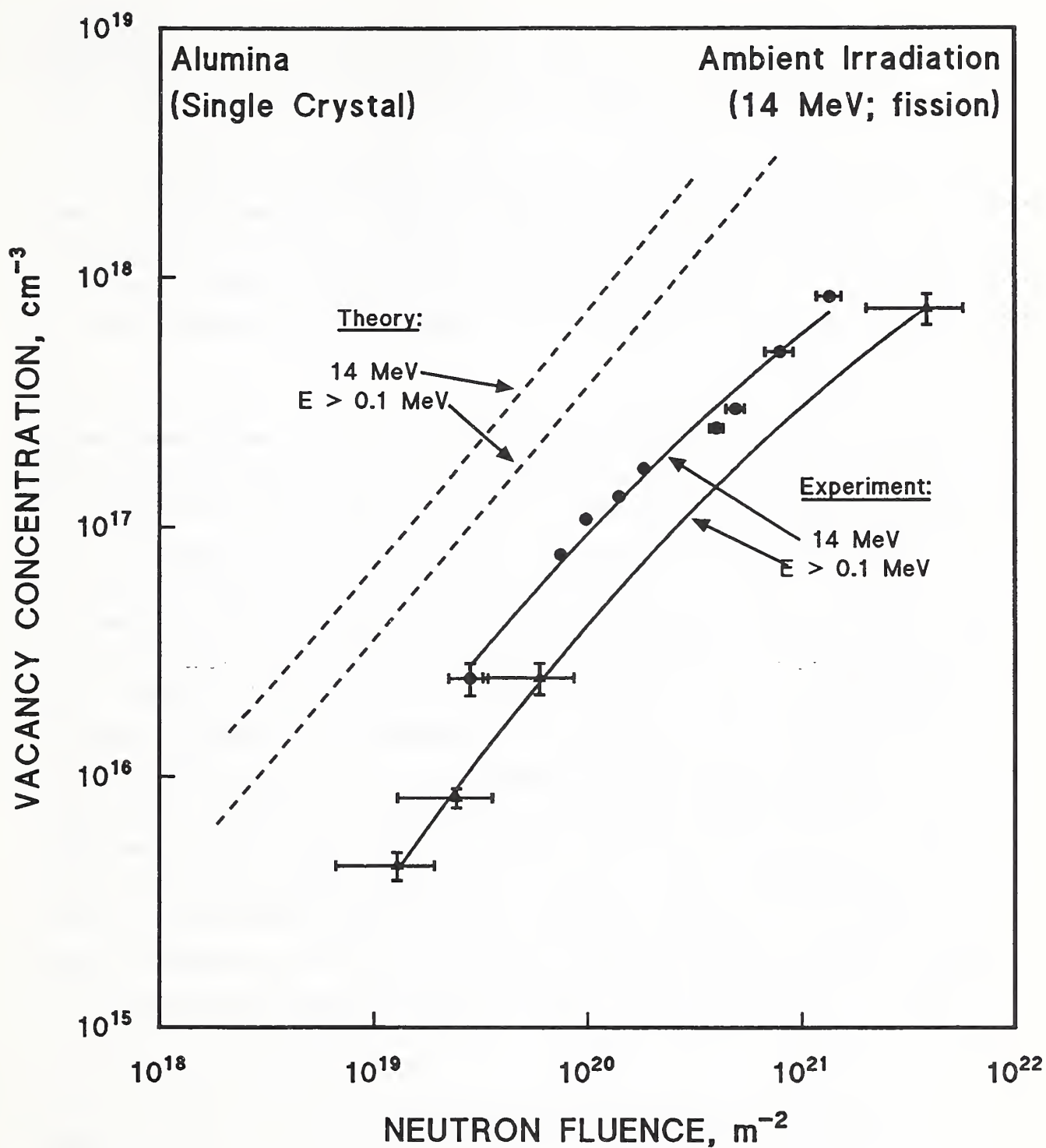


Figure 1.4.5. Oxygen vacancy concentration (F and F^+ centers) in Al_2O_3 produced by 14-MeV neutrons and fission neutrons. Data from Evans and Stapelbroek [1979].

the reactor irradiation may have contributed to a higher degree of swelling. This effect of ionizing energy absorption has been attributed to variations in the charge state of the predominant point defect [Arnold et al., 1974].

Garner et al. [1990] reviewed the translation of fission reactor data to fusion devices, but primarily with regard to alloys irradiated at higher temperatures. However, their cautions on the validity of older data for fluence and temperature, as well as new data on the increase in swelling at lower displacement rates may be relevant to the interpretation of experiments on insulators cited above.

In contrast to these experiments in which defect densities and volume changes were compared, Abdel-Fattah et al. [1981] measured the 14-MeV fluence required for amorphization of porcelain (§5.3). For both quartz and alumina porcelains, amorphization was complete at a fluence of $\sim 2 \times 10^{15}/\text{m}^2$, whereas a fission neutron fluence of $\sim 10^{23}/\text{m}^2$ was required for amorphization of quartz (§6.3). The reason for the factor of $\sim 10^8$ in the effectiveness of 14-MeV neutrons compared to fission-spectrum neutrons instead of the factors of 2 or 4 found by others could be due to the differences in materials compared, or to the nonreversible process of amorphization compared to the lower-fluence processes of volume change, which allow recovery. Long recovery periods may have allowed the density of retained defects from 14-MeV and fission irradiations to approach a similar value; this similarity may not apply to 4-K irradiation damage from very high energy neutrons. All of the examples in which the much smaller factor was found were dependent upon fluence determinations made for the RTNS (Rotating Target Neutron Source) at LLNL (Lawrence Livermore National Laboratory); Abdel-Fattah et al. evidently used an independent source of 14-MeV neutrons.

1.4.3. Production of α Particles and H Atoms

In §9.5.3 below, the possible formation in mica at 4 K of tracks of damaged material or even voids from α particles is discussed with regard to the thermal spike mechanism, which would predict dramatically increased damage as the specific heat decreases at low temperatures. Since the range of α particles is of the order of micrometers, it appears that this aspect of α -particle

damage poses an electrical breakdown problem chiefly for layered materials that may delaminate under irradiation, or for porous or subdivided materials, rather than for bulk insulators. However, surface crazing of vitreous SiO_2 by α beams of energies from 0.5 to 4 MeV has been reported [Primak, 1964], and surface damage could modify bulk electrical breakdown characteristics. The dose in these experiments was not well-defined. Bulk damage in quartz from 1-MeV α particles at ambient temperature was due to atomic collisions, not ionization processes [Toulemonde et al., 1990]. Alpha particle emission energies will typically be of the order of a few MeV.

With regard to the influence of α emission on mechanical properties, several authors have observed or suggested that H and He will tend to deposit at grain boundaries (warm-up may be required for diffusion to such sites) [Clinard, 1979, and citations therein]. This could result in the weakening of materials and even in grain boundary separation [Keilholtz et al., 1964].

The effects of He and H on the microstructure of Al_2O_3 and MgAl_2O_4 have been investigated by simultaneous irradiation with He^+ and Al^+ beams [Zinkle and Kojima, 1991] and by Ar^+ irradiation when He and H had been preimplanted [Yamada et al., 1992]. The He generation rate has been estimated to be ~ 100 appm (atomic parts per million)/dpa at the fusion reactor first wall [e.g., Pells, 1988], but it would be much less in the TF magnets. In these experiments, high ratios of He concentration to dpa were used to simulate first wall conditions, and some irradiation temperatures also were well above ambient. Catastrophic amounts of grain boundary cavitation were observed in MgAl_2O_4 only when the displacement damage was large, ~ 20 dpa. Cavity formation in Al_2O_3 was observed even in specimens irradiated at 25°C , even with a low ratio of ~ 9 appm/dpa that would be characteristic of a fission reactor, and perhaps, TF magnets [Zinkle and Kojima, 1991]. However, a high damage level, ~ 7 to 22 dpa, was achieved in these investigations, and this dpa is not expected at the TF magnets. Cavity formation in Ar^+ -irradiated MgAl_2O_4 occurred only at relatively high temperatures or high doses, but He and H were found to have a much smaller effect on the Al_2O_3 microstructure, since pre-implantation of ions was not necessary for cavity formation [Yamada et al., 1992]. The sizes of the defects were usually about 10 to 15 nm, but in some cases became as large as 100 nm (1000 Å). It is not known if cavity formation

is important for 4-K magnet insulation, since diffusion should be very much inhibited at least until warm-up occurs. However, the dpa expected from a fast neutron fluence of $10^{22}/\text{m}^2$ should be of the order of 10^{-3} to 10^{-4} dpa, using the displacement cross section data for inorganics from Dell and Goland [1981]. This dpa is so far below that at which significant cavity formation was observed at high temperatures that an effect in the ITER TF magnets seems unlikely, although lack of recovery at 4 K could increase some effects.

Pells and Murphy [1991] also simulated transmutation damage in Al_2O_3 and MgAl_2O_4 with preimplantation of He and H, followed by Ar-ion irradiation at high temperatures, from 535 to 1080 K. Figure 1.4.6 shows that polycrystalline Al_2O_3 was not much affected by the preimplantation, but Figure 1.4.7 shows that swelling in MgAl_2O_4 was affected, but only at a high damage dose. Swelling increased from less than 1% to -2% at all irradiation temperatures.

Since there are so many differences between high temperature and cryogenic irradiation, however, exploratory tests of the effects of He and H atoms on the cryogenic damage microstructure would be of interest. The methods described above for high temperature studies could be used, although the lack of cryogenic irradiation facilities may make some procedures unwieldy. Another possibility is the use of isotopically tailored ceramics [Labauve et al., 1988]. In this approach, the thermal neutron reactions $^{17}\text{O}(n,\alpha)^{14}\text{C}$ and $^{14}\text{N}(n,p)^{14}\text{C}$ were used in Al_2O_3 and $\text{Si}_3\text{Al}_3\text{O}_3\text{N}_5$ (sialon) to introduce controlled amounts of He and H. For first wall simulation, 18 to 91% isotope addition was necessary; amounts for TF magnet simulation should be much lower.

Table 1.4.1 from Pells [1988] gives the calculated transmutation product yield per unit dpa for most of the insulators considered in this survey. These calculations were done for a first wall spectrum, but since transmutation production may be about a factor of 10 lower at the TF magnets, the table is useful only in a relative sense. In this sense, the H production for AlN is relatively high, but He production is similar for all of the insulators. Figure 1.4.8 gives the (n,α) cross section for some inorganic insulator atoms of interest: N, O, Mg, Al, and Si.

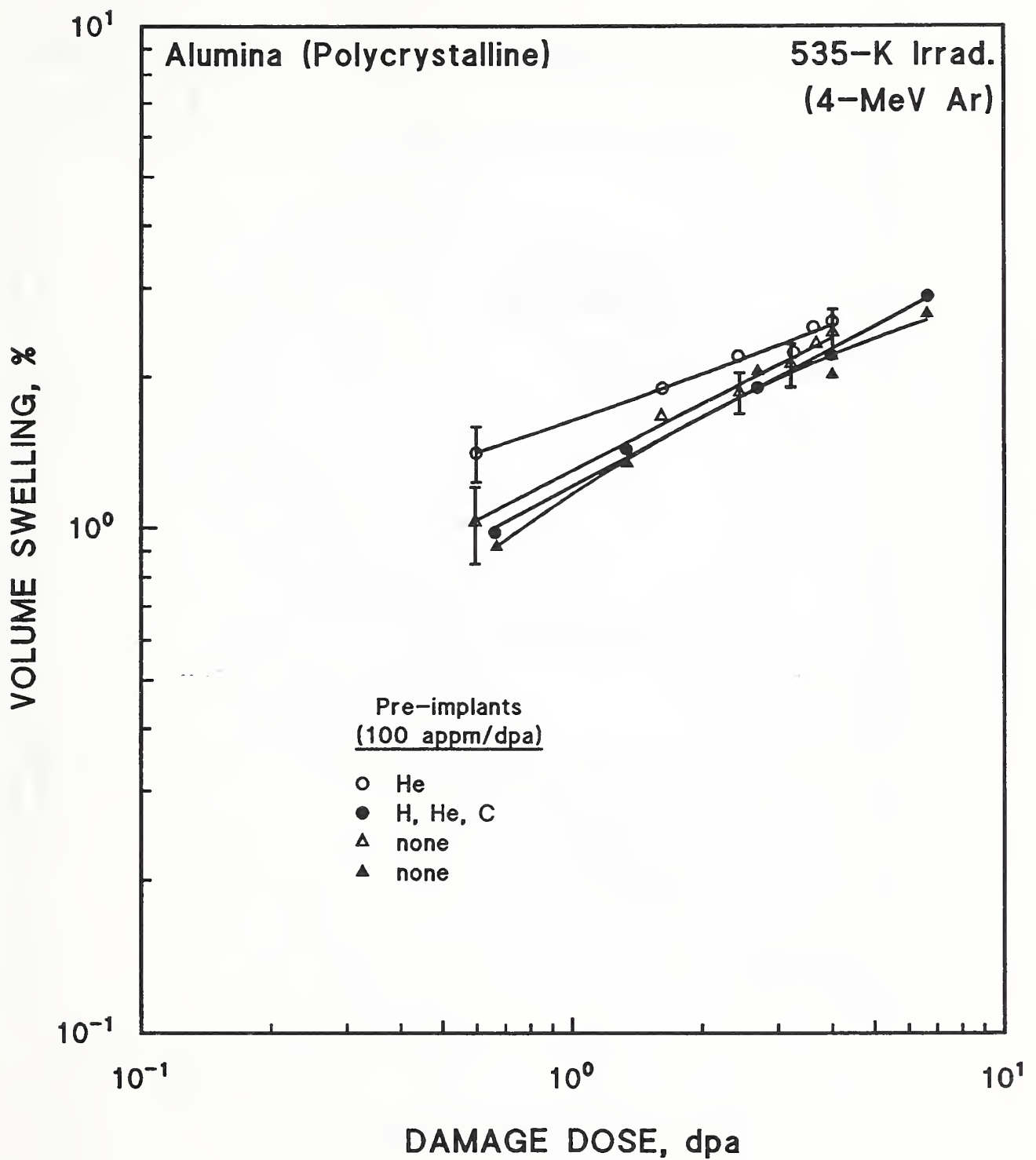


Figure 1.4.6. Swelling of polycrystalline Al_2O_3 after Ar irradiation at 535 K, with and without preimplantation of H and He. Data from Pells and Murphy [1991].

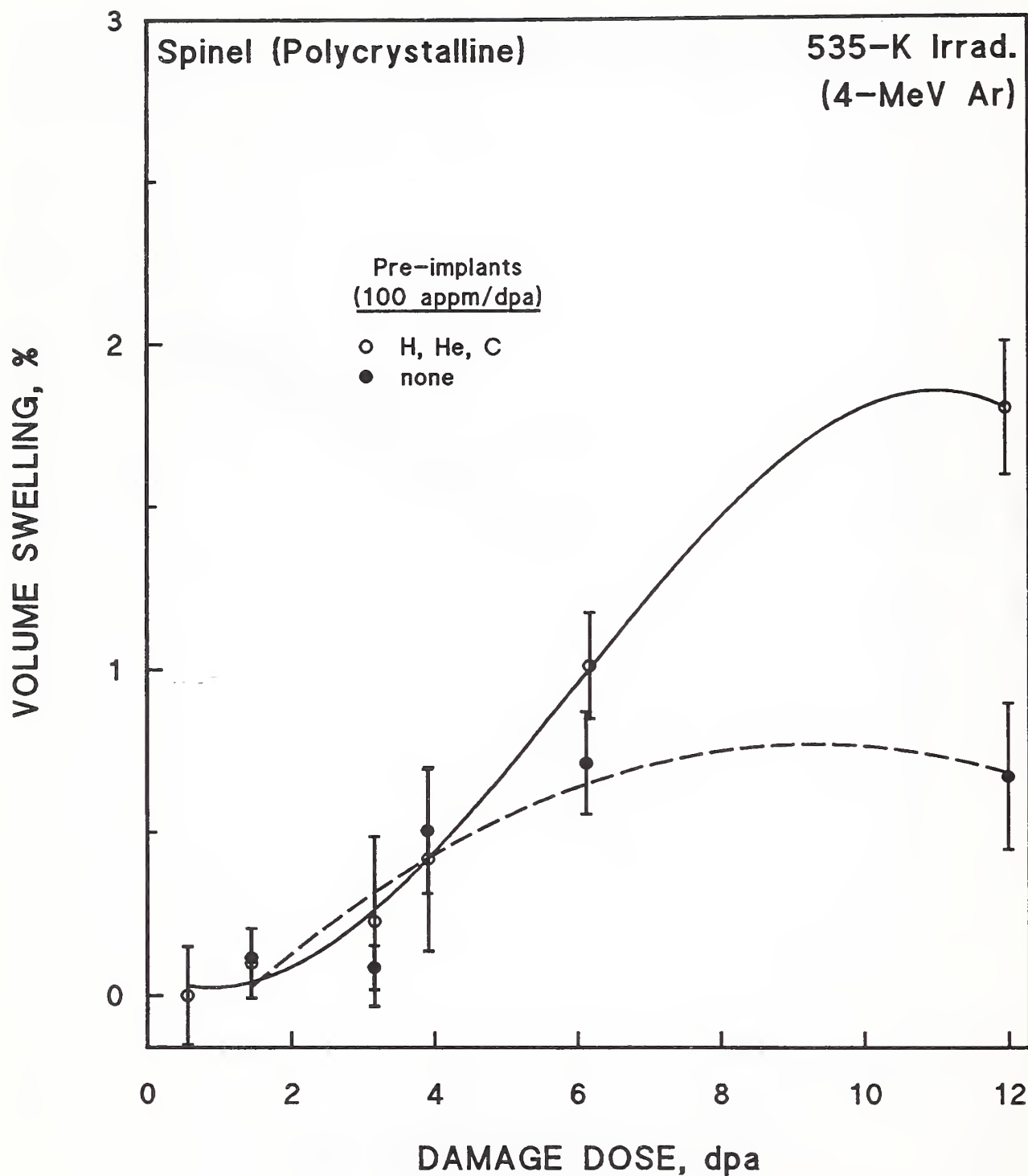


Figure 1.4.7. Swelling of polycrystalline MgAl_2O_4 after Ar irradiation at 535 K, with and without preimplantation of H and He. Data from Pells and Murphy [1991].

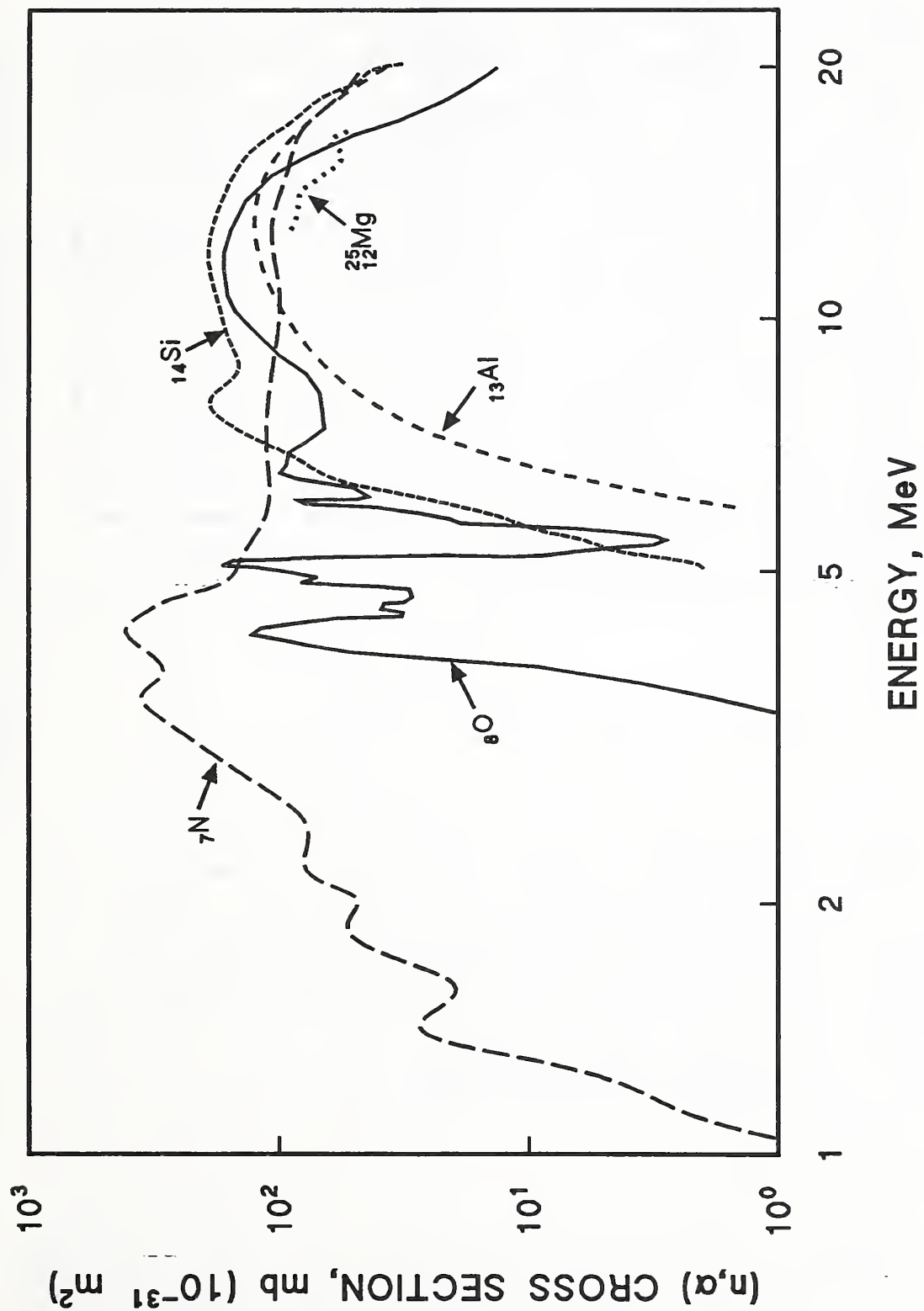


Figure 1.4.8. Cross sections for n, α production for N, O, Mg, Al, and Si. Very sharp resonance spikes and other fine structure in the curves are not shown. Data from McLane et al. [1988].

Table 1.4.1. Calculated Transmutation Product Yields per Unit dpa for Low Z Insulator Atoms. Calculations from Pells [1988].

TRANSMUTATION PRODUCT	TRANSMUTATION PRODUCT YIELD, appm/dpa*				
	MgO	Al ₂ O ₃	MgAl ₂ O ₄	AlN	SiO ₂
He	85	170	134	376	66
H	148	192	165	142	100
B	—	—	—	83	—
C	110	149	128	193	84
N	10	14	12	—	1
Na	31	—	9	—	1
Na	5	—	2	—	1
Mg	—	149	—	206	15
Al	—	—	—	—	1
Si	—	2	1	3	—

* Calculated for $E_d = 40$ eV. The appm/dpa ratio may be adjusted by multiplying by $E_d(\text{new})/40$ eV.

1.5. WARM-UP: RECOVERY AND ANNEALING

It is difficult to obtain guidance from the literature about the extent of recovery, during magnet warm-up at ambient temperature, of damage incurred in insulators at 4 K. A relevant experiment would require that a specimen be irradiated at 4 K and that a property change be measured in situ. Then, anneals would be carried out for specified periods at higher temperatures, after which the property would again be measured at 4 K. Only a few authors have followed this protocol, and only for initial measurements at liquid nitrogen temperatures, rather than at 4 K. The results of McDonald [1963] were shown above, in Figure 1.3.3. McDonald measured the increase in thermal resistivity of BeO in situ after irradiations at about 91 K (Figure 1.5.1), and then measured the recovery, after 15-min anneals, up to ambient temperature. The thermal resistivity increased by a factor of 3 after a fast neutron fluence of $1.5 \times 10^{21}/\text{m}^2$ ($E > 0.6$ MeV), but only about 25% of this increase

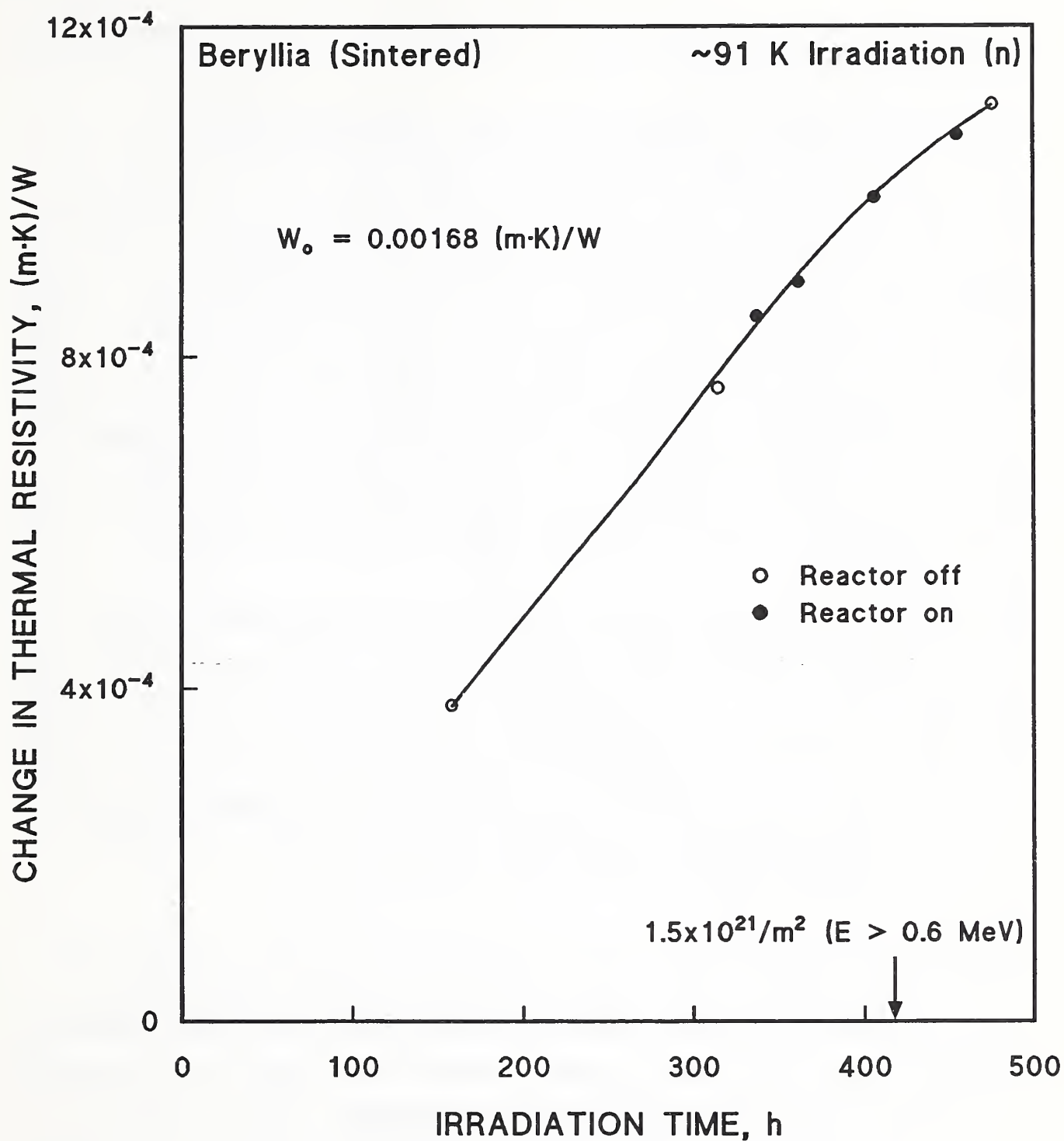


Figure 1.5.I. The increase in thermal resistivity of sintered BeO vs. irradiation time. Both irradiation and measurement at ~91 K. Data from McDonald [1963].

annealed during recovery. However, this may have been due to the short annealing periods of 15 min.

The recovery experiment of McDonald was ideal, at least for the temperature range and annealing times investigated. Several other recovery experiments in which irradiation was also done at cryogenic temperatures are less useful, because the property measurements were made at ambient temperature. For example, Chen et al. [1969] measured the 250-nm optical absorption band of MgO at ambient temperature after irradiation at 153 K. This band indicates the presence of O^- vacancies (§4.1). When the irradiated specimens were annealed at temperatures up to 600°C for unspecified periods, the recovery of the optical absorption was very similar to that recorded for specimens irradiated at about 50 to 70°C. However, in both cases, regardless of the irradiation history, the recovery of defects surviving at ambient temperature was measured; therefore, it was not surprising that the results were similar.

The same problem occurs with the optical absorption measurements of Atobe et al. [1985] on single-crystal Al_2O_3 irradiated at 23 K to a fast neutron fluence of $4 \times 10^{20}/m^2$. The 203-nm optical band monitored also indicated the presence of O^- vacancies or displacements. Again, the recovery curve, shown in Figure 1.5.2, is based on ambient-temperature measurements, so the results indicate the recovery of defects that survived at ambient temperature, not the recovery at ambient temperature of defects generated at 23 K. The latter quantity would be of greater interest for ITER TF magnets.

Nevertheless, these recovery data and Figures 1.5.3 to 1.5.5, covering high temperature recovery of Al_2O_3 , MgO, and vitreous SiO_2 after neutron irradiation at ambient temperature, indicate the persistence of some types of defects to temperatures of about 400 to 600°C. Figure 9.5.11 below, on the annealing of heavy-ion mica tracks, also indicates persistence of damage to approximately this temperature range. These persistent defects probably reflect the stabilization of multi-defect clusters that occur in neutron damage cascades, owing to the proximity of many individual defects. For example, Bowen and Clarke [1964] found that above a critical fluence of about $4 \times 10^{24}/m^2$ ($E > 1$ MeV), defect clusters (dislocation loops) were so large in single-crystal MgO that they degenerated into a tangle of dislocation lines upon heating and

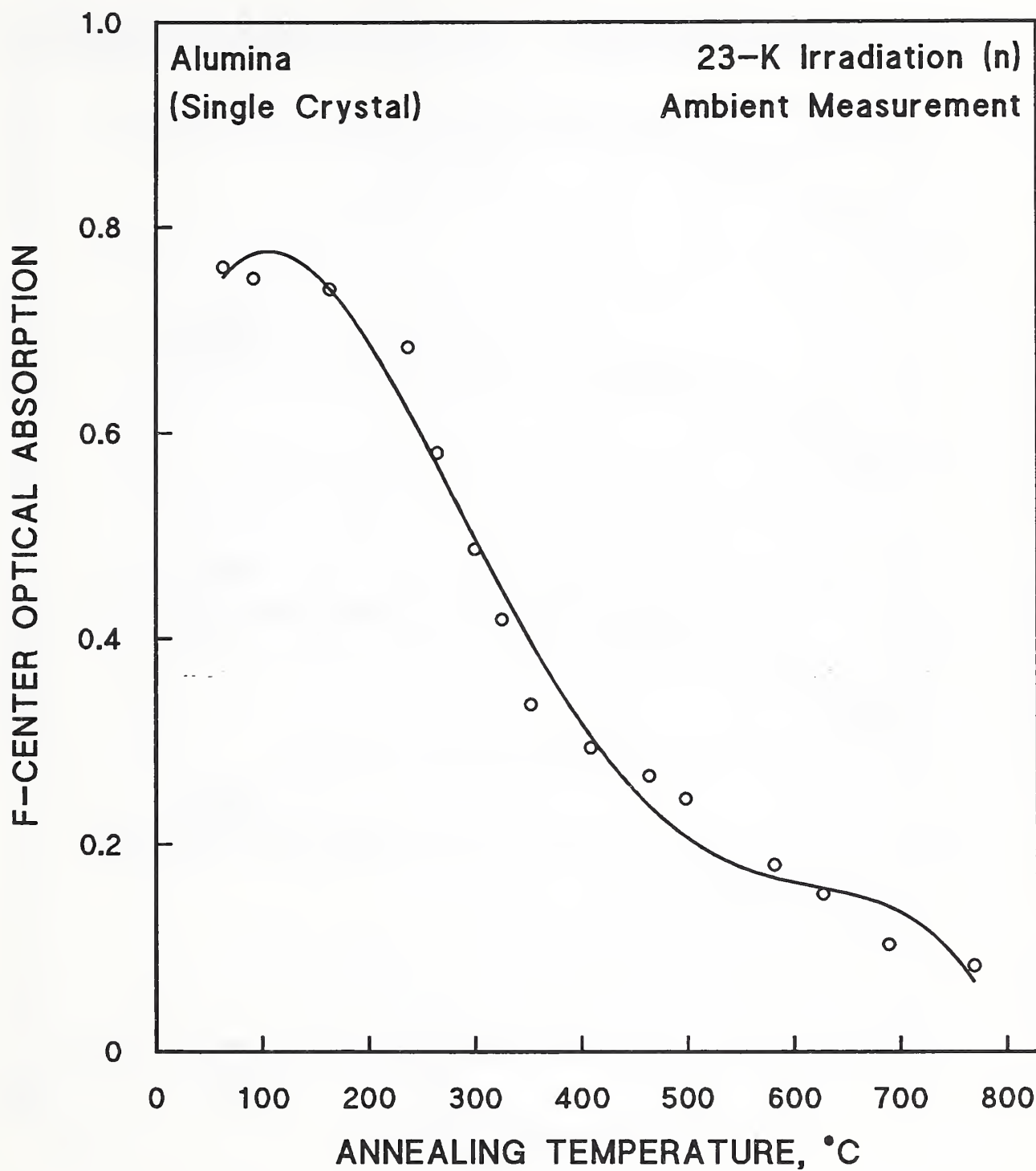


Figure 1.5.2. Decay of the optical absorption band indicating the presence of O vacancies in single-crystal Al_2O_3 after neutron irradiation at 23 K. Optical measurements were made at ambient temperature. Data from Atobe et al. [1985].

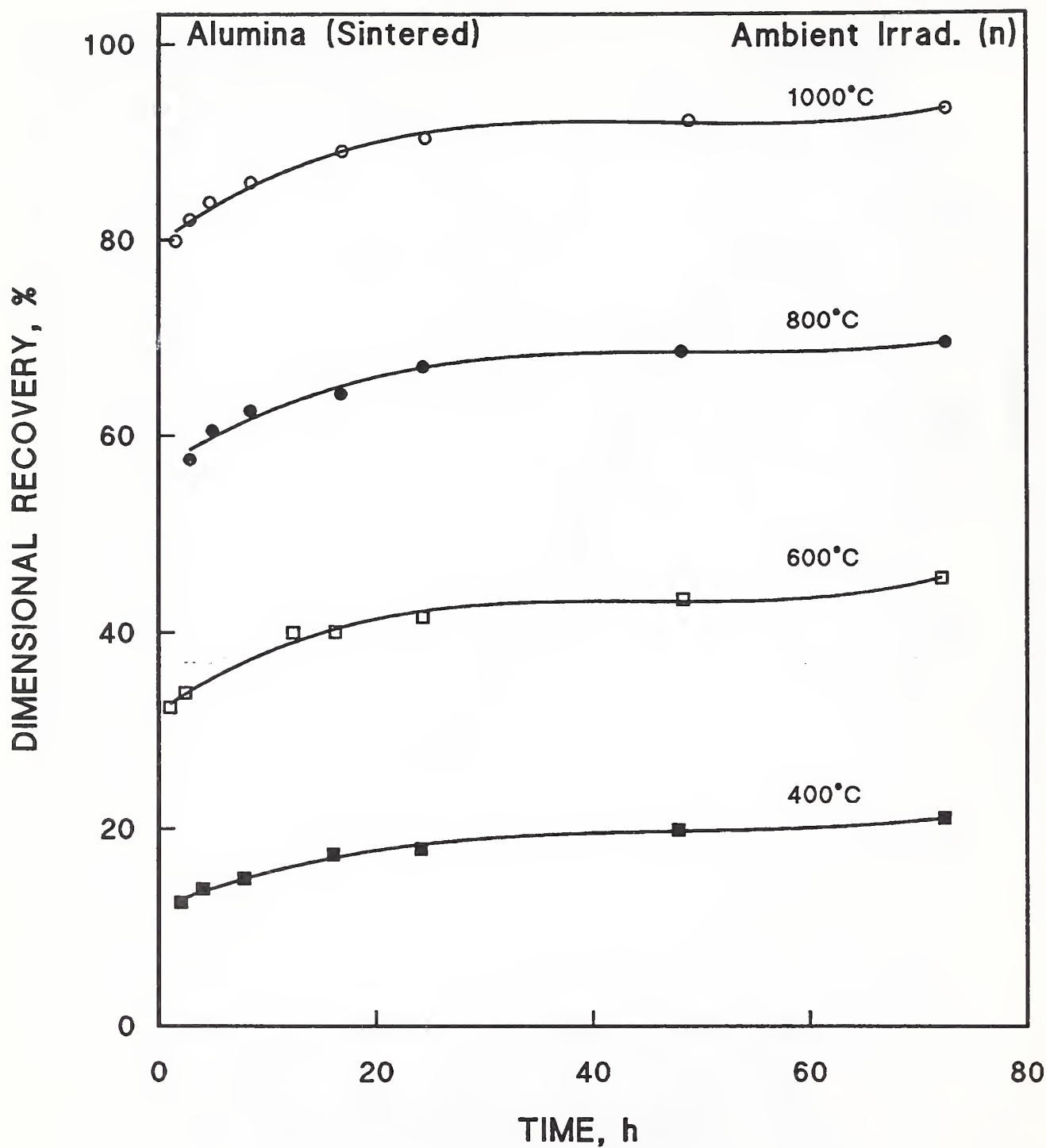


Figure 1.5.3. Isotherms of length recovery of Al_2O_3 irradiated to $1.5 \times 10^{24}/\text{m}^2$. Separate specimens were used at each temperature. Data from Stevanovic and Elston [1967].

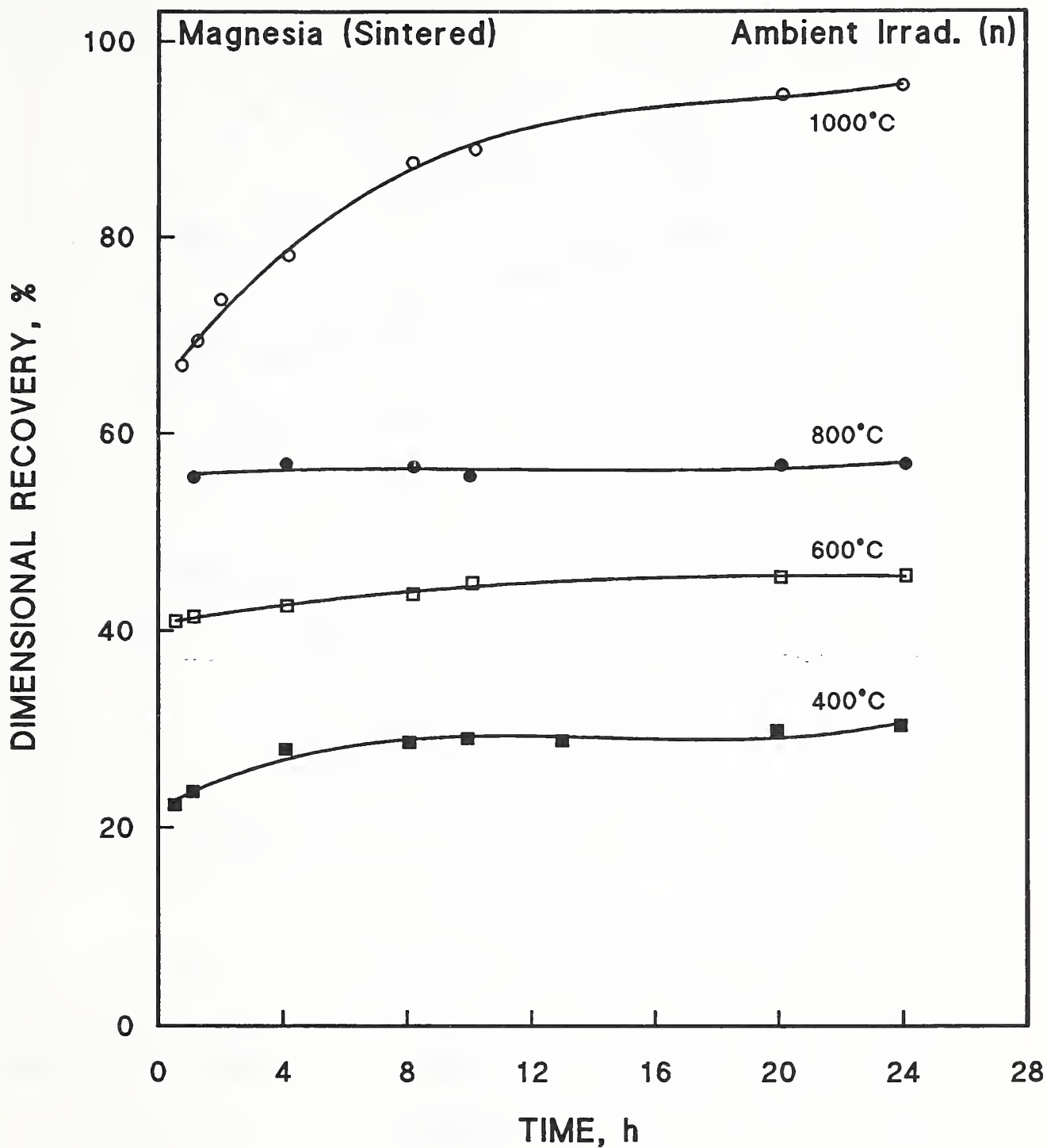


Figure 1.5.4. Isotherms of length recovery of MgO irradiated to $8 \times 10^{23}/\text{m}^2$. All measurements were made on the same specimen. Data from Stevanovic and Elston [1967].

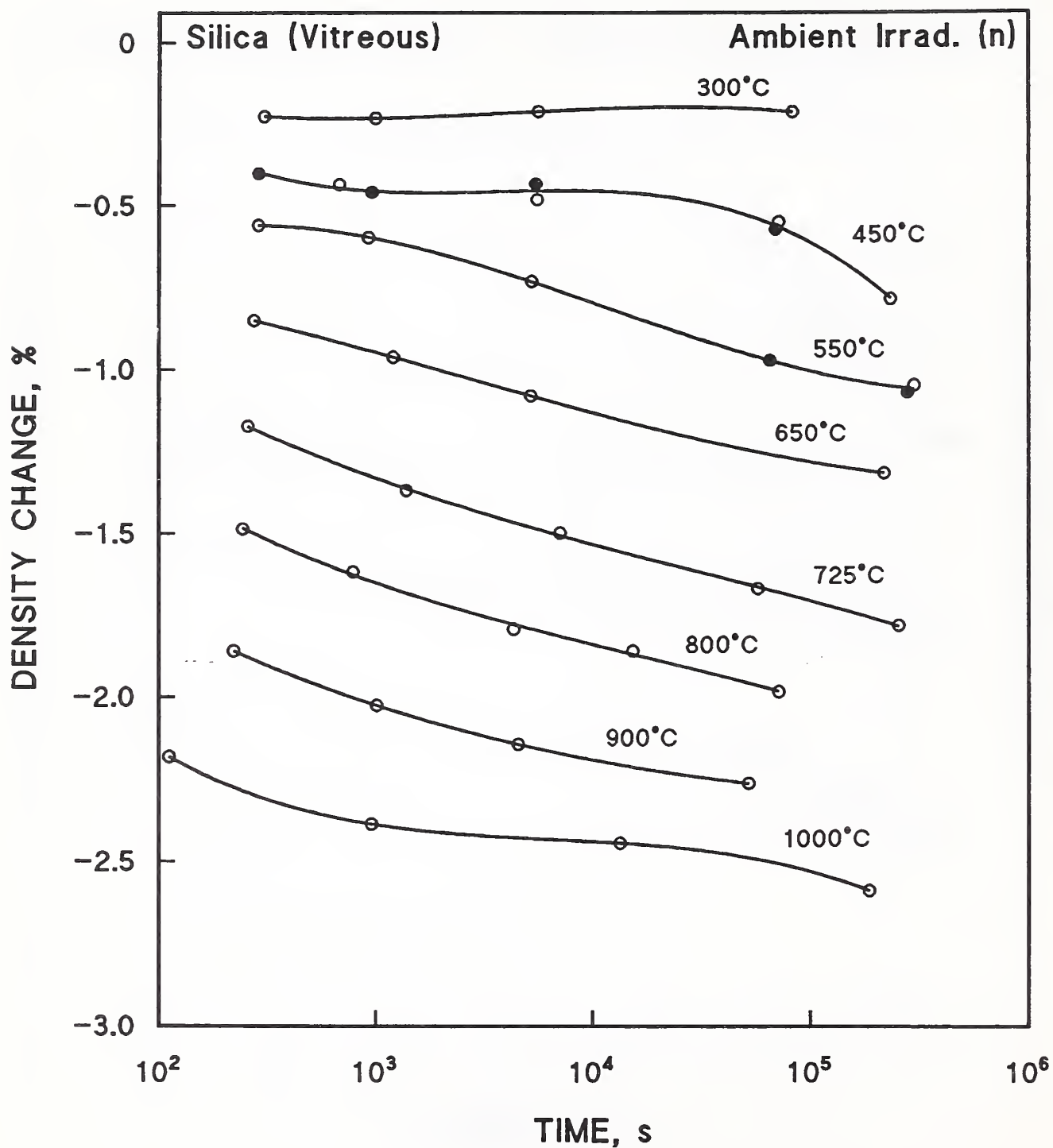


Figure 1.5.5. Isotherms of the recovery of density in vitreous SiO_2 irradiated to $\sim 5.9 \times 10^{23}/\text{m}^2$. The increase in density after irradiation was about 2.7%. Data from Primak and Szymanski [1956].

required temperatures of 1800°C for partial recovery. Even at a lower fluence of $3 \times 10^{23}/\text{m}^2$, defect clusters accounted for about a quarter of the macroscopic growth seen upon annealing. Therefore, a substantial fraction of the defects that survive at ambient temperatures do not anneal out easily. What has not been measured is the fraction of the total number of defects generated at 4 K that these recalcitrant defects compose. There may be more clusters stable at ambient temperature that are generated at 4 K than would be generated with the same fluence at ambient temperature, owing to the lower amount of recovery at 4 K. Therefore, the extent of recovery from 4-K irradiation after ambient-temperature warm-up cannot be predicted at this time, and further research is necessary. Because irradiation damage of crystalline SiO_2 (quartz) is more likely to involve a degree of amorphization, at a given fluence, Primak et al. [1953] noted that recovery for quartz was more difficult than for Al_2O_3 , MgO and MgAl_2O_4 , and that radiation effects were an order of magnitude larger. Since mica also has silicate bonding, recovery is also expected to be more difficult. The next section (§1.6) presents evidence to show that amorphization of ionically bonded solids, such as ceramic oxides, is difficult, whereas amorphization of covalently bonded solids, such as SiO_2 (quartz) occurs more readily. One reason may be that recovery (during irradiation) occurs more easily in ionically bonded solids; if so, ceramic oxides should also recover more completely from 4-K damage during warm-up. Weissman and Nakijima [1963] reported the formation of a hexagonal defect structure in quartz that was very stable and resistant to prolonged annealing at 500°C (see §6.2).

1.6. PRINCIPLES OF MATERIAL SELECTION

Attempts have been made to predict the response of nonmetallic solids to radiation. Naguib and Kelly [1975] examined the response of 72 solids to intermediate and high doses of heavy ions. Table 1.6.1 summarizes their data for the insulators under consideration in this review. Three of the materials under consideration are said to retain crystallinity or, undergo an amorphous-to-crystalline transformation (ZrO_2). Two of the materials undergo a crystalline-to-amorphous transition. Spinel, mica, and porcelain were not included in this analysis.

Table 1.6.1. Response of Nonmetallic Solids to Ion Irradiation.
See Naguib and Kelly [1975] for Discussion and Citations.

INITIAL STATE	STRUCTURE FOR INTERMEDIATE FLUENCES ($\sim 10^{17}$ – $10^{20}/\text{m}^2$)	STRUCTURE FOR HIGH FLUENCES ($\geq 10^{21}/\text{m}^2$)	EXAMPLES
crystalline or amorphous	crystalline	crystalline	AlN, MgO, ZrO ₂
crystalline or amorphous	amorphous	amorphous	α -Al ₂ O ₃ , SiO ₂

Phenomenological criteria were developed by Naguib and Kelly to explain the structural changes (or lack thereof) in these and other solids. Their first criterion, the temperature-ratio criterion, is based on the thermal spike model in which the irradiation ion is thought to create a small, hot disordered region along its path which becomes liquid, but then cools rapidly. An expression for the effective duration of the thermal spike was obtained from the requirement that crystallinity should be preserved during cooling if the crystallization front moves into the disordered region by a distance sufficiently greater than the mean atomic spacing, . This effective duration is typically a few picoseconds. Further analysis allowed the derivation of a condition for amorphization and crystallization, where T_c is the temperature of crystallization and T_m is the melting point:

The substance remains crystalline if $T_c/T_m < (T_c/T_m)^*$, or,
the substance amorphizes if $T_c/T_m > (T_c/T_m)^*$.

Observation on the structure after ion irradiation of a number of substances suggested that the critical ratio, $(T_c/T_m)^* \approx 0.30$. Even if the thermal spike model is not accurate, the criterion that amorphization occurs when T_c/T_m is greater than 0.30 is still empirically valid. This criterion is illustrated in Figure 1.6.1.

An alternate, crystal-structure criterion was proposed by several investigators [citations in Naguib and Kelly, 1975]. In its usual formulation, this criterion states that anisotropic substances tend to amorphize under ion irradiation, whereas cubic substances tend to remain crystalline. However,

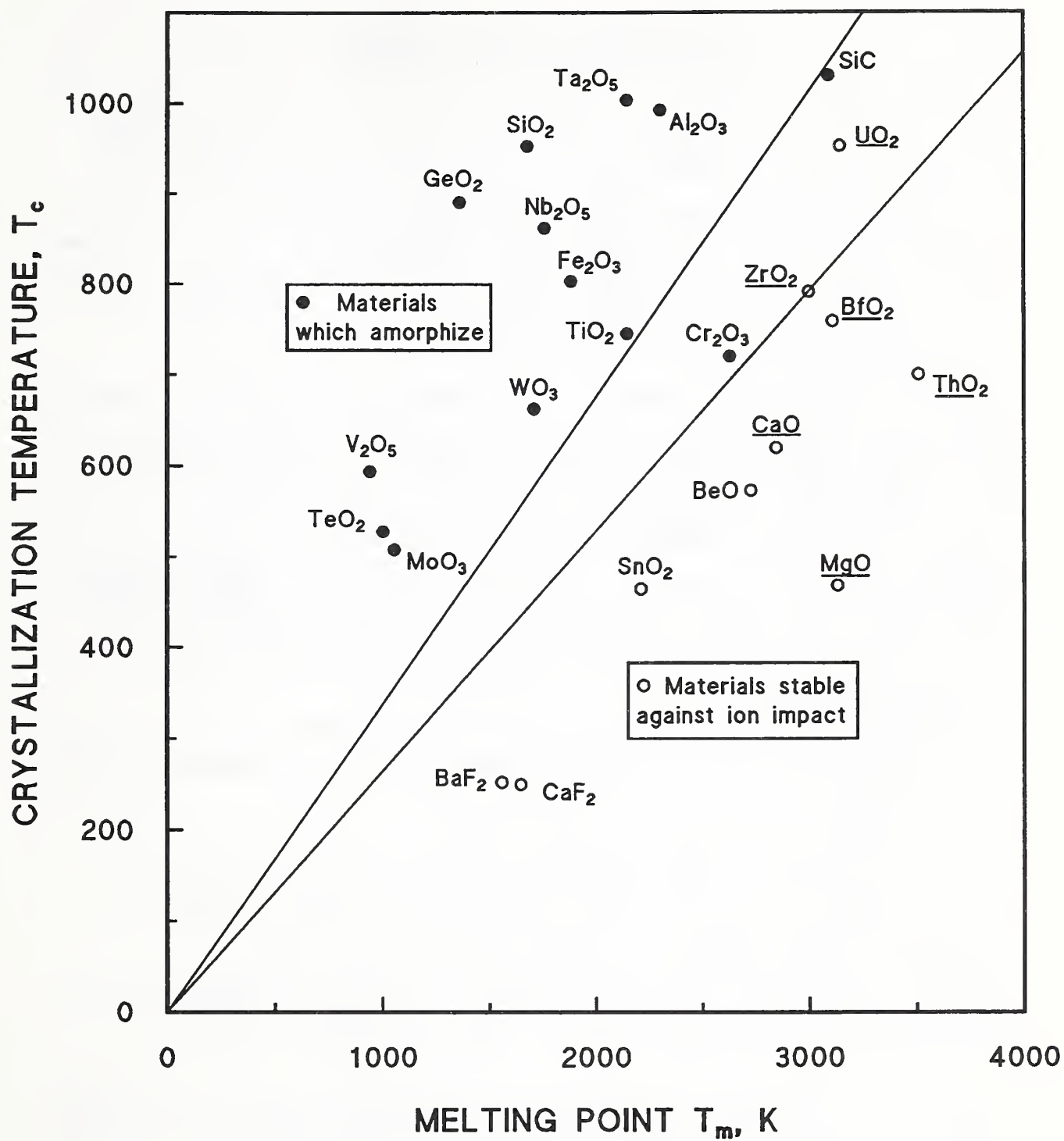


Figure 1.6.1. Thermal criterion for the occurrence of amorphization. Cubic structures are underlined. Data from Naguib and Kelly [1975] and Matzke [1982].

Naguib and Kelly demonstrated that this criterion was unsatisfactory; they found 22 exceptions among 66 materials for which data were available. But, if anisotropy is considered to pertain to bond directionality, 10 out of 11 cubic materials with diamond or zincblende structures, both of which have directional bonds, amorphize readily, whereas all 19 cubic materials with either NaCl or CaF₂ structure, in which bonds are nondirectional, show good radiation stability. However, when the crystal-structure criterion is formulated in this way, it becomes equivalent to a bond-type criterion, discussed below, and need not be considered separately.

Naguib and Kelly cited earlier work on bond-type criteria, that is, ionicity. Figure 1.6.2 illustrates that the order of increasing radiation resistance in materials is also the order of increasing ionicity. Naguib and Kelly found that a total of 25 substances which amorphize on ion irradiation had ionicities ≤ 0.47 and that 18 substances which remained crystalline had values ≥ 0.59 . Variable behavior was found for intermediate ionicities. However, one exception is AlN, which remains crystalline but has covalent bonding (ionicity = 0.39). At least four rationalizations of the ionic-covalent bond criteria have been suggested:

- (1) Amorphization is related to substitutional disorder, and ionic solids do not permit substitutional disorder, because of the large increase in electrostatic energy.
- (2) The directional nature of covalent bonds.
- (3) The fact that covalent bonds involve only short-range interactions.
- (4) The difference in the lattice strain due to a defect dependency or whether the atoms neighboring to the defect are ionic or not.

Since it is difficult to make such arguments quantitative, Naguib and Kelly suggested that the bond-type criterion also be regarded as empirical.

Burnett and Page [1986] extended the work of Naguib and Kelly by noting that more recent irradiation studies showed that materials with ionicities > 0.59 could be rendered amorphous, as shown by TEM or RBS (Rutherford beam scattering) if the fluence were sufficiently high. They introduced an additional quantity, $\rho(E_{\text{crit}})$, a critical value of the energy per unit volume that has been given up through damage processes, that must be exceeded for amorphization to occur. A universal curve was derived that allows estimation of

BOND-TYPE CRITERION

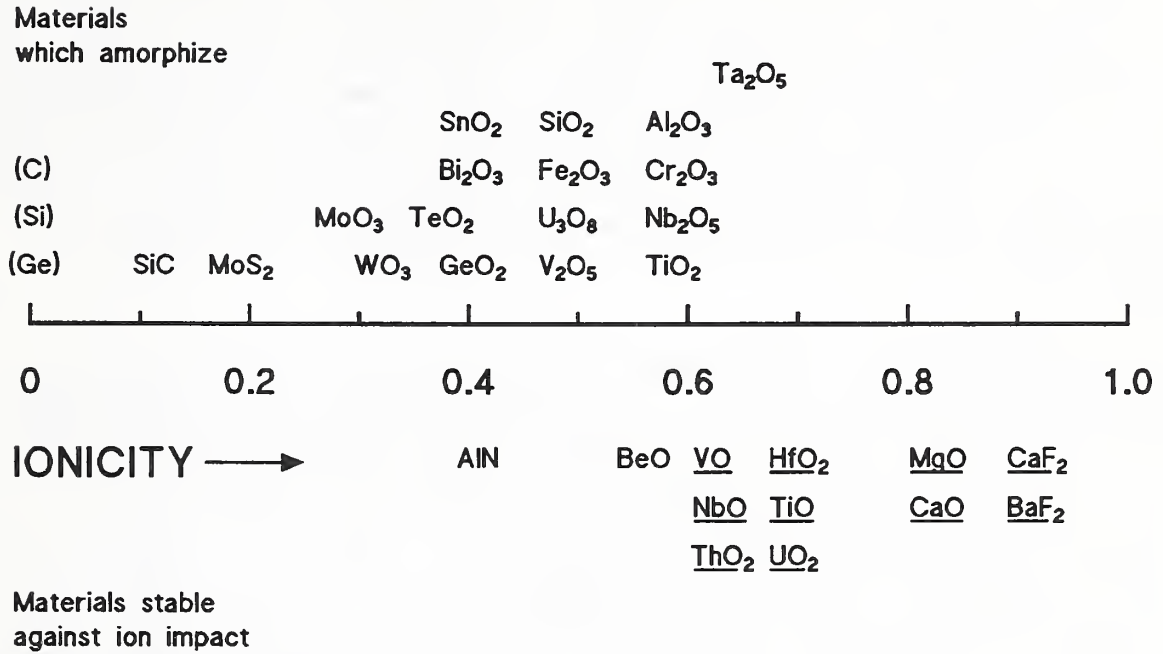


Figure 1.6.2. The bond-type criterion for the occurrence of amorphization. Cubic structures are underlined. Data from Naguib and Kelly [1975] and Matzke [1982].

$\rho(E_{\text{crit}})$ for a wide range of nonmetallic materials (Figure 1.6.3). The more ionically bonded materials require much greater damage energy densities to be rendered amorphous. Burnett and Page stated that the theoretical understanding of this difference in amorphization mechanisms operating in covalent and ionic materials had not yet been attained. They also reported that amorphization was accompanied by considerable softening of the material, so that hardness values, which generally rose with the initial ion irradiation, often fell considerably below the initial (unirradiated) values as the fluence was increased.

A property related to amorphization is the ability of fission fragments to form tracks in insulators, since the tracks are evidence of disordered material. The minimal energy loss per distance necessary for the formation of a track, $(dE/dx)_{\text{crit}}$, has been correlated with the thermal conductivity of the material [Matzke, 1982, and citations therein]. Figure 1.6.4 indicates that mica and fused SiO_2 have low thermal conductivities, and thus, lower values of dE/dx are required for disordering. For Al_2O_3 and MgAl_2O_4 , which have much higher thermal conductivities, fission fragment tracks have not yet been observed, although they have been observed for SiO_2 and mica.

In addition to amorphization, irradiation also may cause changes in stoichiometry that may adversely affect material properties. Naguib and Kelly cited various proposed models to account for stoichiometry changes, but discussed only a sputtering model, which led to a satisfactory criterion for predicting nonstoichiometry. The criterion is related to the heats of atomization for a particular degree of loss of stoichiometry. Their analysis predicted that $\alpha\text{-Al}_2\text{O}_3$, MgO , SiO_2 , and ZrO_2 would remain stoichiometric during irradiation. (Information on other compounds selected for this review was not available at the time of their report.) At high temperatures, however, Pells and Phillips [1979a,b] reported formation of Al colloids after electron irradiation of Al_2O_3 . This was attributed to a lower E_d for Al (~ 18 eV), than that for O (~ 72 eV). (See also §2.1, since this conclusion has been challenged by other workers.) Ghoniem and Chou [1988] used a Monte Carlo simulation of neutron cascade damage to show that the stoichiometry of MgAl_2O_4 was not always preserved during irradiation.

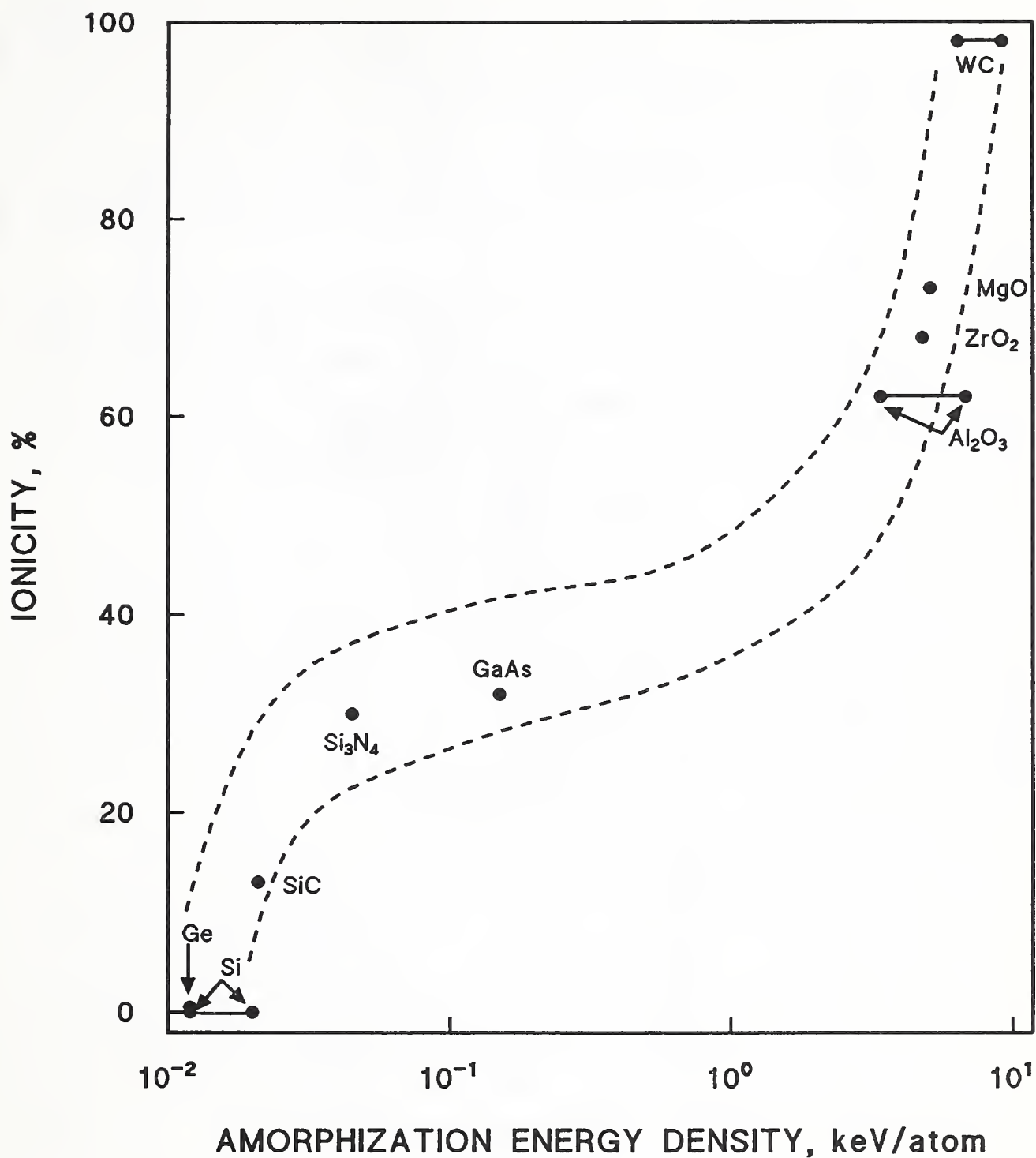


Figure 1.6.3. Relationship between energy density for amorphization and the bonding (ionicity) for several materials. The data fall between the dotted curves, as shown. Data from Burnett and Page [1986].

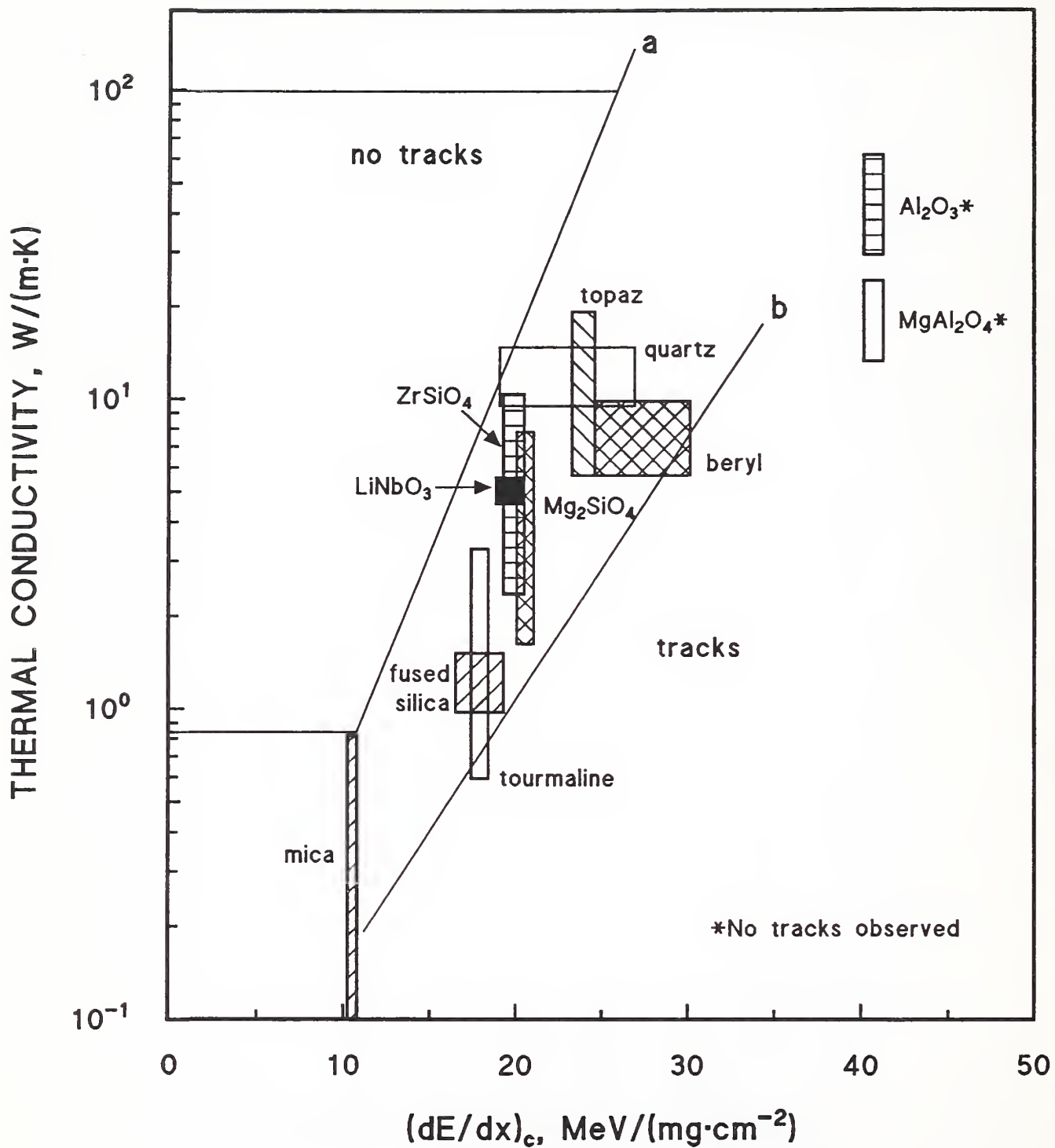


Figure 1.6.4. Thermal conductivity vs. critical energy for track formation in insulators used as nuclear track detectors. Data from Matzke [1982].

Despite the prediction that MgAl_2O_4 would become nonstoichiometric under irradiation, it is generally regarded as relatively resistant to radiation. Youngman [cited in Buckley and Shaibani, 1987] presented evidence that ceramics with more complicated chemical compositions, such as MgAl_2O_4 , were more resistant to fission irradiation than simple binary compounds such as Al_2O_3 and MgO . The unit cell of MgAl_2O_4 contains 56 atoms.

Another factor in the radiation resistance of polycrystalline materials is the atomic structure of the compound. In polycrystalline materials, grain boundary separation may occur if the specimen structure is not cubic, since each grain undergoes anisotropic expansion under irradiation. Thus, a cubic material, such as MgO or MgAl_2O_4 , should be superior to a noncubic material, such as Al_2O_3 .

In addition to the chemical and physical properties of a substance, the form in which it is prepared also has an effect on its radiation resistance. For compacted powder ceramics, Perkins [1984] suggested that neutron damage had no effect on the strength of the material since each grain would be affected individually. Therefore, the fluence limit would be set only by the swelling limit of the bulk material. Since compacted powder ceramics have typical void fractions of 30%, this insulation should have very high radiation limits. The results of Keilholtz et al. [1964] on BeO compacts appear to agree with Perkin's principle, since fracturing associated with grain boundary separation of the hot-pressed samples was reported to be more severe than in cold-pressed samples which should be less like the solid form. Another feature of the compacted powder form of a material is that a cubic structure may not offer any advantage over a noncubic structure, since grains are not closely associated. On the other hand, a compacted powder may not serve well as an electrical barrier, since dc resistivity typically is lower than in the same material in solid form.

To avoid problems with irradiation swelling, a high-porosity form of the material in question is sometimes suggested, since voids are available to take up expansion. However, one experiment indicated that plasma-sprayed MgAl_2O_4 was relatively vulnerable to disorder under irradiation. Amorphization occurred at a lower foreign-ion fluence than that for material of normal density. This

experiment is discussed further in §7.3 below. Furthermore, porous materials can generally be expected to have weaker mechanical properties and lower electrical breakdown strengths.

If the material is in layered form or otherwise subdivided on a fine scale ($\sim 10 \mu\text{m}$ or less), a unique problem may arise with the electrical breakdown strength. If certain impurities are also present, such as ^{235}U , the thermal neutron fluence which accompanies the fast neutron fusion fluence will activate the impurity, resulting in the emission of heavy fission fragments. These heavy ions will make tracks of disordered material in the insulation, typically about $10 \mu\text{m}$ in length. Alpha emission is an even more common occurrence, since the ITER neutron spectrum is now more highly weighted above 5 MeV. Alpha emission is much less likely to result in tracks at ambient temperature than heavy ions are, but the situation at 4 K has not yet been investigated. If tracks are the result of a thermal process, the decrease in the specific heat from 300 to 4 K of about 3 orders of magnitude may allow localized temperatures along the ion track to rise to near the melting point. This could result in tracks of disordered material. Since such tracks are usually only a few micrometers in length, unless they are very numerous, they may not degrade the electrical properties of a bulk material. In a subdivided material, however, the situation is different, as the tracks may link voids. These problems are discussed for the layered structure of mica in §9.5.

Since natural mica always contains some U as an impurity, it is especially vulnerable to the track problem. However, other materials, such as natural quartz, also contain U at or below the parts per 10^9 range [Singh et al., 1984], which appears to be sufficient for the production of numerous tracks under the expected thermal neutron fluence in ITER (see §9.5 for mica; Singh et al. [1984] for quartz). Other elements that have a high cross section for α emission may also be present in a natural material. Therefore, the availability of the material in a synthetic form may be an advantage in some cases, although processing steps for both synthetic and natural materials may introduce impurities. The usual activation analysis may not suffice to determine the existence of these impurities at the very low levels at which they may cause problems; therefore, activation analysis must be supplemented with fission and α track observations. Examples of fission-track analysis

procedures are given in Singh et al. [1984] and in Fleischer and Price [1964]. There is evidence that tracks in some forms of mica anneal to some degree, even at ambient temperature [Price and Walker, 1962a]. Therefore, to validate a material for 4-K use, in situ observations at 4 K after irradiation may be necessary.

The irradiation data base for inorganic materials is well-developed for only a few ceramic insulations, such as Al_2O_3 , MgO , MgAl_2O_4 , AlN , and SiO_2 . Information is available for ambient-temperature irradiation (up to -100°C), on the defect density, change in volume, fluence of amorphization, and effects on mechanical and thermal properties. These data allow some comparison of the materials. Although porcelain, mica, and ZrO_2 are also considered in this review, their irradiation data base is almost nonexistent. Therefore, in selecting material, the extent of irradiation information should also be considered. The availability of the material and its development in various forms is also an important consideration. For example, compressive stress is higher in fine-grained ($\sim 2 \mu\text{m}$) Al_2O_3 , but other ceramic oxides may not be available in fine-grained form.

2. LOW TEMPERATURE IRRADIATION OF ALUMINA

2.1. DEFECT DENSITY

2.1.1. Frenkel Defects

Several experimental and theoretical studies of optical changes induced in Al_2O_3 by fast neutrons have led to the association of certain ultraviolet absorption bands with electron-trapping oxygen vacancies [citations in Evans and Stapelbroek, 1979; Atobe et al., 1985]. Oxygen vacancy sites with a single trapped electron are called F^+ centers; if two electrons are trapped, the site is termed an F center. The concentration of F and F^+ centers is directly proportional to the height of a spectral absorption peak (or the area under the peak), and, therefore, the height (or area) of the peak determines the concentration of defects induced in the material, assuming that the fraction of defects populated by electrons is constant. Bunch and Clinard [1974] used this technique to compare the damage produced by 14-MeV neutrons from the RTNS source with the damage produced by fission-reactor neutrons with $E > 0.1$ MeV. A comparison of the absorption produced by the two neutron sources in Figure 2.1.1 shows that the amount of damage per neutron is about 4 times greater for the 14-MeV fusion neutrons. Evans and Stapelbroek [1979] made a similar comparison of the optical absorption spectra they obtained from Al_2O_3 irradiated in the RTNS source with earlier fission data, but found a somewhat lower damage efficiency ratio of 2.3 ± 1 (Figure 2.1.2). Both investigations used the same source of fission data, that of Levy [1961], but Evans and Stapelbroek used error bars to indicate the sizeable uncertainty in the fission fluence. Both investigations used single-crystal sapphire (evidently the samples examined by Evans and Stapelbroek were those of Bunch and Clinard) and the irradiation temperatures were similar; ~ 300 K for the RTNS source and ~ 345 K for the BNL (Brookhaven National Laboratory) reactor. Note that long recovery periods may have resulted in a similar density of ambient-temperature retained defects for both the 14-MeV and fission irradiations; these results may not apply to 4-K irradiations.

In the examples just described, the optical absorption peak heights and areas were used to compare the ratio of displacement defects produced in Al_2O_3 by

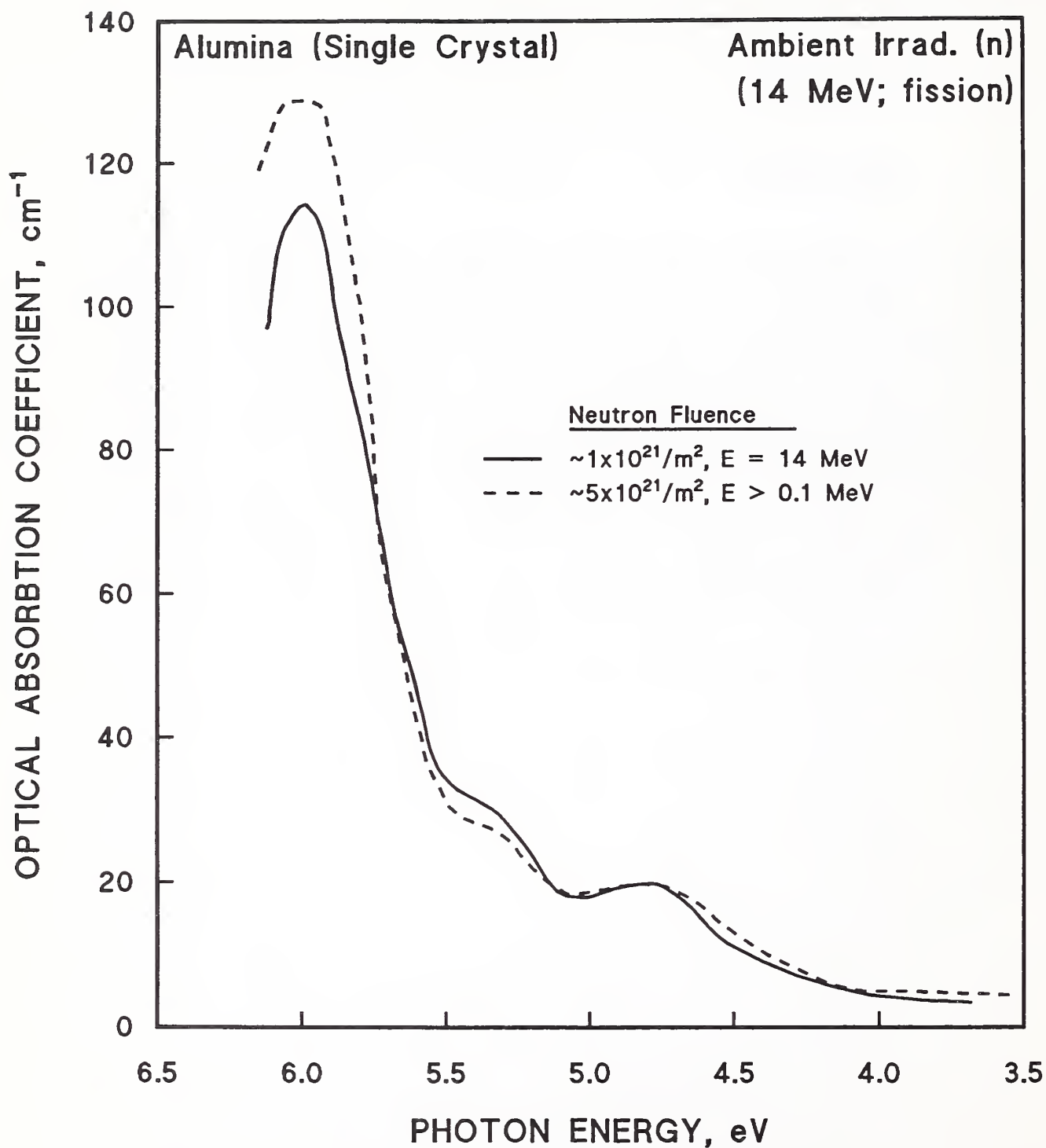


Figure 2.1.1. Optical absorption of single-crystal Al_2O_3 irradiated by 14-MeV neutrons and fission neutrons. Data from Bunch and Clinard [1974].

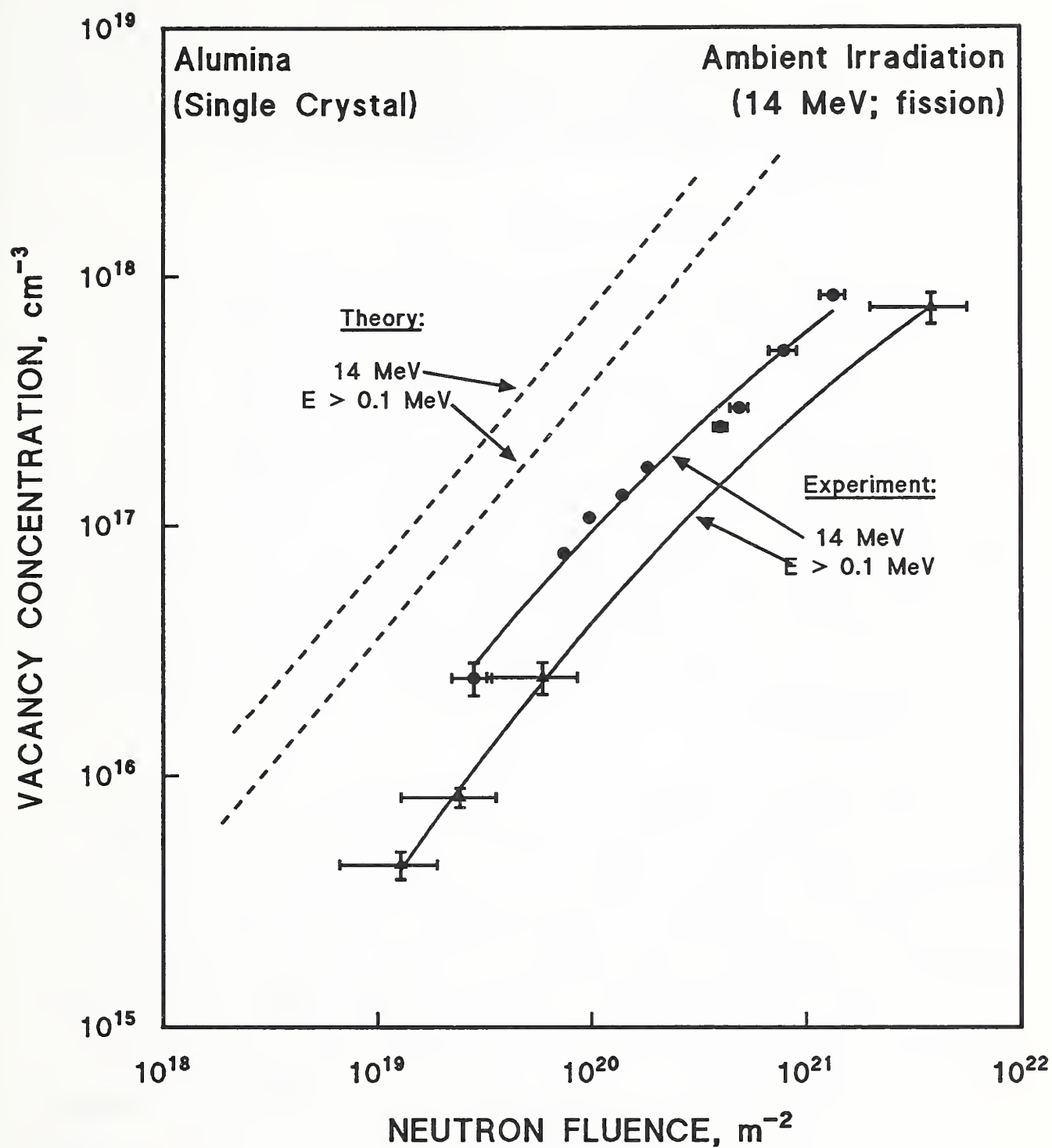


Figure 2.1.2. Oxygen vacancy concentration (F and F^+ centers) of single-crystal Al_2O_3 for 14-MeV neutrons and fission neutrons. Data from Evans and Stapelbroek [1979].

neutrons of different energies. However, the actual number of defects giving rise to the optical absorption peak can also be calculated, if values for certain parameters are known. Evans and Stapelbroek used the equation of Smakula [citation, Evans and Stapelbroek, 1979] to calculate the volume concentration of F and F⁺ centers:

$$Nf(\text{cm}^{-3}) = 0.87 \times 10^{17} [n/(2+n)^2] \alpha \Delta E, \quad (2.1)$$

where n is the optical index of refraction at the absorption band peak, α is the optical absorption coefficient at the band maximum, and ΔE is the band full width at half maximum. The value chosen for the oscillator strength, f , and other details of the calculation are explained in the paper. Figure 2.1.2 shows that there is a difference of an order of magnitude between the theoretical estimate of lattice defects from a modified Kinchin-Pease equation and the observed density of optically determined defects. Using $E_d(0) = 76$ eV as suggested by Pells and Phillips [1979a] instead of 90 eV in the theoretical calculation would increase the disagreement with theory slightly. Using an E_d of 30 eV [Greenwood, 1990] would increase the disagreement with theory by a factor of 3. The reason for the disagreement with theory is probably the high rate of recombination of defects at ambient temperatures, as discussed above in §1.3 (see also §2.2).

By irradiating single-crystal Al_2O_3 at 15 K, in addition to 360 K, Atobe and Nakagawa [1987] were able to show that the density of optically determined defects was indeed higher for the specimens irradiated at 15 K, even though the specimens were stored at 77 K, which allowed recovery before the ambient-temperature measurements. (The authors stated that no recovery occurred between 77 K and ambient temperature, but did not explain the evidence for this statement, nor whether recovery occurred between 15 and 77 K.) Figures 2.1.3 and 2.1.4 show the difference in optical absorption for specimens at the two temperatures, and Figure 2.1.5 compares the vacancy concentrations, calculated with Equation 2.1 (see the reference for details of the calculation.) Figure 2.1.6 compares these results with those found earlier by Evans and Stapelbroek and by Levy (the BNL data). The dpa can be obtained by dividing the defect density by the number of atoms per cubic centimeter, $1.15 \times 10^{23}/\text{cm}^3$, determined from a density of $3.97 \text{ g}/\text{cm}^3$ and a molecular mass of 102 u. From Atobe and Nakagawa's defect density after 15-K irradiation to a fluence of $10^{21}/\text{m}^2$,

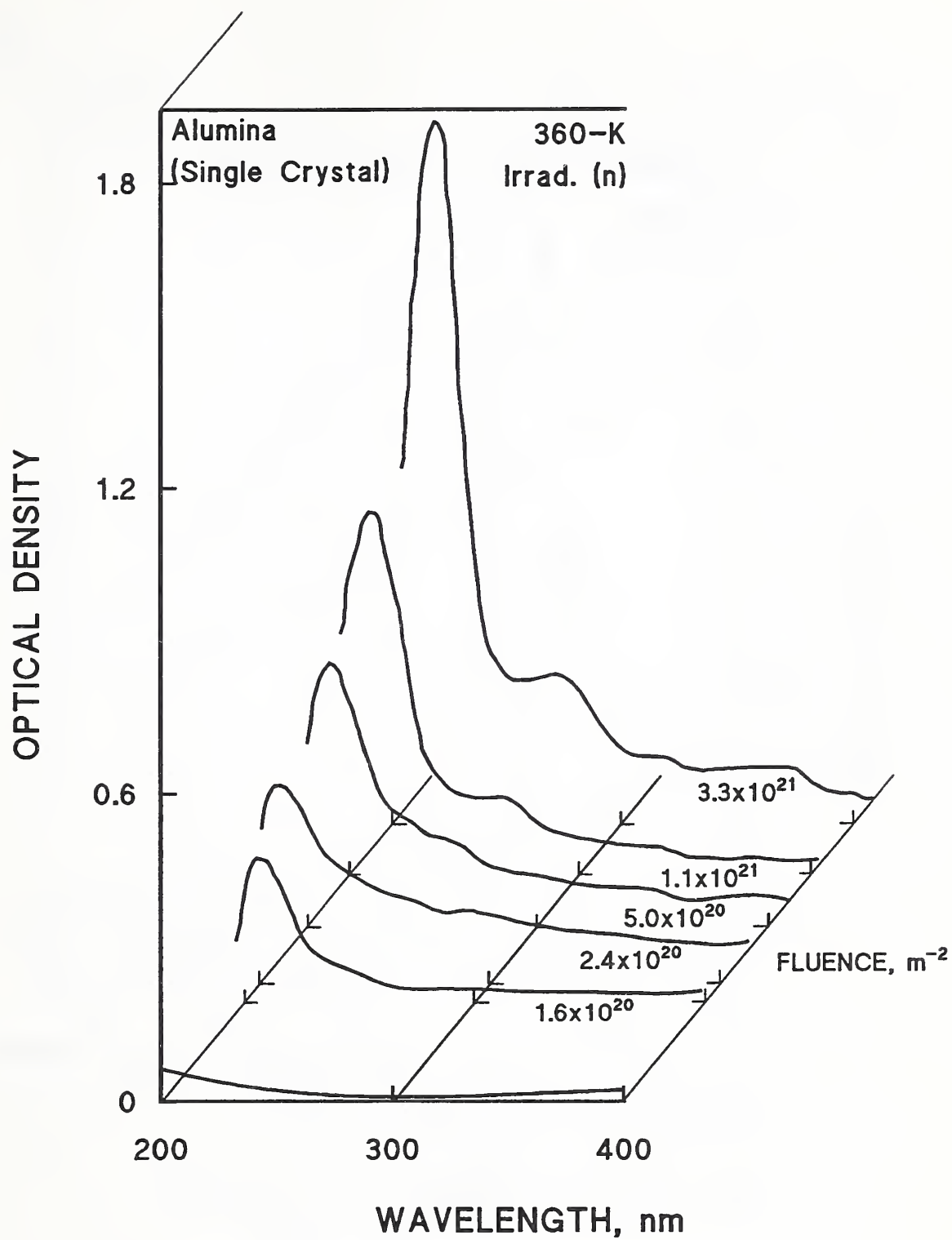


Figure 2.1.3. Optical absorption of single-crystal Al_2O_3 irradiated at 360 K, measured at ambient temperature. Data from Atobe and Nakagawa [1987].

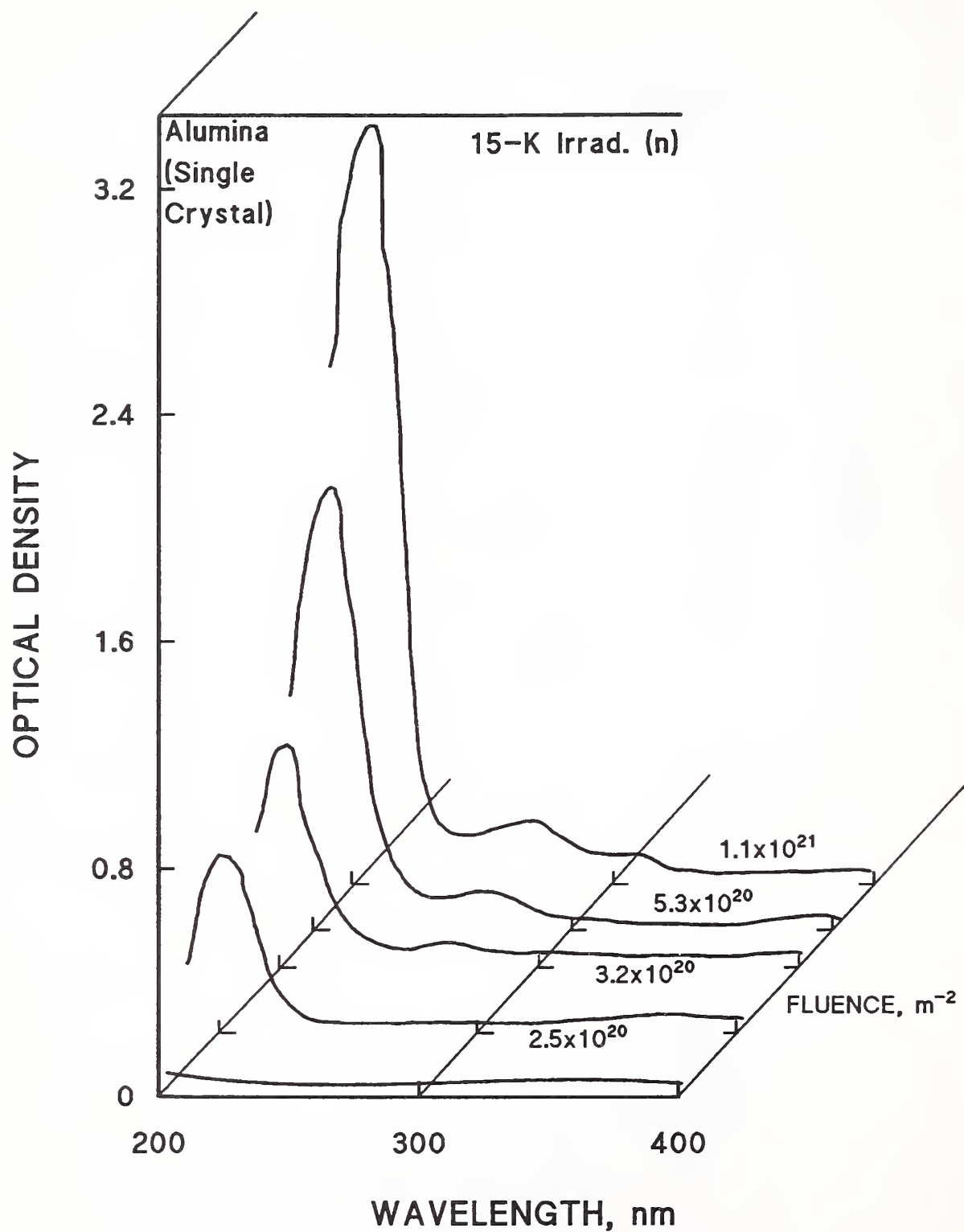


Figure 2.1.4. Optical absorption of single-crystal Al_2O_3 irradiated at 15 K, measured at ambient temperature. Data from Atobe and Nakagawa [1987].

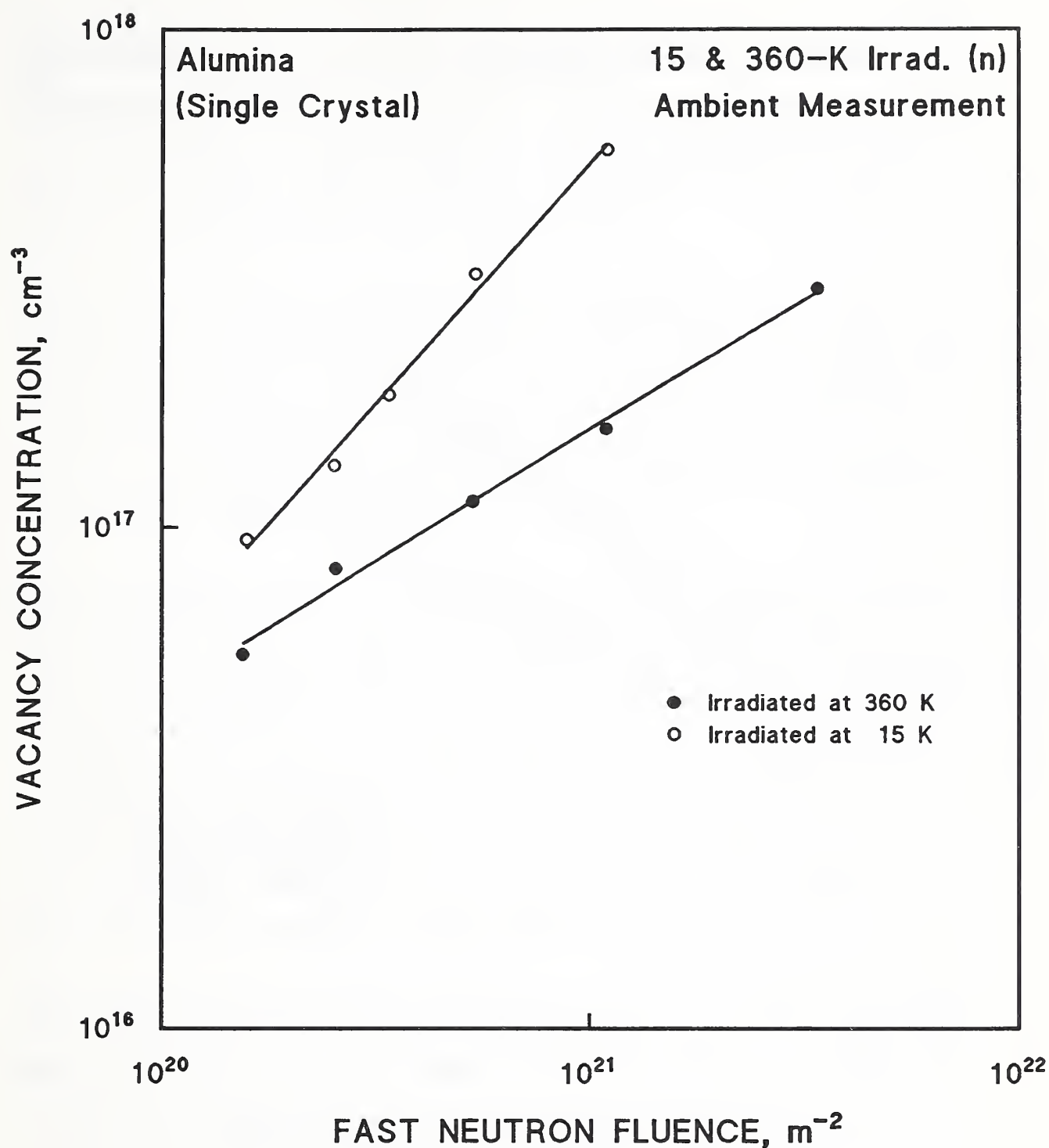


Figure 2.1.5. Comparison of the O vacancy concentration measured at ambient temperature after irradiations of single-crystal Al_2O_3 at 15 and 360 K. Data from Atobe and Nakagawa [1987].

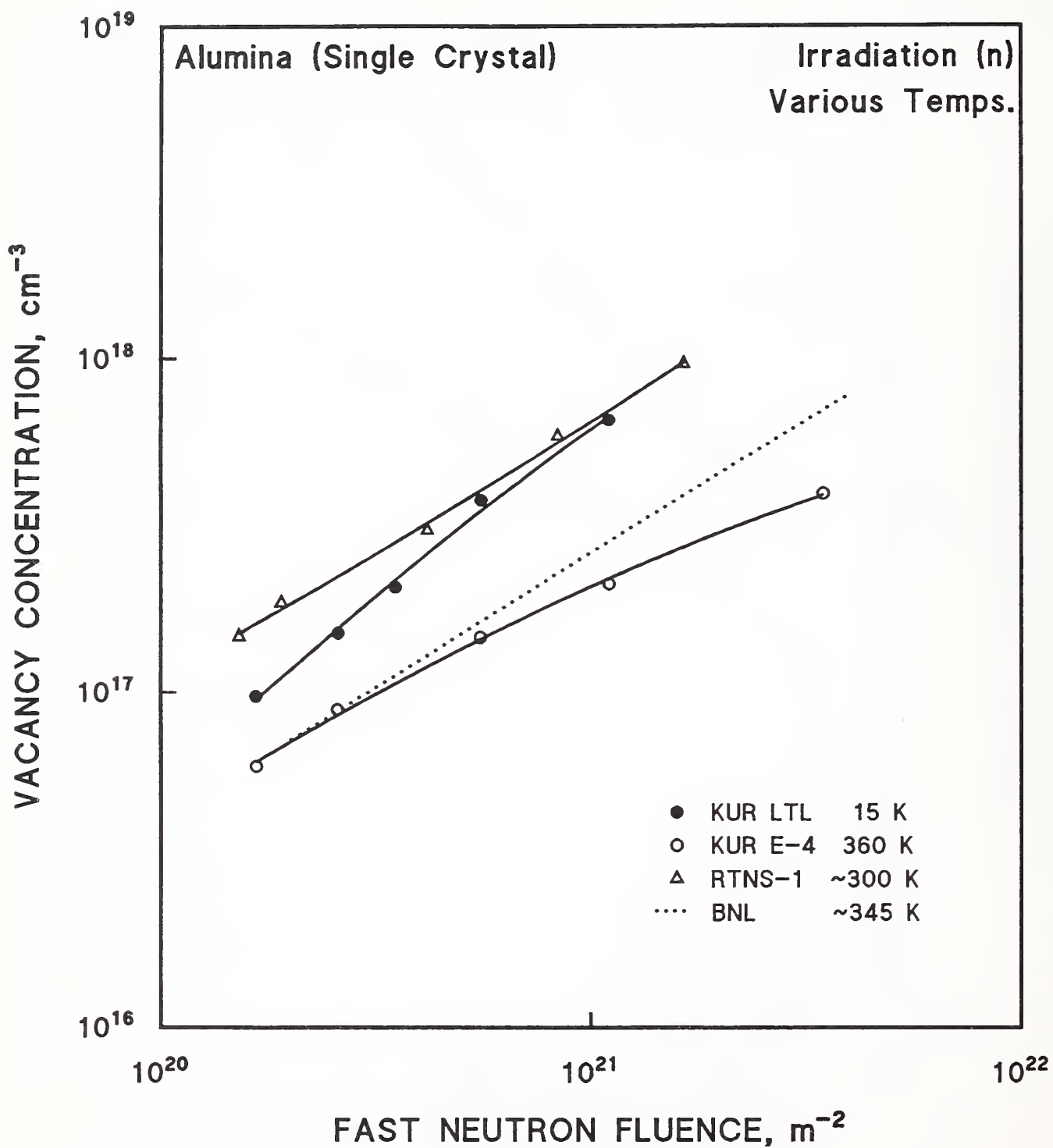


Figure 2.1.6. Comparison of the Atobe and Nakagawa [1987] results with earlier investigations. From Atobe and Nakagawa [1987].

a minimum dpa of $\sim 5 \times 10^{-6}$ is obtained. This represents displacements that survive ambient-temperature recovery processes. Turner and Crawford [1976] have reported that ionizing (γ) radiation enhances absorption at the band identified with an F center, because the band is associated with electrons trapped at a defect created by atomic displacement. Therefore, the actual number of surviving defects could differ somewhat.

The annealing behavior at 670 K of the defects produced at 15 K in a specimen that was held at 77 K is compared to that of 360-K defects in Figure 2.1.7. About 50% of these defects annealed very quickly, and were attributed to F centers. The remaining defects from 15-K irradiation were attributed to a different type of defect. The temperature of the measurements was not reported. However, the short annealing time of about 50% of the 15-K defects is in accord with expectation.

Pells and Murphy [1992] also used optical absorption to investigate the production of defects in polycrystalline Al_2O_3 below ambient temperature. But, in contrast to the experiments of Atobe and Nakagawa, both irradiation (with N^+ ions) and optical band measurements were conducted at the cryogenic temperature, 77 K. These results were discussed above (§1.3). Figure 1.3.9 shows that at low N^+ fluences, comparable to the nominal dpa of 10^{-3} to 10^{-4} expected in the ITER TF magnet, the O-vacancy defects measured at 77 K were about a factor of 30 higher than those measured at 300 K. Pells and Murphy also reported calculations indicating that the number of Al displacements would exceed the number of O displacements by a factor of 2.7.

The theoretical displacement cross section for Al_2O_3 has been published by Dell and Goland [1981]. They used the modified Kinchin-Pease theory as extended by Coulter and Parkin for polyatomic nonmetals. The results were given above, in Table 1.2.3. Values of σ_{dis} , the displacement cross section for O, range from 403 barns for 14-MeV neutrons to about 130 to 200 barns for a reactor fission spectrum. Choosing the EBR II spectrum as approximately comparable to the ITER TF magnet spectrum (although there is less $E > 5$ MeV content), one obtains σ_{dis} values of 5.37 and 2.00×10^{-5} dpa for Al and O, respectively, for a fluence of $10^{21}/\text{m}^2$. This predicted dpa for O is about

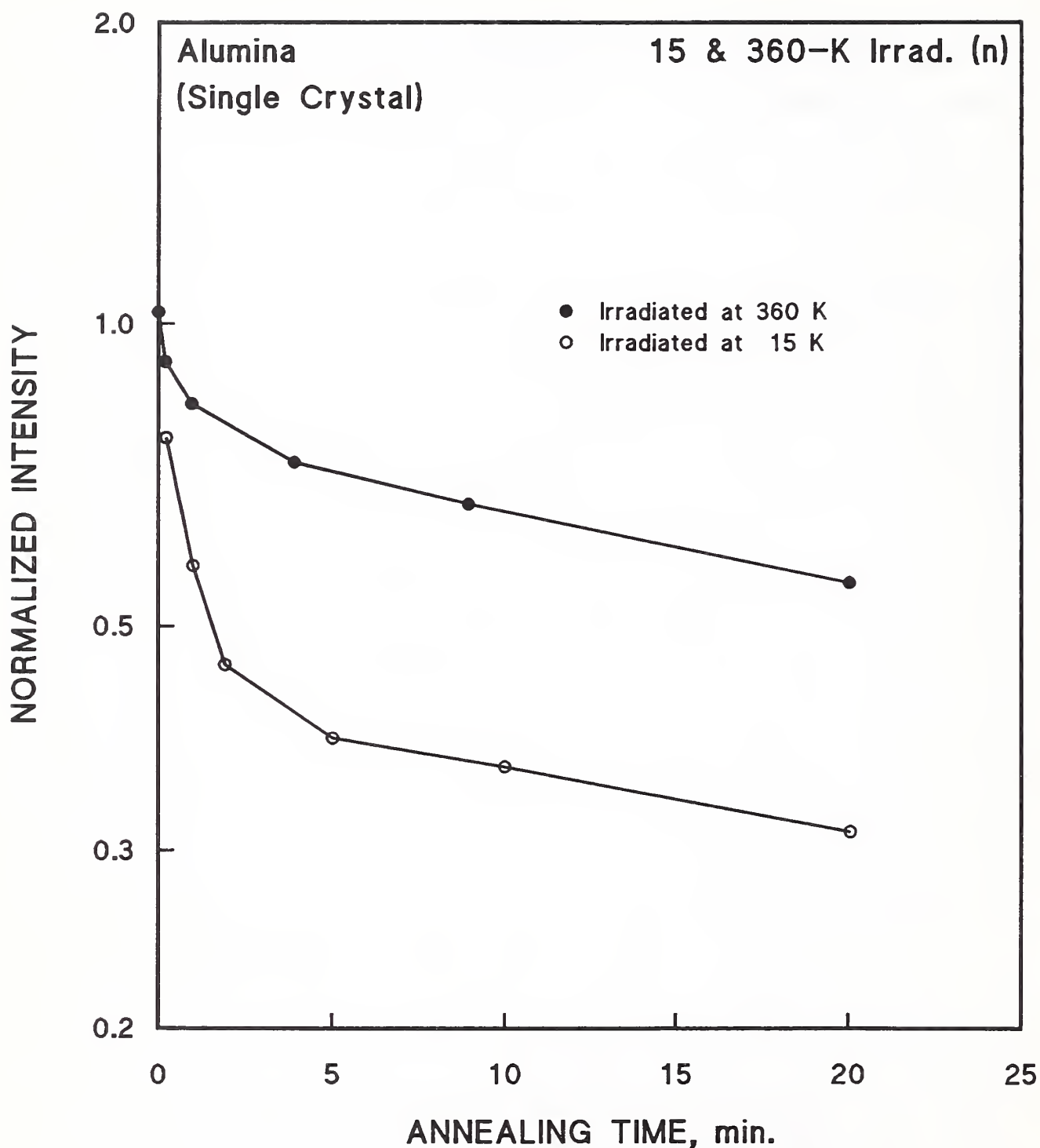


Figure 2.1.7. Annealing behavior at 670 K of defects created at 15 and 360 K in single-crystal Al_2O_3 . Data from Atobe and Nakagawa [1987].

3 times that observed after ambient-temperature measurements of defects created at 15 K by Atobe and Nakagawa.

The calculated σ_{dis} depends inversely upon the value chosen for E_d , and σ_{dis} can be corrected easily if a better value becomes available. The displacement energies for Al_2O_3 were first measured by Arnold and Compton [1960], using optical-absorption techniques to monitor the damage from electron irradiation as the electron energy was increased. The growth of the 205-nm optical absorption band was observed and compared with calculated absorptions that would theoretically occur for various values of E_d , for Al and O. The results at both 77 and ~300 K implied either a value of 50 ± 5 eV for Al or 85 ± 5 eV for O. Since the type of defect responsible for the 205-nm absorption band was unknown at that time, it was not possible to be certain which species was responsible for the observed damage.

Later, Pells and Phillips [1979a] used an alternative method to determine E_d . They examined Al_2O_3 specimens in a HVEM at increasing electron beam energies until observable damage occurred. Although this method is more direct, only dislocations and other large defects can be observed by TEM; hence, the authors also used a Van de Graff electron accelerator and monitored damage by the growth of optical bands. Also, for irradiation near ambient temperature, where the damage was on too fine a scale to be resolvable by the HVEM, the threshold was defined to occur when a general darkening of the image appeared. Figure 2.1.8 shows the temperature dependence of the threshold energy from the HVEM measurement, which is seen to give two values. Since the optical band studies give a value of threshold energy of about 400 keV for O vacancies and about 175 keV for Al vacancies, the higher threshold in Figure 2.1.8 is ascribed to $E_d(O)$ and the lower to $E_d(Al)$, as shown to the right of the figure. Equation (1.5) is used to obtain the portion of threshold energy transferred to the Al or O atom, which gives E_d values of 76 eV for O and 18 eV for Al. Similar high values have been obtained for other $E_d(O)$ measurements in oxides [citations in Pells and Phillips, 1979a].

The temperature dependence of the threshold energy was explained by the method of observation, which required the presence of dislocation damage that was detectable in the TEM. Below 670 K, detectable dislocation damage did not

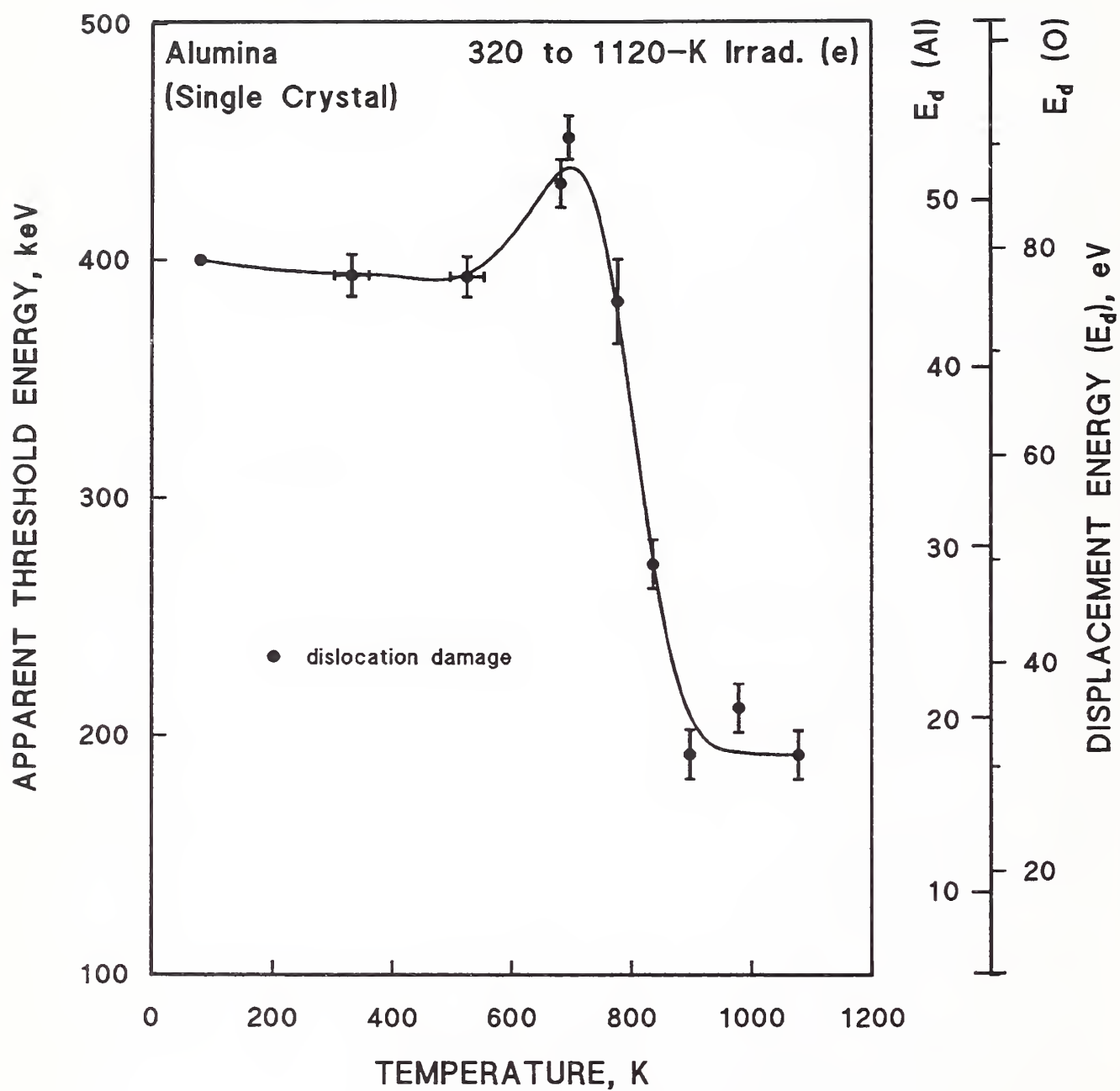


Figure 2.1.8. Threshold energy vs. temperature; derivation of displacement energy for Al and O in Al_2O_3 . Data from Pells and Phillips [1979a].

occur until the incident particle energy was sufficient to displace the more difficult ion, O, while above 870 K it was only necessary to displace the easier atom. In fact, Al diffraction rings observed above 870 K were associated with Al colloidal precipitates. Observations near 77 K indicated no change in the E_d values below ambient temperature, but the data were not reported.

Dell and Goland used the E_d values of Pells and Phillips (18 eV for Al and 76 eV for O) in calculating the σ_{dis} values discussed above. However, Howitt and Mitchell [1981] have published a different interpretation of the data by Pells and Phillips. Their group found a similar decrease in threshold voltage with increasing temperature for MgO; but the effect was ascribed to the thermally activated escape of close Frenkel pairs at high temperatures which would otherwise recombine at lower temperatures [citations in Howitt and Mitchell, 1981]. Under this interpretation, the observations of Pells and Phillips would give an $E_d(Al) \approx 45$ eV and an $E_d(O) \approx 75$ eV at low temperatures, corresponding to the formation of widely-spaced Frenkel pairs, and lower E_d values at high temperatures, corresponding to the formation of close Frenkel pairs. In their HVEM studies of single-crystal Al_2O_3 that was electron-irradiated at high temperature, Howitt and Mitchell also reported another area of disagreement with Pells and Phillips; they did not obtain diffraction evidence for Al and attributed their damage features not to Al metal colloids, but to voids, similar to those obtained in neutron irradiation [citations, Howitt and Mitchell, 1981]. Thus, the use of experimentally determined E_d values to compare the radiation resistance of different materials is not necessarily straightforward.

2.1.2. Dislocation Loops; Defect Aggregates

To show that it is possible that there will not be significant aggregation of displacement defects under 4-K irradiation or ambient temperature warm-up to form dislocation loops or other clustered structures, the results of several comprehensive studies over a range of temperatures will be discussed. First, the HVEM study by Pells and Phillips [1979a,b] discussed above (§2.1.1) did not turn up evidence of dislocation loops in Al_2O_3 until temperatures above about 770 K were reached, although specimens were irradiated near ambient

temperature with 1-MeV electrons, far above the threshold of ~400 keV. Below 770 keV, visible TEM damage consisted of a general darkening of the image dots, thought to result from isolated Frenkel defects. Precipitation of Al colloids, as evidenced by the appearance of Al diffraction rings, was just detectable after annealing damage produced in 300-keV, ambient-temperature irradiation at 658 K.

Since defects produced by electron irradiation are by nature more isolated than those produced by neutrons (§1.2.2), it is also useful to examine the available data from ion irradiation to see if cluster defects are formed. Lee et al. [1985] used TEM to study results of irradiating single-crystal Al_2O_3 from 500 to 900°C with 4-MeV Ne and Ar ions to high doses of ~30 dpa. Half of the specimens were doped with 1000 appm He to simulate the effects of transmutation gas production. For irradiation temperatures of 500 and 600°C, dislocation loops formed, but networks of dislocations did not appear until 700°C. In general, the effect of He on the dislocation microstructure was to increase the loop and network densities. Figure 2.1.9 shows the general trend of data at 500°C. Loop sizes also increased with temperature. Voids were generally not seen at 500 and 600°C. Swelling of ~0.5% was not reported until 700°C, and was increased by He doping. Since irradiation temperatures in this study did not extend below 500°C or to lower doses, it is not possible to conclude from this report that dislocation loops do not form from cascade neutron or ion damage at lower temperatures.

A comparison of the defects observed in neutron-irradiated Al_2O_3 and MgO was made by Stevanovic and Elston [1967] with TEM at ambient temperature. Numerous groups of point defects were found in MgO after irradiation at 60 to 80°C to a fast neutron fluence of $8 \times 10^{23}/\text{m}^2$ ($E > 1$ MeV). In contrast, it was very difficult to observe a few groups of point defects in Al after a higher fluence of $1.5 \times 10^{24}/\text{m}^2$. Gulden [1967] observed only "fine-texture" damage in thin foils of Al_2O_3 irradiated to a fluence of $10^{24}/\text{m}^2$ below 50°C. Dislocation loops developed only on annealing at 1000°C.

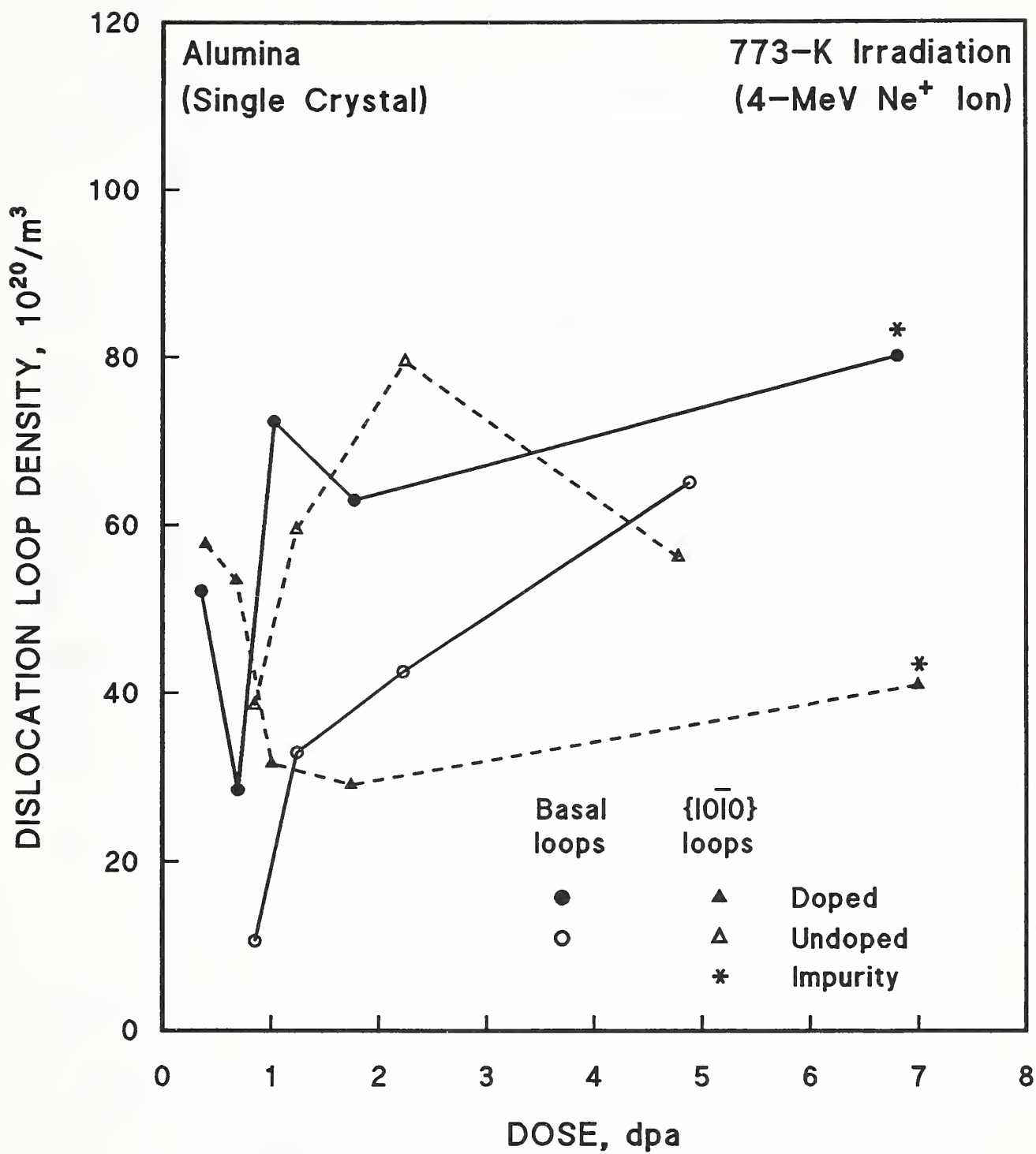


Figure 2.1.9. Dislocation loop density vs. dose, dpa in Al₂O₃. Data from Lee et al. [1985].

2.2. CHANGE IN VOLUME

At low fluences and temperatures, irradiation-induced volume change or swelling is caused by Frenkel pairs or clusters of small size. In the alkali halides, the volume change induced by irradiation has been shown to be proportional to the number of Frenkel pairs [citations in Tanimura et al., 1987]. At higher fluences, and, sometimes, higher temperatures, the anisotropy of expansion of non-cubic material such as Al_2O_3 is of concern, owing to the strains that occur at the grain boundaries of polycrystalline material. Under some conditions, these strains are sufficient to cause intergranular cracking and even powdering of the material [citations in Wilks et al., 1967].

One experiment [Pells and Murphy, 1992] provided limited data on swelling below ambient temperature. Fine-grained, polycrystalline Al_2O_3 was irradiated with 4-MeV Ar ions at temperatures ranging from 800 K to 200 K. After irradiation, the swelling was determined from surface profile measurements to an accuracy of ~ 0.3 vol.%. Although these measurements were made at ambient temperature, which could allow some recovery, a striking increase in volume was observed, as the irradiation temperature decreased, as discussed above in §1.3 (see Figure 1.3.8). The swelling at 200 K (but not, of course, at 4 K) can be estimated by extrapolating the data shown in Figure 2.2.1 to the expected ITER TF-magnet dpa of $\sim 5 \times 10^{-4}$. This gives a value of ~ 0.1 vol.%, a very approximate lower limit for Al_2O_3 under ITER conditions. Because the swelling measurements were obtained at ambient temperature, one could also argue that some degree of recovery had occurred between 200 and 300 K.

Although only limited data on swelling for irradiation of Al_2O_3 below ambient temperature are available, the data for ambient-temperature irradiation cover a range of fast-neutron fluences from 10^{20} to $10^{25}/\text{m}^2$. Data up to about $2.3 \times 10^{21}/\text{m}^2$ were obtained by Tanimura et al. [1987] on single-crystal specimens irradiated at 323 K. Because volume changes at these fluences are relatively small, as Figure 2.2.2 indicates, a capacitance transducer was used to obtain the data. Figure 2.2.2 also indicates the difference in expansion along the a and c axes. Data for MgAl_2O_4 were also obtained and are included in the figure for comparative purposes; these results are discussed further below (§7.2). Tanimura et al. also measured optical absorption spectra at liquid

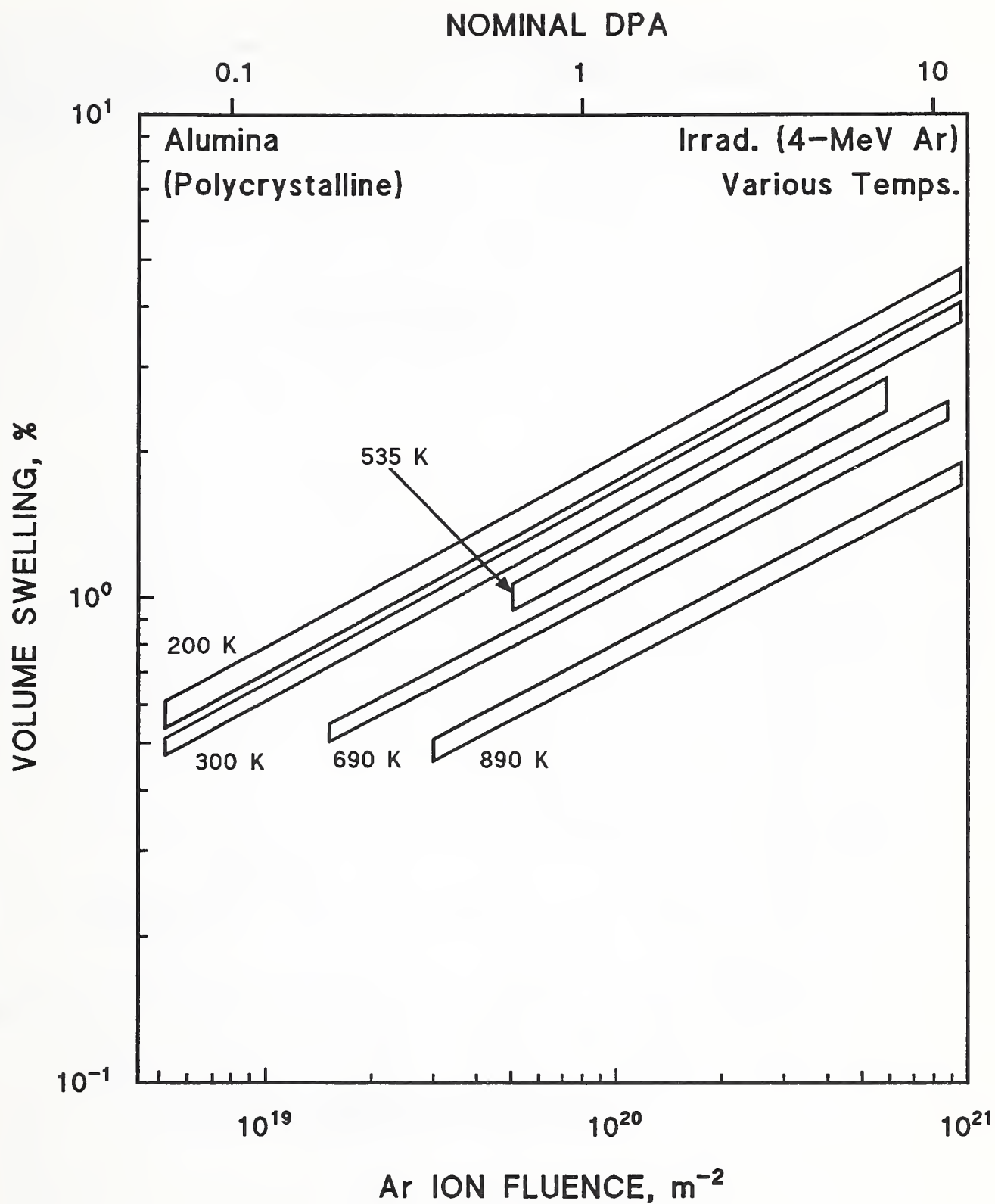


Figure 2.2.1. Log/log dependence of volume swelling upon Ar-ion fluence. The nominal dpa is calculated. Data from Pells and Murphy [1992].

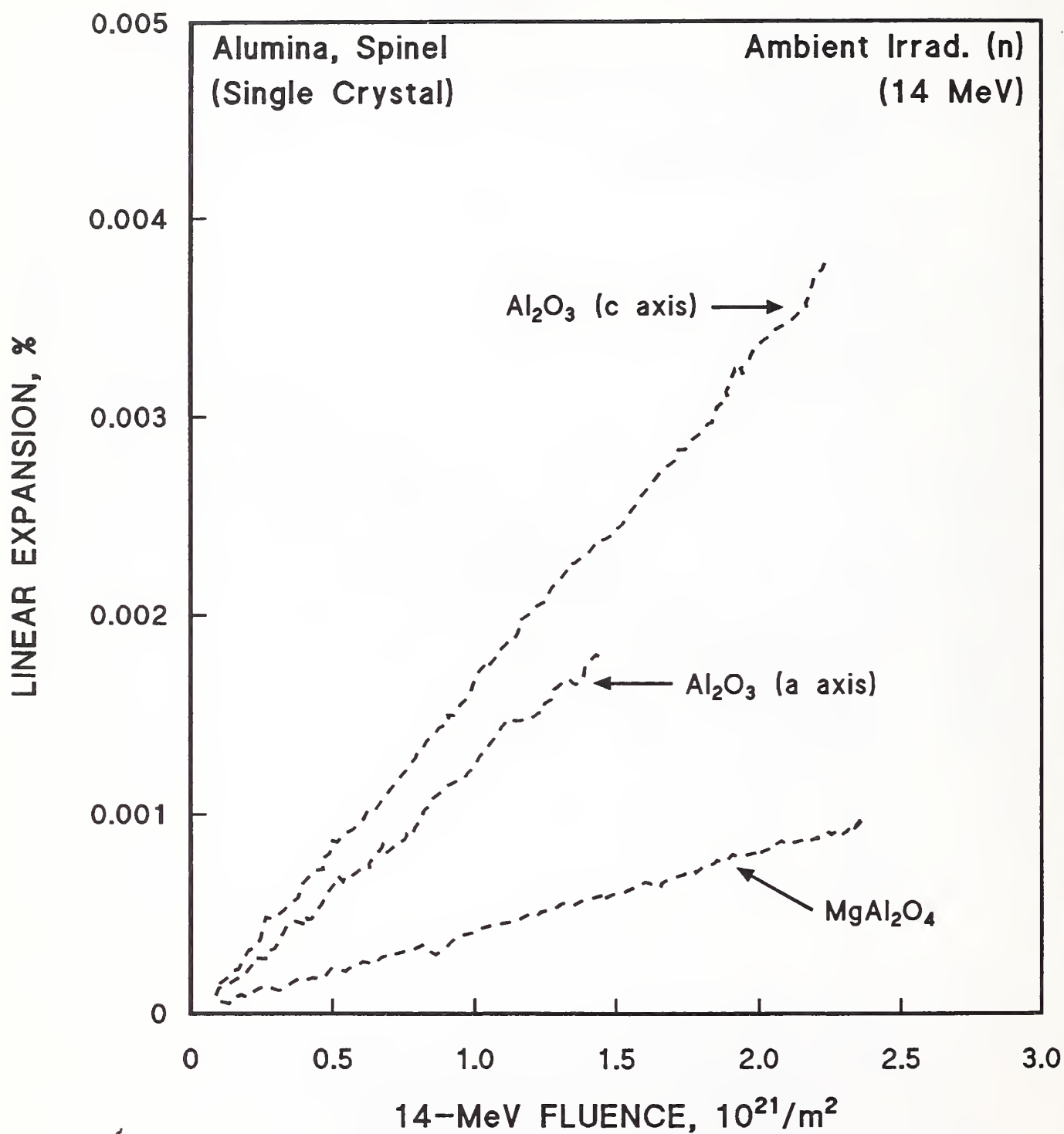


Figure 2.2.2. Linear expansion, $\Delta L/L$, of Al_2O_3 and MgAl_2O_4 . Data from Tanimura et al. [1987].

nitrogen temperature and found the concentration of vacancies generated by irradiation with 2.95×10^{21} neutrons/m² to be 2×10^{18} cm⁻³, which fitted with an extrapolation of the results obtained by Evans and Stapelbroek discussed above (see Figure 2.1.2). This gave a volume per Frenkel pair in Al₂O₃ of 0.4 molecular volume, where the volume change was taken to be the length change along the c axis plus twice that along the a axis. Data at slightly higher fluences at 30°C were obtained by Martin [1959] on single-crystal Al₂O₃. The data are shown in Figure 2.2.3 as a function of slow neutron fluence. The reported accuracy of the length measurements was about 5 ppm (0.0005%). Data at lower fluences appear to be in approximate accord with those of Tanimura et al.

Data for a higher range of fission fast neutron fluence ($E \geq 1$ MeV) were reported by Wilks et al. [1967]. The irradiation temperature was 150°C. These data, also obtained on single-crystal Al for both the a and c axes, are shown in Figure 2.2.4, and are in approximate agreement with the results of Martin. Initially, at fluences below about 10^{23} /m², Wilks et al. reported that the expansion along the c axis was slightly larger than that along the a axis; however, there is a crossover point between 3 and 5×10^{24} /m². This crossover was substantiated when more data were obtained at lower fluences with the "608" apparatus; these data are not shown in Figure 2.2.4. The apparent discontinuity in the expansion was attributed to an uncertainty in the fluence calibration or to differences in spectra. There appears to be some degree of saturation at a fluence of about 1×10^{24} /m² at 150°C, but Pells and Murphy [1992] confirmed that saturation in defect density appeared to be delayed at 77 K, in comparison to 300 K (Figure 1.3.9). Thus, saturation in volume swelling at 4 K cannot be assumed for this range of fluence.

The linear expansion data of Wilks et al. [1967] end at a fast neutron fluence of about 10^{24} /m²; however, data are available from just below this fluence to about 5×10^{24} /m² in a review by Wilks [1968] (Figure 2.2.5). The irradiation temperatures of ~100°C are slightly lower than those of Wilks et al. Not much difference is seen between expansion along the a and c axes until about 4×10^{24} /m². The reversal of a and c expansion reported by Wilks at about 6×10^{24} /m² does not appear (Figure 2.2.4). Some linear expansion data at much

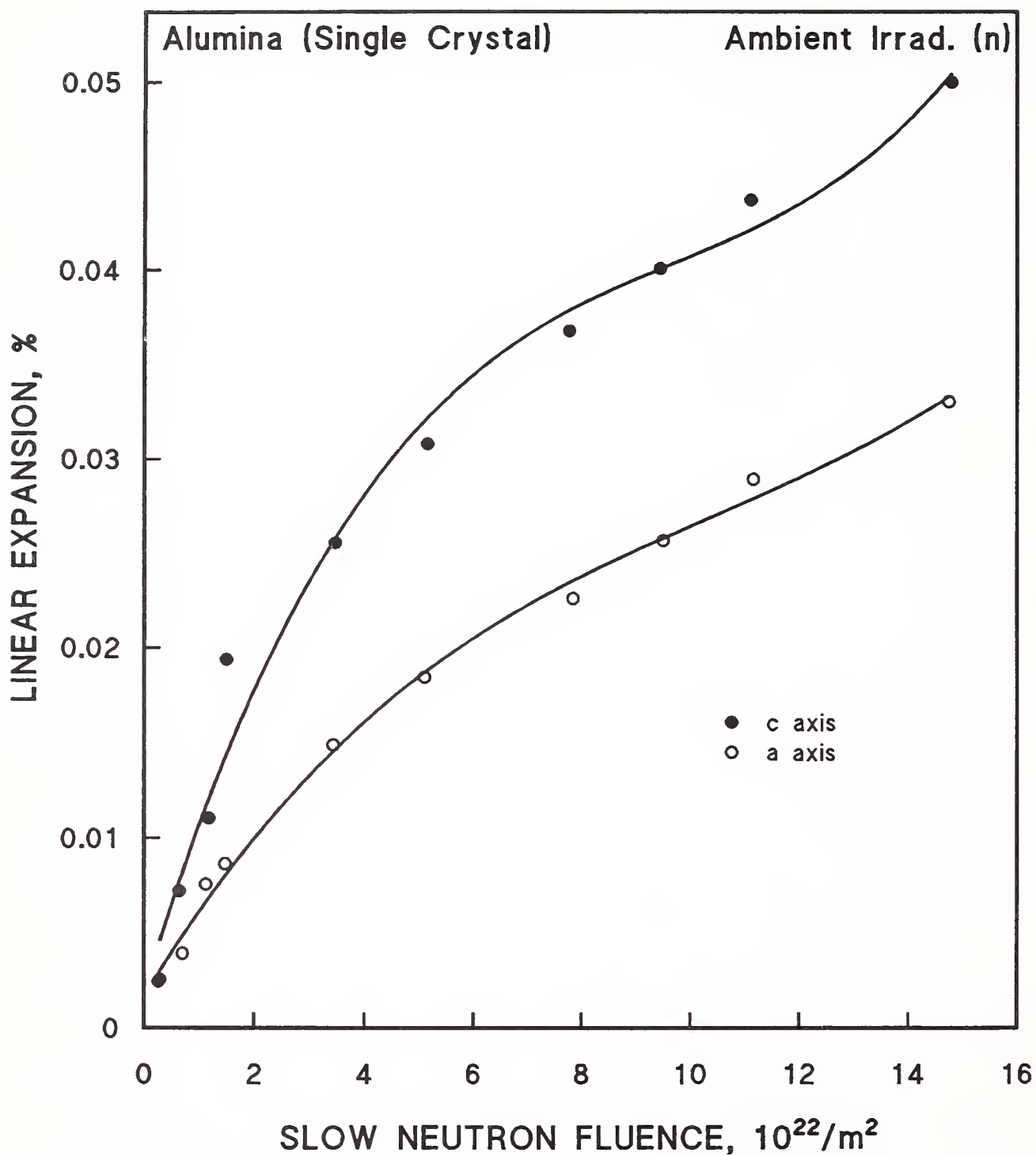


Figure 2.2.3. Linear expansion, $\Delta L/L$, of Al_2O_3 single crystals. Data from Martin [1959].

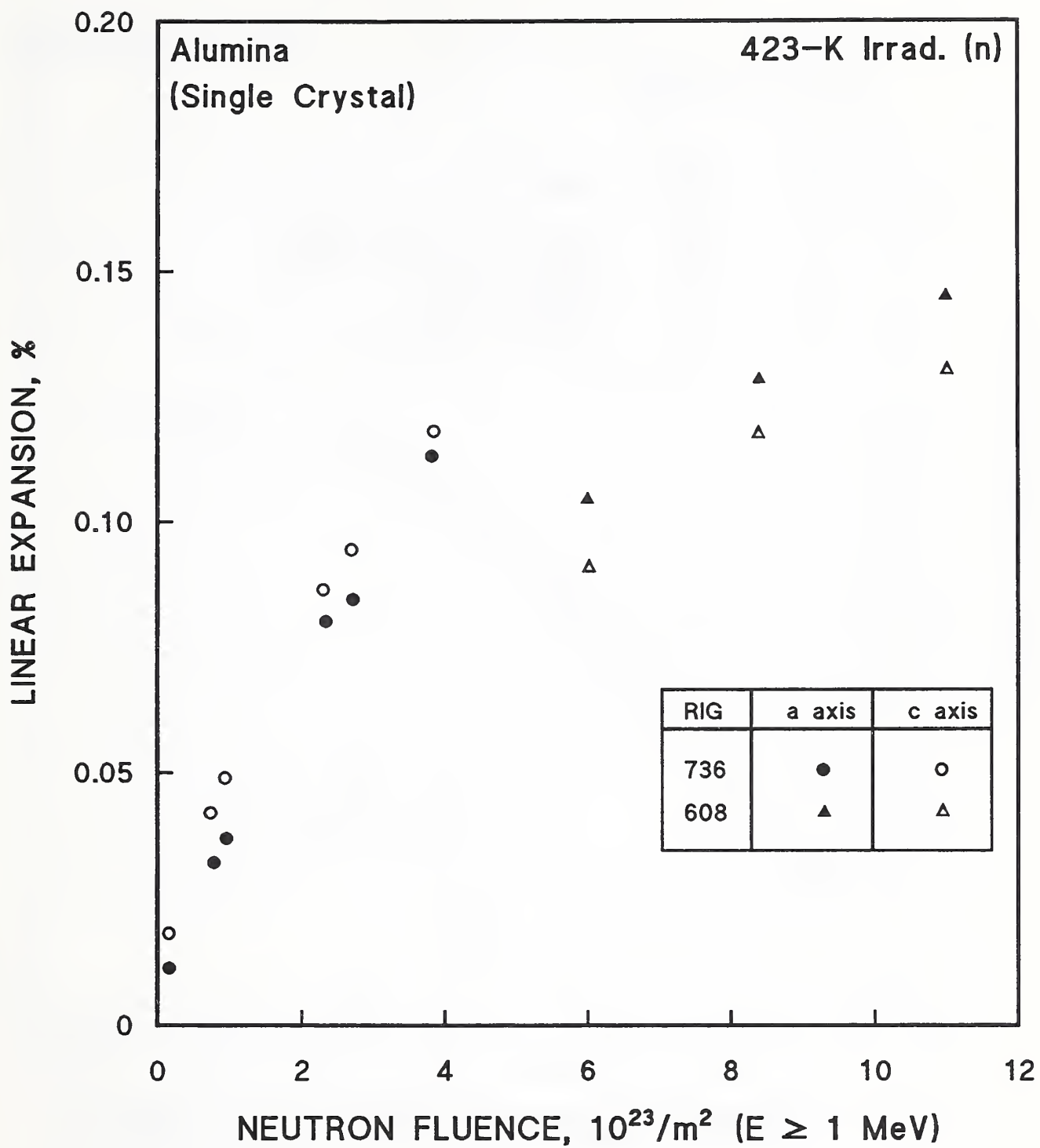


Figure 2.2.4. Linear expansion, $\Delta L/L$, of Al_2O_3 single crystals during neutron irradiation at 423 K. Data from Wilks et al. [1967].

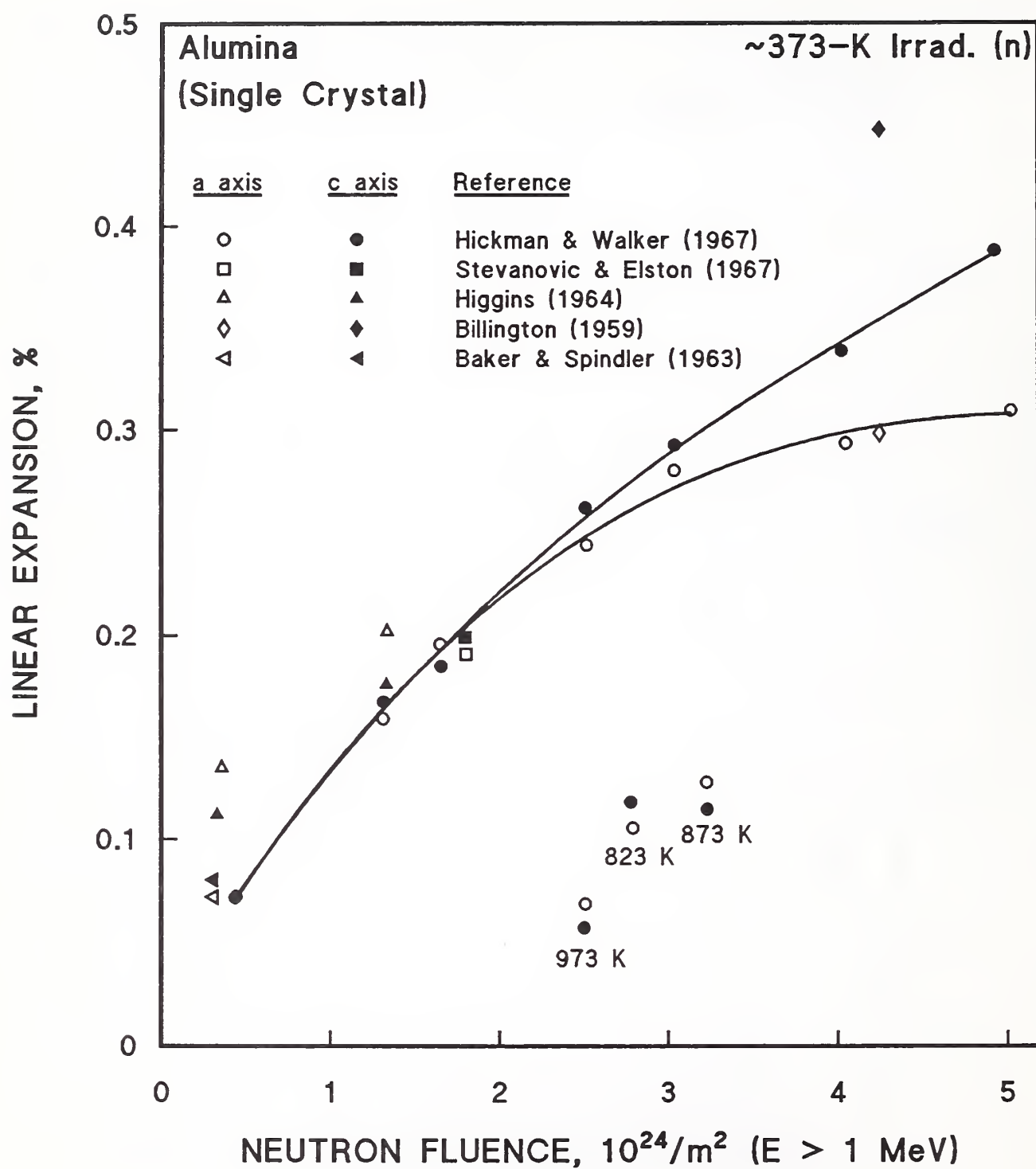


Figure 2.2.5. Linear expansion, $\Delta L/L$, of Al_2O_3 single crystals. A few higher irradiation temperatures are indicated on the graph. Data and citations from Wilks [1968].

higher irradiation temperatures are shown; these values are significantly lower, probably owing to the greater degree of damage recovery.

For irradiation at $\sim 100^\circ\text{C}$ (373 K), Hickman and Walker [citation, Wilks, 1968] reported that the macroscopic density change was not equal to the density change that would be calculated from the change in lattice parameters, as measured by X-ray diffraction. Possible reasons for this are discussed by Wilks [1968]. A review of density changes measured up to a fast neutron fluence of $5 \times 10^{24}/\text{m}^2$ was given by Wilks [1968]; the data are shown in Figure 2.2.6. The lower portion of the curve agrees with a density change of -0.1 to -0.13% reported by Antal and Goland [1958] at a fluence of $1.2 \times 10^{23}/\text{m}^2$ below 40°C . The density change is about -1% at a fluence of $5 \times 10^{24}/\text{m}^2$. This change is in good agreement with the volume change of about $+1\%$ at $5 \times 10^{24}/\text{m}^2$ measured by Keilholtz et al. [1971] that is discussed below (Figure 2.2.7). No microcracking was observed by optical techniques in fluences up to this value [citations, Wilks, 1968]. However, microcracking visualized by X-ray microscopy was reported in polycrystalline material of $50\text{-}\mu\text{m}$ grain size and 7.5% porosity after irradiation at 150°C to a fluence of $3.2 \times 10^{23}/\text{m}^2$, but was said not to occur in single crystals and polycrystalline material of $37\text{-}\mu\text{m}$ grain size and 0.5% porosity, at a higher fluence of $1.3 \times 10^{24}/\text{m}^2$ [Higgins, 1964, citation, Wilks, 1968]. Higgins concluded that microcracking depended upon a high porosity, and that the cracks nucleated at the pores between grains. This could indicate microcracking problems in plasma-sprayed Al_2O_3 , because porosity is usually much higher than in the sintered material.

From their results on single crystals, Wilks et al. [1967] calculated the maximum intergranular strain expected in polycrystalline Al_2O_3 after irradiation at 150°C (423 K), including the residual boundary strain that arises from the anisotropic thermal contraction on cooling from 1000°C . It was assumed that grain boundary relaxation did not occur below 1000°C . The value obtained for the strain, $\epsilon = 1.05 \times 10^{-3}$, after a neutron fluence of $1.1 \times 10^{25}/\text{m}^2$, was then substituted into an expression for the stored strain energy per unit area of grain boundary:

$$U = (1/12)E\epsilon(x - c)/(1 - \nu^2), \quad (2.1)$$

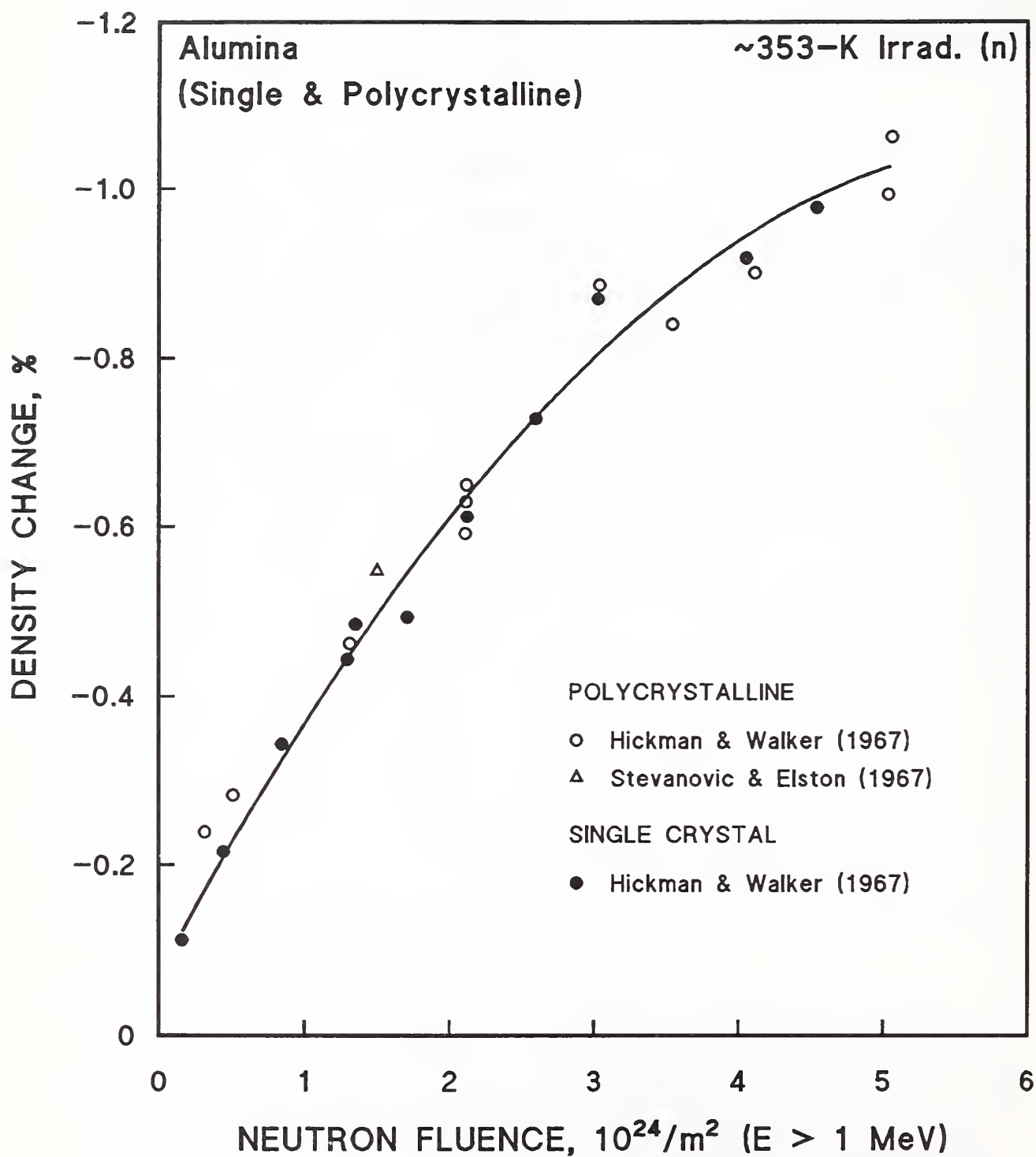
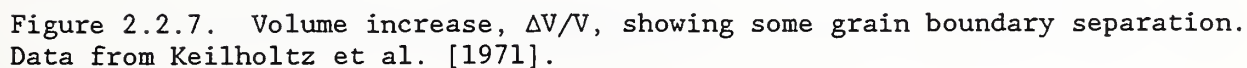


Figure 2.2.6. Density changes of both single and polycrystalline Al_2O_3 . Data and citations from Wilks [1968].



where E is Young's modulus (460 GPa), ν is Poisson's ratio (0.254), $2x$ is the grain diameter (in cm), and c is the general crack length, taken as $x/5$, a typical pore size. For grain sizes below 100 μm , U was less than 2γ , where γ is the surface energy of a boundary, estimated to be larger than 0.9 J/m². Therefore, microcracking was not expected, in agreement with the results cited for fluences in the range of 1 to $5 \times 10^{24}/\text{m}^2$ in polycrystalline Al_2O_3 .

Keilholtz et al. extended the irradiation of polycrystalline Al_2O_3 to somewhat higher fluences at low temperatures, obtaining the volume changes shown in Figure 2.2.7. Grain boundary separation was observed above about $2.3 \times 10^{25}/\text{m}^2$ ($E > 1$ MeV) for irradiations between 110 and 325 °C, but no separation up to $\sim 5.5 \times 10^{25}/\text{m}^2$ if the irradiation was carried out between 70 to 90°C. At the higher irradiation temperatures (110 to 325°C), the grain boundary separation became very severe at a fluence of $4.7 \times 10^{25}/\text{m}^2$, and many of the specimens exposed to fast fluences greater than $3 \times 10^{25}/\text{m}^2$ were extensively fractured. At the lower temperatures (70 to 90°C), even metallographic examination of the specimens did not reveal grain boundary separation. Stevanovic and Elston [1967] also did not find any change in the appearance of the grain boundary in sintered Al_2O_3 irradiated below 80°C for fluences of $\sim 10^{24}/\text{m}^2$. Their observations were made with an optical microscope.

The quoted temperatures of Keilholtz et al. were not directly measured; rather, they were values calculated from the γ -heat generation rate, the thermal conductivities of the materials, and the expected heat transfer properties of the irradiation assemblies. Consequently, the two temperature ranges should be considered valid in a relative, rather than an absolute, sense. Therefore, in attempting to estimate the amount by which the critical fast neutron fluence of about $10^{25}/\text{m}^2$ for grain boundary separation should be downgraded to allow for irradiation at 4 K, the suggested factor of 100 (§1.3) may be too low, if the higher temperature range was actually considerably above 110 to 325°C. However, it is encouraging that no grain boundary separation was observed up to almost $3 \times 10^{25}/\text{m}^2$ in the lower temperature range estimated as 70 to 90°C, and that the volume increase was very comparable for four different types of polycrystalline Al_2O_3 , as shown below in Figure 2.2.8. These data indicate that grain boundary separation is unlikely at 4 K at a fast neutron fluence of $10^{22}/\text{m}^2$, but only in situ testing would provide a

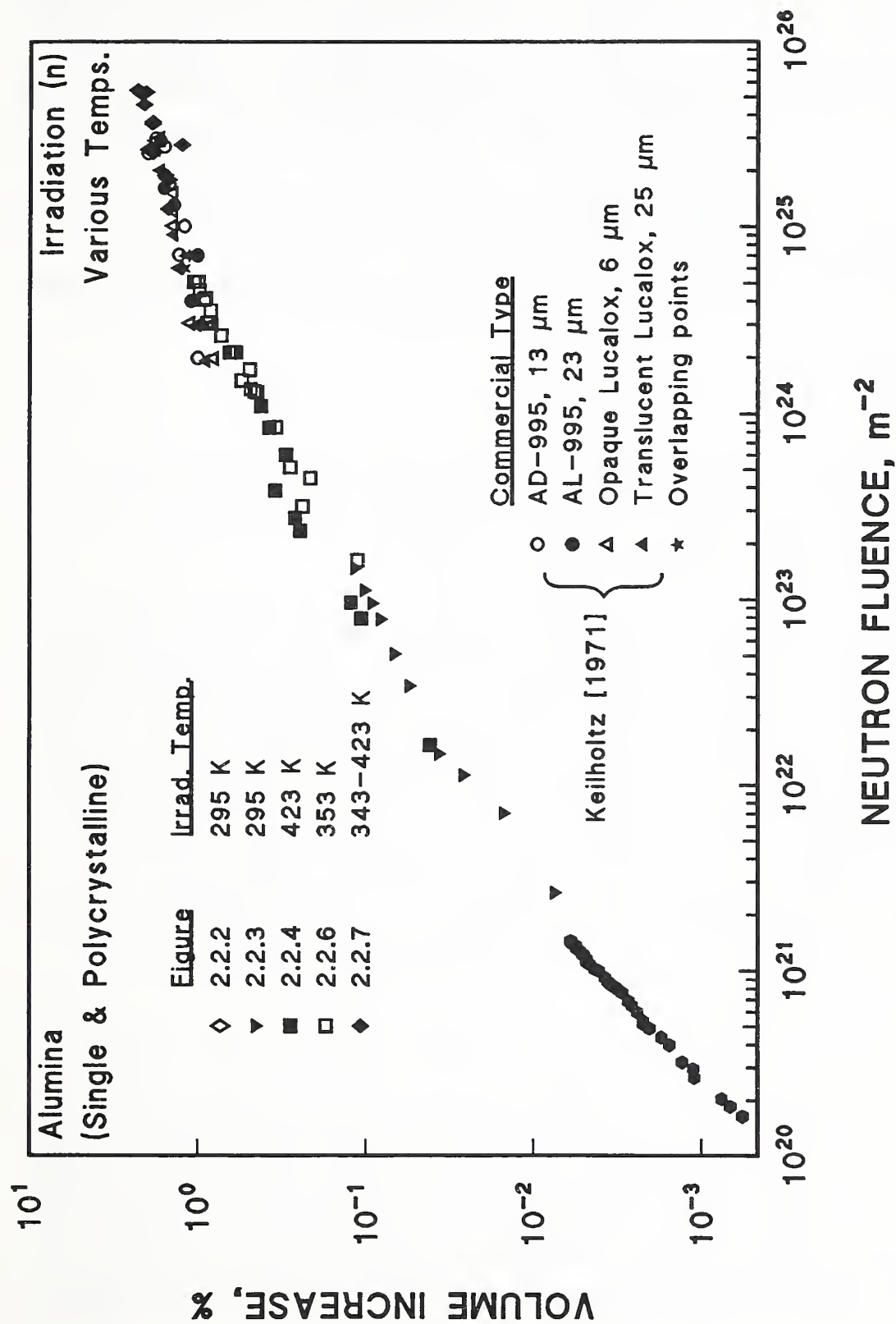


Figure 2.2.8. Comparison of data from the six preceding figures and additional data from Keilholtz et al. [1971].

Table 2.2.1. Characteristics of Commercial Aluminum Products.
Data from Keilholtz et al. [1971].

TYPE OF Al_2O_3^*	SOURCE	BULK DENSITY, g/cm^3	AVERAGE GRAIN SIZE, μm
AD-995	Coors Porcelain Co.	3.86	13
AL-995	Western Gold and Platinum Co.	3.85	23
Opaque Lucalox	General Electric Co.	3.91	6
Translucent Lucalox	General Electric Co.	3.96	25

* All specimens of the same type used in irradiation testing were of the same batch.

definitive answer to this question. Note that the materials tested were all of high density (low porosity) and that the largest grain size was 25 μm . Information on these materials is given in Table 2.2.1.

Figure 2.2.8 is a composite of all of the volume expansion data obtained after irradiation near ambient temperature (~ 323 to 423 K). The expression $\Delta V/V = 2\Delta L_a/L_a + \Delta L_c/L_c$ was used to combine linear data with volume data. The spectrum of the fluences, of course, is not completely comparable, so the agreement is satisfactory. The figure includes additional data from Keilholtz et al. [1971] on four different types of commercial Al_2O_3 products. All show very similar expansion vs. fluence, which is expected because grain size should have no effect on polycrystalline expansion (below the fluence at which grain boundary separation occurs) and purity also should have very little effect.

Finally, results of comparative volume expansion measurements on single crystals of Al_2O_3 and MgO are reviewed. Desport and Smith [1964] found very similar fractional growth for both oxides after neutron irradiation at $<150^\circ\text{C}$ to fluences of $\sim 4 \times 10^{23}/\text{m}^2$ and $\sim 4 \times 10^{24}/\text{m}^2$ ($E > 1$ MeV). The percent volume swelling at the higher fluence was about 0.35 for MgO and 0.41 for Al_2O_3 . At an intermediate fluence of $\sim 1.1 \times 10^{24}/\text{m}^2$, both oxides swelled by about 0.3 vol.% These amounts could be representative of the swelling at 4 K from a

fast neutron fluence about 100 times smaller. At lower neutron irradiation temperatures of 60 to 80°C, Stevanovic and Elston [1967] also reported similar changes in the density of Al_2O_3 and MgO at fluences of about $10^{24}/\text{m}^2$ ($E > 1$ MeV). However, the swelling of MgO per unit fluence was about twice that of Al_2O_3 . The amount of swelling was greater than that reported by Desport and Smith, probably owing to the lower irradiation temperature. This would indicate that the degree of swelling after ambient-temperature irradiation does provide some basis for selection between the two oxides.

2.3. AMORPHIZATION

According to the bond-type criterion of Naguib and Kelly [1975] discussed in §1.6 above, materials with a Pauling ionicity of less than 0.6 should amorphize easily under irradiation. The Pauling ionicity of $\alpha\text{-Al}_2\text{O}_3$ is 0.63 (intermediate ionic bonding). McHargue et al. [1986] irradiated single-crystal Al_2O_3 with various ions at 77, 300, and 640 K and examined the resulting damage states. Fluences ranging from 10^{19} to $10^{21}/\text{m}^2$ were used at energies of 40 to 300 keV. The specimens were examined with Rutherford backscattering-ion channeling techniques (RBS-C) using 2-MeV He ions to determine the depth profile of the implanted ions, the distribution of damage, and the lattice location of the impurity. The chief measure of damage or lattice disorder was the minimum yield, χ_{\min} , as determined at the depth where peak damage occurred. The minimum yield is defined as the ratio of the RBS yield from an aligned specimen to the yield from a randomly-oriented specimen. The data were presented as a function of the calculated dpa, in order to compare the effects from ions of different masses and energy. The dpa were calculated using the modified Kinchin-Pease equation with $E_d(\text{Al}) = 18$ eV and $E_d(\text{O}) = 72$ eV and the treatment of Coulter and Parkin cited above (§2.1.2). Raman spectroscopy and TEM were also used to examine the specimens.

The disorder in the Al sublattice at the peak damage position was found to be about the same for irradiation temperatures of 300 and 640 K, perhaps owing to the considerable degree of recovery at the higher temperature. But irradiation at 77 K by Cr ions gave a significantly higher degree of amorphization for a given dpa than irradiation at 300 K, as Figure 2.3.1 indicates. The amorphous layer, confirmed by TEM, extended well beyond the peak concentration

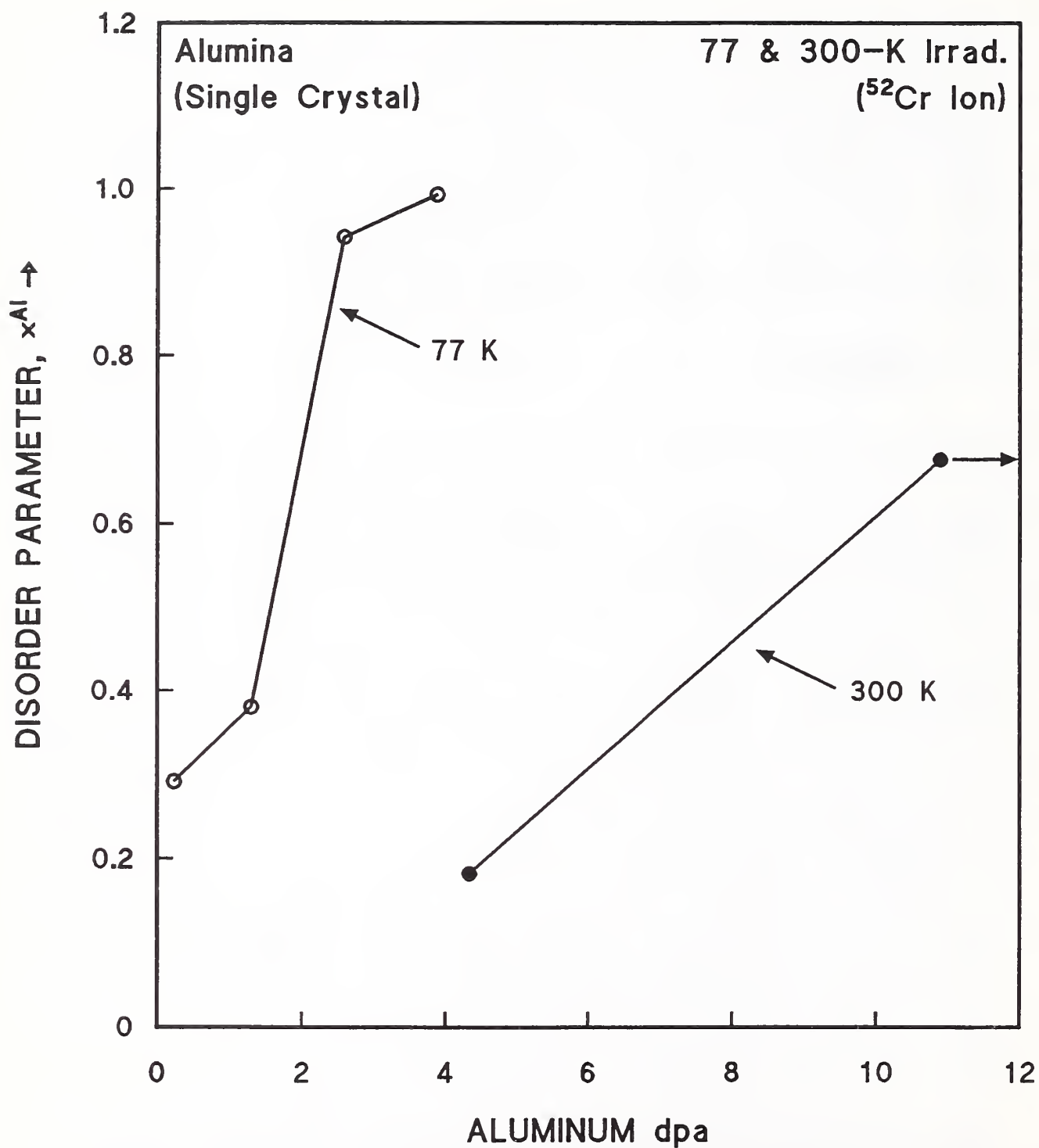


Figure 2.3.1. Disorder of the Al sublattice measured by RBS after Cr-ion implantation of Al_2O_3 at the indicated temperatures. Data from McHargue et al. [1986].

of Cr, to about 120 nm. The critical fluence for amorphization at 77 K corresponded to ~3 dpa. The arrow on the 300-K curve shows that disorder in the Al lattice, χ^{Al} , remained constant at 0.66 for the fluence range required to produce a dpa from 10.9 to 109, indicating that defects were annihilated (recovered) at the same rate as they were produced. However, data from Burnett and Page [citation, McHargue et al., 1986] indicated that amorphization occurred at 300 K for a Cr fluence (300 keV) equivalent to 600 dpa. Hence, McHargue et al. concluded that the critical fluence for Cr amorphization at 77 K (~3 dpa) was about 200 times less than that required at 300 K. Figure 2.3.1 also indicates that the dpa required for a significant degree of lattice disorder, $\chi^{\text{Al}} \approx 0.3$, is over 6 dpa at 300 K, but about 0.2 dpa at 77 K. Since the RBS measurements were evidently made at ~300 K, some recovery of 77-K damage (before complete amorphization) may have occurred.

Because foreign-ion implantation introduces the possibility of chemical effects upon the damage state, specimens were also implanted with similar fluences of Al and O ions at 77 K, in correct stoichiometric ratio. The Al fluence, at 90 keV, was $4 \times 10^{20}/\text{m}^2$; the 55-keV O fluence was $6 \times 10^{20}/\text{m}^2$. The RBS spectra again indicated an amorphous region, to a similar depth of 150 nm. (Apparently, the threshold fluence required for amorphization at 77 K was not established; the fluences used corresponded, approximately, to fast neutron fluences about a factor of 10^4 to 10^6 higher, according to calculations reviewed in §1.2.6.) At 300 K, however, amorphization could only be produced with certain cations, such as Zn and Zr. McHargue et al. concluded that Zr stabilized the defects to prevent recovery processes, or prevented the disordered regions within the cascades from reordering. Because host-ion amorphization occurred at 77 K, damage alone can produce the amorphous state if recovery is suppressed. The degree of recovery that occurs between 4 and 77 K is not known. Therefore, the dpa and fluences required for significant damage in material held at 4 K may be much smaller than expected. Hence, neutron or host atom irradiation of ITER insulation and in situ RBS measurements at 4 K would be highly desirable. If significant amorphization occurs at 4 K, the material may not recover after warm-up, since McHargue et al. were able to measure considerable amorphization induced at 77 K after warm-up for RBS measurements.

Plasma-sprayed coatings of Al_2O_3 may amorphize under lower fluences than those required for a single crystal. A comprehensive study showed that this occurred for MgAl_2O_4 (see §7.3). Iwamoto et al. [1985a] reported than an amorphous layer in plasma-sprayed Al_2O_3 formed at Ar fluences of 10^{20} and $10^{21}/\text{m}^2$.

Matzke and Whitton [1966] irradiated single-crystal specimens of Al_2O_3 and MgO , as well as other materials, in an effort to determine the dose required for amorphization. Electron diffraction was used to examine the perfection of crystals irradiated with 40-keV ions (Kr and Xe). Irradiation temperatures were estimated to be below 70°C . At a fluence of $8 \times 10^{17}/\text{m}^2$, the Kikuchi lines that indicate crystal perfection were weaker in MgO ; at a fluence of $4 \times 10^{18}/\text{m}^2$, the lines had disappeared. In contrast, the Kikuchi lines in Al_2O_3 had disappeared at a dose of $4 \times 10^{17}/\text{m}^2$. This indicates that the anisotropic Al_2O_3 has considerably less structural stability under irradiation than the cubic substance, MgO . (Other cubic substances such as NaCl and CaF_2 were considerably more stable than MgO .) Comparable ambient-temperature fast neutron fluences would be approximately a factor of 10^4 to 10^6 higher (§1.2.6).

In contrast to Matzke and Whitton, Stevanovic and Elston [1967] reported that single-crystal Al_2O_3 X-ray lines were sharp and symmetrical after irradiation to a fast neutron fluence of $1.8 \times 10^{24}/\text{m}^2$ ($E > 1 \text{ MeV}$) at an irradiation temperature of 60 to 80°C , but that some MgO lines were asymmetrical and broadened, particularly on the high-angle side, after a fluence of $1.0 \times 10^{24}/\text{m}^2$. However, the level of damage was considerably below that produced in the foreign-ion irradiations of Matzke and Whitton.

2.4. MECHANICAL PROPERTIES

Little relevant data are available on mechanical properties of Al_2O_3 after low-temperature irradiation. However, point-contact loading often damages ceramic materials, especially if a combination of normal and tangential forces are present. Noda et al. [1985] determined that deposition of a thin metal film on single-crystal Al_2O_3 and additional ion irradiation improved the resistance against cracking under a biaxial loading. Figure 2.4.1 shows the increase in critical peeling load in 100-keV, N-ion irradiated sapphire on which a 220-nm Zr film had been deposited. The film was deposited in vacuum

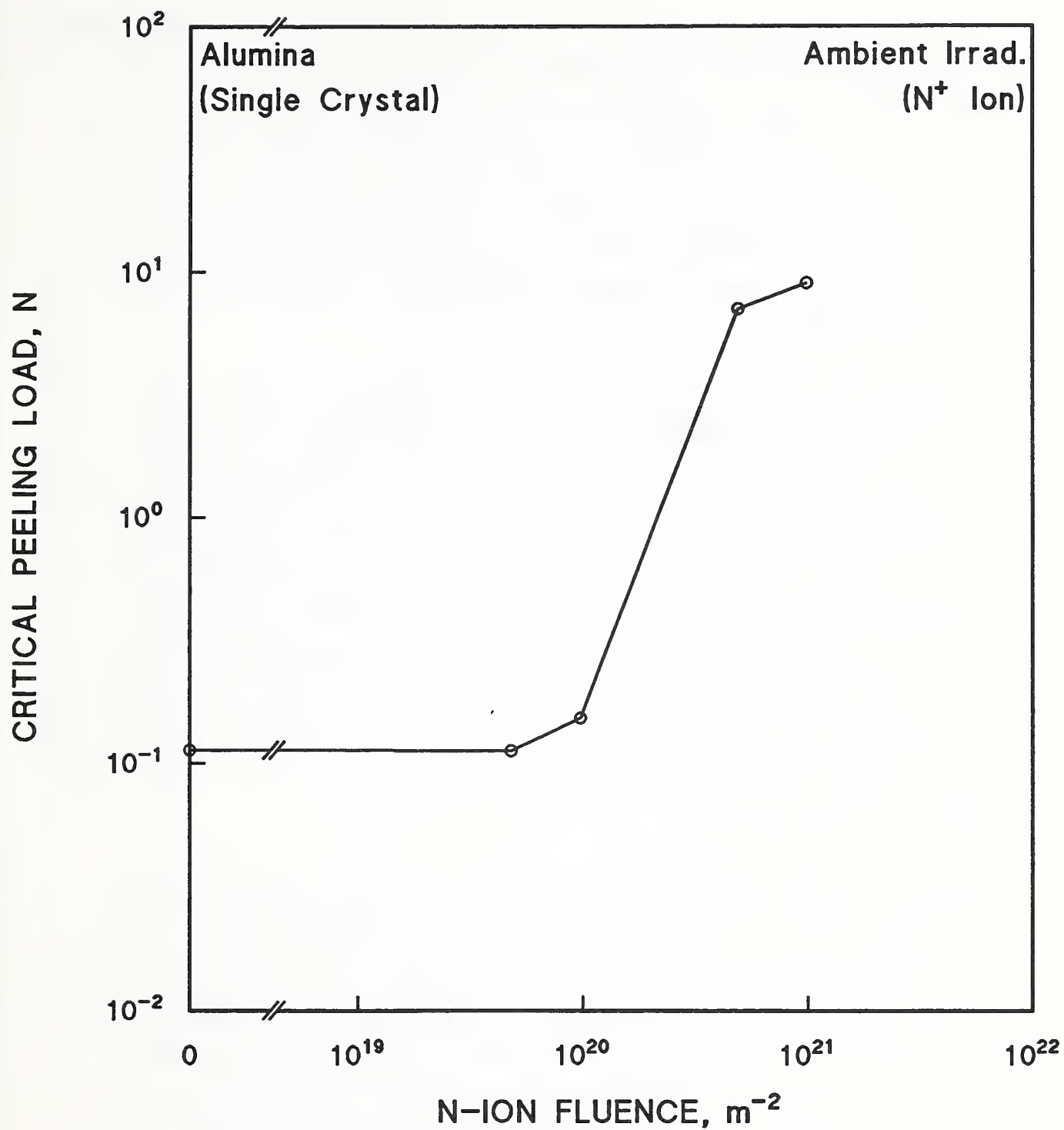


Figure 2.4.1. Critical peeling load of Zr film on Al₂O₃ with 0.1-mm radius diamond stylus and scratching speed of 50 mm/min. Data from Noda et al. [1985].

(5×10^{-4} Pa) onto a mirror-polished surface. The peeling load was determined by scratching the surface with a diamond stylus of 0.1-mm width under the load. The scratching also caused cracking of the sapphire surface above a critical load. However, Figure 2.4.2 shows that this critical cracking load first increases and then decreases with ion fluence. The results were explained by suggesting that the compressive stress generated from expansion under irradiation compensated the tensile stress generated by the scratching. The adhesive metal layer also increases resistance. Further details may be found in the paper.

The relative decrease of Young's modulus in sintered Al_2O_3 after a fast neutron fluence of $1.5 \times 10^{24}/\text{m}^2$ ($E > 1$ MeV) was found to be 3.4% [Stevanovic and Elston, 1967]. These authors also measured the change in Vickers microhardness with an accuracy of $\pm 2\%$. For a fluence of $1.2 \times 10^{24}/\text{m}^2$, the average increase was 16.7%. The Wigner energy was measured in a differential thermal-analysis calorimeter after the same fluence. It was 105 ± 8 kJ/kg. All of these measurements were made at ambient temperature. The reactor temperature was between 60 and 80°C (333 and 353 K). For much higher temperatures of irradiation, between 400 and 600°C, Dienst [1992] also found a decrease in Young's modulus at a fast neutron fluence of about $2 \times 10^{26}/\text{m}^2$ ($E > 0.1$ MeV). This decrease of about 13%, from 375 to 325 GPa, apparently applied to both the single and polycrystalline Al_2O_3 studied.

Dienst cites other high temperature irradiation studies that appeared to indicate that the strength of single-crystal Al_2O_3 should remain unchanged under irradiation [Clinard et al., 1984], because strength changes would be governed by the formation of grain boundary cracks. Clinard et al. measured small increases in the 4-point bending strength after a fast neutron fluence of $\sim 2 \times 10^{26}/\text{m}^2$ ($E > 0.1$ MeV) at 407 and 542°C. However, Dienst showed a deterioration, between fluences of 10^{24} and $10^{25}/\text{m}^2$ ($E > 0.1$ MeV), in the 4-point bending strength of both single-crystal and polycrystalline Al_2O_3 (Figure 2.4.3) and also a decrease in the Weibull modulus (Figure 2.4.4), which indicated a broadening in the distribution of the ultimate strength, owing to an increased number of specimens of very low strength. Dienst correlated this deterioration with the increase in volume of Al_2O_3 (similar results were obtained for AlN), as shown in Figures 2.4.5 through 2.4.7.

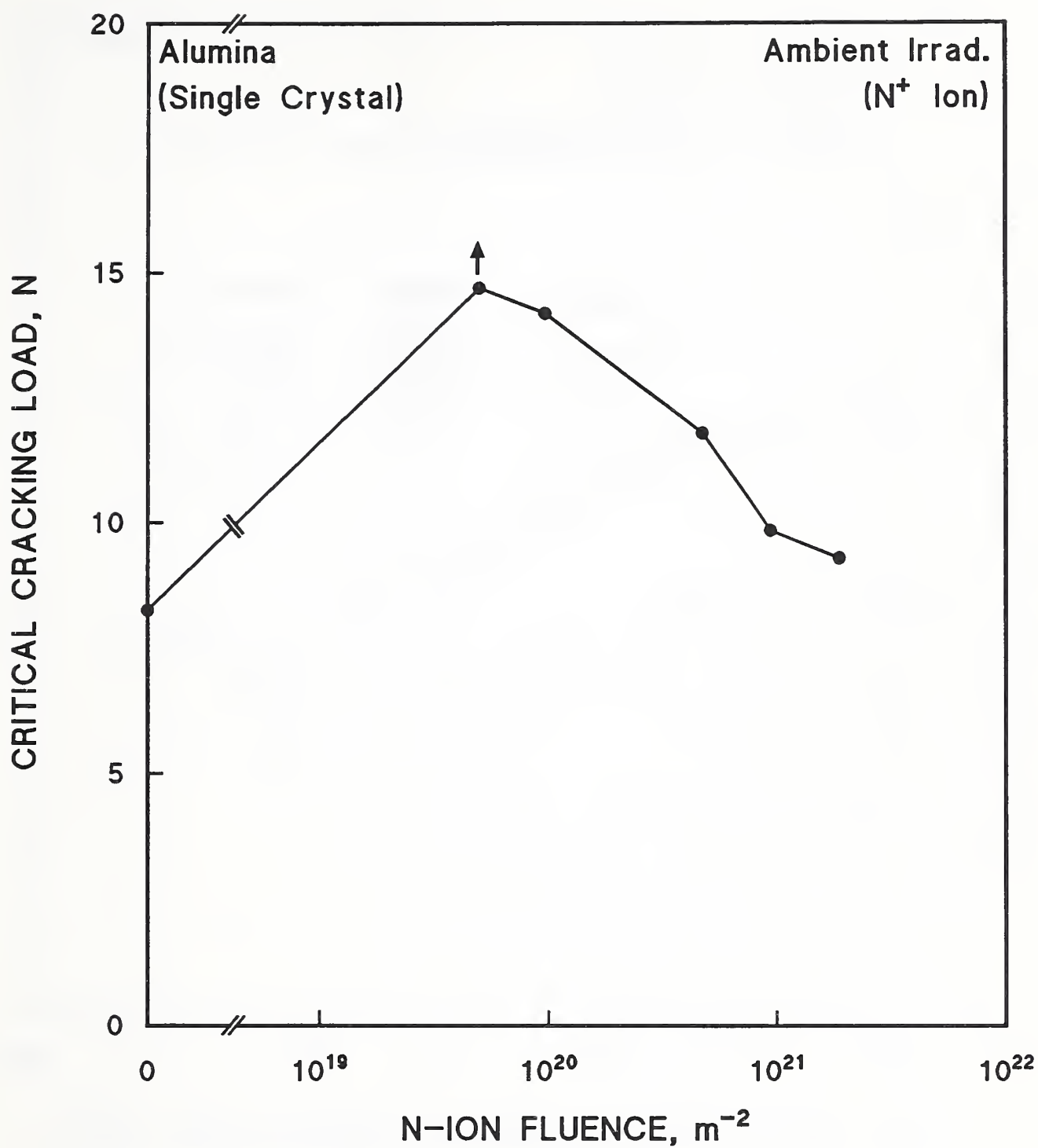


Figure 2.4.2. Critical cracking load of Ti film on Al_2O_3 with 0.1-mm radius diamond stylus and scratching speed of 50 mm/min. Data from Noda et al. [1985].

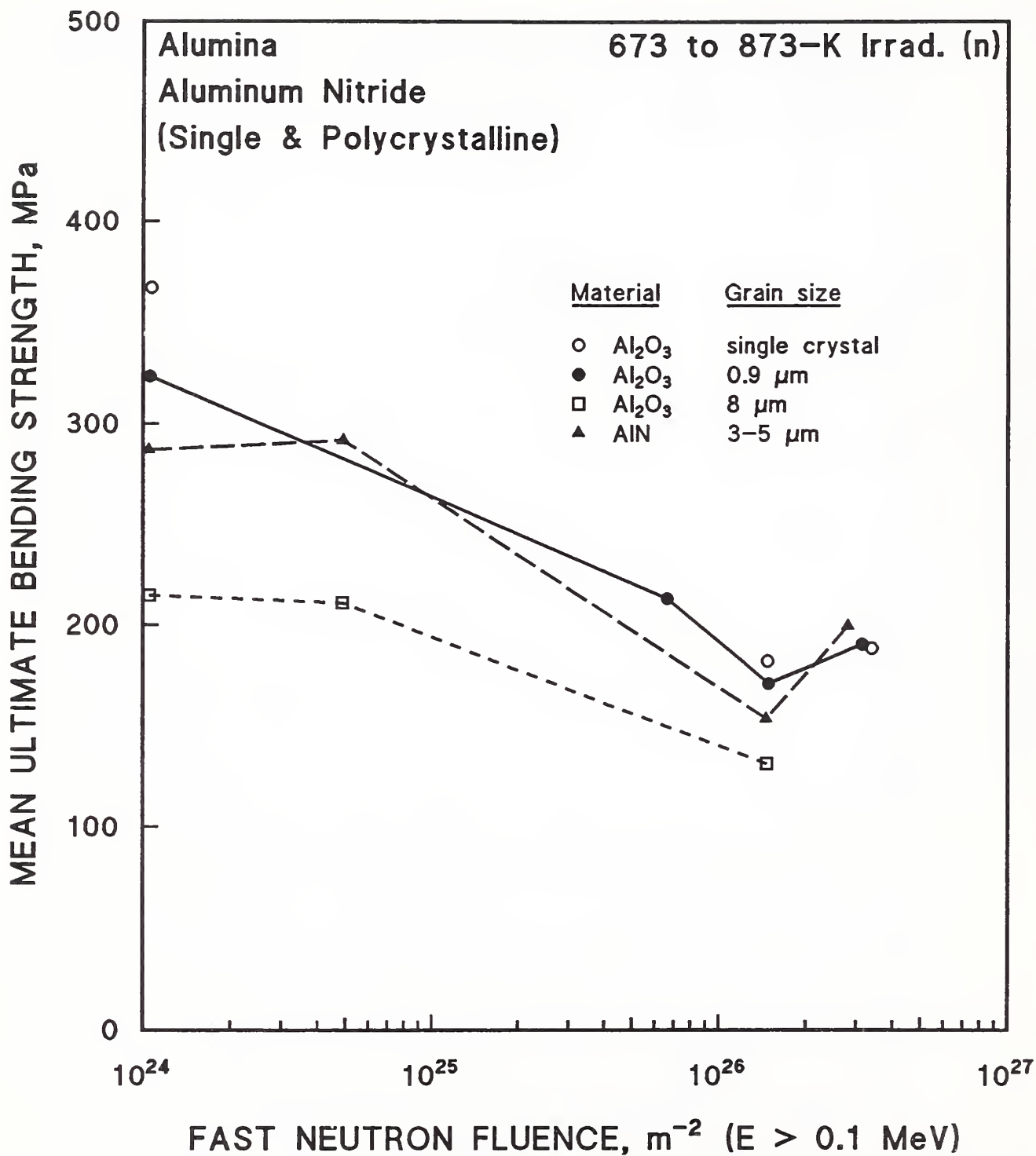


Figure 2.4.3. Decrease of four-point bending strength in Al_2O_3 and AlN with irradiation at ~ 400 – 600°C . Data from Dienst [1992].

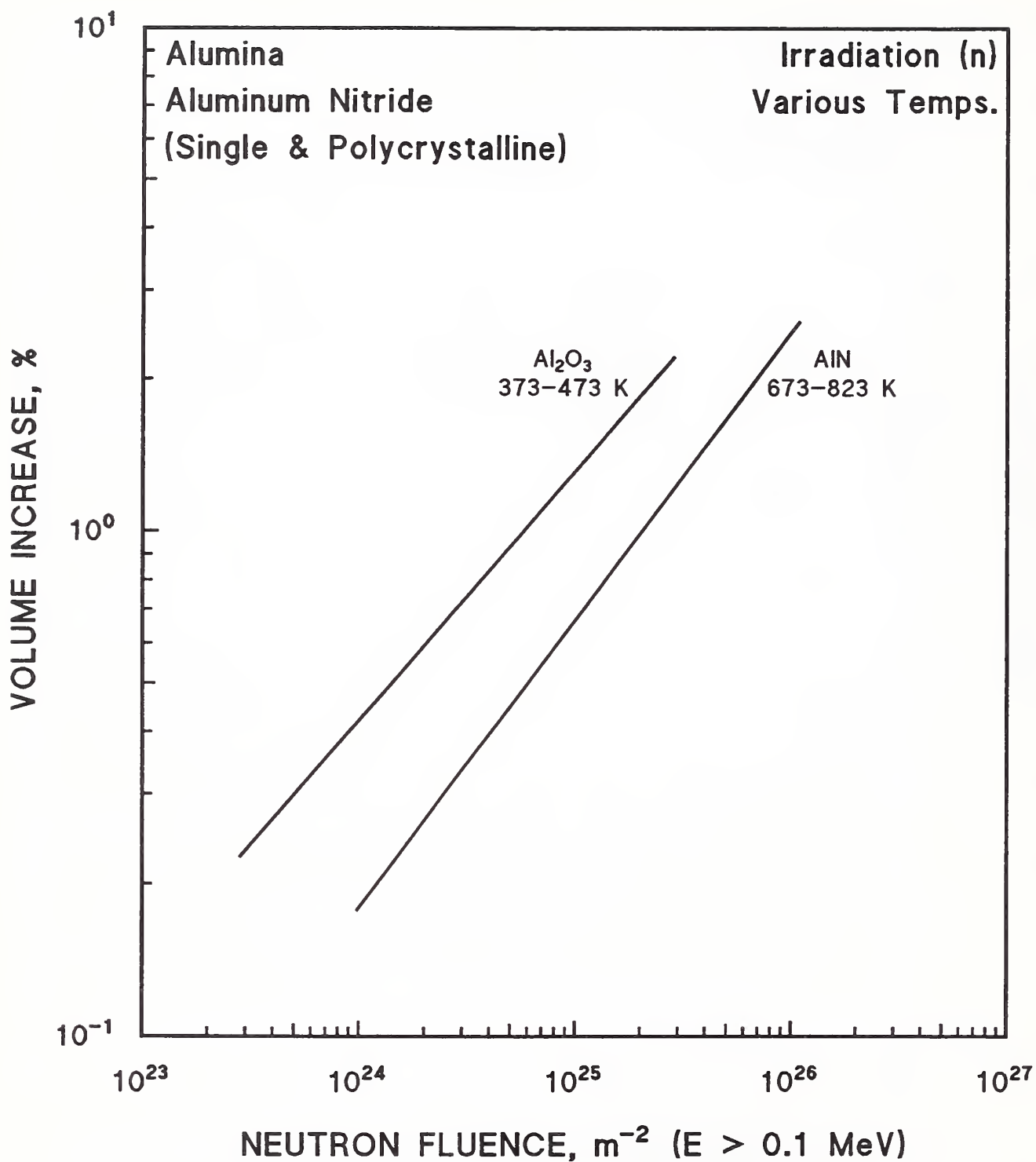


Figure 2.4.5. Volume change in Al_2O_3 and AlN after neutron irradiation at the indicated temperatures. Data from Dienst [1992].

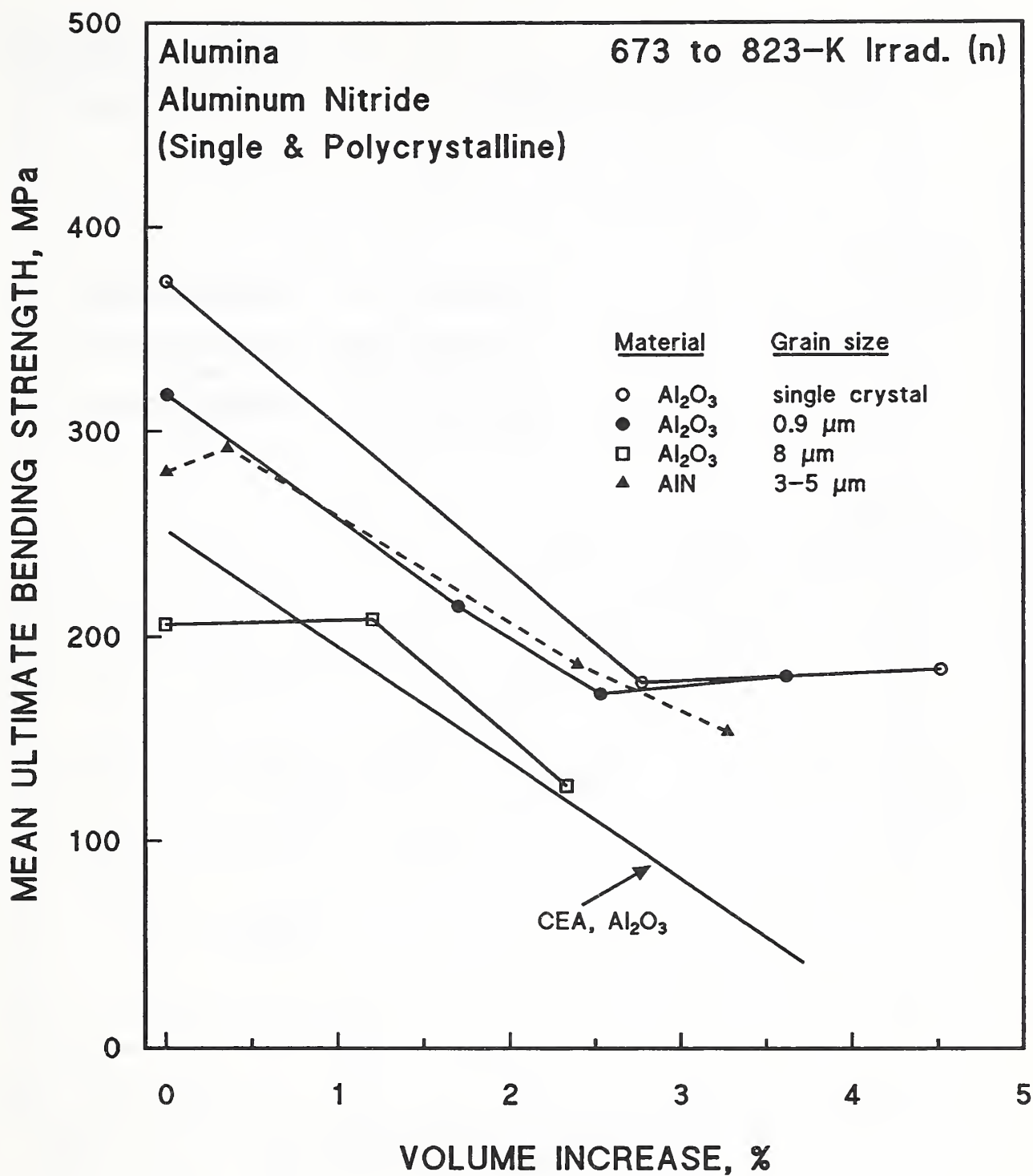


Figure 2.4.6. Decrease in the fracture strength of Al_2O_3 and AlN with volume increase. Data from Dienst [1992]. (No citation was given for the additional curve labeled as CEA.)

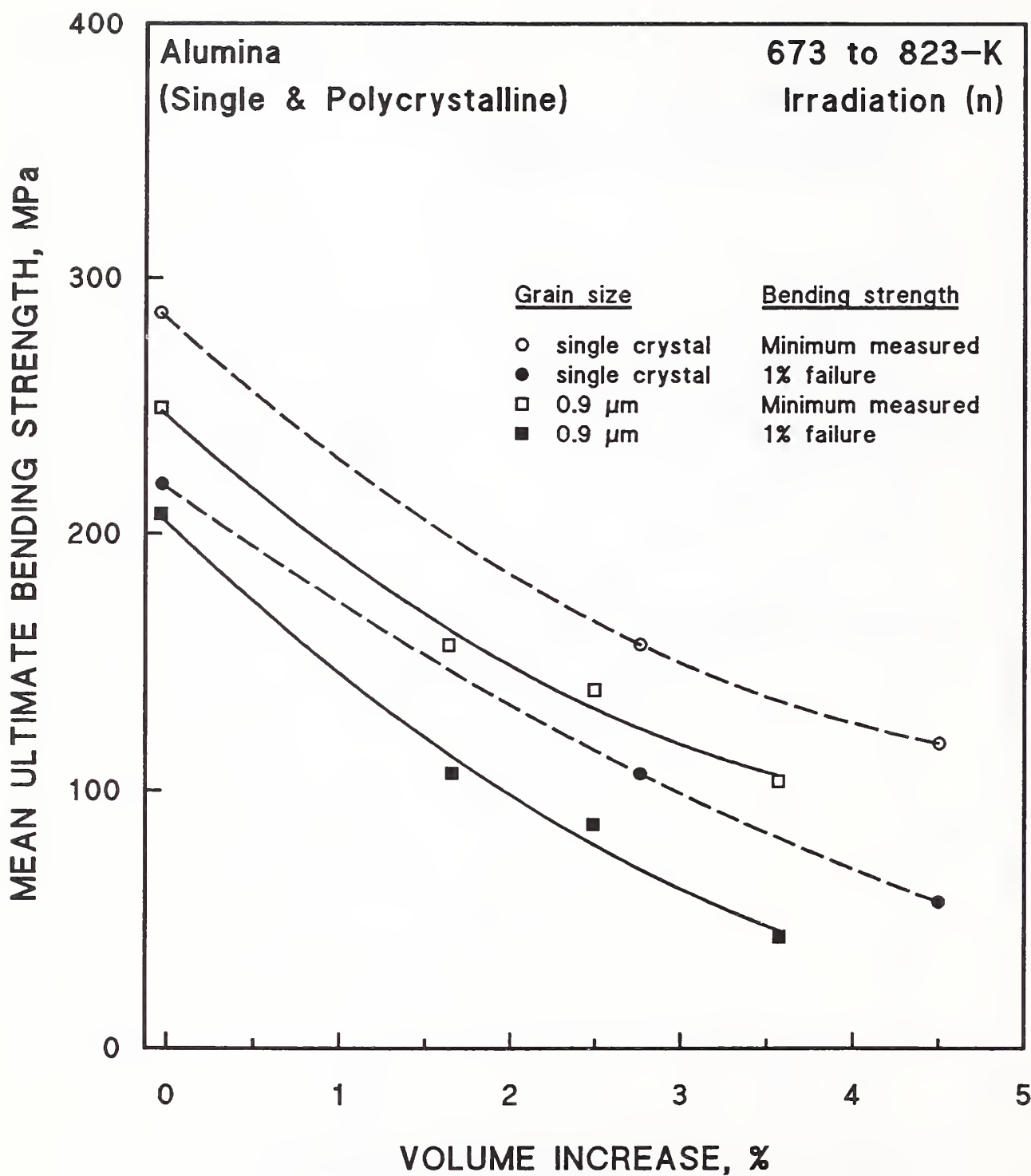


Figure 2.4.7. Decrease in minimum and 1% failure bending strength of Al_2O_3 with volume increase. Data from Dienst [1992].

The latter figure shows the severe decline in minimum measured strengths and 1% failure probability with volume increase. This suggested a major influence of large defect aggregates upon both the volume and strength. The defects were thought to decrease the effective crack toughness. On the other hand, Clinard et al., observing an opposite, strengthening effect of irradiation, especially in MgAl_2O_4 , had suggested that irradiation defects might impede crack propagation. However, they were unable to verify this for their Al_2O_3 samples. The results of Dienst are based upon a larger number of specimens: 20 unirradiated controls and 10 specimens per irradiation point (per material). Clinard et al. tested 7 or 8 unirradiated controls and 4 specimens per material per irradiation point. Perhaps the apparent discrepancy is due to scatter in the smaller set of specimens tested by Clinard et al.

Very recent results of Dienst and Zimmermann [1994] at lower irradiation temperatures and fluences on several materials of interest for this survey are discussed below, in §12.4.1, which compares the materials reviewed in this report. These recent results indicate deterioration of the mechanical strength of Al_2O_3 at a fluence of ~ 3 to $5 \times 10^{24}/\text{m}^2$ at $\sim 100^\circ\text{C}$.

Diametral compression tests on polycrystalline Al_2O_3 showed a decrease of 25.6% in tensile strength after a fluence at 660 K of $2 \times 10^{26}/\text{m}^2$ ($E > 0.1$ MeV). These tests, by Tucker et al. [1986], are discussed in more detail and the results compared to those for MgAl_2O_4 , in §7.4, below.

2.5. THERMAL PROPERTIES

2.5.1. Thermal Conductivity

The thermal conductivity of sapphire single crystals and sintered Al_2O_3 was measured between 2 and 100 K after both reactor and γ -ray irradiation [Berman et al., 1960b]. Figure 2.5.1 shows that there was little change in thermal conductivity of the single crystal after ^{60}Co - γ irradiation, but a decrease of over an order of magnitude in the peak value at about 30 K after neutron (reactor) irradiation. The fast neutron fluence was about $7 \times 10^{22}/\text{m}^2$. The conductivity at 5 K after this ambient-temperature irradiation was about 30% of the initial value. Figure 2.5.2 shows that ambient γ irradiation had

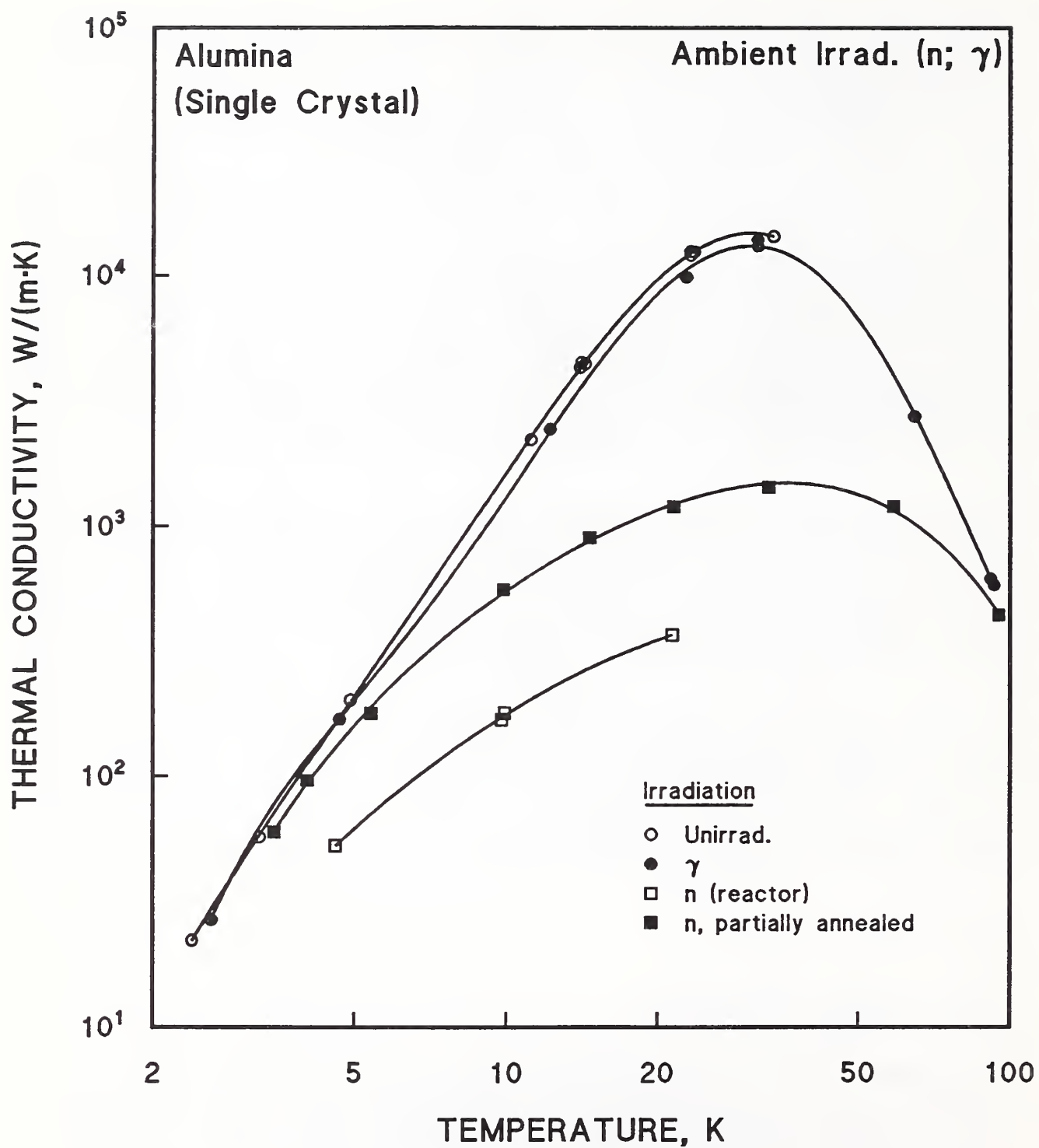


Figure 2.5.1. Thermal conductivity of single-crystal Al_2O_3 after γ and neutron irradiation. Data from Berman et al. [1960b].

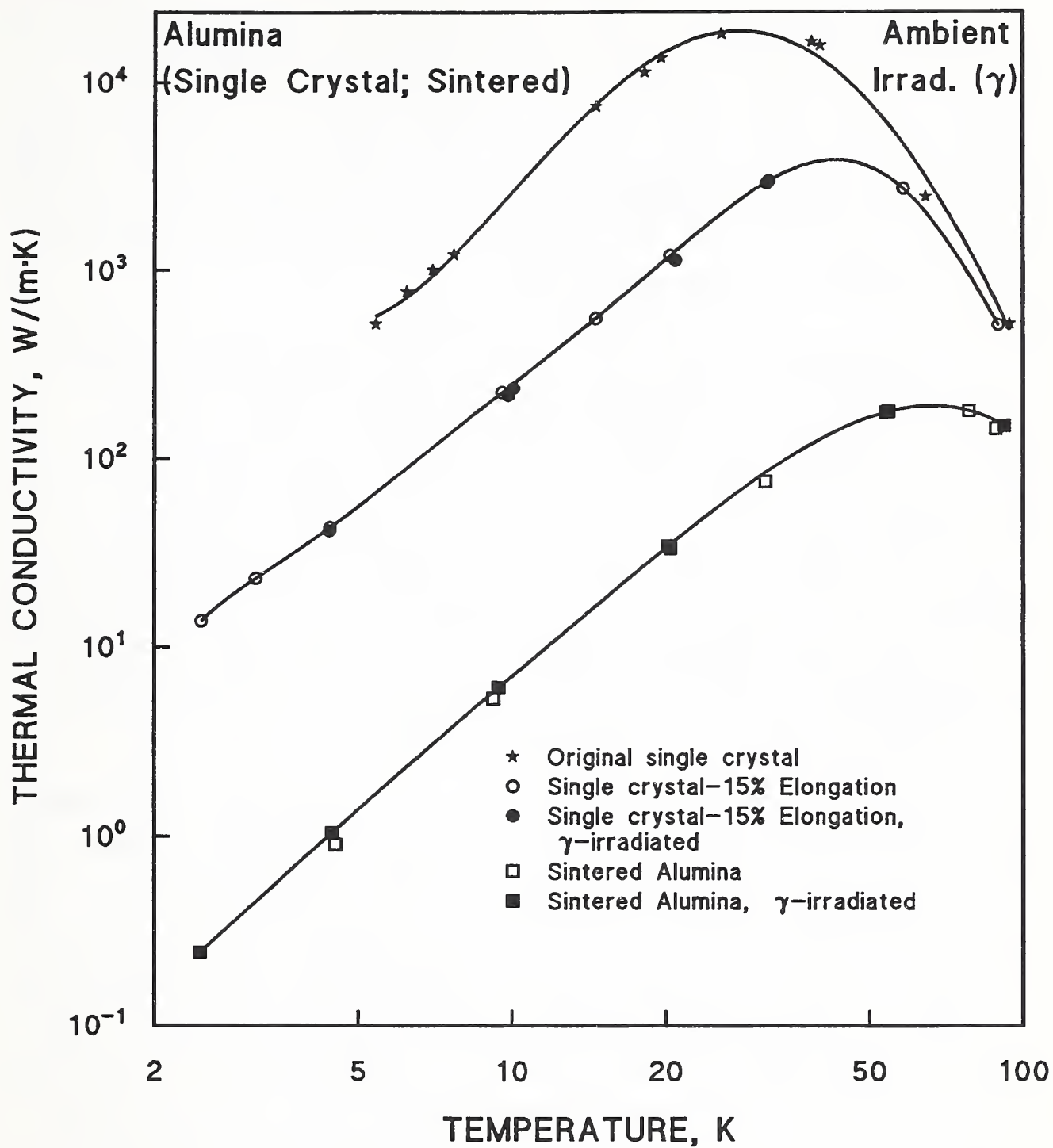


Figure 2.5.2. Thermal conductivity of single-crystal and sintered Al_2O_3 after γ irradiation. Data from Berman et al. [1960b].

little effect on the cryogenic thermal conductivity of a sapphire crystal stretched at 1400°C and of sintered Al_2O_3 . Furthermore, increasing the γ -irradiation dose did not increase the thermal resistance of single crystals [Berman et al., 1955; 1960], although sizeable increases in cryogenic thermal resistance with increasing neutron fluence were observed (Figure 2.5.3). Of course, the decrease in thermal conductivity in 4-K irradiated Al_2O_3 would be expected to be much larger, since many of the defects would have annealed at ambient temperature in these experiments.

These measurements by Berman's group appear to be the only ones on cryogenic thermal conductivity after irradiation. The effect of neutron irradiation on sintered, polycrystalline Al_2O_3 was apparently not measured. Although the decrease in thermal conductivity of polycrystalline Al_2O_3 might be expected to be less than that of the single-crystal material, sizeable conductivity decreases have been found at ambient temperature in sintered, polycrystalline Al_2O_3 . For example, Crawford and Wittels [citation, Penkovskii, 1964] found a decrease at 30°C from 17 to 9.6 W/(m·K) after an intermediate neutron fluence of $3 \times 10^{23}/\text{m}^2$ and a further decrease to 0.38 ± 0.2 W/(m·K) after $4 \times 10^{24}/\text{m}^2$. Percentage decreases of similar magnitude were reported for single crystals after similar fluences of "intermediate" neutrons ($E > 100$ eV).

Thorne and Howard [1967] also measured large fractional decrease in the thermal conductivity of polycrystalline Al_2O_3 at ambient temperature, although their irradiation, reported as the fast neutron fluence, was carried out at 250°C. Figure 2.5.4 shows these results. The fractional decrease in conductivity was similar for both porous and dense material. Although a sizeable decrease ($K \approx K_0/3.5$) was produced after a fluence of $4 \times 10^{24}/\text{m}^2$, this was not as large as the decrease ($K \approx K_0/44$) reported by Crawford and Wittels. Probably, Crawford and Wittels used a much lower irradiation temperature; this was not reported in the review by Penkovskii and their original report was not available. Since a fast neutron fluence of $\sim 10^{24}/\text{m}^2$ at ambient temperature may be roughly equivalent to $10^{22}/\text{m}^2$ at 4 K in terms of retained defects, the 4-K thermal conductivity of polycrystalline Al_2O_3 could fall to a very low fraction of the initial value under the ITER irradiation conditions. Ambient temperature annealing might not completely restore the thermal conductivity

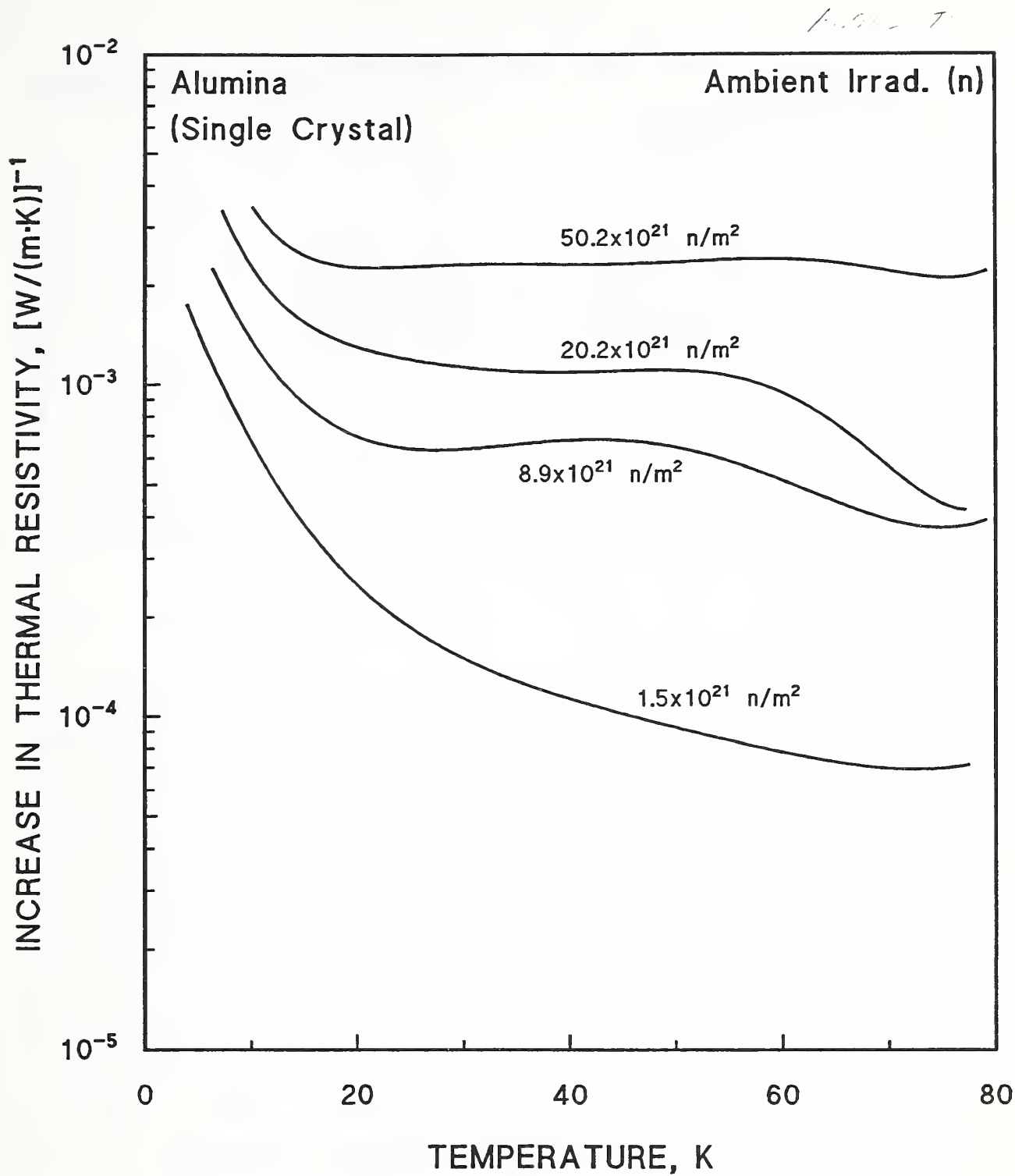


Figure 2.5.3. Increase in thermal resistance of Al_2O_3 after neutron irradiation. Data from Berman et al. [1955].

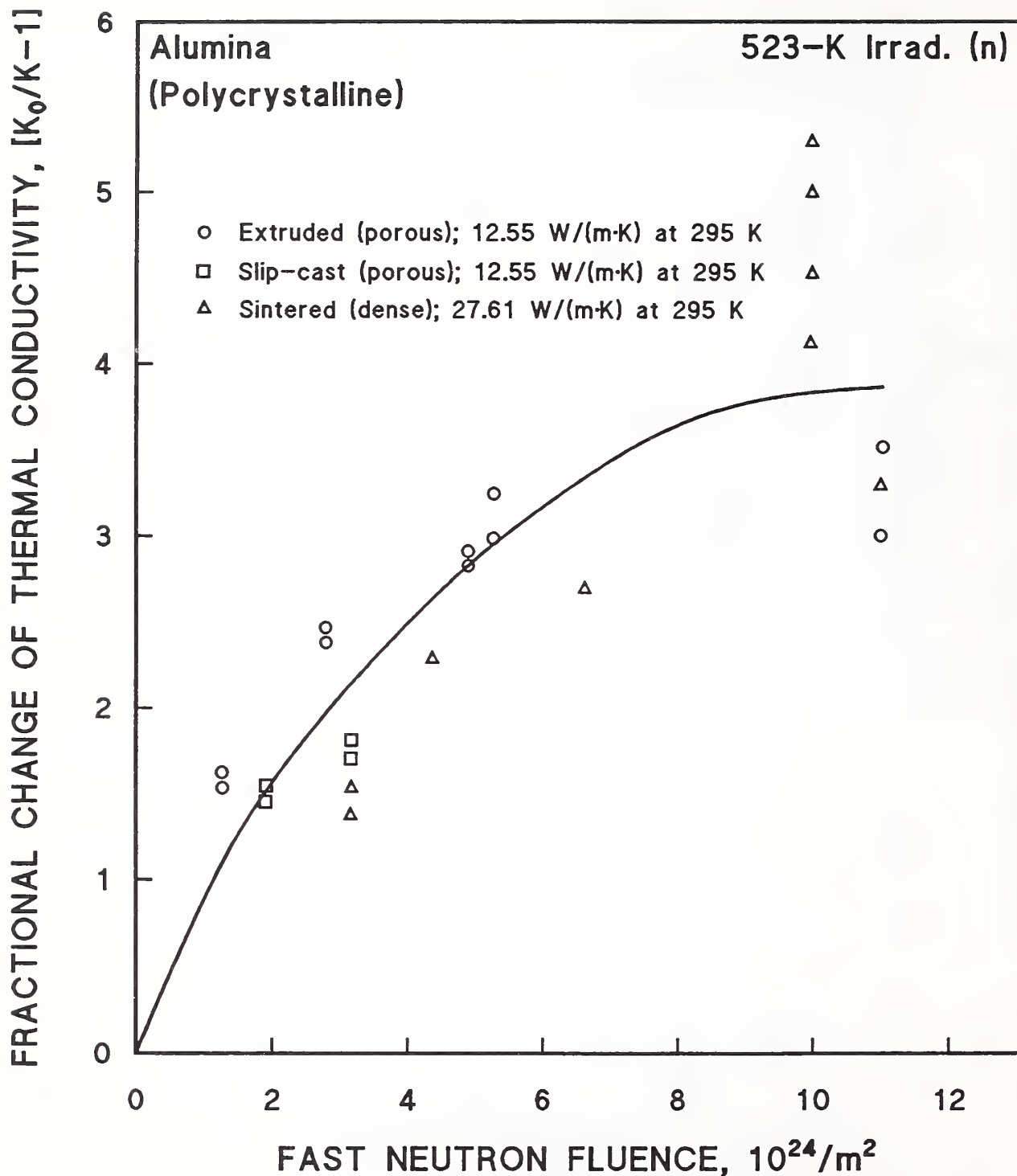


Figure 2.5.4. Fractional change of thermal conductivity, K , of Al_2O_3 after 523-K irradiation (K_0 = Initial Conductivity). Data from Thorne and Howard [1967].

to its original value, since large decreases in thermal conductivity were observed under ambient conditions.

Rohde and Schulz [1992] compared the high temperature thermal conductivity of several ceramics after irradiation. The thermal conductivity of both single and polycrystalline Al_2O_3 and single-crystal MgAl_2O_4 and polycrystalline AlN were measured after fast neutron fluences up to $4 \times 10^{25}/\text{m}^2$ (from various sources) at temperatures from 473 to 823 K. As Figures 2.5.5 and 2.5.6 indicate, decreases in thermal conductivity were similar for both single-crystal and polycrystalline Al_2O_3 . In comparing the LAMPF (Los Alamos Meson Physics Facility) results with those on AlN and MgAl_2O_4 , Rohde and Schulz found decreases to 70 and 80% of the original value for Al_2O_3 , but much larger decreases, to 52% for MgAl_2O_4 and to 36% for AlN . However, AlN had the highest initial thermal conductivity at ambient temperature (§§3.5 and 7.5).

2.5.2. Thermal Expansion

Only limited, γ -irradiation measurements were found for the change in thermal expansion of single-crystal Al_2O_3 at 4 K [Brown and Brown, 1981]. Figure 2.5.7 shows the change in specimen length as a function of temperature after an unspecified amount of γ irradiation. Figure 2.5.8 shows the thermal expansion after irradiation; however, unirradiated material was not measured in the same apparatus, and the authors stated that the small negative coefficient could have been an "apparatus effect." At least at ambient temperature, neutron irradiation produces swelling, not compaction, so it would be of interest to see if the trend below 8 K shown in Figure 2.5.8 is applicable for 4-K irradiation and testing.

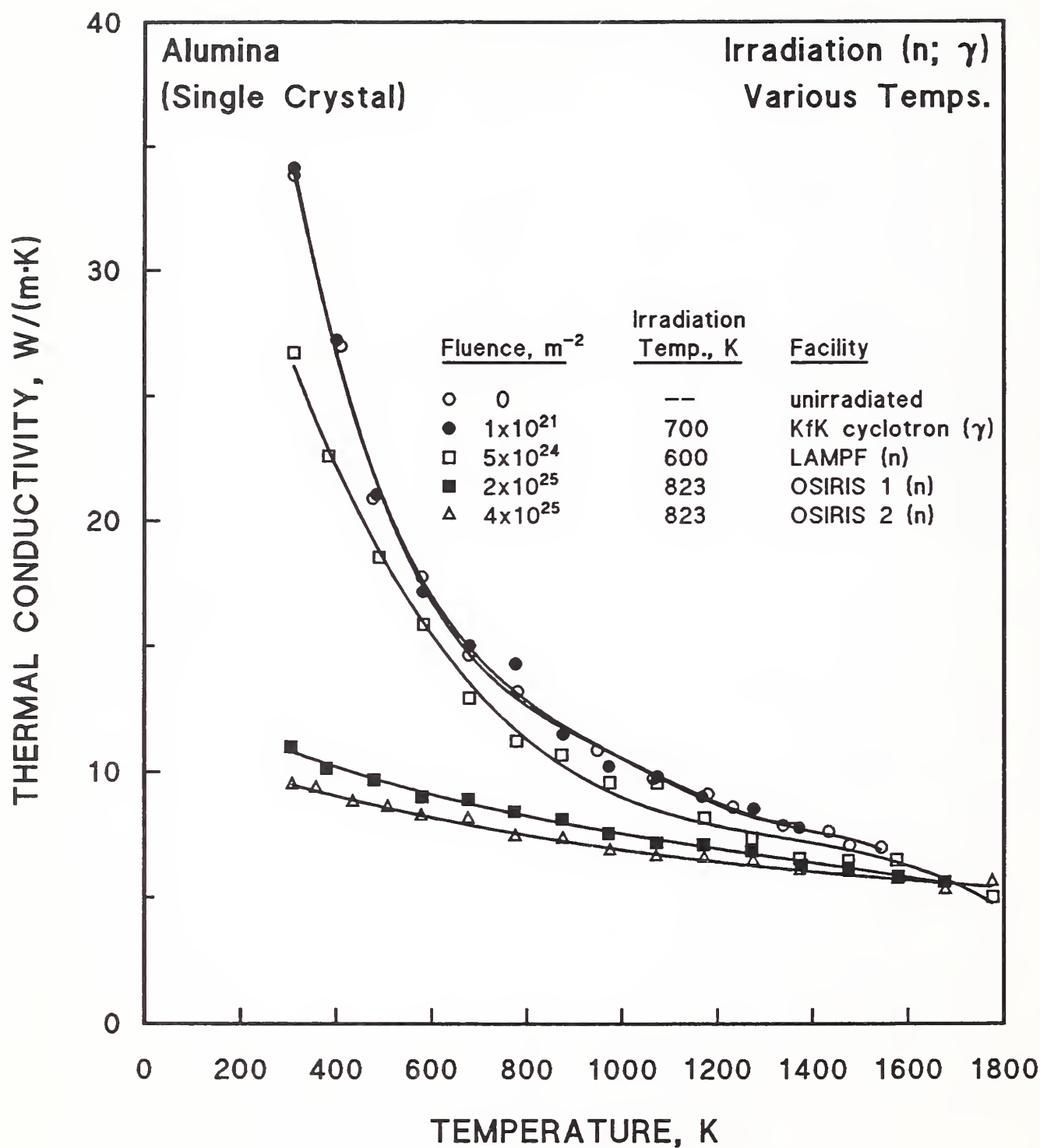


Figure 2.5.5. Thermal conductivity of single-crystal Al_2O_3 after high temperature irradiation at several facilities. Data from Rohde and Schulz [1992].

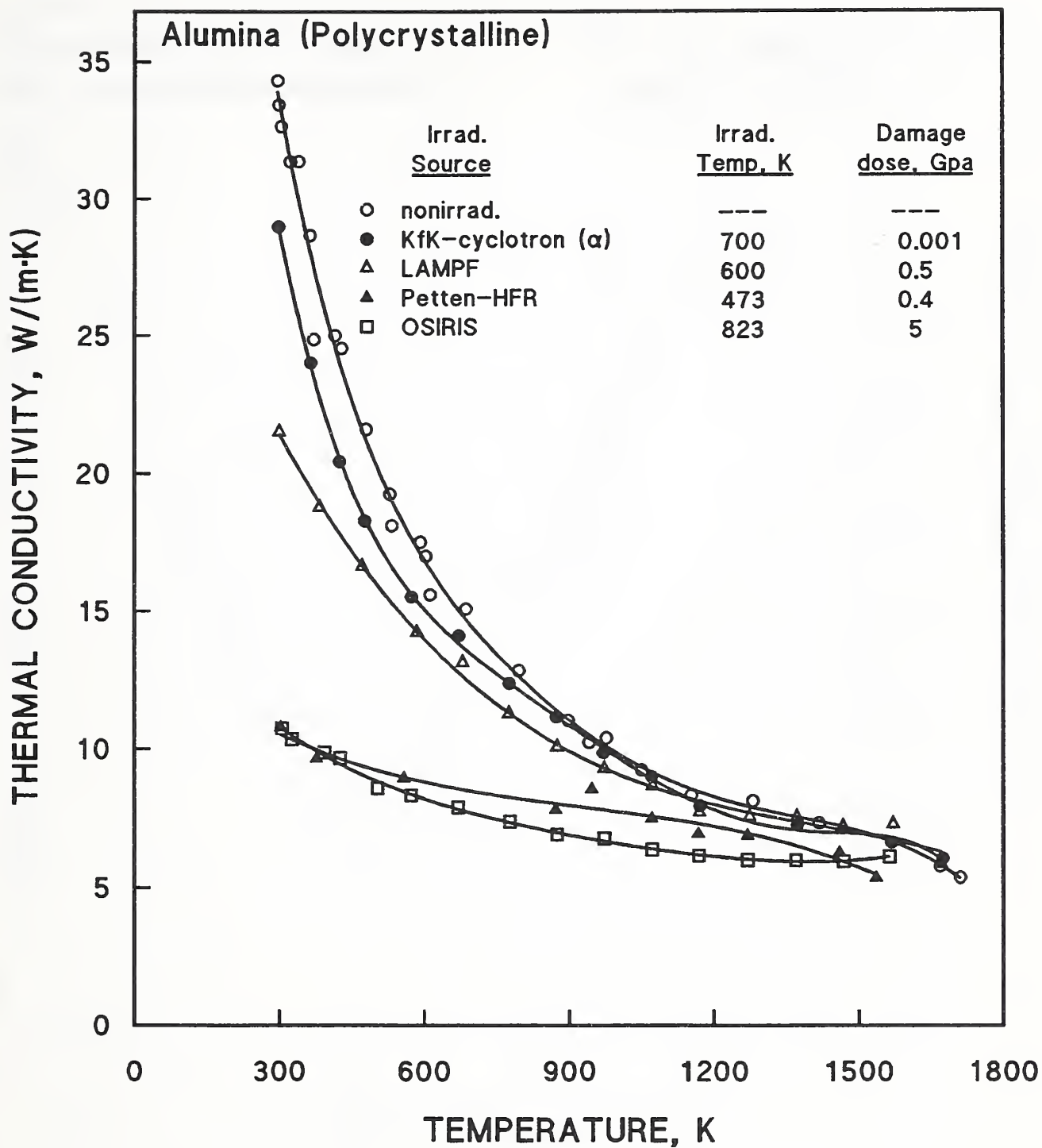


Figure 2.5.6. Thermal conductivity of polycrystalline Al_2O_3 after high temperature irradiation at several facilities. Data from Rohde and Schulz [1992].

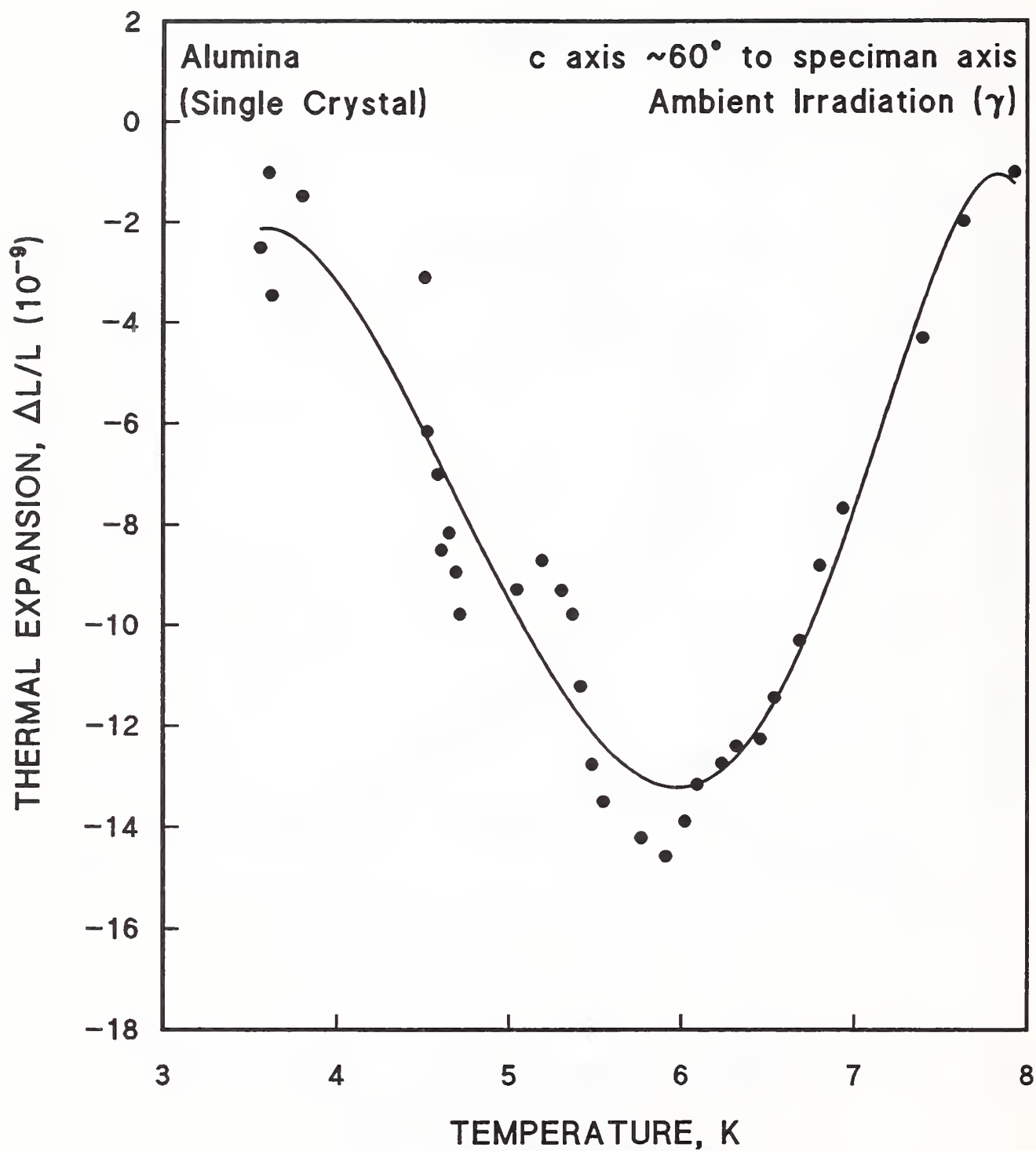


Figure 2.5.7. Thermal contraction, $\Delta L/L$, of single-crystal Al_2O_3 . Data from Brown and Brown [1981].

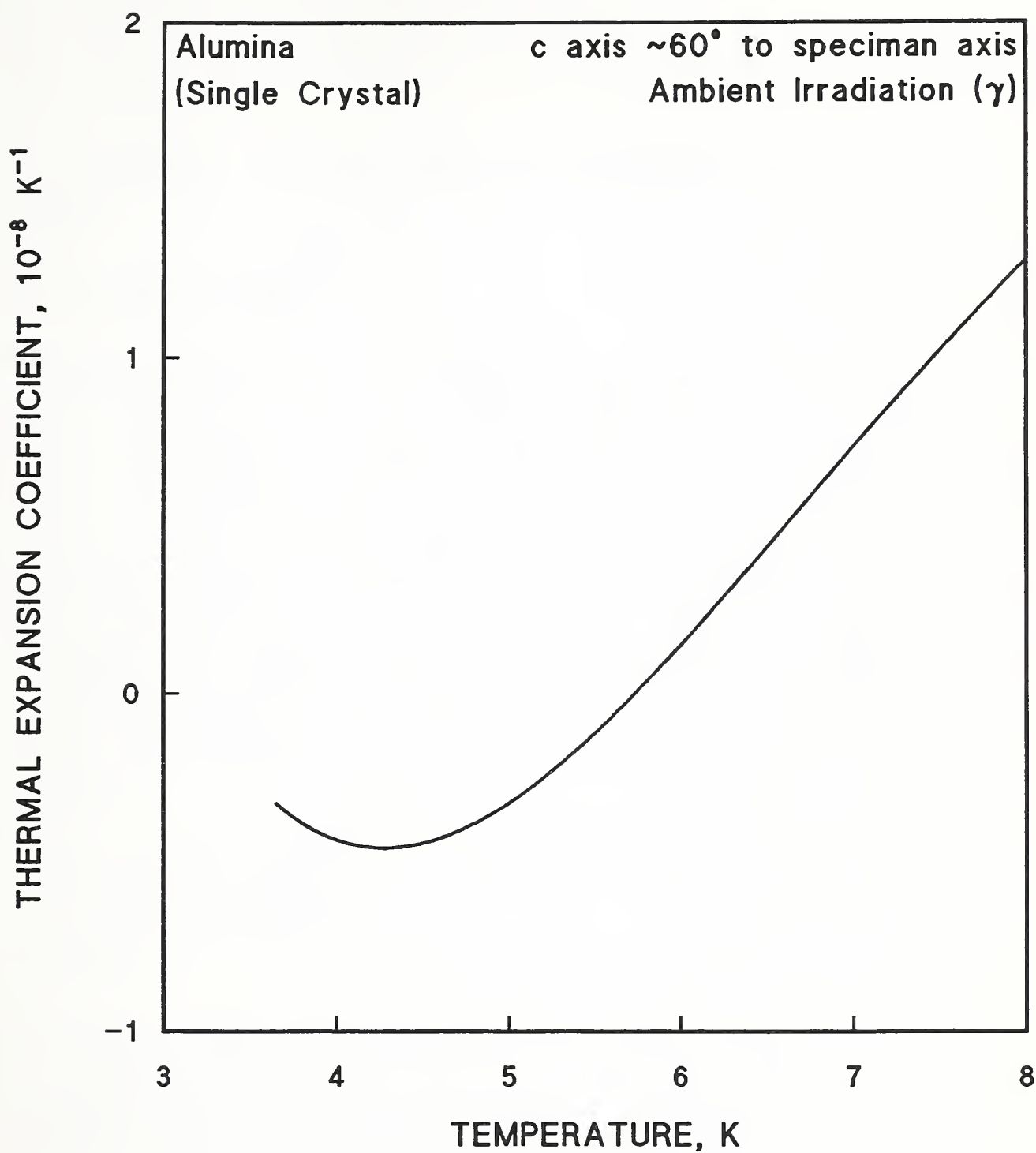


Figure 2.5.8. Thermal expansion coefficient, $\Delta L/L$, of single-crystal Al_2O_3 . Data from Brown and Brown [1981].

3. LOW TEMPERATURE IRRADIATION OF ALUMINUM NITRIDE

3.1. DEFECT DENSITY

No measurements of the defect density for AlN were obtained in the literature search.

3.2. CHANGE IN VOLUME

Aluminum nitride crystallizes in the wurtzite hexagonal system: each atom is at the center of a tetrahedron in which the vertexes are occupied by atoms of the opposite species. This produces the non-cubic unit cell shown in Figure 3.2.1. The oxygen sublattice of Al_2O_3 has the same hexagonal wurtzite structure, and Al_2O_3 expands anisotropically under irradiation. Hickman and Jostsons [1969] first measured the changes in lattice parameter of AlN after irradiation, using X-ray diffraction. Single-crystal whiskers were irradiated at 75 to 100°C, to a fluence of $3.7 \times 10^{24}/\text{m}^2$ ($E > 1$ MeV). The results, shown in Figure 3.2.2, indicated that the expansion is highly anisotropic, much more so than that of Al_2O_3 (§2.2). The volume expansion, also depicted in Figure 3.2.2, was obtained by summing the c-axis expansion and twice the a-axis expansion.

Lattice parameter changes at a lower fluence of $8.3 \times 10^{22}/\text{m}^2$ ($E > 1.0$ MeV) were reported by Yano and Iseki [1991] after irradiation at 100°C: 0.096% for the a axis and 0.092% for the c axis. A volume expansion of about 0.3% was reported.

Billy et al. [1984] also found that the a and c axes expanded in unequal proportions after irradiation. However, as Figure 3.2.3 indicates, the expansion did not become markedly anisotropic until a fast neutron fluence of about $7 \times 10^{23}/\text{m}^2$ was reached, when the a axis had expanded by 0.09 and the c axis had expanded by 0.16%. These results were obtained by the time of flight neutron diffraction method after an irradiation of AlN powder at a temperature below 660°C. Aluminum nitride is thermally stable at that temperature. An extrapolation of the volume change shown in Figure 3.2.3 to a fast neutron fluence of $10^{24}/\text{m}^2$ gives a value of about 0.45%, whereas the results

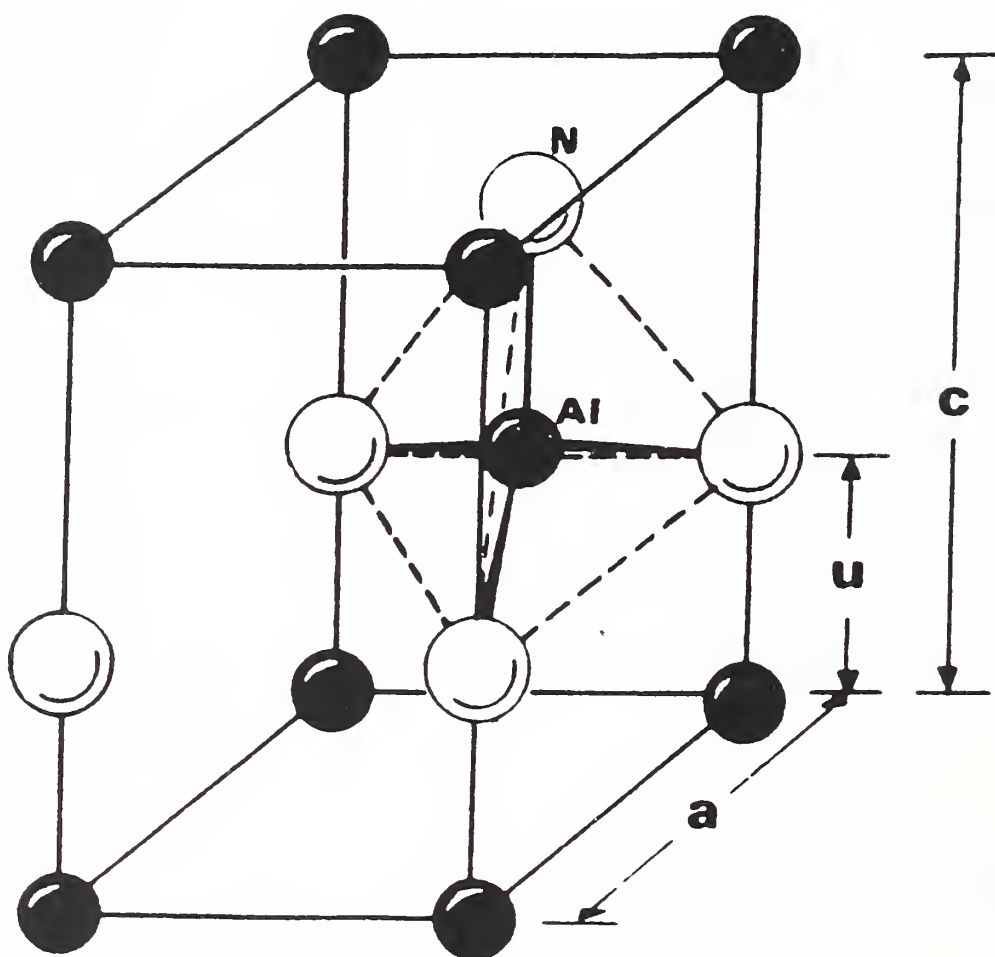


Figure 3.2.1. Arrangement of three unit cells in the wurtzite structure of AlN.

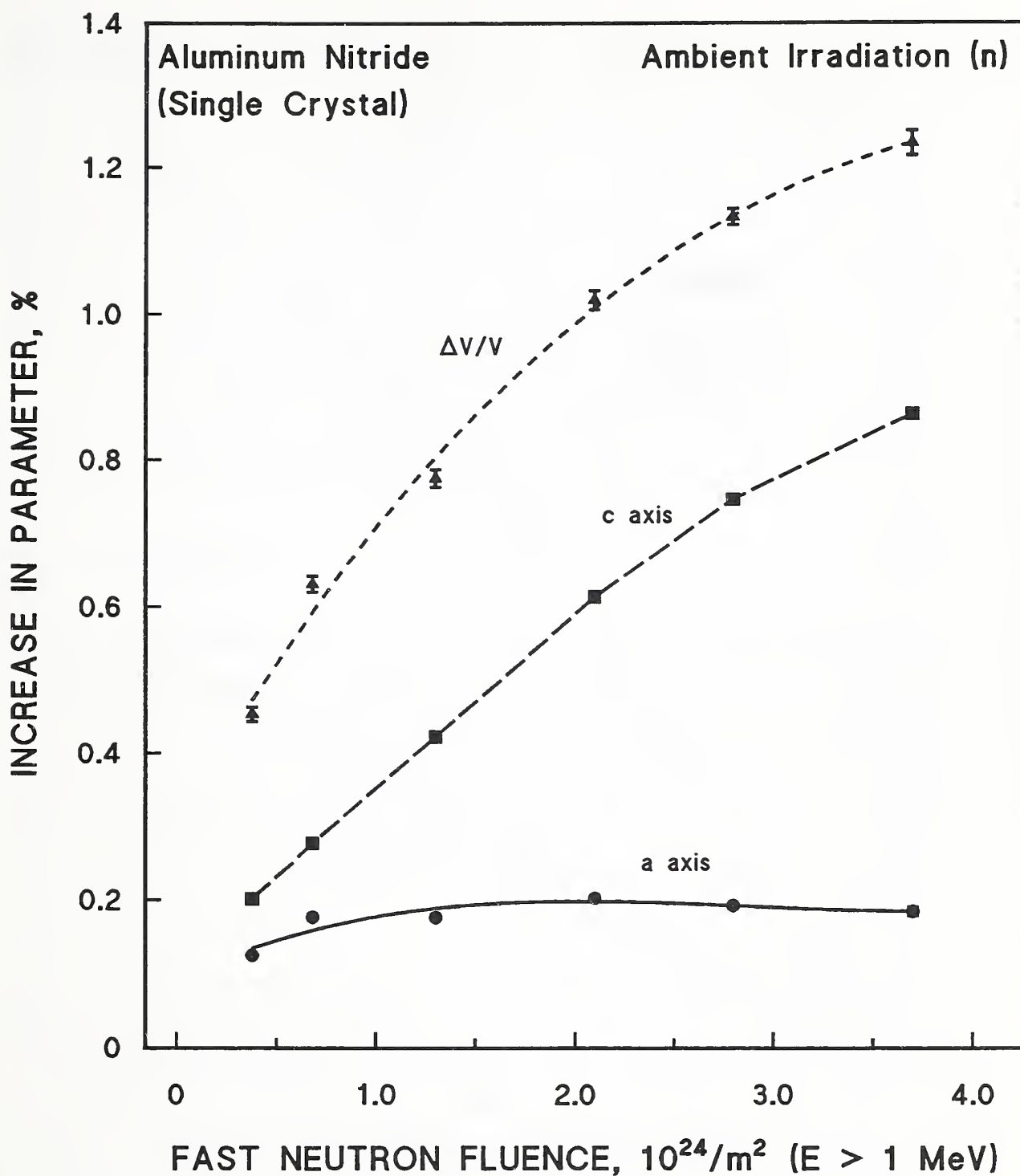


Figure 3.2.2. Increase of the a and c lattice parameters and total volume of AlN under neutron irradiation. Data from Hickman and Jostsons [1969].

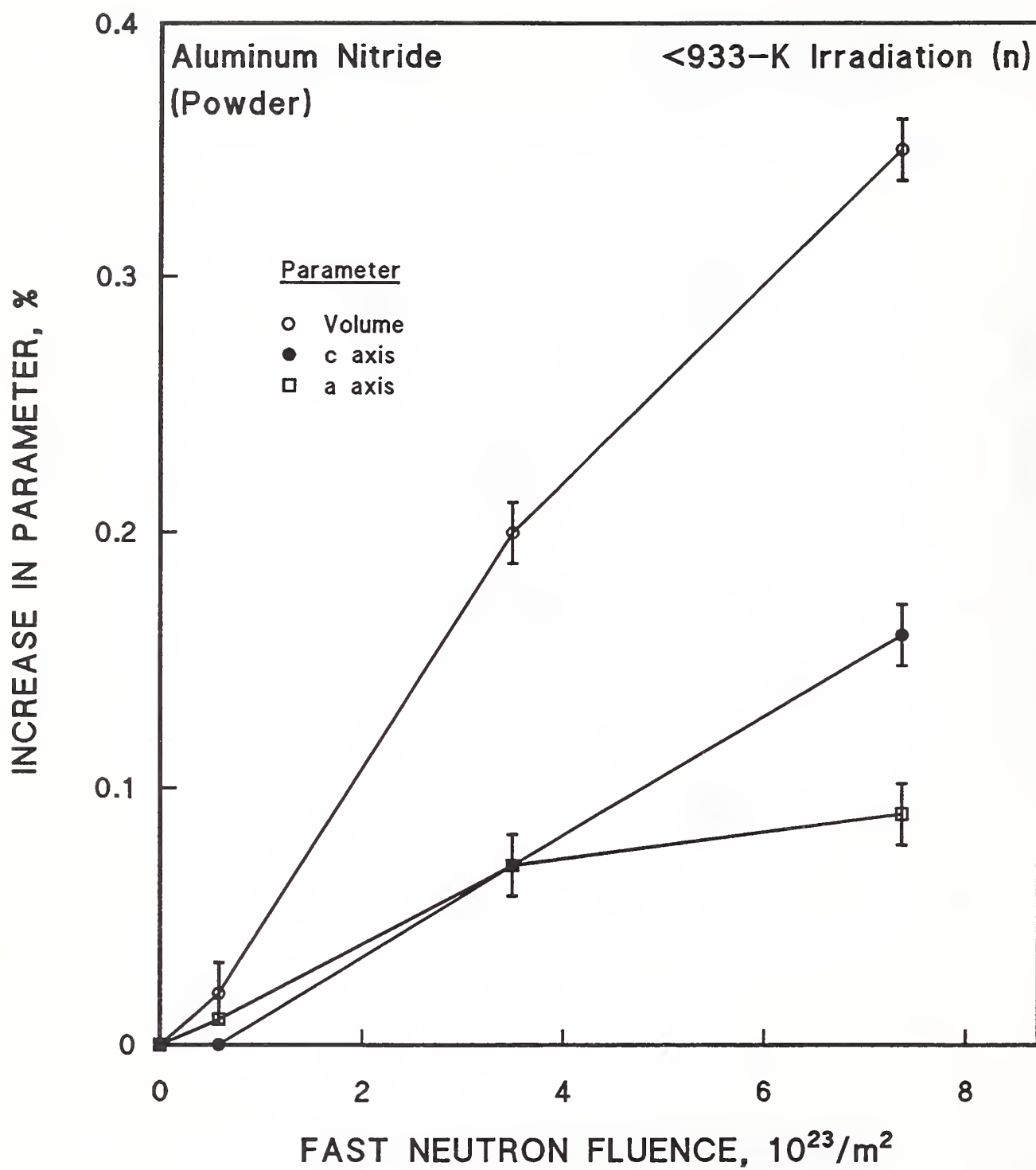


Figure 3.2.3. Increase of the a and c lattice parameters and total volume of AlN under neutron irradiation. Data from Billy et al. [1984].

of Hickman and Jostsons give about 0.7% at that fluence. Since the irradiation of Billy et al. was performed at a very high temperature, some of the defects that cause expansion probably were annealed. It would be preferable to apply the usual fluence-estimating factor of ~100 to the data of Hickman and Jostsons from irradiations at 75 to 100°C to obtain an approximate upper limit for 4-K expansion. Dienst [1992] reported a somewhat lower volume increase at a fluence of $10^{24}/\text{m}^2$, based upon literature data and measurements on 4-point bending specimens irradiated at 400 to 550°C (Figure 2.4.5). Note also that significant anisotropy was found at a lower fluence, $<4 \times 10^{23}/\text{m}^2$, in the lower temperature irradiations. This might imply problems with grain boundary separation in polycrystalline material, but it is not known if this occurs at low temperatures (see Figure 2.2.7 for Al_2O_3 , which, however, exhibits a much lower degree of anisotropic expansion).

3.3. AMORPHIZATION

Billy et al. [1984] observed that the peaks in their AlN diffraction pattern remained sharp and well-defined after irradiation to a fast neutron fluence of $7.3 \times 10^{23}/\text{m}^2$ at 660°C, despite the presence of a strong background continuum. They concluded that AlN had good resistance to amorphization, but did not quantify the extent to which amorphization might have occurred, as evidenced by the increased background signal after irradiation. Such high temperature results do not apply to ambient and cryogenic temperatures, owing to the possibility for high temperature recovery. Furthermore, since AlN is covalently bonded, one would expect a lower resistance to irradiation than that of a more ionically bonded oxide ceramic. However, Hickman and Jostsons [1969] noted that their X-ray reflection patterns (taken after 75 to 100°C irradiations) remained sharp up to $2.8 \times 10^{24}/\text{m}^2$ and showed only very weak streaks in the c-axis direction after $3.7 \times 10^{24}/\text{m}^2$. Therefore, AlN was added to Figure 1.6.2 in §1.6, above, as a stable material. Naguib and Kelly (Table 1.6.1) also reported that AlN was relatively stable to amorphization. Clusters of damage were observed by Hickman and Jostsons at both fluences with TEM on flakes obtained by crushing the irradiated crystals.

3.4. MECHANICAL PROPERTIES

Four-point bending tests were performed at ambient temperature on several ceramics, including AlN, that had been irradiated at various facilities, including LAMPF, at temperatures ranging mostly from 400 to 600°C [Dienst, 1992]. These results were summarized above, in Figures 2.4.3 and 2.4.4 (§2.4). The first figure shows that the bending strength of AlN, while initially lower than that of both single-crystal and some polycrystalline Al₂O₃, is comparable after a fast neutron fluence of about 10²⁶/m² (E > 0.1 MeV). The second figure shows a broadening of the strength distribution after irradiation, as represented by the decrease of the Weibull modulus. The distribution of ultimate bending strengths was widened chiefly by an increased number of specimens with very low strengths. Twenty specimens were tested to obtain the unirradiated control strengths, and about 10 at each post-irradiation examination. Dienst noted that the favorable, but somewhat erratic behavior of the AlN samples may have been due to the relatively high Al₂O₃ content (about 5%) of the HIP (isostatically hot-pressed) grade used, which could give composite-like properties. Very recent further investigations of Dienst and Zimmermann [1994] at lower fluences and lower irradiation temperatures that compare a sintered AlN with Al₂O₃ and MgAl₂O₄ are discussed below in §12.4.1.

The decrease of fracture strength was shown to correlate with an increase in volume under irradiation for both Al₂O₃ and AlN in Figure 2.4.5 above. No saturation in the decrease of strength with the increase of volume is evident, as apparently occurs with Al₂O₃. However, Dienst showed that this apparent leveling off did not really occur for Al₂O₃, since minimum strengths observed continued to decline as the volume increased (Figure 2.4.4, above). Therefore, the apparent difference in saturation behavior should probably not be used to discriminate between AlN and Al₂O₃ unless more data show significant differences in behavior with regard to minimum strengths. The very recent data discussed below in §12.4.1 does indicate a more severe deterioration of strength in sintered AlN than in polycrystalline Al₂O₃ at 2×10^{25} /m².

A reduction in Young's modulus from 310 to 210 GPa was found by Dienst for a fast neutron fluence of 2×10^{26} /m². This decrease for AlN was somewhat larger, in percentage, than that observed for Al₂O₃; the Al₂O₃ modulus

decreased from 375 to 325 GPa after the same fluence. The larger decrease in AlN could be due to its multiphase microstructure. Ultrasonic techniques were used to measure these moduli.

Yano and Iseki [1991] measured the decrease in 4-point bending strength of sintered AlN (99% of theoretical density, >99.5% AlN) as a function of volume swelling (Figure 3.4.1). However, only the lowest swelling point was obtained at 100°C ($8.3 \times 10^{22}/\text{m}^2$), a relatively low irradiation temperature. As fluence (and swelling) increased, the irradiation temperature also increased: to 470°C at $2.4 \times 10^{24}/\text{m}^2$ and to 785°C at $5.2 \times 10^{24}/\text{m}^2$ ($E > 1.0$ MeV). Some additional mechanical-property data, the change in Vickers hardness and the fracture toughness (estimated by the indentation microfracture method), were also obtained at these three different irradiation temperatures. These data are shown in Figure 3.4.2. Hardness and fracture toughness increased with fluence. Yano and Iseki also measured lattice parameter changes at the two higher fluences and temperatures, finding a total volume swelling of about 0.44% at $5 \times 10^{24}/\text{m}^2$ (785°C). This is much smaller than the values obtained by other authors at lower irradiation temperatures (§3.2); hence, the conclusions of Yano and Iseki with regard to microcracking and voids (neither was observed with TEM) may not be valid for lower irradiation temperatures, especially since they also reported a much smaller anisotropy in expansion than the other authors.

3.5. THERMAL PROPERTIES

Cryogenic measurements of thermal properties of AlN after irradiation were not found in the literature search. Figure 3.5.1 shows the behavior of the high temperature thermal conductivity of polycrystalline AlN after irradiation temperatures of 353 to 700 K and α -particle and neutron fluences of 10^{21} to $5 \times 10^{24}/\text{m}^2$ [Rohde and Schulz, 1992]. Both higher fluences and lower irradiation temperatures appear to lower the thermal conductivity significantly. Comparative irradiations at LAMPF showed reductions in the thermal conductivity to 80 and 70% of the initial value for single and polycrystalline Al_2O_3 , to 52% for MgAl_2O_4 , and to 36% for AlN. This appears to indicate that AlN, a covalently bonded material, is damaged more heavily than the more ionically bonded oxide ceramics (see §1.6). The extent of the post-irradiation reduction in the 4-K

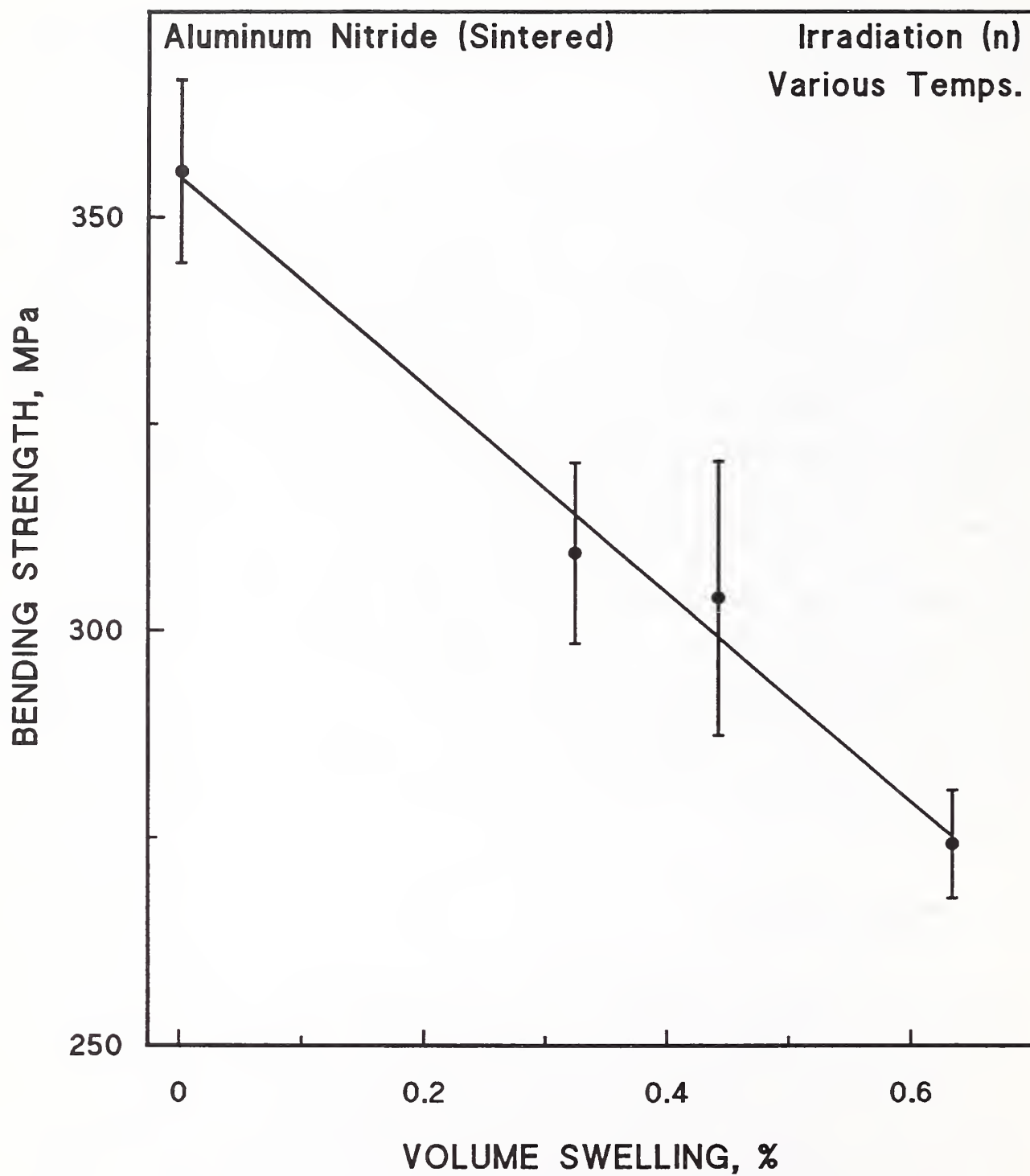


Figure 3.4.1. Four-point bending strength of AlN as a function of volume swelling (see text). Data from Yano and Iseki [1991].

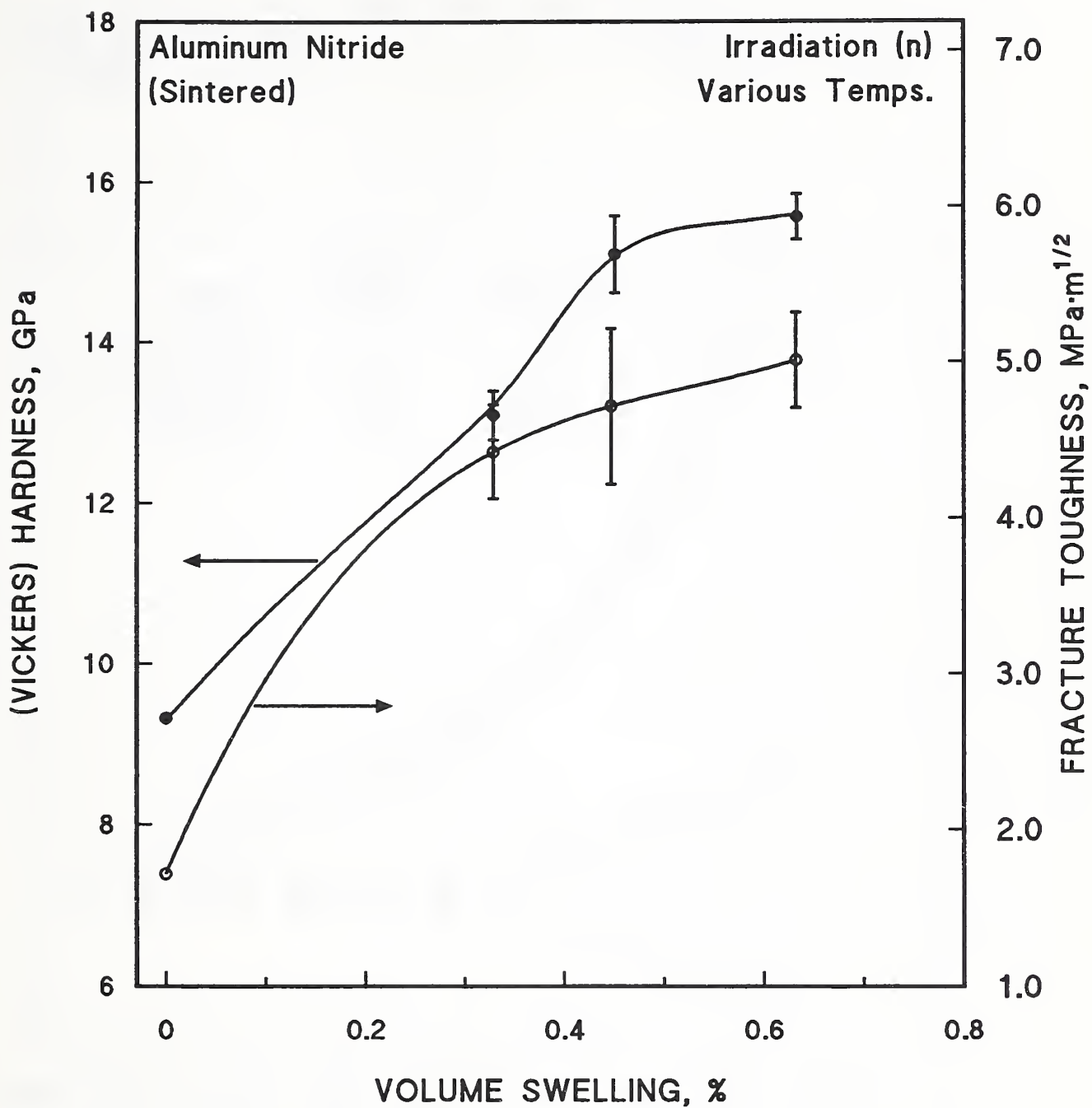


Figure 3.4.2. Increase of Vickers hardness and fracture toughness of AlN as a function of volume swelling (see text). Data from Yano and Iseki [1991].

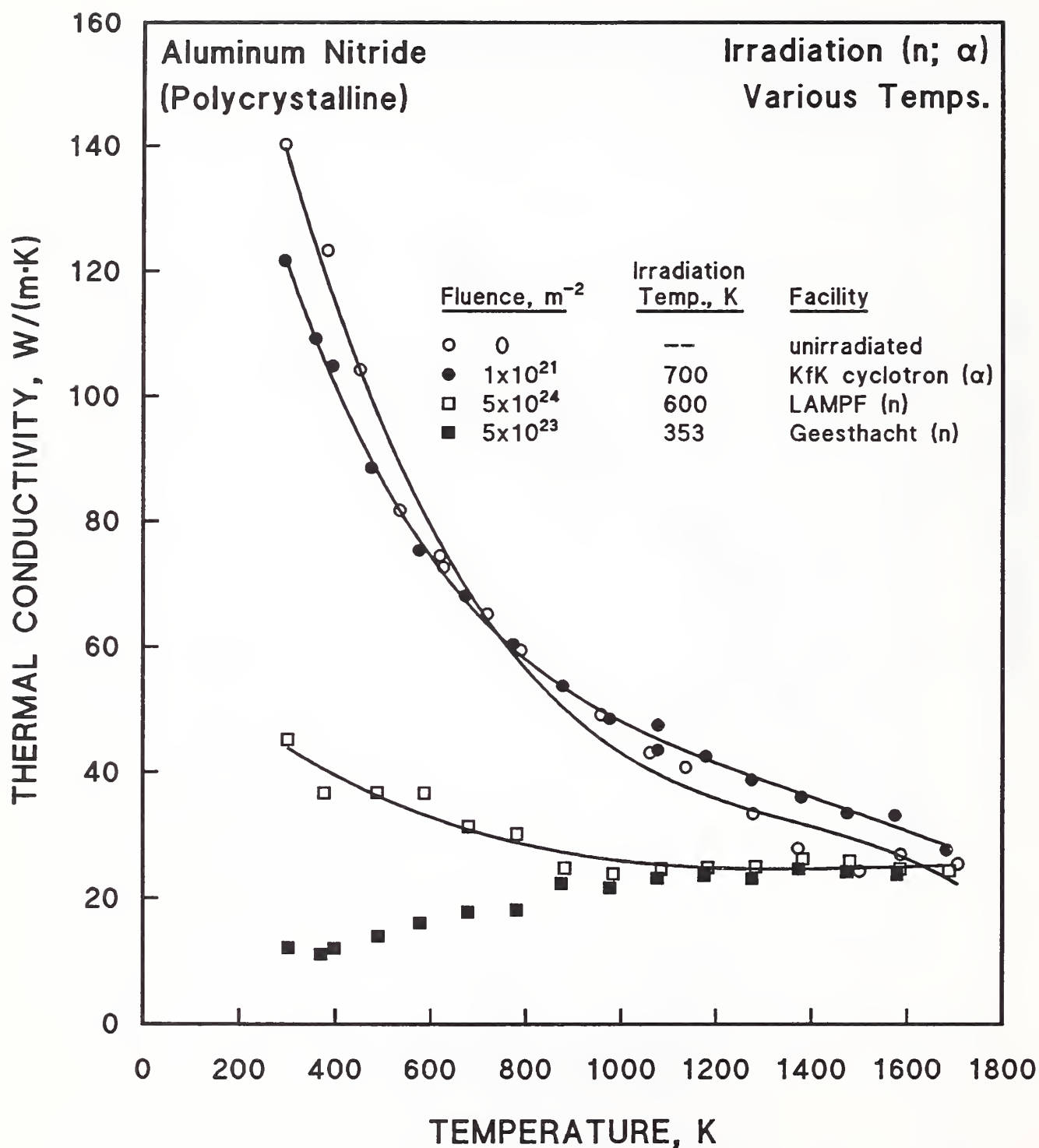


Figure 3.5.1. Decrease of high temperature thermal conductivity of AlN after neutron irradiation at high temperatures. Data from Rohde and Schulz [1992].

thermal conductivity of these ceramics has been measured only for single-crystal Al_2O_3 . The 300-K thermal conductivity of AlN was very significantly decreased after the 353-K irradiation.

Additional data on the reduction of ambient-temperature thermal conductivity of polycrystalline AlN were reported by Yano and Iseki [1991]. Figure 3.5.2 shows both the thermal conductivity and diffusivity after irradiation at 100°C ($8.3 \times 10^{22}/\text{m}^2$) and 470°C ($2.4 \times 10^{24}/\text{m}^2$). The reduction is comparable to that reported by Rohde and Schulz, after a similar temperature of irradiation (353 K). This sintered material was >99.5% AlN and had a density which was 99% of the theoretical density.

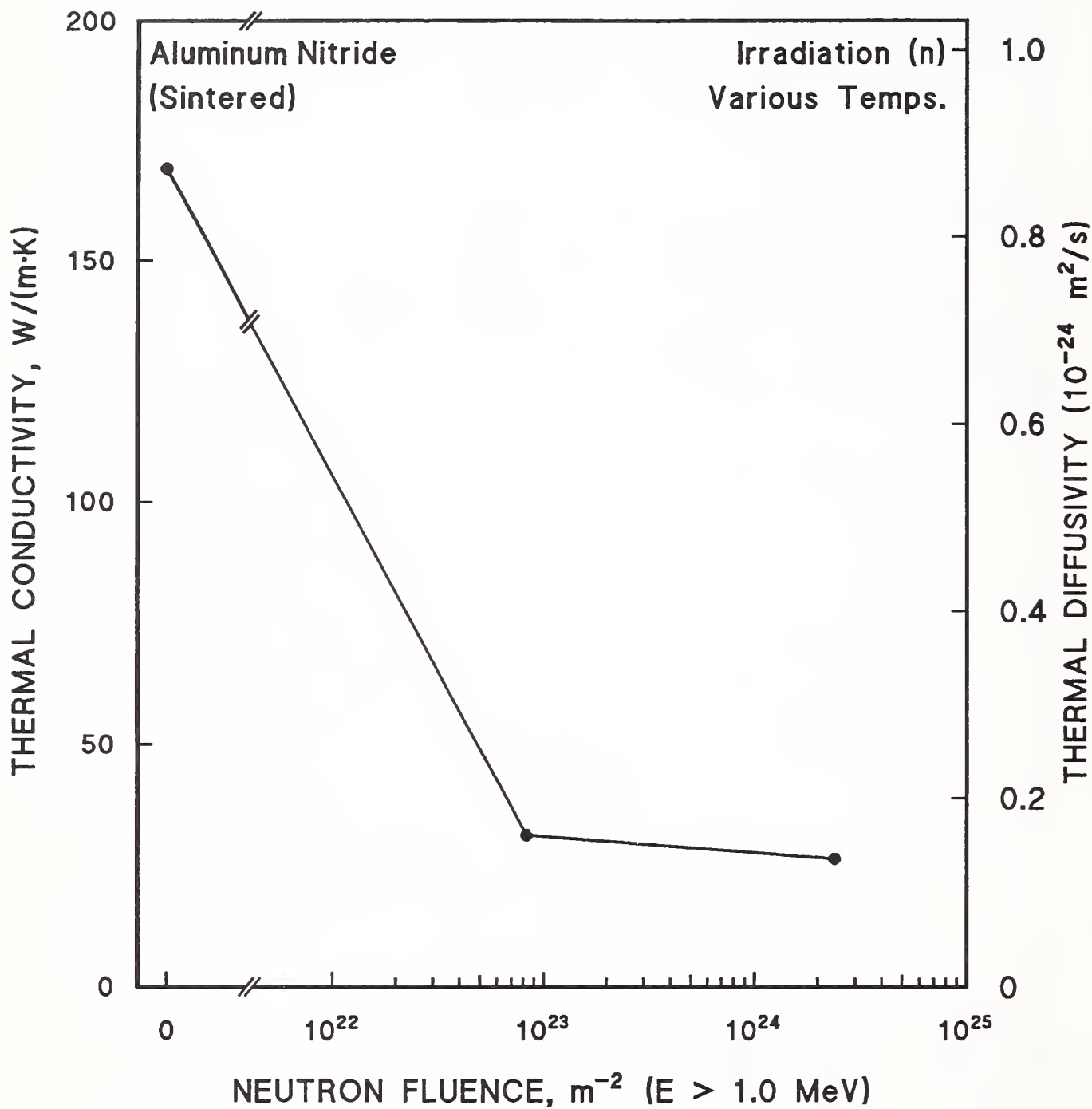


Figure 3.5.2. Decrease of thermal conductivity and thermal diffusivity of AlN after neutron irradiation at various temperatures. Data from Yano and Iseki [1991].

4. LOW TEMPERATURE IRRADIATION OF MAGNESIA

4.1. DEFECT DENSITY

4.1.1. Frenkel Defects

Information on the concentration of Frenkel defects produced at low fast neutron fluences of 10^{21} to $10^{23}/\text{m}^2$ at ~ 70 to 100°C was reviewed by Henderson and Bowen [1971]. Optical absorption and ESR studies showed that O vacancies were the prominent defect in this temperature range. (Since an ITER fluence of $10^{22}/\text{m}^2$ at 4 K may be equivalent to a fast neutron fluence of $\sim 10^{24}/\text{m}^2$ at ambient temperature, more extensive damage in addition to Frenkel defects may be present after these fluences at 4 K.) Cation vacancies (Mg^{2+}) are usually not monitored, because they may anneal more readily and techniques more complex than optical absorption are required to confirm their presence [To et al., 1969; Evans et al., 1972; Sibley and Chen, 1967]. Figure 4.1.1 shows the increase in defects with fluence, as well as the lattice parameter change that Henderson and Bowen obtained with single crystals of MgO . At very low fluences, Henderson and Bowen found a value of 8 to 9 atomic volumes of dilation per Frenkel defect pair. Values of atomic volume per defect pair suggested by other authors are discussed by Henderson and Bowen.

Sibley and Chen [1967] also measured Frenkel defects at relatively low neutron fluences, up to $7 \times 10^{21}/\text{m}^2$ ($E > 1$ MeV). The Smakula equation (§2.1) was used to calculate the number of defects from the optical absorption. Figure 4.1.2 shows the number of defects vs. the neutron fluence. Irradiation with 1.6-MeV electrons was also used by Sibley and Chen to produce defects from displacement damage. Figure 4.1.3 shows the number of defects vs. electron fluence in a format similar to that of Figure 4.1.2 for neutrons. These results could be used to determine, experimentally, the fluence of electrons required to simulate a given neutron fluence, but the results apply only to very low fluences. The ratio of electron-to-neutron fluence required for simulation is about 50. Note that only individual O vacancies (250-nm absorption) were monitored in this comparative study. Additional absorption lines found only in neutron irradiation indicate that clustering of O vacancies produces different types

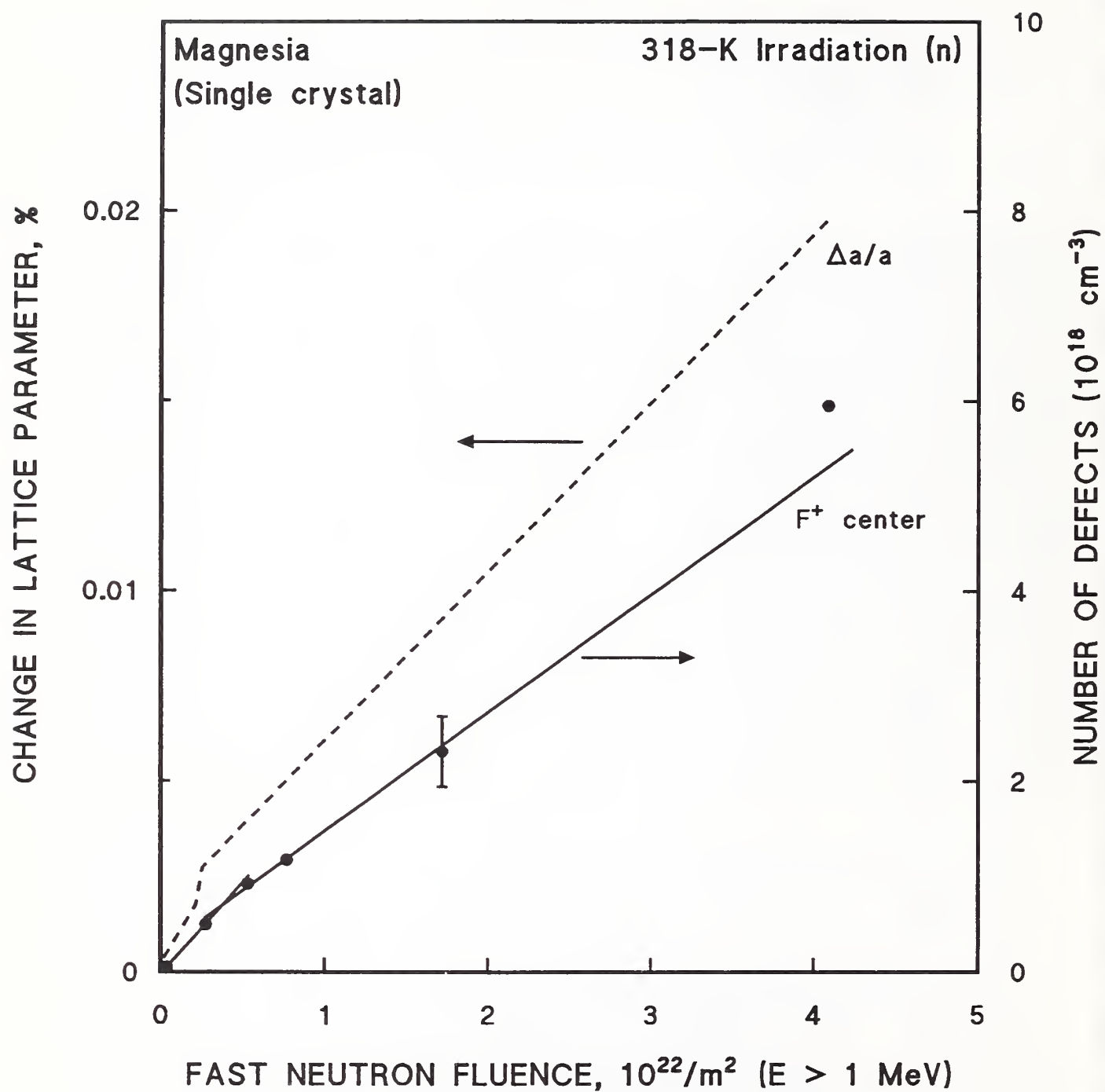


Figure 4.1.1. Fractional change of lattice parameter and number of F^+ centers created in MgO after irradiation. Data from Henderson and Bowen [1971].

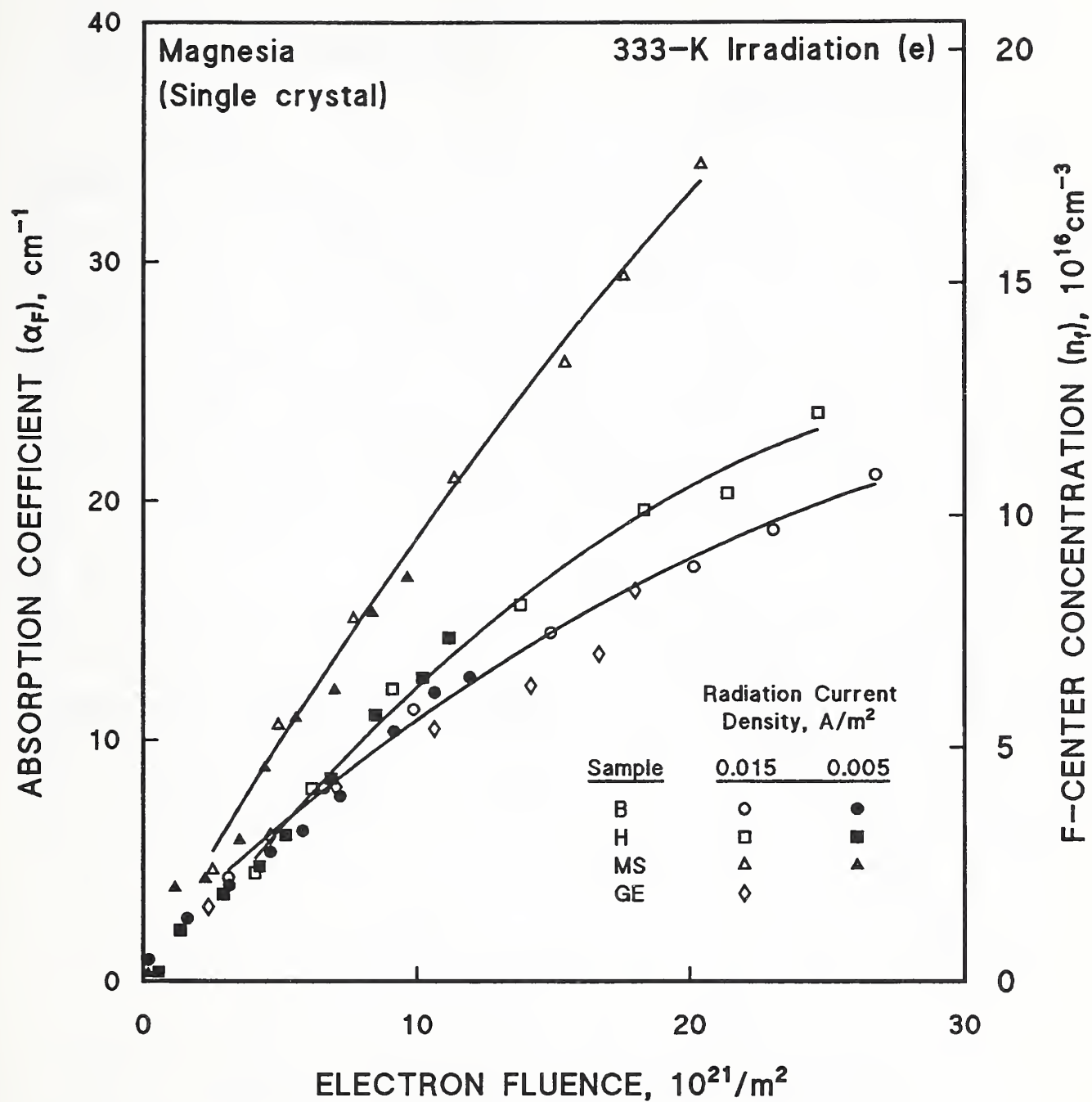


Figure 4.1.2. Absorption coefficient and defect-center concentration of MgO after electron irradiation. See text for sample differences. Data from Sibley and Chen [1967].

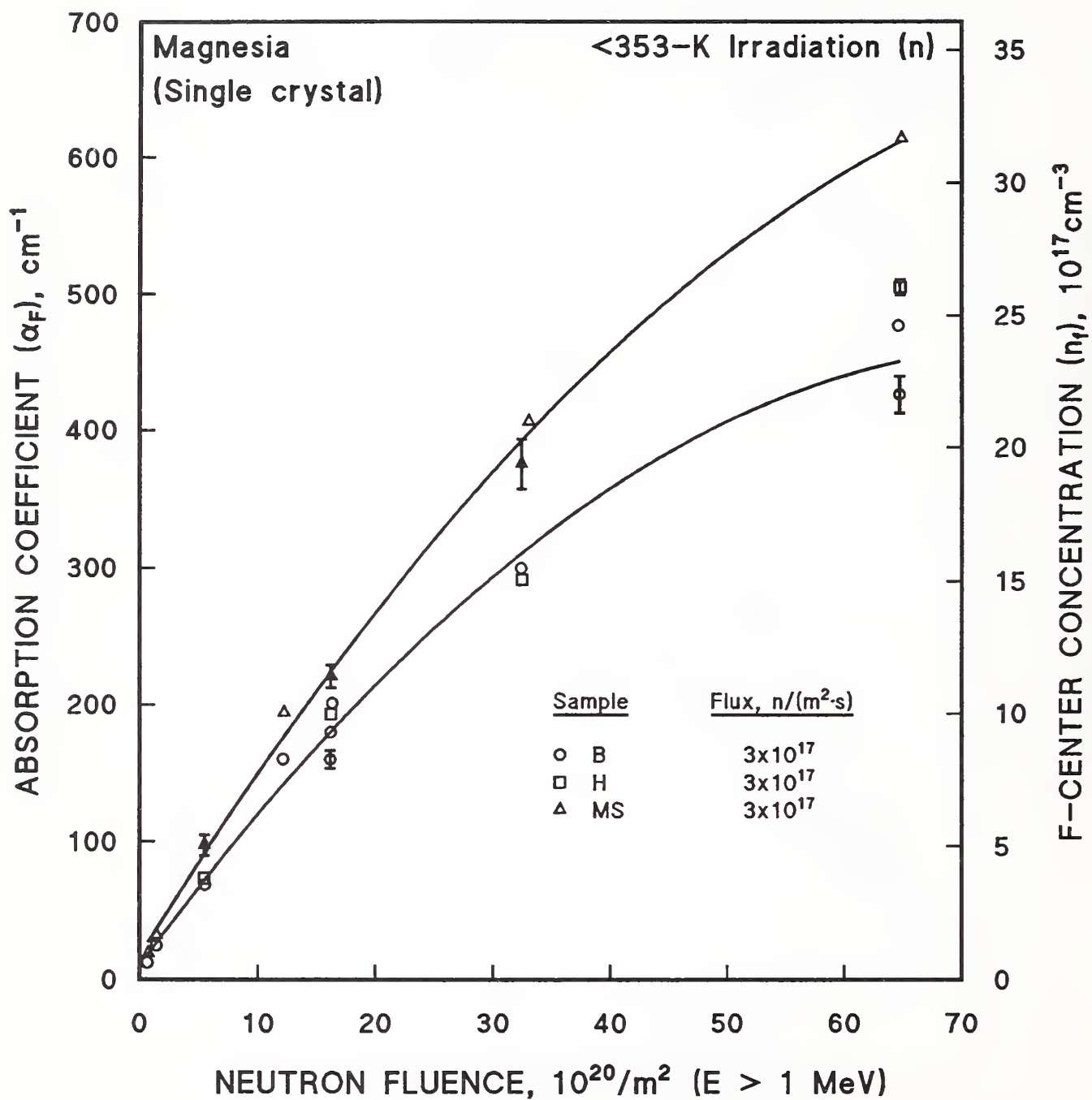


Figure 4.1.3. Absorption coefficient and defect-center concentration of MgO after neutron irradiation. See text for sample differences. Data from Sibley and Chen [1967].

of defects in neutron cascades [Chen et al., 1969]. These defects are not produced by electron irradiation.

The effect of impurities on damage was also studied. Both figures indicate that somewhat higher damage is sustained by the samples labeled MS, which were obtained from Muscle Shoals and contained about 60 ppm Fe. The other MgO single crystals had a lower impurity content; for example, the H (Harwell) samples had only 10 ppm Fe. Sibley [1971] suggested that the Fe impurities stabilized some of the defects at ambient temperature. The interstitial is mobile and diffuses through the lattice until it recombines or is trapped by an impurity ion. Therefore, the impure samples exhibit more damage for a given fluence. Since the purity of MgO has improved dramatically over time, this process of damage stabilization could account for differences in results between different groups. However, the results in Figure 4.1.2 compare well with those in Figure 4.1.1.

Chen et al.[1975] compared the number of defects produced by 14-MeV fusion neutrons with the number produced with a fission spectrum. High purity MgO single crystals were irradiated at ~300 K in the RTNS or at 325 K in a fission reactor. The defect concentrations were determined by measuring the intensity of the 250-nm band (4.95 eV). Both one-electron and two-electron O vacancies (F^+ and F centers, respectively) absorb at this energy. The results, shown in Figure 4.1.4, indicated that the fusion neutrons produced about twice as many defects per neutron as fission neutrons. This result is in accord with theoretical calculations [citations, Chen et al., 1975] and with a similar study by Evans and Stapelbroek [1979] on Al_2O_3 , discussed in §2.1.1 (Figure 2.1.2).

Electron irradiation was also used by Sibley and Chen [1967] to establish a threshold damage energy for MgO. Figure 4.1.5 shows that many fewer defects are produced with an electron energy of 700 keV than were produced with 1.6 MeV. Very few defects were produced with an electron energy of 330 keV. This establishes an $E_d(0)$ of about 50 eV, with the aid of Equation (1.5). Like Henderson and Bowen, Sibley and Chen also observed that Mg vacancies appeared to be harder to create (or observation may be more difficult). A positive-ion vacancy with a trapped hole is known as a V_1 center. The optical absorption band for V_1 centers grew rapidly at low electron doses and saturated before

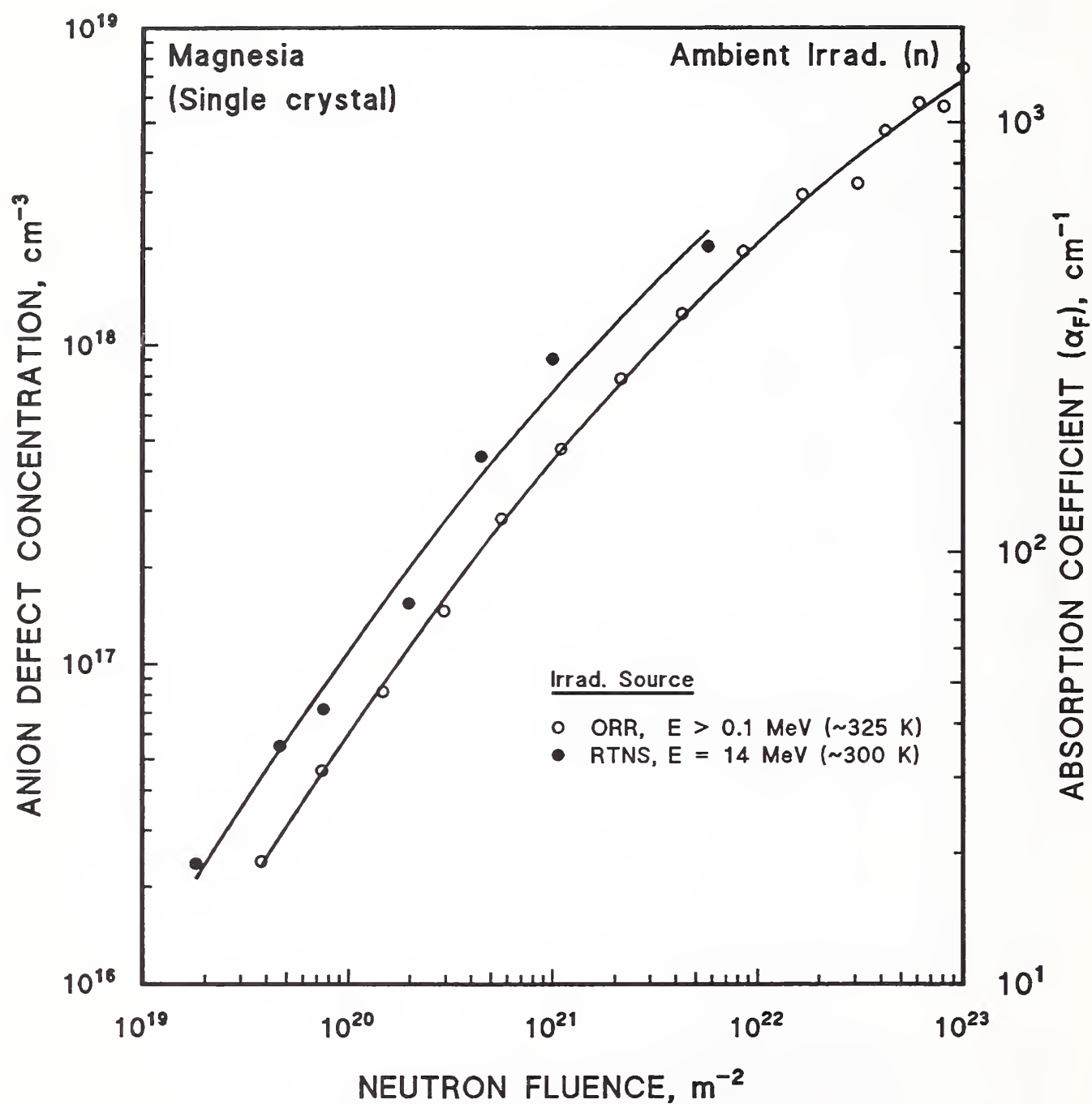


Figure 4.1.4. Absorption coefficient and defect-center concentration after neutron irradiation at different energies. Data from Chen et al. [1975].

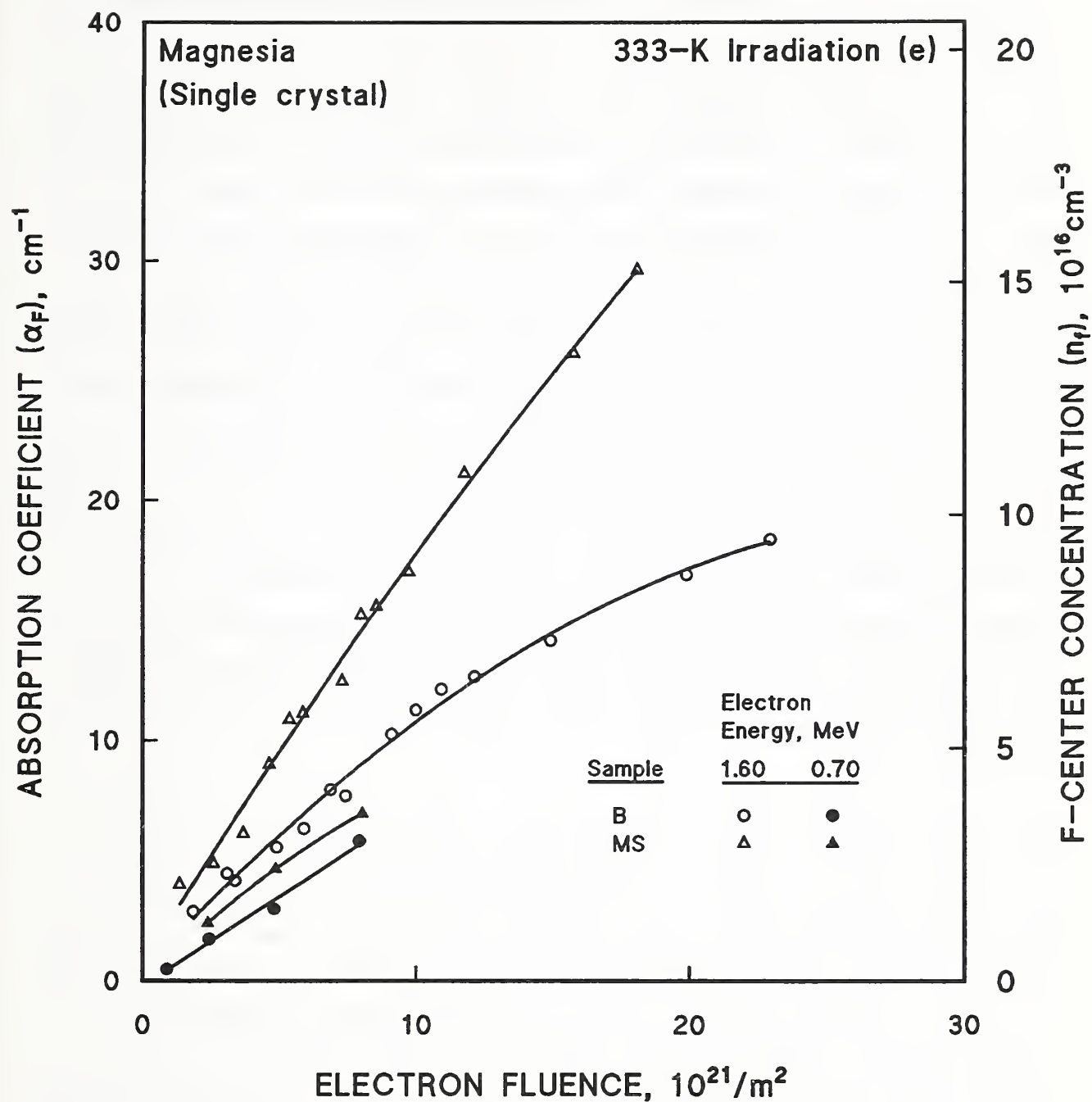


Figure 4.1.5. Effect of electron radiation energy on production of defects in MgO. See text for sample differences. Data from Sibley and Chen [1967].

F-center absorption occurred. This may have been due to ionization damage (see below).

Pells [1982] obtained an $E_d(O)$ of 53 eV for MgO, similar to the value obtained by Sibley and Chen. However, his measurements were made at 90 K, with optical techniques. Higher temperature, HVEM measurements of the threshold damage energy, obtained by monitoring the growth of visible gross radiation damage, such as dislocation loops, gave an effective threshold voltage which varied considerably with the temperature. A higher threshold found at ambient temperature was presumed to be due to Mg vacancies, giving an $E_d(Mg)$ of 60 ± 3 eV. Later work by Caulfield et al. [1990] used time resolved luminescence spectroscopy after pulsed electron irradiation to study specific isolated ionic displacements, as opposed to the gross damage monitored by Pells. This group (see also Grant et al. [1989]) found an $E_d(Mg)$ of 52 ± 2 eV at 83 K and either a second $E_d(Mg)$ of 37 ± 2 eV or an $E_d(O)$ of 55 ± 2 eV at 83 and 293 K. No effect of temperature was found on the threshold for production of F^+ centers by O displacement. The $E_d(O)$ for this process was determined to be 55 ± 3 eV at both 83 and 293 K. These newer techniques indicate that the concept of a single displacement energy for each sublattice atom may need revision in some cases.

In addition to their studies of displacement defects in MgO, Chen and Sibley also [1967] studied ionization defects by irradiating single-crystal MgO with a γ source (^{60}Co) from about 7 to 305 K, and measuring the optical spectra at the irradiation temperature. Since MgO is a strongly polar substance, when an impurity of valence state different from that of the host is incorporated into the lattice, another defect with a balancing charge must be incorporated. Ionizing radiation changes valence states, and, hence, changes the concentration of various impurity-related defects. However, the positive-ion vacancies corresponding to these defects were not created by the γ radiation. Similarly, the O-vacancy F and F^+ centers were not observed after γ radiation. The positive-ion defects were quenched in when the specimens were produced, and the γ radiation generated electron-hole pairs so that holes could be trapped at the vacancy. Then, the positive-ion vacancy with a trapped hole (a V_1 center) could be detected optically.

A strong temperature effect was observed in the decay of these ionization-created V_1 defects. Figure 4.1.6 shows the ambient-temperature decay rate of V_1 centers, ascribed to positive-ion vacancies that have trapped holes. Their half life is 2 to 7 h, with a strong impurity dependence. In contrast, at 78 K, only a small decay rate was observed, and at 5 K, the optical absorption band that reflects the defects was stable with time. However, this decay may just reflect a change in the charge state of the vacancy.

Surprisingly, Sibley and Chen [1967] did not observe annealing of displacement-produced damage from electron irradiation between 80 K and ambient temperature, within their experimental accuracy of 5%. Measurements were made by rapidly warming irradiated specimens and holding at an annealing temperature for 10 min, and then recooling to 80 K for the optical absorption measurement. This contrasts to RBS studies of McHargue et al. [1986] on Al_2O_3 irradiated with Cr ions at 77 and 300 K, discussed above in §2.3 (Figure 2.3.1), in which much greater damage was observed at 77 K than at 300 K for a given fluence. Sibley and Chen noted that the presence of a strong background signal resulting from surface contamination of specimens in their cryostat complicated their 80-K observations. However, these authors thought that this background absorption did not change during annealing, and could be subtracted.

4.1.2. Dislocation Loops; Defect Aggregates

Hurley et al. [1981] used TEM to examine polycrystalline MgO specimens after a fast neutron fluence of $2.1 \times 10^{26}/m^2$ ($E > 0.2$ MeV) at 430 K. A high density of small, elongated loops was found.

From detailed measurements of both the a-lattice parameter and the density, Henderson and Bowen [1971] concluded that clusters were present above a fluence of $5.8 \times 10^{23}/m^2$ at $-100^\circ C$. This value was deduced from a difference in the slope of $\Delta a/a$ and $\Delta \rho/3\rho$ versus fluence; that is, Frenkel vacancies migrated to form clusters of defects. This is shown in Figures 4.2.1 and 4.2.2 in the following section. Bowen and Clark [1964] found that interstitial clusters could be observed with TEM at a slightly lower fast neutron fluence of $3 \times 10^{23}/m^2$ ($E > 1$ MeV) after irradiation at $150^\circ C$. Further studies

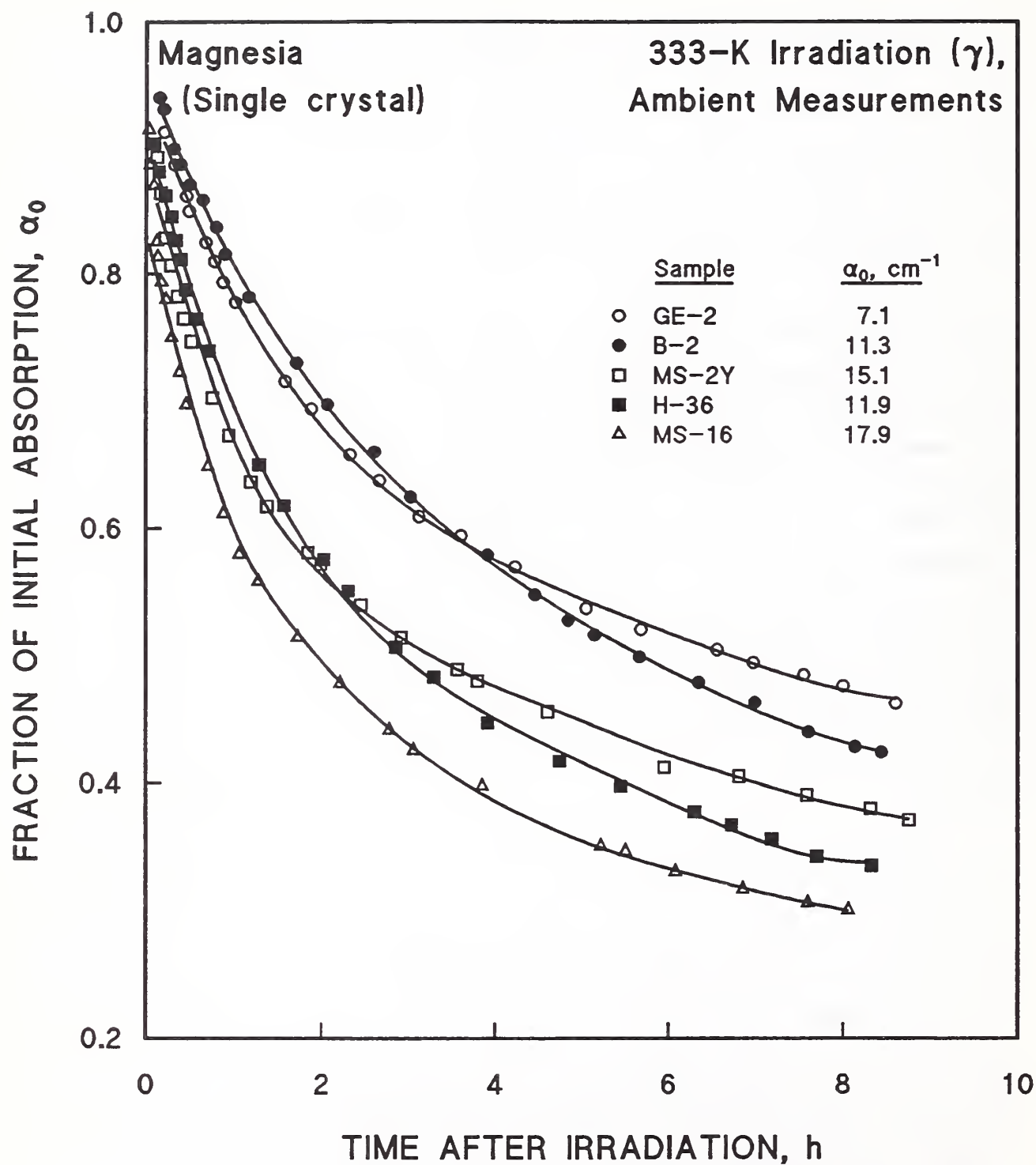


Figure 4.1.6. Ambient temperature decay rates of V_i centers (Mg^{2+} vacancies plus holes) produced after saturation γ irradiation (2.3-eV absorption). Data from Chen and Sibley [1967].

indicated that these clusters consisted of interstitial dislocation loops lying in the $\{110\}$ plane. Henderson and Bowen cited other work showing formation of cluster defects above fluences of $\sim 10^{23}/\text{m}^2$. At a fluence of $4 \times 10^{24}/\text{m}^2$, Bowen and Clark found that the loops became so large that they disintegrated into a tangle of dislocation lines and were very resistant to annealing. At 4 K, or after warm-up, cluster defects could arise at lower fluences, since defects lying close to each other in a cascade will not anneal as easily as isolated defects at ambient temperature.

4.2. CHANGE IN VOLUME

Henderson and Bowen [1971] made careful measurements of the a-axis lattice parameter and density changes in single-crystal MgO after 318-K fast neutron fluences from 10^{21} to $8 \times 10^{23}/\text{m}^2$. (The energy range was not specified.) Their results in the lower range for $\Delta a/a$ were shown above in Figure 4.1.1. Figures 4.2.1 and 4.2.2 show the continuation of their work to higher fluences, and include the density change, $\Delta\rho/3\rho$. (By multiplying $\Delta\rho/3\rho$ by 3, one obtains a volume change of $\sim 0.6\%$ at a fluence of $8 \times 10^{23}/\text{m}^2$.) The value, 0.2% , for $\Delta a/a$ at $8 \times 10^{23}/\text{m}^2$ can be compared with the lattice parameter data reviewed by Wilks [1968] and shown in Figure 4.2.3. These data were obtained from irradiations at ~ 375 K, whereas the irradiations of Henderson and Bowen were at 318 K. Possibly, the higher temperature of irradiation could explain the discrepancy, since these data do not attain the saturation value of $\sim 0.2\%$ until a fluence of $2 \times 10^{24}/\text{m}^2$, somewhat above that of Henderson and Bowen.

The observed decline in the lattice parameter is not reflected in the total volume expansion. This is shown in the review of density measurements by Wilks [1968] given in Figure 4.2.4. The departure of the correlation in slope of the lattice parameter curve (Figure 4.2.3) and the volume expansion curve is thought to represent formation of cluster damage above $\sim 7 \times 10^{23}/\text{m}^2$ [citations, Wilks, 1968]. (For Al_2O_3 , Wilks found that the density change correlated with the lattice parameter change in a similar range of fluence; therefore, the density change in Al_2O_3 was ascribed to interstitials and vacancies, and the cluster damage was thought to be relatively low.) The results of Hurley et al. [1981] do not support the apparent saturation of the density change at $\sim 1\%$ shown in Figure 4.2.4 at a fluence of ~ 4 to $6 \times 10^{24}/\text{m}^2$.

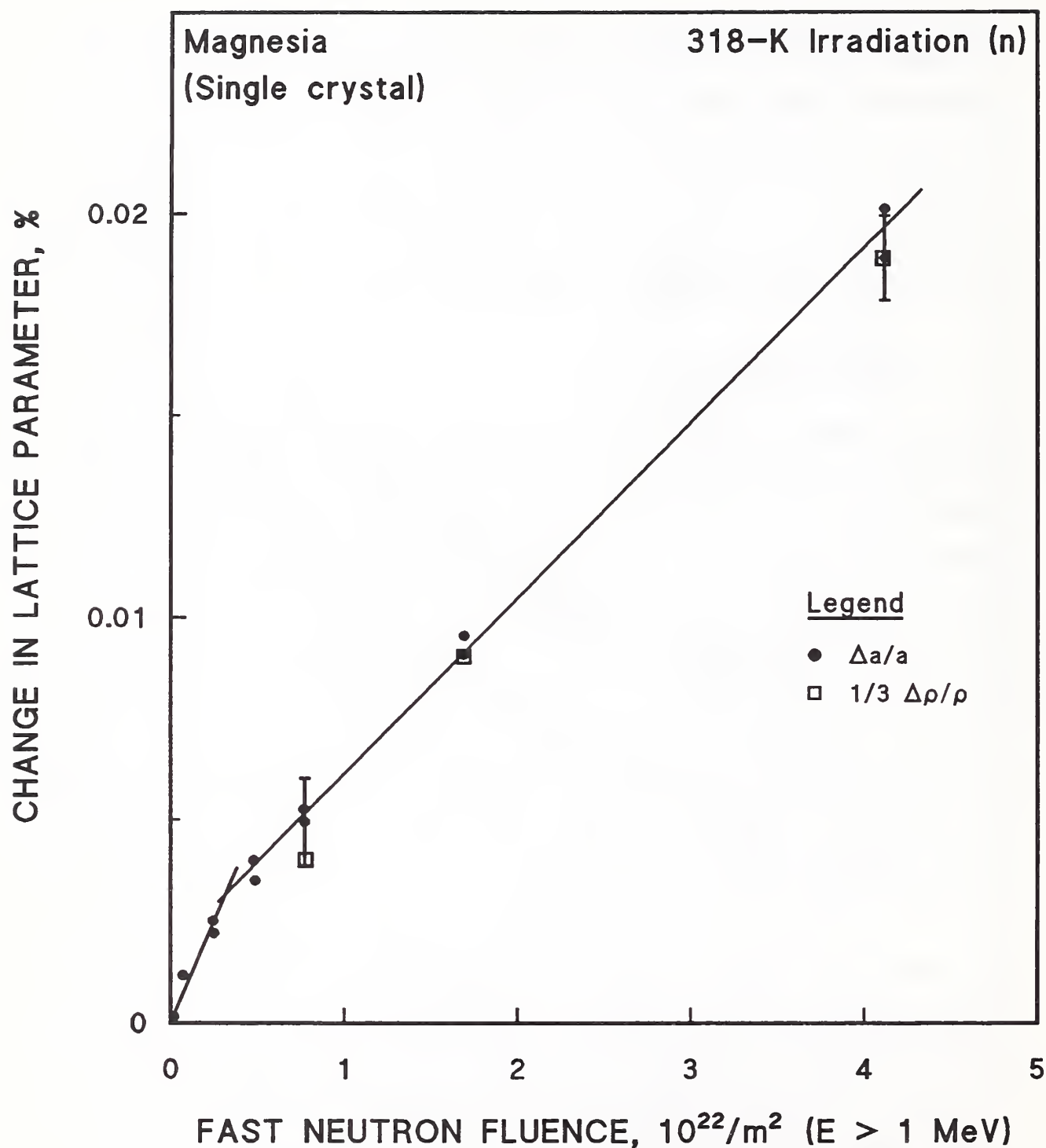


Figure 4.2.1. The change of lattice parameter ($\Delta a/a$) and crystal density ($\Delta \rho/\rho$) with neutron irradiation of MgO at 318 K. Data from Henderson and Bowen [1971].

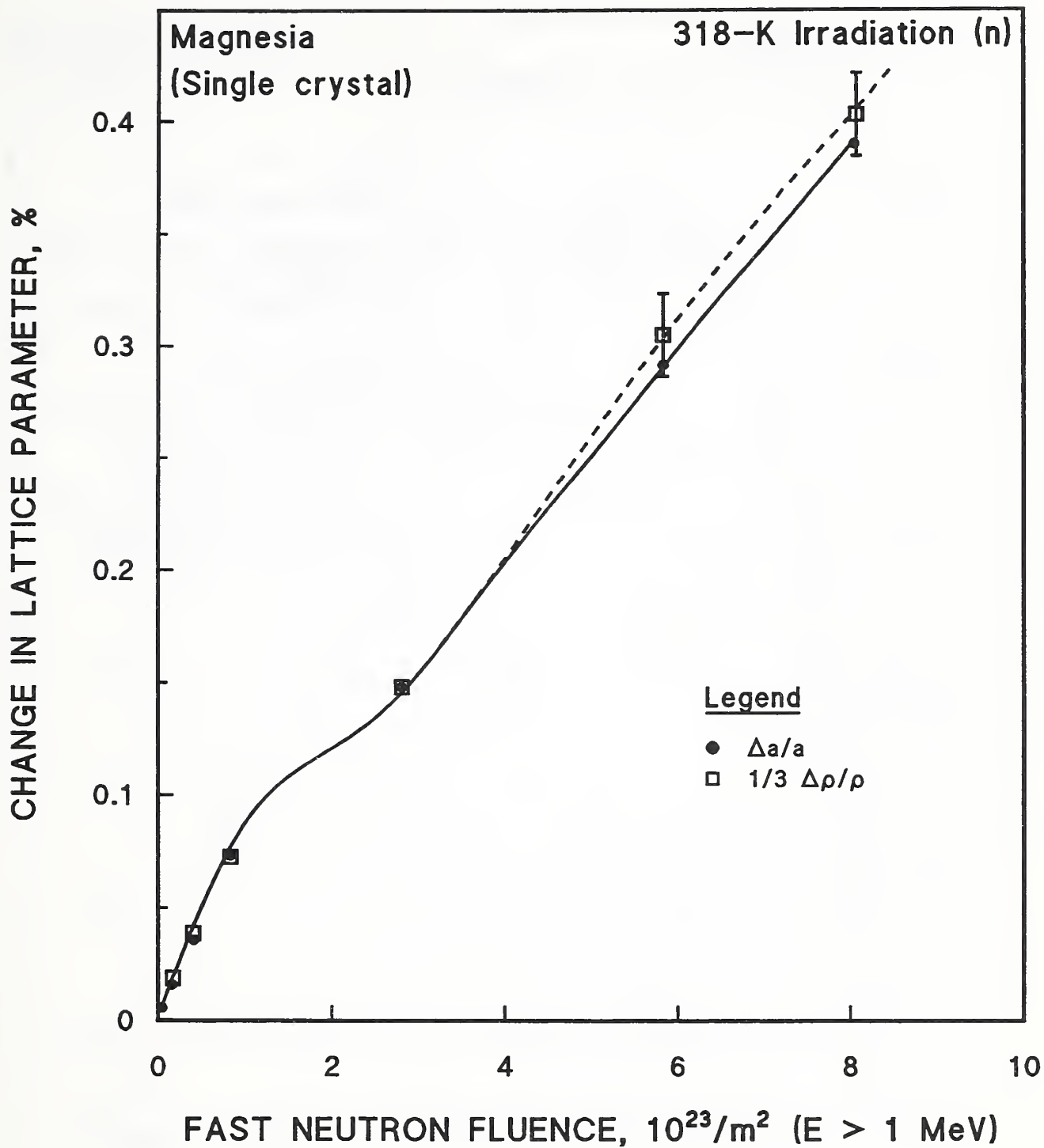


Figure 4.2.2. The change of lattice parameter ($\Delta a/a$) and crystal density ($\Delta \rho/\rho$) with neutron irradiation of MgO at 318 K. Data at higher fluence. From Henderson and Bowen [1971].

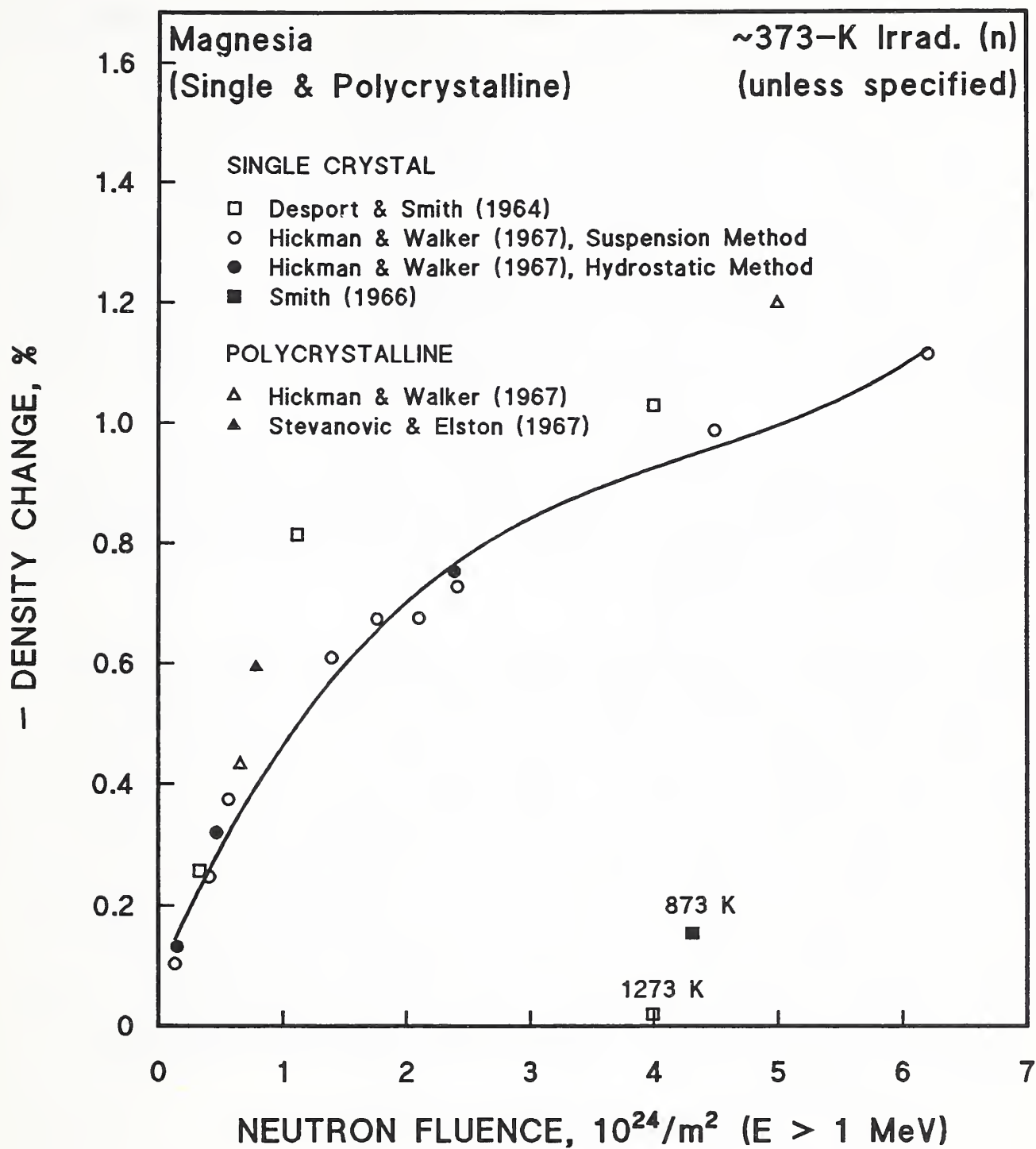


Figure 4.2.4. Density change of MgO with neutron irradiation. Data and citations from Wilks [1968].

When Hurley et al. irradiated polycrystalline MgO to a fast neutron fluence of $2.1 \times 10^{26}/\text{m}^2$ ($E > 0.2$ MeV) at 430 K, they found volume swelling of 2.6 and 3.0 % in two samples. The two samples were from different suppliers; the differences in swelling, if significant, could arise from different impurity content. These polycrystalline specimens had impurity levels of up to 1.7%. Keilholtz et al. [1971] found swelling of 1.1 and 1.3% in single-crystal MgO irradiated at 60 to 90°C to intermediate fluences of 1.2 and $2.1 \times 10^{25}/\text{m}^2$ ($E > 1$ MeV). Thus, it appears that saturation in swelling is not reached, at least at the fluence attained at low irradiation temperatures. When all of the volume swelling data are plotted together, as in Figure 4.2.5, saturation is not indicated.

Stevanovic and Elston [1967] found no changes in the grain size or appearance of the grain boundary in sintered MgO after irradiation below 80°C to a fast neutron fluence of $\sim 10^{24}/\text{m}^2$ ($E > 1$ MeV). The transcrystalline fracture of the material also was not changed.

The X-ray diffraction line profiles found by Stevanovic and Elston indicated greater strains in MgO than in Al_2O_3 for similar fluences. Point defects tended to remain scattered or annihilated in Al_2O_3 , but in the MgO lattice they were clustered. The authors suggested that the occurrence of Mg^{2+} interstitials of ion radius 0.078 nm (0.78 Å) causes strains in the MgO structure, which is like that of NaCl. These strains are greater than those of Al^{3+} interstitials of ion radius 0.057 nm (0.57 Å) in the corundum lattice, and the Al^{3+} ions may be displaced to normally unoccupied octahedral holes, since Al^{3+} ions occupy only 2/3 of these sites in the hexagonal close packing of O^{2-} ions. However, in MgO, the Mg^{2+} ions occupy all the octahedral holes, so the interstitials must be located in the tetrahedral holes, which disturbs the lattice structure much more.

4.3. AMORPHIZATION

Wilks [1968] reviewed X-ray studies of line broadening in MgO. At an irradiation temperature of 150°C, no X-ray line broadening was observed at a fluence of $3 \times 10^{23}/\text{m}^2$, but considerable broadening was observed at $4 \times 10^{24}/\text{m}^2$ (E not specified). Irradiations at 100°C gave approximately the same result, except

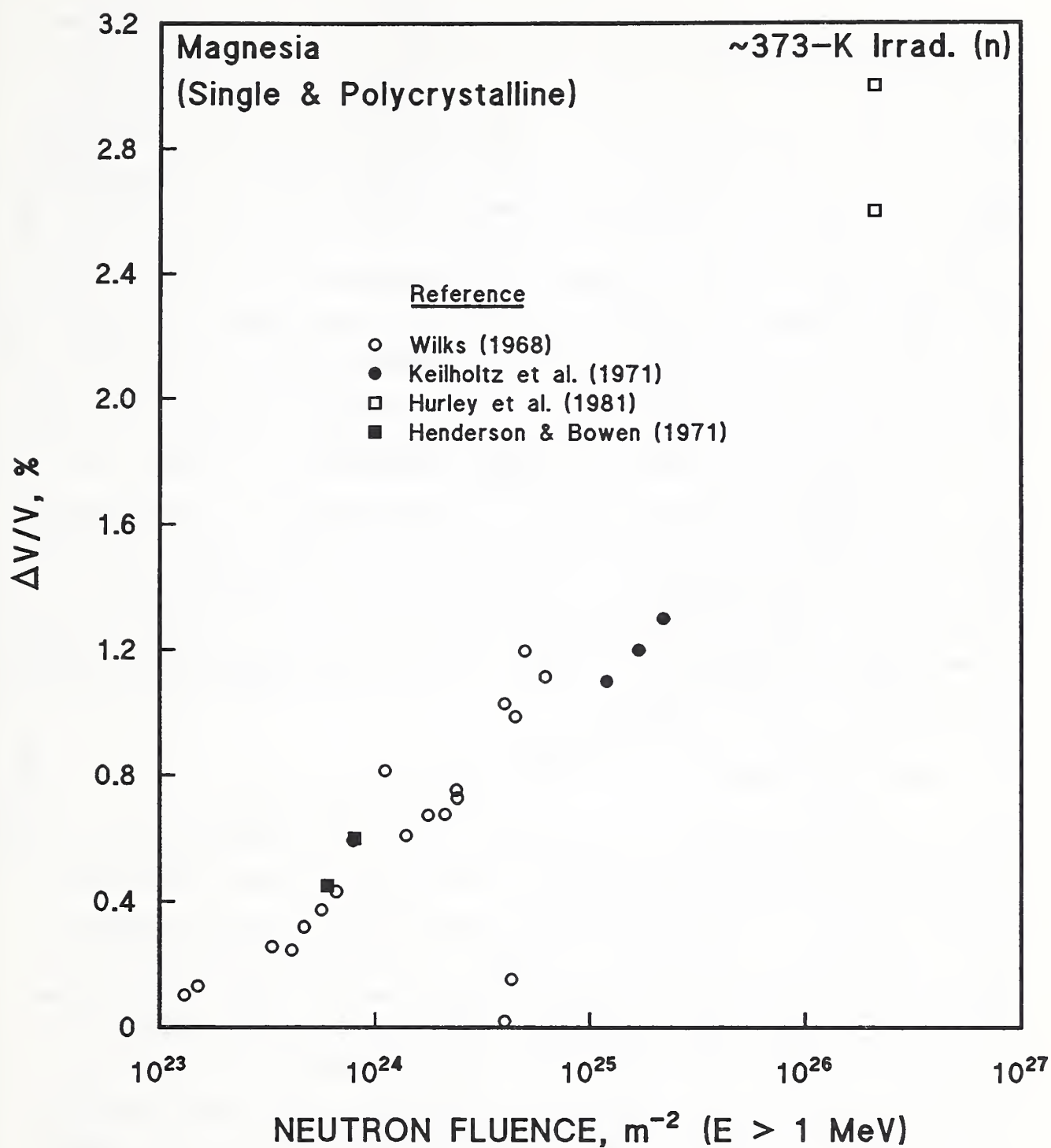


Figure 4.2.5. Compilation of volume swelling data on MgO.

that slight broadening was observed at $4.2 \times 10^{23}/\text{m}^2$. The line broadening was attributed chiefly to strain from dislocation loops, but a particle size contribution was reported at $4 \times 10^{24}/\text{m}^2$. It was suggested that this contribution was from interactions between the dislocation loops that led to formation of a cellular structure similar to that of a cold-worked metal. Primak [1954] irradiated a number of inorganics at a temperature below 100°C to the same fluence, estimated as about $1.2 \times 10^{24}/\text{m}^2$ ($0.01 < E < 1\text{--}2 \text{ MeV}$). Only small percentage changes in lattice parameter were observed for MgO and MgAl_2O_4 at this fluence; however, the diffraction pattern of quartz became so diffuse that line positions could not be measured. Matzke and Whitton [1966] also compared X-ray evidence for structural changes in a number of substances after 40-keV Xe or Kr ion irradiation. Although MgO is a cubic substance, it showed considerable lattice disorder at the highest ion fluence of $2 \times 10^{20}/\text{m}^2$ when other cubic substances showed no change in lattice perfection. Kikuchi lines indicating crystal perfection had disappeared at $4 \times 10^{18}/\text{m}^2$. The anisotropic Al_2O_3 exhibited a disappearance of crystallinity at lower fluences (§2.3). Although data on the fluence at 4 K that causes considerable lattice disorder or amorphization do not exist, it appears that the relative order of stability is $\text{MgO}, \text{MgAl}_2\text{O}_4 > \text{Al}_2\text{O}_3 > \text{SiO}_2$.

4.4. MECHANICAL PROPERTIES

Single crystals of MgO were irradiated with fast neutron fluences up to $8 \times 10^{21}/\text{m}^2$ ($E > 1 \text{ MeV}$) before measurements of the critical resolved shear stress [Davidge, 1968]. The optical absorption spectrum and the lattice parameter were also measured as a function of fluence. All measurements were made at ambient temperature, and the irradiation temperature was $\sim 343 \text{ K}$. The critical resolved shear stress was estimated by an indentation wing size technique [citation, Davidge, 1968]. Figure 4.4.1 shows the increase in critical resolved shear stress, τ , with fluence, ϕ . These data can be fitted with an expression of the form $\tau = \tau_0 + A\phi^{1/2}$, where τ_0 is the critical resolved shear stress before irradiation. Since the number of trapped interstitials was proportional to the fluence, for the optical absorption measurements that Davidge also performed, the hardening was proportional to $c^{1/2}$, where c is the concentration of interstitials. This result has been obtained in other systems, such

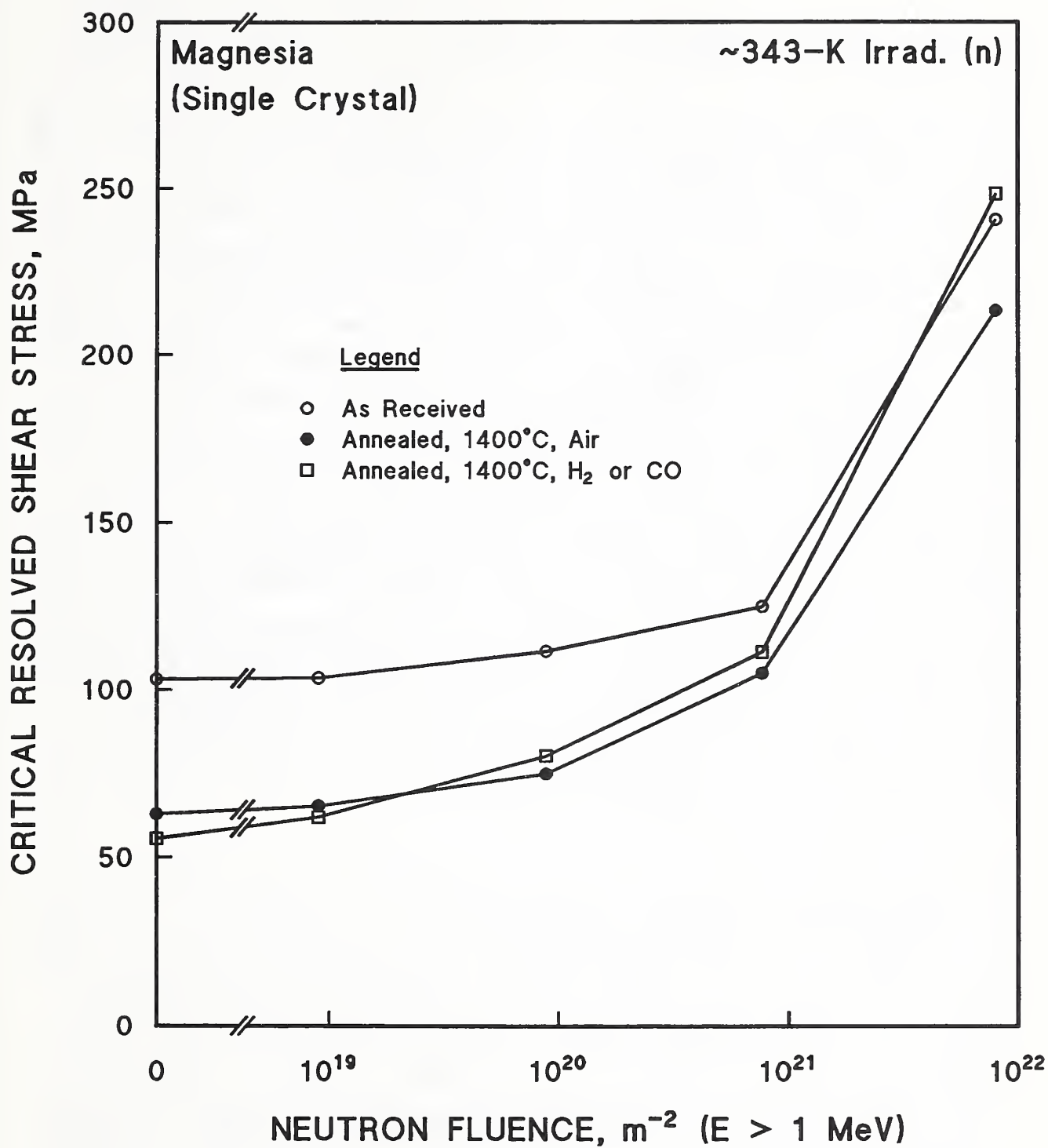


Figure 4.4.1. Critical resolved shear stress (see text) of single-crystal MgO after neutron irradiation. Data from Davidge [1968].

as the alkali halide system [citations, Davidge, 1968]. Davidge concluded that vacancies played a minor role in hardening.

McGowan and Sibley [1969] verified and extended this work by irradiating single-crystal MgO specimens of higher purity with both electrons and neutrons. Irradiation with electrons produces only isolated defects and relatively few clusters, in comparison to irradiation with neutrons (§1.2). Therefore, the optical measurements of the 250-nm absorption band gave the concentration of the negative-ion vacancies (§4.1), and, thus, a good estimate of the concentration of interstitials. Since flow strength measurements in this investigation were made by compression tests, the validity of the indentation technique was not an issue. However, extreme care was necessary to obtain useful results from the compression testing. Specimens that were diamond-sawn were about 20% harder than those that were cleaved. Only specimens that had no observable cleavage steps or grain boundaries were used, and because of the extreme brittleness of the irradiated specimens, the compression ends had to be very flat and parallel, so that fracture did not occur before the flow point was reached. To minimize material variability, samples for a particular experiment were taken from the same part of one crystal ingot. Four specimens were normally tested and results averaged for each irradiation data point. Compression specimens were 5 to 10 mm in length with a cross sectional area of about 1 to 10 mm².

Irradiation temperatures for both electrons and neutrons ranged from 40 to 60°C (313 to 333 K). Because ionizing radiation was also thought to be effective in changing the flow strength of MgO, some specimens were irradiated with 10⁴ Gy of ⁶⁰Co γ radiation (Figure 4.4.2). This increased the flow strength by about 4 to 6 MPa, probably because ionizing radiation changes the valence state of some impurities and forms V₁ centers (§4.1) [citation, McGowan and Sibley, 1969]. Since optical bleaching removes most of the damage produced by ionizing radiation, this and other techniques were used to obtain consistent flow strength data. Figure 4.4.3 shows the data as a function of the concentration of vacancy centers, calculated from an equation similar to Equation (2.1). The data for electron irradiation have a slope of ~0.5, as Davidge found, but the neutron data had to be fitted to fluence, rather than to defect concentration as measured by optical absorption, to obtain a slope of 0.5,

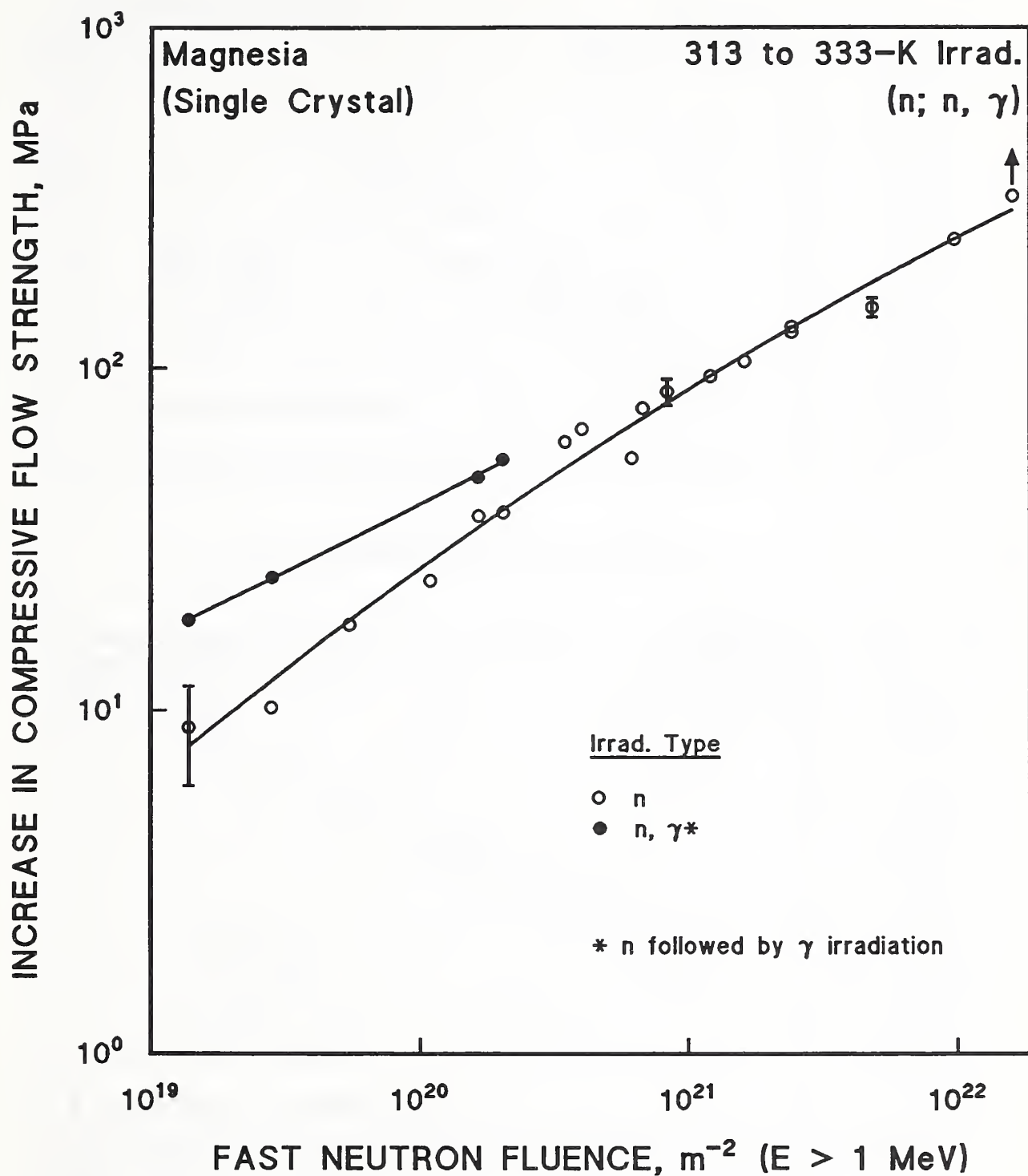


Figure 4.4.2. Increase in compressive flow strength of single-crystal MgO after neutron irradiation. The arrow indicates that only one sample was useable at this fluence; the others underwent brittle fracture before yielding. Data from McGowan and Sibley [1969].

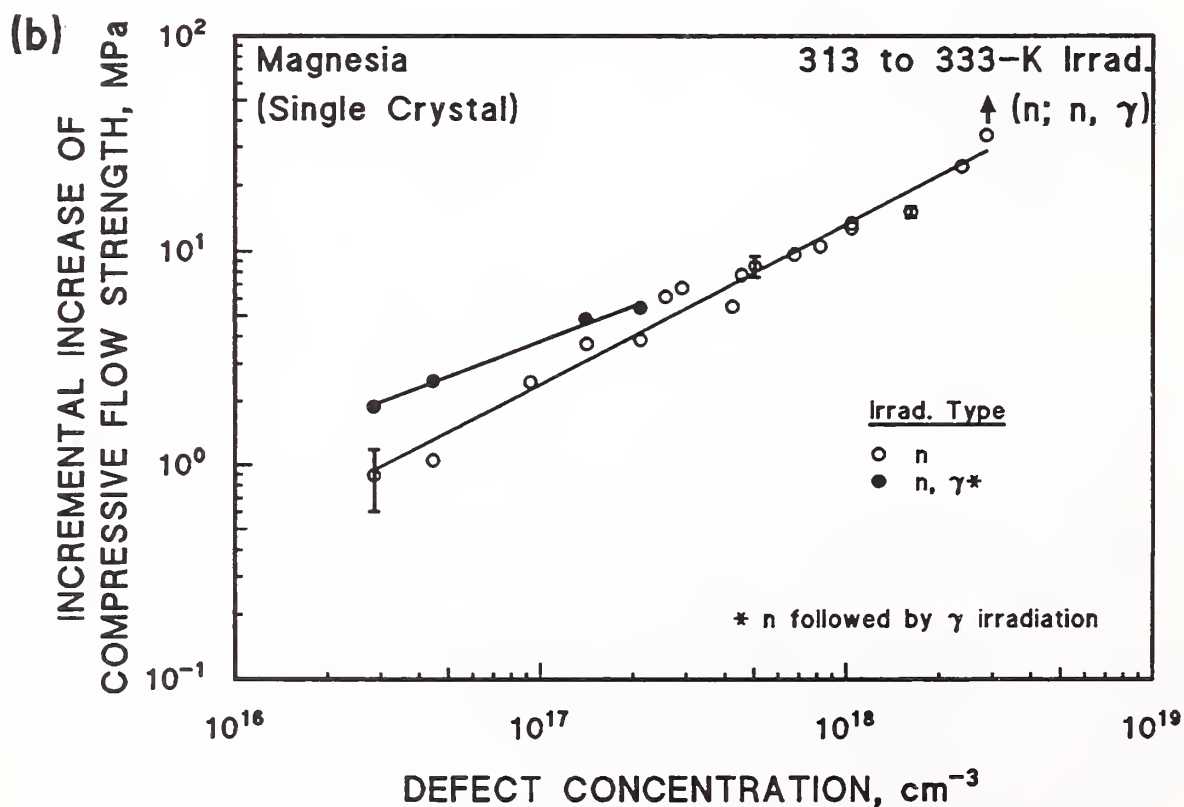
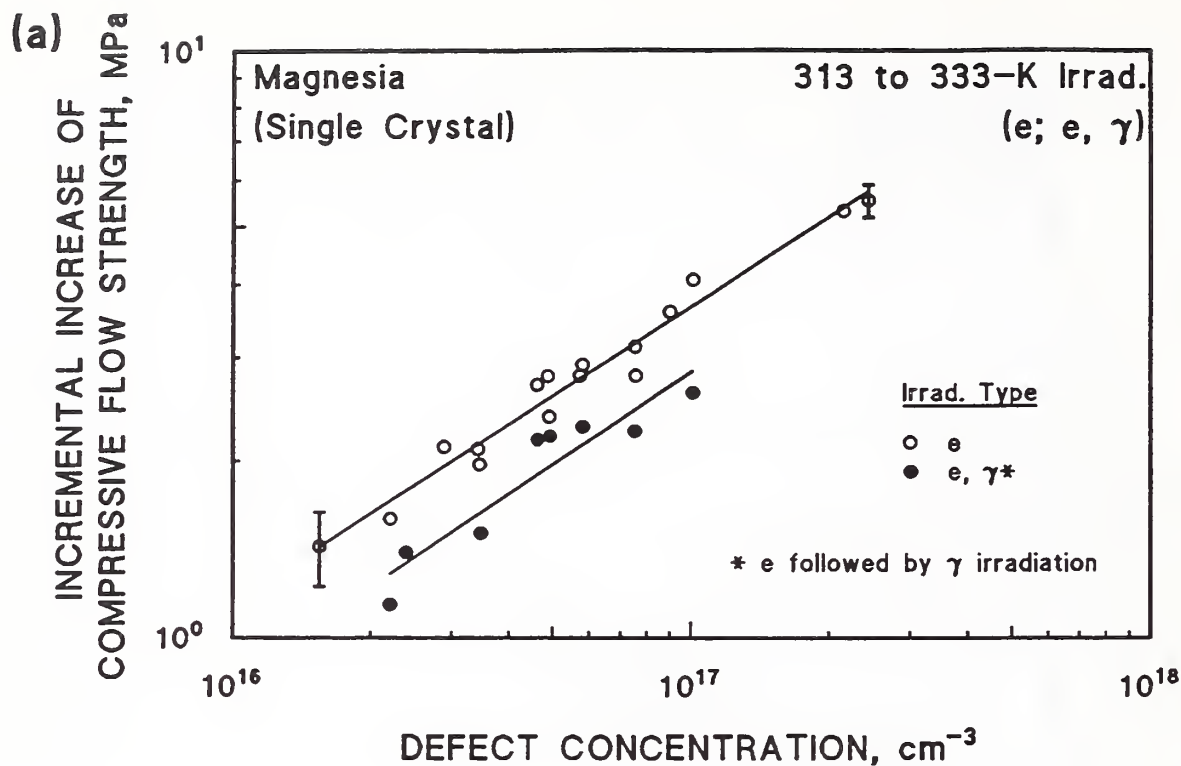


Figure 4.4.3. Incremental increase of compressive flow strength of single-crystal MgO for (a) electron and (b) neutron irradiation. The error bars represent only statistical, not systematic, errors. The arrow indicates that only one sample was useable at this fluence; the others underwent brittle fracture before yielding. Data from McGowan and Sibley [1969].

since additional cluster defects were created. Figure 4.4.2 shows the increase in compressive flow strength with fluence. The data were also plotted to give a direct comparison with the investigation of Davidge; the agreement was very good (Figure 4.4.4). However, data at a fluence just below $2 \times 10^{22}/\text{m}^2$ (see arrow in figures) were difficult to obtain, since most specimens underwent brittle fracture before yield occurred, after irradiation to this fluence. An analysis of the electron irradiation data was made with the expression $\Delta r = (G/K)c^{1/2}$, where G is the shear modulus, c is the mole fraction of defects, and K is related to the tetragonal lattice strain associated with the defect. This showed that K had the value expected for interstitial lattice strain. McGowan and Sibley therefore concluded that the hardening was caused by interstitials and that vacancies could be excluded as a cause of hardening by other work they did with doped crystals.

An important point raised in this work for the possible use of MgO in ITER TF magnets was the brittle behavior of specimens irradiated at ambient temperature to a fluence of $\sim 2 \times 10^{22}/\text{m}^2$. Brittle behavior was not reported by Davidge, but his specimens were more impure and the highest fast neutron fluence was slightly lower, $8 \times 10^{21}/\text{m}^2$ (Figure 4.4.1). Also, Davidge used an indentation technique that was less likely to reveal brittle behavior. Since a considerable degree of defect annealing is expected at ambient temperature, if brittle fracture under compression is not acceptable in the magnet, then fluences would have to be kept below $\sim 10^{22}/\text{m}^2/100$, or $\sim 10^{20}/\text{m}^2$, before periodic ambient-temperature anneals, and additional testing on this point would surely be warranted. The value of the compressive flow strength had increased by more than 300 MPa under irradiation, before brittle failures occurred (Figure 4.4.2). Perhaps the compressive strength of sintered, polycrystalline material will be less sensitive to neutron irradiation, but this possibility must be experimentally verified. Compressive tests were found only for MgO in the literature search. Compressive testing with an aspect ratio that corresponds to the geometry of the ITER TF magnet insulation should also be carried out, since the insulation thickness is expected to be only about 1.5 mm (Figures 1.1.1 and 1.1.2).

Evans and Davidge [1969] studied the fracture in 4-point bending of dense, polycrystalline MgO in which the grain size varied from 10 to 500 μm . The

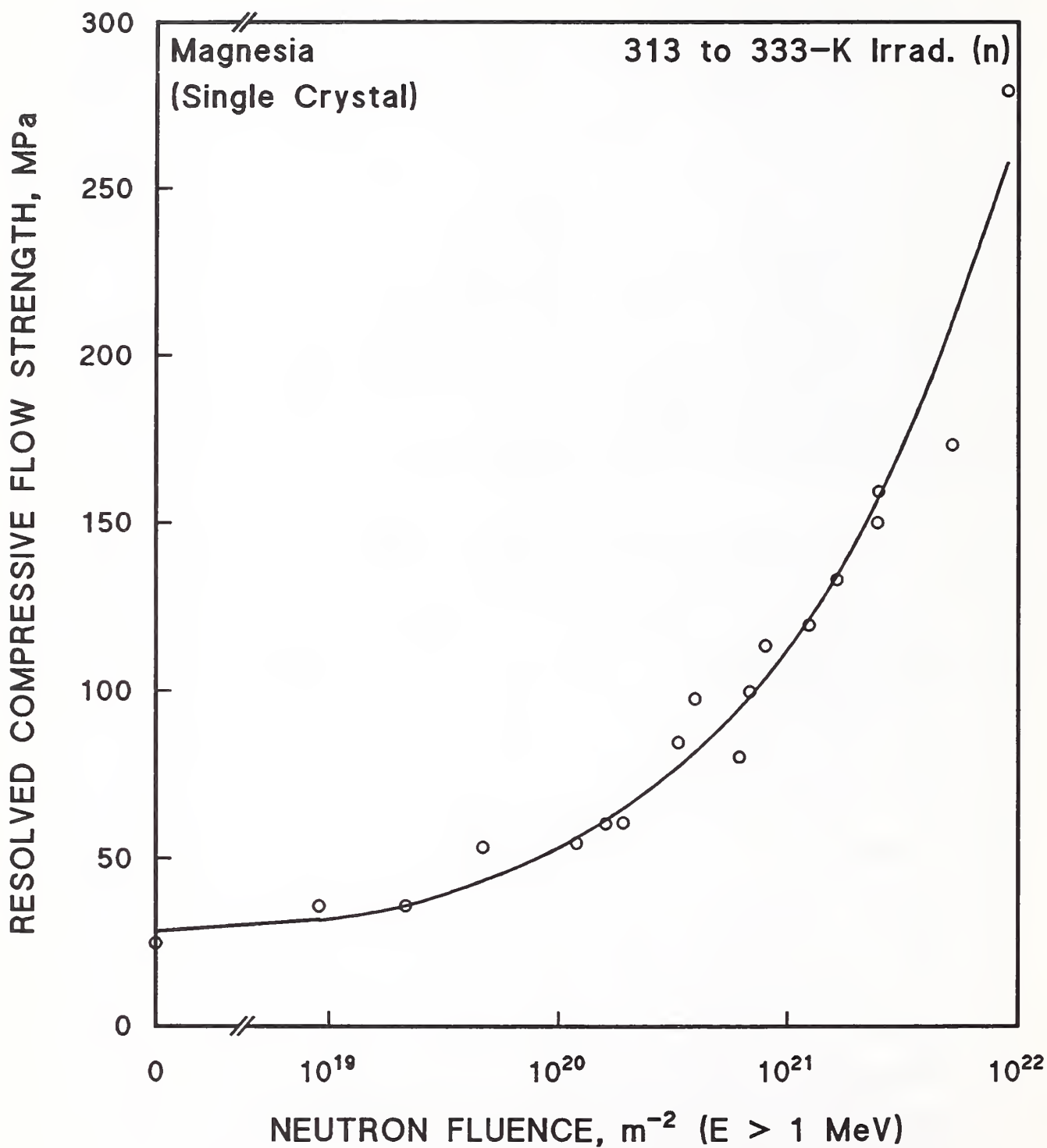


Figure 4.4.4. The compressive flow strength of single-crystal MgO plotted as a function of fluence, for comparison with Figure 4.4.1. Data from McGowan and Sibley [1969].

fracture in chemically polished specimens initiated by plastic flow, whereas in machined specimens, fracture occurred by the extension of flaws produced by machining. A relatively low fluence of reactor neutron irradiation, $\sim 3 \times 10^{15}/\text{m}^2$, was used in an attempt to strengthen the material. The irradiation temperature was $\sim 150^\circ\text{C}$ (423 K). Figure 4.4.5 shows that the irradiation slightly decreased the fracture strength of the machined specimens, but the figure also indicates that the strength of chemically polished specimens was increased. Evans and Davidge concluded that fracture of the irradiated, chemically polished material was nucleated at surface flaws, instead of by dislocation motion, as in the unirradiated material. In mechanically polished specimens, dislocation-initiated fracture was not possible, and so fracture probably occurred by extension of existing flaws.

The diametral compression strength of cylinders of polycrystalline MgO loaded on their sides between parallel platens was measured by Hurley et al. [1981] after neutron irradiation at 430 ± 5 K to $2.1 \times 10^{26}/\text{m}^2$ ($E > 0.2$ MeV). Stress analysis [citation, Hurley et al., 1981] shows that uniform tensile stress is produced by this configuration, owing to the selection of padding. The results on two materials are shown in Figure 4.4.6; this test was also carried out on polycrystalline MgAl_2O_4 (§7.4). All of the failures occurred by parting on the midplane or by triple cleft failure, and were considered to be tensile. Fracture in both irradiated and control specimens was largely transgranular, but in the control material, significant areas of intergranular fracture were observed. The strength of both control and irradiated MgAl_2O_4 was much higher, and fracture origin was traced to locations at the free surface. This suggested that fractures originated at machining flaws. Significant swelling ($\sim 3\%$) was observed in MgO (§4.2); that of MgAl_2O_4 was lower, but still significant ($\sim 0.8\%$).

Several other ambient-temperature mechanical properties of sintered MgO and single crystals were measured by Stevanovic and Elston [1967] after irradiation below 80°C (353 K) to fast neutron fluences in the $10^{24}/\text{m}^2$ ($E > 1$ MeV) range. A resonance method was used to determine the change of Young's modulus in sintered MgO at 293 K: a decrease of 4.85% was observed after $8 \times 10^{23}/\text{m}^2$. The Vickers microhardness was measured on single crystals at ambient temperature with an estimated accuracy of $\pm 2\%$ on the (001) plane for fluences of

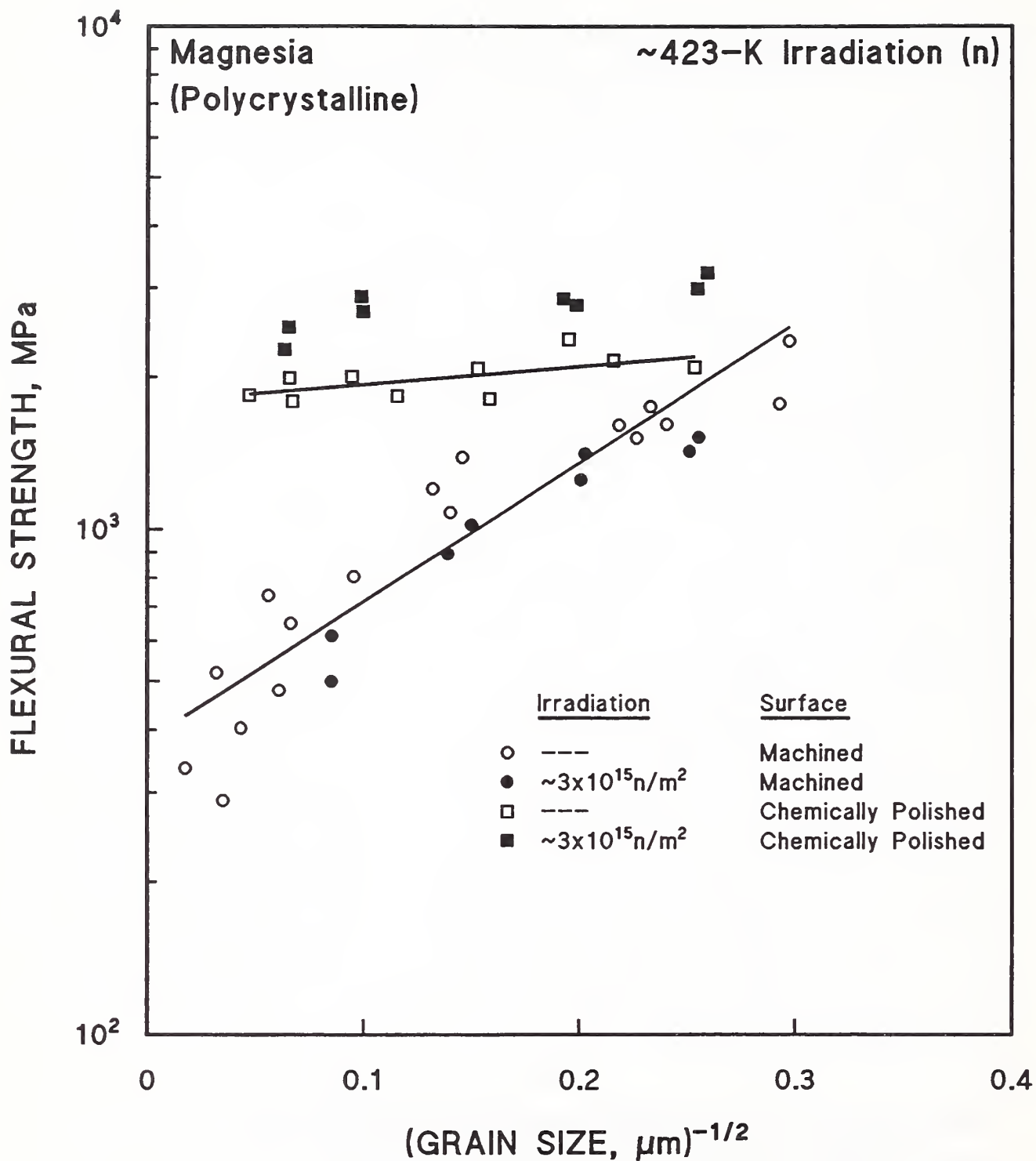


Figure 4.4.5. Four-point bending strength vs. reciprocal square root of grain size before and after irradiation for two types of surface finish. Data from Evans and Davidge [1969] on polycrystalline MgO.

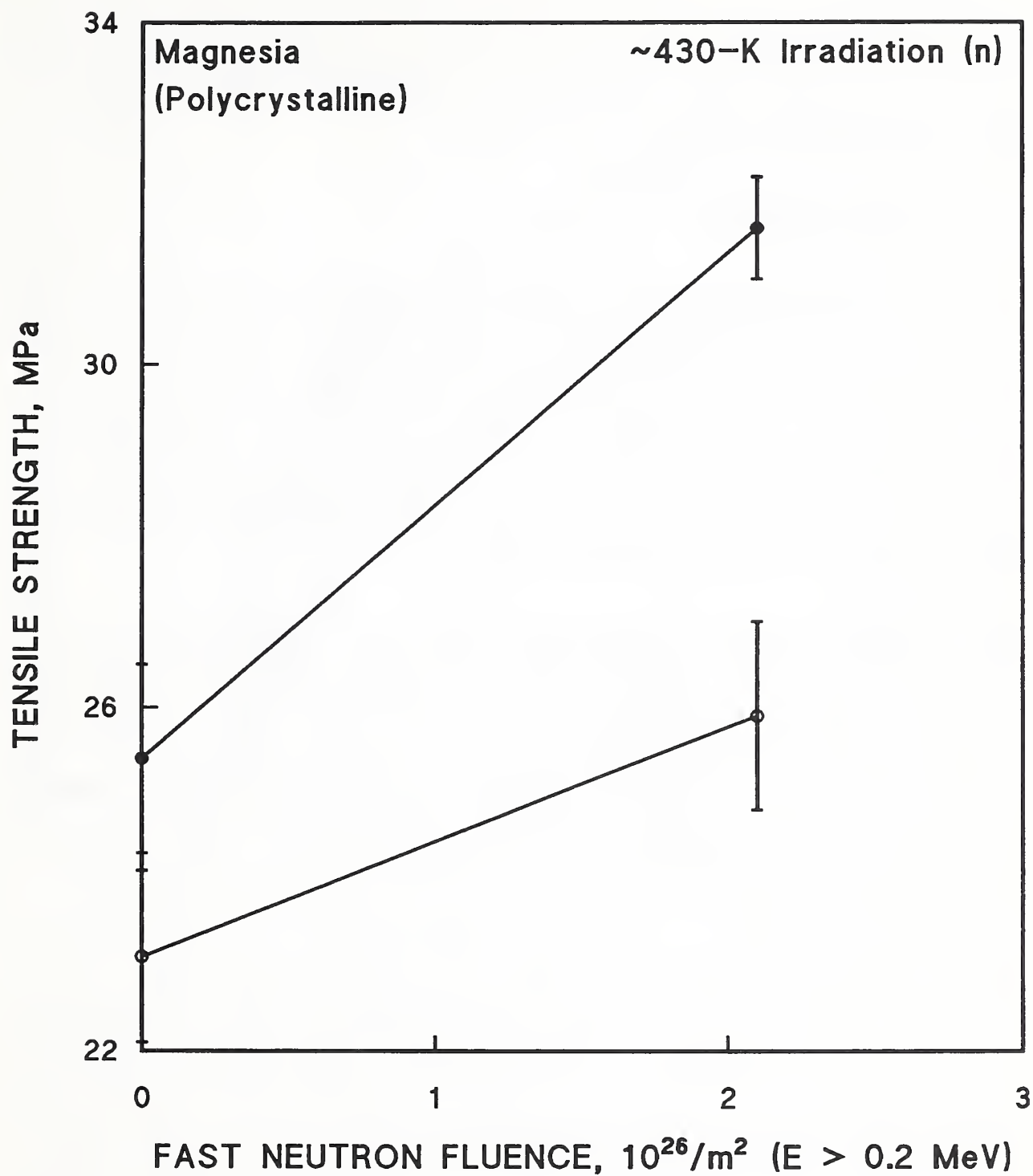


Figure 4.4.6. Diametral compressive strength of polycrystalline MgO specimens after neutron irradiation. Data from Hurley et al. [1981].

5×10^{23} and $1.2 \times 10^{24}/\text{m}^2$. The average increases in directions [010] and [100] were 24.2 and 26.7%. Stored energy after irradiation was measured on a differential thermal analysis calorimeter. The Wigner's energy in sintered MgO after $8 \times 10^{23}/\text{m}^2$ was about 72 ± 8 kJ/kg.

4.5. THERMAL PROPERTIES

Thermal conductivity at cryogenic temperatures was measured after ambient temperature γ irradiation by Abramishvili et al. [1981]. Figure 4.5.1 shows that the effect of the γ irradiation on a single crystal appeared to saturate after about 2.5×10^3 Gy, and that annealing at 625°C restored the original values. The change in conductivity was related to valence changes caused by the ionizing radiation which affected the impurity ions Fe and Cr, present at 40 and 4.5 ppm, respectively. The valence changes were observed by annealing studies combined with optical spectroscopy.

Thermal conductivity and specific heat of single-crystal MgO were measured between 0.1 and 10 K by Gardner and Anderson [1981b] after ambient-temperature (value not reported) irradiation to fast neutron fluences up to $3 \times 10^{23}/\text{m}^2$ ($E > 0.1$ MeV). The results of the single-crystal measurements are shown in Figures 4.5.2 and 4.5.3. The investigation was made to determine if evidence existed for "glassy" or amorphous behavior after irradiation. At cryogenic temperatures, the thermal properties of amorphous materials differ significantly from those observed in crystalline solids. The properties may be ascribed to localized excitations, each having a ground state and one excited state of energy, E , well-separated from other states of higher energy. This energy scheme for the localized excitations manifests itself in a contribution to the specific heat linear in the temperature, T , and a thermal conductivity proportional to T^2 . The temperature dependence and magnitude of the specific heat increases from the two irradiations were similar to those observed in crystalline SiO_2 after a similar low exposure to neutron irradiation. Analysis of the thermal conductivity results suggested also that localized excitations were not significant. The density of localized excitations in MgO was found to be a factor of about 300 smaller than the density produced in crystalline SiO_2 by the same fluence. This result suggested that many polymorphs

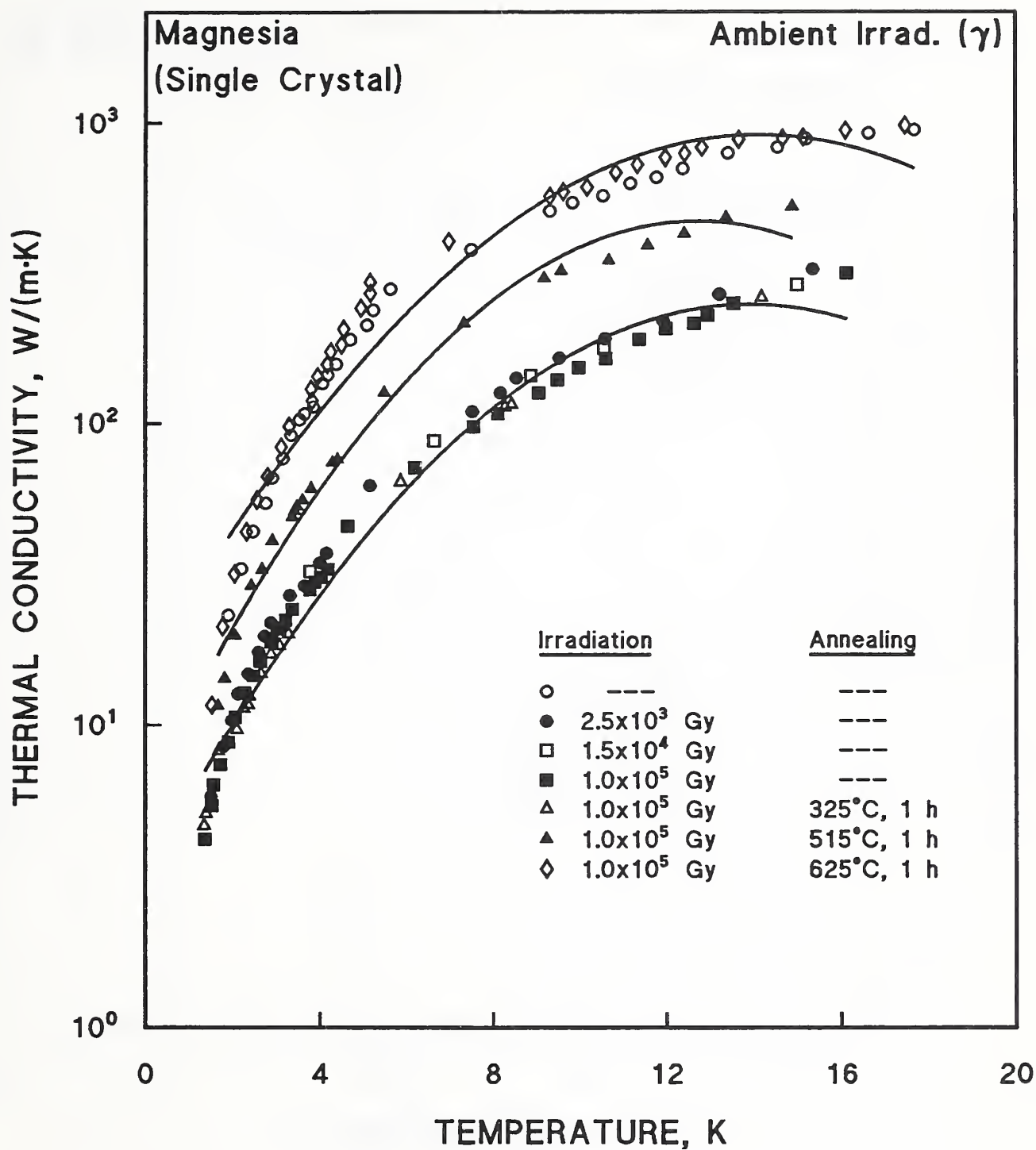


Figure 4.5.1. Thermal conductivity of single-crystal MgO after ambient γ irradiation. Data from Abramishvili et al. [1981].

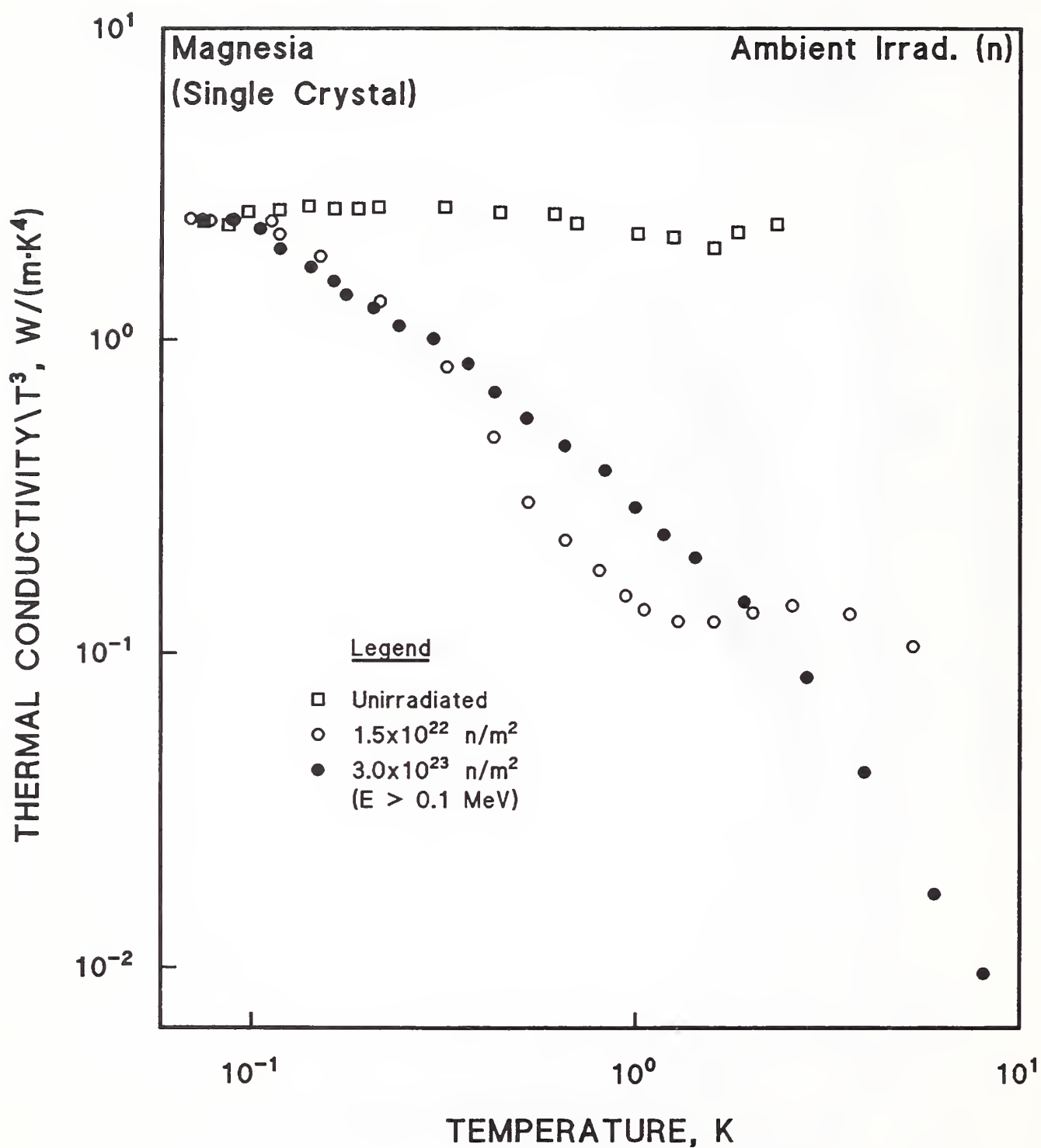


Figure 4.5.2. Thermal conductivity of single-crystal MgO after ambient neutron irradiation. Data from Gardner and Anderson [1981b].

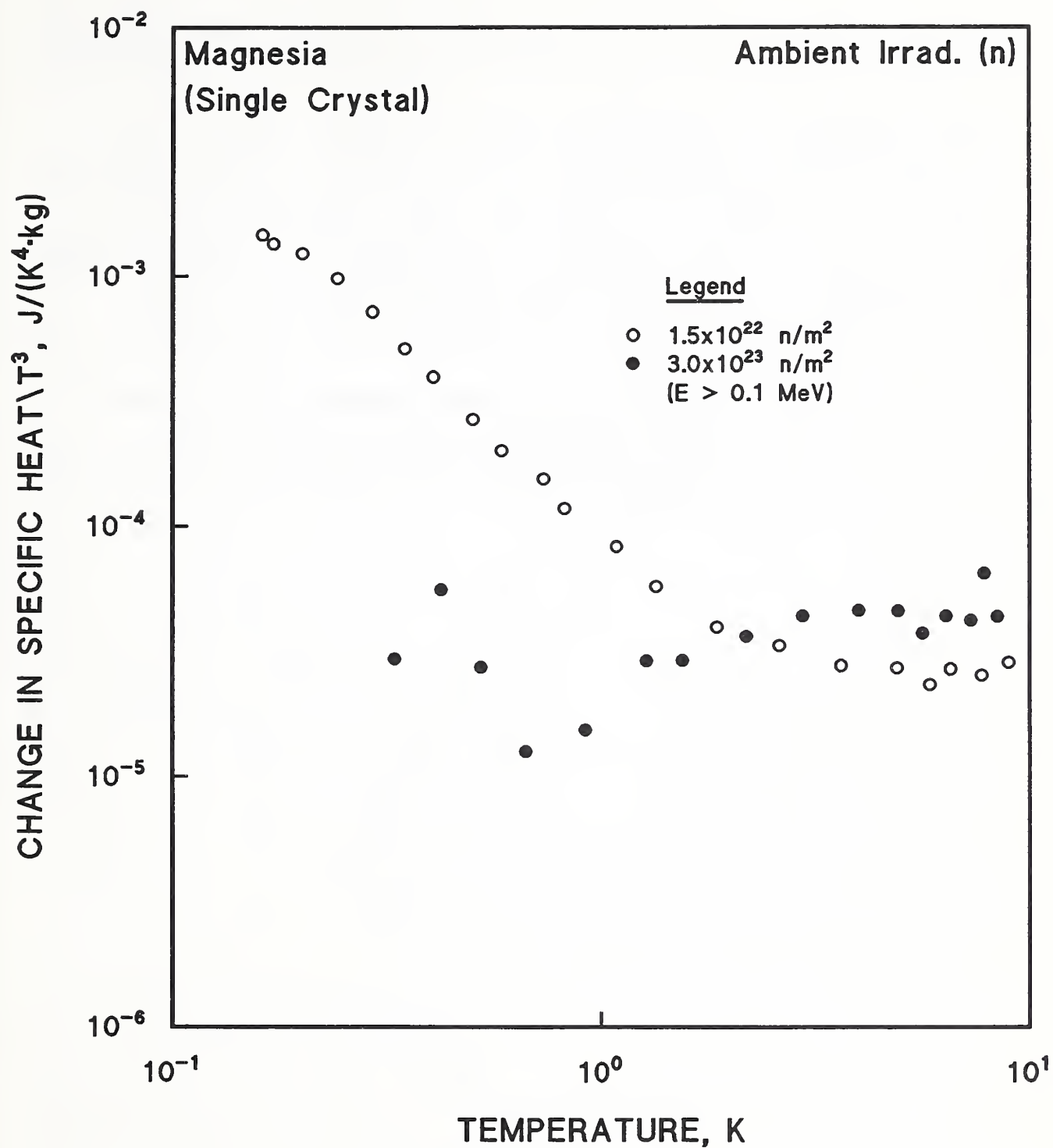


Figure 4.5.3. Change in specific heat of single-crystal MgO after ambient neutron irradiation. Data from Gardner and Anderson [1981b].

of SiO_2 are conducive to forming a glass and that since MgO occurs only in the cubic phase known as periclase, it would be less susceptible to amorphization.

Thermal conductivity of single-crystal MgO over a wider cryogenic range of 0.4 to 80 K was measured by Kupperman et al. [1973] after neutron irradiation below 323 K to fluences to $2 \times 10^{23}/\text{m}^2$ ($E > 1$ MeV). Features of the data, shown in Figure 4.5.4, were explained by a resonance model. Impurity effects were eliminated by further experiments in magnetic fields. At 4 K, the decrease in thermal conductivity was less than an order of magnitude.

Since all of these irradiations to test thermal properties were at ambient temperature, results are not representative of 4-K irradiation results, although they may correspond very approximately to results from fluences about a factor of 100 lower at 4 K.

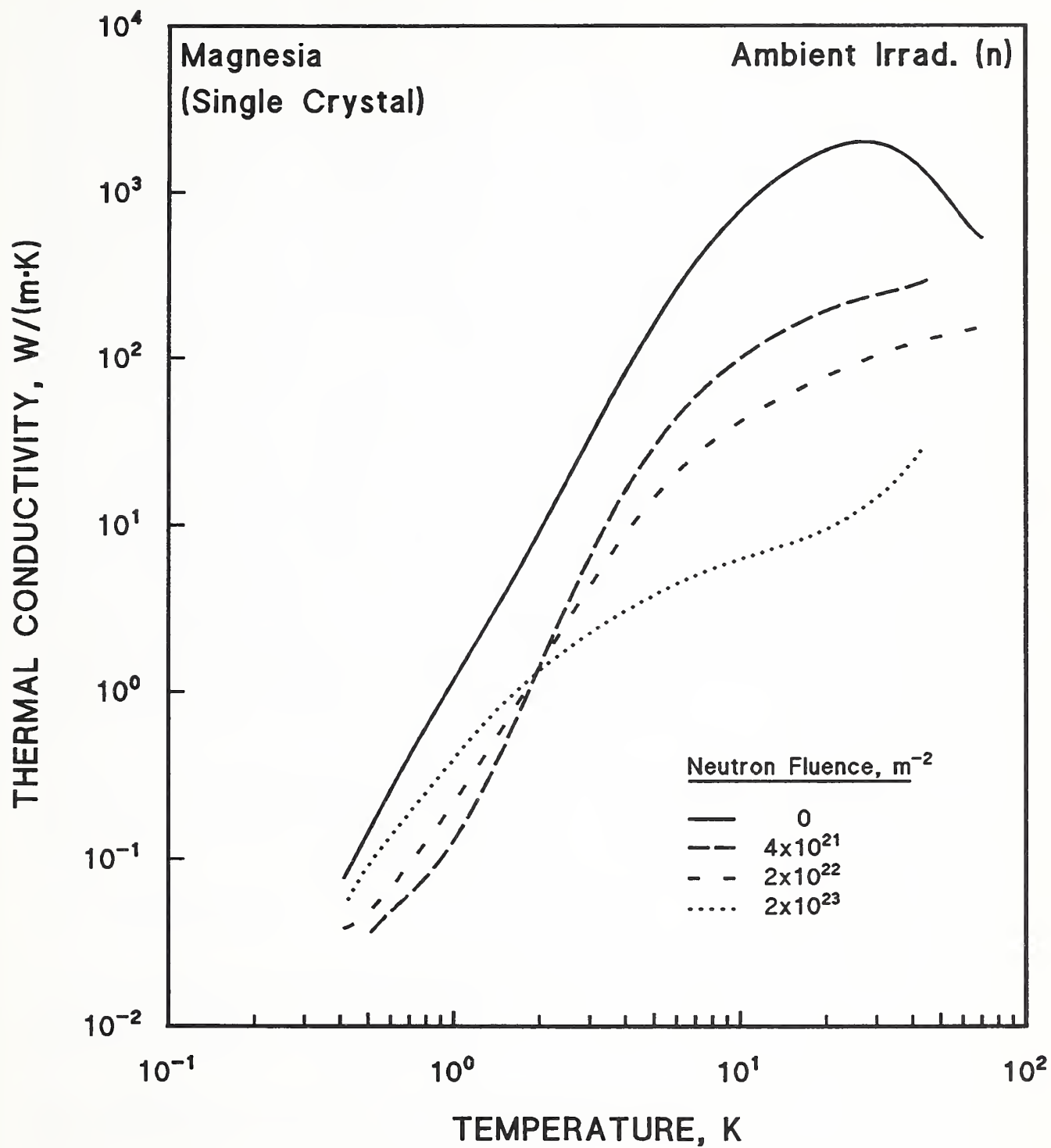


Figure 4.5.4. Thermal conductivity of single-crystal MgO after ambient neutron irradiation. Data from Kupperman et al. [1973].

5. LOW TEMPERATURE IRRADIATION OF PORCELAIN

Porcelain is a heterogeneous dielectric that consists of both a glassy matrix and crystals. The classic composition is 50% clay, 25% quartz, and 25% feldspar. Clay consists primarily of hydrated silicates of Al such as kaolinite, $\text{Al}_2\text{O}_3 \cdot 2\text{SiO}_2 \cdot 2\text{H}_2\text{O}$. Feldspar consists of silicates of Al with K, Na, Ca, and, sometimes, Ba. The composition of an electrical porcelain has been given, in mass percent, as 37% ball clay, 16% kaolin, 28% feldspar, and 19% flint (SiO_2) [Clark and Logsdon, 1974]. In addition to supplying the plasticity necessary for forming operations, clays react with the liquid fluxing material to form mullite ($3\text{Al}_2\text{O}_3 \cdot 2\text{SiO}_2$) crystals, which act as reinforcing strengtheners when present in the glassy matrix in acicular form. Potash feldspar is an effective liquid former for mullite needle growth. Alumina-containing compounds must be added to attain the composition necessary for mullite formation. Commercial electrical porcelains contain a high degree of closed porosity, 5 to 10% [Schroeder and Guertin, 1978]. Classical porcelain contains quartz to control thermal expansion and shrinkage, but often cracking occurs as the result of quartz phase transformation. Thus, quartz-containing porcelains are generally weaker than alumina-containing porcelains.

Owing to its heterogeneous structure, its variability in composition, and the presence of silicate bonds, which are not radiation resistant, porcelain does not appear to be a promising material for the ITER TF magnets.

5.1. DEFECT DENSITY

No measurements of the defect density for porcelain were obtained in the literature search.

5.2. CHANGE IN VOLUME

The dimensional stability of a porcelain was surveyed in an ORNL investigation of the radiation resistance of ceramics [Sisman et al., 1957]. Exposures at $<100^\circ\text{C}$ were made to intermediate-energy ($E > 100$ eV) fluences of $6 \times 10^{23}/\text{m}^2$ and $4 \times 10^{24}/\text{m}^2$ in the ORNL MTR reactor. As Table 5.2.1 indicates, the porcelain tested had a high degree of relative dimensional stability in this

Table 5.2.1. Effect of Radiation upon Thermal Conductivity and Density of Insulators.
Data from Sisman et al. [1957].

MATERIAL	INITIAL VALUE		EXPOSURE C, 10 ²³ neutrons/m ²	AFTER EXPOSURE C		EXPOSURE D, 10 ²³ neutrons/m ²	AFTER EXPOSURE D	
	THERMAL CONDUCTIVITY, * W/(m·K)	DENSITY, † g/cm ³		THERMAL CONDUCTIVITY, * W/(m·K)	DENSITY, † g/cm ³		THERMAL CONDUCTIVITY, * W/(m·K)	DENSITY, † g/cm ³
Sapphire	25 ± 8	3.983 ± 0.001	6	12 ± 2.5	3.969 ± 0.001	60	84 ± 1.2	3.944 ± 0.001
Al ₂ O ₃ , sintered	17 ± 4	3.559 ± 0.001	3	10 ± 1.7	3.553 ± 0.002	40	3.6 ± 0.2	3.80 ± 0.04
BeO	25 ± 8	2.84 ± 0.03	7	17 ± 4	2.85 ± 0.02			
Spinel	10 ± 2	3.60 ± 0.01	7	5.4 ± 0.4	3.60 ± 0.01	40	5.4 ± 0.4	3.60 ± 0.01
Forsterite 243	10 ± 2	3.056 ± 0.004	7	3.1 ± 0.4	3.03 ± 0.01		5.4 ± 0.4	3.60 ± 0.01
Zircon 475	5.0 ± 0.4	3.73 ± 0.01	5	0.96 ± 0.4	3.48 ± 0.01	30		3.39 ± 0.01
Steatite	3.2 ± 0.2	2.796 ± 0.005	7	1.2 ± 0.04	2.760 ± 0.005			
Cordierite 202	3.0 ± 0.2		5	0.8 ± 0.08		30	0.8 ± 0.08	
TiO ₂ 192	7.0 ± 0.8	4.01 ± 0.01	6	4.6 ± 0.4	3.99 ± 0.01	30	2.7 ± 0.2	3.98 ± 0.01
Porcelain 576	11 ± 2	3.41 ± 0.01	6	5.0 ± 0.4	3.40 ± 0.01	40	3.6 ± 0.2	3.39 ± 0.01
Mica	0.71 ± 0.04	2.845 ± 0.001	4	0.8 ± 0.08	2.738 ± 0.002	20	1.2 ± 0.12	2.444 ± 0.002
Plate glass	1.0 ± 0.04	2.509 ± 0.001	3		2.530 ± 0.001	60		2.515 ± 0.001
Silica glass	1.5 ± 0.04	2.204 ± 0.001	7		2.255 ± 0.001	40		2.23 ± 0.01
Quartz, Brazilian		2.65 ± 0.01	5		2.27 ± 0.01	40		2.24 ± 0.01

* at 30°C; † at 25°C.

fluence range, which is probably approximately equivalent to the expected 4-K ITER fluence of $10^{22}/\text{m}^2$, except for the unknown proportion of higher energy neutrons. The increase in volume of porcelain was $0.6 \pm 0.3\%$ at the highest fluence, as opposed to -1.2% for vitreous SiO_2 , 1% for single-crystal Al_2O_3 , and 0 (within 0.3% accuracy) for MgAl_2O_4 . In contrast, at half this fluence, mica expanded by 14% . The density changes were measured by alternately weighing specimens in air and in kerosene. An earlier, X-ray survey of ceramics found no observable change in the lattice parameters or diffraction pattern of a porcelain at a fluence of $2 \times 10^{24}/\text{m}^2$ ($E > 100$ eV) [Klein, 1955].

5.3. AMORPHIZATION

In contrast to this report by Klein of a crystalline X-ray diffraction pattern for porcelain after an intermediate neutron fluence of $2 \times 10^{24}/\text{m}^2$ ($E > 100$ eV), Abdel-Fattah et al. [1981] reported a significant amount of amorphous material in both quartz (67%) and alumina (53%) porcelains irradiated to 14-MeV fluences above $8.4 \times 10^{14}/\text{m}^2$. Evidence from both X-ray and electron diffraction showed that destruction of crystallinity was fairly complete by a fluence of $2.1 \times 10^{15}/\text{m}^2$. Destruction of the crystallinity of quartz usually requires a fluence of about $10^{23}/\text{m}^2$, although the neutrons have a fission spectrum [citations in Abdel-Fattah et al., 1981]. Abdel-Fattah et al. ascribed the disparity in their results with those of earlier investigations to the higher energy of their neutron fluence, yet earlier investigators reported only a factor of 2 or 4 in the difference in the effectiveness of 14-MeV and fission neutrons in Al_2O_3 and MgO (§§1.4, 2.1, 4.1), and theoretical calculations quoted in Fowler et al. [1981] gave a factor of 14 for the difference in Al_2O_3 of ionization dose per neutron. Sawan [1993] quotes a factor of 5.74 for the damage effectiveness of fission neutrons ($E > 0.1$ MeV) compared to 14-MeV neutrons. However, most of the experimental measurements were made on Frenkel defects and volume changes, at fluences below those necessary for amorphization at ambient temperature; thus, long recovery periods may have permitted the density of retained defects to approach similar values, despite the difference in neutron energy. Fowler et al. did observe some damage (not quantified) in the mica phase of a glass-mica composite (§10.1) after a much higher RTNS 14-MeV fluence of $10^{22}/\text{m}^2$. However, since the 14-MeV fluence necessary for amorphization of quartz or mullite was not found in the present literature search, the report of Abdel-Fattah et al. suggests that

porcelain should not be employed in the ITER TF magnet unless 4-K, in situ testing with 14 MeV neutrons validates adequate property values, or unless ambient temperature studies of porcelains with a 14-MeV source disprove the results of Abdel-Fattah et al. Of course, the apparent discrepancy between the results of Klein and those of Abdel-Fattah et al. could be due to differences in material composition and preparation, as well as to the large difference in neutron energy. Also, Abdel-Fattah et al. did not report the temperature of their irradiations. However, the 14-MeV fluence at the ITER magnets is estimated as about $3.1 \times 10^{20}/\text{m}^2$, from the calculations of Sawan [1993], allowing for a reduction of a factor of 3.6 in the total fast neutron fluence after the calculations were performed (Table 1.1.1). This 14-MeV fluence is far above that reported by Abdel-Fattah et al. as necessary for amorphization of the crystalline, strengthening phases in porcelain.

Caution in using porcelains is also suggested because there is very little information in the literature on irradiation damage. Porcelain is generally considered to be a lower-grade ceramic. It is severely degraded by electrolysis at relatively low electrical fields and temperatures, for example, by 100 V/mm at 150°C for 600 h, whereas single-crystal Al_2O_3 survives exposure to 1 kV/mm for 100 h at 1000°C [Weeks et al., 1978]. Since the high-temperature electrical breakdown properties of ceramics appear to correlate with their behavior under both an electric field and neutron irradiation (see §11), it appears from the available information that porcelain is not a conservative choice for the TF magnets, where fields of ~1 kV/mm are expected (Table 1.1.1).

5.4. MECHANICAL PROPERTIES

Some properties of an "ultra-porcelain" that contained ~70% Al_2O_3 were compared with those of Al_2O_3 and steatite (a form of talc) by Kostyukov et al. [1981]. Figure 5.5.1 shows the flexural strength at ambient temperature of these three insulators, after neutron irradiation at temperatures ranging up to 660°C for the highest fluence of $4.2 \times 10^{25}/\text{m}^2$. The authors also reported that the dielectric loss tangent of the "ultra-porcelain" showed the least change (in comparison to Al_2O_3 and steatite) after irradiation to $1.5 \times 10^{24}/\text{m}^2$ at an irradiation temperature below 200°C. The "ultra-porcelain" is a mullite-corundum material. The good properties were ascribed to an opposite

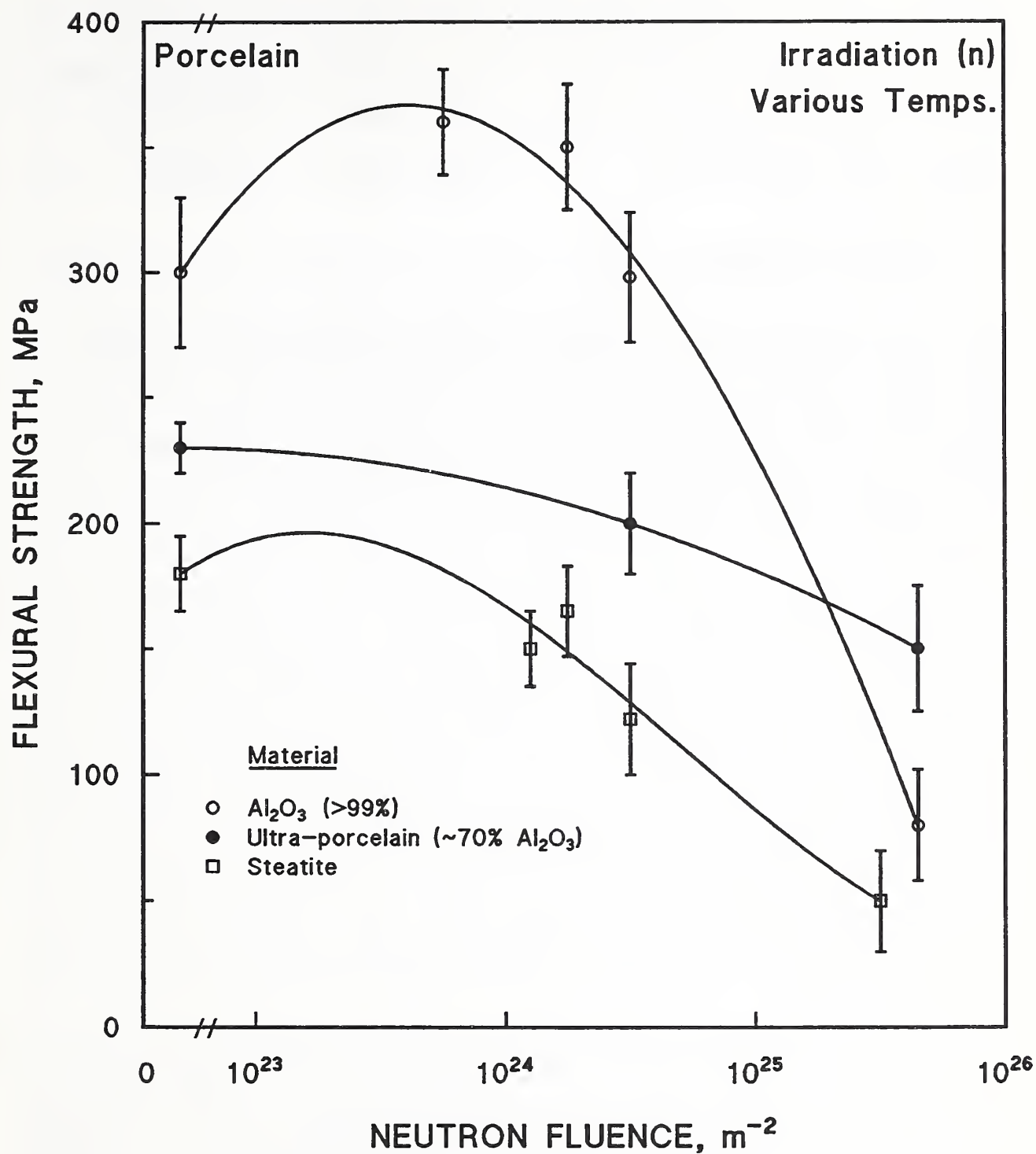


Figure 5.5.1. Flexural strength vs. fast neutron fluence for Al_2O_3 , ultra-porcelain, and steatite. Data from Kostyukov et al. [1981].

change in direction of the volume change under irradiation of the crystalline phases, e.g., mullite, and the glassy phase. The crystalline phase expands, and the glassy phase contracts. However, a borosilicate glass-mica ceramic was also found to have these opposing expansion properties, but the consequences for the strength were considered to be unfavorable [Coghlan and Clinard, 1991] (see §10.1.2).

5.5. THERMAL PROPERTIES

The thermal conductivity of a porcelain at ambient temperature was also measured by Sisman et al. [1957], as shown in Table 5.2.1, above. In contrast to the dimensional stability, the thermal conductivity exhibited a large decrease: to 44% of the initial value after an intermediate-energy neutron fluence of $6 \times 10^{23}/\text{m}^2$ and then, to 31% of the initial value after $4 \times 10^{24}/\text{m}^2$ ($E > 100$ eV).

6. LOW TEMPERATURE IRRADIATION OF VITREOUS SILICA AND QUARTZ

6.1. DEFECT PRODUCTION AND DENSITY

6.1.1. Displacement Threshold Energy

In quartz, highly strained Si—O configurations are susceptible to rupture by trapping electrons or holes, so Baeta and Ashbee [1975] suggested that displacement mechanisms involving electron excitation or multiple ionizations are responsible for the observed displacement damage from predominantly ionizing irradiation sources. In vitreous SiO₂, densification processes can be used to increase the number of "strained" Si—O—Si bonds. Defect creation from ionizing γ irradiation is then very much enhanced, as Figure 6.1.1 from Devine [1990] indicates. Therefore, O vacancy creation evidently arises from strained bond cleavage, and ionizing irradiation actually does induce stable O atom displacements. This process in SiO₂ is sometimes called radiolysis [Howitt and Mitchell, 1981]. Earlier evidence for displacement from ionization is given in Figure 6.1.2 from Levy [1960], which shows that γ irradiation of vitreous SiO₂ gives an optical absorption band at 5.85 eV that is similar to the band produced by neutron irradiation. Similar data were obtained by Nelson [1957]. The 5.85-eV optical absorption band has been identified as an O vacancy site in both quartz and vitreous SiO₂. Figure 6.1.3 of Nelson indicates that the 5.85-eV (235-nm) optical absorption bands of vitreous SiO₂ and quartz become more similar as the neutron irradiation reaches a fast neutron fluence of $2.9 \times 10^{24}/\text{m}^2$. This and other point defect and radiation damage processes in quartz were reviewed in detail by Griscom [1979].

Usually E_d can be determined by irradiating a material with electrons of increasing energy, as described for Al₂O₃ (§2.1.1), MgO (§4.1.1), and MgAl₂O₄ (§7.1.1). However, this method is difficult to use for vitreous SiO₂, because compaction ($-\Delta V/V$) due to displacement damage results from ionization [Primak, 1972]. Owing to the difficulty in determining E_d with electron irradiation, Primak used data on the initial negative dilation of vitreous SiO₂ per incident bombarding ion to determine this quantity. Ion energies were 40 and 140 keV for H⁺, D⁺, He⁺, Ne⁺, and Ar⁺, and 80 keV for He⁺. The total negative dilation associated with these ions was plotted against the energy dissipated

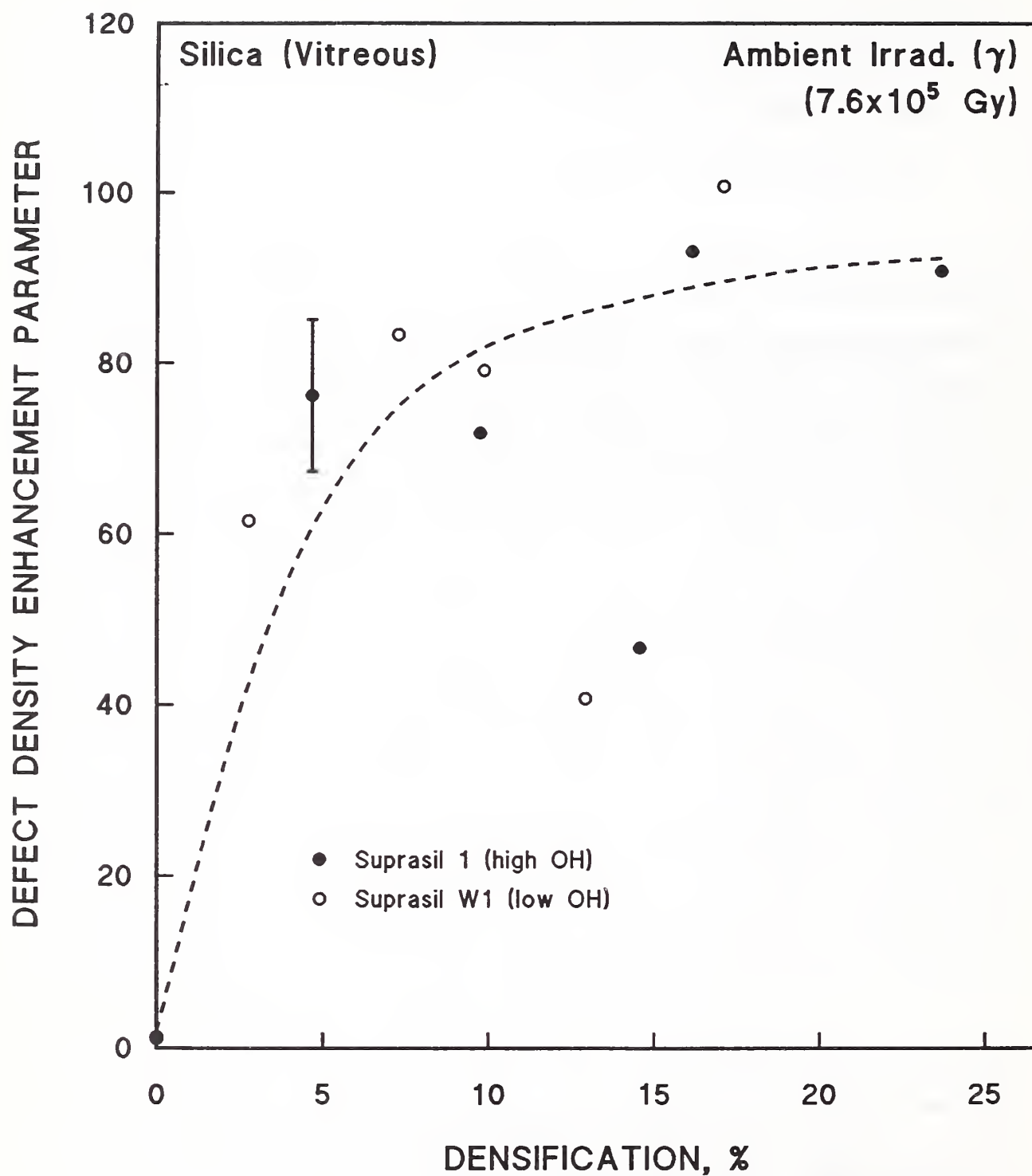


Figure 6.1.1. Enhancement of defect density of amorphous SiO_2 with compaction. Data from Devine [1990].

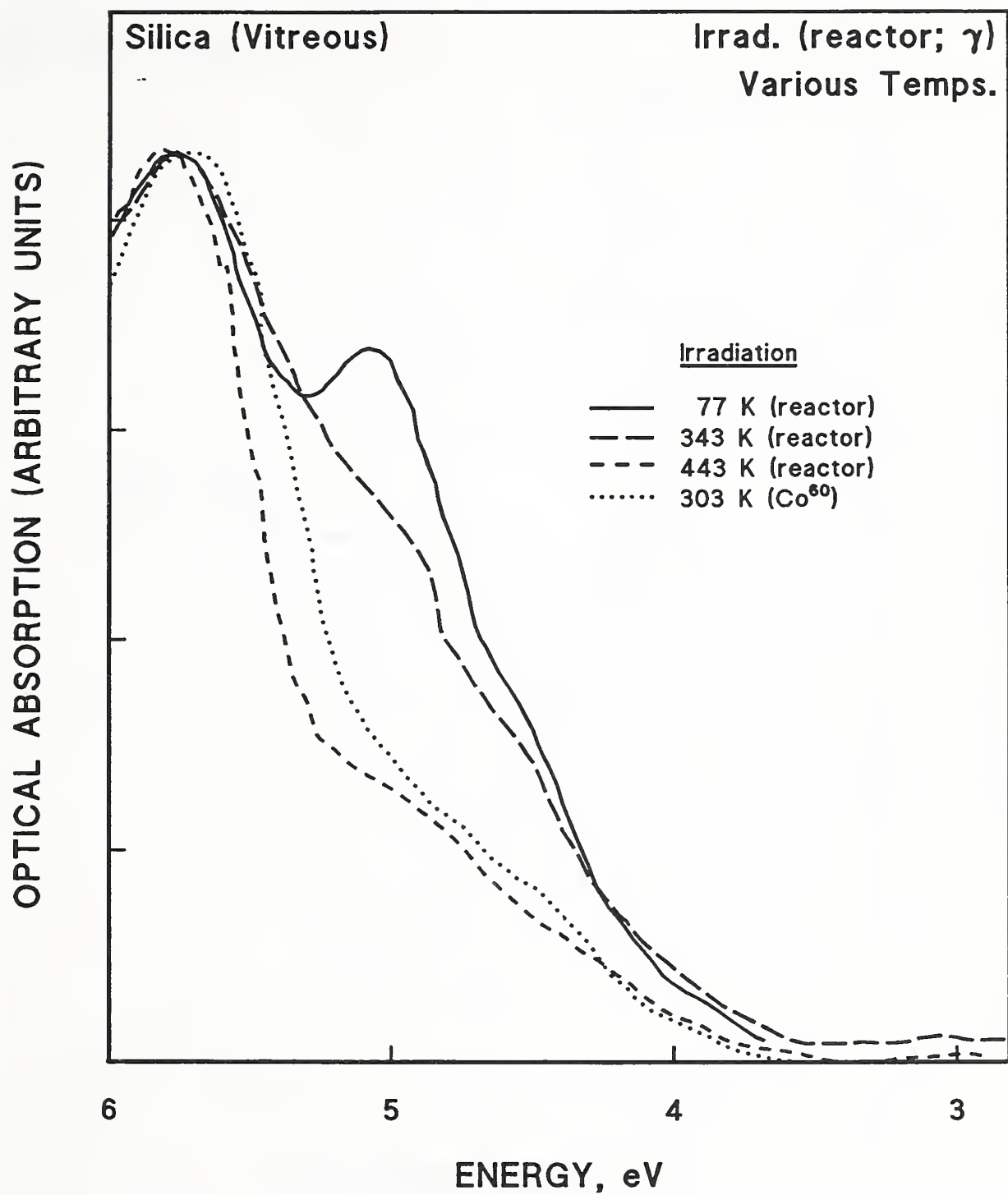


Figure 6.1.2. Optical absorption of vitreous SiO_2 from reactor and γ irradiation. Spectra were normalized to the same height at points of maximum absorbance. Data from Levy [1960].

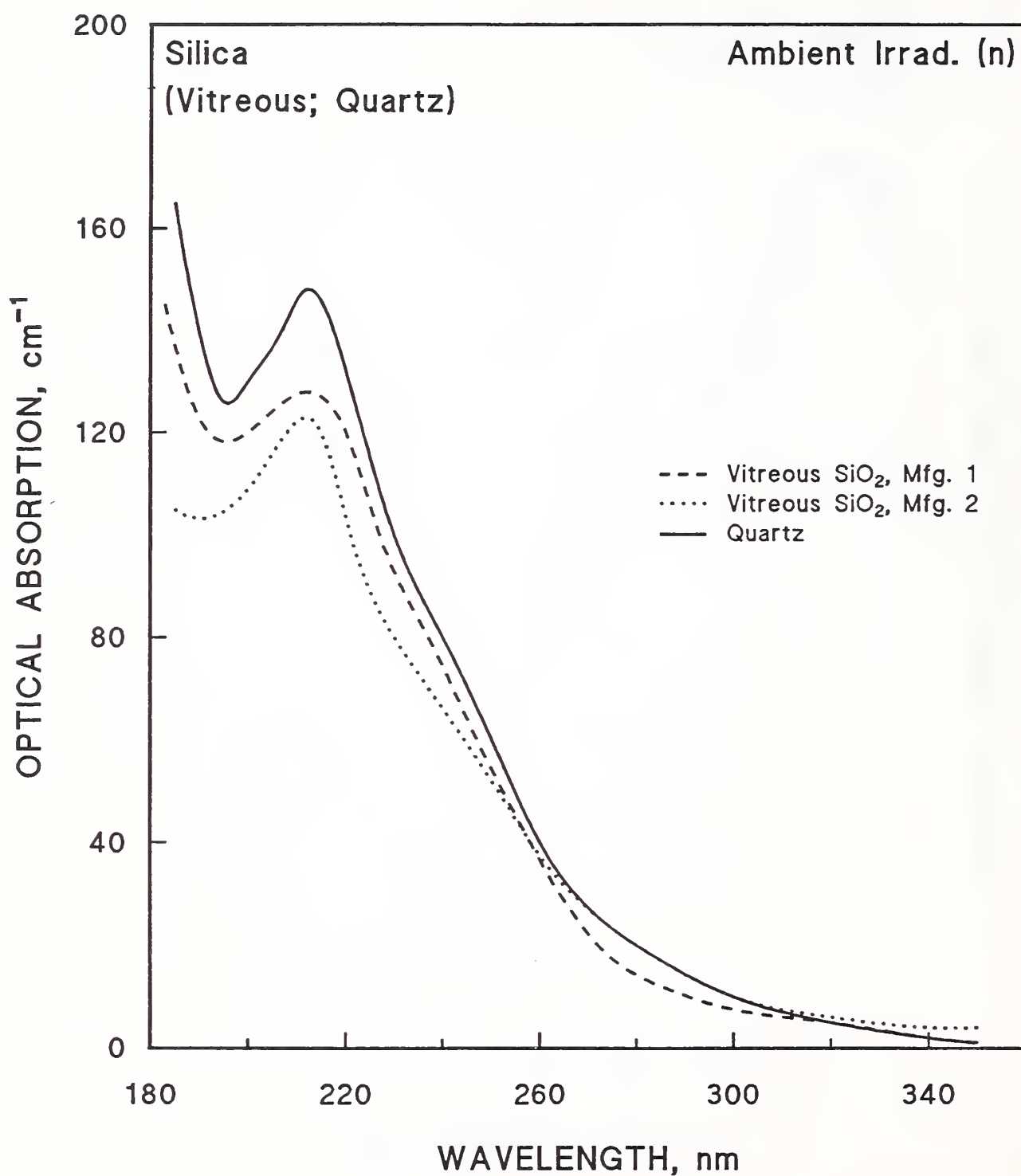


Figure 6.1.3. Optical absorption of vitreous SiO₂ and quartz after neutron irradiation to $2.9 \times 10^{24}/\text{m}^2$. Data from Nelson [1957].

by the ions in atomic collisions. The slope, in a log/log plot, indicates that the threshold energy for negative dilation, or compaction of vitreous SiO_2 , is very low compared to a typical E_d of at least 25 eV. Primak then treated data of Hines and Arndt [citation in Primak, 1972] on the disordering of quartz by ion irradiation in a similar fashion, and obtained a threshold energy of ~25 eV. Details of the analysis and experimental uncertainties are discussed in the paper by Primak. Although an E_d determined in this manner may not be strictly comparable to one determined by electron irradiation, a lower threshold energy would be expected from the covalent structure of SiO_2 , in comparison to the ionically bonded ceramics, such as Al_2O_3 , MgO , and MgAl_2O_4 . This bond structure criterion was discussed above in §1.6. (See Table 1.2.2 for E_d s of ceramic oxides and AlN .)

Bäeta and Ashbee [1973] noted that quartz specimens examined at 100 and 200 keV in TEM deteriorated rapidly, eventually becoming amorphous. Das and Mitchell [1974] used a HVEM to determine a threshold voltage for displacement damage in quartz. The displacement damage was identified with small black spots and loops that first appeared in the center of the electron beam where current density was greatest. The threshold voltage determined by these spots was less than 50 keV, far below the values of ~400 to 500 keV measured for ceramic oxides. From this threshold voltage, Das and Mitchell derived values of $E_d(\text{Si}) \approx 5.4$ eV and $E_d(\text{O}) \approx 9.5$ eV. Again, these values are considerably below those of other ceramic oxides. Das and Mitchell noted that while MgO and Al_2O_3 have higher binding energies than SiO_2 , their structures are also more closely packed. Displacement of ions in quartz should be much easier, owing to the open nature of the crystal structure.

In addition to their study of displacement damage, Das and Mitchell also found evidence to clarify the role of ionization damage in quartz. Figure 6.1.4 shows the electron fluence required to induce amorphization in quartz as a function of the electron energy. Because the required fluence is higher at higher electron energy, the rate at which the amorphous transition occurs is decreasing. However, the production of displacement damage, determined by the rate of formation of black spots, increases with electron energy. Therefore, two different damage processes are probably occurring. The behavior shown in

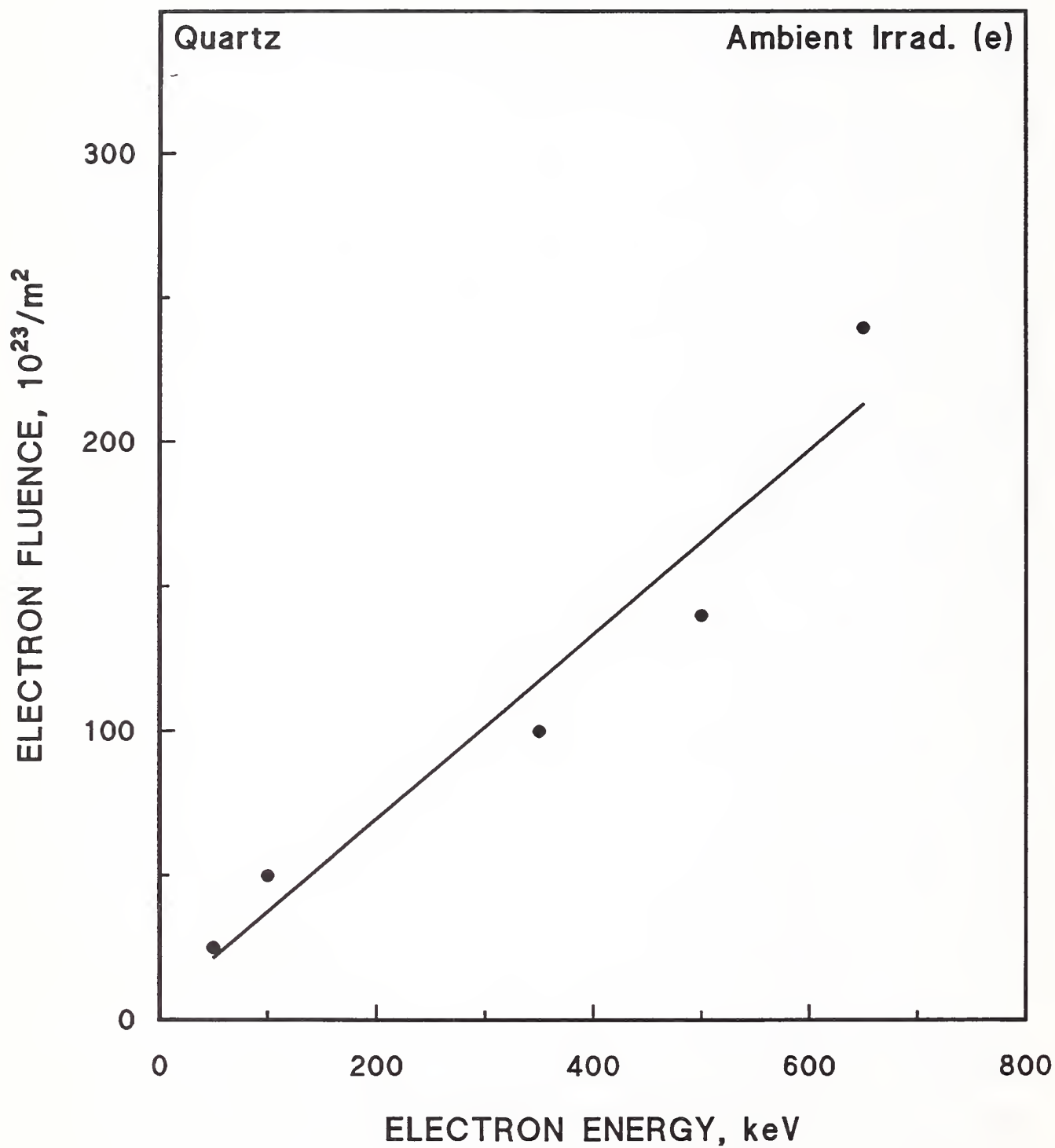


Figure 6.1.4. Electron fluence required to amorphize quartz as a function of increasing electron energy. Data from Das and Mitchell [1974].

Figure 6.1.4 is similar to that observed in polymers, where the crystalline-to-amorphous transition also occurred more slowly at higher electron energy [citations, Das and Mitchell, 1974]. In polymers, the destruction of crystallinity is thought to be due to ionization and subsequent crosslinking. The damage process in quartz may be similar: the SiO_4 tetrahedra become ionized by electrons so that small movements and rotations enable the tetrahedra to "crosslink" in a more random way to produce an amorphous structure. This amorphization process is facilitated by the open structure of quartz.

6.1.2. Defect Density

Weeks [1963] has measured the production of the $\sim 230\text{-nm}$ 0 vacancy in synthetic quartz crystals with ESR and found $\sim 5 \times 10^{16}/\text{cm}^3$ after a γ -irradiation dose of $\sim 2 \times 10^7$ Gy. The dpa calculated from $5 \times 10^{16}/\text{cm}^3$ is $\sim 6 \times 10^{-7}$. The γ dose of 2×10^7 Gy is comparable to that expected at ITER TF magnets (Table 1.1.1); however, these irradiation and optical measurements were made at ambient temperature, so the 4-K dpa could be larger, owing to fewer recombinations of defects at 4 K, or smaller, because of lowered mobility of the SiO_4 tetrahedra.

Shamfarov and Smirnova [1963] and Shamfarov [1967] have reported defect densities in quartz based on EPR (electron paramagnetic resonance) after ambient temperature neutron fluences of 3×10^{22} and $3 \times 10^{23}/\text{m}^2$ (E not specified). Their estimates (based on the EPR signal) showed that the spin concentrations associated with these defects were 10^{18} and $10^{19}/\text{cm}^3$, respectively, for the lower and higher fluence. This is equivalent to dpas (for the defect detected) of $\sim 1.2 \times 10^{-5}$ and $\sim 1.2 \times 10^{-4}$.

6.2. CHANGE IN VOLUME

Vitreous SiO_2 contracts under neutron irradiation and quartz expands. The relative sizes of these effects, at fluences to $2 \times 10^{22}/\text{m}^2$ ($E > 0.01$ MeV) are indicated in Figure 6.2.1 [Primak et al., 1955]. In vitreous SiO_2 , atoms may be displaced to the large holes in the structure, permitting the Si—O tetrahedra to relax into a more compact arrangement; quartz may expand because atoms are displaced to parts of the structure not large enough to accommodate them and because bonds are broken or strained. Although the contraction of

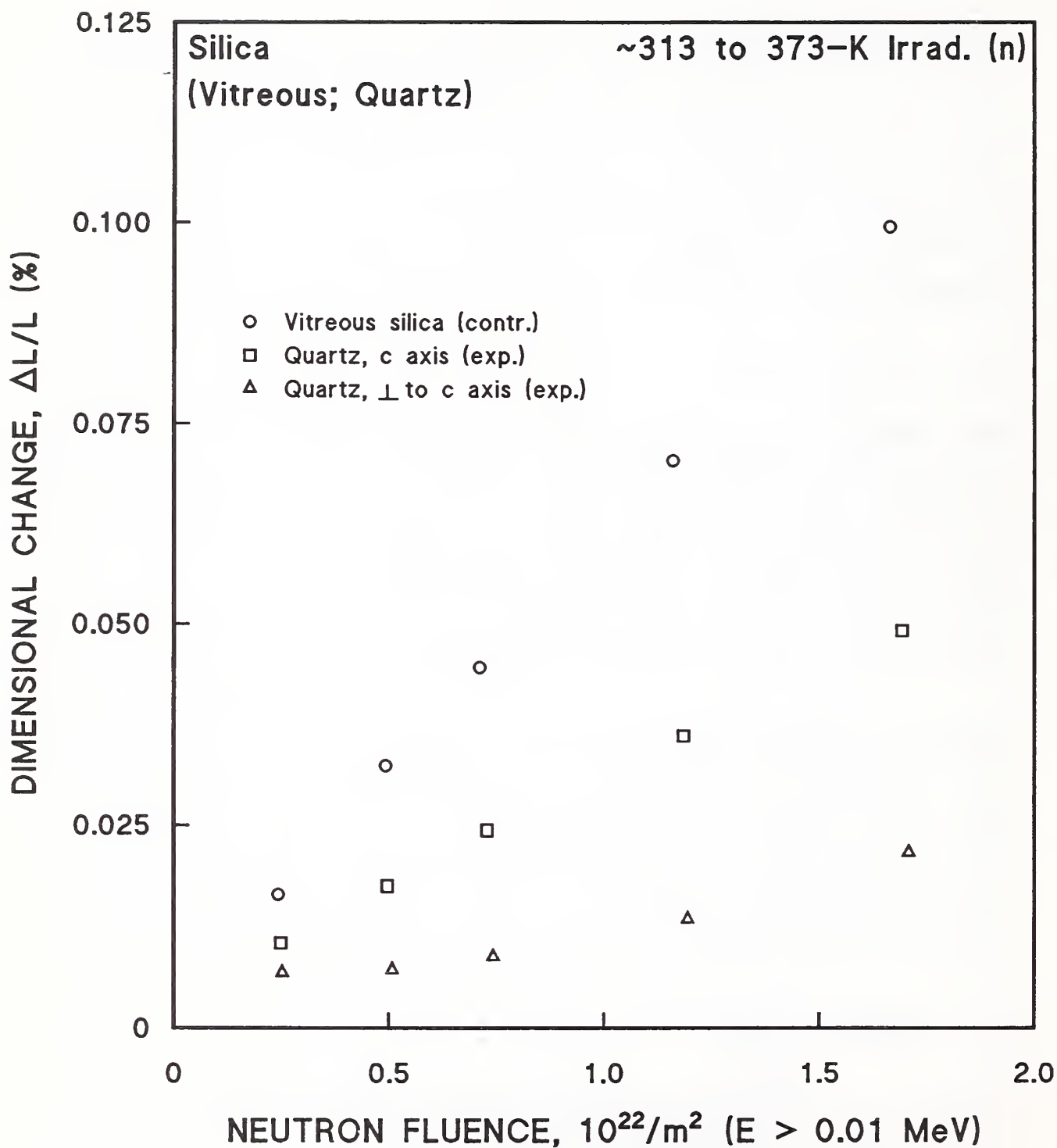


Figure 6.2.1. Dimensional change of vitreous SiO_2 and in quartz after neutron irradiation. The irradiation temperature for the highest fluence was estimated as $\sim 250\text{--}300^\circ\text{C}$. Data from Primak et al. [1955].

vitreous SiO_2 is initially more rapid than the expansion of quartz, the contraction soon saturates with increasing fluence, while the expansion of quartz proceeds until the density of the material is similar to that of vitreous SiO_2 . The change in density for both vitreous SiO_2 and quartz is shown in Figures 6.2.2 and 6.2.3 from Primak [1958]. These figures include some data at higher fluences that indicate a saturation at about $2 \times 10^{24}/\text{m}^2$. Data from Simon [1957] at a fluence of $1.4 \times 10^{24}/\text{m}^2$ are in agreement with those of Primak. Although Simon estimated that the dpa from his irradiation was only $\sim 1.4 \times 10^{-4}$, the density of quartz decreased by 16%. X-ray and infrared studies made by Simon showed that the structure of irradiated quartz was very similar to that of vitreous SiO_2 . Such a rearrangement should only have resulted if each displaced O atom had produced disordering in a region containing about 5300 surrounding Si atoms.

The trend lines for quartz and vitreous SiO_2 are combined in Figure 6.2.4, which shows that the two materials approach a similar density [Lell et al., 1966]. Lell et al. state that the difference between vitreous SiO_2 and heavily irradiated quartz is not in the Si—O bond length, which was said to be the same, but in a decreased Si—Si distance, indicating a smaller Si—O—Si bond angle, as found by Simon [1957]. Distances to nearest neighbors show a wider distribution in neutron-disordered quartz than in vitreous SiO_2 .

Weissman and Nakajima [1963] used X-rays and TEM to correlate the density changes in quartz with the growth in clusters of interstitial Si atoms. Figure 6.2.5 shows this correlation. These authors also found that the size and density of the clusters increased with increasing radiation dose. At a fast neutron fluence of about $8 \times 10^{23}/\text{m}^2$, the number of clusters was so high that mutual interaction occurred between the clusters. Increasing radiation fluences (~ 1 to $1.5 \times 10^{24}/\text{m}^2$) led to the formation of a hexagonal defect structure which was very stable and resistant to prolonged annealing at 500°C . However, even at $1.5 \times 10^{24}/\text{m}^2$, crystals still exhibited considerable long-range order and yielded single-crystal electron diffraction patterns. These irradiations were performed in the Oak Ridge reactor, but the temperature and spectrum of the irradiation were not reported. The aggregation of defects into clusters apparently occurred near ambient temperature. It is not known

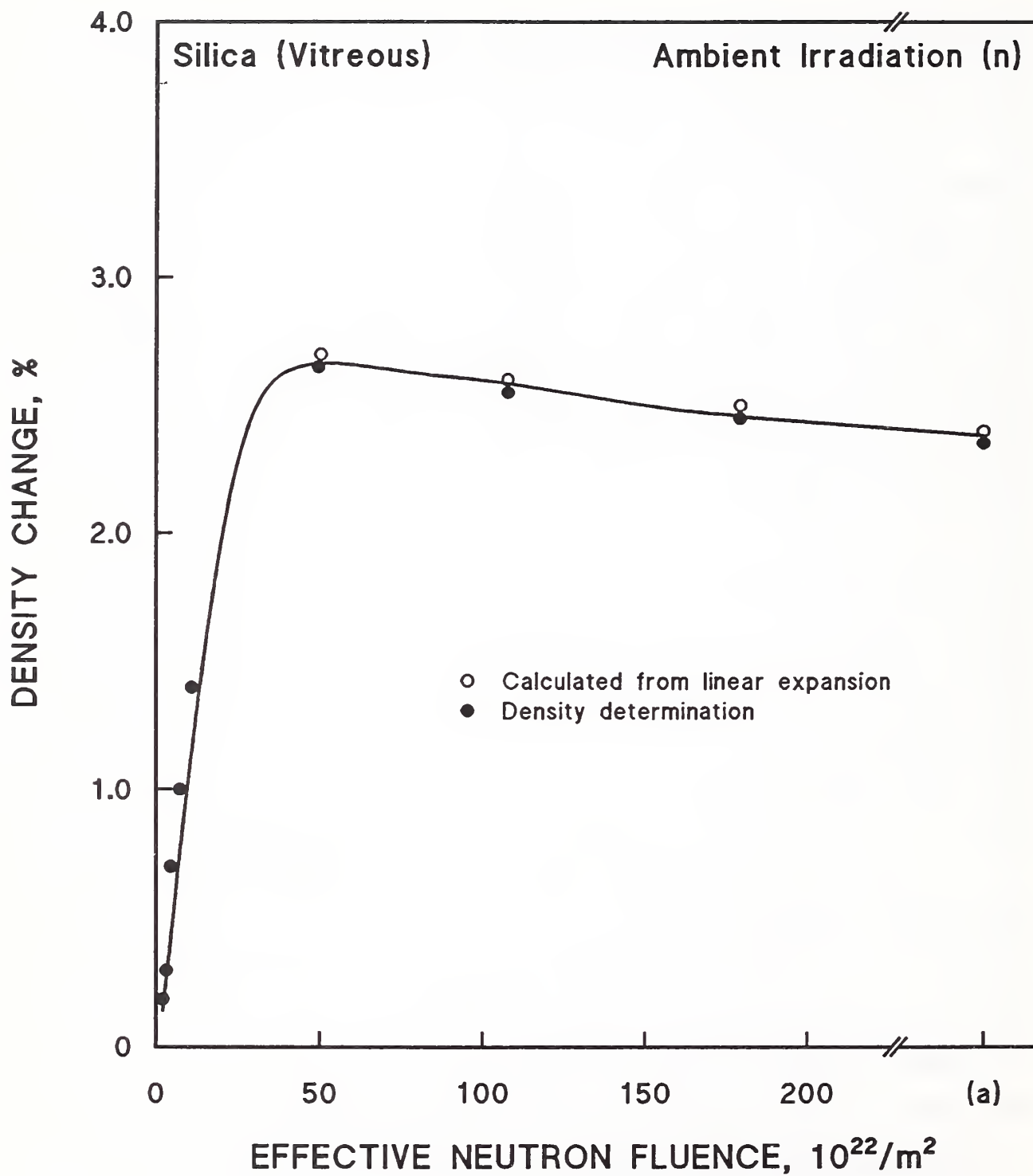


Figure 6.2.2. Density change of vitreous SiO_2 after neutron irradiation. The fluence at (a) is estimated at 2.5 to $4.0 \times 10^{24}/\text{m}^2$. Data from Primak [1958].

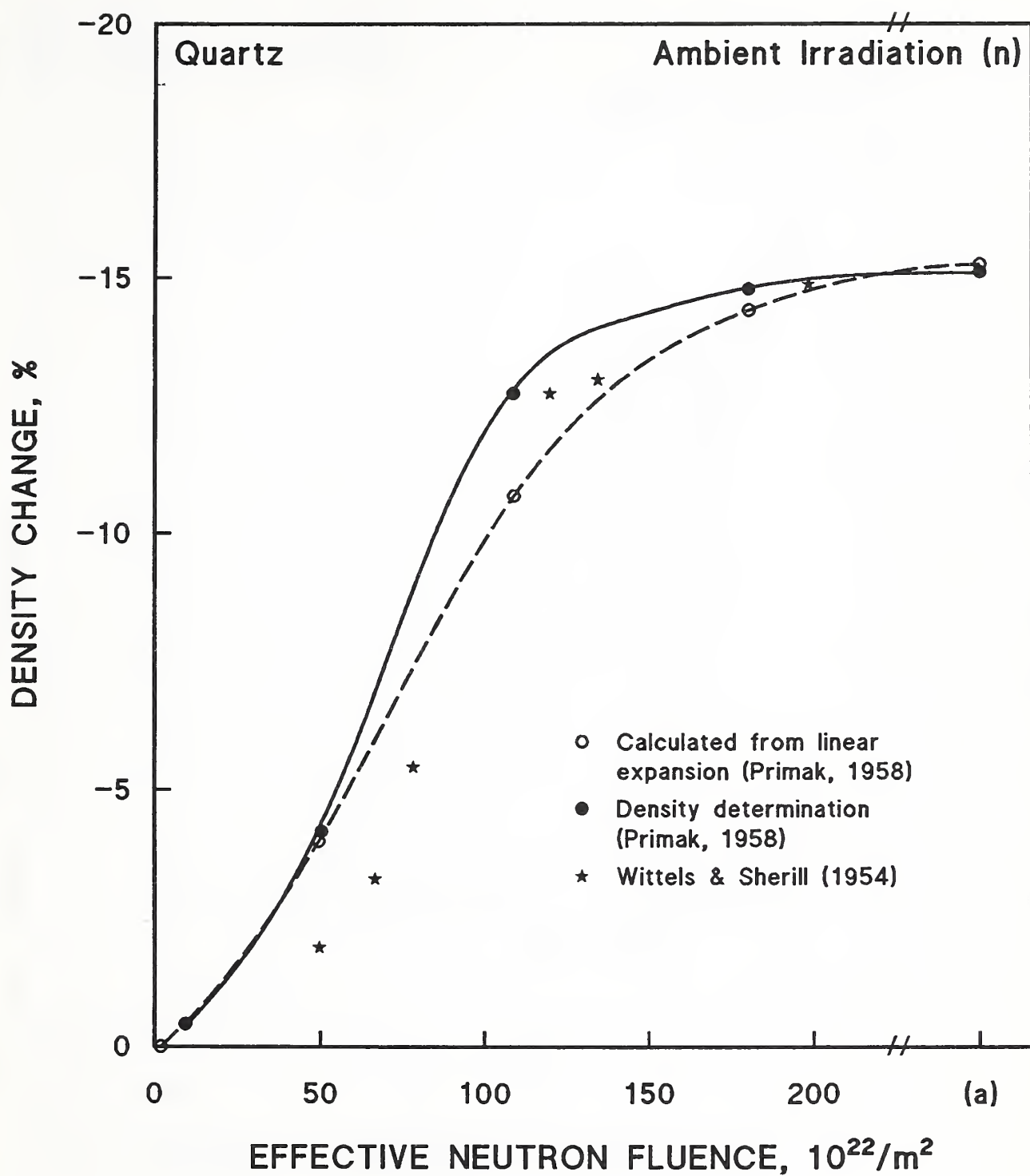


Figure 6.2.3. Density change of quartz after neutron irradiation. The fluence at (a) is estimated at 2.5 to $4.0 \times 10^{24}/\text{m}^2$. Data from Primak [1958].

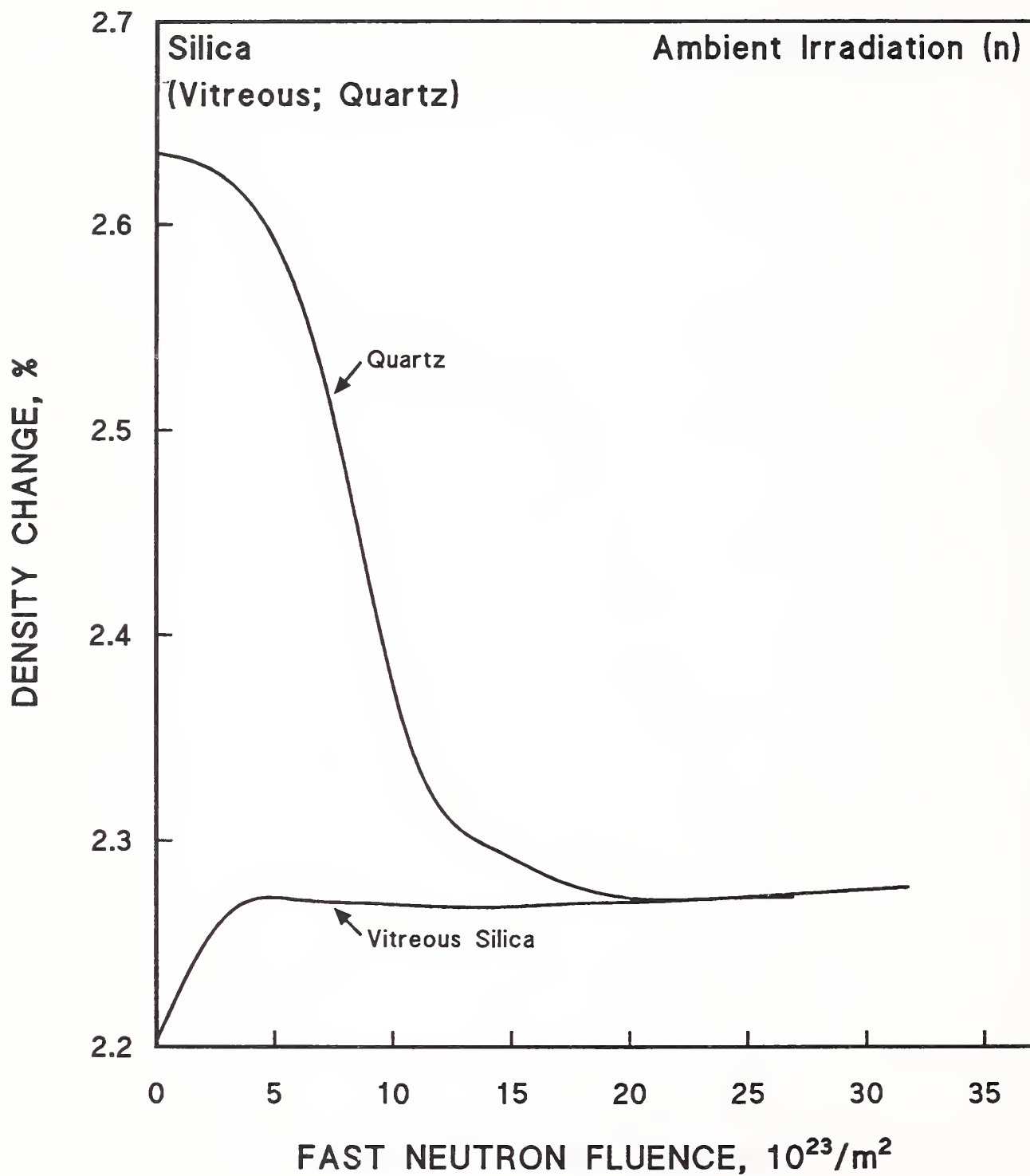


Figure 6.2.4. Comparison of density change of vitreous SiO_2 and quartz after neutron irradiation. Data from Lell et al. [1966].

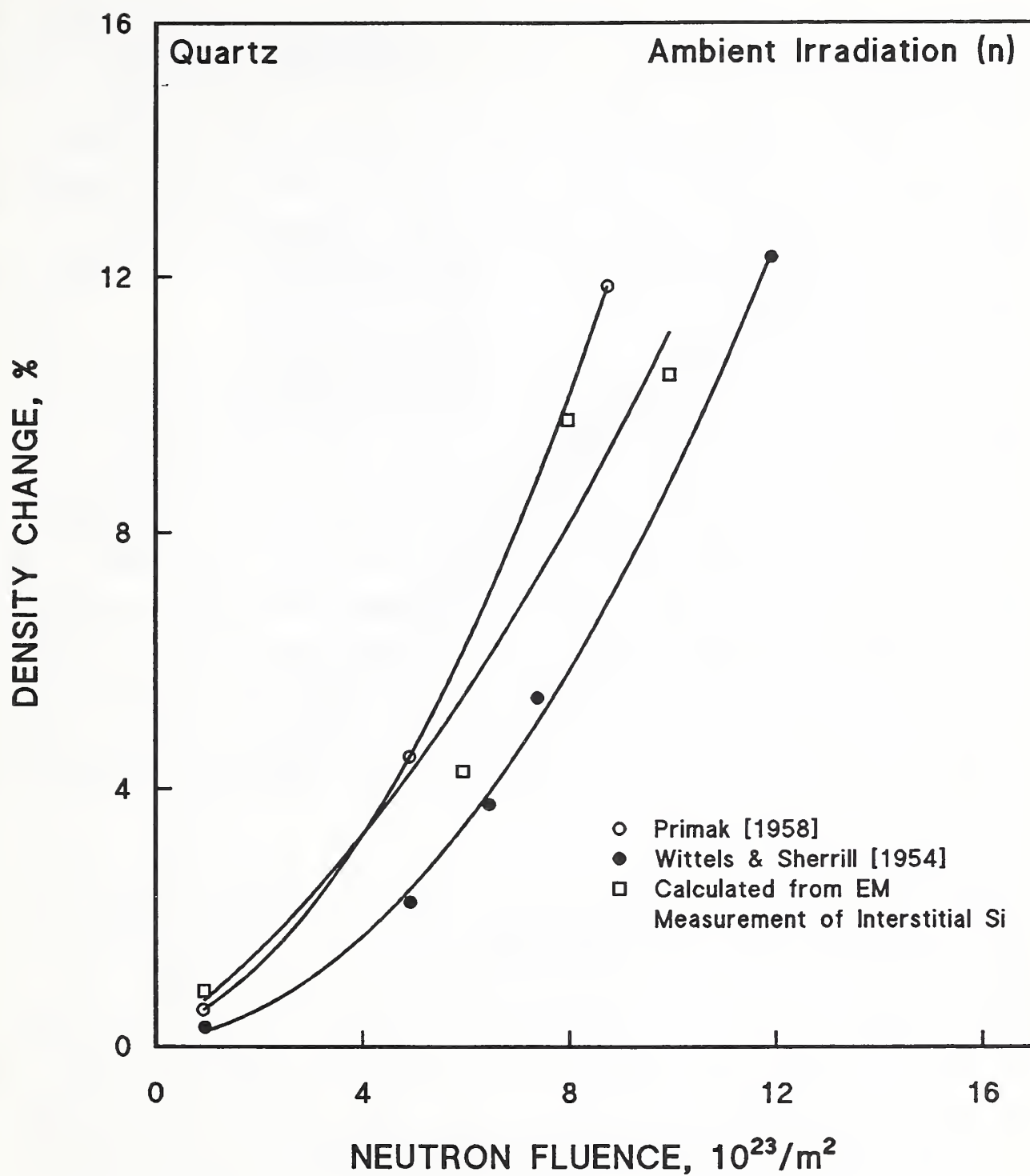


Figure 6.2.5. Correlation of density change of quartz after neutron irradiation with formation of clusters of interstitial Si atoms, detected by electron microscopy. Data from Weissman and Nakajima [1963].

whether the higher densities of retained defects expected in 4-K irradiation would lead to cluster formation at fluences below $8 \times 10^{23}/\text{m}^2$ or whether warming material to ambient temperature would anneal out defects or cause cluster formation. The studies of Weissman and Nakajima showed that defects in quartz might not anneal as readily upon warm-up as defects in ionic oxides, such as Al_2O_3 and MgAl_2O_4 , would be expected to do. Wittels and Sherrill [1954] believed that permanent damage in quartz was induced at an ambient-temperature fluence of $\sim 2 \times 10^{23}/\text{m}^2$.

The data discussed above concern volume changes arising primarily from displacements by neutron irradiation. Yet, in §6.1, the existence of volume changes from ionizing irradiation was emphasized. Data on the compaction of vitreous SiO_2 from ionization alone were produced by Norris and EerNisse [1974] using 18-keV electron irradiation. It is unlikely that a significant number of atomic displacements arises from 18-keV electrons. Furthermore, Norris and EerNisse found that there was no apparent threshold for the onset of the compaction mechanism between 2.2 and 18 keV. These results for 18-keV electrons, as well as those of Primak and Kampworth [citation, Norris and EerNisse, 1974] over a range of electron energies, are given in Figure 6.2.6. Further work with 18-keV electron irradiation showed significant changes in the index of refraction from this ionizing irradiation [Dellin et al., 1977].

Additional studies on the effect of ionizing radiation have been done. Some of this work is reviewed by Primak [1975]. Figure 6.2.7 shows the effect of the γ irradiation dose on the volume decrease of various commercial borosilicate glasses, to illustrate the effect of composition [Shelby, 1980]. All show a higher response to γ radiation than does pure SiO_2 . Figure 6.2.8, also from Shelby, indicates the effect of volume compaction on refractive index, and Figure 6.2.9 shows the large effect of the volume compaction on the relative coefficient of thermal expansion for these glasses between 173 and 273 K. The $^{10}\text{B}(n,\alpha)^7\text{Li}$ reaction does not affect these results, since only ^{60}Co γ radiation was used. In pure SiO_2 , Iida et al. [1991] reported that 14-MeV neutron fluences of 1 to $3 \times 10^{19}/\text{m}^2$ significantly decreased the light transmission efficiency.

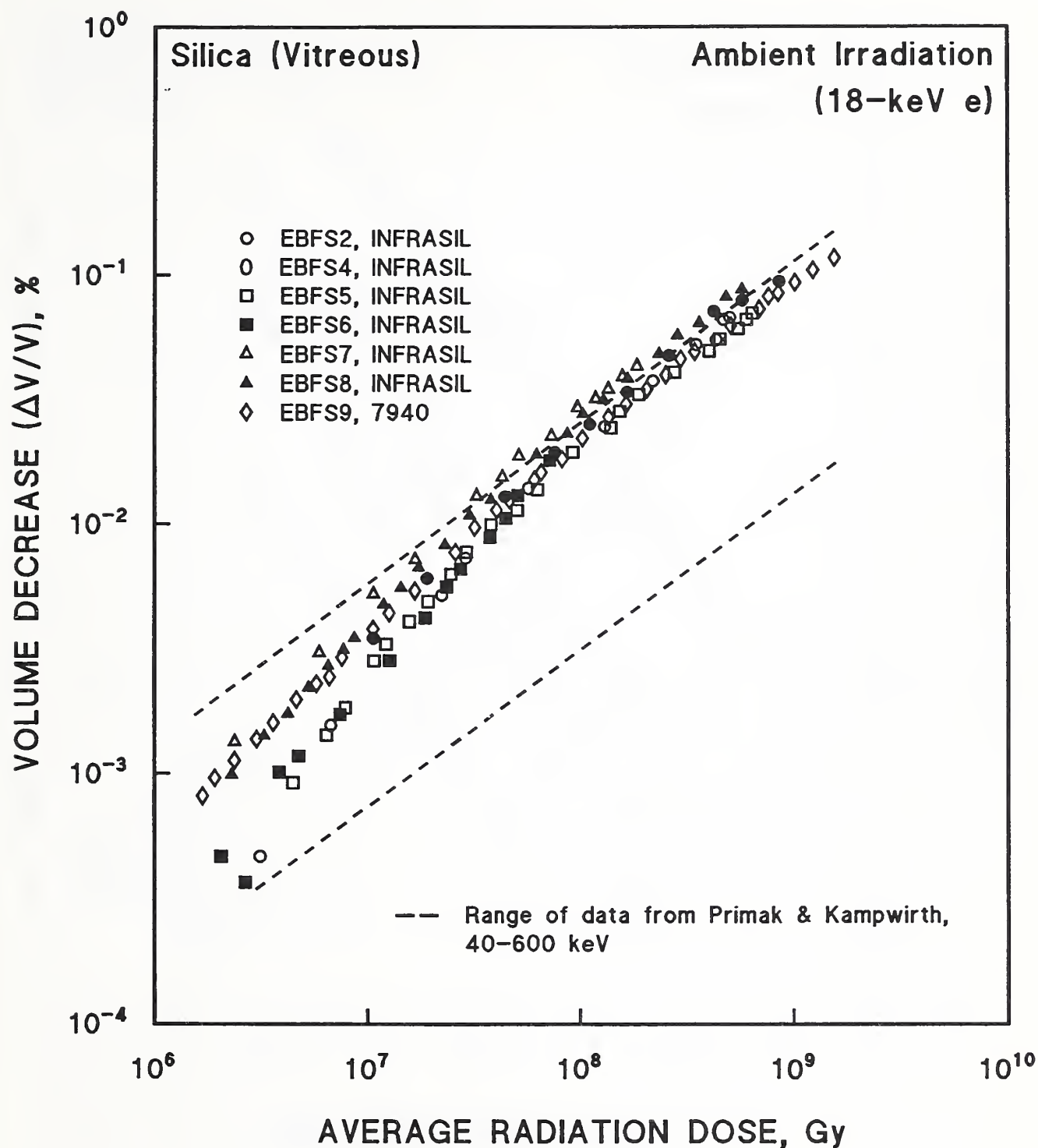


Figure 6.2.6. Volume compaction of vitreous SiO_2 after 18-keV electron irradiation. Data from Norris and EerNisse [1974].

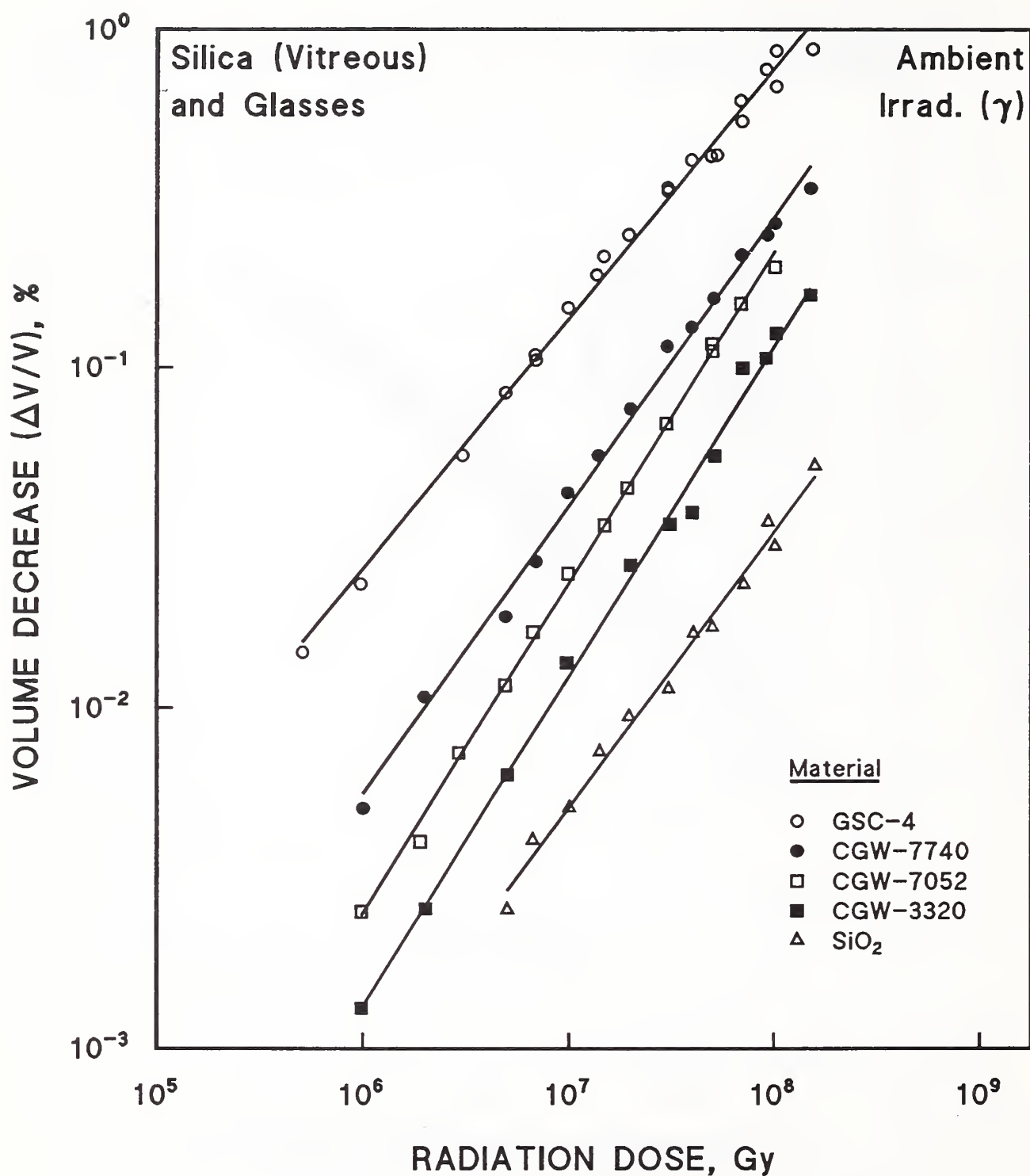


Figure 6.2.7. Volume compaction after γ irradiation of SiO₂ and various commercial borosilicate glasses. Data from Shelby [1980].

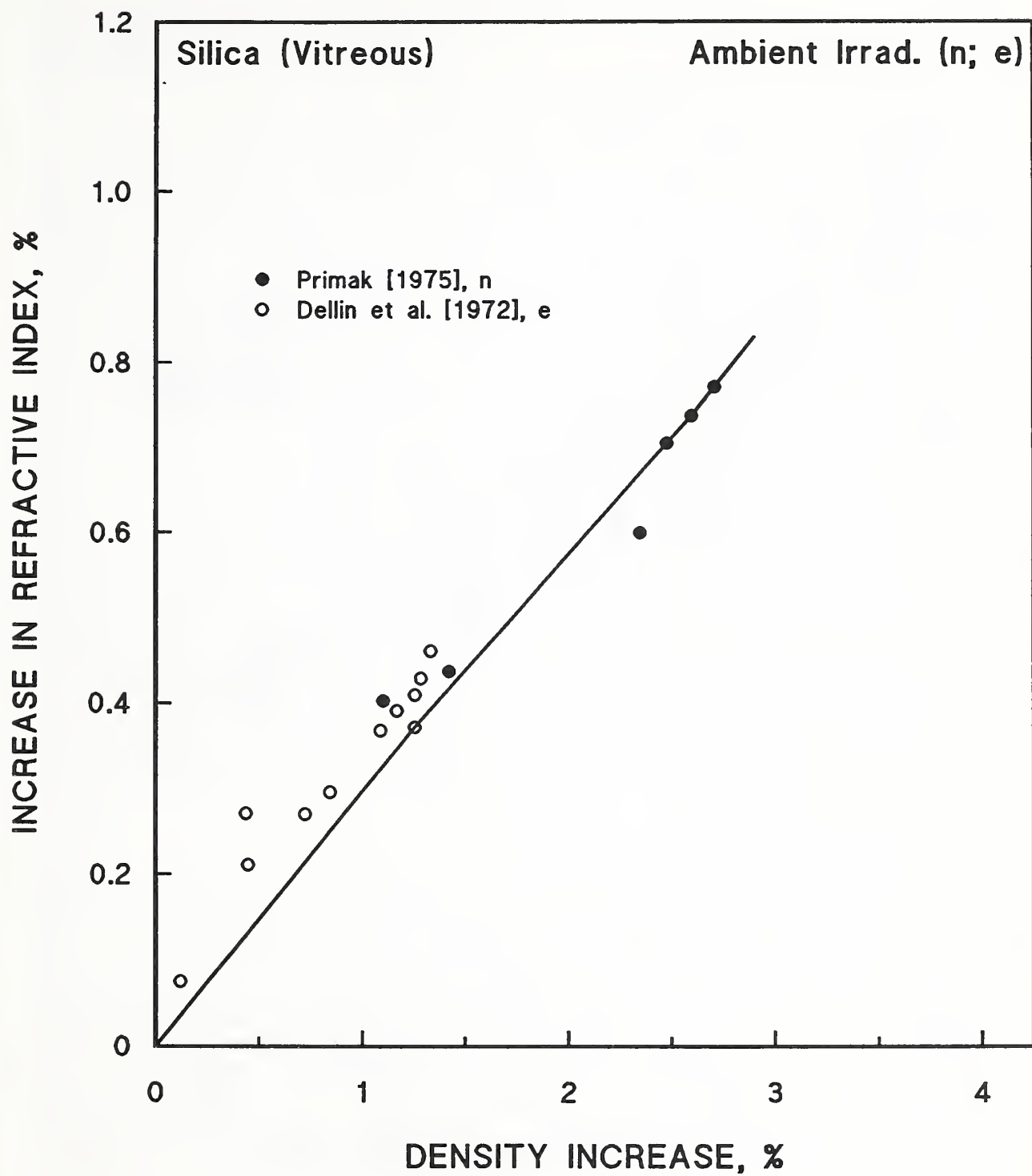


Figure 6.2.8. Increase of refractive index after neutron and electron irradiation of SiO_2 . Data from Shelby [1980].

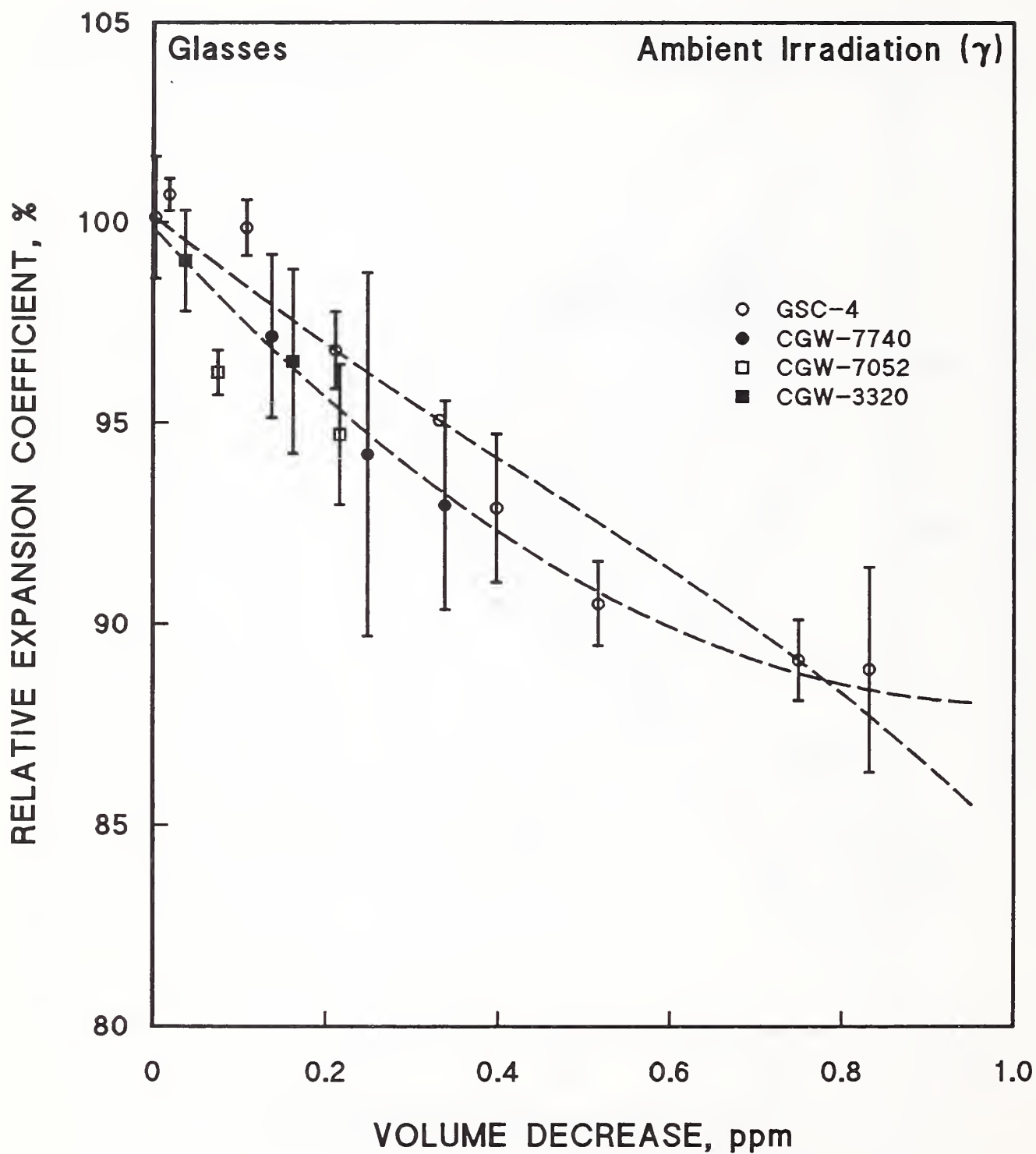


Figure 6.2.9. Decrease of relative thermal expansion (between 173 and 273 K) after γ irradiation in various commercial borosilicate glasses. Data from Shelby [1980].

6.3. AMORPHIZATION

Wittels and Sherrill [1954] found that the onset of permanent damage in quartz occurred at a neutron fluence of about $2 \times 10^{23}/\text{m}^2$. They also showed that both neutron-irradiated quartz and vitreous SiO_2 were transformed into a disordered, amorphous modification above a fast neutron fluence of about $1.2 \times 10^{24}/\text{m}^2$. The transformed quartz has a density of about 2.3 g/cm^2 and a refractive index of about 1.467, whereas the density of vitreous SiO_2 is about 2.21 g/cm^3 and its refractive index is 1.457 [Simon, 1957]. Therefore, the structure of amorphized quartz is not expected to be precisely the same as that of vitreous SiO_2 . Simon [1957] used X-ray diffraction after neutron irradiation to $1.4 \times 10^{24}/\text{m}^2$ ($E > 1 \text{ MeV}$) to show that the average Si—O distance in the quartz was the same as that in vitreous silica, but the distance for the Si atom to the next nearest Si atom was somewhat smaller than in vitreous SiO_2 . This indicates that the bond angle is slightly smaller in the disordered quartz. The radial distances of O atoms and Si atoms to second-neighbor O atoms showed a wider distribution in the disordered quartz than in unirradiated vitreous SiO_2 . This early work with X-ray techniques has been confirmed by Tsumbu et al. [1982] and van den Bosch et al. [1983], who used positron-annihilation measurements in neutron-irradiated quartz and vitreous SiO_2 to show that their physical state is different.

Despite the considerable degree of disorder and density change in irradiated quartz, the dpa from direct neutron collisions was estimated to be only 1.4×10^{-4} . Simon estimated that this disorder could have occurred only if each PKA produced disorder in a region containing about 5300 surrounding Si atoms. Since the disordering fluence at ambient temperature is only about 100 times the ITER TF magnet fluence at 4 K, significant disorder could arise from the ITER fluence in vitreous or crystalline SiO_2 , especially since warm-up is less likely to restore the original state (§1.5).

Other aspects of the formation and nature of the disordered state in quartz have been investigated by several authors. Baeta and Ashbee [1975] suggested that the formation of a glassy state occurred as follows: after Si atom displacement, four SiO_4 tetrahedron corners become unlinked. The adjoining tetrahedra then have considerable freedom of movement, and when unsaturated corners

subsequently approach closely enough to form a bond, the tetrahedra are unlikely to be oriented according to a crystalline lattice.

Pascucci et al. [1983, and citations therein] further discussed the rearrangement of SiO_4 tetrahedra upon radiolysis. Evidence from their TEM ultrahigh-resolution structure imaging, and convergent-beam electron diffraction studies supported a transformation model in which progressive disorder evolved from local rearrangements of individual $[\text{SiO}_4]$ units rendered less constrained by lowered connectivity afforded by the unlinked tetrahedra. The rate of amorphization was found to be more than a factor of two lower at 10 K than at ambient temperature. However, this observation was based on electron irradiation, which induces amorphization from ionizing radiation. Displacive radiation from neutron irradiation is much more efficient at inducing amorphization, owing to the greater disorder within displacement cascades that makes the necessary cooperative rotations easier than the stepwise accumulation of broken $\text{Si}-\text{O}-\text{Si}$ linkages arising from radiolysis in electron irradiation. Therefore, it is not clear whether neutron-induced amorphization and disorder damage at 4 K would be significantly retarded over that observed at ambient temperature. However, ionization-induced amorphization probably would be retarded, owing to the role of thermal motion in the process.

The noncrystalline form of quartz produced by rearrangement of tetrahedra may not be completely glassy. One of the characteristics of a glassy state is that at 4 K and below, localized excitations known as tunneling systems exist. These tunneling systems are effective scatterers of phonons, and affect thermal properties, as is discussed below (§6.5). Since tunneling systems can be detected by phonon echo techniques, Golding and Graebner [1980] used this technique to investigate whether glassy regions exist in crystalline quartz into which only a small amount of disorder has been introduced by irradiation. Such investigations give information on the effect of irradiation upon properties. After ambient irradiation to $6 \times 10^{22}/\text{m}^2$, considerably below the amorphizing fluence of $\sim 2 \times 10^{24}/\text{m}^2$, Golding and Graebner found that their specimen was essentially indistinguishable from unirradiated quartz in terms of sound velocity, density, and piezoelectric activity. Sharp Bragg X-ray reflections were still present. However, a phonon echo study at 20 mK gave evidence of resonant centers with the same properties as those of vitreous

SiO₂. Because the change in density at their irradiation fluence was only 0.1%, whereas the difference in density between quartz and vitreous SiO₂ is 20%, Golding and Graebner argued that any local regions melted by thermal spikes could constitute only a small fraction of the total volume of the crystal and could not be the only loci of resonant systems, because the density of states would not be large enough. They therefore concluded that tunneling systems could exist in the inhomogeneously strained matrix surrounding displacement regions, and that complete disorder was not required for detection of the glassy state. Their X-ray studies suggested that these regions contained clusters of interstitials, and were on the scale of nanometers, perhaps ranging up to 5 nm (50 Å) in extent.

Laermans [1979] obtained results similar to those of Golding and Graebner. She irradiated quartz to the same fast neutron fluence, $\sim 6 \times 10^{22}/\text{m}^2$ ($E \approx 1$ MeV) at about 60°C. The temperature-dependent behavior of the hypersonic attenuation at 9.4 GHz between 1.4 and 4.2 K was completely different from that of a pure unirradiated sample, although quartz is known to maintain long-range order at this fluence. The results were explained by a two-level system model used to describe disordered, amorphous materials, but it was postulated that the disorder occurred only in localized regions. The nature of the local disorder was not determined.

Fischer et al. [1983a] also studied the formation of disorder in quartz. They used RBS to investigate the degree of disorder by implantation of He⁺, B⁺, and Ar⁺ ions at ambient temperature. First, they noted that structural defects in SiO₂ could be created by electronic energy deposition, as shown by electron and light ion experiments [citations, Fischer et al., 1983a] and by evidence discussed above in §§6.1 and 6.2. In the ionization process, Si—O bonds are broken with subsequent formation of Si—O—Si bridges and changes in the arrangement of neighboring SiO₄ tetrahedra. However, the efficiency of this ionization-induced damage is about 200 times less than the damage produced by nuclear collisions. Fischer et al. investigated the relative contributions of both electronic and nuclear energy deposition to the creation of the amorphous or disordered state. They found that disorder formation due to electronic processes was possible only in predamaged crystals, and that the predominant damage was produced by nuclear processes only. Figure 6.3.1 shows that there

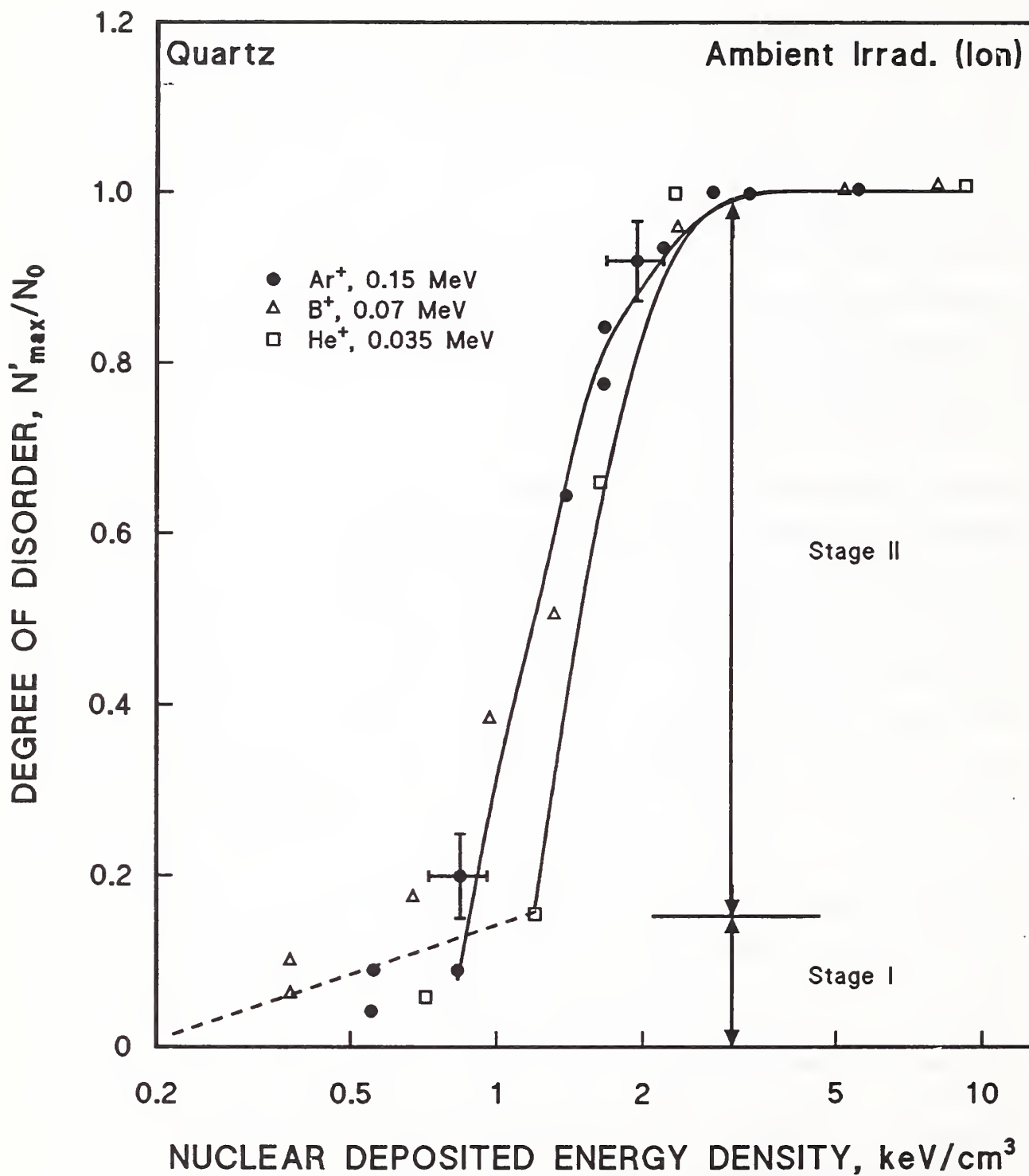


Figure 6.3.1. Degree of disorder of ion-bombarded quartz. Data from Fischer et al. [1983a].

is an initial region (Stage I) with a low degree of disorder, ($N'_{\text{max}}/N_0 < 0.15$) produced by Frenkel defects, in which $\leq 1 \times 10^{20}$ keV/cm³ is deposited. This is followed by formation of amorphized microregions around each particle trajectory up to $\sim 2.5 \times 10^{20}$ keV/cm³. Drastic structural and physical property changes, such as a large volume expansion, occur at the higher energy deposition. The number of disordered atoms per keV of incident energy was much higher than predicted by the Kinchin-Pease model (§1.2.1). Using $E_d = 25$ eV for quartz, as determined by Primak (§6.1), the model gives an averaged nuclear deposited energy of about 60 eV for the production of one Frenkel pair. The observed average nuclear deposited energy for the generation of one disordered atom was only 8 eV in Stage I. The discrepancy with theory would be smaller if the values of Das and Mitchell [1974] for E_d were used instead of the value of Primak, since these values were 5.4 eV (Si) and 9.5 eV (O). However, in Stage II, at higher defect concentration, this average nuclear deposited energy drops to about 1 eV. The discrepancy was attributed to a shifting of SiO₄ tetrahedra against each other that yielded RBS-amorphous microregions.

Finally, with regard to the amorphization of quartz by neutron fluences of $\sim 10^{23}$ to 10^{24} /m², note that comparative X-ray studies of other oxides, such as MgO and MgAl₂O₄, that were exposed to this fluence have shown little difference in the X-ray diffraction pattern from that of the unirradiated material [Primak, 1954]. Thus, quartz appears more subject to severe radiation damage than other ceramic oxides. For comparison with other ion irradiation studies, note that Fischer et al. [1983b] found that a quasi-random arrangement of both Si and O atoms was obtained from 150-keV Ar⁺ fluences $\geq 5 \times 10^{17}$ /m², according to RBS examination.

Vitreous SiO₂ is already amorphous, and its cryogenic properties, such as thermal conductivity and specific heat, can be explained by the tunneling-states model for localized excitations that was used above to explain disorder in quartz after irradiation. Neutron irradiation of vitreous SiO₂ should reduce the number of localized excitations, but the amorphous nature of the material should not be lost. Smith et al. [1978] irradiated vitreous SiO₂ to fluences to 5×10^{23} /m² at ambient temperatures and then measured the thermal conductivity and specific heat between 0.1 and 100 K. The results are

presented in Figures 6.5.1 and 6.5.9 in §6.5. The thermal conductivity increased and the specific heat decreased. Smith et al. explained their results by a change of density of tunneling states owing to a modification of the already-amorphous structure.

6.4. MECHANICAL PROPERTIES

6.4.1. Flexural Strength

Because several cases of shattering of SiO_2 glass at 77 K had been observed when it was used in the construction of apparatus for irradiation, Thompson [1957] tested vitreous SiO_2 rods in 3-point bending tests at 77 K. Specimens were irradiated at 100°C and tested at 77 K in sets of 12; the mean values from these sets and their standard deviations are shown in Figure 6.4.1. The large standard deviations are due to the influence of surface conditions on the fracture strength. One set of rods was irradiated at 77 K. Whether or not these specimens were warmed to ambient temperature before being inserted into the testing apparatus was not reported, but warm-up seems likely, because the diagram of the apparatus indicated that one specimen at a time was tested. Thompson concluded that there was no change in strength, greater than 10%, for fluences of the order of $10^{22}/\text{m}^2$, and that shattering under irradiation was not due to loss of strength. However, the author did not account for the possible annealing of damage at 100°C or during specimen warm-up, after the irradiation was conducted at 77 K. Therefore, the conditions under which vitreous SiO_2 failed in service were apparently not completely reproduced in the tests. It is of interest that the 293-K value of flexural strength of a set of unirradiated specimens was 17.3 ± 1.4 Mpa. Figure 6.4.1 shows that an increase of about 70% in the strength of the glass occurred at 77 K. Perhaps a drop in fracture toughness rather than a change in strength under irradiation was responsible for the failures in vitreous SiO_2 .

Flexural strength measurements on borosilicate and soda-lime glasses were made by Mike et al. [1960] after irradiation by 2-MeV electrons. No effect on the strength was found from doses up to 3×10^6 Gy. Flexural strengths reported were about 49 and 69 MPa for borosilicate and soda-lime glasses, respectively, considerably above the strengths reported for vitreous SiO_2 by Thompson. The

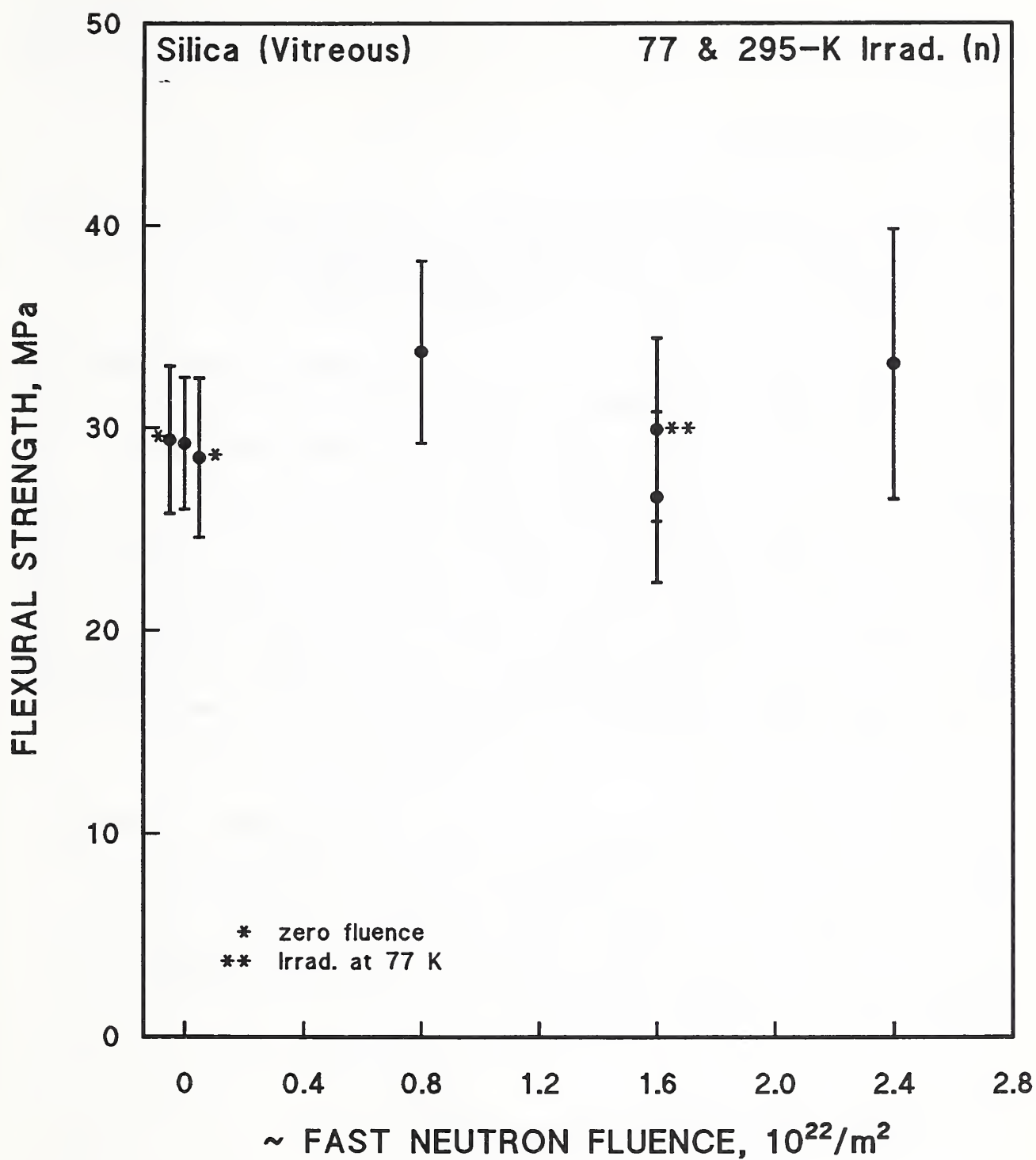


Figure 6.4.1. Flexural strength of vitreous SiO_2 at 77 K after neutron irradiation at ambient and 77-K temperatures. Data from Thompson [1957].

relatively small dose in these electron irradiations did not produce a density change.

6.4.2. Elastic Moduli

An increase in Young's modulus of 1.42% and a decrease in the shear modulus of 3.8 % were measured by Mayer and Gigon [citation, Wullaert et al., 1964] for vitreous SiO₂ after a fast neutron fluence of $7 \times 10^{22}/\text{m}^2$ at 55°C.

Strakna et al. [1963] irradiated vitreous SiO₂ specimens of optical quality at an unspecified ambient temperature to a higher fast neutron fluence of more than $5 \times 10^{23}/\text{m}^2$ ($E > 0.01$ MeV). The unirradiated samples had a density of 2.203 g/cm³ and the irradiated samples had a density of 2.26 g/cm³. The specimens may have been stored for a considerable period before the ultrasonic attenuation and shear longitudinal velocities were measured at cryogenic temperatures. In an isotropic solid, the shear modulus and compressibility can be determined from these velocities. The results are shown in Figures 6.4.2 and 6.4.3. The absolute value of the shear modulus changed by less than 2%, at the lowest temperature and the 300-K change was below that reported by Mayer and Gigon. However, the compressibility decreased by ~20%.

Paymal and LeClerc [1964] measured the change in Young's modulus in various glasses by thermal neutron irradiation of up to $\sim 4 \times 10^{22}/\text{m}^2$ at about 150°C. The effect of the neutrons was magnified through the $^{10}\text{B}(n,\alpha)^7\text{Li}$ reaction, since B was added to all glasses. Both increases and decreases of several percent in Young's modulus were measured by the longitudinal vibration resonance method in a number of glasses.

6.5. THERMAL PROPERTIES

6.5.1. Specific Heat

Neutron irradiation of vitreous SiO₂ at ambient temperatures decreases the specific heat at cryogenic temperatures but increases the thermal conductivity [citations, Smith et al., 1978]. Several authors have suggested that the

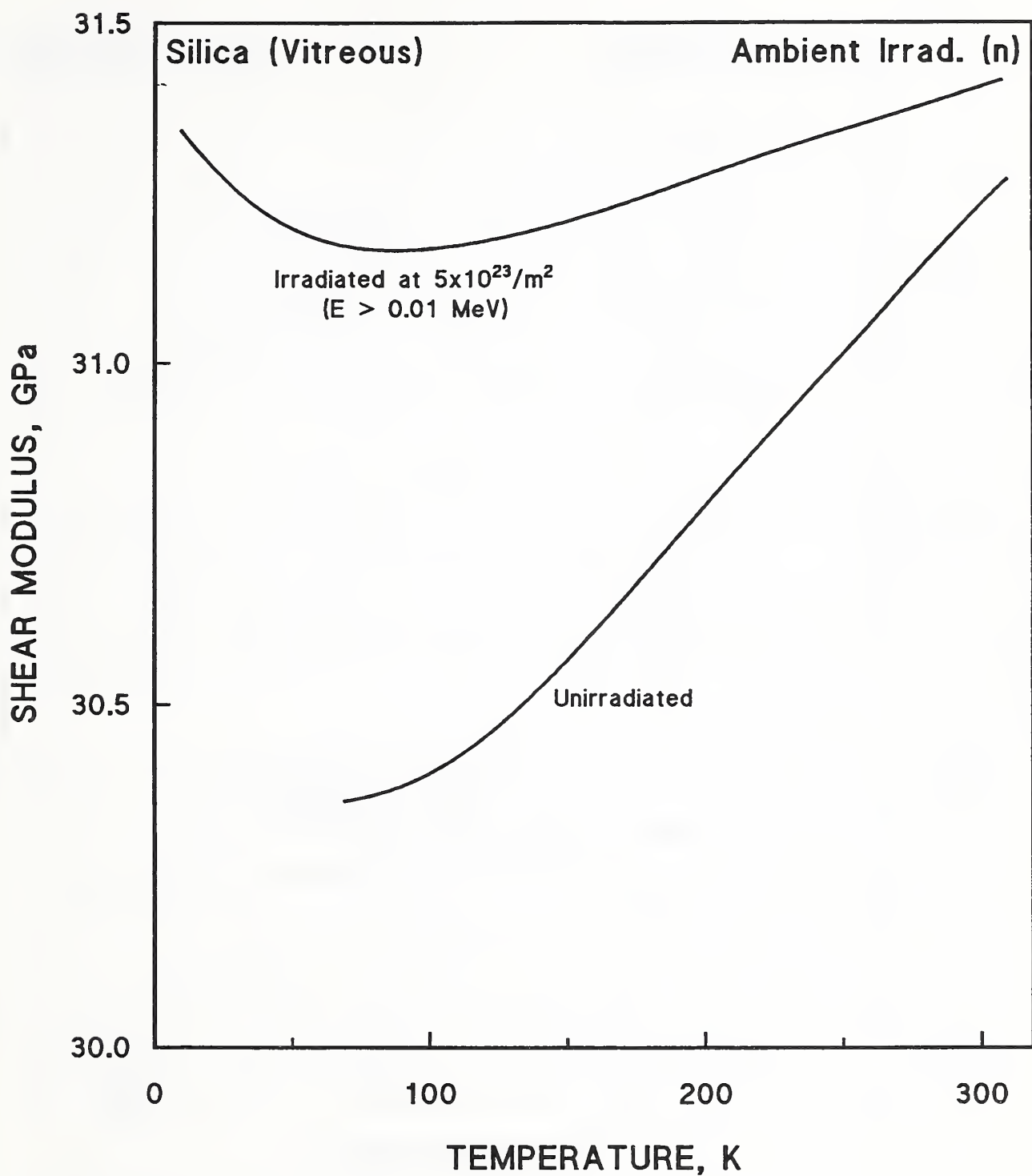


Figure 6.4.2. Effect of neutron irradiation upon the cryogenic shear modulus of vitreous SiO_2 . Data from Strakna et al. [1963].

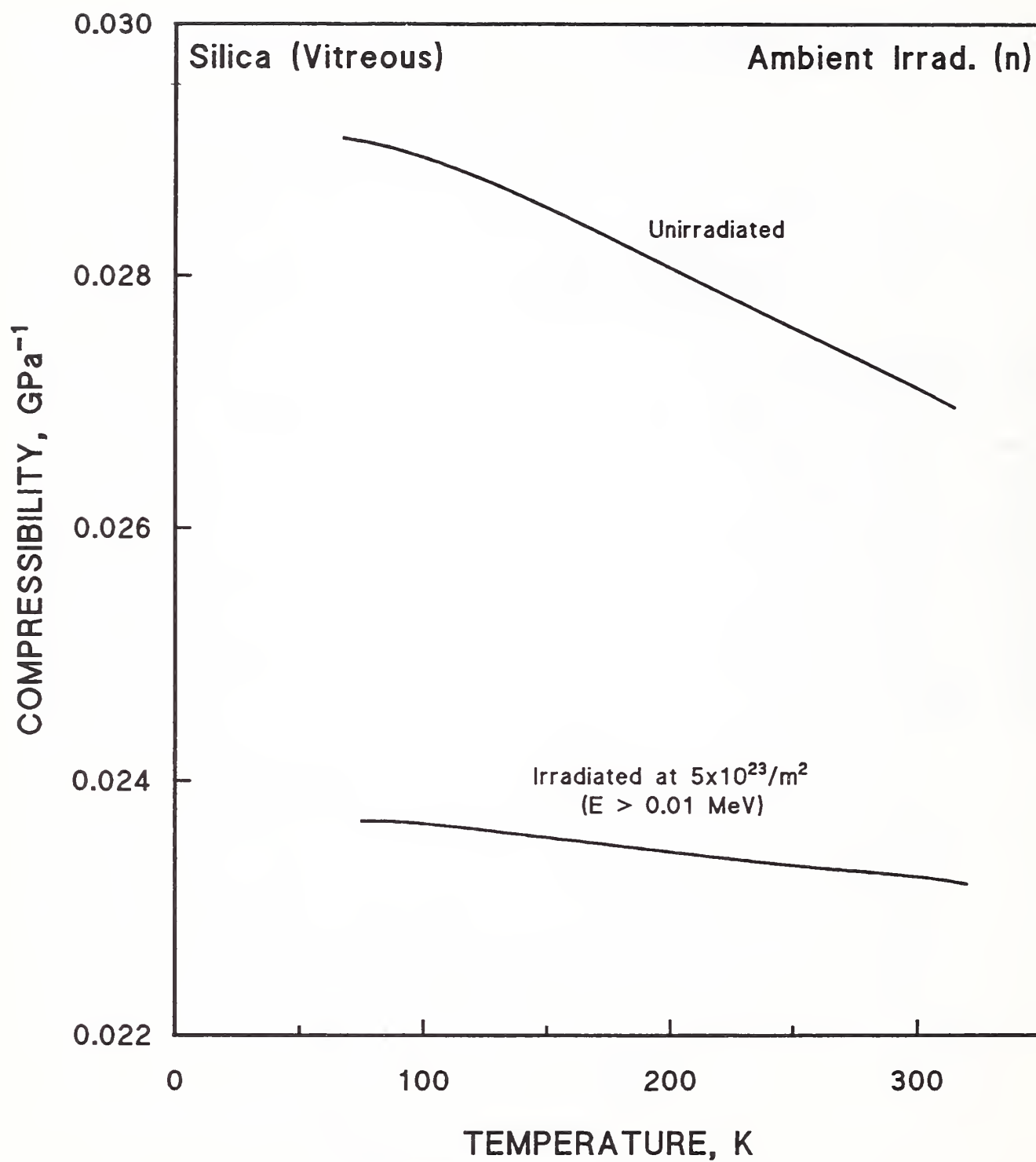


Figure 6.4.3. Effect of neutron irradiation upon the compressibility of vitreous SiO_2 . Data from Strakna et al. [1963].

irradiation reduces the number of localized excitations, but does not alter the amorphous nature of vitreous SiO_2 [citations, Smith et al., 1978]. When specific heat and thermal conductivity measurements were made before and after irradiation on samples cut from a single piece of vitreous SiO_2 , a localized excitation model was used to explain the results quantitatively. The changes in specific heat and thermal conductivity were attributed to a change in the density of localized excitations (tunneling-states model) [Smith et al., 1978]. As a practical matter, however, the decrease in specific heat at ~ 4 K is relatively small, even for an ambient irradiation of $1.7 \times 10^{23}/\text{m}^2$ ($E > 0.1$ MeV), as Figure 6.5.1 indicates. Whether or not the change in specific heat would be more significant for 4-K irradiation is not known.

In contrast to the vitreous material, the specific heat of quartz increased somewhat after neutron irradiation. Figure 6.5.2 indicates this change after ambient irradiation to $5.3 \times 10^{22}/\text{m}^2$ ($E > 1$ MeV) [Saint-Paul and Lasjaunias, 1981]. There is no recovery after thermal annealing of 2 h at 400°C . The specific heat of the irradiated quartz became similar to that of unirradiated vitreous SiO_2 .

Gardner and Anderson [1981a] carried out a similar experiment, but irradiated quartz to a higher fluence, $2 \times 10^{24}/\text{m}^2$ ($E > 0.1$ MeV). Their results, divided by T^3 to emphasize the departure from the Debye behavior of the undamaged crystal, are shown in Figure 6.5.3. The effect at ~ 4 K seems to be somewhat smaller than at lower temperatures. This presentation of the data, (specific heat)/ T^3 , indicates the differences between the specific heat of unirradiated quartz and unirradiated vitreous SiO_2 . Both Gardner and Anderson [1981a] and Saint-Paul et al. [1982] published extensive theoretical interpretations of their results. This discussion is perhaps most relevant to the lower temperature data well below 4 K. One theoretical curve is shown in Figure 6.5.3.

Chaussey et al. [1979] also found a significant increase in the cryogenic specific heat of quartz after γ irradiation up to 10^5 Gy. However, the measurements did not extend to 4 K and the specific heats of the irradiated specimens appeared to be approaching that of the unirradiated specimen at ~ 2 K (Figure 6.5.4). In agreement with the γ -irradiation results, no significant changes were observed above 3 K in the specific heat after 3-MeV electron

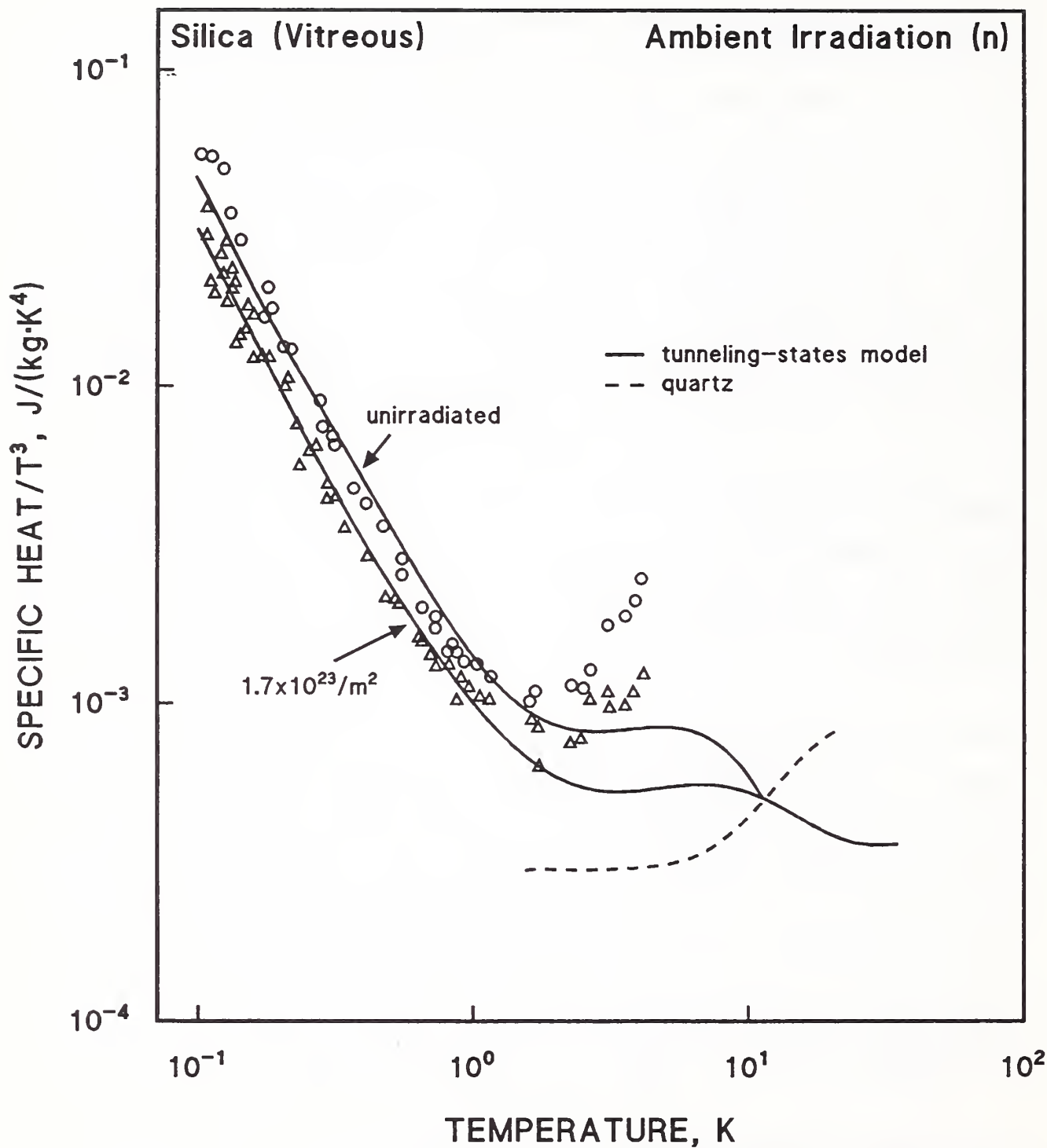


Figure 6.5.1. Cryogenic specific heat/ T^3 of vitreous SiO_2 after neutron irradiation. Higher fluence data omitted for clarity. Solid lines indicate calculations from model. Data from Smith et al. [1978].

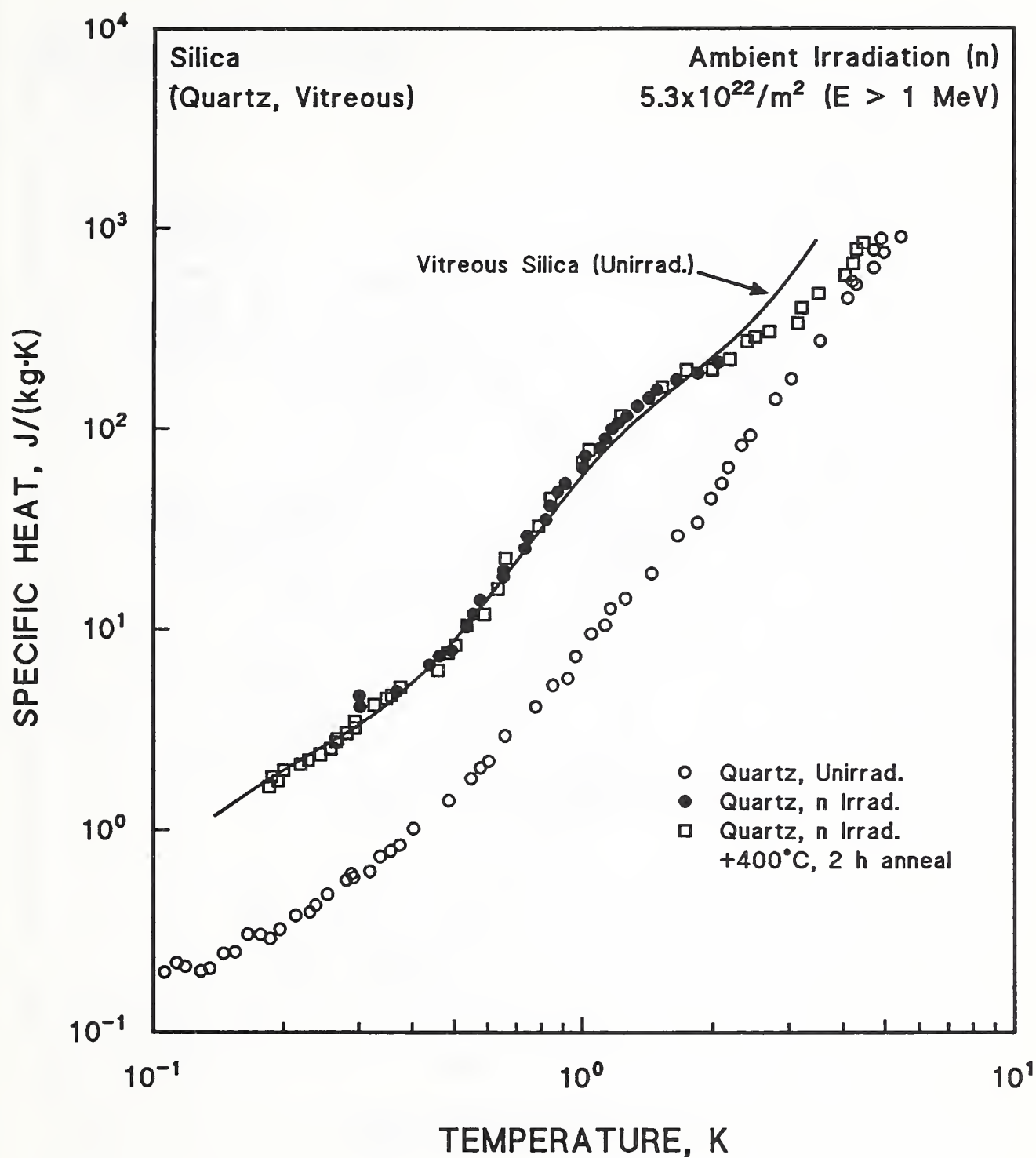


Figure 6.5.2. Specific heat of quartz after neutron irradiation and thermal annealing, compared to specific heat of unirradiated vitreous silica. Data from Saint-Paul and Lasjaunias [1981].

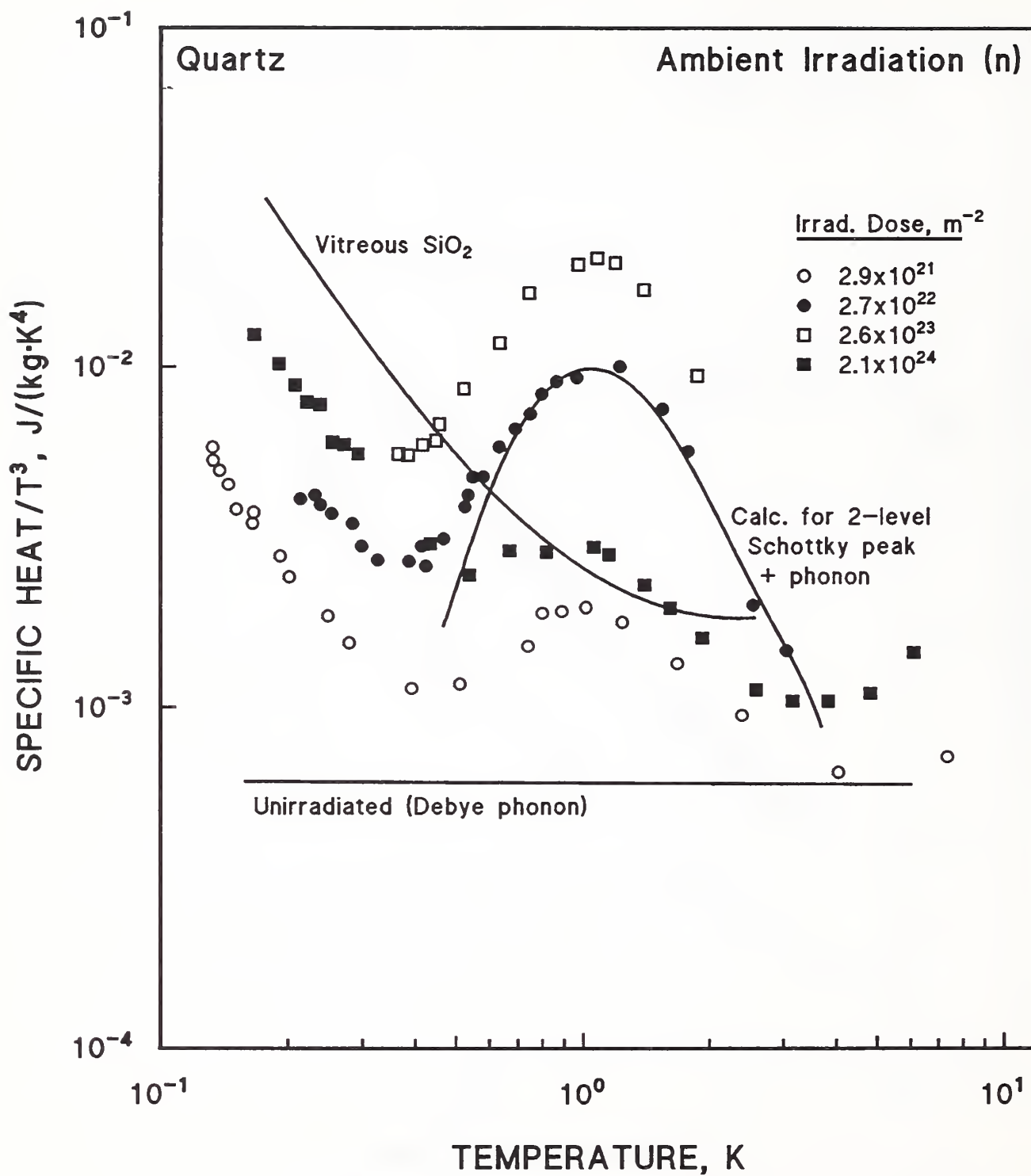


Figure 6.5.3. Specific heat/ T^3 of quartz after neutron irradiation, compared to that of unirradiated vitreous silica and a theoretical calculation. Data from Gardner and Anderson [1981a].

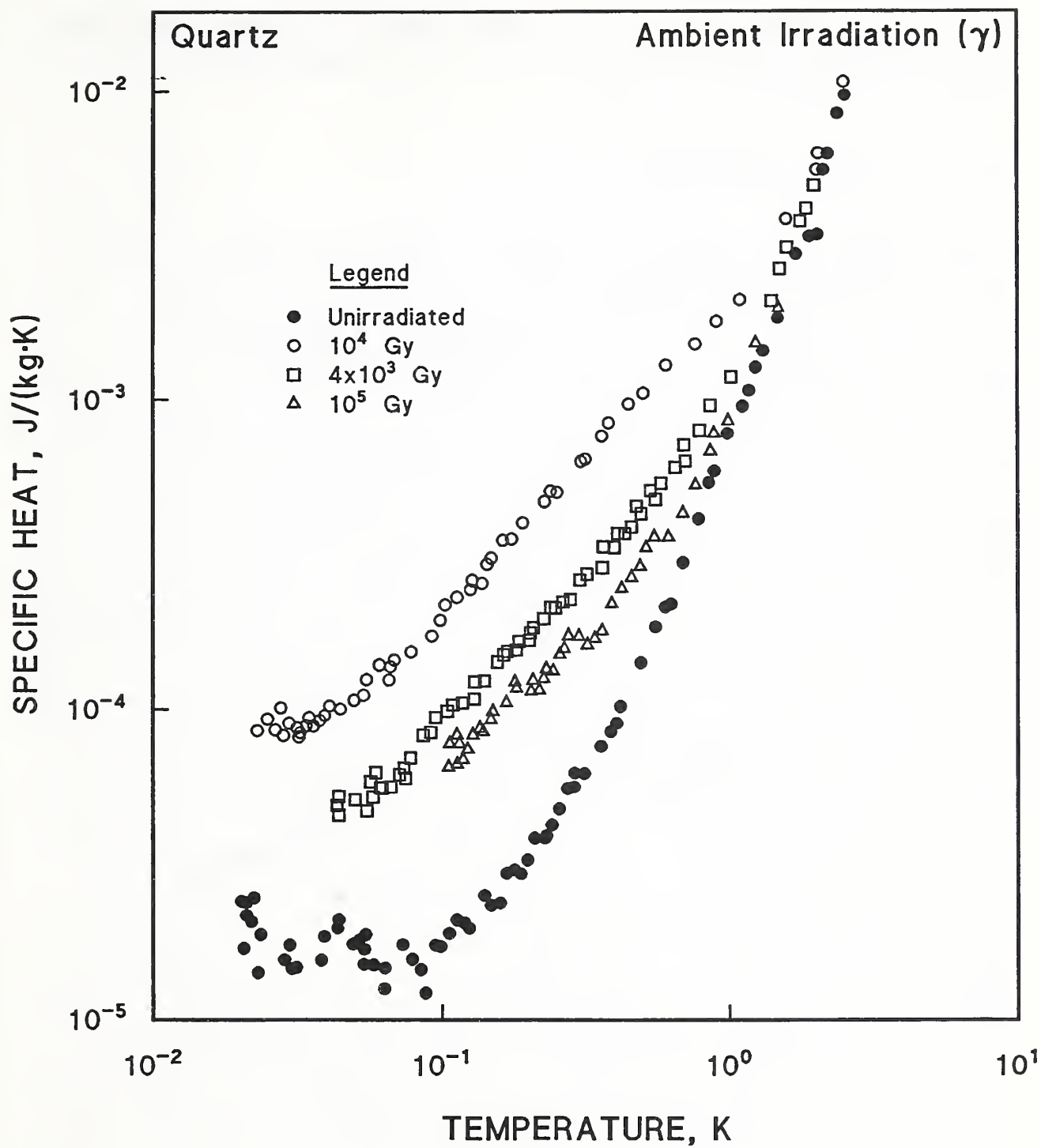


Figure 6.5.4. Specific heat of quartz after γ irradiation. Data from Chaussy et al. [1979].

irradiation, although deviations again were seen at lower temperatures (Figure 6.5.5) [Hofacker and Löhneysen, 1981]. The electron fluence was $1.9 \times 10^{23}/\text{m}^2$.

6.5.2. Thermal Conductivity

Berman [1951, 1952] measured the cryogenic thermal conductivity of quartz irradiated at a temperature below 100°C to (thermal) neutron fluences up to $3.4 \times 10^{23}/\text{m}^2$. Figure 6.5.6 shows these data; the thermal conductivity approaches that of vitreous SiO_2 as the fluence is increased. No difference was detected when specimens were kept at 100°C for 3 weeks. Laermans and Daudin [1980] and Laermans et al. [1980] extended this type of measurement down to lower temperatures; the fast neutron fluence was probably lower, $6 \times 10^{22}/\text{m}^2$, but the results, shown in Figure 6.5.7, are consistent, given the uncertainties in the irradiation conditions. This investigation was also an extension of the work of Golding and Graebner [1980] on low energy, localized excitations (2LS) in neutron-irradiated quartz; this work was described above (§6.3). It had shown that phonon echoes in irradiated quartz were similar to those in vitreous SiO_2 . Laermans and Daudin noted that the fast-neutron irradiation of quartz introduces the 2LS while the irradiation of the vitreous material reduced the number of such systems. They made acoustic measurements to detect the 2LS in electron- as well as neutron-irradiated quartz. As discussed above (§1.2.2), electrons give rise to single, scattered defects, whereas neutrons cause both single defects and clusters of defects. The thermal conductivity data gave no evidence for 2LS in the electron-irradiated sample, but did in the case of neutron irradiation. These excitations are detected by a T^2 behavior at very low temperatures. From Figure 6.5.7, it is clear that the temperature dependence of the thermal conductivity of the neutron-irradiated specimens resembles that of the glass, while that of the electron-irradiated specimen remains similar to quartz. When Hofacker and Löhneysen [1981] irradiated quartz with electrons, a similar shift of the peak to a higher temperature was observed (Figure 6.5.8).

Gardner and Anderson [1981a] have extended this type of measurement down to even lower temperatures below 0.1 K. Figure 6.5.9 shows that a continuation of the decrease in thermal conductivity and the T^2 temperature dependence was

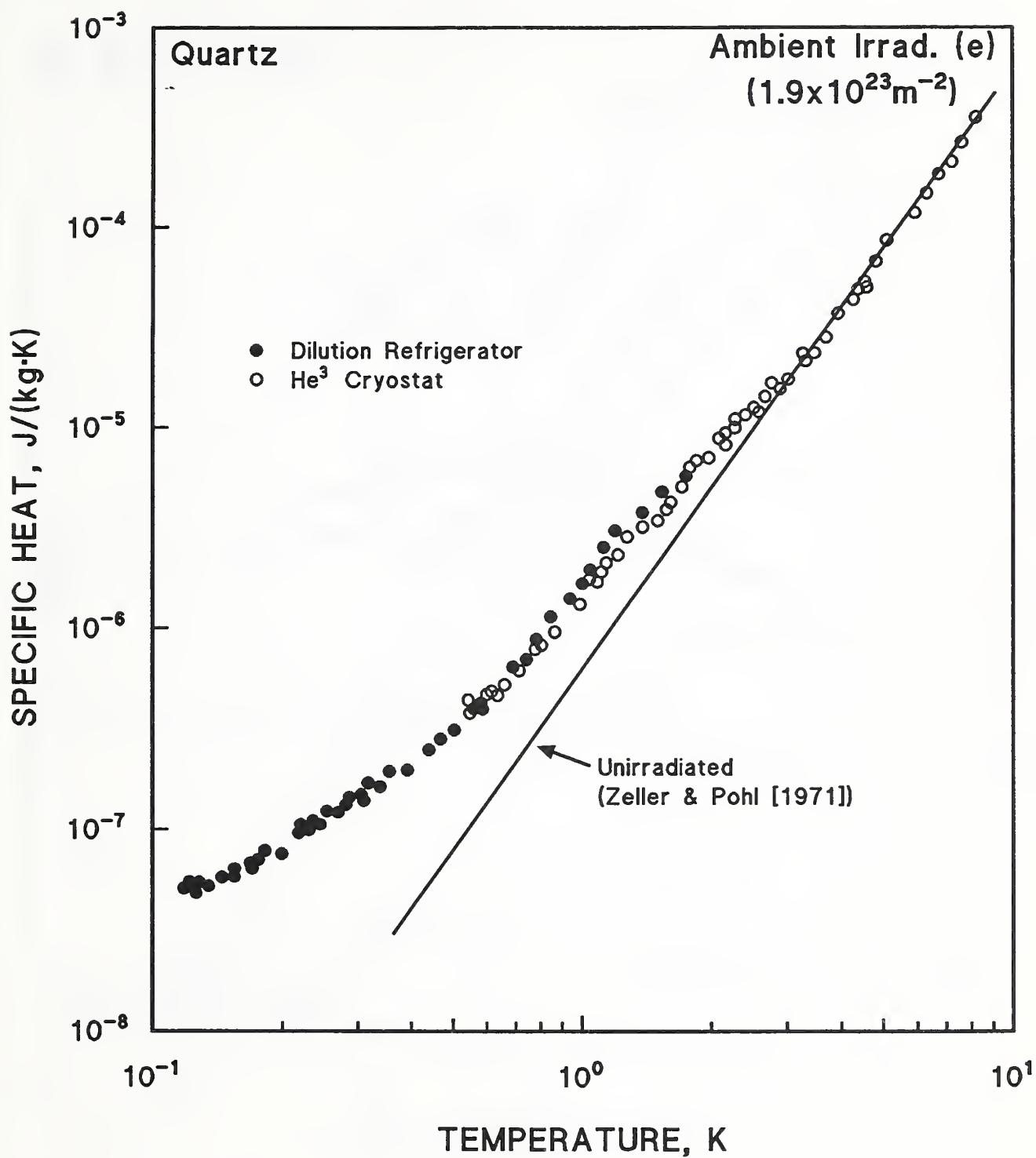


Figure 6.5.5. Specific heat of quartz after electron irradiation. Data and citation from Hofacker and Löhneysen [1981].

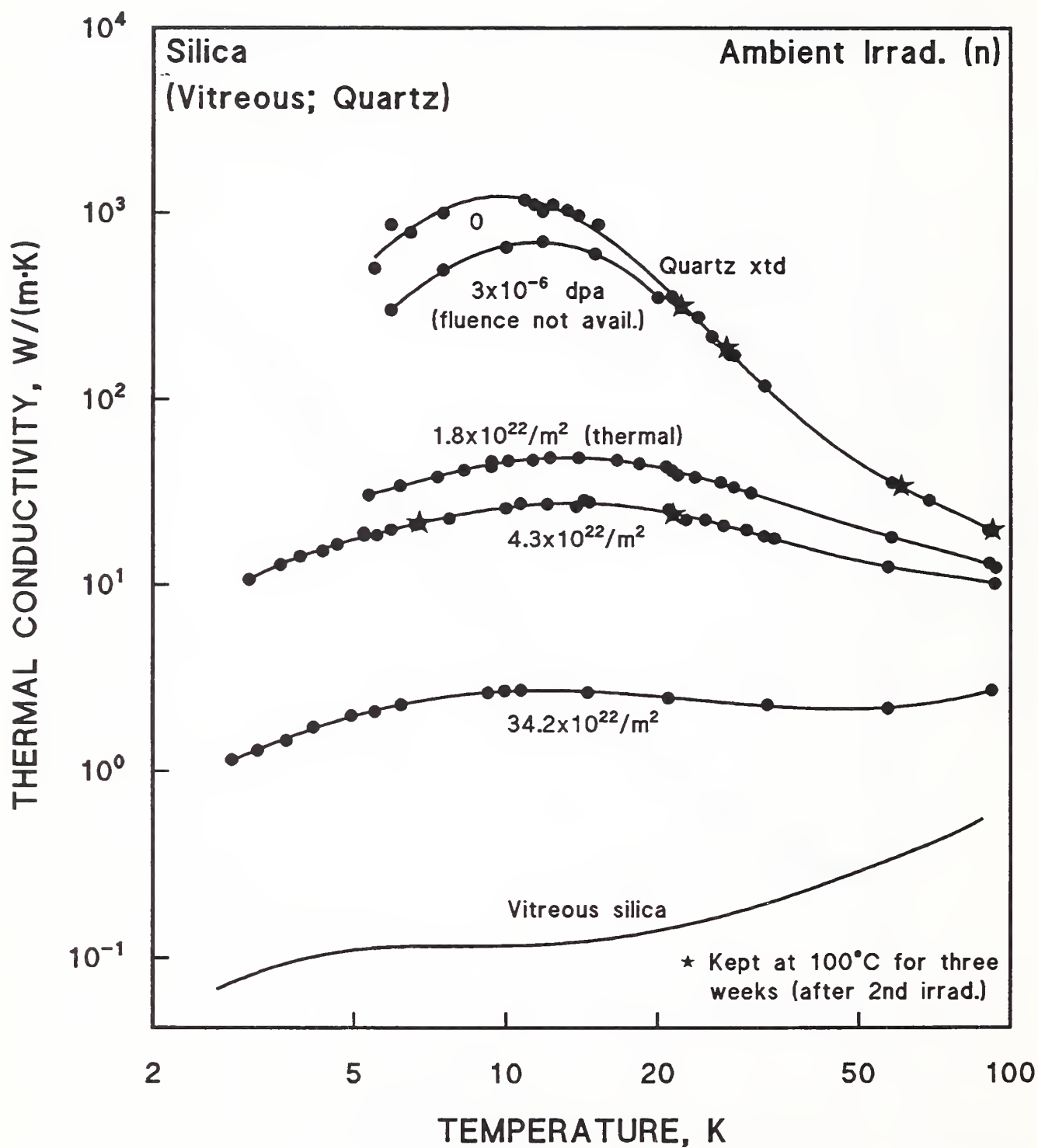


Figure 6.5.6. Thermal conductivity of quartz after neutron irradiation, compared with vitreous SiO_2 . Data from Berman [1951, 1952] and Berman et al. [1950].

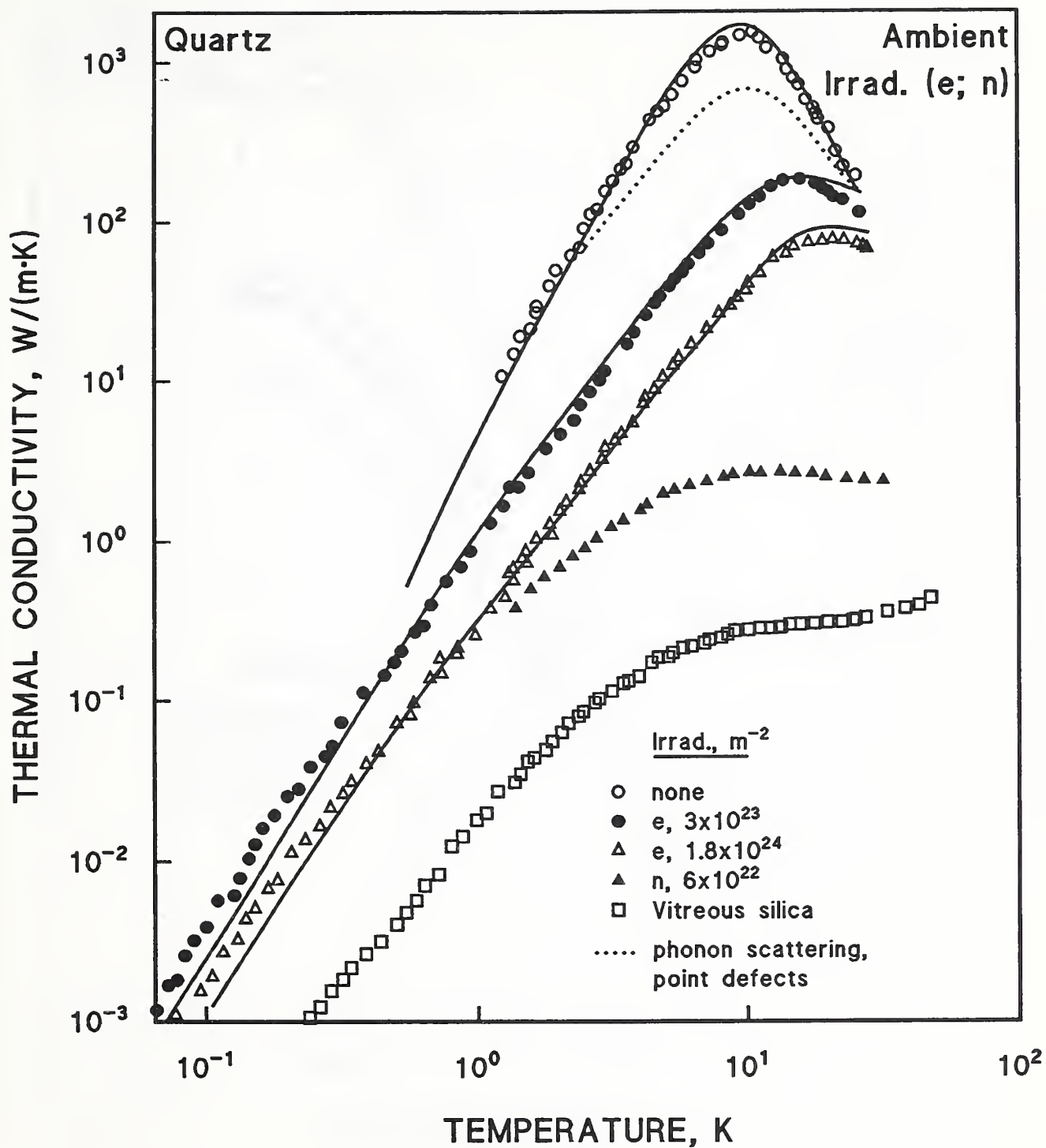


Figure 6.5.7. Thermal conductivity of neutron- and electron-irradiated quartz, compared with that of vitreous SiO_2 . Only a portion of the original data points is shown. Data from Laermans et al. [1980].

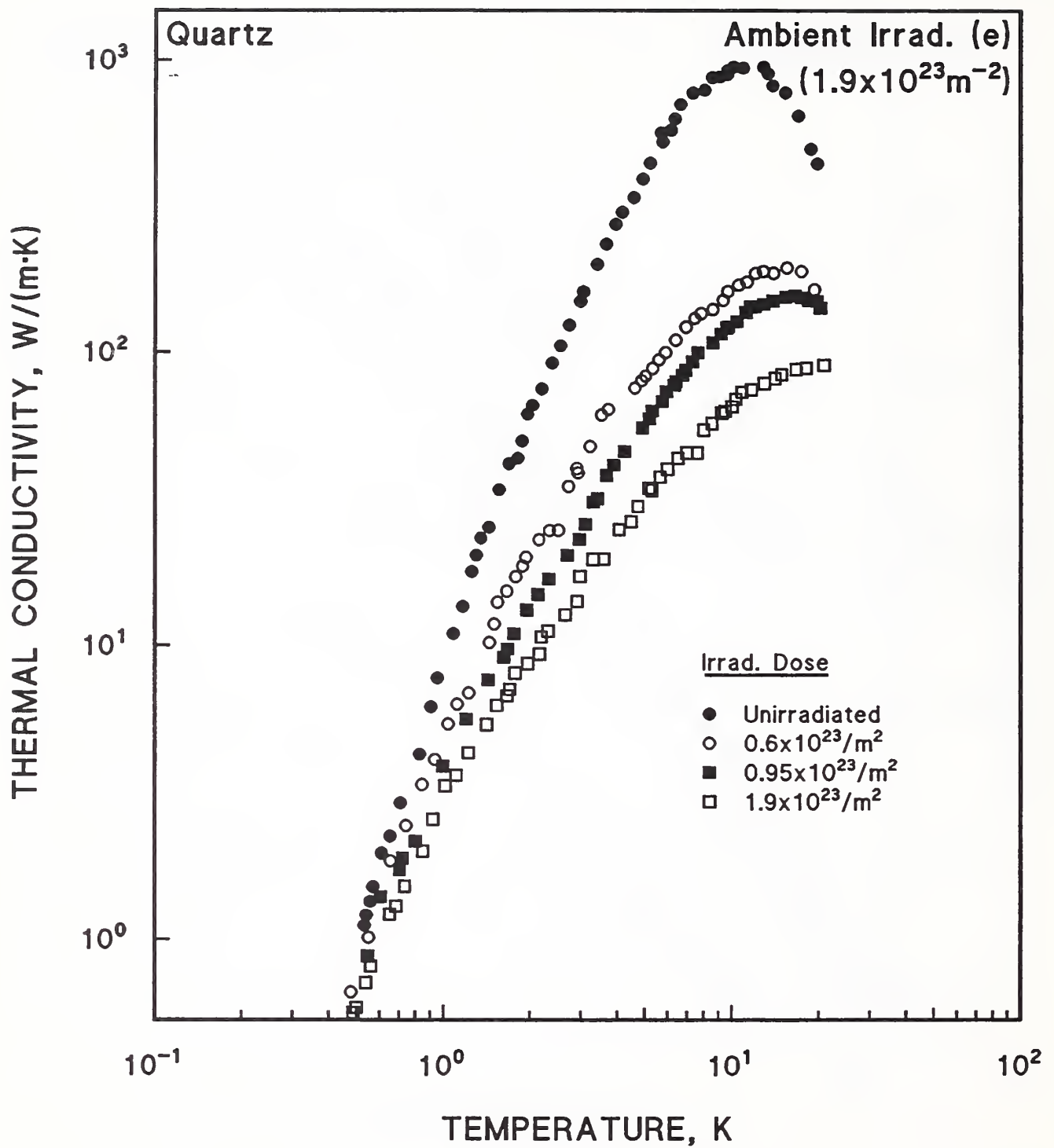


Figure 6.5.8. Thermal conductivity of quartz after electron irradiation. Data from Hofacker and Löhneysen [1981].

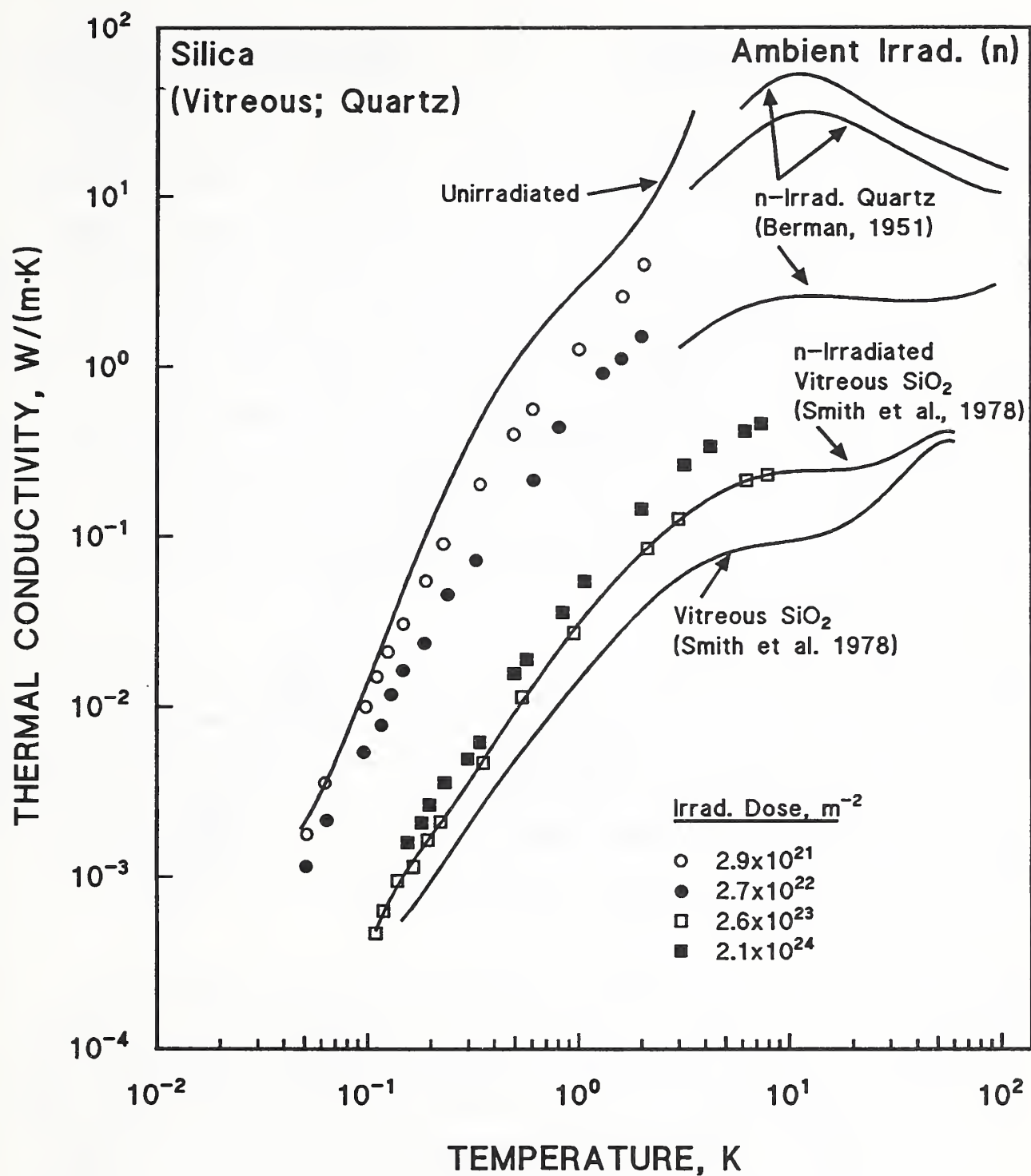


Figure 6.5.9. Thermal conductivity of quartz after neutron irradiation, compared with that of vitreous SiO₂. Data from Gardner and Anderson [1981a].

observed at fluences up to $2.1 \times 10^{24}/\text{m}^2$ ($E > 0.1$ MeV). In addition, the results of Berman are plotted in this figure, as well as data on the irradiation of vitreous SiO_2 from Smith et al. [1978]. In the case of the vitreous material, the neutron irradiation improves the thermal conductivity. This is presumably in agreement with the decrease of 2LS under neutron irradiation noted above. These data on vitreous SiO_2 are shown in more detail in Figure 6.5.10, along with theoretical calculations. This interesting result is corroborated by the work of Raychaudhuri and Pohl [1982], shown in Figure 6.5.11. These data are related to the change in density of the irradiated material in Figure 6.5.12; that is, they are shown to have approximately the same dependence upon fluence and saturation. Despite the increase in conductivity after irradiation, Raychaudhuri and Pohl observed that neutron-irradiated vitreous SiO_2 was considered to be more disordered than unirradiated vitreous SiO_2 . The theories of the increase in thermal conductivity with irradiation are discussed in detail by both Raychaudhuri and Pohl and by Gardner and Anderson.

For historical accuracy, note that the increase in thermal conductivity in vitreous SiO_2 after neutron irradiation (at higher cryogenic temperatures) was reported much earlier, by Cohen [1958]. These results are shown in Figure 6.5.13. At that time, somewhat different theoretical explanations were advanced (e.g., Klemens, [1958]). Cohen also measured the density increase. For the highest fluence, it approached the limiting density for both quartz and vitreous SiO_2 after prolonged neutron irradiation.

The relevance of all these ambient-irradiation data for the ITER TF magnet conditions at 4 K is that for both crystalline and vitreous SiO_2 , the saturation changes in thermal conductivity (decrease or increase, respectively) can be taken as an approximation to the situation which should obtain after extensive 4-K irradiation in which the fluence may be lower, but the defects retained may approximate those of ambient-temperature fluences about 100 times higher. However, direct measurements of the thermal conductivity after 4-K irradiation with warm-up would be essential to obtain design data.

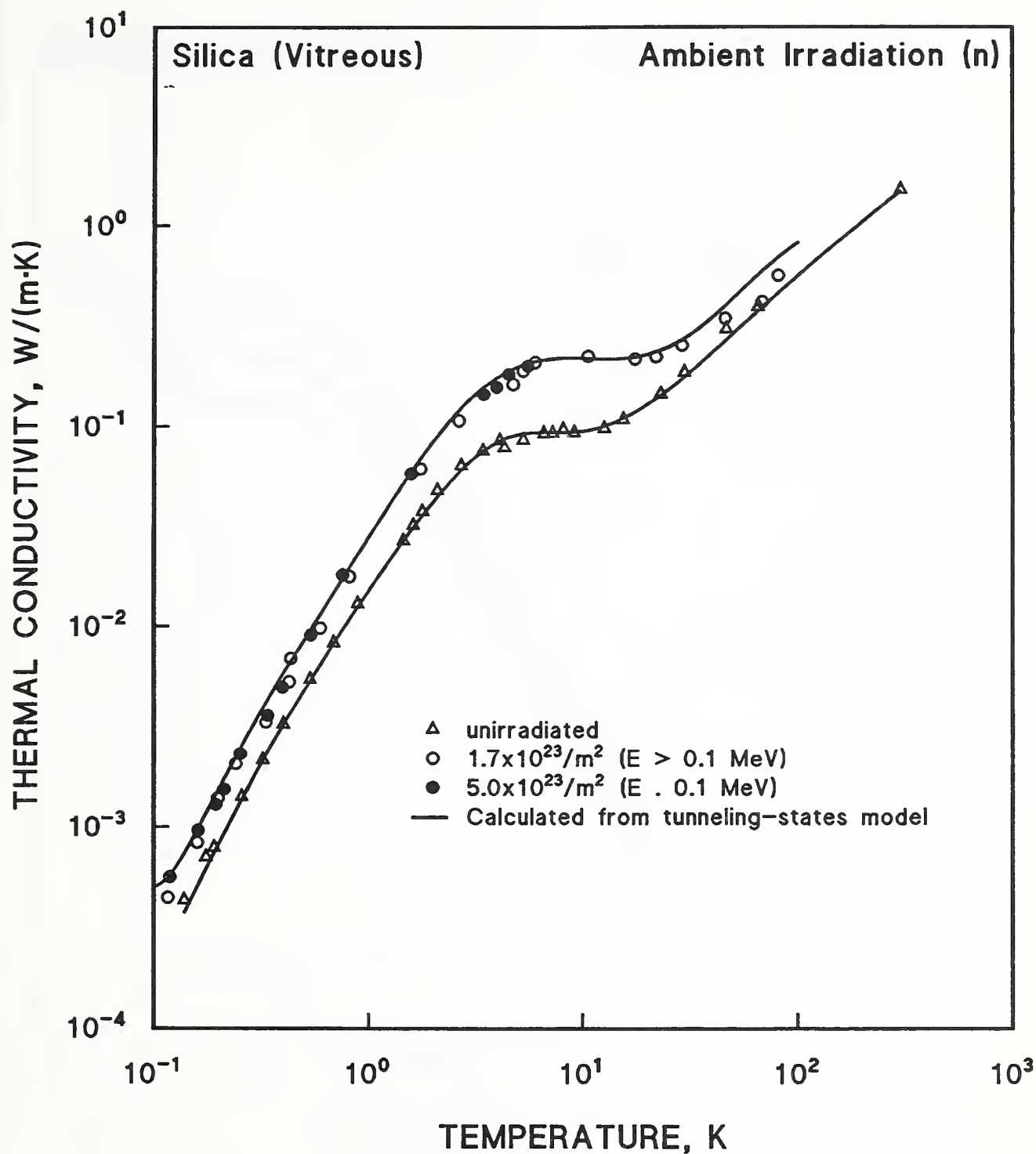


Figure 6.5.10. Thermal conductivity of vitreous SiO_2 after neutron irradiation. Solid lines are calculated from the tunneling states model. Data from Smith et al. [1978].

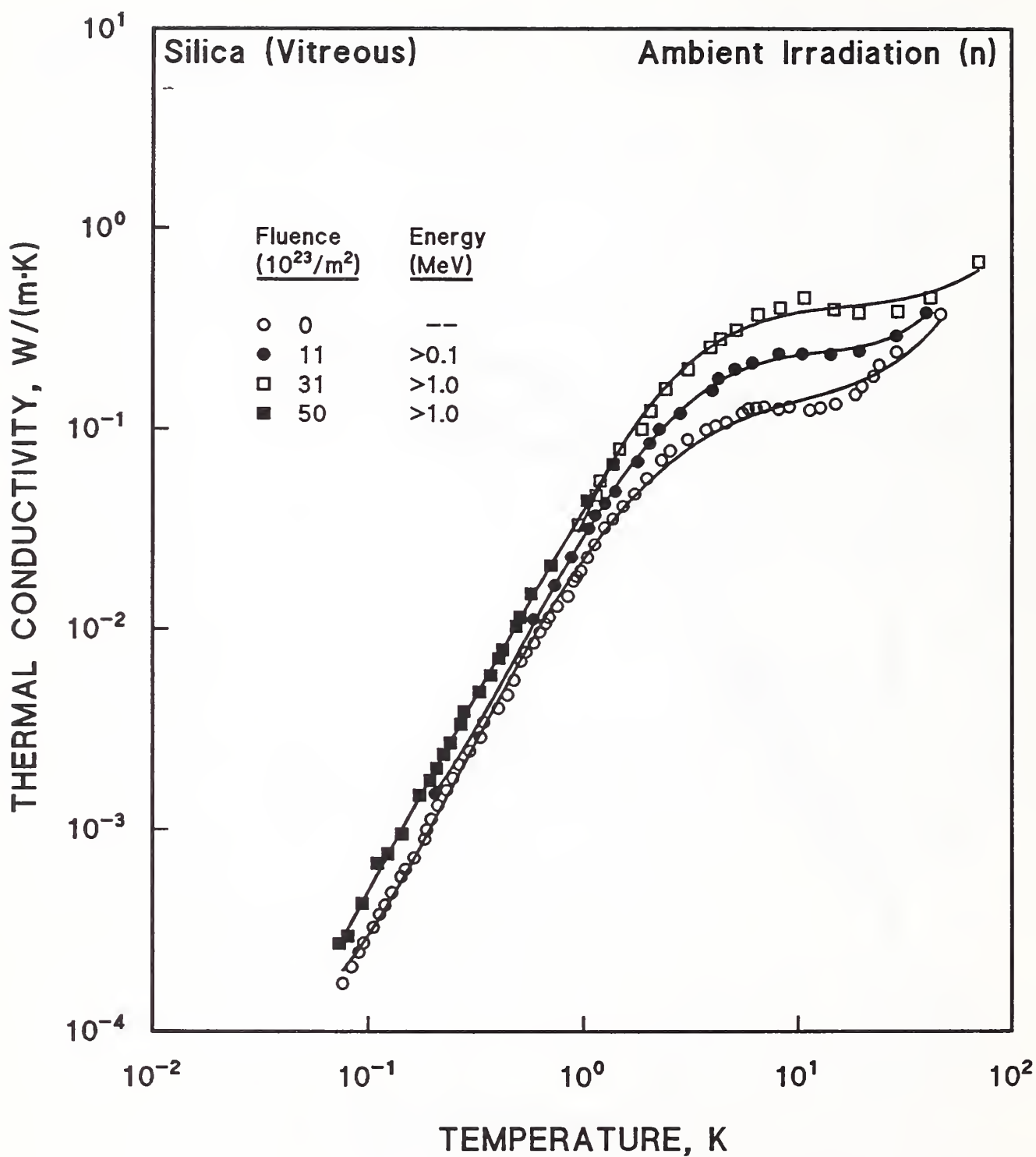


Figure 6.5.11. Thermal conductivity of vitreous SiO_2 after neutron irradiation. Data from Raychaudhuri and Pohl [1982].

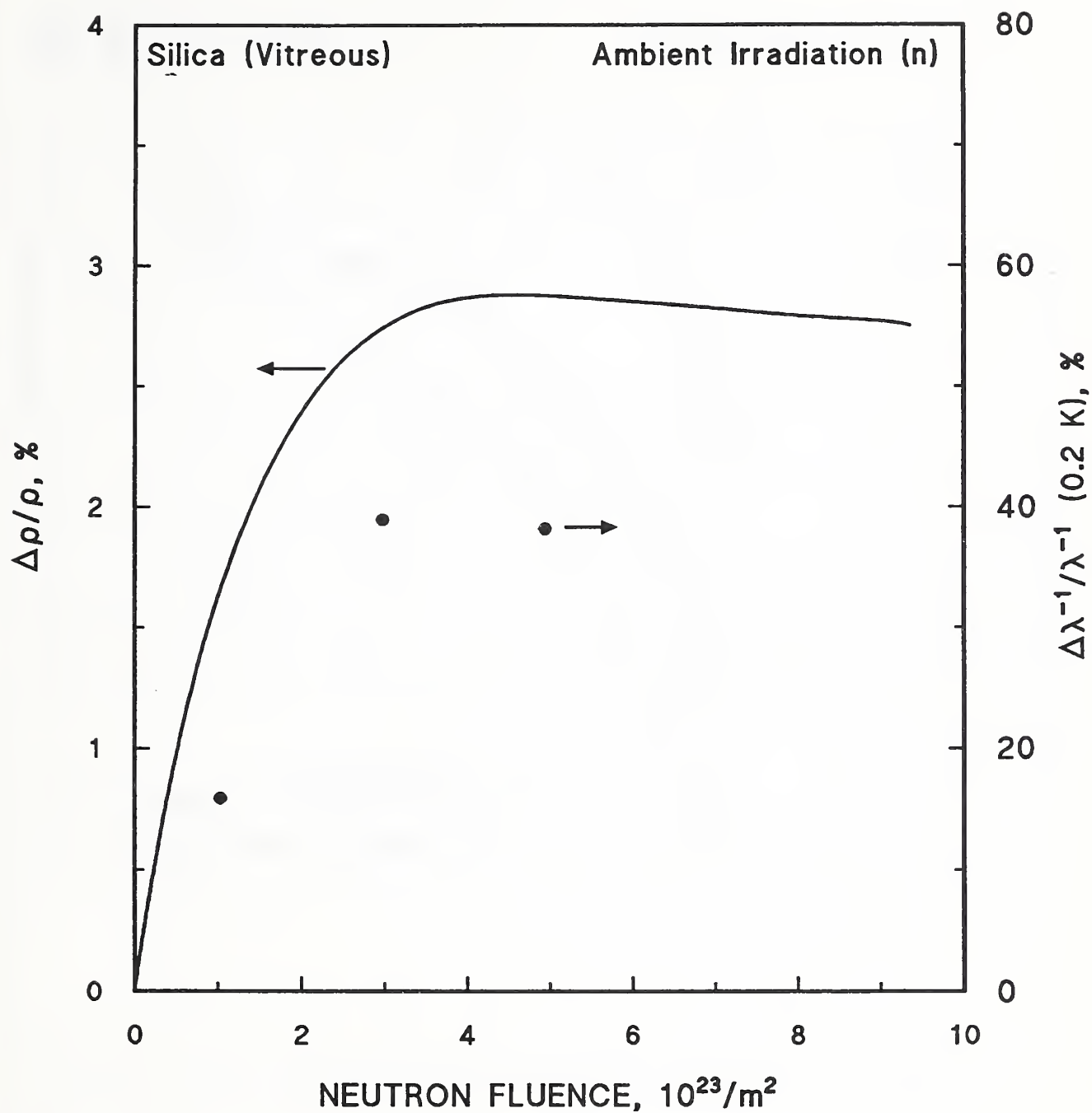


Figure 6.5.12. Relative change of density and thermal resistivity of vitreous SiO_2 with increasing neutron fluence. Data from Raychaudhuri and Pohl [1982].

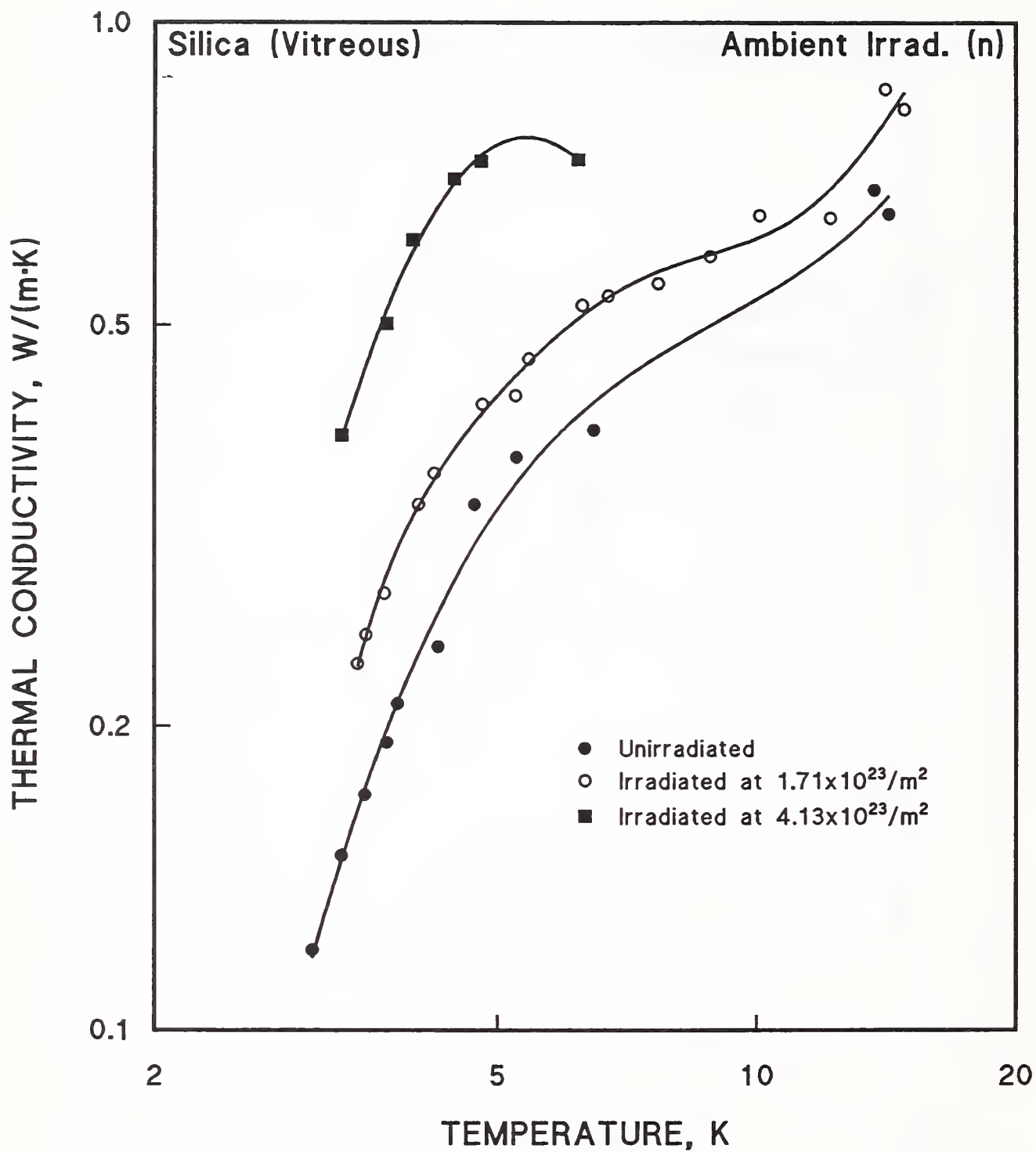


Figure 6.5.13. Thermal conductivity of vitreous SiO_2 after neutron irradiation. Data from Cohen [1958].

6.5.3. Thermal Expansion

At ambient temperature, Meyer and Gigon [citation, Wullaert et al., 1964] reported no significant changes in the coefficients of thermal expansion of both quartz and vitreous SiO_2 after a fast neutron fluence of $7 \times 10^{22}/\text{m}^2$ at 55°C . When Simon [1958] measured the thermal expansion of quartz after a higher fluence that produced vitrification, he found a value approximately equivalent to that of vitreous SiO_2 .

Some thermal expansion properties at cryogenic temperature of quartz and vitreous SiO_2 were measured after ambient-temperature neutron irradiation by White and Birch [1965]. Figure 6.5.14 shows the small increase in thermal expansion of quartz between 4 and 8 K after a neutron fluence of $10^{23}/\text{m}^2$ which decreased the density by only 0.5%. (A higher fluence of $5 \times 10^{23}/\text{m}^2$ cracked the quartz cylinder.) Between 10 and 20 K, the thermal expansion was increased by ~10%, from 20 to 25 K, by only 5%, and at 293 K, by only 1.4%. Perhaps, this is an example of the greater effect of radiation upon cryogenic properties than upon ambient-temperature properties.

In contrast to quartz, the thermal expansion coefficient of vitreous SiO_2 , which is negative below ~200 K, is 2 to 4 times smaller (in magnitude) after irradiation, as shown in Figure 6.5.15. But, again, the effect of radiation on the thermal expansion appears to decrease as the temperature increases.

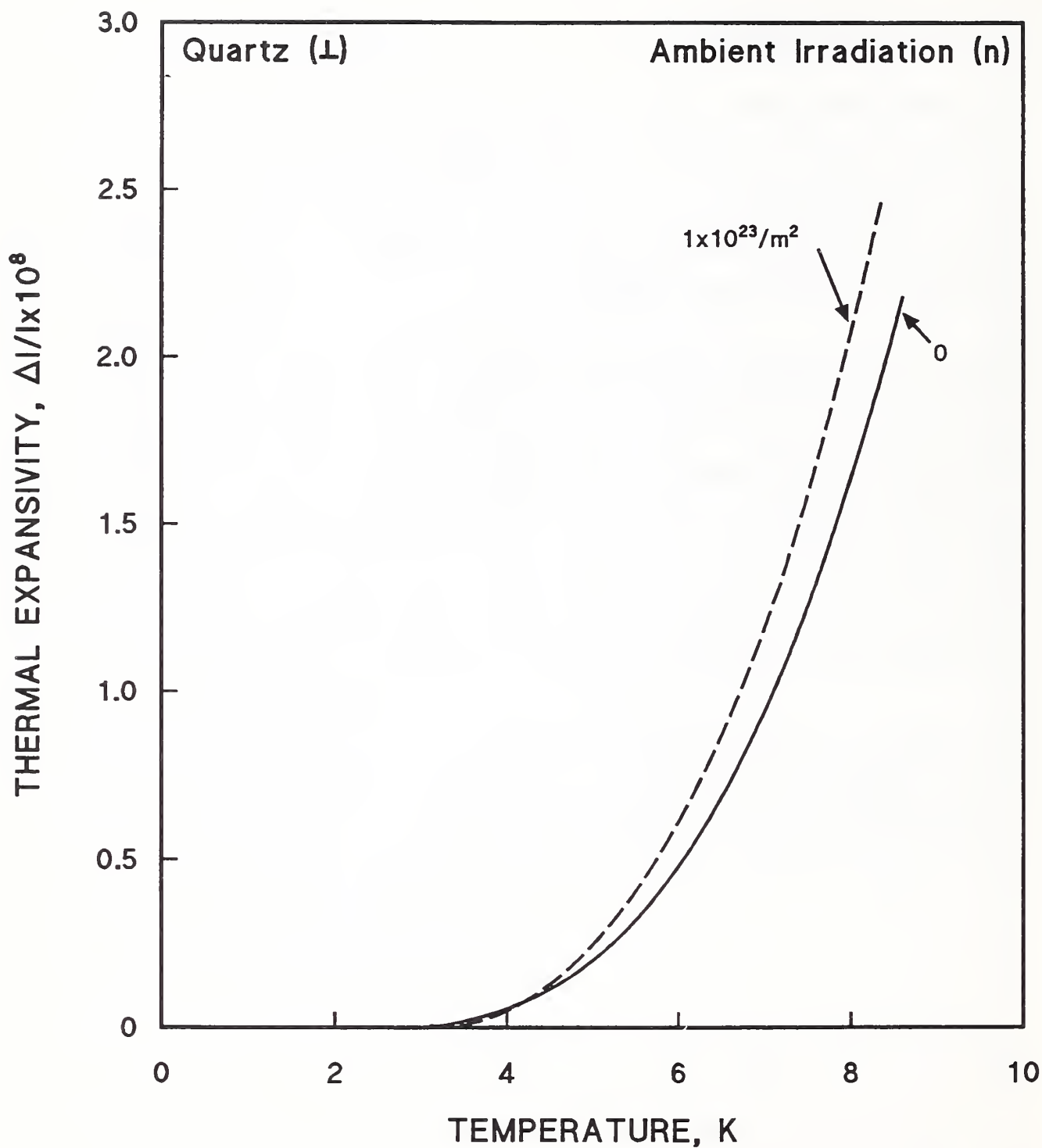


Figure 6.5.14. Linear thermal expansion per unit length of quartz, before and after an ambient-temperature neutron fluence of $10^{23}/\text{m}^2$. The cylinder axis was normal to the optic axis. Data from White and Birch [1965].

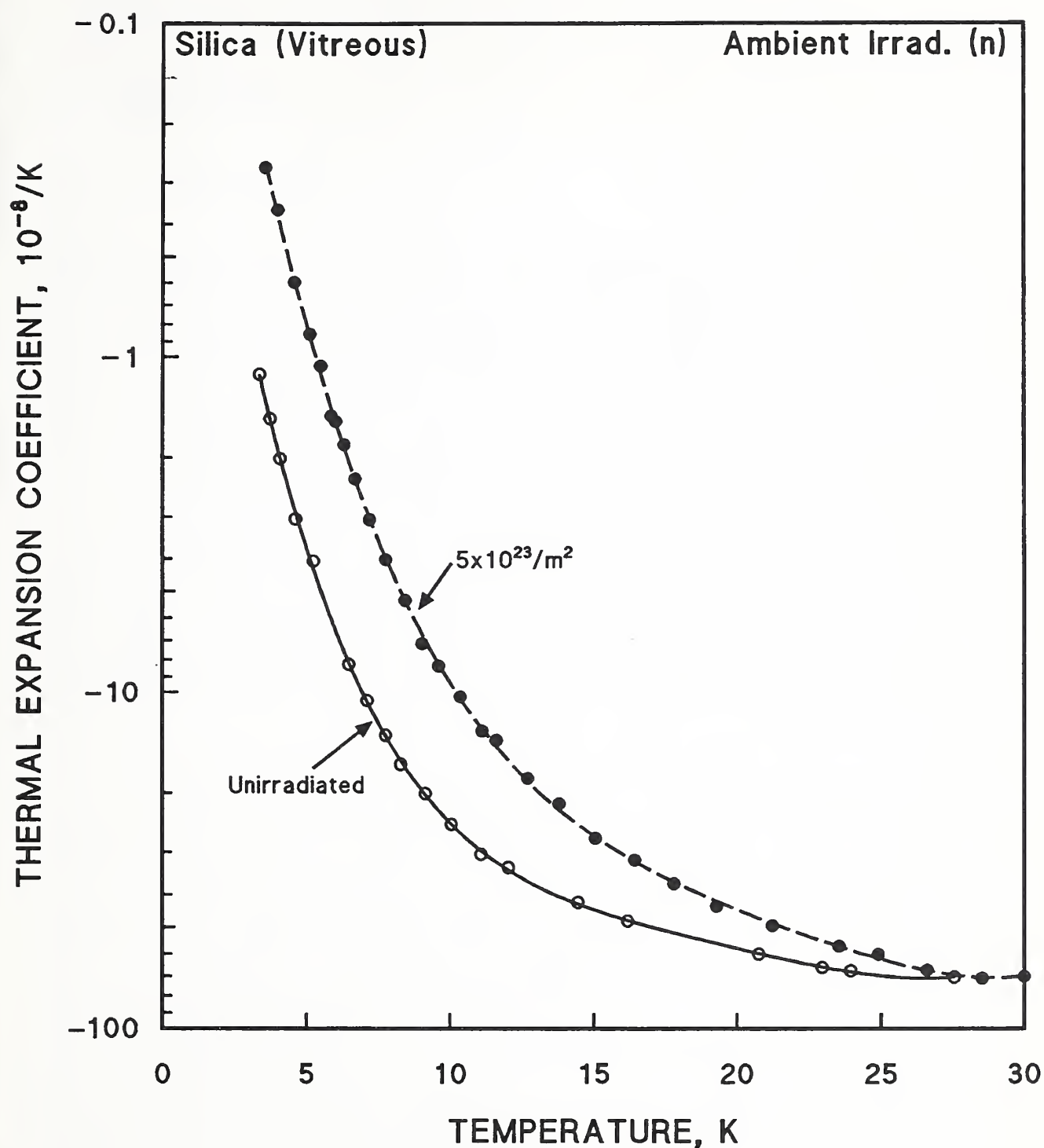


Figure 6.5.15. Thermal expansion coefficient of vitreous SiO_2 , before and after an ambient-temperature neutron fluence of $5 \times 10^{23}/m^2$. Data from White and Birch [1965].

7. LOW TEMPERATURE IRRADIATION OF SPINEL

7.1. DEFECT DENSITY

7.1.1. Frenkel Defects

Optical band absorption has been the usual method of measuring the density of Frenkel defects of insulators after irradiation. Perhaps because the identification of absorption bands with trapped electron defect centers has been less certain for MgAl_2O_4 than for Al_2O_3 and MgO [Crawford, 1984], there are fewer studies in the literature. A careful investigation that identified the bands associated with the F^+ center (one electron trapped at an O-ion vacancy) and the F center (two electrons trapped at an O-ion vacancy) did not appear until 1980 [Summers et al., 1980]. (However, the 5.3-eV band was associated by Bunch [1977a] with O displacement on the basis of an energy relationship with other oxides.) Another complication is that additional optical absorption bands are associated with impurity effects produced by the ionizing radiation that accompanies displacive radiation [Cain et al., 1988]. Summers et al. carried out their study using specimens of low Fe content of 76 or 20 ppm.

These authors then used the 5.3-eV absorption band identified with the F center as an index of the O^{2-} displacement process to determine the threshold energy for creating O^{2-} vacancies by electron ion irradiation. Electron irradiation was carried out at 77 K as well as at ambient temperature, but the specimens were warmed to ambient temperature before the optical absorption spectrum was measured. The threshold energy obtained at 77 K was 325 keV (Figure 7.1.1a), which gives an $E_d(0)$ of 59 eV [Equation (1.5)]. The use of Smakula's equation [Equation (2.1)] indicated that about 30 incident electrons of 0.5 MeV energy produced one O vacancy at 77 K. At the same electron energy at 300 K, the rate of defect production was at least a factor of 6 lower. The results for the threshold at 300 K were also different (Figure 7.1.1b), giving an apparent E_d of 130 eV. Summers et al. explained the difference with the 77-K value by noting that what is measured by the threshold is not the individual displacement event, but a stable damage complex, owing to the interval between irradiation and measurement. The displaced O^{2-} is expected to immediately lose one electron and to become O^- , which is much smaller and moves

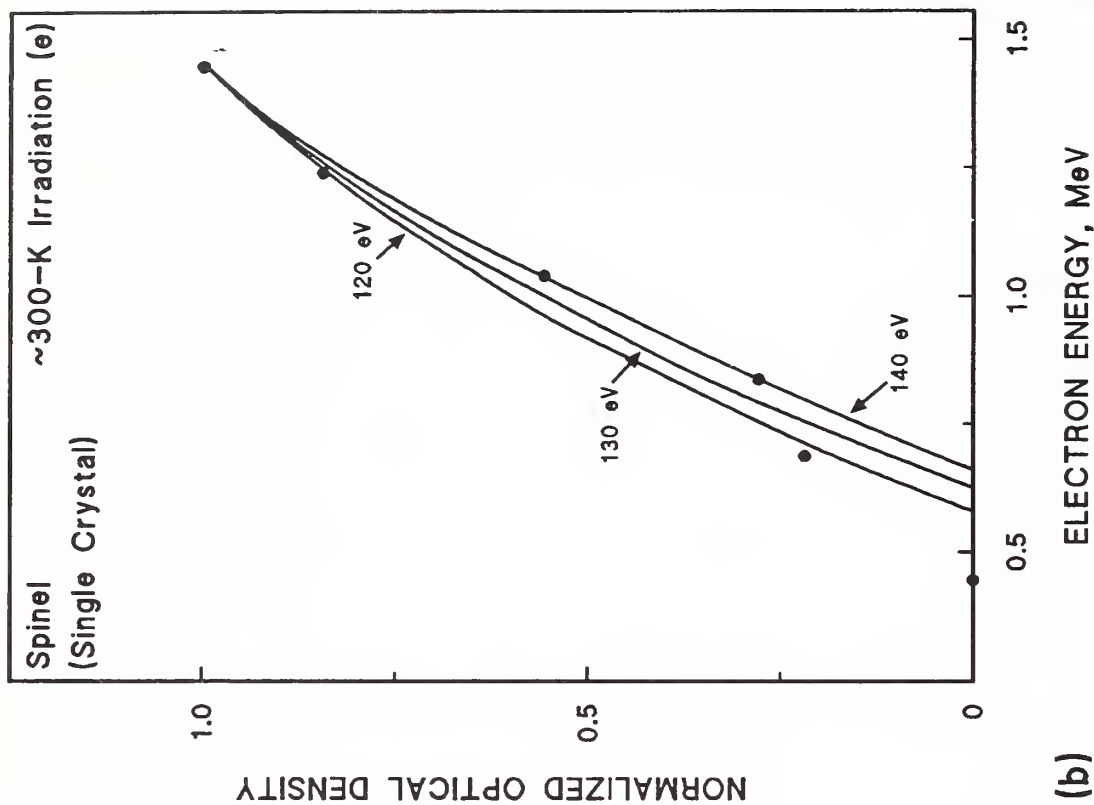
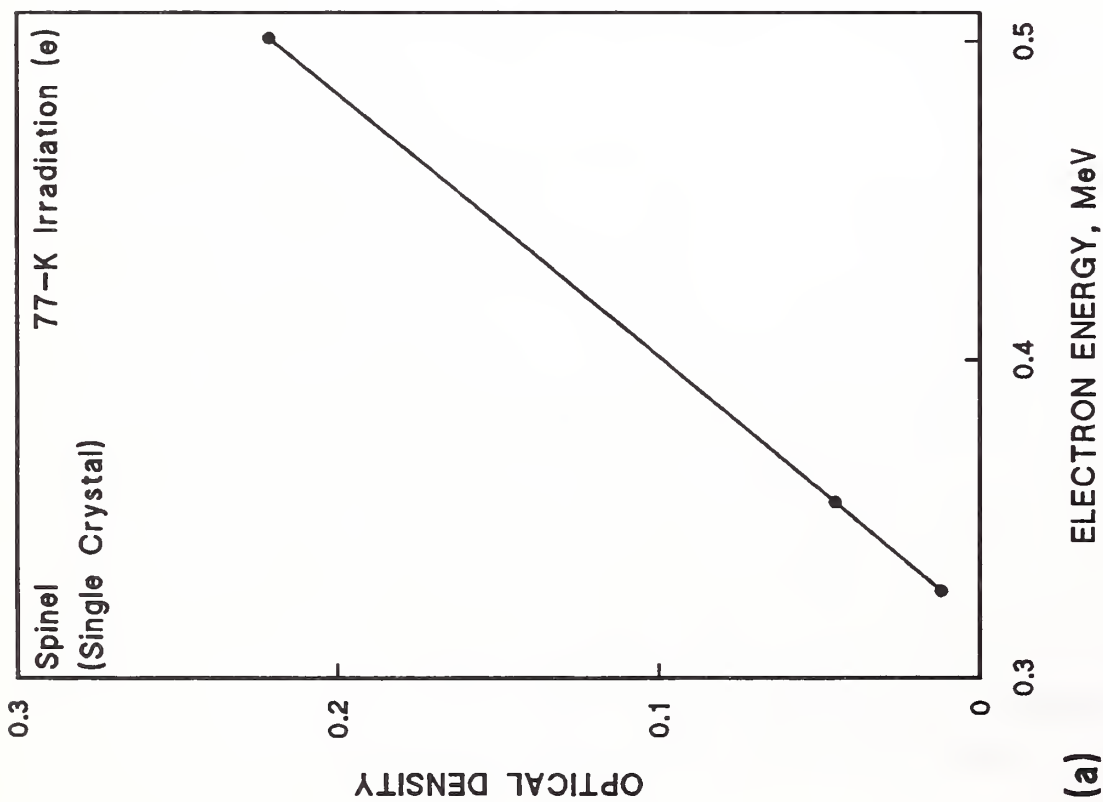


Figure 7.1.1. Optical density at the 5.3-eV (235-nm) absorption peak as a function of incident electron energy measured at ~300 K, after (a) 77-K or (b) ~300-K irradiation. Corrected for thickness losses. Data from Summers et al. [1980].

easily through the lattice, so its probability of recombination with an interstitial is quite large. Thus, the creation of stable O vacancies requires the trapping of corresponding interstitials. This trapping would occur more easily at 77 K. The E_d of 130 eV is much higher than those of most other ceramics. Parker et al. [1985] noted that ceramics with a complex structure and larger unit cell probably were more resistant to radiation effects because it is more difficult to nucleate defect aggregates within them.

As described above in §§1.2.1 and 2.1.1, Dell and Goland [1981] published calculated values of the displacement cross section for several multicomponent nonmetals. Their results for Al_2O_3 and MgAl_2O_4 were given above in Table 1.2.3. For comparable neutron spectra, the σ_{dis} for MgAl_2O_4 are lower by a factor of about 13 for Al and by a factor of about 2 for O than those for Al_2O_3 . However, the MgAl_2O_4 calculations are based upon E_d values of 86, 77, and 130 eV for Mg, Al, and O, respectively. Because the value chosen for E_d enters into the calculation only as E_d^{-1} , the displacement cross sections of Dell and Goland can be easily recalculated for different value of E_d . Since their value of $E_d(\text{Al})$ in Al_2O_3 was 18 eV, but was 77 eV in MgAl_2O_4 , it is possible that additional measurements of $E_d(\text{Al})$ could lower the apparent favorable factor of 13 for Al displacement in MgAl_2O_4 as compared to Al_2O_3 . In fact, the 86 eV value for $E_d(\text{Mg})$ and the 77 eV value for $E_d(\text{Al})$ are based upon one threshold energy published in an abstract used by Dell and Goland [Crawford et al., 1978]. The abstract was published before the defect responsible for the threshold energy was identified as an O vacancy [Summers et al., 1980], and so gave only potential E_d values for Mg and Al. Strictly speaking, the E_d values published in this abstract for Mg and Al have no foundation, although they have been widely quoted in the literature. More recently, Zinkle [1989] noted that values of 60 eV for Mg and 20 eV for Al were suggested by Parker [1984, cited in Zinkle, 1989]. Furthermore, since Dell and Goland chose the ambient-temperature $E_d(\text{O})$ value of 130 eV rather than the 77-K value of 59 eV discussed above, their σ_{dis} for O at 4 K should probably be at least a factor of 2 higher. The $E_d(\text{O})$ in Al_2O_3 did not appear to be lower at 77 K than at ambient temperature (§2.1.1, Pells and Phillips [1979a]). If the EBR II spectrum of Dell and Goland is chosen as approximately representative of the ITER TF magnet spectrum, but the $E_d(\text{O})$ determined at 77 K is used, then the fluence of $10^{22}/\text{m}^2$ times the displacement cross sections for Mg, Al, and O

gives 4.38, 9.95, and 23.5×10^{-5} dpa, respectively, considerably below the dpas for Al_2O_3 determined by the same procedure (§2.1.1). However, since none of the E_d values have been determined at 4 K, the σ_{dis} and dpas at 4 K may actually be about the same for Al_2O_3 and MgAl_2O_4 , and their apparent inequality in the paper by Dell and Goland should not be used to discriminate between the two ceramics at present.

The change in optical absorption of MgAl_2O_4 after cryogenic irradiation, presumably at ~ 4 K, in the Low Temperature Neutron Irradiation Facility of the Oak Ridge National Laboratory was reported by Cain et al. [1988]. The results, which apply to 0 displacements, are shown in Figure 7.1.2. However, the parameters to use in the Smakula equation [Equation (2.1)] were not given, and, apparently, the absorption was measured at ambient temperature, allowing recovery of a major portion of the defects produced at the cryogenic temperature. Therefore, these data do not provide an estimate of the 4-K dpa. Although the authors state that saturation began above $10^{21}/\text{m}^2$, the same considerations of recovery apply to this conclusion, so the fluence at which saturation begins in MgAl_2O_4 at 4 K is also unknown.

Optical absorption and other techniques have been used to study MgAl_2O_4 after ionizing radiation (X-ray or γ) [Ibarra et al., 1991a,b]. In this case, the unirradiated material has a large number of lattice defects, owing to the extensive cation disorder and nonstoichiometry, and the ionizing radiation only induces changes in the electric-charge state of preexisting defects. No evidence has been presented for displacement damage in MgAl_2O_4 as a result of ionizing radiation, as was reported for SiO_2 (§6.1). However, this possibility is discussed by Zinkle [1991]. The intensities of various ionization phenomena were higher by a factor of about 2.5 when irradiation and detection took place at 90 K rather than at 300 K [Ibarra et al., 1991a].

7.1.2. Dislocation Loops; Defect Aggregates

Buckley [1986] irradiated polycrystalline MgAl_2O_4 with intense 1-MeV electron beams at temperatures from 880 to 1320 K, but did not observe any dislocation loops with TEM. The doses exceeded 10 and 30 dpa on the respective cation and anion sublattices in the range of 800 to 1300 K. In contrast, both Al_2O_3 and

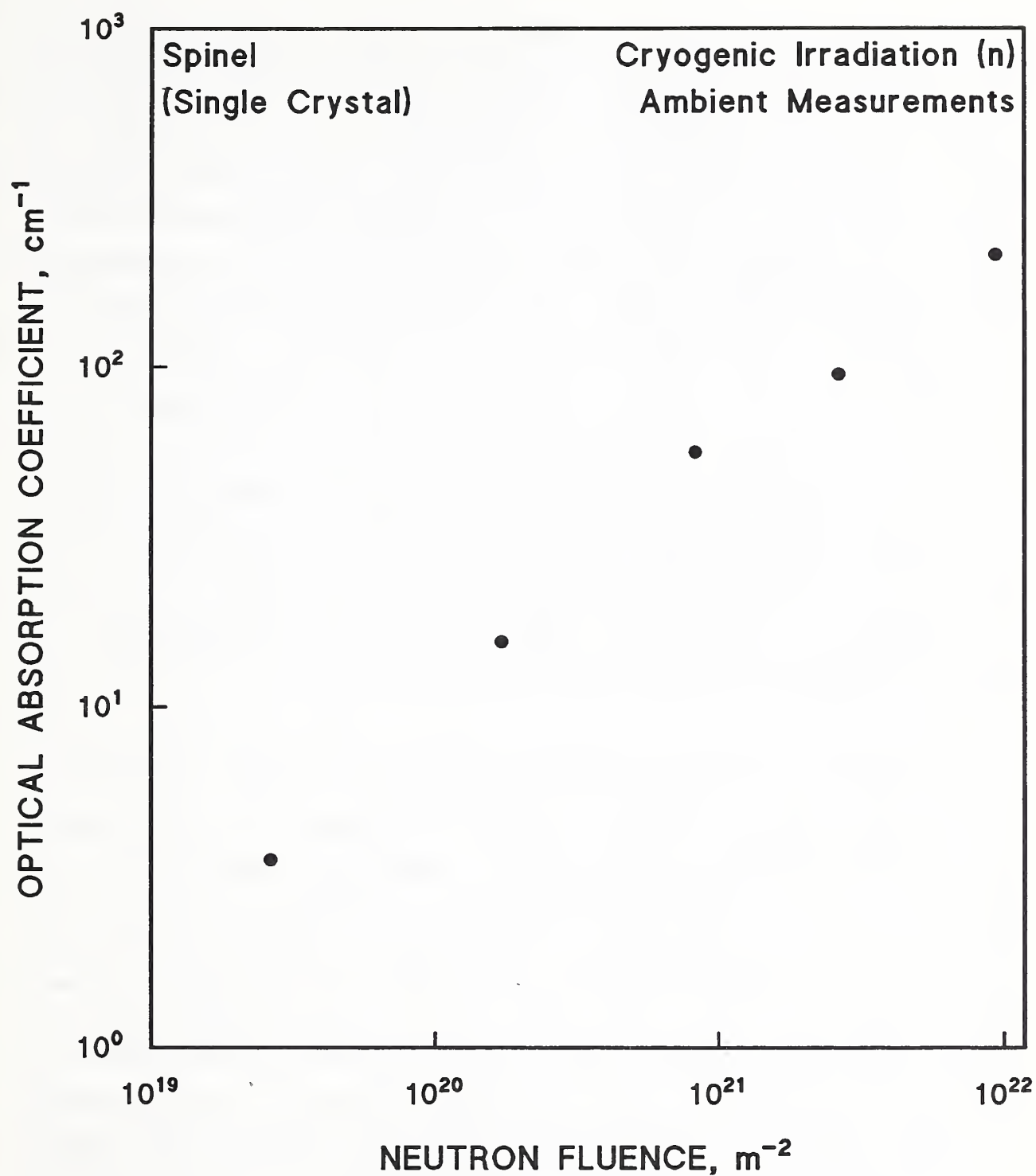


Figure 7.1.2. The magnitude of the peak optical absorption coefficient of the F center (at 5.3 eV) after cryogenic neutron irradiation of MgAl_2O_4 . Data from Cain et al. [1988].

MgO were reported to nucleate dislocation loops easily at these doses. Visible structural damage in MgAl_2O_4 was observed above $\sim 10^{26}$ electrons/ m^2 , more quickly at the higher temperatures. Various structures were described by Buckley, but these observations apparently were made only between 800 and 1300 K. Implanted He (1000 ppm) did not nucleate dislocations in this polycrystalline material. Although previous measurements at high temperatures on single-crystal MgAl_2O_4 had indicated resistance to voids, it was conceivable that He gas bubbles derived from (n,α) reactions in grain boundary impurities might allow nucleation in polycrystalline material. However, Parker [citation in Buckley and Shaibani, 1987] did observe evolution of dislocation loops without void production in hyperstoichiometric crystals using the same model of electron microscope. Buckley and Shaibani therefore ascribed the disparity in results to differences in material composition. Furthermore, neutron irradiation also produced dislocation loops, but observations again were made above ambient temperature (680 and 815 K) [Parker et al., 1985]. When Fukushima et al. [1990] irradiated nonstoichiometric spinel to a fluence of $8.3 \times 10^{22}/\text{m}^2$ ($E > 1$ MeV) at 373 K, TEM revealed no evidence of aggregate damage. The $\text{Al}_2\text{O}_3/\text{MgO}$ ratio of these specimens was 3.

An investigation of light ion irradiation damage in Al_2O_3 , MgO, and MgAl_2O_4 by Zinkle [1991] has illuminated the differences in response of these three ceramic oxides. Spinel was found to have a suppression of dislocation loop formation compared to that of Al_2O_3 ; MgO was intermediate between the two. The difference was traced to the ratio of ionizing to displacive energy loss. This ratio evidently must be less than ~ 10 to produce resolvable defect aggregates in MgAl_2O_4 at 650°C , but defects will be produced in Al_2O_3 for ionizing-to-displacive dose ratios of up to ~ 1000 . The dose ratio in MgO is similar to that of Al_2O_3 [Zinkle, 1993b]. Since this dose ratio is ~ 10 to 20 during neutron irradiation of ceramics, this observation explains the relative radiation resistance of MgAl_2O_4 compared to Al_2O_3 . Zinkle lists various possible effects of ionizing radiation upon displacive damage processes; this area is not well understood, but significant effects have been demonstrated. Zinkle also notes that the critical ratio of ionizing to displacive energy losses for producing defect aggregates depends strongly upon the irradiation temperature. For example, irradiation of Al_2O_3 with $^3\text{He}^+$ ions at ambient temperature did not produce observable damage, although dislocation loops were found at 800°C .

Therefore, the distinction in radiation resistance between MgAl_2O_4 , MgO , and Al_2O_3 may be primarily a high-temperature phenomenon that does not necessarily apply to 4-K irradiations. In fact, Zinkle [1989] noted that small dislocation loops (~ 1 to 10 nm) were observed in a nonirradiated MgAl_2O_4 that was prepared by 6-keV Ar ion milling at ambient temperature and even at 77 K. In contrast to this observation, Cain et al. [1988] found "little evidence for the formation of optical bands attributable to cluster defects from neutron irradiation." Cain et al. irradiated MgAl_2O_4 specimens cryogenically, but, evidently, optical observations were made subsequently at ambient temperature.

7.2. CHANGE IN VOLUME

The change of volume of single-crystal MgAl_2O_4 after irradiation with 14-MeV neutrons at 50°C (323 K) was measured by Tanimura et al. [1987]. The results were shown in Figure 2.2.2 (§2.2, above), since single-crystal Al_2O_3 was also irradiated. A volume change of about 0.003% was observed at a fluence of about $2.5 \times 10^{21}/\text{m}^2$. This volume change in MgAl_2O_4 was found to be smaller than that of Al_2O_3 by a factor of about 3.5. Furthermore, since the volume change is isotropic, because MgAl_2O_4 is cubic, there is less tendency for grain boundary decohesion in irradiated polycrystalline material.

The swelling of polycrystalline MgAl_2O_4 was compared with that of polycrystalline MgO by Hurley et al. [1981]. In this case, the irradiation temperature was somewhat higher, 430 ± 5 K, and one measurement was made after a much higher fast neutron fission fluence of $2.1 \times 10^{26}/\text{m}^2$ ($E > 0.2$ MeV). A swelling of 0.8% was reported, compared to 2.6 to 3.0% for MgO .

The measurements of Coghlan et al. [1986] span a range of fluences between these extremes of 10^{21} and $10^{26}/\text{m}^2$, but do not appear to agree exactly with either result. As Figure 7.2.1 indicates, Coghlan et al. found a linear fluence/swelling relationship below $2 \times 10^{22}/\text{m}^2$, which would predict about 0.004% volume swelling at a fission-neutron fluence of $\sim 2 \times 10^{21}/\text{m}^2$, and perhaps 0.008% for a 14-MeV fluence, whereas 0.003% was reported by Tanimura et al. However, the latter value was measured during the 14-MeV irradiation, and Coghlan et al. reported that their MgAl_2O_4 crystals continued to swell at ambient temperature for several months after irradiation. Gamma radiation was

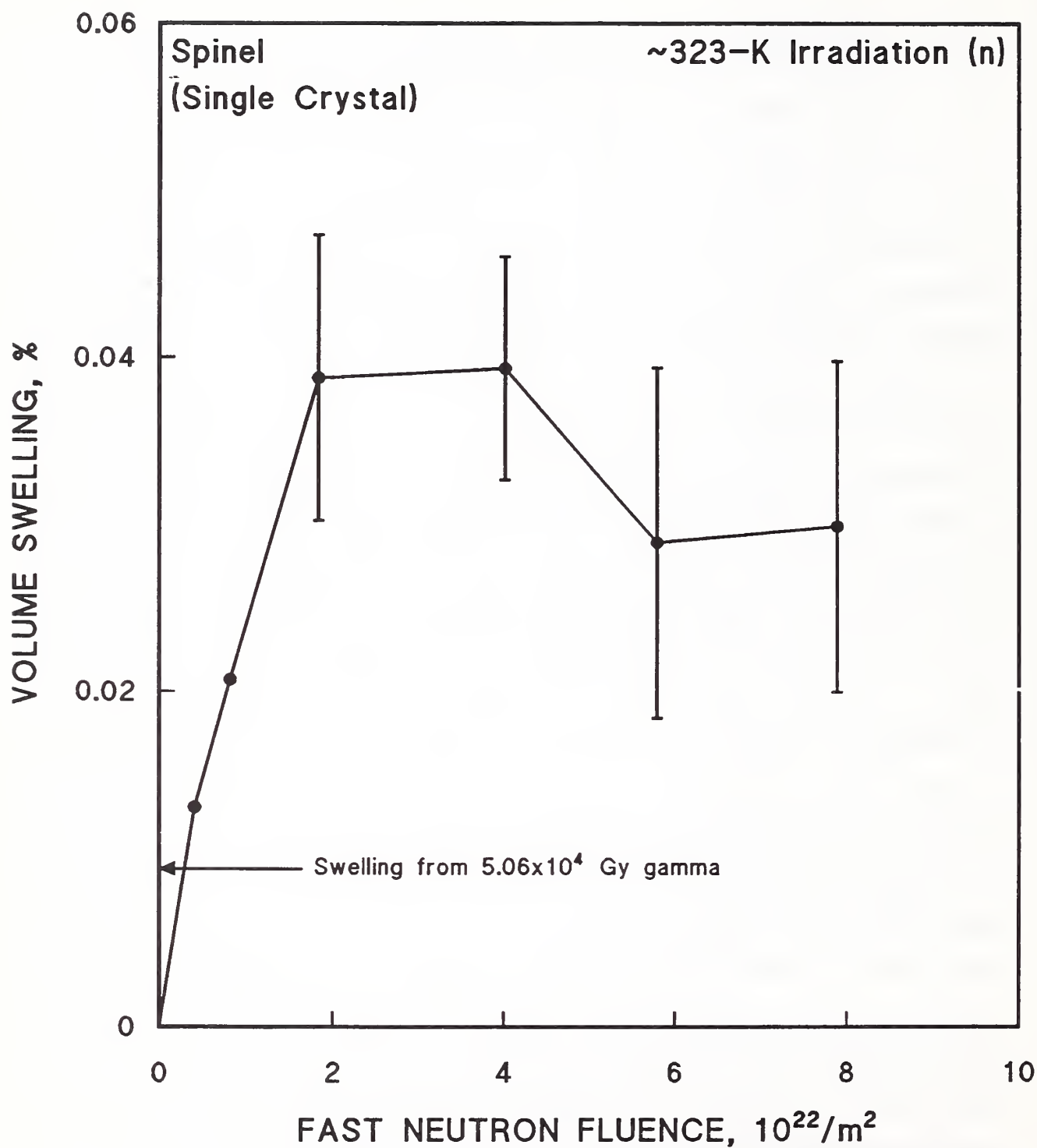


Figure 7.2.1. Swelling of single-crystal MgAl_2O_4 after neutron irradiation. Data from Coghlan et al. [1986].

also present in the irradiation by Coghlan et al., and, according to Tanimura et al., may have also contributed to swelling. Nevertheless, this disparity in results is surprising, since for both Al_2O_3 and MgO , at least twice as many vacancies are reported to be created by 14-MeV neutrons as by fission neutrons of the same fluence (§§2.1, 4.1). The saturation shown in Figure 7.2.1 is not in accord with the higher-fluence results of Hurley et al. Perhaps, the saturation reported by Tanimura et al. is temporary, since otherwise the volume swelling of 0.8% at a higher fluence reported by Hurley et al. would not be possible.

At fluences above $2 \times 10^{22}/\text{m}^2$ ($E > 0.1$ MeV), Coghlan et al. observed saturation of the volume change, at 0.04%, whereas Hurley et al. had found a swelling of 0.8% at a fluence of $2.1 \times 10^{26}/\text{m}^2$. However, Coghlan et al. suggested that their apparent saturation was temporary, and that swelling would continue if voids or other volume-producing defect clusters formed at higher fluences. The saturation volume change shown in Figure 7.2.1 is consistent with that expected from the dpa of about 2×10^{-3} calculated with lower E_d values than those used by Dell and Goland, a swelling contribution of one atomic volume per defect pair, and a fraction of 0.28 of defects surviving recombination. The figure also shows a small amount of swelling arising from a γ irradiation to 5×10^4 Gy carried out separately. An additional observation of interest was the continued growth of swelling during storage, after the irradiation was ended. Figure 7.2.2 shows this result. One explanation given for the continued swelling was the diffusion and clustering of interstitial defects in a manner that increased the total volume of the crystal.

The volume expansion produced in nonstoichiometric spinel ($\text{Al}_2\text{O}_3/\text{MgO} = 3$) after a fluence of $8.3 \times 10^{22}/\text{m}^2$ ($E > 1$ MeV) at 373 K was 0.195% [Fukushima et al., 1990]. Comparing this with the results of Coghlan et al. above seems to indicate that the use of nonstoichiometric spinel in fusion reactors is not advantageous.

At an irradiation temperature of 660 K, Tucker et al. [1986] observed a compaction of 0.316% in MgAl_2O_4 after a fast neutron fluence of about $2 \times 10^{26}/\text{m}^2$ ($E > 0.1$ MeV). Other investigators have also observed compaction at high temperatures [citations in Tucker et al., 1986]. Jones et al. [1985] used

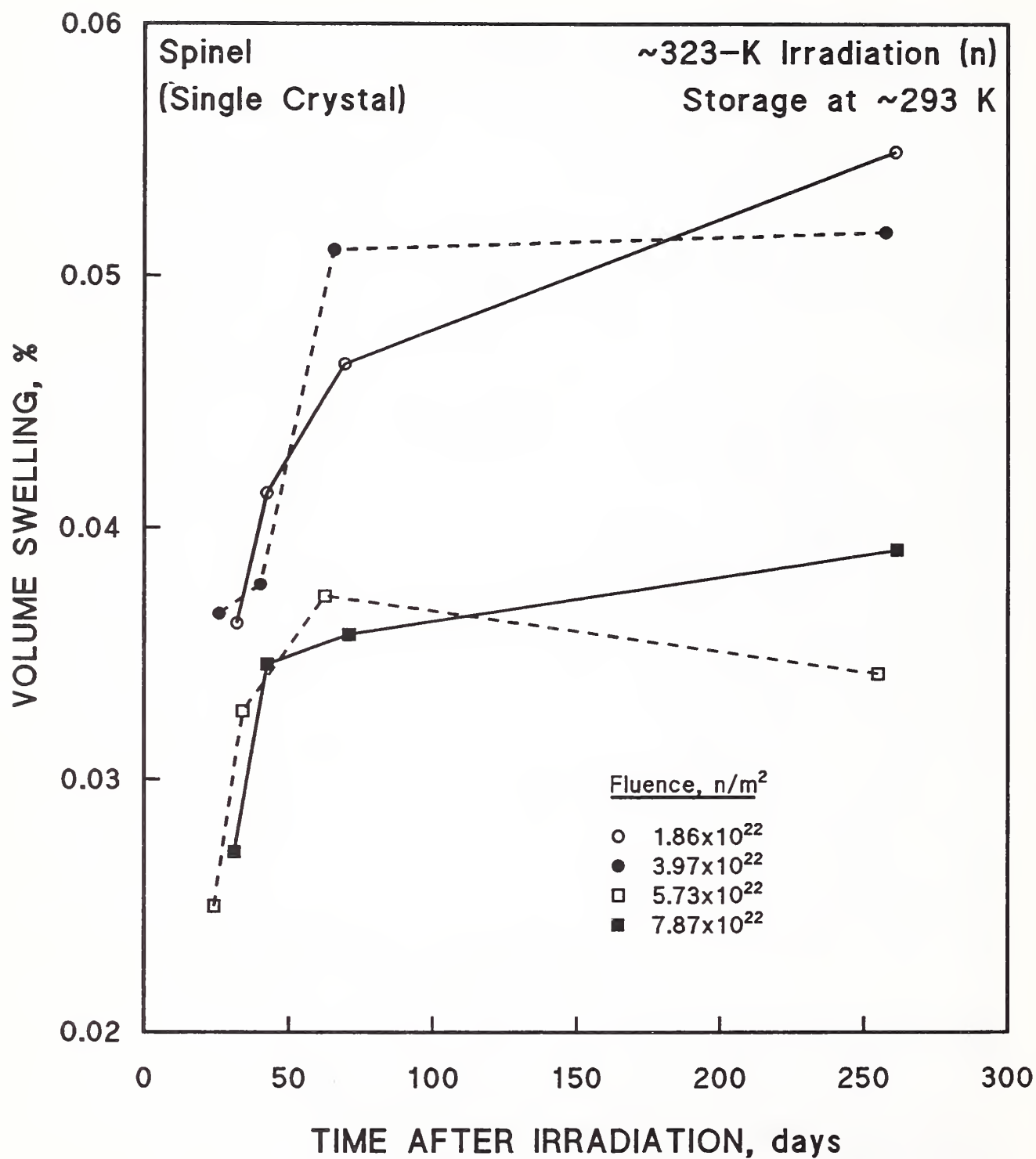


Figure 7.2.2. Swelling of single-crystal $MgAl_2O_4$, as a function of storage time, after neutron irradiation. Data from Coghlan et al. [1986].

positron annihilation spectroscopy to probe neutron irradiation damage in both Al_2O_3 and MgAl_2O_4 at high temperatures. They found that a temperature of 550°C served to reduce the concentration of inherent, grown-in, vacancy-type defects, probably by recombination at grain boundaries and grain growth. This phenomenon alone was not sufficient to explain the contraction, but Jones et al. also suggested that interstitial dislocation loops might predominate over vacancy generation, which would be expected to produce volume swelling. The reasons for the volume compaction in MgAl_2O_4 at high temperatures are not yet completely understood, but, presumably, this anomaly is irrelevant for ITER TF magnet conditions. However, since this compaction phenomenon is partly responsible for the low swelling and high radiation resistance attributed to MgAl_2O_4 , caution should be exercised in applying high temperature radiation results to 4-K conditions.

7.3. AMORPHIZATION

The amount of displacement damage required to produce amorphization is somewhat dependent upon the type of chemical bonding (§1.5). Burnett and Page [1986] suggested that for the strongly ionic bonding of MgAl_2O_4 , damage levels of ~ 5 keV/atom would be necessary to induce amorphization. To test this suggestion, Zinkle and Kojima [1990] used 2-MeV Al or 2.4-MeV Mg ions to irradiate polycrystalline MgAl_2O_4 at 300 K to peak damage levels up to 8 keV/atom ($3 \times 10^{21} \text{ Mg}^+/\text{m}^2$). The host ion species was chosen to minimize chemical effects associated with ion implantation. Although the peak damage level was very high [8 keV/atom \approx 80 dpa; Equations (1.2 and (1.4)], TEM examination of the specimens indicated that amorphization did not occur. Dislocation loops and dislocation tangles were observed, and Zinkle and Kojima suggested that the presence of a network of dislocation lines inhibited the buildup of a critical concentration of point defects necessary of amorphization, because the dislocations absorbed point defects produced by displacement damage. The authors also suggested that failure to observe dislocation networks in MgAl_2O_4 foils irradiated in a HVEM at elevated temperatures [e.g., Buckley, 1986; Buckley and Shaibani, 1987] could be due to the absence of a layer thick enough to allow nucleation of growth of interstitial clusters. Surprisingly, Zinkle and Kojima did not suggest that their failure to observe amorphization was simply due to recovery of damage at 300 K from the host ion irradiation,

although they noted that McHargue et al. [1986] had been able to induce amorphization in Al_2O_3 at 300 K only with certain foreign ion species that stabilized the damage states. Host ion amorphization was achieved at 77 K in Al_2O_3 with fluences $\sim 10^{20}/\text{m}^2$, since recovery was suppressed.

Although host ion amorphization was not observed under the conditions of 8 keV/atom in polycrystalline MgAl_2O_4 , amorphization was observed at a lower damage level of about 3 keV/atom ($10^{21} \text{ Ar}^+/\text{m}^2$, 100-keV ions) when the MgAl_2O_4 was in a plasma-sprayed form [Iwamoto et al., 1986]. It is unlikely that the use of a foreign ion species was solely responsible for the amorphization of the plasma sprayed MgAl_2O_4 , since single-crystal MgAl_2O_4 irradiated under the same conditions did not amorphize. Both RBS and XPS (X-ray photoelectron spectra) techniques were used to examine the ion-irradiated specimens. Plasma-sprayed Al_2O_3 amorphized at an Ar fluence above $10^{20}/\text{m}^2$, a lower dose than required for plasma-sprayed MgAl_2O_4 [Iwamoto et al., 1985a].

Another technique, TSEE (thermally stimulated exoelectron emission) was also used by this group to examine differences between single-crystal and plasma-sprayed MgAl_2O_4 [Iwamoto et al., 1985b]. This field emission technique is reviewed by Kawanishi [1985]. The intensities of the TSEE peaks in sprayed MgAl_2O_4 were weaker than those in single-crystal MgAl_2O_4 after Ar ion irradiation. This again indicated that the plasma-sprayed material was more easily amorphized than the single-crystal form. In this investigation, a comparison was also made between Ar-irradiated, single-crystal Al_2O_3 and single-crystal MgAl_2O_4 . The formation of an amorphous layer by Ar-ion irradiation was more difficult in MgAl_2O_4 than in Al_2O_3 . This finding is in accord with other results indicating lower volume expansion under irradiation of MgAl_2O_4 than of Al_2O_3 (Figure 2.2.2).

Buckley [1984] also reported severe structural damage in MgAl_2O_4 . He used a HVEM at temperatures from 900 to 1130 K. Three stages of damage were found: (1) dislocation loop nucleation and growth, followed by (2) precipitation of metallic Mg on the external surfaces of the specimen and gross shrinkage of the material manifested by microcracks, and finally, (3) metal precipitation within the bulk, coupled with nucleation and growth of gas bubbles, material dilation, and healing of microcracks. The damage was ascribed to charge

segregation associated with the ionizing radiation, which produced secondary electrons and δ rays (§1.2.2). Solid-state electrolysis then occurred, because the material had a significant ionic component of conductivity at high temperatures. Presumably, even though this is a charge-driven process, these phenomena would not occur under 4-K ionizing irradiation or during ambient-temperature warm-up, because the temperature-dependent ionic conductivity would be much lower than in Buckley's experiments. However, possible effects of ionizing radiation in ceramics have not been investigated at 4 K. The electron fluences in Buckley's investigations were in the range of 4 to $12 \times 10^{26}/\text{m}^2$.

In another investigation of amorphization, the cross section for metamict (noncrystalline) damage was determined for MgAl_2O_4 and a compound, pollucite ($\text{CsAlSi}_2\text{O}_6$), in which the crystal structure is much less closely packed [Vance et al., 1983]. The cross section for MgAl_2O_4 was lower by almost four orders of magnitude. The attenuation of crystalline Bragg X-ray diffraction intensities were used to derive the amount of amorphization, and, hence, the cross section. The X-ray attenuation results, shown in Figure 7.3.1, were obtained with 3-MeV Ar ions, with fluences up to $2 \times 10^{20}/\text{m}^2$. The highest fluences are not shown in the figure, but were used to derive the curves shown. Since another closely packed compound, magnetoplumbite, also was highly resistant to amorphization, Vance et al. concluded that such closely packed crystal structures conferred resistance, whereas more open crystal structures were more likely to become amorphous under irradiation.

7.4. MECHANICAL PROPERTIES

Both single-crystal and polycrystalline MgAl_2O_4 have exhibited significant increases in flexural strength after irradiation to fast neutron fluences of $2.2 \times 10^{26}/\text{m}^2$ at 680 and 815 K [Clinard et al., 1984]. Both irradiated and control strengths were measured in 4-point bending tests for Al_2O_3 and MgAl_2O_4 . The unirradiated flexural strength of MgAl_2O_4 was about half that of Al_2O_3 , but the strengths after this high temperature, high dose irradiation were similar. Because of the high temperatures and fluences, the applicability of the results to ITER TF magnet conditions is uncertain.

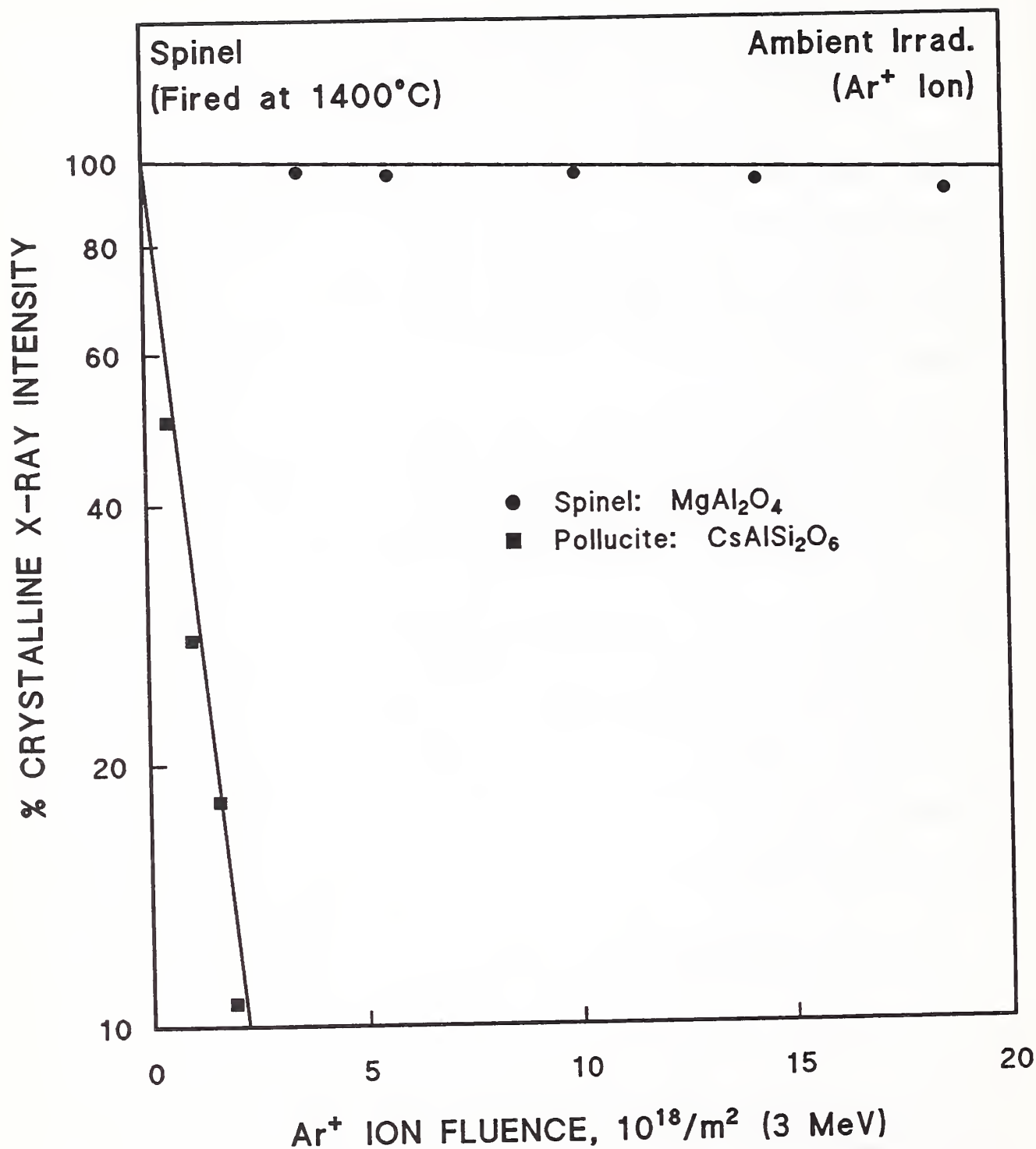


Figure 7.3.1. Percentage of crystalline X-ray diffraction peak intensity for MgAl₂O₄ and pollucite (CsAlSi₂O₆) vs. ion fluence. Data from Vance et al. [1983].

Tucker et al. [1986] also compared tensile strength of MgAl_2O_4 and Al_2O_3 at high temperatures (660 K) and fluences ($2 \times 10^{26}/\text{m}^2$; $E > 0.1$ MeV). In this case, cylindrical specimens were tested in diametral compression. The cylinders were loaded on their sides between parallel platens. Analysis shows that a uniform tensile stress is produced along the midplane parallel to the applied compressive load [citation, Tucker et al., 1986]. The magnitude of the tensile stress is controlled by the choice of padding material. In the 4-point bending tests of Clinard et al., the strengths of the Al_2O_3 specimens had improved after irradiation, but to a much lesser degree than those of the MgAl_2O_4 specimens. Only single-crystal Al_2O_3 was tested, however. In the diametral compression test, the strength of the polycrystalline Al_2O_3 actually decreased by 25.6%, while the strength of the polycrystalline MgAl_2O_4 increased by 24.4%, in accord with the previous results (Figure 7.4.1). Ten specimens were irradiated, but the standard deviations were not reported. A large swelling of 3.22% occurred in the Al_2O_3 specimens, while the MgAl_2O_4 densified slightly (0.316%). The large swelling, plus the significant anisotropy in Al_2O_3 (see, e.g., Figure 2.2.2) leads to stresses in polycrystalline Al_2O_3 and weakening and failure along grain boundaries. The failure mode was intergranular in irradiated specimens of Al_2O_3 , but was transgranular in MgAl_2O_4 . However, the tensile strength of Al_2O_3 after irradiation damage is still larger than that of MgAl_2O_4 .

There are several additional ambient-temperature measurements of mechanical properties, but, again, stresses were primarily tensile. The diametral compression test was carried out in both polycrystalline MgAl_2O_4 and MgO specimens after irradiation to a fast neutron fluence of $2.1 \times 10^{26}/\text{m}^2$ ($E > 0.2$ MeV) at 430 ± 5 K [Hurley et al., 1981]. At this lower temperature, as noted above (§7.2), MgAl_2O_4 swelled to 0.8%, but the two specimens of MgO swelled by 2.6 and 3.0%. The increases in tensile strength were 20% for MgAl_2O_4 and 12 and 24% for MgO . These results are shown in Figures 7.4.2 and 4.4.6. The initial tensile strength of MgO is considerably below that of MgAl_2O_4 . Thus, with regard to this test, MgAl_2O_4 performs better than both MgO and Al_2O_3 . In some very recent comparative 3-point bending tests discussed in §12.4.1 below, MgAl_2O_4 specimens irradiated at -100°C had somewhat better retention of strength than Al_2O_3 or AlN [Dienst and Zimmermann, 1994].

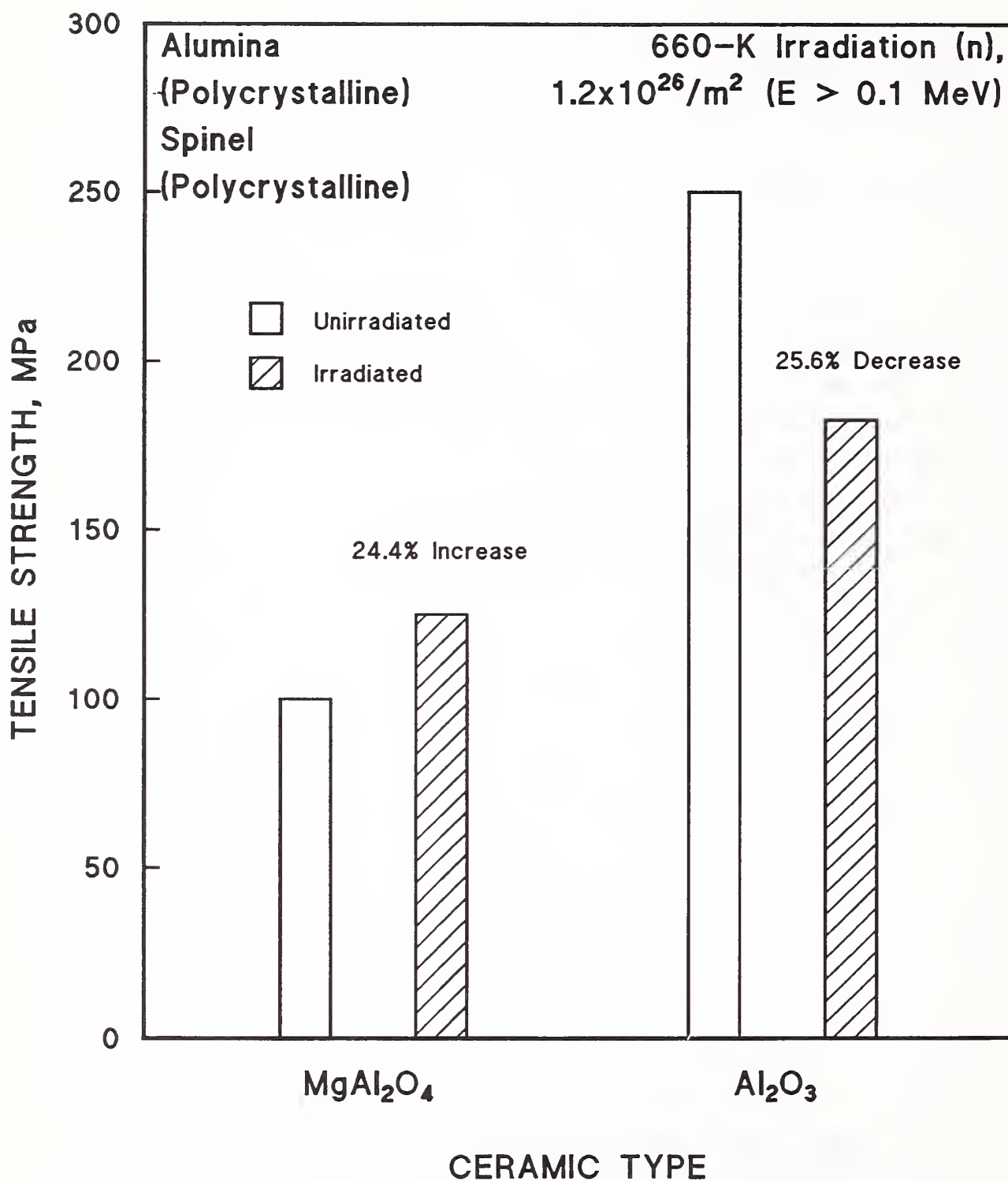


Figure 7.4.1. Tensile strength of polycrystalline Al_2O_3 and MgAl_2O_4 as measured in the diametral compression test after neutron irradiation at 660 K. Data from Tucker et al. [1986].

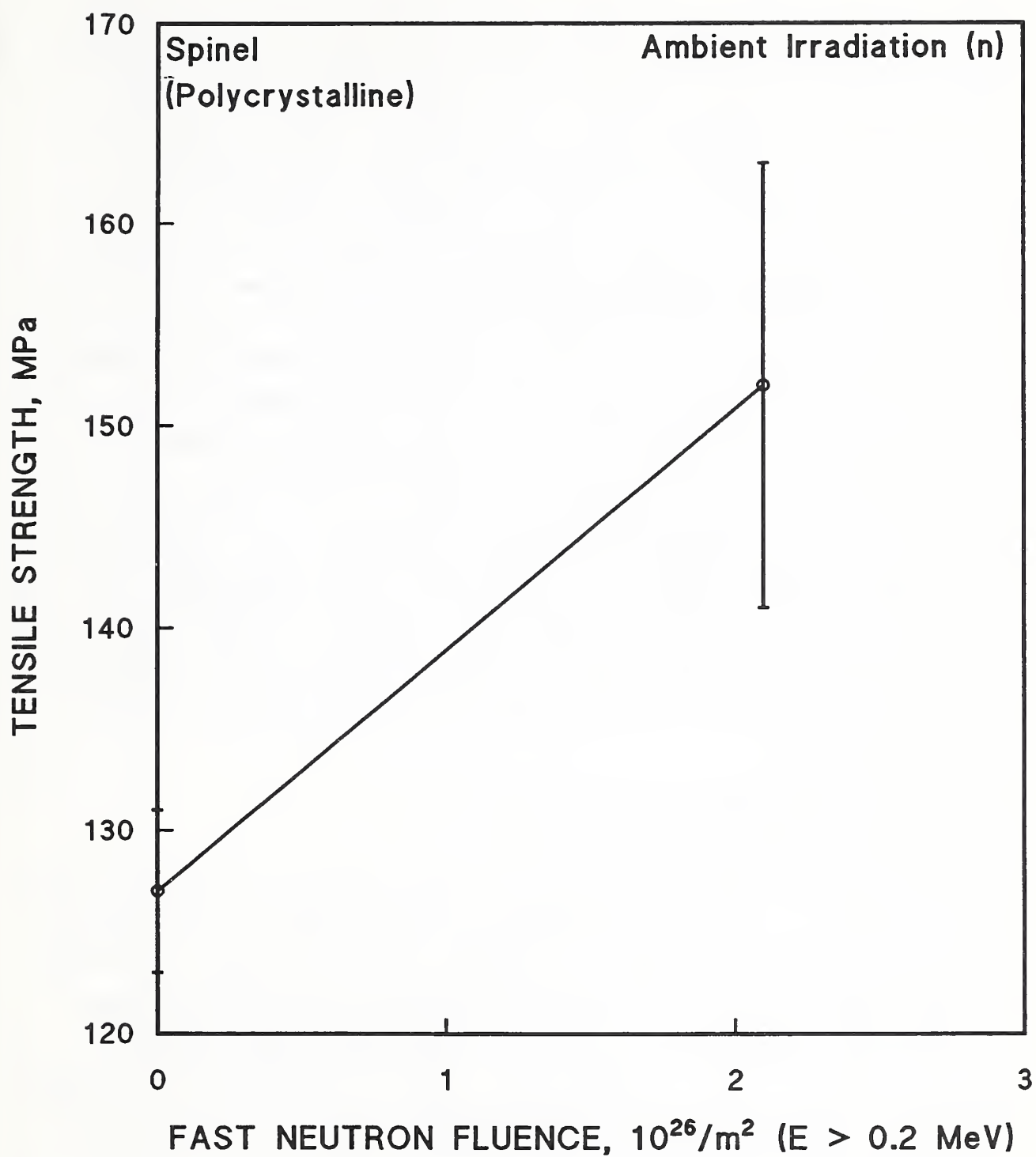


Figure 7.4.2. Tensile strength of polycrystalline MgAl_2O_4 as measured in the diametral compression test after neutron irradiation. Data from Hurley et al. [1981].

The hardness of polycrystalline MgAl_2O_4 was measured as a function of depth after 298-K irradiation with 2.4-MeV Mg ions to a fluence of $1.4 \times 10^{21}/\text{m}^2$ [Zinkle, 1989]. The grain size was 30 μm . The calculated dpa for this fluence was 35, assuming $E_d = 40$ eV. The results are shown in Figure 7.4.3. Control values were obtained from measurements made on the unirradiated periphery of the TEM disks. At least 8 indentations were made for each irradiation condition. The results suggested to Zinkle that the material was still in the Stage I of hardness, where hardness is increased, owing to lattice defects created by the irradiation. In later stages, when irradiation damage is severe enough that the material becomes partly amorphous, softening is observed. Zinkle and Kojima (§7.3) observed no amorphization at a fluence of $3 \times 10^{21} \text{ Mg}^+/\text{m}^2$, which could correspond to a fast neutron fluence of 10^{25} to $10^{27}/\text{m}^2$, more than the factor of 100 above the ITER 4-K fluence of $10^{22}/\text{m}^2$, which allows for the greater retention of defects at 4 K. However, host ions were used in these amorphization attempts, and McHargue et al. [1986] demonstrated that host ion amorphization for Al_2O_3 was impossible at 300 K, but easy at 77 K, where recovery was suppressed. Therefore, one should not assume that the material will remain in Stage I at 4 K, until 4-K hardness and other relevant mechanical tests have been carried out, in situ, after 4-K irradiation.

7.5. THERMAL PROPERTIES

No information on the effects of irradiation upon cryogenic thermal properties of MgAl_2O_4 was obtained from the literature search. Rohde and Schulz [1992] obtained comparative information on the high temperature thermal conductivity of Al_2O_3 , MgAl_2O_4 , and AlN after neutron irradiations in various facilities at temperatures ranging from 353 to 823 K. For MgAl_2O_4 , the irradiation source was the LAMPF-SNS (Los Alamos Meson Physics Facility-Spallation Neutron Source). The neutron spectrum of LAMPF-SNS reassembles that of a fission-neutron spectrum at low energies, but includes a high-energy tail above 20 MeV, so transmutation gases will be produced, as expected in the ITER first wall and, to a much lesser extent, in the TF magnets. However, the irradiation temperature was 600 K. From the fluence of $5 \times 10^{24}/\text{m}^2$, a damage dose of 0.5 dpa was calculated. This dose was evidently intended to apply to all three irradiated substances.

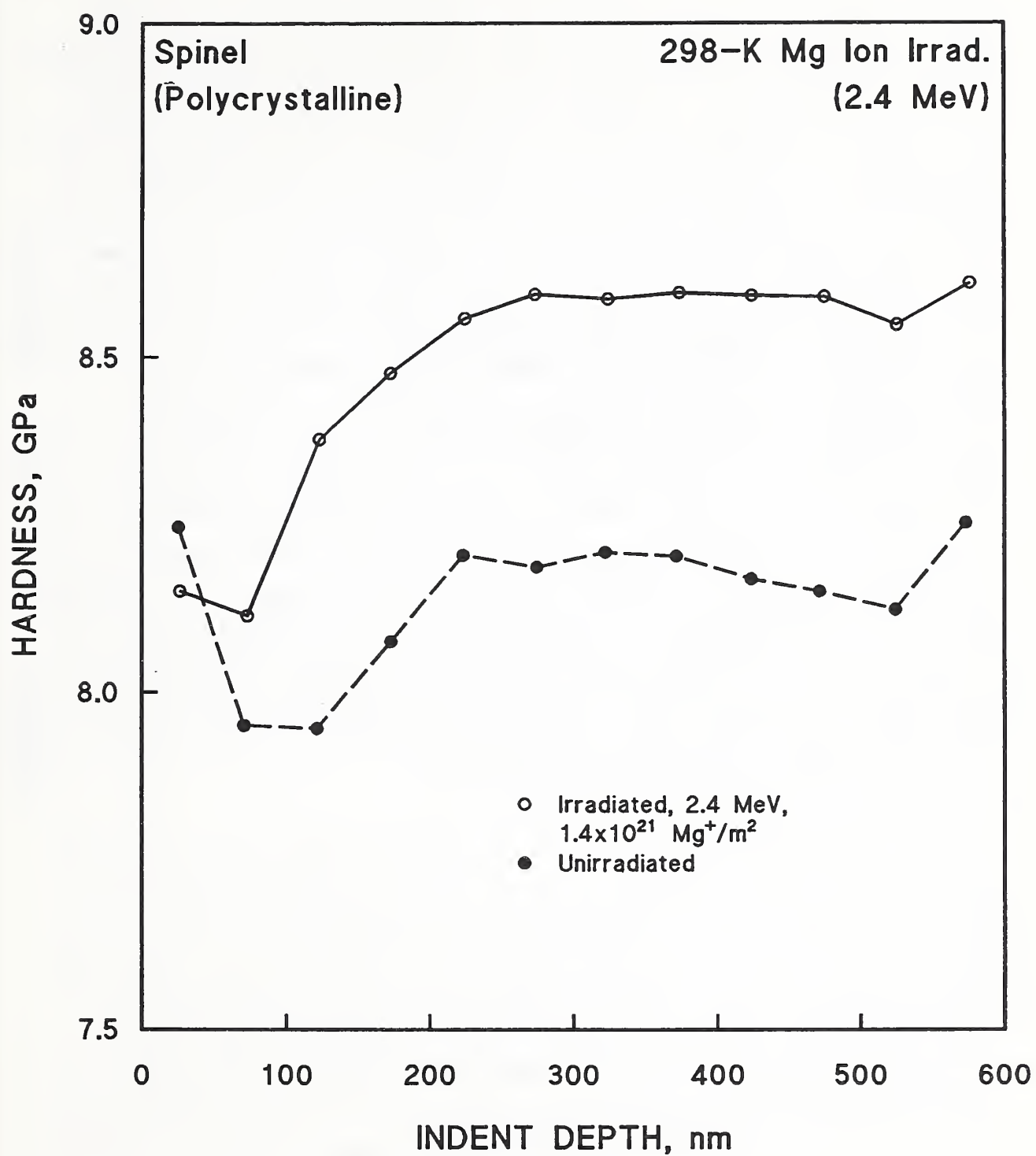


Figure 7.4.3. Hardness of MgAl_2O_4 as a function of depth after Mg-ion irradiation. Data from Zinkle [1989].

Figure 7.5.1 shows the reduction in thermal conductivity after irradiation. Earlier measurements of the thermal diffusivity of samples irradiated at 100 K indicated no degradation at damage doses below 3 dpa [citation, Rohde and Schulz, 1992]. Therefore, it was concluded that the concentration of isolated point defects was very low in irradiated MgAl_2O_4 , since these defects are the most effective scatterers of phonons. However, Figure 7.5.1 shows a reduction of the 300-K thermal conductivity of more than 40%, which would correspond to a defect concentration of about 1 atomic %, from equations relating the thermal conductivity to the phonon mean free path. This defect concentration should be accompanied by a volume change, $\Delta V/V$, of 0.14%, if each point defect contributes one atomic volume to the macroscopic density change. In fact, the volume change observed was 0.01%, which actually is higher than the compaction of 0.316% reported by Tucker et al. [1986] (§7.2) after irradiation to a higher fluence at 660 K. Rohde and Schulz ascribed the discrepancy between $\Delta V/V$ and the change in thermal conductivity to the complicated atomic stacking in the unit cell of MgAl_2O_4 , which contains 56 atoms. They suggested that a slight rearrangement of the stacking due to the irradiation could affect the thermal conductivity, but leave the density nearly unchanged. The large change in thermal conductivity after 600-K irradiation in comparison to the 1000-K thermal diffusivity results was ascribed to the greater retention of defects at the lower irradiation temperature.

The comparative results of irradiation of different ceramics with the LAMPF facility are as follows: for single-crystal Al_2O_3 , the thermal conductivity was reduced to 80% of the original value; for polycrystalline Al_2O_3 , it was reduced to 70%. For single-crystal MgAl_2O_4 , the reduction was to 52% of the original value, and for polycrystalline AlN , the thermal conductivity was reduced to 36% of the original value. Rohde and Schulz concluded that the two oxides, with their predominantly ionic bonding, were more resistant to radiation than AlN , with its covalent bonding (§1.6). However, the absolute values of the thermal conductivity at 300 K were highest for AlN .

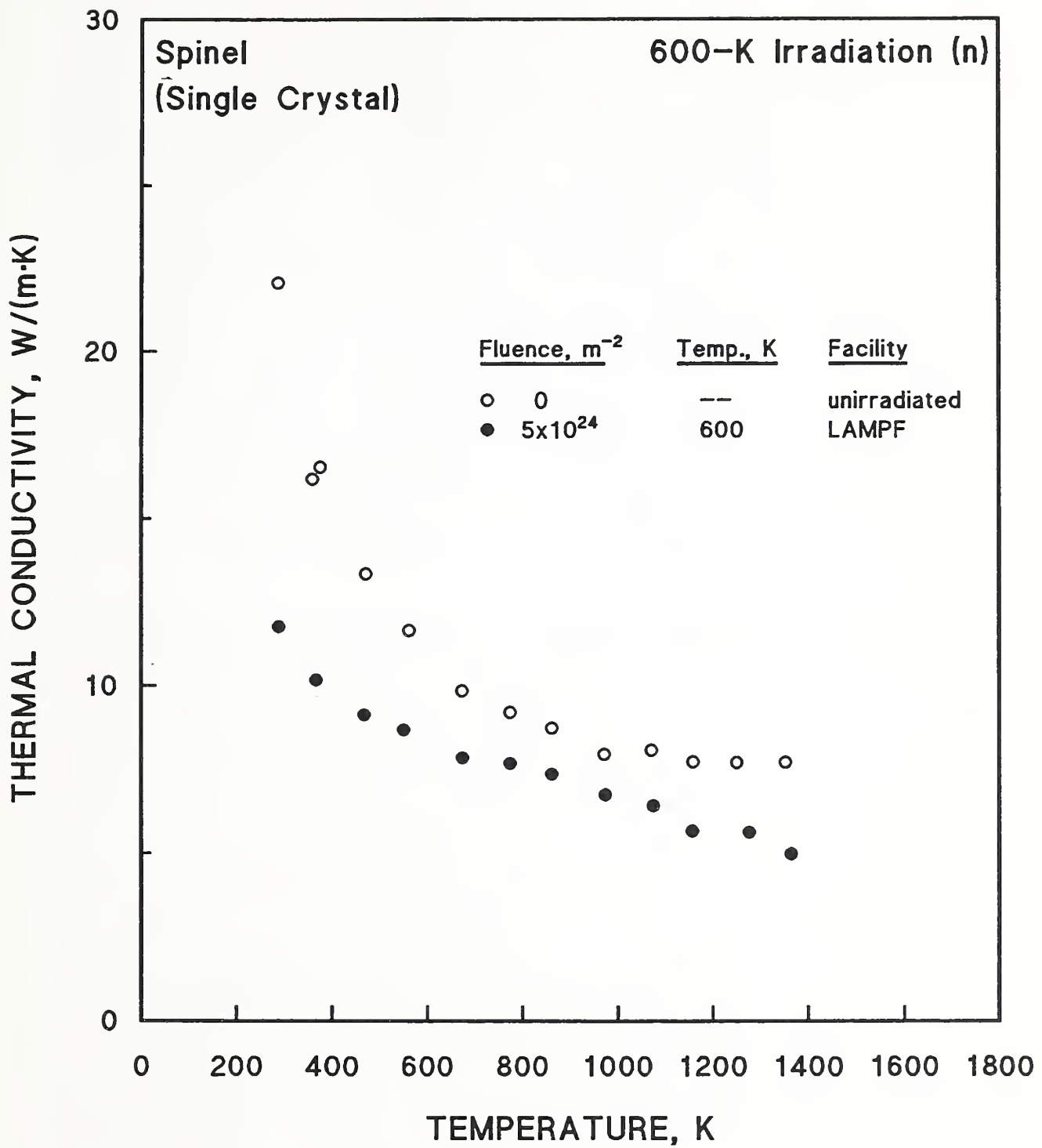


Figure 7.5.1. Reduction of high temperature thermal conductivity of MgAl_2O_4 after irradiation at 600 K. Data from Rohde and Schulz [1992].

8. LOW TEMPERATURE IRRADIATION OF ZIRCONIA

When pure ZrO_2 is cooled from high temperatures, it undergoes phase transformations: at about 1900°C , the cubic structure transforms to a tetragonal structure, and at 1100°C , the tetragonal structure transforms to a monoclinic structure that is the usual form at ambient temperature. For engineering uses, the high-temperature cubic structure is stabilized by the addition of such oxides as CaO , MgO , or Y_2O_3 . Unfortunately, the available evidence indicates that some of the stabilized cubic forms transform back to the monoclinic phase below ambient temperature, and that mechanical properties consequently may deteriorate at cryogenic temperatures [e.g., Veitch et al., 1987]. The phase stability and mechanical properties have not yet been fully determined down to 4 K for any of the ZrO_2 materials that are stabilized at ambient temperature, although the preliminary work of Veitch et al. indicated that Y_2O_3 -stabilized ZrO_2 may be the most promising material (see also Simon [1994]).

In addition to the lack of structure and property information on stabilized zirconias at 4 K, there is very little information on their radiation resistance. Most of the irradiation damage experiments on ZrO_2 were performed to study the phase transition that occurs in the unstabilized material. This work was reviewed by Wullaert et al. [1964] and by Penkovskii [1964]. Briefly, spectroscopically pure, monoclinic ZrO_2 was eventually found to be stable under fast neutron fluences up to $6.3 \times 10^{24}/\text{m}^2$. However, natural ZrO_2 usually contains sufficient impurity ^{235}U content that induced fission fragment damage will induce a phase change, perhaps from the disorder produced in the material by thermal spikes along the fission fragment paths. Additional chemical impurities are evidently not required for transformation [citations, Wullaert et al., 1964]. In technical-grade ZrO_2 , which is a mixture of 75% of the monoclinic phase and 25% of the tetragonal phase, this phase ratio was reported to remain unchanged up to a fast neutron fluence of $1.9 \times 10^{23}/\text{m}^2$ [Penkovskii, 1964].

In the remainder of this section, radiation damage of all forms of zirconias tested will be surveyed. Zirconias are not strong candidates for use in the TF magnets at present, owing to the possibility of undesirable phase transformations initiated both by neutron irradiation and by cryogenic temperatures,

and by the relative lack of radiation damage studies, in comparison to other materials, such as Al_2O_3 and MgAl_2O_4 . However, it is possible that sufficient research might uncover a radiation-resistant, stabilized ZrO_2 despite the present inadequate data base. Use of spectroscopically pure, monoclinic ZrO_2 in ITER TF magnets must be approached with caution, owing to the possibility of incorporating impurities during fabrication and the transformation, by (n,α) reactions above ~ 5 MeV, of pure material. Impurities apparently act as nucleation centers for phase transformation. Furthermore, mechanical properties of monoclinic ZrO_2 may not be satisfactory.

8.1. DEFECT DENSITY

Harrop et al. [1967] noted that the study of point defects in ZrO_2 had been hindered because the preparation of single crystals was difficult, owing to the monoclinic phase transition at about 1100°C . However, these authors initiated the study of ZrO_2 films that are substantially crystalline and nearly stoichiometric. The onset of observable changes in the 1-kHz electronic conductivity occurred for a 65-keV Ne-ion fluence of (very approximately) $10^{21}/\text{m}^2$ and a fast neutron fluence of $\sim 10^{24}/\text{m}^2$ ($E > 1$ MeV). The threshold of the electrical effect was estimated by Harrop et al. to require about 10^{19} vacancies/ cm^3 .

8.2. CHANGE IN VOLUME

Some results on the change in monoclinic lattice dimensions attributed to Berman et al. [1960a] are quoted by Wullaert et al. [1964], but they apparently are not stated in the article cited. These results indicate an unusually large effect of neutron irradiation upon volume: at a fast neutron fluence of $1.5 \times 10^{22}/\text{m}^2$ at 100°C , the a axis decreased by 0.39%, the b axis by 1.2%, and the c axis by 1.94%. The expected volume change, from summation, is -3.53% at $1.5 \times 10^{22}/\text{m}^2$. The negative sign of the effect is perhaps a reflection of a phase change, since the cubic phase is more dense than the monoclinic. Wittels and Sherrill [1956] found that the monoclinic phase was progressively replaced by the cubic phase in neutron irradiation, under conditions in which transformation could occur.

Although Klein [1955] identified a material only as ZrO_2 , for which no expansion was observed at an epithermal fluence of $10^{24}/\text{m}^2$, and a 0.28% expansion was observed in the a axis at $2 \times 10^{24}/\text{m}^2$ ($E > 100$ eV), Wullaert et al. [1964] reported that these data pertain to stabilized ZrO_2 . Klein also reported X-ray diffraction data on Hf-free ZrO_2 : "diminution in monoclinic phase" at $1 \times 10^{24}/\text{m}^2$; "monoclinic phase disappears, cubic phase remains" at $2 \times 10^{24}/\text{m}^2$. No information on the density changes accompanying these phase transformations was supplied, owing to the nature of the investigation. It is unclear why Wullaert also refers to this material as a Hf-free "stabilized zirconia," since it is the nonstabilized ZrO_2 in the monoclinic form which under certain conditions (see above) undergoes transformation under neutron irradiation into the cubic phase. It is possible that the Hf-free ZrO_2 data pertain to partially stabilized material, or simply to one of the cases in which transformation to the cubic phase was observed under irradiation. The low-expansion data may apply to very pure ZrO_2 in which transformation does not occur. See also §8.3 below.

Clinard et al. [1977] evaluated dimensional and microstructural changes in a 6 mol% Y_2O_3 -stabilized ZrO_2 after irradiation to fast neutron fluences of up to $4.4 \times 10^{25}/\text{m}^2$. Unfortunately, the irradiation temperatures were 650 K and above. However, very little volume change, $0.21 \pm 0.12\%$, was observed at this fluence at 650 K. Also, a low concentration of dislocation loops was found. This report is not relevant to the stability problem at 4 K, where irradiation damage might nucleate some degree of transformation. It is not known if the Y_2O_3 -stabilized zirconias remain stable for long periods at this temperature, even without irradiation, since in situ X-ray investigations have not been found in the literature.

8.3. AMORPHIZATION AND TRANSFORMATION

Wittels and Sherrill [1959] used X-ray diffraction to show that synthetic single crystals of monoclinic ZrO_2 remained crystalline and untransformed to a fast neutron fluence of $3.6 \times 10^{24}/\text{m}^2$ (E not specified). On the other hand, natural ZrO_2 , containing U and Th in concentrations of 3550 and 39.2 ppm, respectively, underwent a complete transformation into the high-temperature cubic phases at lower fluences. Evidently, the apparent irradiation-induced

transformation was produced by the action of fission fragments from activated impurities, such as ^{235}U . Further work at ORNL [citation, Wullaert et al., 1964] showed that no transformation occurred up to $6.3 \times 10^{24}/\text{m}^2$, but that 10^{15} to 10^{16} fissions/ cm^3 would produce a phase change, and that the presence of chemical impurities in the amounts usually necessary for stabilization of the cubic phase was not required. Because the number of displaced atoms theoretically expected from the ~ 100 -MeV fission fragments was not sufficient to effect the transformation, it appeared likely that localized heating ("thermal spikes") from the large amount of energy deposited over the short range of $\sim 8 \mu\text{m}$ of each fission fragment was responsible for the phase change. Such localized heating might be even more effective at 4 K (see §9.5.3 below). The conclusion with relevance to ITER TF magnets is that natural ZrO_2 might pose serious stability problems, but synthetic, nonstabilized, monoclinic ZrO_2 could be satisfactory, if its mechanical properties were adequate, and if the impurity level could be controlled during fabrication and during operating conditions that include irradiation at very high energy ($E > 5 \text{ MeV}$).

Tawfik et al. [1985] subjected monoclinic, sintered ZrO_2 (99.0% pure) to γ irradiation and found that the X-ray diffraction patterns were mostly unchanged, up to a dose of 10^5 Gy . However, broadening and weakening of some peaks were observed and attributed to a slight distortion of the monoclinic structure to a tetragonal structure. This γ dose is considerably below the expected TF magnet dose of about 10^7 Gy (Table 1.1.1). However, the ORNL reactor fluence of $6.3 \times 10^{24}/\text{m}^2$ that did not effect a phase transformation in pure ZrO_2 was probably accompanied by a significant γ dose.

Unfortunately, stabilized, cubic ZrO_2 is not immune from phase transformation under irradiation. Hasegawa et al. [1986] irradiated fully stabilized, 10 mol% Y_2O_3 - ZrO_2 with 1-MeV N ions with fluences from $1.3 \times 10^{18}/\text{m}^2$ to $4 \times 10^{20}/\text{m}^2$ and found transformation to a phase with rhombohedral symmetry. At a fluence of $1 \times 10^{20}/\text{m}^2$, the depth of the transformed zone extended beyond the projected ion range by a factor of 2, and the fraction of transformed material was estimated to be 74%. Figure 8.3.1 shows that even at the lowest fluence, some transformation has occurred, because X-ray diffraction shows a change in the lattice parameter. Even at this fluence, approximately equivalent to a neutron fluence of $10^{23}/\text{m}^2$, a significant swelling of 1.1% was present.

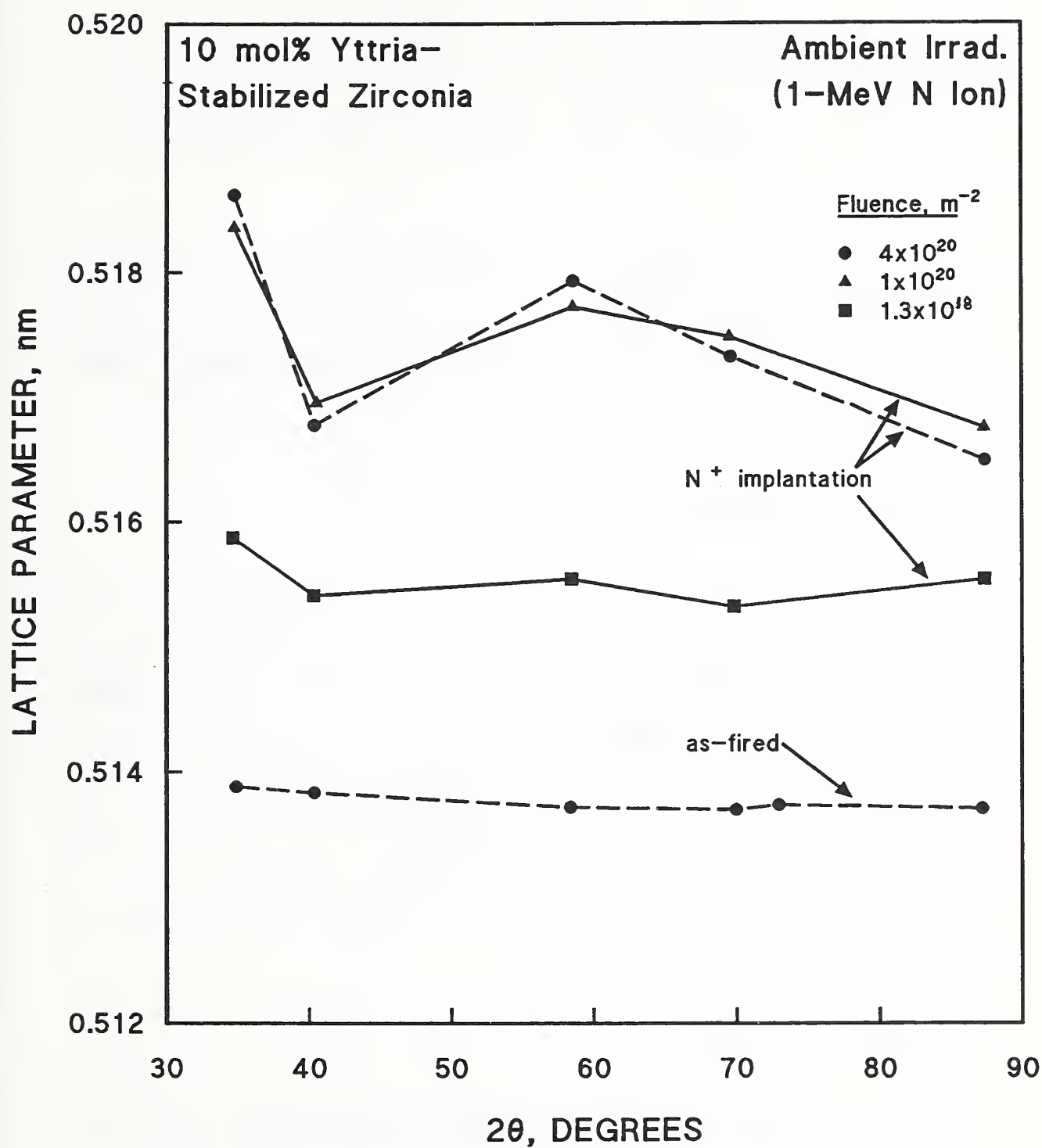


Figure 8.3.1. Plot of lattice parameters of cubic phase and new phase induced by N ion bombardment vs. diffraction angle, 2θ . Lattice parameters of new phase calculated on assumption of face-centered cubic structure. Data on 10-mol% $\text{Y}_2\text{O}_3\text{-ZrO}_2$ from Hasegawa et al. [1986].

Therefore, Y_2O_3 -stabilized ZrO_2 cannot be recommended for use in the TF magnets, because the 4-K neutron-equivalent fluence of this ion fluence is approaching the expected ITER value. It is not known if the 4-K temperature could suppress transformation, but, in that event, transformation could occur upon warm-up.

Wullaert et al. [1964] reported transformation in "Hf-free, stabilized" ZrO_2 at intermediate neutron fluences of 1 and $2 \times 10^{24}/\text{m}^2$ ($E > 100$ eV). However, these data are attributed to Klein [1955], who does not identify the material as stabilized. In fact, since the ZrO_2 transformed from monoclinic to cubic structure, it was, at least, not completely stabilized in the cubic phase before irradiation.

8.4. MECHANICAL PROPERTIES

The onset of mechanical degradation of pure ZrO_2 , as demonstrated by a bending test of an oxide-metal sandwich, appeared at a neutron fluence of about $5 \times 10^{23}/\text{m}^2$ ($E > 1$ MeV). Figure 8.4.1 shows the surface-fracture strain of the 640-nm (6400-Å) film at ambient temperature [Harrop et al., 1967]. However, the authors noted that the mechanical properties of the metal could also have been affected by this fluence. Cracking between microhardness indentations was also examined as a possible test of embrittlement, but the effect of radiation was not observable in this test. The dynamic Young's modulus of ZrO_2 was reported to decrease by less than 10% at fluences from 0.3 to $1.6 \times 10^{24}/\text{m}^2$ ($E > 100$ eV) [citation, Wullaert et al., 1964]. The temperature of irradiation was about 50°C.

8.5. THERMAL PROPERTIES

The ambient-temperature thermal conductivity of "No. 550" ZrO_2 decreased by 24% at a fluence of $2 \times 10^{24}/\text{m}^2$ ($E > 100$ eV) [Sisman et al., 1955]. In this series of comparative measurements, the thermal conductivity of single-crystal and polycrystalline Al_2O_3 and vitreous SiO_2 did not decrease appreciably at this fluence, but that of MgAl_2O_4 decreased by more than 40%. The thermal conductivity of mica decreased by 38%.

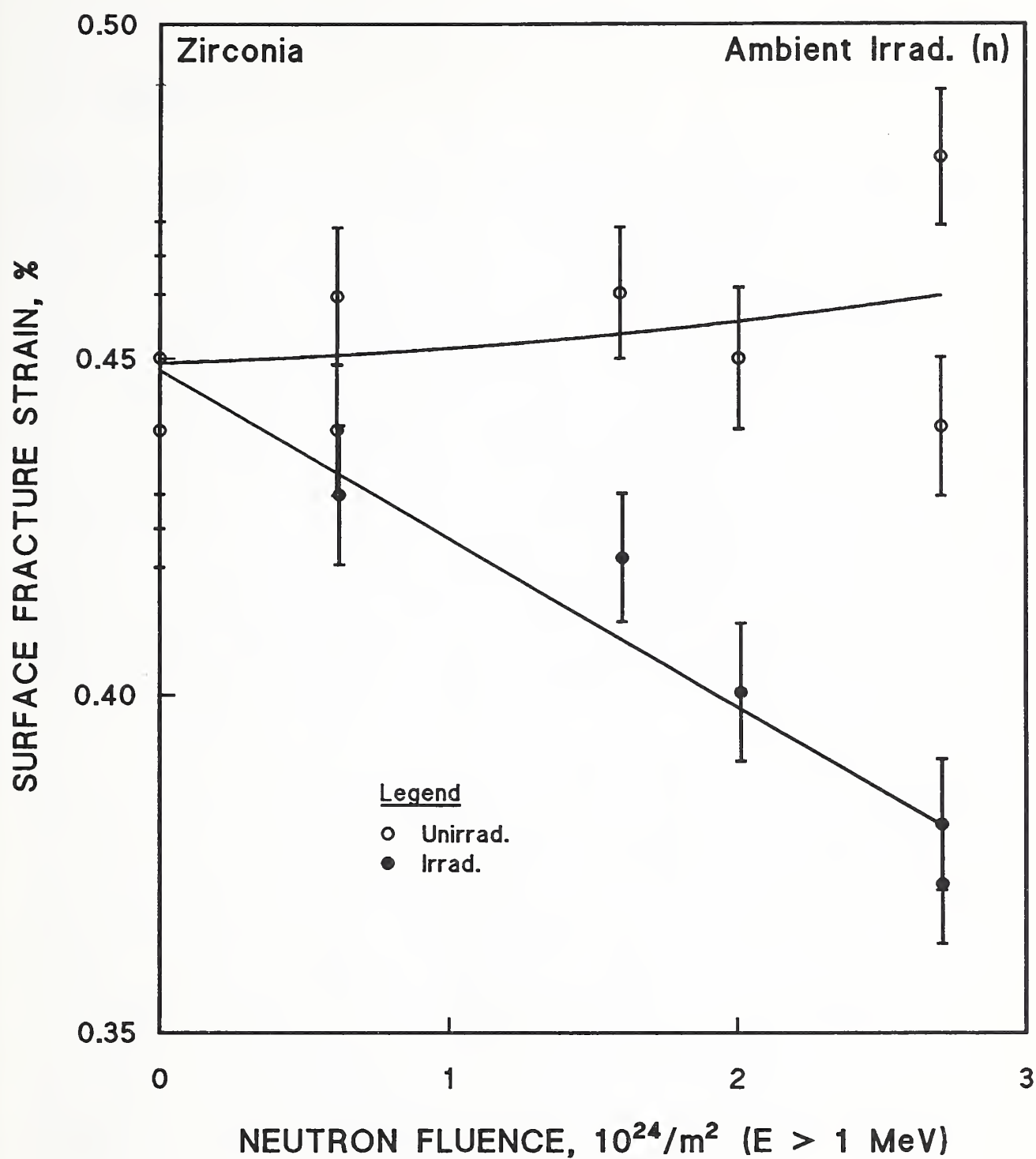


Figure 8.4.1. Surface-fracture strain of 640-nm (6400-Å) anodic film on Zr vs. neutron fluence. Data from Harrop et al. [1967].

9. MICA: RADIATION PROBLEMS OF A LAYERED STRUCTURE

9.1. STRUCTURE OF MICA

Micas are silicate minerals with a layered structure that poses unique radiation problems when contrasted to the ceramics and inorganics usually considered for service in fusion reactors. Mica crystallizes in sheet-like form and has an easy cleavage plane parallel to the layers. This structure is illustrated in Figure 9.1.1 for muscovite mica, the form most commonly used in commercial mica insulations. The approximate chemical formula of muscovite mica is $\text{KAl}_2(\text{Si}_3\text{Al})\text{O}_{10}(\text{OH},\text{F})_2$. Large, negatively charged anions, O, OH, and, occasionally, F, are arranged in octahedra around the smaller, positively charged cations, Si and Al, shown as the smaller spheres in Figure 9.1.1. The oxygen ions lie in two planes in a close-packed arrangement. This layered structure has an overall negative charge that is neutralized by the interlayer cation, K^+ , identified in the figure. Bonding between the negatively-charged layers is strong and specific because the K ions occupy well-defined positions ("holes") between the adjacent planes of O atoms. The width of one layer in the mica structure is about 1 nm (10 Å).

Mica structures have been extensively studied: useful references are Brindley [1981] and Pauling [1930]. In addition to muscovite, two other micas similarly bound by interlayer K ions have been investigated to a small extent after irradiation. These are phlogopite, $\text{KMg}_3(\text{Si}_3\text{Al})\text{O}_{10}(\text{OH},\text{F})_2$, and biotite, $\text{K}(\text{Mg},\text{Fe}^{2+})_3(\text{Si}_3\text{Al})\text{O}_{10}(\text{OH},\text{F})_2$. In both of these micas, Mg substitutes partially for the Al atoms of muscovite; biotite also contains Fe^{2+} as an Al substitute. The amounts of impurities can be surprisingly large in natural micas; for muscovite, Povarennykh [1972] quotes: Ba, $\leq 10\%$; Fe^{3+} , $\leq 6.6\%$; Cr, $\leq 4.8\%$; $\text{V}^{3,4+}$, $\leq 3.5\%$; Fe^{2+} , $\leq 3.2\%$; Na, $\leq 2.9\%$; Mg, $\leq 2.8\%$; F, $\leq 2.1\%$; Rb, $\leq 1.4\%$; Li, $\leq 1.8\%$; and Ca, $\leq 1.1\%$. Synthetic mica would not have these impurity problems, but evidently is not much used for commercial electrical insulation.

Several obvious concerns with the use of mica in a fusion reactor arise from its layered structure. First, since mica cleaves so easily, the stability of the K-ion interlayer bond under displacive neutron irradiation is questionable. Second, silicate bonds are not considered very resistant, even to

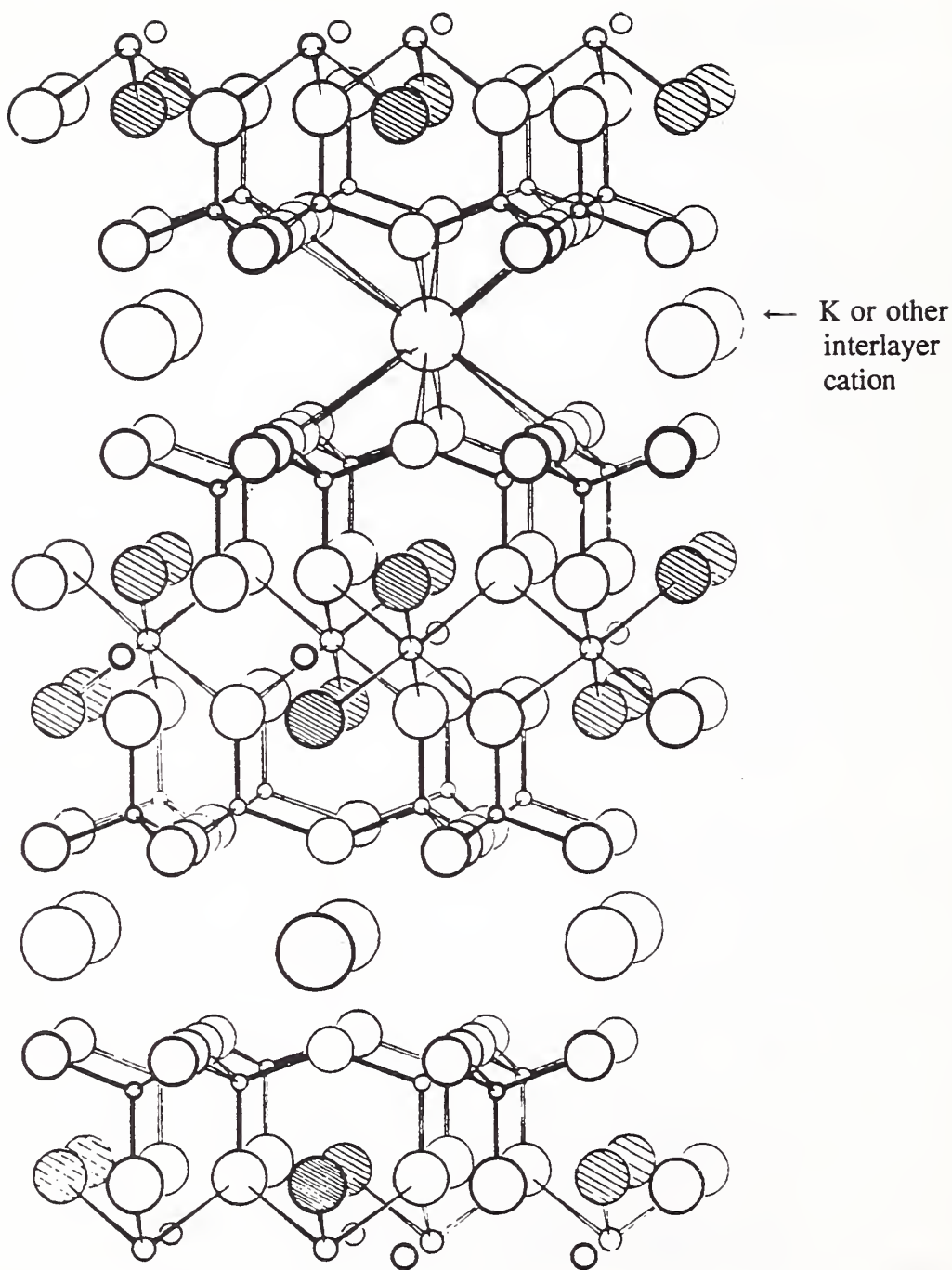


Figure 9.1.1. Schematic of structure of mica. Data from Brindley [1981].

ionizing radiation (§§6.1, 6.3), and the bonds within the mica layers are of this type. A third concern arises from other factors: the use of mica as a solid-state track detector and as a geological dating system from tracks naturally present in the material from spontaneous ^{238}U fission, and possibly, from recoil nuclei in ^{238}U decay. Any lack of cohesion of the layers under irradiation could open up channels along which electrical breakdown could occur. Of course, thermal-neutron irradiation will cause additional ^{235}U fission fragment tracks, in addition to the naturally occurring porosity of the individual layers. The well-known ^{235}U thermal fission cross section is large, ~550 barns, although the isotopic abundance of ^{235}U is <1%. There is also a fast neutron fission cross section of ~0.5 barns for ^{238}U above about 2 MeV, which may also be of some importance, since the isotopic abundance of ^{238}U is >99%, and about 7% of the magnet neutron spectrum is above 5 MeV. The evidence for all of these potential problems is discussed in the following sections.

9.2. DIRECT OBSERVATIONS OF RADIATION DAMAGE

In an early survey of ceramics and inorganic insulation, Klein [1955] used a shielded X-ray diffractometer to show that mica had a low resistance to neutron irradiation damage in comparison to Al_2O_3 , MgO , MgAl_2O_4 , porcelain, SiO_2 , and ZrO_2 . In contrast to these materials, which generally exhibited little or no change in their diffraction pattern and lattice constants for an epithermal neutron fluence of $10^{24}/\text{m}^2$ ($E > 100$ eV), mica showed line broadening and a significant 1.3% expansion of the c-axis lattice constant (Table 9.2.1). Figure 9.2.1 depicts the change in lattice constant. Bopp et al. [1960] reported swelling of about 14% in muscovite mica for an epithermal neutron fluence of $2 \times 10^{24}/\text{m}^2$, as indicated by the density changes in Figure 9.2.2. As Coghlan and Clinard [1991] noted, since the irradiation was carried out to investigate the release of water from mica, which causes shrinkage, the intrinsic radiation swelling of dehydrated mica should be larger. Thus, calcined mica could be expected to show even larger swelling for comparable fluences. (Calcined mica is mica that has been heated to drive off the water.)

The effect of the same radiation fluence upon the ambient-temperature thermal conductivity was also measured [Sisman et al., 1957]. The initial thermal

Table 9.2.1. Results of X-Ray Examination of Ceramics.
Data from Klein [1955]

Sample	Results When Irradiated with 1×10^{20} neutrons/cm ²	Activity (at 1 cm)	Results When Irradiated with 2×10^{20} neutrons/cm ²	Activity (at 1 cm)
Single-crystal Al ₂ O ₃	No change in pattern	1.5 mr/h	No change in pattern	1.5 mr/h
Hot-pressed Al ₂ O ₃	No change in pattern	6 mr/h	No change in pattern	10 mr/h
Spinel	No change in pattern	1.5 mr/h	No change in pattern	5 mr/h
Forsterite	No change in pattern	15 mr/h	No change in pattern	60 mr/h
Porcelain	No change in pattern	40 mr/h	No change in pattern	40 mr/h
Steatite	No change in pattern	80 mr/h	No change in pattern	80 mr/h
TiO ₂	No change in pattern	170 mr/h	No change in pattern	230 mr/h
Silica glass	Halo broadening	2 mr/h	Halo broadening	2 mr/h
Plate glass	Halo broadening	10 mr/h	Halo broadening	15 mr/h
Pyrex glass	Halo broadening	10 mr/h	Diminution in halo intensity; broadening	30 mr/h
Lead glass*	Lead plus other devitrification products	500 mr/h	Lead plus other devitrification products	900 mr/h
Mica	Line broadening; 1.3% expansion in c_0	120 mr/h	Line broadening; 1.7% expansion in c_0	170 mr/h
Enamel ground coat	Loss in crystallinity	6.7 r/h	Loss in crystallinity	11 r/h 7 r/h (gamma)
ZrO ₂	No change in pattern	6 r/h	0.28% expansion in a_0	10.4 r/h 600 mr/h (gamma)
Hf-free ZrO ₂	Diminution in monoclinic phase	800 mr/h	Monoclinic phase disappears; cubic phase remains	1.2 r/h
Zircon	1.9% expansion; large loss in crystallinity	2.2 r/h	No lines detectable; large loss in crystallinity	6.8 r/h
SiC	Line broadening; 0.3% expansion	10 mr/h	Expansion and loss in crystallinity	10 mr/h
BeO	Very slight expansion in c_0	9 mr/h	Approximately 0.3% expansion in c_0 ; none in a_0	25 mr/h
Lava	Loss in crystallinity	170 mr/h	No lines detectable	220 mr/h
Cordierite	No change in pattern	100 mr/h	Line broadening	150 mr/h
MgO	No change in pattern	15 mr/h	MgO + MgO·4CO ₂ ·5H ₂ O + MgCO ₃ ·3H ₂ O	15 mr/h
BaTiO ₃	2.03% expansion in a_0	80 mr/h	2.87% expansion in a_0 ; reflections broadened	170 mr/h

*Confirmed by petrographic analysis.

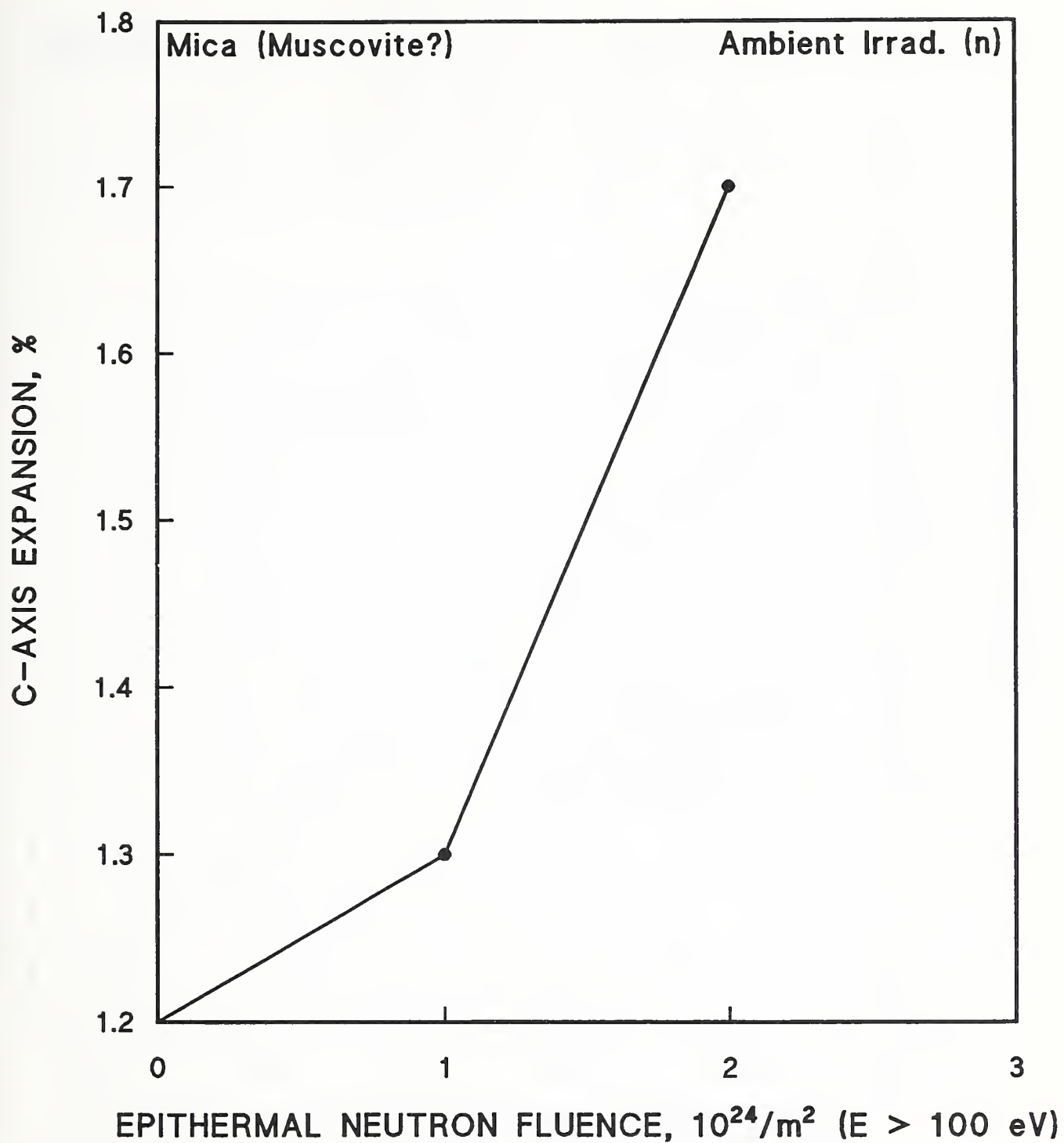


Figure 9.2.1. Expansion in the c-axis direction of mica after neutron irradiation. Data from Klein [1955].

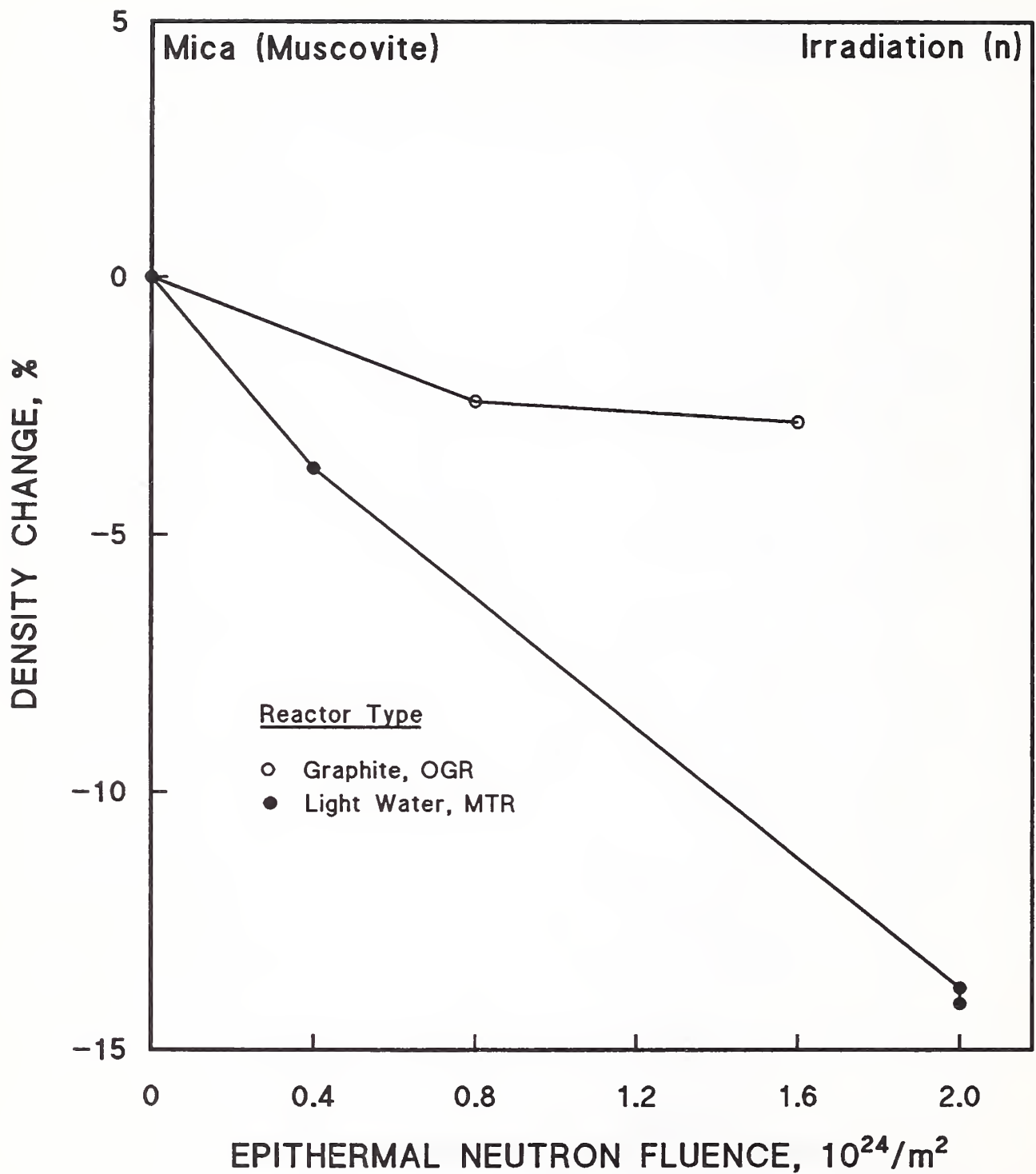


Figure 9.2.2. Density change of mica after neutron irradiation; the average energy of the neutrons in the MTR reactor is greater than that in the OGR reactor, which accounts for the greater degree of damage per indicated total fluence. Data from Bopp et al. [1960].

conductivity in air was $0.71 \pm 0.04 \text{ W/(m}\cdot\text{K)}$. After an epithermal fluence of $4 \times 10^{23}/\text{m}^2$, the conductivity decreased to $0.50 \pm 0.04 \text{ W/(m}\cdot\text{K)}$; after an exposure to $2 \times 10^{24}/\text{m}^2$, the conductivity had increased above the initial value to $1.2 \pm 0.1 \text{ W/(m}\cdot\text{K)}$. The reason for this somewhat unusual behavior was not discussed, and the orientation of specimens also was not reported, either in this or in an earlier report [Sisman et al., 1955].

The various materials in the irradiation of Sisman et al. were subject to corrosion by the reactor cooling water in which they were immersed. Several of the materials, but not mica, were found to be largely dissolved by the corrosive action of the water. Mica was not reported to be dissolved, but glass-bonded mica was said to be broken up because of a large loss of strength. The report is not entirely clear on this point, but apparently specimens of another form of mica survived the irradiation procedure. After the highest fluence, the Knoop hardness of this mica was measured with an indenter. A light mass of 100 g was evidently employed in this test to prevent fracturing, but the report is unclear on this point, because it also states that a 2-kg mass was used for coarser-grained, pressed materials to obtain a distinct impression. The Knoop hardness of mica initially was 113 ± 10 ; after the exposure, it was 440 ± 10 . Plate glass exhibited similar hardness characteristics before and after irradiation, perhaps owing to the similar chemistry of the silicate bonds in both materials. However, lead and Pyrex glass specimens were too broken up to be tested. The initial hardness of a polycrystalline Brazilian quartz material was much higher than that of mica; after irradiation, hardness was lower, comparable to that of the irradiated mica. Since the fluence received by the Brazilian quartz was higher, $6 \times 10^{24}/\text{m}^2$, and probably sufficient for amorphization, the softening of the quartz was probably due to amorphization, which is known to soften hard materials. It is possible, owing to the similarity in bonding and nearly identical hardness values, that the mica had also attained a similar amorphous state after a fluence of $2 \times 10^{24}/\text{m}^2$, but that the hardness of this state was greater than that of unirradiated mica.

Some information is available on the effects of ionizing radiation on electrical properties of mica hybrid insulators [Aki et al., 1983]. Figure 9.2.3 shows that under creep, there is no substantial lowering of the surface

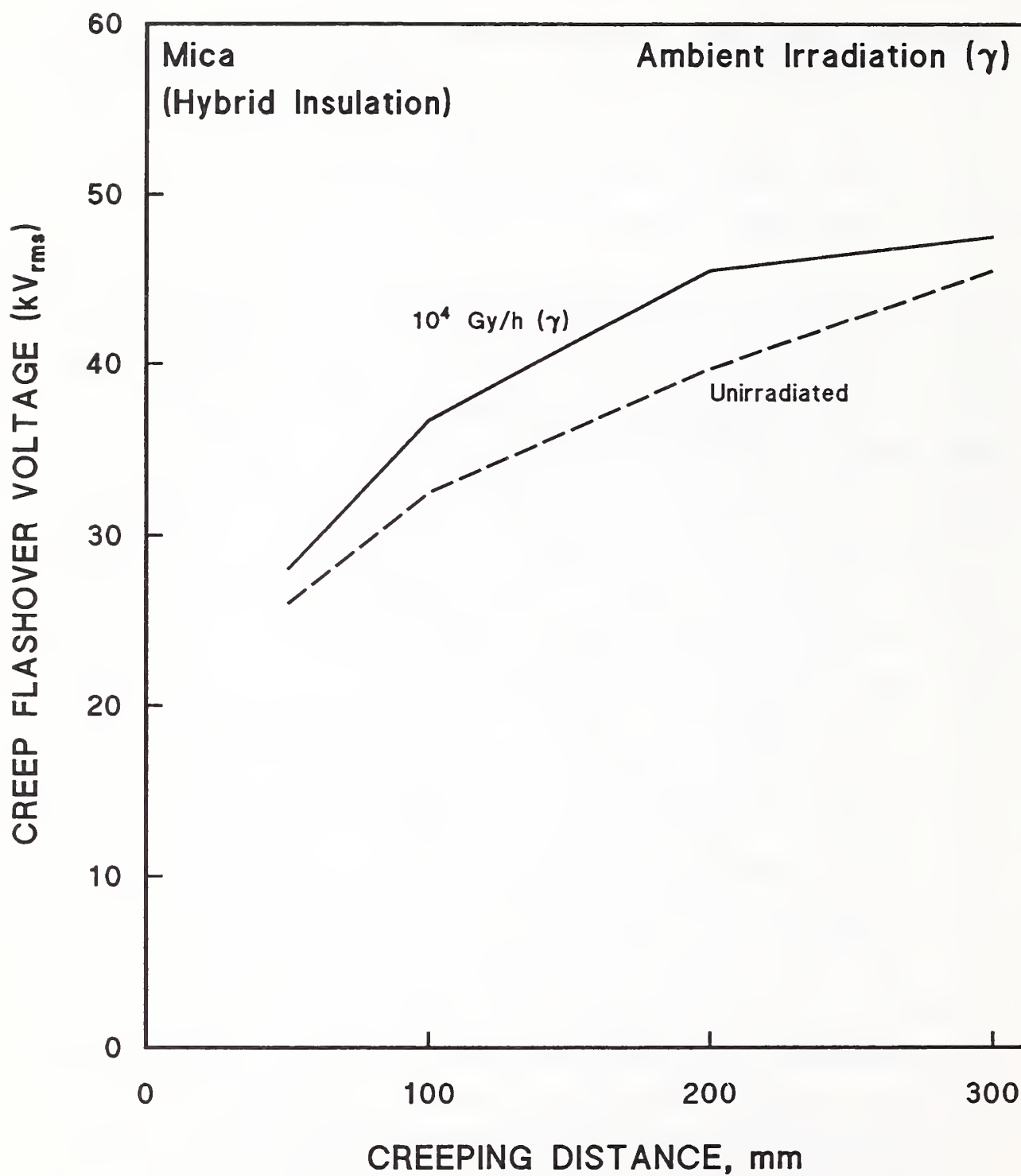


Figure 9.2.3. Creeping flashover voltage characteristics in hybrid mica insulation under γ irradiation. Data from Aki et al. [1983].

flashover voltage of hybrid insulation upon exposure to γ radiation at 10^4 Gy/h. See the paper for further details of the tests. Other results reported in this paper indicated that this hybrid insulation may have consisted of a polyimide film, mica paper, mica flakes, and glass cloth tape. Electrical breakdown results on hybrid insulation by the same group are discussed in §9.5.1 below. All tests were evidently done at ambient temperature.

Since the early surveys at ORNL indicated that mica had low radiation resistance, compared with other insulators, it was apparently not considered to be a viable candidate insulator for fusion reactors; consequently, there is little further irradiation research on this material in the literature. However, some additional information may be gleaned from three other areas of research on mica: (1) HVEM studies, as reported in mineralogy journals; (2) ion-irradiation solubility studies; and (3) the use of mica as a solid-state track detector for high energy ions.

9.3. ELECTRON MICROSCOPY

When high energy transmission electron microscopy is used to investigate the microstructure and microchemistry of mica, beam damage is a serious problem. The damage to micas caused by loss of the interlayer bonding cations was reviewed by Ahn et al. [1986], who examined a Na mica, paragonite, with a 100-keV electron beam. Paragonite has the same composition and structure as muscovite (Figure 9.1.1), except that the interlayer K ions are replaced by Na ions. Electron micrographs of paragonite showed prominent lenticular features (Figure 9.3.1). An examination with minimal electron beam exposure determined that these fissures were not part of the original microstructure, but were caused by beam damage. Ten seconds of exposure to the 100-keV electron beam produced abundant fissures that appeared at thin edges. As Figure 9.3.1 indicates, these fissures were elongated in a direction perpendicular to the *c* axis. Their size varied from barely observable to almost 10 nm (100 Å) in width. Furthermore, electron diffraction images of the damaged area showed diffuse patterns both parallel and perpendicular to the *c* axis. The diffuseness perpendicular to the *c* axis was attributed by Ahn et al. to misorientations of the split lamellae, whereas that along the *c* axis was said to

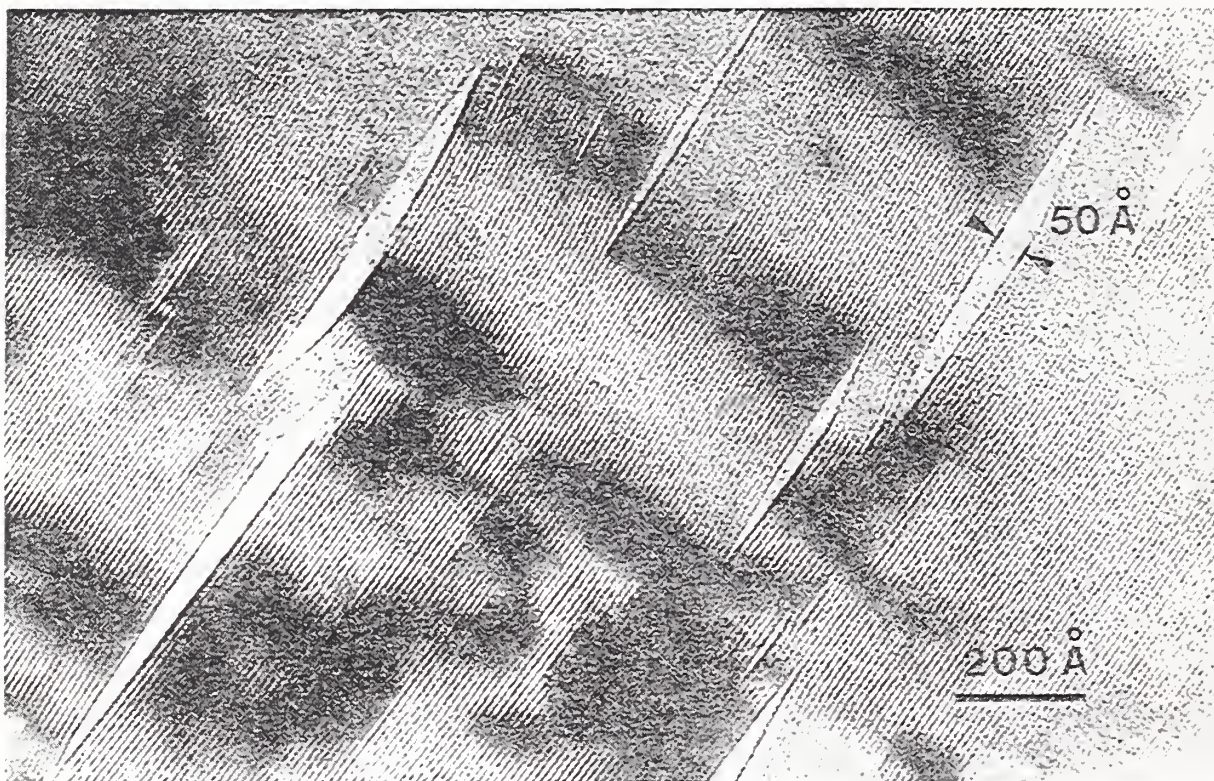


Figure 9.3.1. Image of electron-beam damaged paragonite showing lenticular fissures along layers. From Ahn, J.H.; Peacor, D.R.; Essene, E.J. 1986. Cation-Diffusion-Induced Characteristic Beam Damage in Transmission Electron Microscope Images of Micas. *Ultramicroscopy* 19. pp. 375-382. Reprinted with permission from Elsevier Science.

indicate a change in basal spacing such that the structure or chemistry of some layers had been affected by the beam.

Quantitative X-ray analysis showed a considerable decrease in the Na content relative to the Al and Si content, which were unchanged. Beam-induced loss of light elements is a not uncommon problem in electron microscopy. In addition, the rate of cation diffusion is much greater along the mica layers than perpendicular to them. Therefore, Na can easily diffuse or be volatilized from the thin edges of specimens.

Ahn et al. proposed that loss of Na, an interlayer cation, would eventually cause collapse of the paragonite structure to a structure without interlayer cations. Local collapse may cause mechanical separation of layers. Because the bonding between mica layers is much weaker than that across the tetrahedral and octahedral layers, the fissures were inferred to occur along the interlayers of paragonite. Similar fissures were observed by other investigators in other Na-type micas [citations, Ahn et al., 1986]. Earlier observations by the same group on phlogopite, a K mica, indicated that it was relatively stable under electron beam irradiation, and did not show any layer separation [Yau et al., 1984]. In contrast to Figure 9.3.1, Figure 9.3.2 shows that regular spacing of the ordered phlogopite mica layers was maintained under the same conditions of observation (100-keV electron beam). Ahn et al. attributed this difference to a greater mobility of Na than of K in the interlayer sites, although they noted that displacement could not be ruled out. However, as Equation (1.5) shows, an electron with an energy of 100 keV can transfer a maximum of 10.4 eV to a Na atom, but only 6.1 keV to a K atom, owing to its greater mass. M. M. Mills pointed out in 1950 [Billington and Crawford, 1961; p. 24] that electron irradiation in increments of increasing energy could be used to determine E_d , the threshold energy necessary to displace an atom in a particular solid. Since 10.4 eV is a relatively low value for E_d , as indicated in Table 1.2.2, what the groups led by Ahn and by Kau at the Department of Geological Sciences at the University of Michigan may have found were preliminary limits between 6 and 10 eV for the E_d s of the interlayer cations in micas. (However, Van der Pluijm et al. [1988] ascribed these fissure phenomena to diffusion of K rather than to sputtering.)

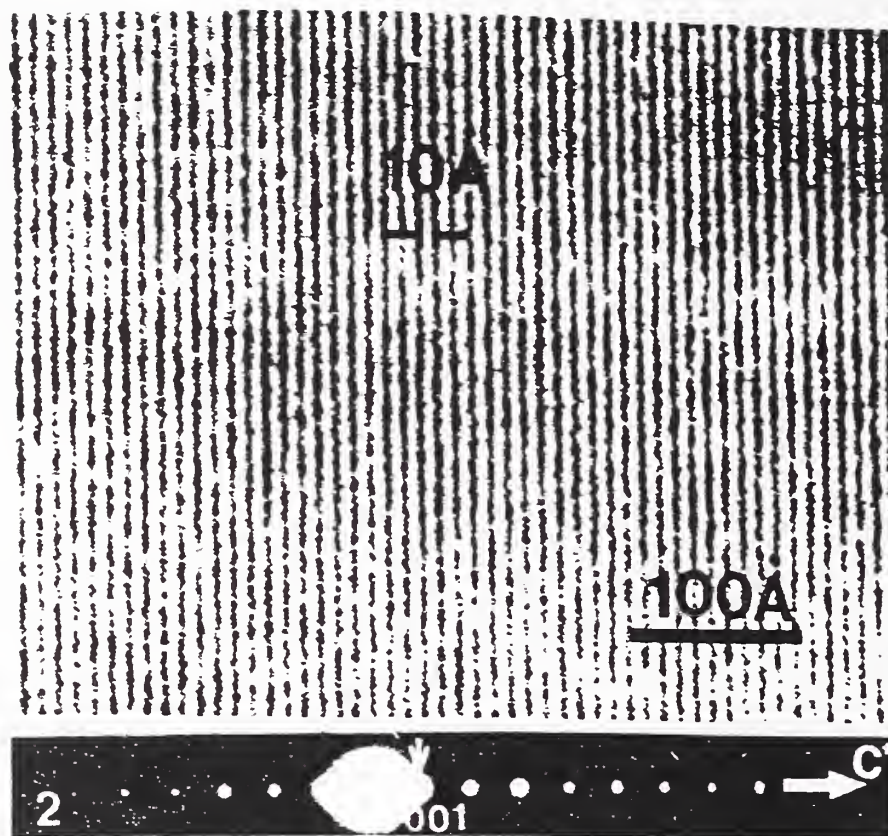


Figure 9.3.2. Electron microscope image (100 keV) of phlogopite mica showing ordered, undamaged 1 nm (10 Å) stacking sequence. From Yau, Y.; Anovitz, L.M.; Essene, E.J.; Peacor, D.R. 1984. Phlogopite-Chlorite Reaction Mechanisms and Physical Conditions during Retrograde Reactions in the Marble Formation, Franklin, New Jersey. *Contributions to Mineralogy and Petrology* 88. p. 302. Copyright by Springer-Verlag. Reprinted with permission.

Ahn et al. also cited TEM observations of similar fissures in two other K micas, biotite and muscovite, by Iijima and Zhu [1982], but noted that they apparently were not as prominent and abundant as those found in the Na micas. Figure 9.3.3 from Iijima and Zhu shows definite, but narrower, fissures. These fissures were not attributed to beam damage by Iijima and Zhu, but a careful search for their origin was apparently not carried out. Since Iijima and Zhu (at Arizona State University) used an electron microscope with a 200-keV beam energy, in contrast to the 100-keV machine at the University of Michigan, a maximum energy of 13.3 eV could be transmitted to the K ion, instead of the maximum of 6.1 eV available to Yau et al. An E_d of 10 or 13 eV is somewhat below the region of normal displacement energies for ceramic oxides, but is not an unexpected value for a silicate material (§6.1). Obviously, irradiation of mica by neutrons of much higher energy than one or two hundred keV will easily displace the interlayer K ions. The ease of displacing the interlayer cations that hold the mica layers together and subsequent occurrence of fissures, or voids, is probably the explanation for the large expansion in the c-axis direction noted above for low energy neutron irradiation (§9.2, Figure 9.2.1).

In contrast to this apparent damage from 200-keV electrons, Figure 2.1.8 above from Pells and Phillips [1979a,b] shows the results of a very comprehensive HVEM investigation of the E_d s in Al_2O_3 for both Al atoms (18 eV) and O atoms (76 eV) as an apparent function of temperature. This figure shows that an electron beam energy of about 400 keV was necessary to displace O ions even though they are much lighter than Na or K ions. This is an indication of the lack of radiation resistance of mica, in comparison to that of other inorganic insulators. Although the $E_d(Al)$ suggested by Pells [1988] (Table 1.2.2) is only 18 ± 3 eV, other authors have suggested higher values [e.g., Greenwood, 1990].

At higher electron beam energies, Iijima and Zhu [1982] observed vitrification of muscovite, although not of biotite exposed in the same beam. (The two forms of mica were extracted from a geological formation in intergrown crystal form, so that sections in which both forms were joined together [Figure 9.3.3] were placed in the electron microscope.) These authors stated that resistance of the material to vitrification from electron beam ionization depends upon

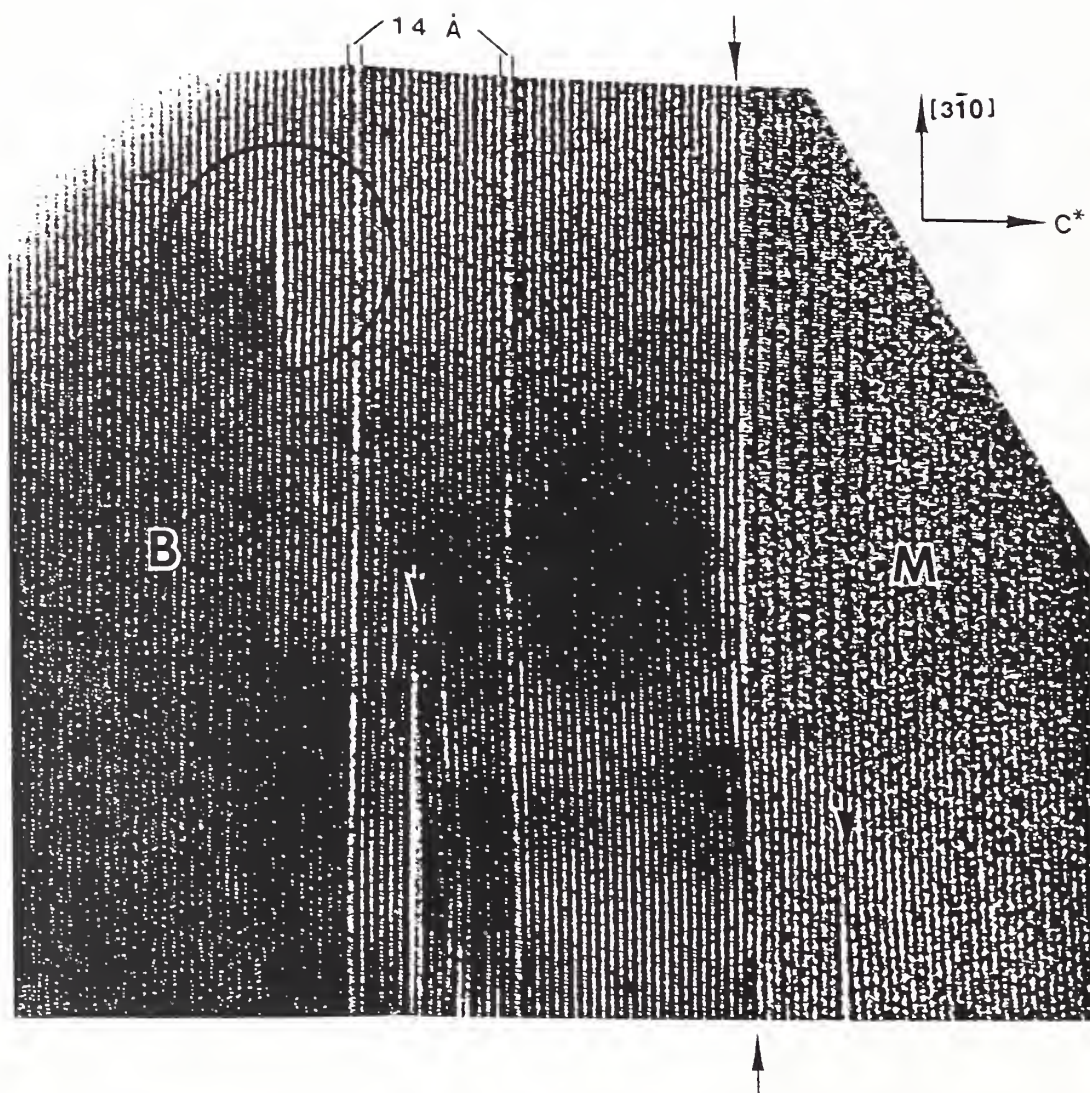


Figure 9.3.3. Electron microscope image of muscovite mica (on the left) and biotite mica showing fissures between the layers, probably from the 200-keV electron beam. From Iijima, S.; Zhu, J. 1982. Electron Microscopy of a Muscovite-Biotite Interface. *American Mineralogist* 67. pp. 1195-1205. Figure 7. Copyright by the Mineralogical Society of America. Reprinted with permission.

the percentage of OH ions present. Their evidence for this was that chlorite was less stable than micas. [Chlorites have the structure $(\text{Mg}_{6-x}\text{Al}_x)(\text{Si}_{4-x}\text{Al}_x)\text{O}_{10}(\text{OH})_8$, so the OH group has a much higher representation than in the micas.] Also, clay minerals containing much more water were more rapidly damaged by the electron beam. Biotite is richer in Fe ions than muscovite. The Fe ions may have a higher ionization energy than the Al ions in muscovite. Muscovite is also commonly poorer in F and richer in OH than biotite. The dose required for muscovite vitrification was not reported.

9.4. ION-IRRADIATION ENHANCED SOLUBILITY

The surface layer of a solid that has been irradiated by ions with an energy of a few keV will have a changed chemical reactivity, including an enhanced solubility. Because the disordered surface layer damaged by ions is thin, of the order of 1 to 10 nm for ion energies in the keV region, a special technique was devised to monitor the change in solubility. This monitoring technique involved the injection of radioactive tracer atoms into the previously irradiated surface [Jech, 1967]. The conditions for tracer injection were chosen to minimize any additional damage, and autoradiography was used to determine the tracer activity before and after dissolution treatment. Alpha- Al_2O_3 was compared with a mica of unspecified type and chemistry under Kr irradiated from 2 to 10 keV. (The mean atomic mass of both solids is similar, so the ion ranges are also similar.) For mica after 10-keV irradiation, an enhanced solubility (in 3% HF) was observed for a fluence as low as 5×10^{16} ions/ m^2 , while a fluence about 10 times larger was sufficient to ensure complete removal of all activity during dissolution. For Al_2O_3 , an increased solubility (in NaOH) was only observed for a fluence almost an order of magnitude higher, $3 \times 10^{17}/\text{m}^2$. Heating to 800°C in N restored the original solubility in Al_2O_3 ; however, in mica, this thermal treatment up to 500°C did not remove the enhanced solubility. Because enhanced solubility reflects a disordered or amorphous state, it is evident that mica is less resistant to irradiation-induced amorphization than Al_2O_3 is. This low resistance to amorphization is related to the use of mica as a nuclear-particle track detector: tracks of heavy ionizing particles in mica can be observed with TEM and are readily visualized when the disordered regions of the lattice are dissolved by etching, as discussed in the following section.

9.5. FORMATION OF ETCHABLE TRACKS IN MICA

9.5.1. Critical Dose

In mica and some other insulators, the tracks of heavy ions can be readily etched to optical dimensions of the order of 10 nm (100 Å). Theories of track formation are controversial and are discussed in §9.5.3 below with respect to their implications for 4-K track enhancement, but the empirical evidence regarding the energy/u required for etchable tracks at ambient temperature is well-established [Katz and Kobetich, 1968; Fleischer et al., 1964]. Figures 9.5.1 and 9.5.2 show an interesting contrast between a typical organic material (cellulose nitrate) and muscovite mica. The horizontal line shows the dose, in Gy, above which etchable tracks are formed. For the organic material, data are available to correlate this critical dose of ionization energy with the γ -ray dose for microscopic damage of the bulk material. Figure 9.5.1 shows that the critical dose of about 2×10^4 Gy lies in the region of moderate damage. No comparable bulk damage information is available for mica, but an expected dose for moderate bulk damage of about 3×10^5 Gy could be inferred from Figure 9.5.2, by analogy with the results for cellulose nitrate in Figure 9.5.1, which also apply to at least one other organic, bisphenol-A polycarbonate [Katz and Kobetich, 1968]. In tests which measured the breakdown voltage of composites containing mica flakes or mica paper, over 90% of the initial breakdown strength was observed after 10^6 Gy of γ radiation at a temperature of 155°C [Aki et al., 1983]. These results are shown in Figure 9.5.3. Also, the same authors reported that the breakdown voltage vs. bending cycles of hybrid mica insulation remained unchanged at 2×10^6 Gy (Figure 9.5.4). Therefore, the moderate damage level for bulk mica from ambient γ irradiation may be in the range of 10^5 to 10^6 Gy. Such γ -ray doses are far below the level required for observable damage to ceramics such as Al_2O_3 , MgO , and MgAl_2O_4 . Khan and Khan [1983] found that heavy damage (amorphization) in mica did not occur until $\sim 10^9$ to 10^{10} Gy in muscovite or $\sim 10^8$ to 10^9 Gy in biotite. These doses were from electron irradiation. [This relative sensitivity to amorphization of muscovite and biotite is the reverse of that reported by Iijima and Zhu [1982] (§9.3).] Hurley and Clinard [1980] found clusters of defects in muscovite mica at an ionizing dose of $\sim 10^{10}$ Gy, the lowest dose attainable with their electron microscope.

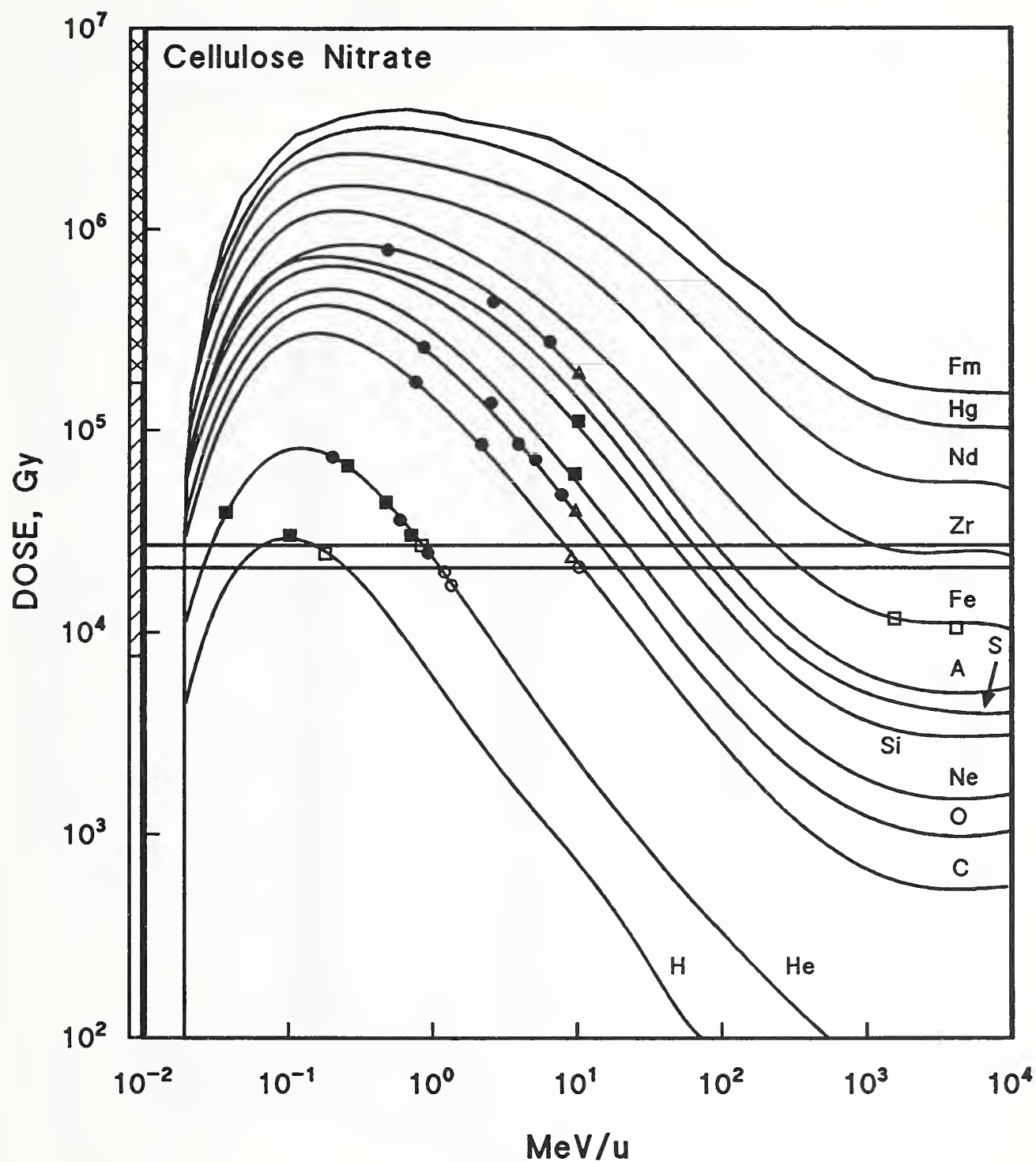


Figure 9.5.1. Calculated dose of ionization energy in cellulose nitrate at 1.5 nm (15 Å) as a function of the ion type and energy. Solid symbols indicate formation of etchable tracks; open symbols otherwise. Squares: Fleischer et al. [1967]; circles: Benton [1967]; triangles: overlapped points. Partial track formation (not plotted) is observed along the dividing line of critical dose. Shading along y-axis gives response to γ irradiation: X = severe damage; / = moderate damage; open = negligible damage. Data from Katz and Kobetich [1968].

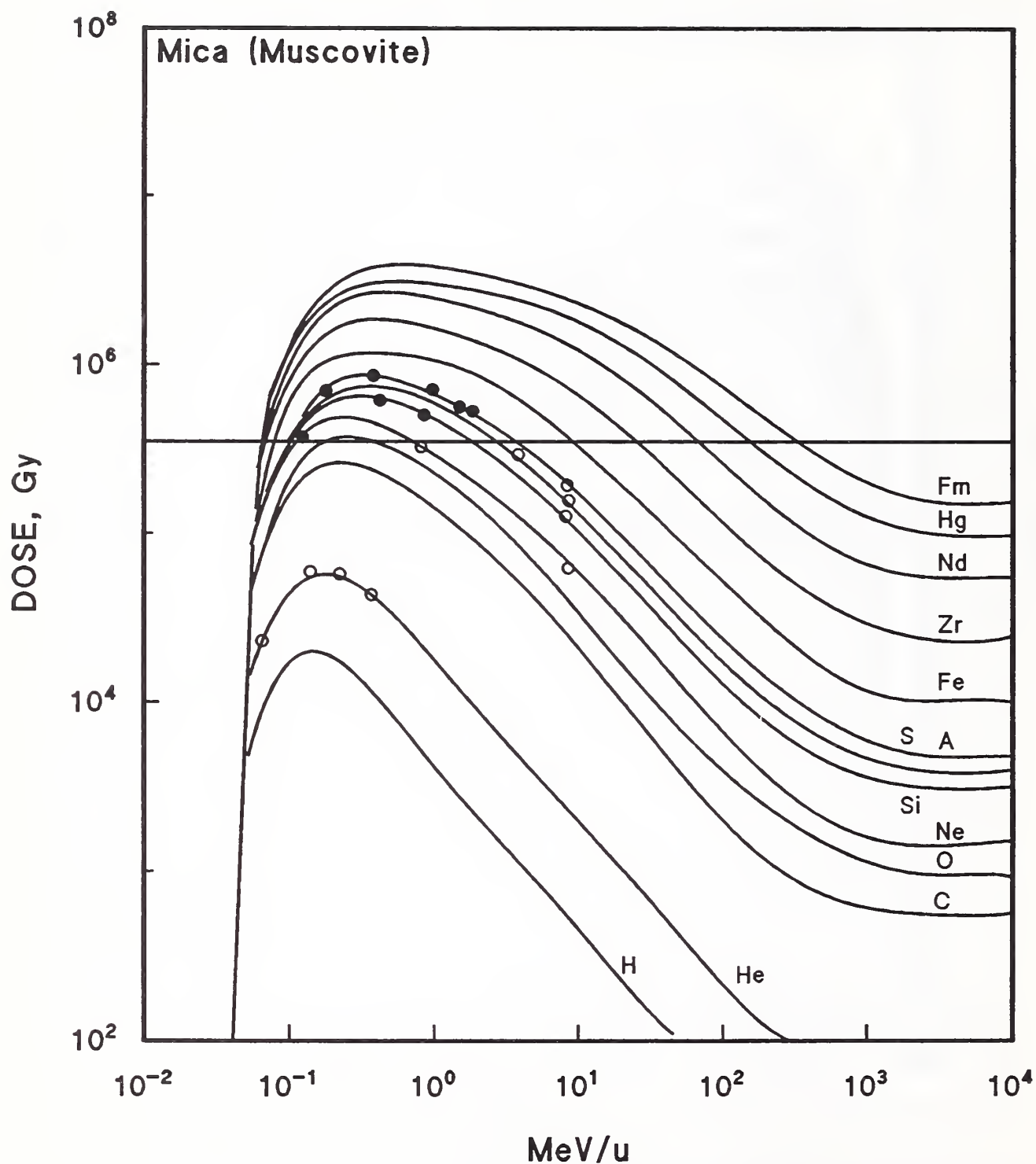


Figure 9.5.2. Calculated dose of ionization energy in cellulose nitrate at 1.9 nm (19 Å) as a function of the ion type and energy. Solid circles indicate formation of etchable tracks; open circles otherwise. Partial track formation (not plotted) is observed along the dividing line of critical dose. Data from Katz and Kobetich [1968].

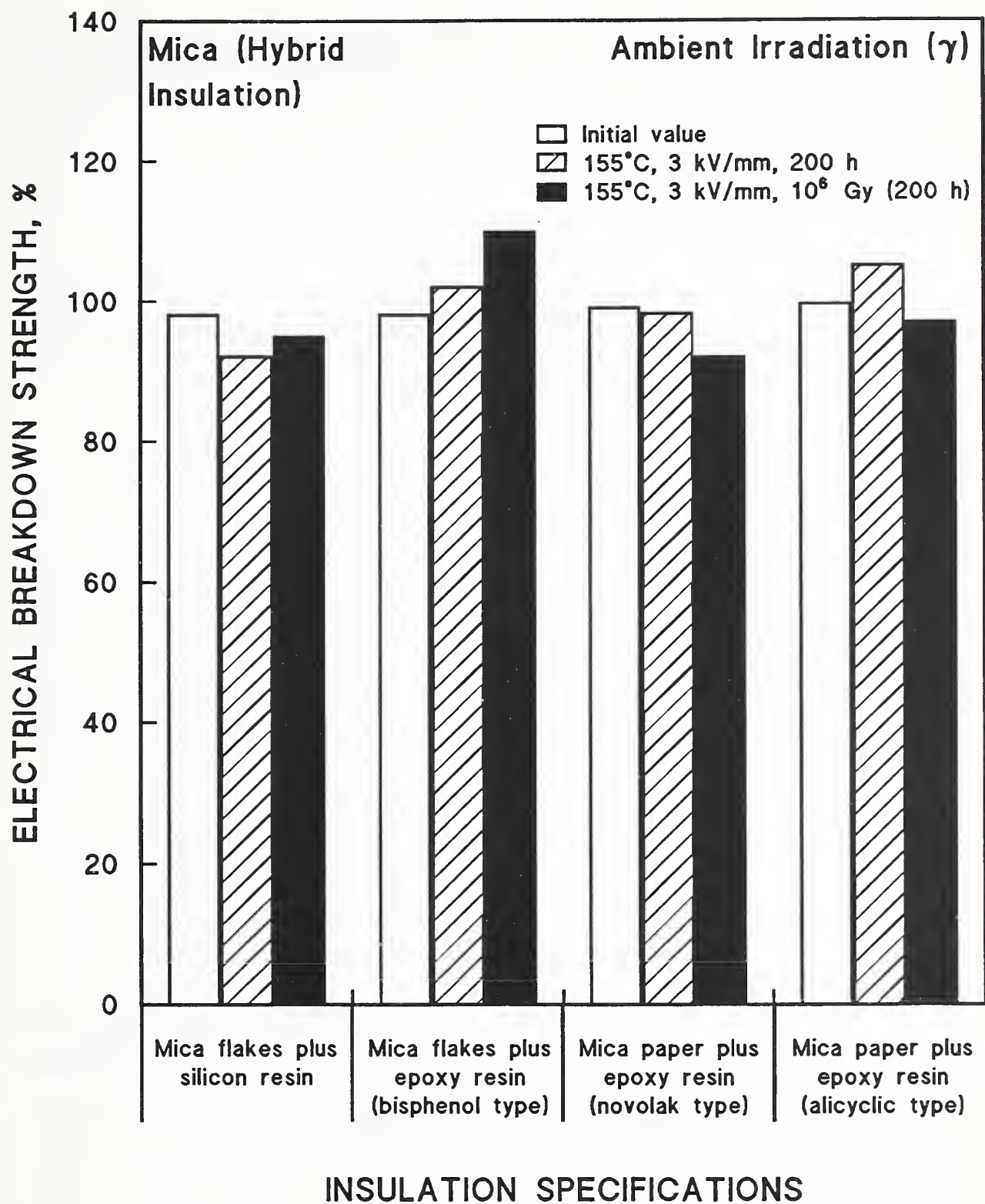


Figure 9.5.3. Model coil insulation characteristics of hybrid mica/organic insulators after 10^6 Gy of γ irradiation at 3 kV/mm and 155°C. Data from Aki et al. [1983].

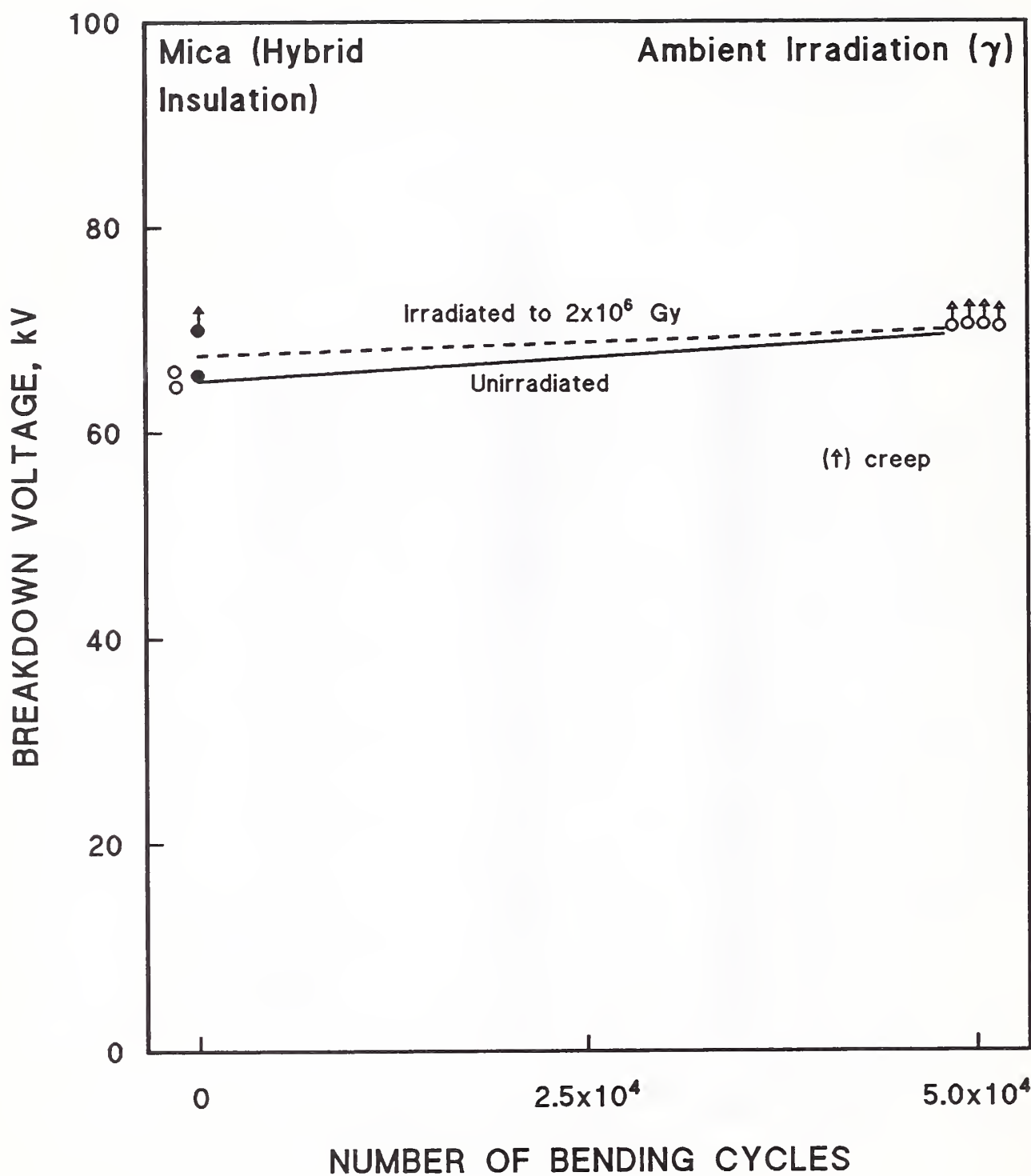


Figure 9.5.4. Electrical breakdown voltage vs. coil bending fatigue cycles of hybrid mica/organic insulation with and without 2×10^6 Gy of γ irradiation. Data from Aki et al. [1983].

9.5.2. Mica Tracks from U Fission

The as-mined, natural forms of mica will usually contain tracks from fission fragments and recoil nuclei stemming from the spontaneous fission and radioactive decay of ^{238}U impurities over geologic times. Uranium impurities are usually associated with zircon (ZrSiO_4) inclusions. The density of the tracks varies from low, unobservable values to $>5 \times 10^4/\text{cm}^2$. Track densities were higher in the biotites and phlogopites studied by Price and Walker [1963] and lower in muscovites, but this generalization may not apply to micas obtained from different sources. Figure 9.5.5 shows naturally occurring "fossil" tracks in a Madagascar phlogopite at a density of about $5 \times 10^4/\text{cm}^2$. The track lengths are of the order of $10 \mu\text{m}$.

When natural mica is processed to form mica paper, it is delaminated by mechanical, chemical, or water-jet processes and then the delaminated material is recohered to form an inorganic "paper" or mat [see, e.g., Ketterer, 1964]. Thus, processing removes track coherence. However, this processing apparently does not remove the U impurities, measured by Price and Walker [1963] to range from 10^{-8} to 10^{-11} atomic fraction in unprocessed micas. The U in inclusions and grain boundaries might tend to separate out to some extent during processing, although no information is available from processors on this point. Figure 9.5.6 shows the same mica material as that of Figure 9.5.5, but after reactor irradiation with a thermal neutron fluence of $10^{21}/\text{m}^2$. The density of tracks resulting from the neutron-induced fission of ^{235}U is about $4 \times 10^5/\text{cm}^2$. Depino and Dahl [1967] obtained a similar density of induced tracks, $7 \times 10^4/\text{cm}^2$, after irradiation of a phlogopite mica to a total neutron fluence of $\sim 10^{23}/\text{m}^2$. The induced track lengths are approximately $10 \mu\text{m}$, the same length as the fossil tracks. Maurette [1966] reported a similar value for the range, $2.1 \text{ mg}/\text{cm}^2$. Track diameters range from about 5 to 15 nm (50 to 150 Å). The tracks shown in the figures above have been etched with HF to allow visualization, although the tracks of unetched, disordered material (diameter $\sim 10 \text{ nm}$) can also be seen in the electron microscope (Figure 9.5.7). Since muscovite mica is most commonly used in insulation products, it is fortunate that the usual track etching time of 30 min is longer for this type of mica than for phlogopite and biotite, which have etching times of 1 min and 20 s, respectively. The undamaged cleavage plane surface of muscovite mica does not dissolve with the etching treatments used [Fleischer et al., 1964]. Figure 9.5.8



Figure 9.5.5. "Fossil" tracks in Madagascar phlogopite from ^{238}U spontaneous fission fragments after visualization by etching for 1 min. in 15% HF at 50°C. Track density is $\sim 5 \times 10^4/\text{cm}^2$. From Price, P.B.; Walker, R.M. Fossil Tracks of Charged Particles in Mica and the Age of Minerals. *Journal of Geophysical Research* 68. pp. 4847-4862. 1963. Copyright by the American Geophysical Union. Reprinted with permission.

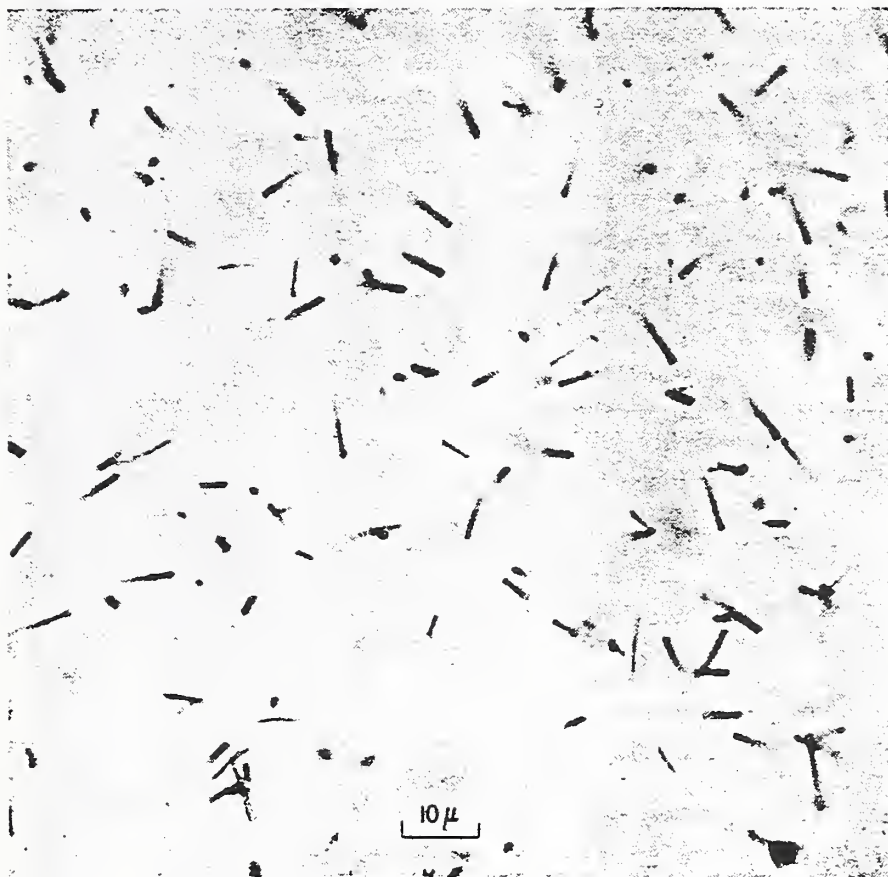


Figure 9.5.6. Induced tracks in Madagascar phlogopite from ^{238}U fission after thermal-neutron fluence of $10^{21}/\text{m}^2$. New track density is $\sim 4 \times 10^5/\text{cm}^2$. Same specimen as shown in Figure 9.5.5 before activation. From Price, P.B.; Walker, R.M. Fossil Tracks of Charged Particles in Mica and the Age of Minerals. *Journal of Geophysical Research* 68. pp. 4847-4862. 1963. Copyright by the American Geophysical Union. Reprinted with permission.

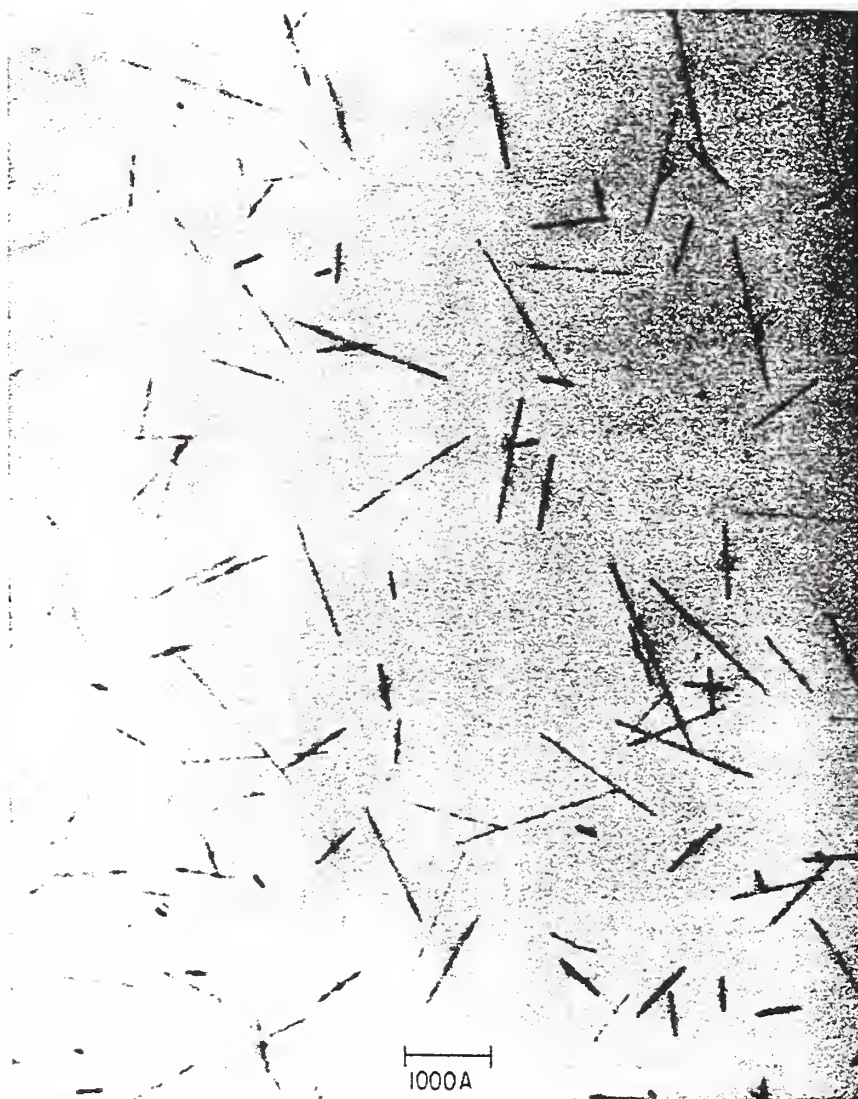


Figure 9.5.7. Fission fragment tracks in synthetic mica, observed by TEM. The material was irradiated with fission fragments from ^{235}U . From Price, P.B.; Walker, R.M. Fossil Tracks of Charged Particles in Mica and the Age of Minerals. *Journal of Geophysical Research* 68. pp. 4847-4862. 1963. Copyright by the American Geophysical Union. Reprinted with permission.

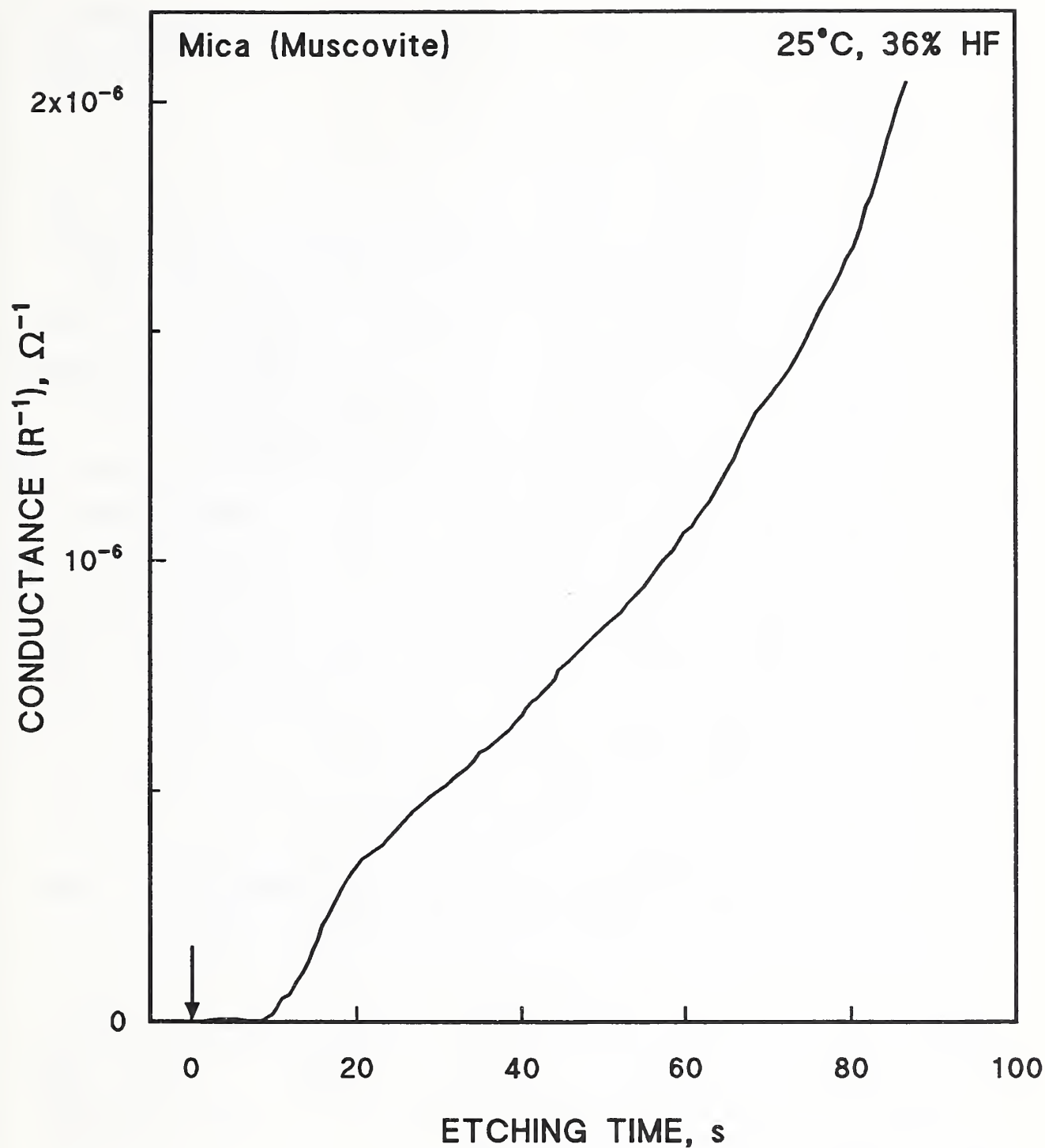


Figure 9.5.8. Conductance as a function of time for 7.1- μm thick mica of track density $4 \times 10^5/\text{cm}^2$. Etched in 35.7% HF at 25°C. Arrow indicates addition of acid. Data from Bean et al. [1970].

indicates a latent time of perhaps 10 s in etching muscovite mica at 25°C before enough material is removed to allow passage of conducting ions through the materia [Bean et al., 1970]. However, Figure 9.5.9, from the same investigation, indicates shorter latent periods for other types of mica, and Maurette [1966] states that the initial attack of the etchant is very fast, requiring less than a second to form a channel of 3-nm (30-Å) diameter. Presumably, the longer latent time for a conductance current to appear in muscovite mica indicates that continuous voids are not present along the track; rather, the material is altered so that it dissolves very easily, as occurred in the ion-irradiation studies of Jech, discussed in §9.4 above. Even though voids may not be present, or at least, are not continuous along the tracks, Davidson and Yoffe [1965] found that fission-fragment tracks do lower the electrical breakdown strength of mica. Figure 9.5.10 is an electron micrograph of these breakdown sites, after ambient irradiation of muscovite mica with fission fragments. These authors did not quantify the effects they observed, although their track density of 10^{11} tracks/cm² is higher than would be expected from fission of ²³⁵U impurities subjected to the expected thermal neutron fluence in the TF magnets, based on the limited results of Price and Walker [1963] discussed above. Of course, as the discussion in the following §9.5.3 indicates, fission fragment and α -recoil damage may be much heavier, or of different character at 4 K. Berman et al. [1960a] reported that fission fragments appeared to act synergistically with reactor neutrons to increase damage (in Al₂O₃). Also, the expected separation of the layered mica structure from fast neutron displacement damage (§9.3, above) should connect paths in individual layers and perhaps, lower breakdown strength catastrophically under fusion conditions. In contrast, Bunch [1977b] found no electrical breakdown degradation in neutron-irradiated Al₂O₃ with voids of 9-nm (90 Å) diameter (see also Clinard and Hobbs [1986]). A pulsed breakdown field up to 180 kV/mm was applied. Clinard and Hobbs did not specify the neutron fluence, but reported that the material was irradiated to 12 dpa at 1100 K. Bunch reported a neutron fluence of 1 to 2×10^{26} /m².

Because extremely small amounts of U impurity may give rise to a significant density of tracks, activation or other analysis of mica intended for use in fusion reactors would have to determine U impurity levels to the range of one

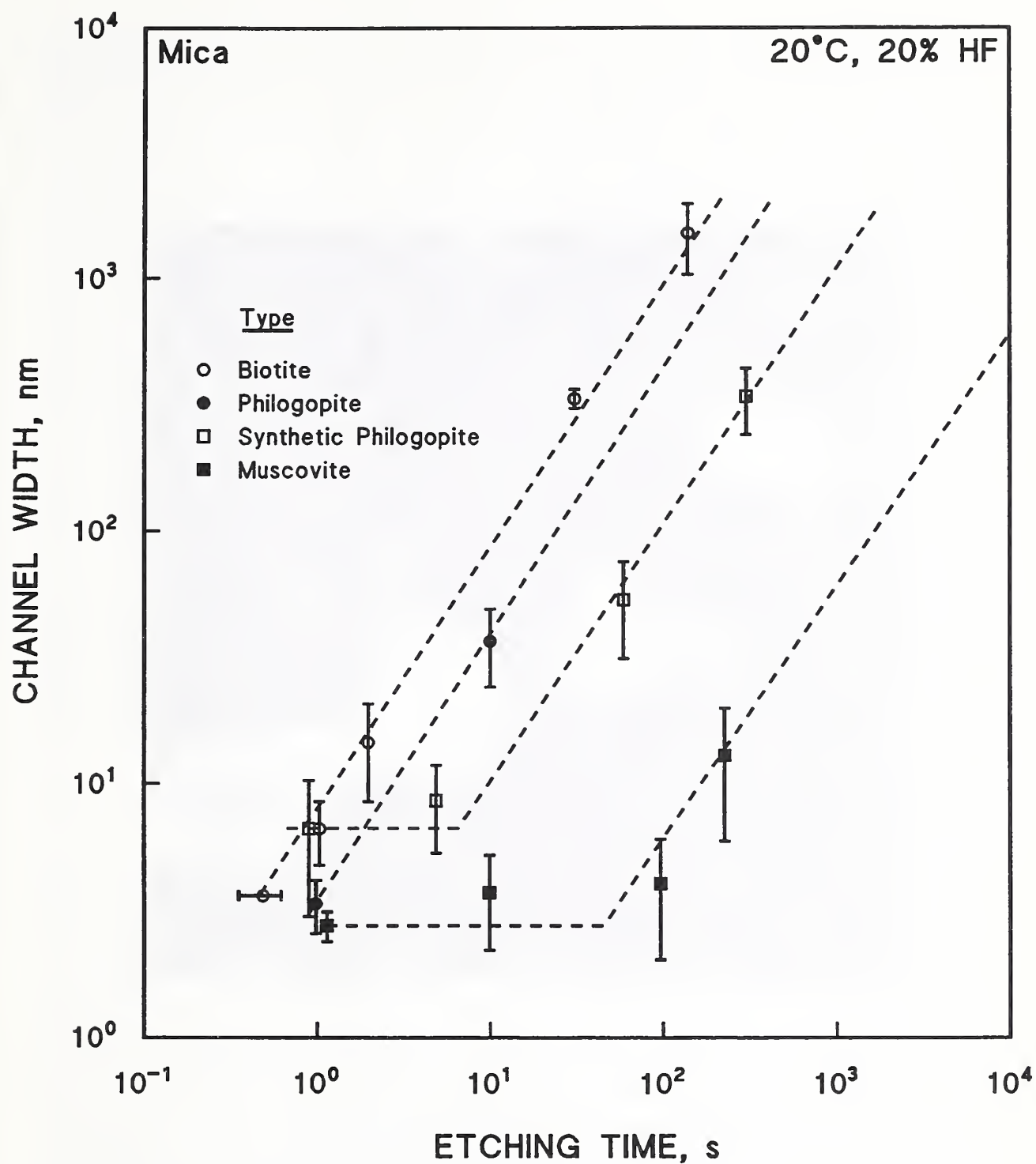


Figure 9.5.9. Etching rates of tracks in several types of mica. From Price and Walker [1962b].

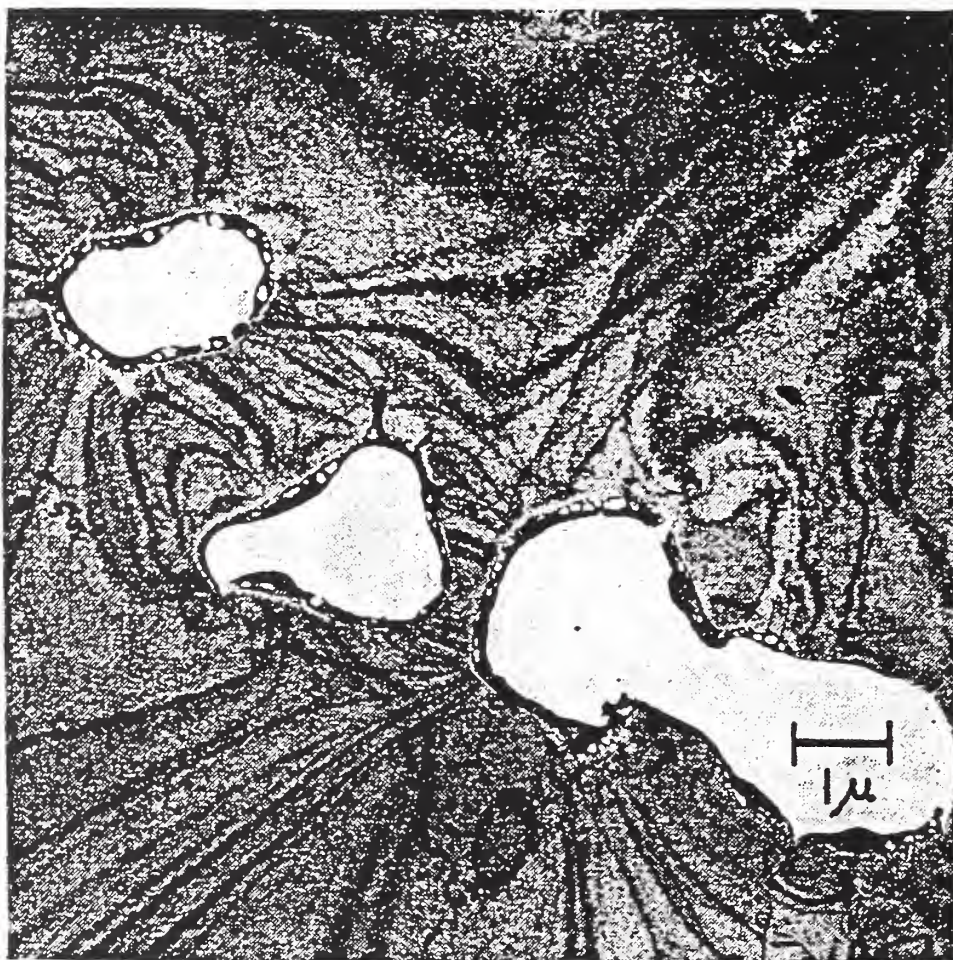


Figure 9.5.10. Electron micrograph of electrical breakdown sites in muscovite mica after irradiation with fission fragments. Track density: $10^{11}/\text{cm}^2$. From Davidson, A.T.; Yoffe, A.D. 1965. Dielectric Breakdown in Thin Mica Crystals. *Nature* 206. pp. 1247-1248. Reprinted with permission from *Nature*; copyright 1965; Macmillan Magazines Limited.

atomic part per 10^8 to 10^{11} . Price and Walker [1963] obtained induced track densities up to $4 \times 10^5/\text{cm}^2$ from this approximate range of U impurity. In one mica tested, a thermal-neutron fluence of $10^{21}/\text{m}^2$ was used to induce a fission track density of $4 \times 10^5/\text{cm}^2$. This is comparable to the thermal-neutron fluence expected in the ITER TF magnets. (More specifically, a thermal-neutron fluence of $0.5 \times 10^{21}/\text{m}^2$ [$0.022 \text{ eV} \leq E \leq 0.87 \text{ eV}$] is obtained by scaling the results of Sawan [1993] for a fast neutron fluence of $3.6 \times 10^{22}/\text{m}^2$; the ^{235}U fission cross section ranges from about 545 barns in the thermal energy range to about 100 barns at 1 eV; and the fast fission cross section of ^{238}U [~99% isotopic abundance] is about 0.5 barns at 3 MeV [Lapp and Andrews, 1954].) Fleischer and Price [1964] have described counting and thermal neutron exposure techniques that could be used to determine U concentration and expected track densities. However, since the ITER exposure will occur at 4 K, allowance must be made for some recovery of damage before ambient-temperature etching or electron microscopy is performed. Knowledge of the zircon (ZrSiO_4) content may also be useful in determining or estimating the U content, since this mineral may contain U as a substitution solid solution up to about 0.1%. Then, in addition, several times as much U and Th may be contained by the zircon in the form of small crystal inclusions [Hurley and Fairbairn, 1952].

9.5.3. Temperature Effect upon Track Recovery and Formation

Track fading has been studied as a function of temperature [Fleischer et al., 1965a]. If track fading were governed by a single activation energy, there would be a linear relationship between the logarithm of the annealing time and T^{-1} , where T is the absolute temperature. Although Fleischer et al. noted that there was evidence that a single activation energy was not correct for phlogopite mica, they were able to obtain an Arrhenius line when they plotted the time for 50% of the tracks to decrease in length to less than 1 μm . Extrapolating this line to 22°C would give a fading time of many years, but such an extrapolation may be unwarranted, because measurements were made only between 400 and 500°C. Khan et al. [1984] extended annealing studies to 850°C for tracks produced by very energetic (3975 MeV) ^{238}U ions. A significant recovery, as measured by a sharp decrease in the etching velocity, did not occur until specimens were warmed to about 550 and 600°C (Figure 9.5.11). Both the high temperature data of Fleischer et al. and that of Khan et al.

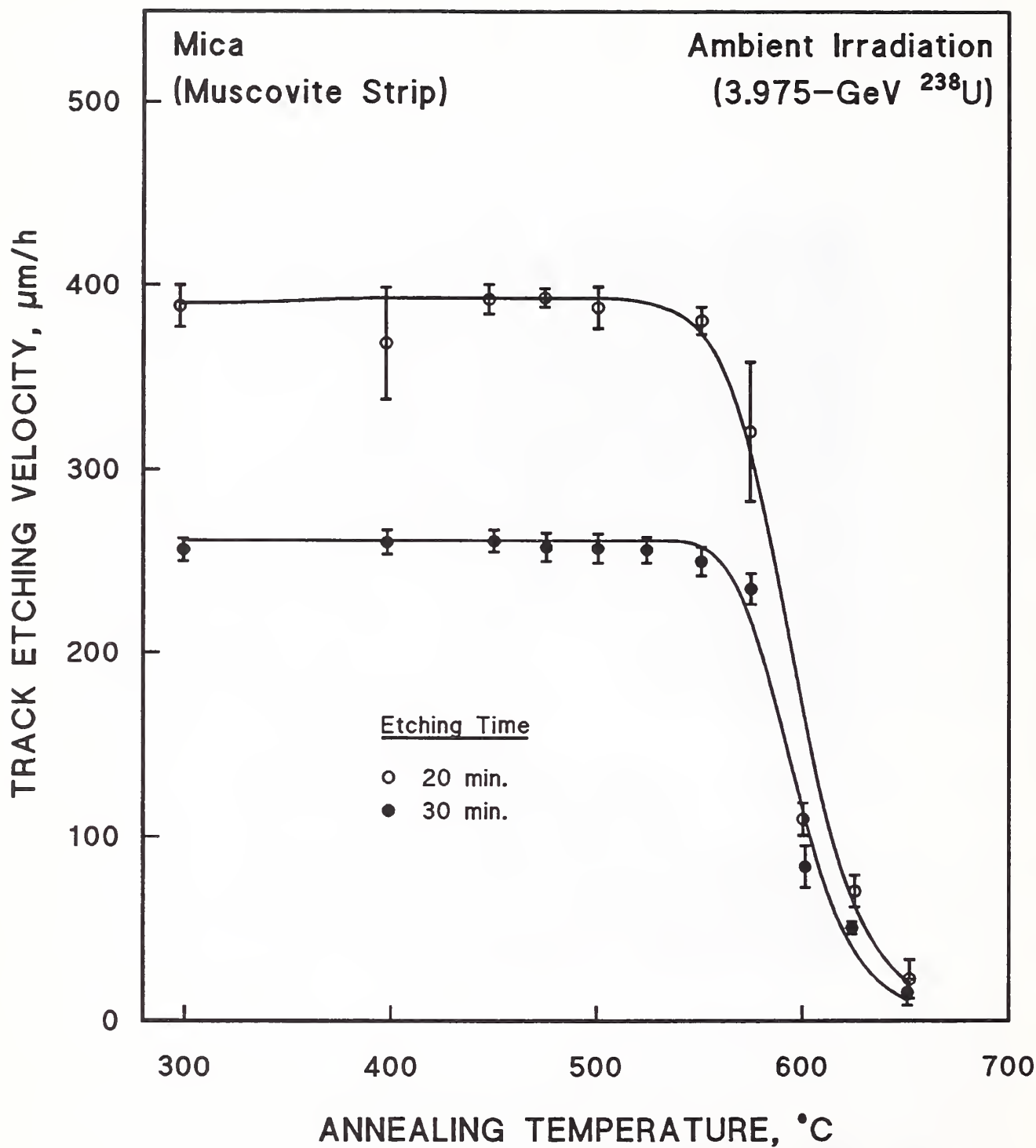


Figure 9.5.11. Annealing of ^{238}U -ion tracks (3.9-GeV) in mica, as determined by the track etching velocity. Data from Khan et al. [1984].

appear to indicate that ambient-temperature warm-up will not suffice to anneal track damage, at least from very energetic, heavy ions. However, fading of ^{235}U fission fragment tracks in biotite, phlogopite, and muscovite has been observed, either at ambient temperature or in the electron microscope [Bonfiglioli et al., 1961; Price and Walker, 1962a]. Bonfiglioli et al. stored irradiated specimens in liquid nitrogen until they were placed in the EM, and attributed discontinuous tracks to partial recovery. A cryogenic temperature stage in the TEM was required for the observation of tracks in biotite. Since any fissuring in mica from 4-K displacement of K atoms may also anneal somewhat at ambient temperature, this effect upon breakdown strength will also have to be observed in situ, at 4 K. In the TEM studies, the interlayer Na or K cations diffused away, because very thin sections were used; this would not be the case for larger specimens or for mica insulation in the TF magnets.

Whether charged particles of much lower mass, such as α particles, would form tracks at 4 K even though such tracks are not observed at ambient temperatures (Figure 9.5.2) depends upon the mechanism of track formation. One of the first groups to report tracks in mica suggested that a thermal spike mechanism was operating, and explained differences in the observed track radii in different types of mica on the basis of this thermal model [Bonfiglioli et al., 1961]. Tracks were said to represent material thermally altered by heat spikes generated by the intense ionization along the path of a fusion fragment. The radius of such a thermally altered region can be approximated by

$$r = [Q/e\pi CT_c]^{1/2}, \quad (9.1)$$

where Q is the heat released per unit path length, C is the specific heat, and T_c is the thermal decomposition temperature [Sherman, 1962 and citations therein]. This equation accounted for the larger diameter tracks in muscovite ($T_c = 700^\circ\text{C}$) than in fluorophlogopite ($T_c = 1200^\circ\text{C}$). Since the tracks were not etched, but, instead, were observed in an electron microscope, the lack of tracks in biotite ($T_c = 500^\circ\text{C}$) was attributed to recovery during beam heating. Although many other authors have subscribed to the thermal spike model [e.g., Chadderton, 1965; Matzke, 1982], Price and Walker [1962a] questioned this interpretation and proposed instead an ion-explosion spike mechanism [Fleischer et al., 1965b]. In this model, mutual repulsion of positive ions

ejects them into the surrounding lattice. However, Price and Walker [1962a] also found that track fading in biotite could be arrested by cooling the sample to 77 K during electron microscopy, and that tracks in this form of mica were much wider than in other micas, indicating some involvement of a thermal mechanism. Furthermore, tracks in synthetic fluorophlogopite were found to be narrower and stable under observation. Sigrist and Balzer [1977] later showed that the latent-track etchability threshold could be better scaled by thermodynamic parameters than by parameters of an ion-explosion mechanism. Khan and Khan [1983] found that the dose from the secondary, δ -ray electrons, about 10^6 Gy, would be inadequate to produce etchable damage, as postulated in the ionization spike model. About 10^9 Gy were required to produce observable etchable damage in muscovite mica. Hashemi-Nezhad et al. [1982] came to a similar conclusion for biotite mica; the Ne ion is the lightest ion to produce etchable tracks in biotite (at ambient temperature), but the dose from 1-MeV electrons necessary to produce coloration and enhanced bulk etching (amorphization) was $\sim 10^8$ to 10^9 Gy, much higher than the electron dose from δ rays in the path of a Ne ion.

Dartyge et al. [1976] challenged the existence of an energy threshold mechanism for track registration: their small angle X-ray scattering experiments on latent tracks indicated that zones of disordered material were formed and the size and separation of these zones determined the chemical etchability of the latent track. However, these results were criticized by Albrecht et al. [1985], who again found an energy loss dependence. These authors determined that a very large number of atoms were displaced per nm of track: 480 ± 200 for ^{238}U ; 190 ± 90 for ^{132}Xe ; and 60 ± 30 for ^{84}Kr ions. A large amount of displacement damage would appear to facilitate a decrease in electric breakdown strength after track formation.

Toulemonde et al. [1989, 1990] also conducted experiments that related the level of damage in tracks to the electronic stopping power of the ion in the medium. Ritchie and Claussen [1982] noted that although the ions lost most of their energy to electrons in the stopping medium, atomic displacement was necessary for track registration. They suggested that for insulators, the excited electrons formed a core electron-ion plasma, leading to transfer of the electronic energy to the lattice, and causing a transiently heated region.

In metals and semiconductors, higher electron mobility evidently prevents the energy deposited in the electronic system from being confined long enough to form a transiently heated region.

In accord with the model of Ritchie and Claussen, Toulemonde et al. [1992] used a thermal-spike calculation to describe the effects of high energy, heavy-ion irradiation in amorphous metals and semiconductors. Instead of a simpler early model [Equation (9.1)], Toulemonde et al. used a more sophisticated formalism, noting that the phase transformations induced by heavy-ion irradiation may result from an increase of the lattice temperature in a two-step process. First, the energy deposited in electron excitation is shared with the "cold" electrons (in $<10^{-14}$ s), and then the energy is transferred to the lattice by electron-atom interactions ($\sim 5 \times 10^{-13}$ s). Since the electron and lattice systems are not in thermal equilibrium, the space and time evolution of the electronic system and lattice temperatures are governed by a set of coupled nonlinear differential equations which Toulemonde et al. solved numerically in cylindrical geometry. This procedure requires many additional thermodynamic parameters beyond those in the simple Equation (9.1). Nevertheless, the rise in local temperature is again inversely proportional to the specific heat, as in Equation (9.1). Thus, the thermal spike mechanism, even when couched in more advanced formalism, would evidently predict an enhancement of track formation and track diameter at 4 K, since the specific heat of mica is expected to be several orders of magnitude lower at 4 K than at ambient temperature. Even α particles may therefore induce tracks at 4 K, although it is well-established that they do not at ambient temperature (Figure 9.5.2). Since about 7% of the neutron fluence at the TF magnets is expected to have an energy above 5 MeV, production of α particles is not insignificant. At ambient temperature, particles with atomic mass below about 30 u are not expected to cause formation of etchable tracks in mica [Price and Walker, 1962a], and, since the average atomic mass for mica is about 20, the recoil ions from α -particle reactions would not be expected to produce tracks. Again, however, under the assumption of a thermal mechanism, track formation for recoils of ~ 20 -u atoms could be significant at 4 K. Toulemonde et al. [1987] used a Mössbauer spectroscopic technique to show that the change in magnetic properties in a ferrimagnetic oxide was dependent upon the electronic stopping power, as discussed above, both at 77 and 300 K. However, their data

were normalized, so they did not publish a comparison of the magnitude of the effect at the two temperatures. Hence, the data of Toulemonde et al. do not necessarily disagree with the hypothesis of an increase in the latent track damage at cryogenic temperatures.

Track formation in an unidentified mica from fission fragments of ^{252}Cf at 77 K was studied by Fleischer et al. [1965a]. This was done by observing the density and length distribution of etched tracks. Within the experimental error of $\pm 10\%$, the track density and length were found to be unchanged at 77 K, when irradiation with fission fragments occurred. However, etching and measurement of tracks evidently took place at ambient temperature, which could have permitted some recovery of 77-K damage, and caused the 77-K results to appear similar to those from ambient-temperature irradiation. Furthermore, Fleischer et al. expected that a difference in track registration sensitivity at 77 K would be manifested by a change in the track length distribution. Actually, the range of fission fragments would be unchanged, to a first approximation, at lower temperatures, but the track radius would increase, as predicted by Equation (9.1) and the pronounced dependence of the specific heat upon temperature below 300 K. A much stronger effect should occur at 4 K than at 77 K. Fischer et al. evidently did not measure the track radius from 77-K irradiation with fission fragments for comparison with ambient-temperature results.

The individual mica flakes that are separated and then reconstituted to form a mica insulation product have an inherent degree of porosity [e.g., Noren and Ball, 1969; Klein, 1981]. Therefore, even if track formation does not occur, or does not degrade the electrical breakdown strength significantly, the likely separation of mica layers under displacive neutron irradiation, as discussed above in §9.3, may decrease electrical breakdown strength, because connecting void paths will open up, to some degree. The possible degradation of electrical breakdown strength in mica must be tested in situ, after 4-K irradiation, because some of the interlayer K cations may diffuse back to bonding positions during warm-up. The interlayer cations in the TEM experiments discussed above were permanently removed, owing to the use of thin sections in the electron microscope.

9.5.4. Electric-Field Enhancement of Tracks

The topic of possible electric-field enhancement of track formation must be briefly discussed, because the insulation in the TF magnets is exposed to an electric field and at least two papers noting such effects have appeared in the literature. In the first, Crannell et al. [1970] found that the application of fields up to 55 kV/mm to cellulose nitrate during α -particle irradiation enhanced the efficiency for etchable track formation in an α -particle energy range from 3.4 to 4.0 MeV. However, prior application of the field also produced considerable enhancement, so the authors hypothesized that ozone formed by corona discharge was the activating agent. (The experiments were performed in air.)

Blanford et al. [citation, Fleischer et al., 1975] observed a sensitivity enhancement when bisphenol polycarbonate was irradiated in the presence of a spark discharge. In this case, the enhancement was probably due to production of one of the nitrogen oxides produced in the discharge. This work was reviewed by Fleischer et al. [1975] in a book that extensively reviews track production in mica and other substances. However, comparable experiments in mica were not cited. Because no intrinsic electric field effect has been substantiated in other materials, and, apparently, the possible production of such an effect in mica has not been investigated, electric field enhancement of track production in mica remains a topic for further research at this writing.

9.6. AMORPHIZATION

Estimates of the dose of ionizing radiation required for amorphization of mica vary somewhat, perhaps because some estimates were obtained from indirect evidence, rather than from X-ray or electron diffraction techniques. Spitzer [1970] used mica splittings (type unspecified) as support films for TEM studies with 100-keV electrons. He reported that the support films became completely amorphous at a total dose of $500 \text{ (A}\cdot\text{s)/cm}^2$, equivalent to an electron fluence of $3.1 \times 10^{21}/\text{cm}^2$. Using the stopping power for 100-keV electrons in SiO_2 from Berger and Seltzer [1982] gives $(3.1 \times 10^{21}/\text{cm}^2) \times (3.4 \text{ MeV cm}^2/\text{g}) = 1.05 \times 10^{25} \text{ MeV/kg} = 1.7 \times 10^{12} \text{ Gy}$.

In contrast, Hashemi-Nezhad et al. [1982] concluded that a dose of only $\sim 10^8$ to 10^9 Gy from 1-MeV electrons was necessary to produce enhanced bulk etching in biotite (§9.5.3). (As noted above in §9.4, the enhanced solubility of a material signals the onset of amorphization.) Khan and Khan [1983] found that about 10^9 Gy were necessary for improved etching in muscovite mica. Their required dose for biotite was about an order of magnitude smaller than that required for muscovite, and these authors reported that their estimates of critical doses were about an order of magnitude greater than those of Hashemi-Nezhad. This result appears to disagree with a report of Iijima and Zhu [1982], who found that muscovite vitrified before biotite under TEM (§9.3). Khan and Khan used 1-MeV electrons, 10-MeV protons, and 40-MeV α particles.

Jech [1967], who studied solubility with a radioactive tracer technique rather than with physical measurements and EM, apparently found a lower limit for the onset of amorphization (§9.4). The critical ion fluence with 10-keV Kr ions was $\sim 5 \times 10^{16}/\text{m}^2$, equivalent to a fast neutron fluence of roughly $5 \times 10^{21}/\text{m}^2$, using the approximate rule of Evans et al. [1972] discussed above in §1.2.6. Using the conversion factor of 7.7×10^{-17} Gy/(neutron/ m^2) published for fast neutrons in Al_2O_3 [Egusa et al., 1984] would give an ionization dose of only about 4×10^5 Gy. More complete disorder required $\sim 4 \times 10^6$ Gy. However, this ionization dose was accompanied by a much higher proportion of displacement damage than that from electrons and protons (Table 1.2.7). This would account for the difference of several orders of magnitude with the results of Khan and Khan and Hashemi-Nezhad. Also, Jech did not report the form of mica that was studied, and Khan and Khan found a difference of an order of magnitude in the amorphization dose of two types of mica. Fowler et al. [1981] also found many orders of magnitude difference in the ionization dose required for damage to phlogopite mica in the glass ceramic Macor, depending upon whether or not the ionizing dose was accompanied by significant displacive damage, as was the case for the 14-MeV irradiations (§10.1.3, below).

Comparatively, Jech found that mica amorphized at a fluence about an order of magnitude below that of Al_2O_3 . X-ray studies of amorphization in Al_2O_3 by Matzke and Whitton [1966] (§2.3) indicated an ion fluence of $8 \times 10^{17}/\text{m}^2$ was required; this was in agreement with the onset fluence of $3 \times 10^{17}/\text{m}^2$ found by Jech. Matzke and Whitton used 40-keV Kr and Xe ions and Jech used 10-keV Kr

ions. Since Matzke and Whitton also observed that MgO amorphized less easily than Al_2O_3 , and Jech observed that mica amorphized at a lower fluence than Al_2O_3 , the order of relative stability is probably $\text{MgO} > \text{Al}_2\text{O}_3 > \text{mica}$. Evidence for the relative stability of the two forms of mica, biotite and muscovite, is unclear, as noted above. It is difficult to extrapolate to the values of fast neutron amorphization fluences at 4 K from these data, because McHargue et al. [1986] found that the amorphization fluence for Al_2O_3 was two orders of magnitude lower at 77 K than at 300 K, for foreign ions, and probably many orders of magnitude lower for host ion or fast neutron amorphization.

10. RADIATION RESISTANCE OF HYBRID INSULATION

Because differential swelling of a two-component material under radiation may cause stresses at the interface, hybrid insulations may be especially sensitive to radiation. Very little research has been done in this area. The approach in this report will be to review results on hybrid mica insulation, considering both radiation damage to the mica-glass ceramic, Macor, and to mica-epoxy hybrids. Then, the theoretical treatments of this subject will be briefly surveyed.

10.1. LOW TEMPERATURE IRRADIATION OF A MICA-GLASS CERAMIC

The machinable glass ceramic, Macor, consists of interlocking, but noncontiguous fluorophlogopite crystals ($\text{KMg}_3\text{AlSi}_3\text{O}_{10}\text{F}_2$) in a borosilicate glass matrix. The machinability is comparable to that of a soft metal. Vitreous SiO_2 densifies and exhibits an increase in refractive index at a relatively low neutron fluence of about 10^{22} to $10^{23}/\text{m}^2$. A muscovite mica exhibited very large swelling at $2 \times 10^{24}/\text{m}^2$ ([Bopp et al., 1960], §9.2), but TEM studies indicated that a fluorophlogopite mica, lacking the OH ion, would be more resistant to vitrification than other micas ([Iijima and Zhu, 1982], §9.3). However, mica is considerably less radiation resistant than the ceramic oxides (e.g., §§9.2, 9.4), as is vitreous SiO_2 , so their hybrid combination should be most useful in regions of lower fluence. A further problem is that the B-free forms of Macor investigated by Porter et al. [1981] at high irradiation temperatures are no longer available. The ^{10}B isotope produces α particles both from thermal and very high energy neutron fluences.

10.1.1. Defect Density

Measurements of the defect density in irradiated Macor were not found in the literature search.

10.1.2. Change in Volume

Fowler et al. [1981] irradiated Macor at ambient temperature with 14-MeV neutrons from the RTNS source at fluences up to $10^{22}/\text{m}^2$. An observable density

change was detectable only at the highest fluence of $10^{22}/\text{m}^2$. It was an increase of 0.05 to 0.1%. Coghlan and Clinard [1991] continued the irradiation (also at ambient temperature) to a maximum 14-MeV fluence of $4 \times 10^{22}/\text{m}^2$, observing first an increase in volume, and then a decrease, as shown in Figure 10.1.1. Coghlan and Clinard noted that this unusual result was consistent with two competing processes in the composite: an increase in the volume of the mica (§9.2, Figure 9.2.2) and a decrease in the volume of the glass (§6.2, Figure 6.2.4). Coghlan and Clinard used mathematical expressions for the density as a function of fluence with three adjustable parameters to fit the densities of the two components, mica and glass, and that of the composite. (See the paper for details of the procedure.) The three density functions are shown graphically in Figure 10.1.2. Then, Figure 10.1.3 shows that the swelling of Macor calculated from these density functions is in reasonable agreement with the experimental results (Figure 10.1.1). Although the model predicts a limiting value for the swelling of Macor of less than 0.5 vol.% at high fluences, the authors cautioned that differential swelling of the two phases of the composite material could lead to reduction of strength, and, eventually, to the separation of the phases and total destruction of the material. Clinard et al. [1984] had observed this behavior earlier in a SiC/graphite composite irradiated to a high fission fluence: the composite suffered almost complete delamination as the result of swelling of the SiC and densification of the graphite.

10.1.3. Microstructural Changes; Amorphization

The Macor irradiated by Fowler et al. was ion-thinned for examination in a TEM, along with unirradiated control specimens. Only the material irradiated to $10^{22}/\text{m}^2$ showed noticeable change: occasional areas of barely visible mottled damage in the mica phase. Using correlations for the ionization dose for Al_2O_3 [citation, Fowler et al., 1981], the ionization dose from this 14-MeV fluence was found to be $\sim 6 \times 10^6$ Gy and the ionization dose from a fission irradiation that caused ~4% swelling in mica was $\sim 2 \times 10^7$ Gy (Figure 9.2.2). Ionizing doses were also generated in the TEM. A dose of $\sim 10^{11}$ Gy was necessary to cause observable damage to the mica constituent of Macor, whereas slightly lower doses caused pores to appear in the glassy matrix. Thus, there is a difference of about 4 or 5 orders of magnitude in the effects of

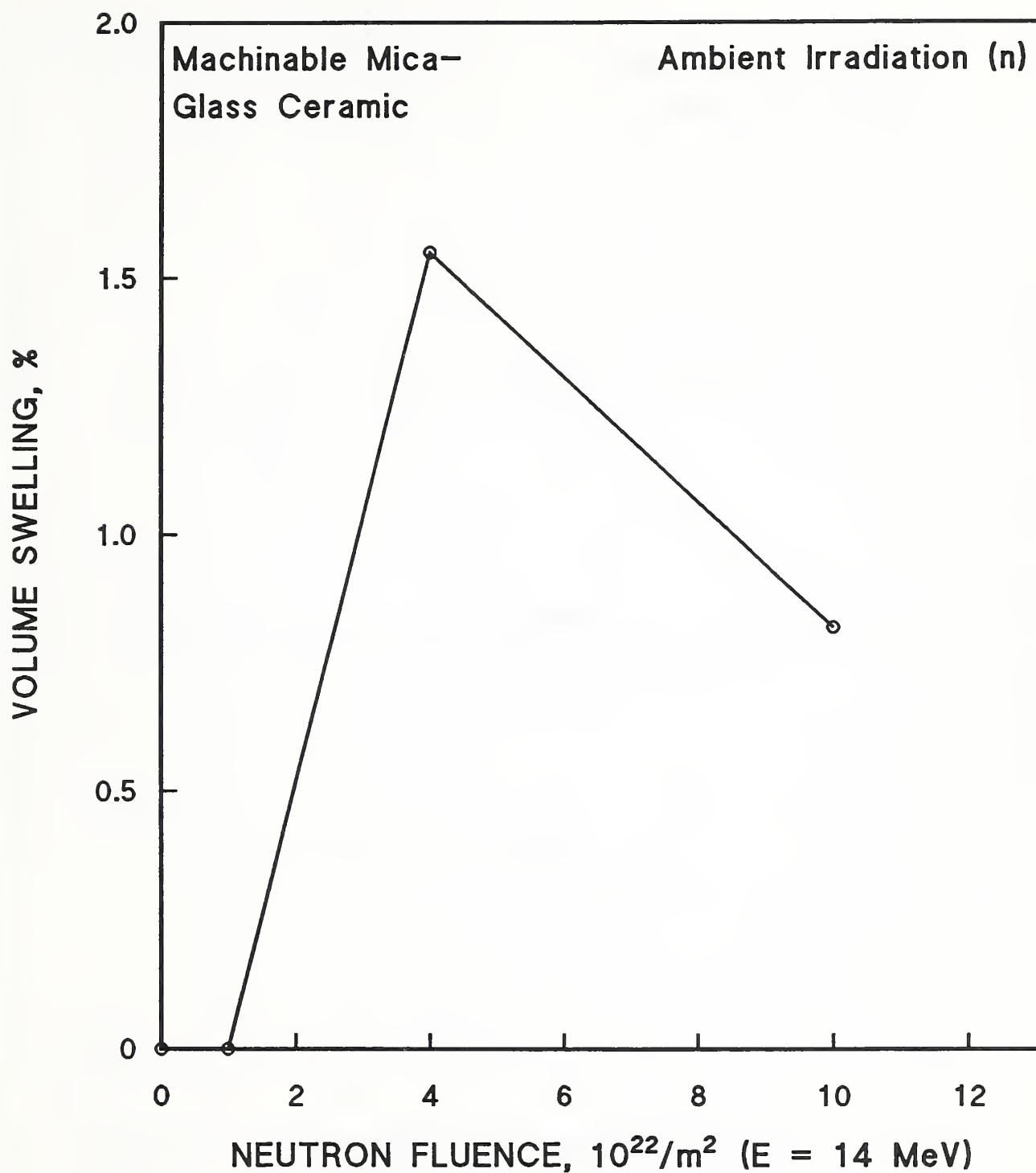


Figure 10.1.1. Experimental values for the swelling of Macor as a function of the 14-MeV neutron fluence. Data from Coghlan and Clinard [1991]. The value of zero for the swelling at a fluence of $10^{22}/\text{m}^2$ is roughly consistent with the increase of +0.05 to +0.1% in the density observed by Fowler et al. [1981], which would require initial compaction ($-\Delta V/V$).

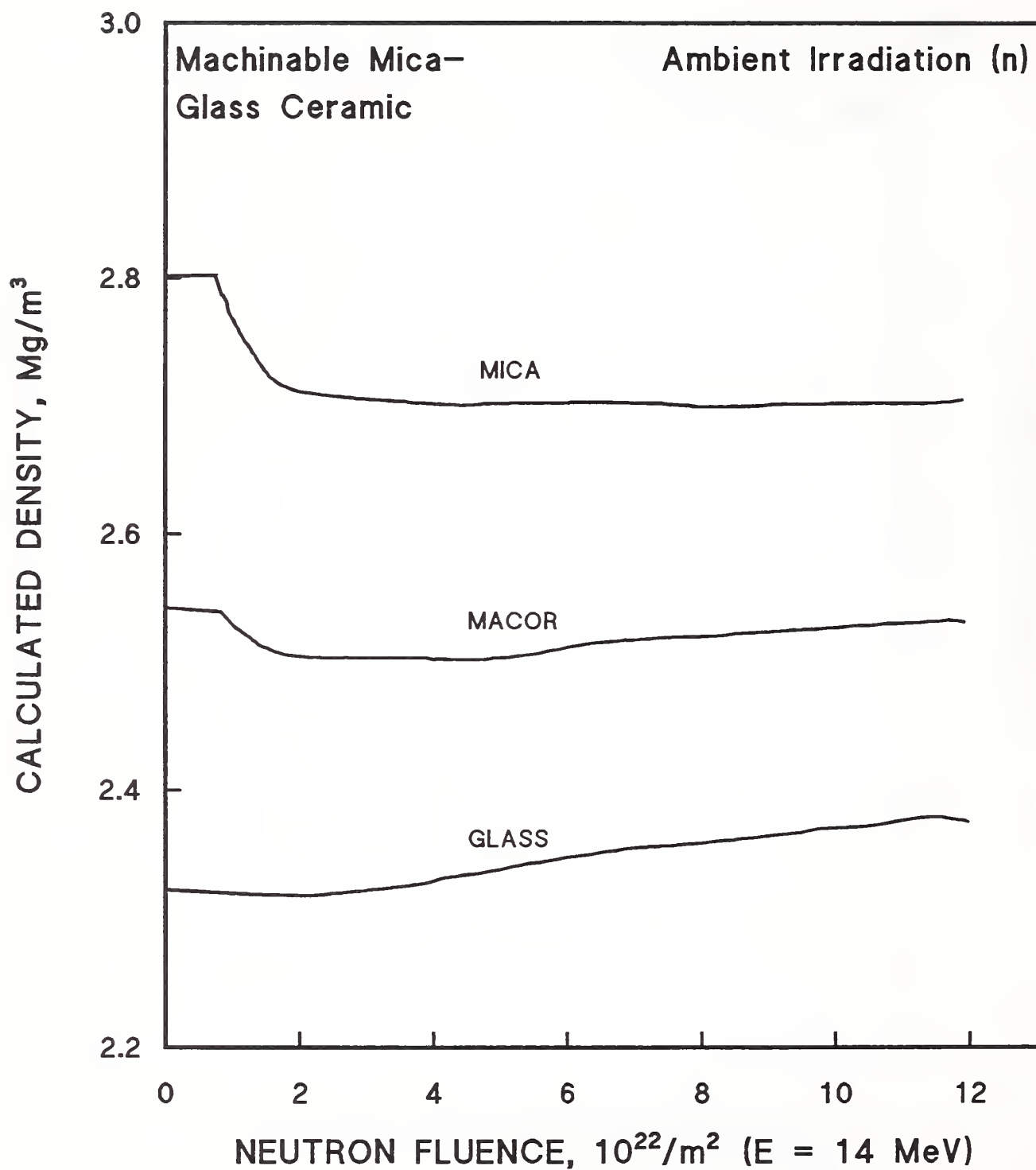


Figure 10.1.2. Calculated density of Macor and its two constituent phases, as a function of the 14-MeV neutron fluence. Data from Coghlan and Clinard [1991].

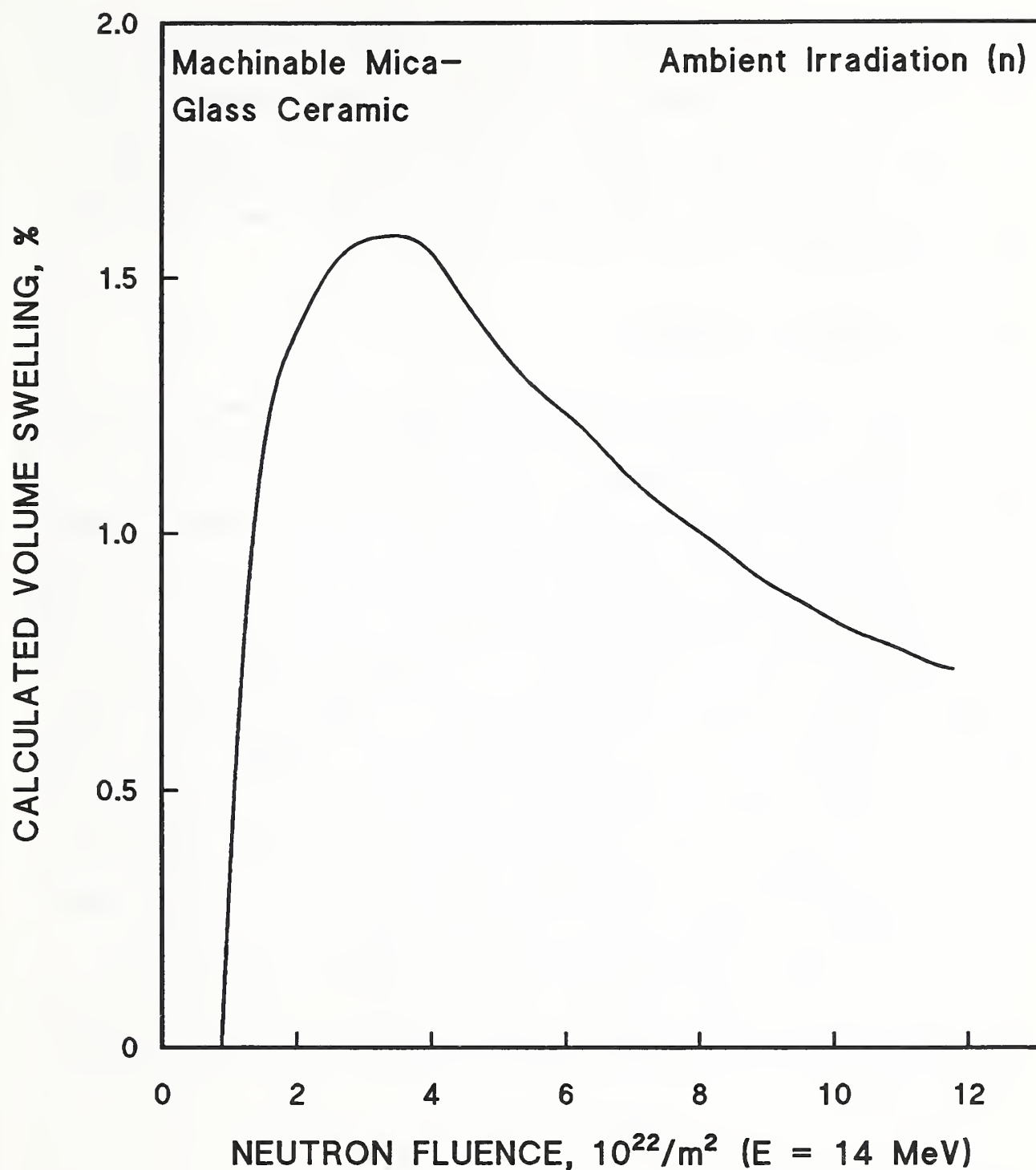


Figure 10.1.3. Calculated swelling of Macor, following the procedures described in the text, as a function of the 14-MeV neutron fluence. Data from Coghlan and Clinard [1991].

the ionizing doses from neutrons and electrons. This presumably reflects the heavier displacement damage that accompanies the ionizing dose from neutrons (e.g., Table 1.2.7). Coghlan and Clinard did not report microstructural observations of their Macor specimens irradiated to a higher 14-MeV fluence of $4 \times 10^{22}/\text{m}^2$. However, they did report that some specimens fractured from handling after irradiation. These specimens were 16-mm diameter disks that were 0.55 mm thick.

10.1.4. Mechanical Properties

Fowler et al. [1981] performed three-point bending tests on Macor specimens irradiated to 10^{20} and $10^{22}/\text{m}^2$ with 14-MeV neutrons. A very slight, but consistent, strengthening was observed. The initial flexural strength was 104 ± 4 MPa (24 specimens); at the highest fluence it was 109 ± 4 MPa (14 specimens). Coghlan and Clinard [1991] did not conduct similar flexural strength tests on the Macor they irradiated to higher fluences, but measured the hardness of two irradiated specimens and a control. These measurements are shown, for two indenter masses, in Figure 10.1.4. The large standard deviations reflect the fact that the sizes and distribution lengths of the mica flakes were of the order of the sizes of the indentations. In regard to the strength of the irradiated material, Coghlan and Clinard noted that some of their irradiated disks were fractured in handling and others were damaged by attempts to remove the Kapton tape (also damaged) that was used to hold the assemblage together during the irradiation. Specimens of one of the B-free mica-glass ceramics irradiated by Porter et al. [1981] to fission fluences of $\sim 2.5 \times 10^{22}/\text{m}^2$ ($E > 0.1$ MeV) at 400 and 550°C also often broke in handling, but Macor and other mica-glass ceramics evidently did not. Porter et al. reported that the hardness of all of these materials increased significantly after irradiation.

10.1.5. Thermal Properties

Some reduction in thermal diffusivity would be expected from irradiation damage. A reduction to 97.8% of the original value of diffusivity ($4.5 \times 10^{-7} \text{ m}^2/\text{s}$) was reported by Fowler et al. [1981] at their highest 14-MeV irradiation fluence of $10^{22}/\text{m}^2$.

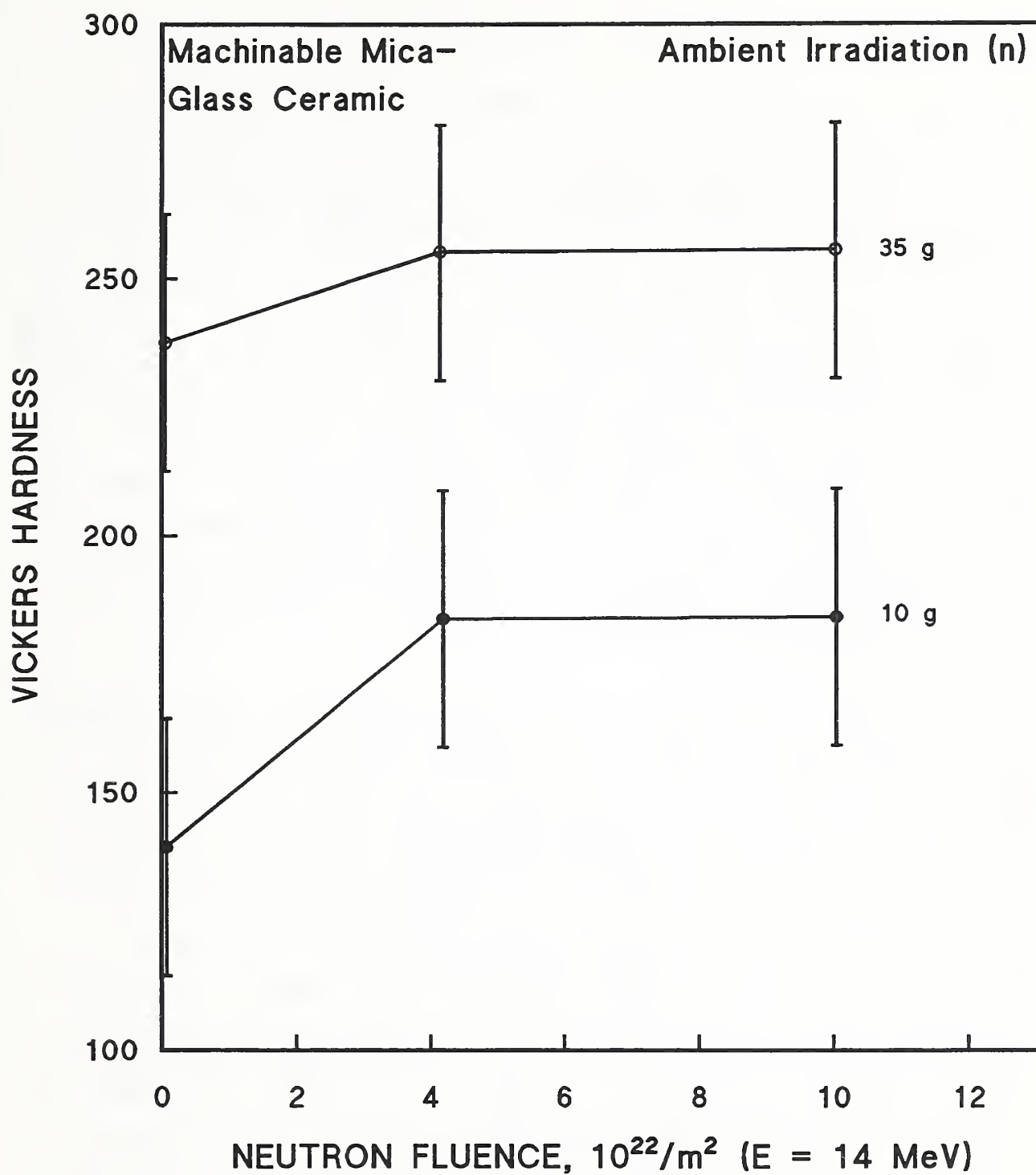


Figure 10.1.4. Change in Vickers hardness of Macor as a function of 14-MeV neutron fluence. Data from Coghlan and Clinard [1991].

10.2. IRRADIATION OF HYBRID MICA INSULATION

A material identified only as glass-bonded mica was reported to break up because of a large loss in strength when irradiated to an epithermal fluence of 2 to $6 \times 10^{24}/\text{m}^2$ ($E > 100$ eV) [Sisman et al., 1957]. Apparently, non-bonded mica (not further identified) and plate glass survived a similar fluence ($2 \times 10^{24}/\text{m}^2$) and were tested for hardness and change of thermal conductivity, but lead and pyrex glass specimens were broken up (§9.2). This fluence range is similar to that required for devitrification of glass; however, it was unclear whether the destruction of the glass or effects of the interface were responsible for the break-up of the glass-bonded mica. As noted above in §10.1.2, severe interfacial stress might be expected, owing to the large expansion of mica during irradiation, combined with compaction of the glass. A comparison of Figures 9.2.1 and 9.2.2 shows that the c-axis expansion cannot account for all of the radiation swelling in mica; therefore, it may not be correct to assume that most of the expansion of mica flake or mica paper occurs perpendicular to the plane of the interface.

Properties after γ irradiation of a hybrid mica insulation system consisting of mica paper tape, mica flakes, and polyimide film were described above in §§9.2 and 9.5 [Aki et al., 1983]. Figures 9.2.3, 9.5.3, and 9.5.4 present data on creep properties and electrical breakdown voltage after an ambient dose of $\sim 2 \times 10^6$ Gy. Good retention of properties after this ionization dose was observed. But note from §10.1.3 that an electron ionization dose of $\sim 10^{11}$ Gy was required before significant damage to a glass-mica ceramic was observed, but that the ionization dose from a 14-MeV neutron fluence required to generate about the same level of damage was about a factor of 10^5 lower. This is apparently due to the greater level of displacement damage accompanying the neutron ionization dose. Therefore, results of Aki et al. [1983] on ambient γ irradiation of hybrid mica insulation cannot be extrapolated to those for 4-K neutron irradiation at the expected ITER fluence. Also, note that these authors found that the strain from a small bending radius caused severe deterioration in the electrical breakdown strength of both mica flake and mica paper insulation, unless it was reinforced by a polyimide film (Kapton). The results of static bending tests of small bar coils are shown in Figure 10.2.1. The dielectric strength of the polyimide film withstands

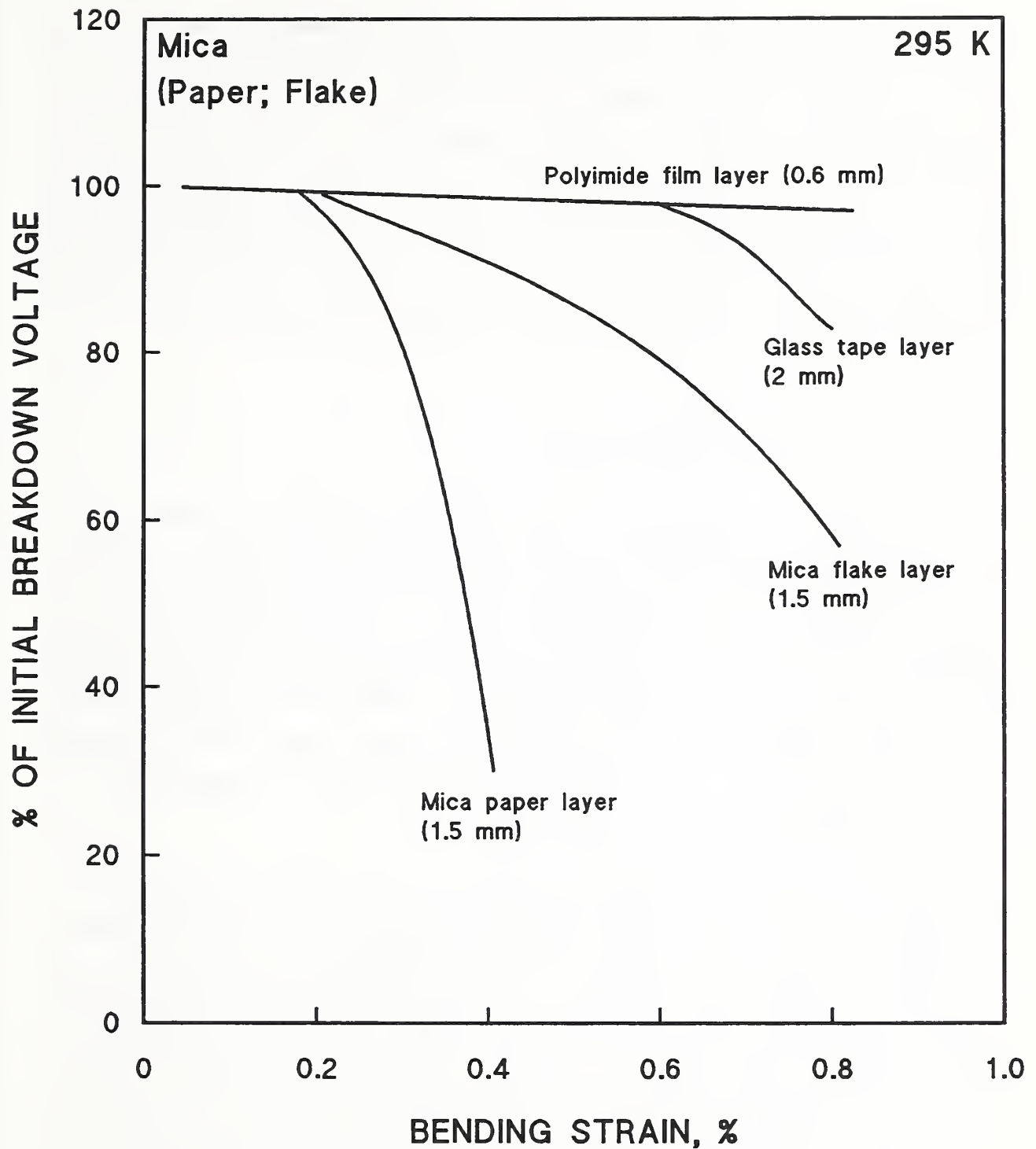


Figure 10.2.1. Deterioration of electrical breakdown strength of mica-paper and mica-flake layered insulation under static bending load, with respect to performance of polyimide film. Data from Aki et al. [1983].

the largest bending strain. Unfortunately, tensile-strength measurements of such polyimide films showed that deterioration began to occur above an ambient-temperature, 14-MeV fluence of $\sim 5 \times 10^{20}/\text{m}^2$ [Abe et al., 1987]; since the ITER 14-MeV, 4-K fluence at the TF magnets is $\sim 3 \times 10^{20}/\text{m}^2$, and this represents only about 1% of the total neutron fluence, it is quite possible that such polyimide reinforcements will not survive the 4-K ITER irradiation with good electrical and mechanical properties. (The 14-MeV fluence expected at the TF magnets is obtained from a spectrum from Sawan [1993] for a fast neutron fluence of $3.6 \times 10^{22}/\text{m}^2$ scaled to reflect the decrease to $1 \times 10^{22}/\text{m}^2$.)

10.3. IRRADIATION OF DUPLEX STRUCTURES

Several theoretical investigations of stresses in a duplex, or bonded structure in a fusion environment will be briefly described. Glasgow and Wolfer [1985] considered two bonded metals and performed a one-dimensional inelastic stress analysis of a thin-walled shell element. Their analysis encompassed temperature-dependent material properties, radiation-induced swelling, thermal and irradiation creep, and thermal expansion. They derived an equation for the case of a duplex plate constrained from bending. When stress distribution was followed with time, a near steady-state distribution was approached, depending upon swelling, and, especially, creep.

Blanchard [1988] also considered the influence of swelling and irradiation creep in bonded fusion components. Boundary-layer stress intensities were analyzed for two systems: graphite on Cu (both assumed to be creep-free) and W on V (high irradiation creep rate). Blanchard and Ghoniem [1990] analyzed thermal and swelling stress fields using a model of two thin, rectangular strips perfectly bonded along one surface. Logarithmic or algebraic singularities were found for the solutions of the stress fields near the edge of the structure. For further details of these calculations and additional references, the reader is referred to the original reports and to the citations therein.

Ceramic-metal bonds have been tested after neutron irradiation [Patrick, 1965; Barr et al., 1990]. Patrick found that Al_2O_3 ceramics maintained good bonding

after a fast neutron fluence of $\sim 3 \times 10^{24}/\text{m}^2$ at temperatures of 700 to 900 K. Spinel and MgO disks tested under the same conditions showed extensive damage and were judged unusable. Perhaps for this reason, bonded specimens of these ceramics were not tested. Barr et al. tested Al_2O_3 , MgAl_2O_4 , and mica-glass ceramic-to-metal seals with a leak detector after a spallation neutron fluence of $3.8 \times 10^{23}/\text{m}^2$. Only the mica-glass ceramics showed a measurable leak, but this may have arisen from fittings that connected the seals to the leak detector.

11. RADIATION-INDUCED ELECTRICAL DEGRADATION (ELECTRIC FIELD EFFECT)

11.1. ELECTRICAL CONDUCTIVITY IN INSULATORS

Valence electrons in both insulators and metals have energies that fall into discrete bands separated by forbidden regions, or band gaps, in which no electronic energy states are allowed. The difference between insulators and metal conductors is schematically indicated in Figure 11.1.1: the valence electrons of insulators exactly fill one or more bands, so an external electric field will not cause a flow of current. If there are a few vacant states at the top of a band, these are called holes. Then, an applied electric field will cause the electrons to move in the direction opposite to that of the field, in momentum space, but the vacancy, or hole, will move along the field direction as if it had a positive charge. Therefore, both electrons and holes are considered to be charge carriers that respond to electric fields. At ambient and lower temperatures, very few holes exist, and the typical insulator has a very high resistivity, sometimes $\sim 10^{12} \Omega \cdot \text{m}$. As the temperature is increased, charge carriers are thermally excited across the band gap into higher energy states (a conduction band), and typical resistivities for ceramics such as Al_2O_3 drop to 10^4 to $10^7 \Omega \cdot \text{m}$ at 1000 K.

Irradiation can affect resistivity both by causing structural (displacement) damage and by depositing ionization energy. Structural changes can introduce trapping, recombination, or scattering centers so that resistivity could increase or decrease. But, ionizing energy can generate a density of charge carriers far above that arising from thermal effects. For example, Davis [citation, Clinard, 1979] found that resistivities of several insulators decreased from about 10^{12} to about $10^9 \Omega \cdot \text{m}$ below 400 to 700 K with an ionizing dose rate of $\sim 5 \times 10^4 \text{ Gy/h}$ from γ radiation. The increase in conductivity of single-crystal Al_2O_3 with irradiation in this dose rate range is shown in Figure 11.1.2 [citation, Clinard, 1979]; the effect is reduced at lower temperatures. The data for Cr-doped crystals are included because transmutation reactions will alter the purity of insulators in a fusion reactor over a period of time. The variation in conductivity with dose rate is reviewed in more detail by Clinard [1979] and by Pells [1986]. More information on conduction mechanisms in ceramics may be found in Tuller [1986].

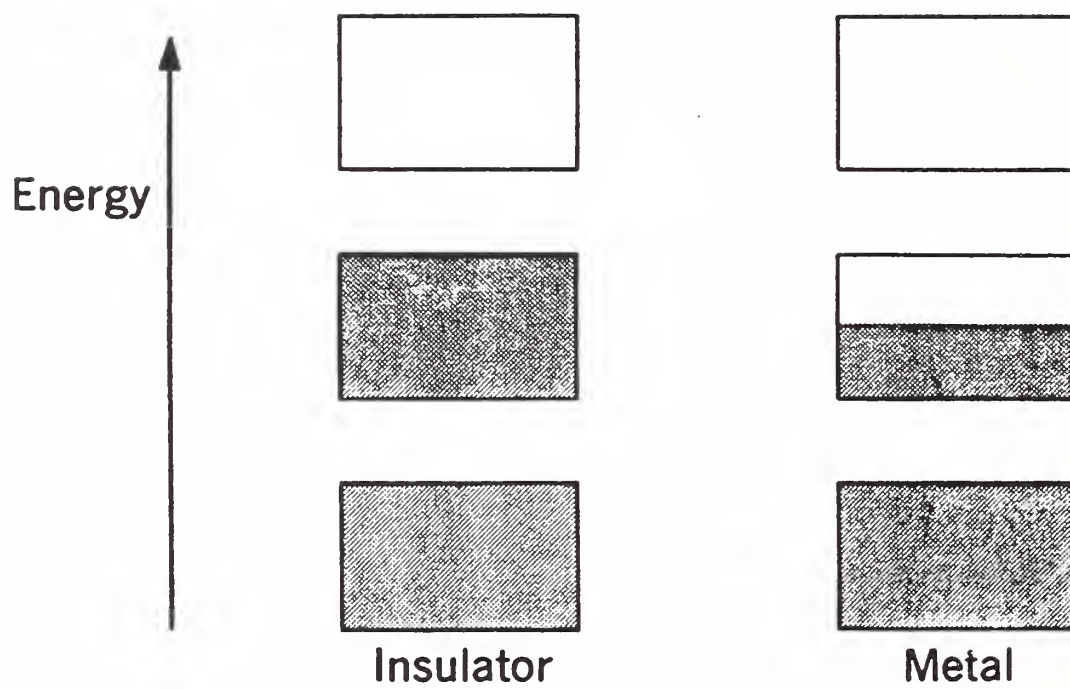


Figure 11.1.1. Schematic occupancy by electrons of allowed energy bands in an insulator and a metal.

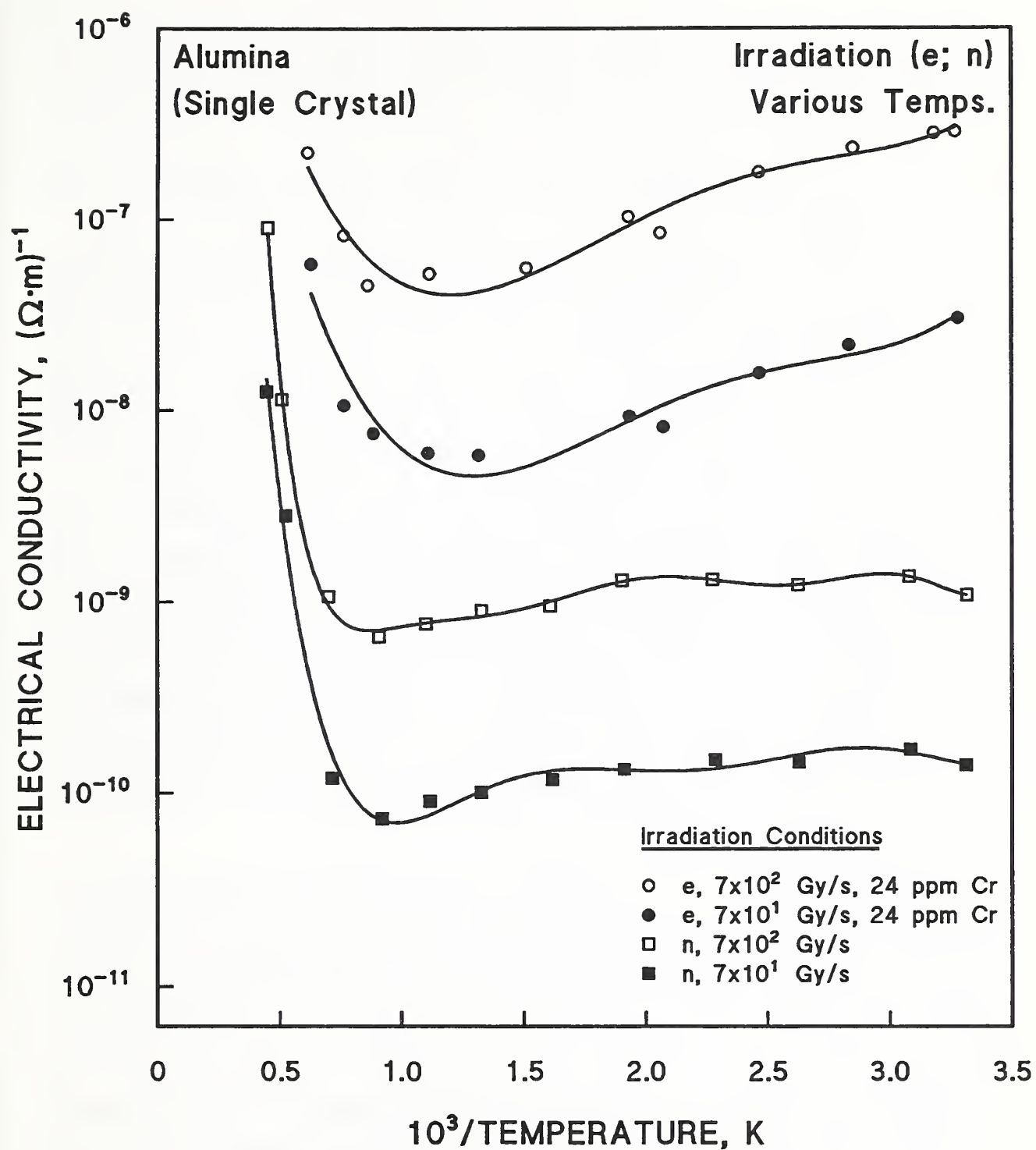


Figure 11.1.2. The RIC of single-crystal Al_2O_3 for electron and neutron irradiation. Data from Klaffky et al. [citation in Clinard, 1979].

Ions, as well as electrons and holes, contribute to the bulk conductivity in insulators. Two ceramics reviewed in this report, Al_2O_3 and ZrO_2 , exhibit at least some ionic conduction, in addition to that of electronic charge carriers. The fraction of conductivity due to ions may become more significant as the temperature rises [citations, Clinard, 1979]. Under dc fields, separation of anionic and cationic species occurs, causing serious degradation (electrolysis). Since diffusivity is enhanced by irradiation, electrolysis will be accelerated in a neutron flux. However, electrolysis should be much less significant at cryogenic temperatures.

Electrical breakdown of insulators occurs by either the thermal or avalanche mechanism. In the thermal mechanism, operative above ~ 450 K, Joule heating arises from a small current flow and conductivity accelerates to breakdown. In the avalanche mechanism, seen below ~ 450 K, ionization and multiplication from electron collision causes the "avalanche" breakdown. Radiation can fill traps with charge carriers which are then available as avalanche collision targets [Clinard, 1979]. Even without irradiation, when an insulator is exposed beyond a critical voltage gradient, or electric field, a steady state does not result. Instead, after a certain incubation time, a distinct increase in the current may occur, leading often to delayed dielectric breakdown. Therefore, a time period of operation, as well as the voltage gradient, must be specified for safe operation [Heidinger, 1991].

In the remainder of this section, experimental results on several related topics will be reviewed: radiation-induced conductivity (RIC) due to both ionization and displacement damage, electrolysis, and degradation of the breakdown voltage. Since all experiments were carried out at ambient temperature or above, the consequences for 4-K irradiation of insulators are speculative, at present. For example, Banford [1984] suggested that at very low temperatures much of the charge generated from electron-hole pairs created by both ionizing and displacive radiation would become trapped, owing to reduced carrier mobilities. The result could be a frozen-in space charge. This space charge would cause field distortion and intensification at the cathode of an applied field, which would result in increased collisional ionization and further field distortion and intensification. Finally, the insulator could be destroyed by massive electron emission from the cathode caused by

an enhanced field strength. The type of irradiation experiments undertaken so far would not detect this phenomenon, because the 4-K electrical breakdown was not measured under field, in situ.

11.2. INVESTIGATIONS OF RADIATION-INDUCED CONDUCTIVITY

A number of investigations have indicated that both ionization and displacement damage contribute to the total RIC. For example, Figure 11.2.1 shows a somewhat greater increase in the conductivity of polycrystalline Al_2O_3 when the irradiation species is protons, instead of X-rays, although equivalent dose rates were not used [Pells, 1986]. The response of the RIC to the dose rate is usually described by

$$\sigma = KR^\delta + \sigma_0, \quad (11.1)$$

where R is the dose rate and δ is obtained from a log/log plot of the conductivity versus the ionization dose rate. The behavior of δ with the temperature of irradiation shows a difference between proton and X-ray irradiation (Figure 11.2.2), although the proportionality constant, K , did not differ, within the considerable scatter. However, Shikama et al. [1992a] found that similarity between γ and neutron irradiation was displayed in the log/log plot used to determine δ at one temperature (Figure 11.2.3). The data of Shikama et al. pertain to irradiation of Al_2O_3 , at about 600 to 630 K.

The constant of proportionality, K , in Equation (11.1) was measured by Pells and found to decrease significantly below 400°C (Figure 11.2.4). The decrease appeared to level off below about 50°C, however; this could indicate persistence of an effect below ambient temperatures, into the cryogenic temperature range.

By varying the voltage used in electron irradiation of Al_2O_3 , Hodgson [1991] could irradiate above and below the displacement threshold for Al_2O_3 (~0.40 MeV; see also §§1.2.2 and 2.1). Part 4 of the curve shown in Figure 11.2.5 pertains to irradiation at 0.30 MeV, and no decrease in conductivity was observed, which indicates that displacement damage is necessary for an RIC effect. All results shown in this figure were obtained at or slightly below the rather high dose rate of 10^6 Gy/h, at 500°C. Reducing the ionizing dose

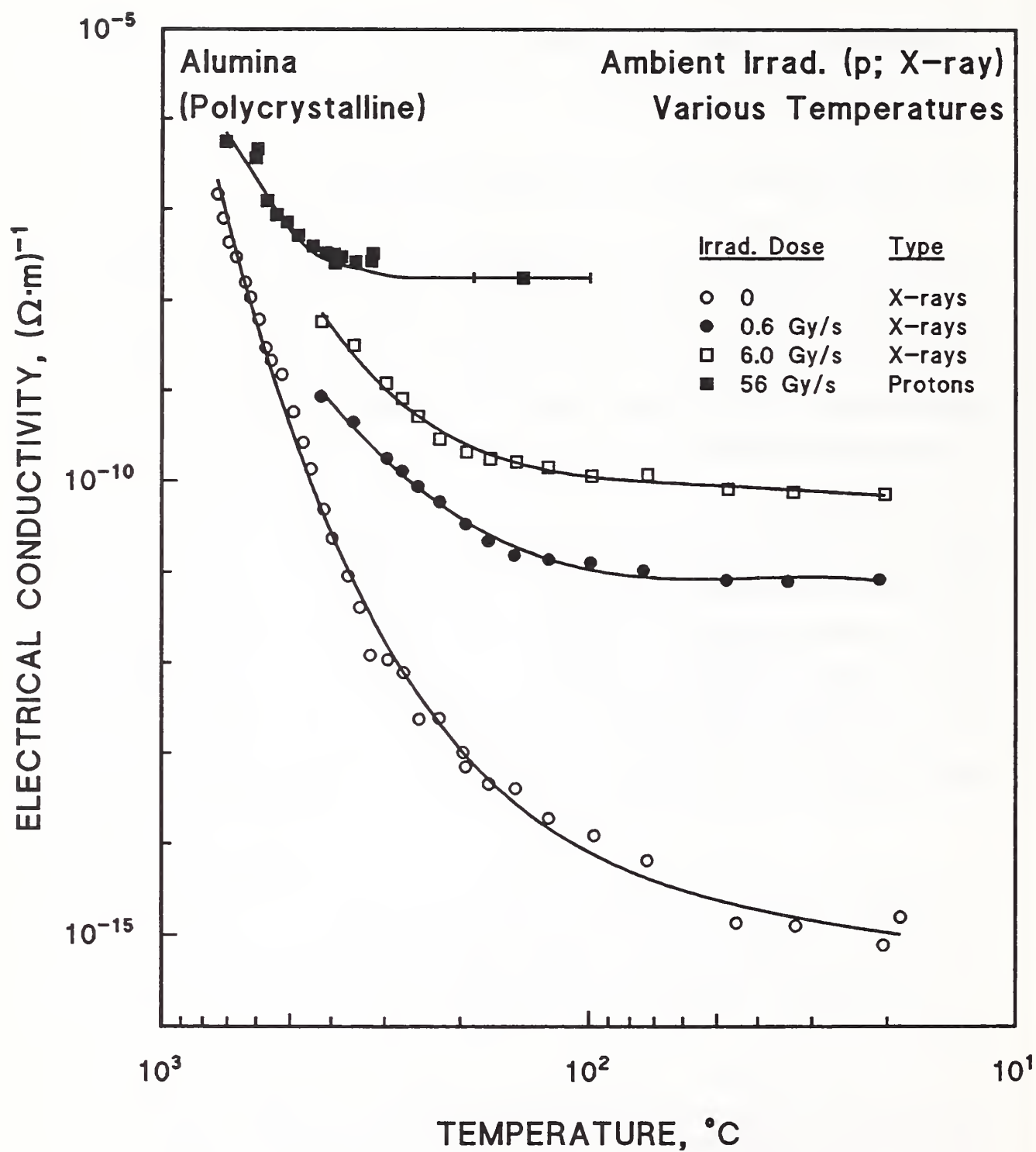


Figure 11.2.1. Increase of DC conductivity of polycrystalline Al_2O_3 after 20-MeV proton and X-ray irradiation. Data from Pells [1986].

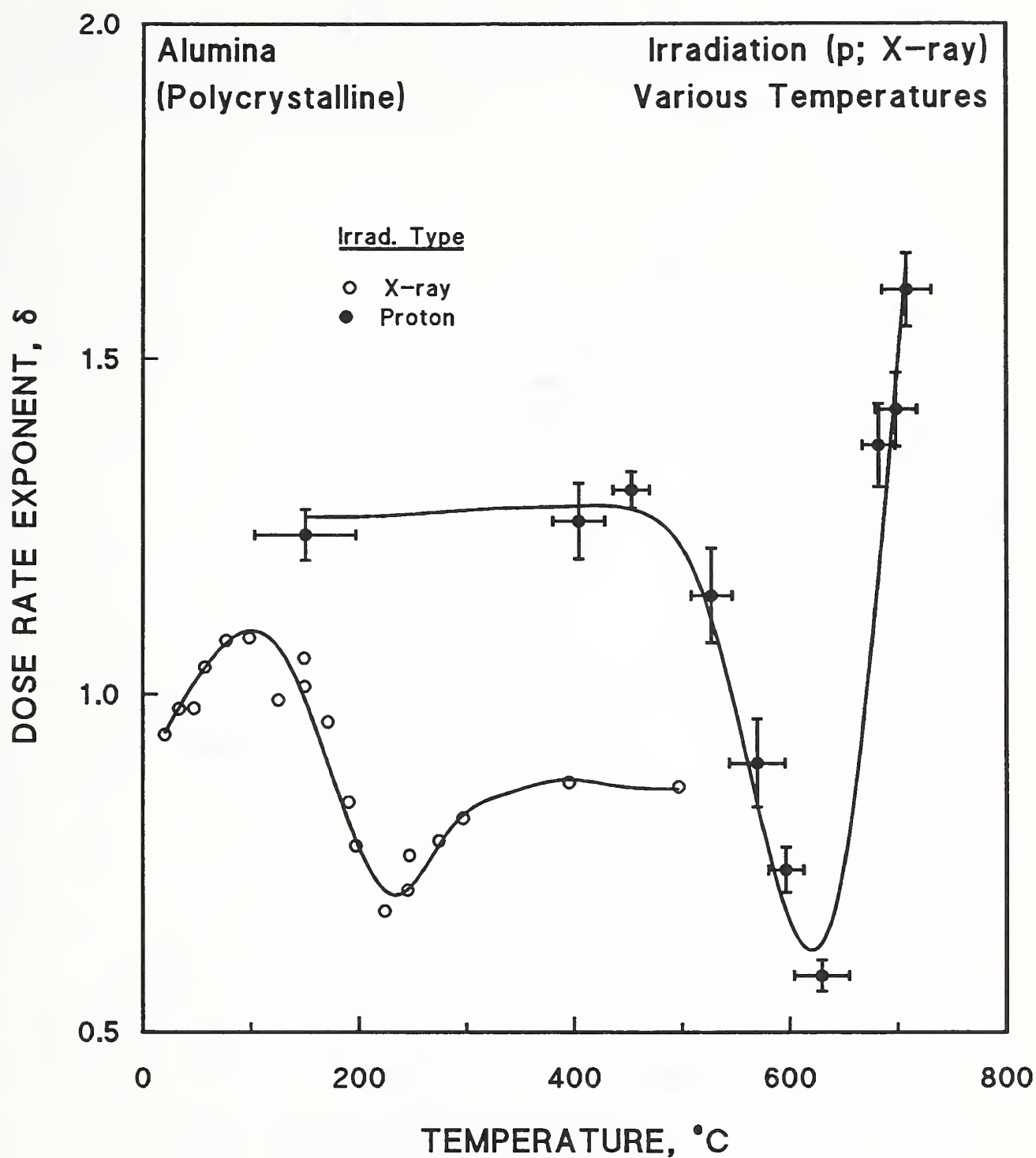


Figure 11.2.2. The dose rate exponent, δ , for proton and X-ray irradiation of polycrystalline Al_2O_3 . Data from Pells [1986].

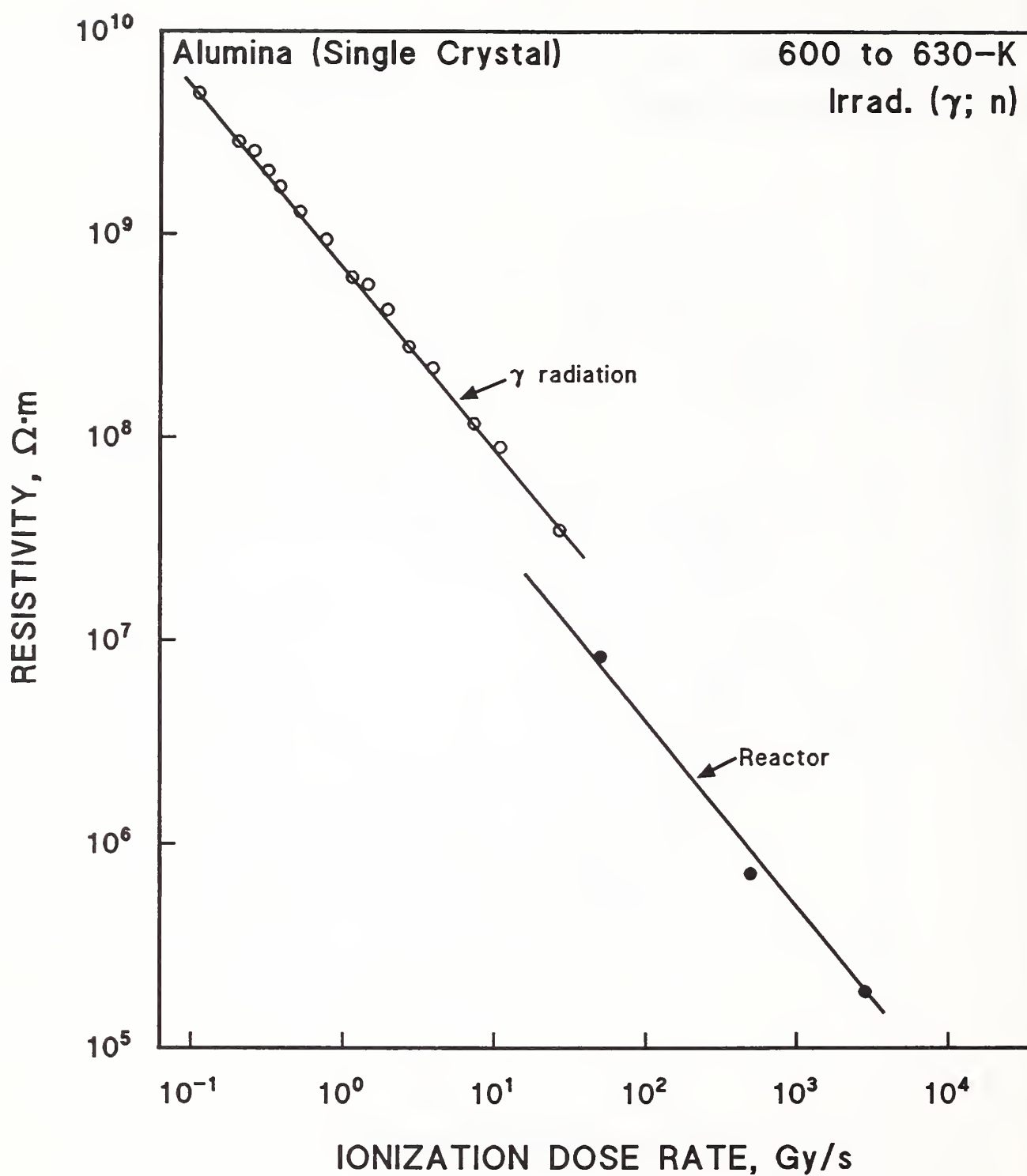


Figure 11.2.3. The RIC vs. ionization dose rate for γ (^{60}Co) and reactor irradiation of single-crystal Al_2O_3 . Data from Shikama et al. [1992a].

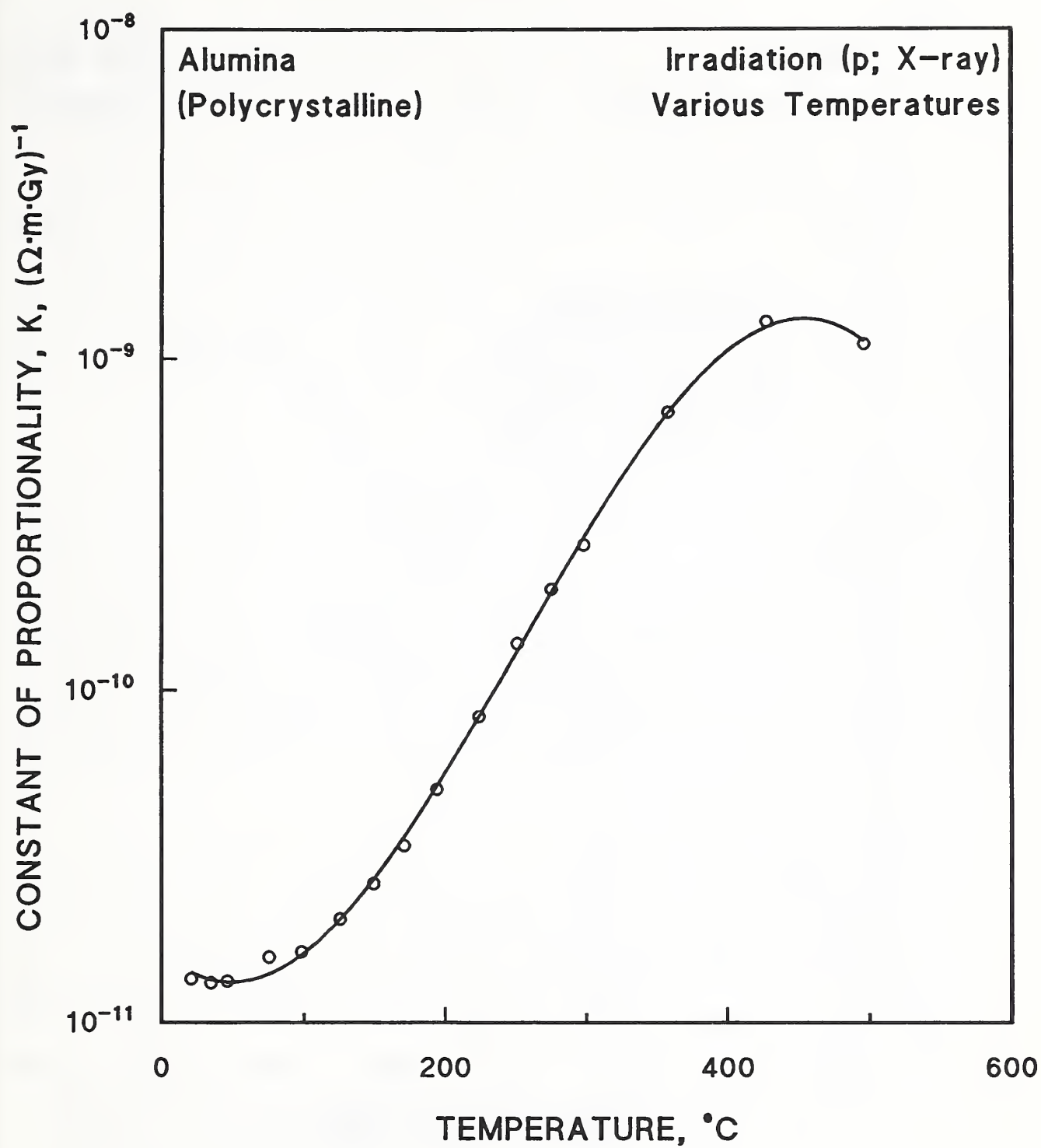


Figure 11.2.4. The constant, K , for RIC of polycrystalline Al_2O_3 vs. temperature. Data from Pells [1986].

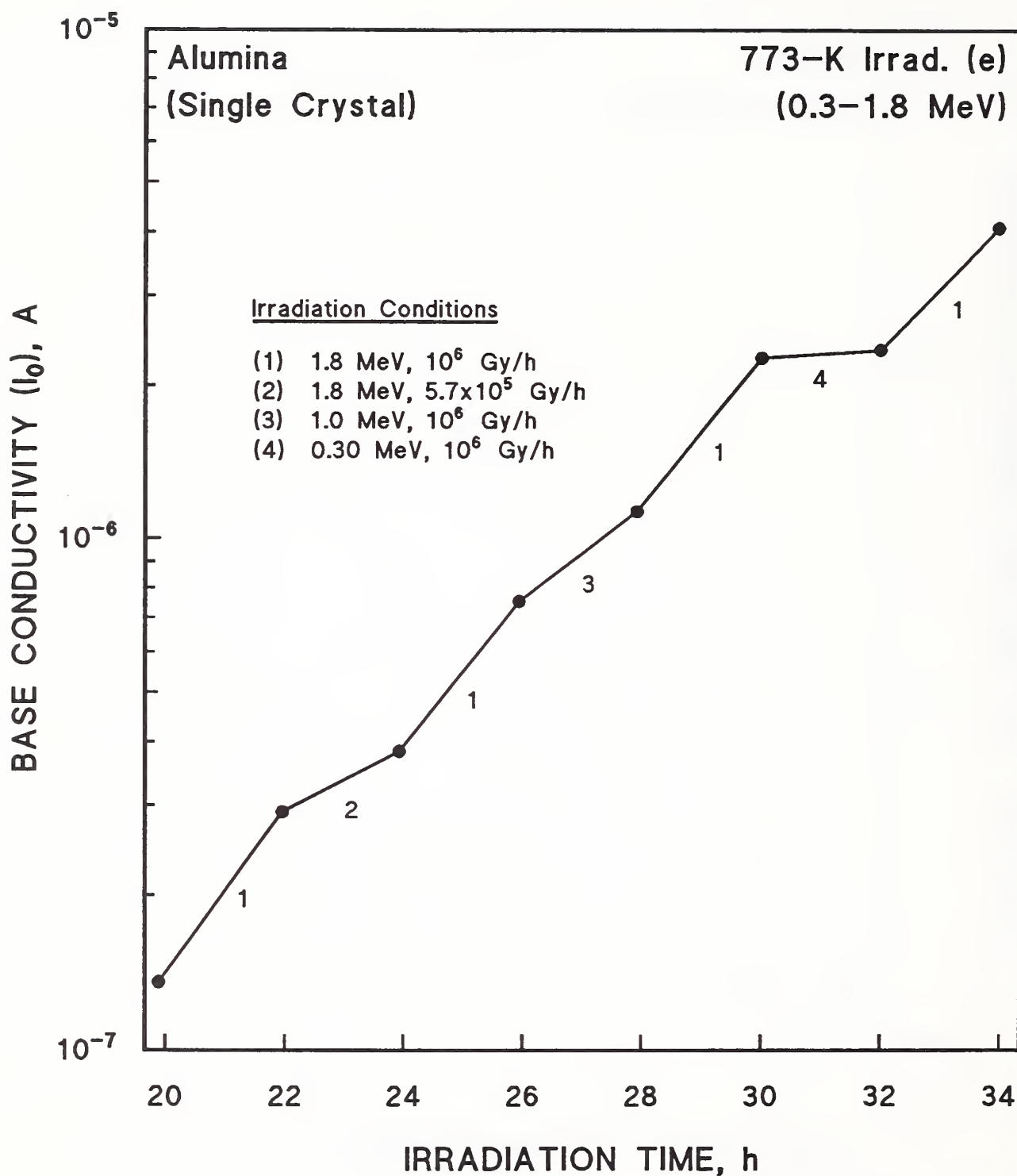


Figure 11.2.5. Increasing base conductivity, I_0 , in single-crystal Al_2O_3 for different electron irradiation conditions. Data from Hodgson [1991].

rate also affected the base current or conductivity. These results indicate that both displacive and ionizing radiation affect the RIC, and that concurrence of both radiation types is necessary for the effect. This is analogous to the growth of colloids in alkali halides, according to Hodgson, indicating that the mechanism involves diffusion of both radiation-enhanced vacancies and lattice ions. Pells explained that the effect of exposure to ionizing radiation was to produce electron-hole pairs by exciting electrons from the valence band into the conduction band (Figure 11.1.1). An Al vacancy is a good candidate for a hole-trapping center, and the dependence of δ upon temperature for proton (displacive) irradiation can be explained by a consideration of energy levels available at the defect.

Although the RIC is affected by both ionizing and displacive radiation, only data on the effect of ionizing radiation were found for SiO_2 , 10 mol% Y_2O_3 - ZrO_2 , ZrO_2 and mica in the literature survey. Figure 11.2.6 presents data on the resistivity of SiO_2 -insulated cable (18% compaction); Figure 11.2.7 shows comparative data for MgO -insulated cable (80% compaction). Both types of cable were exposed to 2.6×10^5 R/h at the temperatures indicated [Cannon, 1982]. Although MgO gave superior breakdown voltage thresholds, SiO_2 consistently had insulation resistance one or two decades higher. Cable of Al_2O_3 was expected to perform similarly to the MgO cable.

Figure 11.2.8 presents the dc electrical conductivity of 10 mol% Y_2O_3 - ZrO_2 before and after a γ dose of 5.3×10^5 Gy [Abou Sekkina et al., 1987]. The porosity of the sintered specimens was about 26%. Figure 11.2.9 shows the increase in electrical conductivity of monoclinic, sintered ZrO_2 for increasing doses of γ irradiation [Tawfik et al., 1985].

Several forms of mica, including natural mica (type not specified), silicone-impregnated mica mat, synthetic mica, and reconstituted mica paper were irradiated with electrons in air of variable humidity [Bradley et al., 1959]. None showed significant increases in induced conductivity at doses up to $\sim 6 \times 10^6$ Gy. Generally, the 25-°C conductivities were $\sim 10^{-16}$ ($\Omega \cdot \text{cm}$)⁻¹.

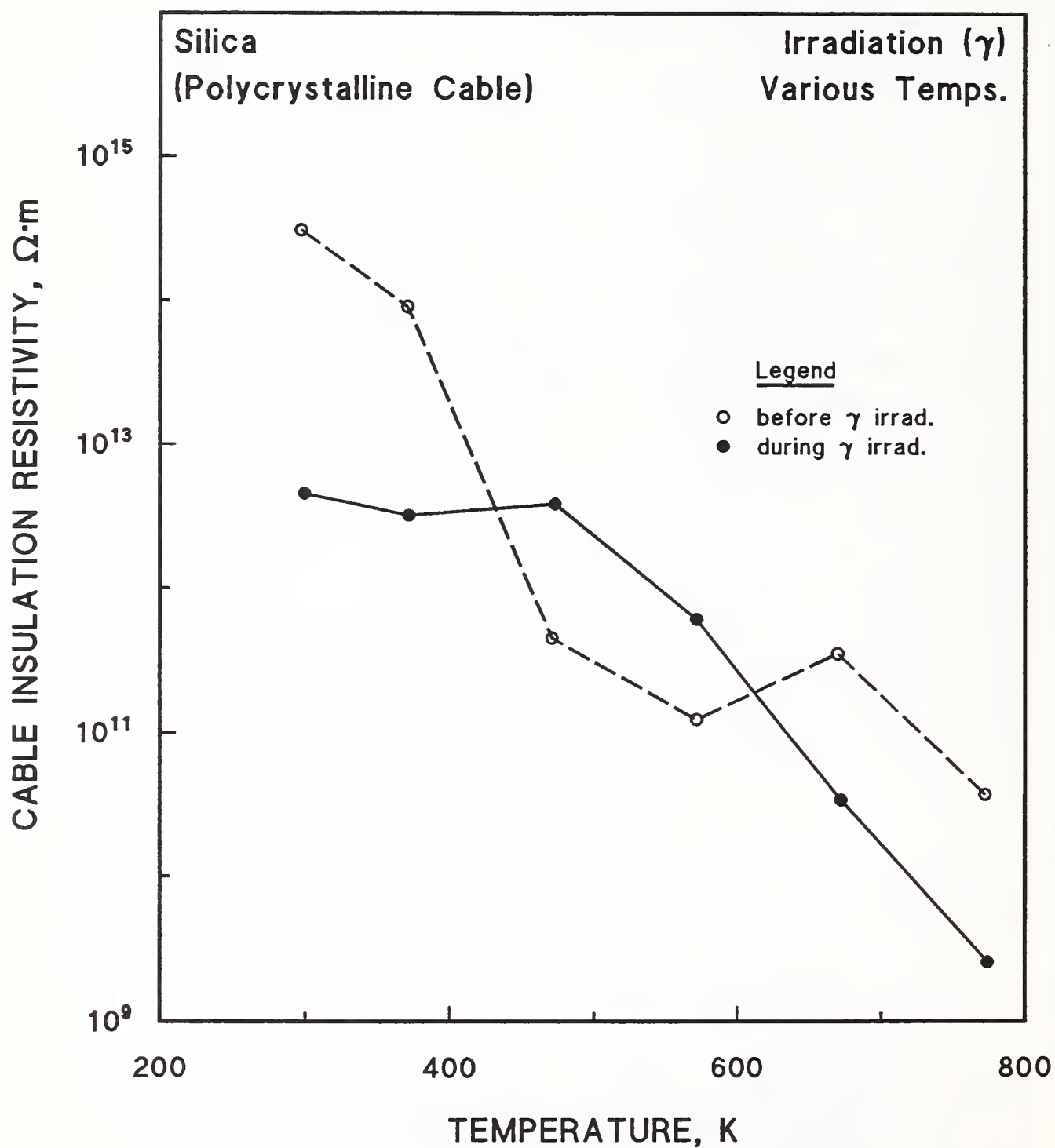


Figure 11.2.6. SiO_2 cable insulation resistivity vs. temperature before and during a γ flux of 2.6×10^6 R/h. (Converted to $\Omega\cdot m$ from $\Omega\cdot ft$, assuming $\Omega\cdot mil\cdot ft$ was not the intended unit). Data from Cannon [1982].

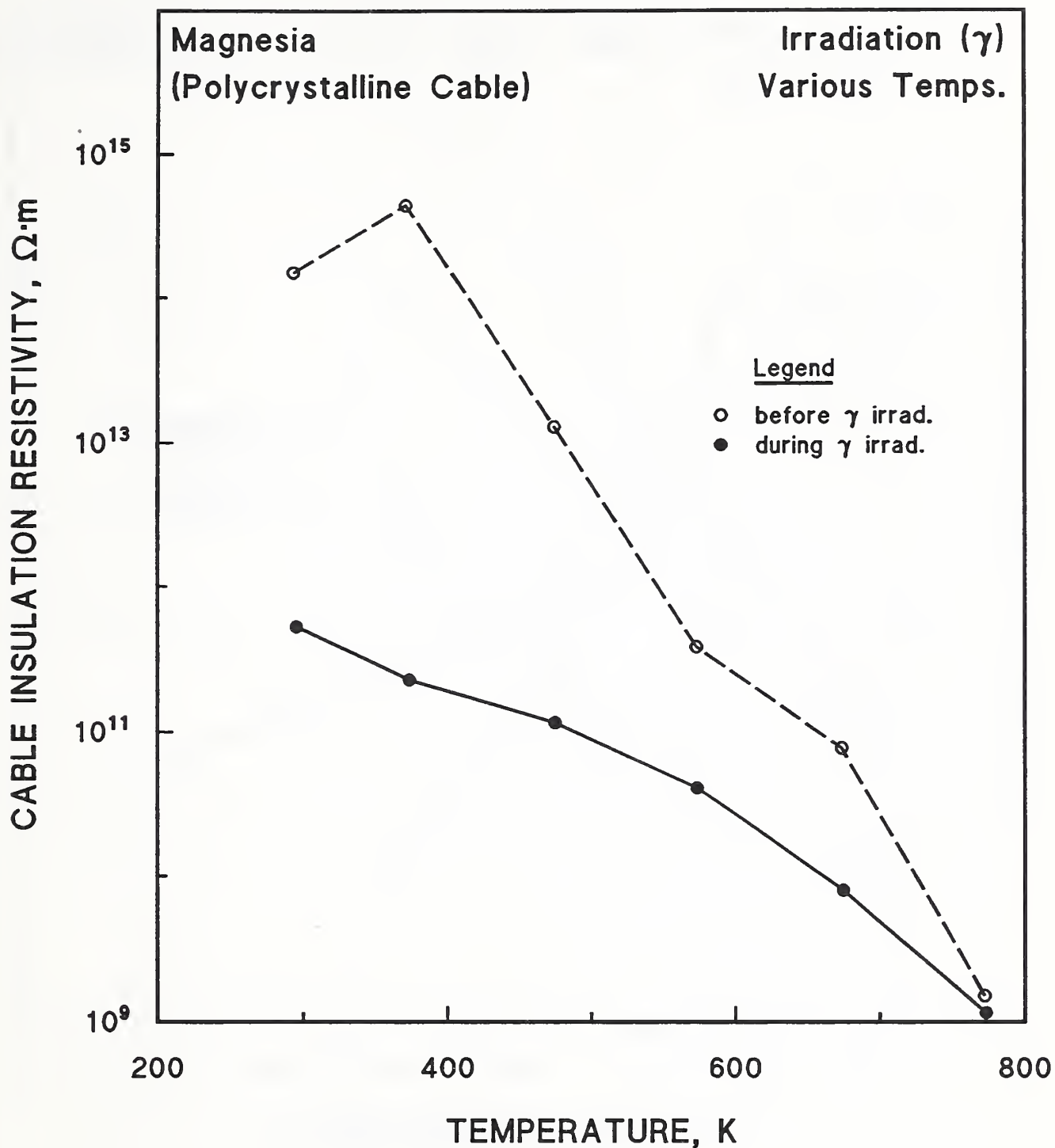


Figure 11.2.7. MgO cable insulation resistivity vs. temperature before and during a γ flux of 2.6×10^6 R/h. (Converted to $\Omega\cdot\text{m}$ from $\Omega\cdot\text{ft}$, assuming $\Omega\cdot\text{mil}\cdot\text{ft}$ was not the intended unit). Data from Cannon [1982].

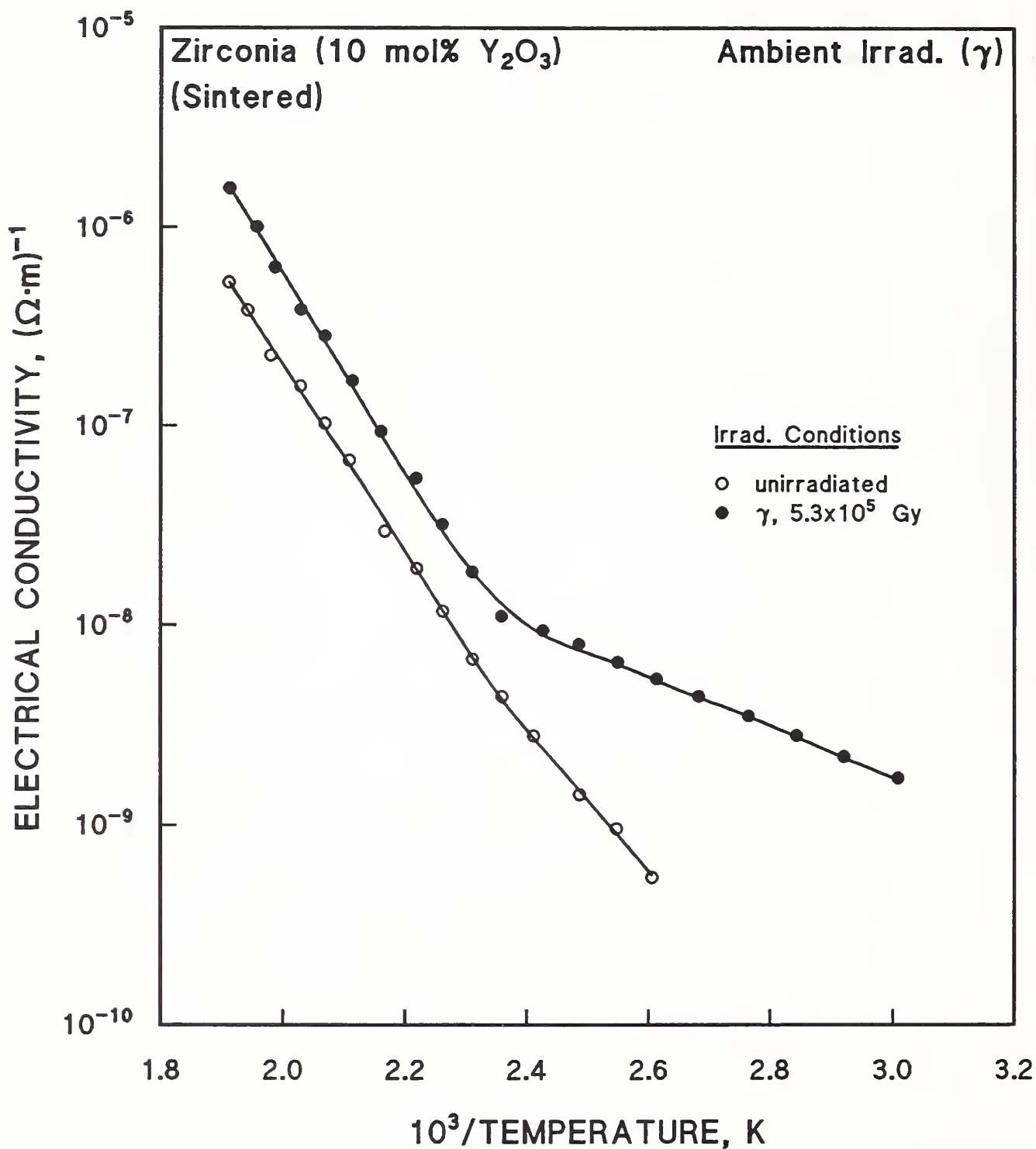


Figure 11.2.8. DC electrical conductivity of 10 mol% Y_2O_3 - ZrO_2 vs. temperature before and after a γ dose of 5.3×10^5 Gy. Data from Abou Sekkina et al. [1987].

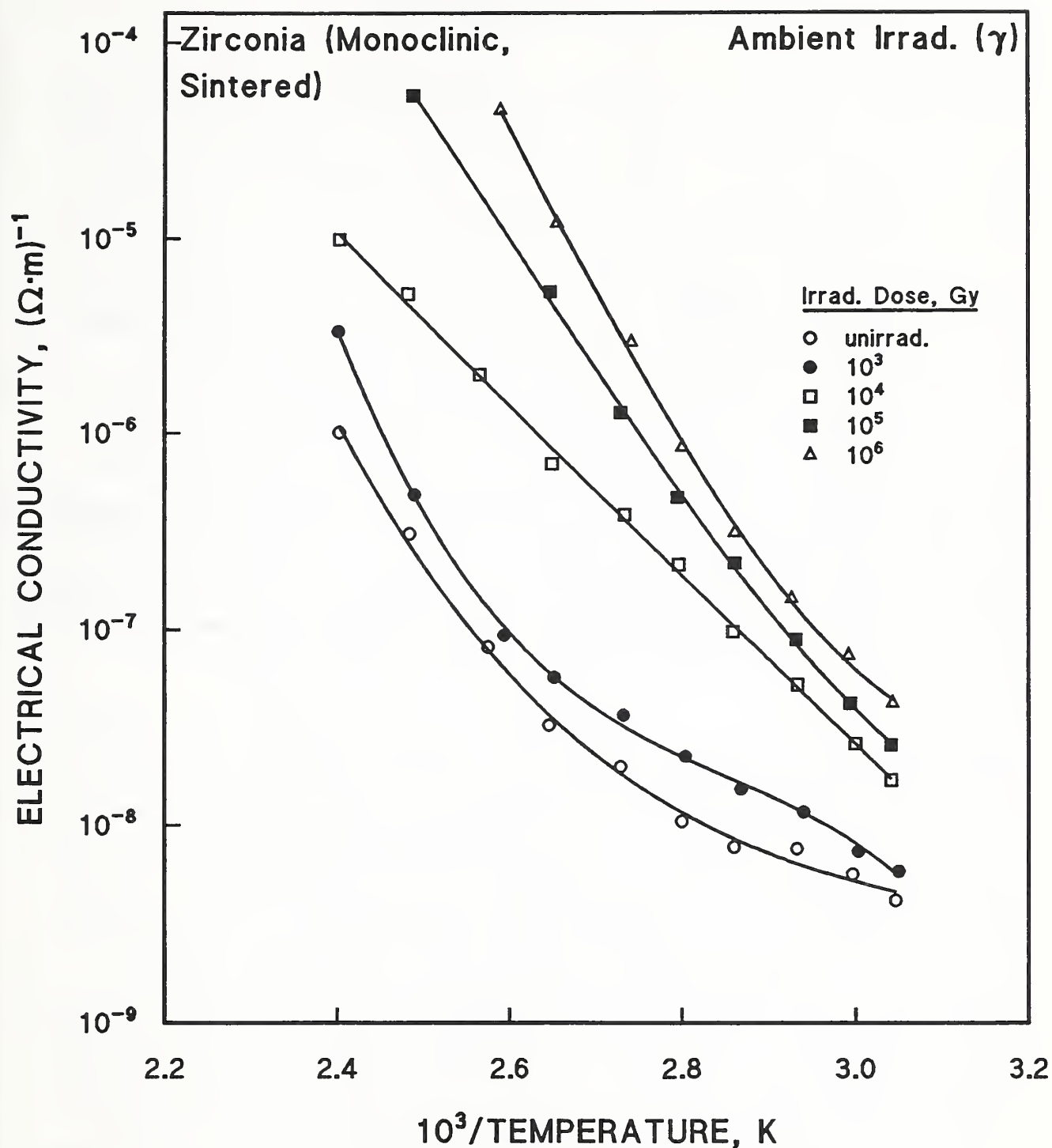


Figure 11.2.9. DC electrical conductivity of monoclinic, unstabilized ZrO_2 vs. temperature before and after several γ radiation doses. Data from Tawfik et al. [1985].

11.3. INVESTIGATIONS OF FIELD-INDUCED DEGRADATION

Figure 11.3.1, from the investigation by Hodgson [1991] described above, shows a decrease in activation energy, as measured by the temperature dependence of the base conductivity, σ_0 . This increase in the base conductivity was maintained after irradiation; therefore, there was no recovery. Since the primary displacement damage was calculated to be low, $\sim 2 \times 10^{-5}$ dpa, the degradation was attributed to the presence of an electric field, and subsequent radiation-enhanced electrolysis, rather than to structural damage from atomic displacements. Hodgson [1991] also reported that when Al_2O_3 was irradiated with 1.8-MeV electrons at 10^6 Gy/h at 450°C , but with no electric field, no post-irradiation degradation was observed [Hodgson, 1989]. He also cited investigations that showed that neutron irradiation without an electric field decreased the RIC but that neutron irradiation with an applied field markedly increased the RIC [Ivanov et al., 1981]. Figure 11.3.2 shows this conductivity increase in plasma-deposited Al_2O_3 and MgAl_2O_4 as a function of neutron fluence at about 700 K. The electric field during the measurements has been inferred to be 10 to 20 kV/m (or, 10 to 20 V/mm) [Pells, 1990].

Hodgson [1989] showed that electric-field dependent breakdown had not been reported previously, owing to shorter periods of observation. Since RIC appears to be an enhancement of thermal effects, and since several ceramic insulators were shown to break down only after ~ 100 h at temperatures above 1000°C (MgO , Al_2O_3 , MgAl_2O_4) and 200°C (porcelain) [citations, Clinard et al., 1983], Hodgson carried out prolonged measurements. The results for Al_2O_3 and MgO at 450°C and 0.13 kV/mm are shown in Figure 11.3.3. MgO seems to exhibit the approximately exponential increase in conductivity at a much earlier time than Al_2O_3 , which is expected because of the somewhat greater resistance of Al_2O_3 to thermal breakdown above 1000°C . (Single-crystal Al_2O_3 withstands 10 kV/mm at 1000°C for over 100 h [Weeks et al., 1978].) The dose rate of 10^6 Gy/h is very much higher than that expected in the TF magnets; however, a lower dose rate of 5.7×10^5 Gy/h simply postponed the onset of the breakdown process. Strictly, the exponential growth of conductivity is defined as a precursor stage before actual electrical breakdown occurs.

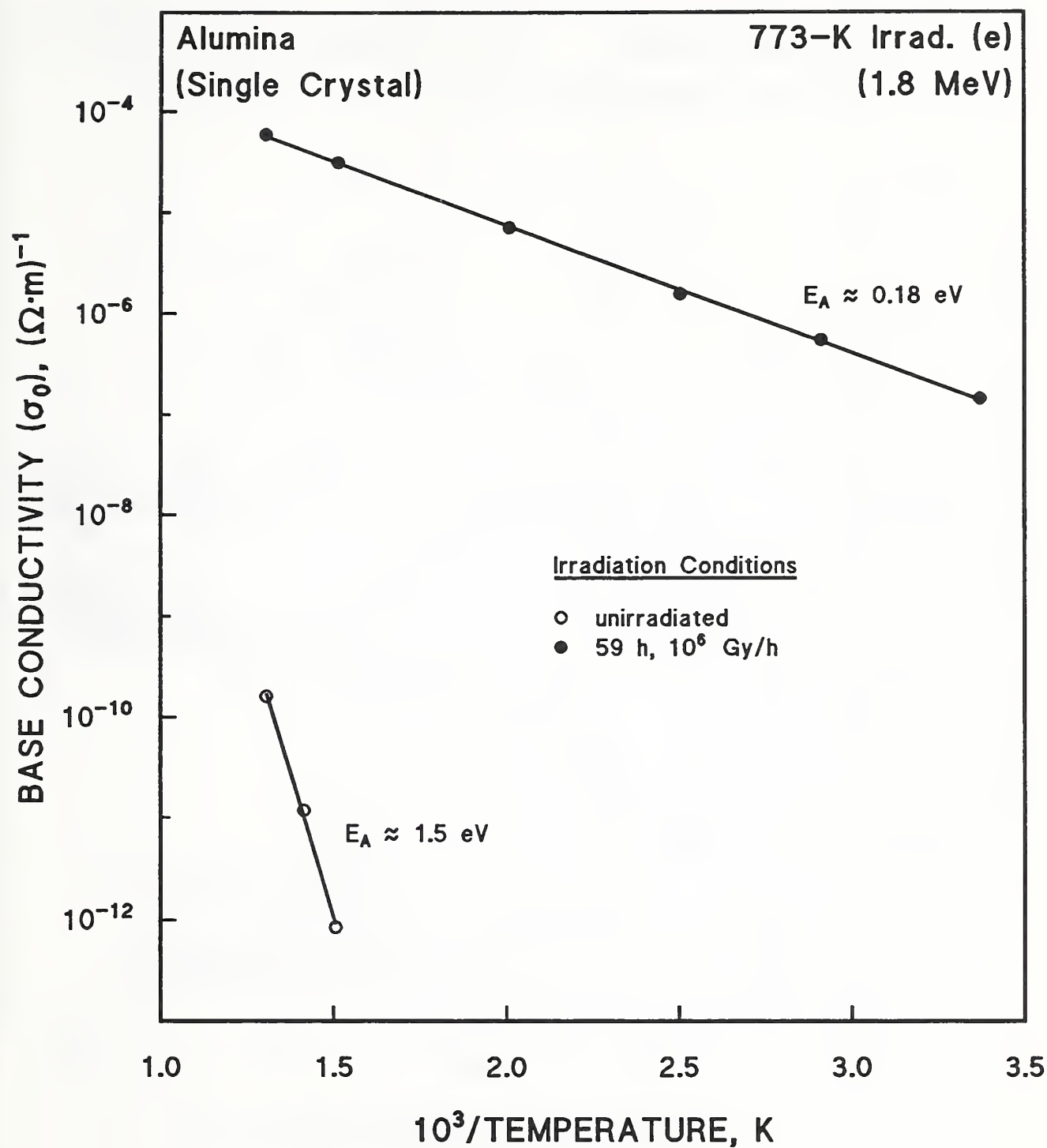


Figure 11.3.1. Base conductivity, σ_0 , in Al_2O_3 for 773-K electron irradiation, indicating change in activation energy, E_A . Data from Hodgson [1991].

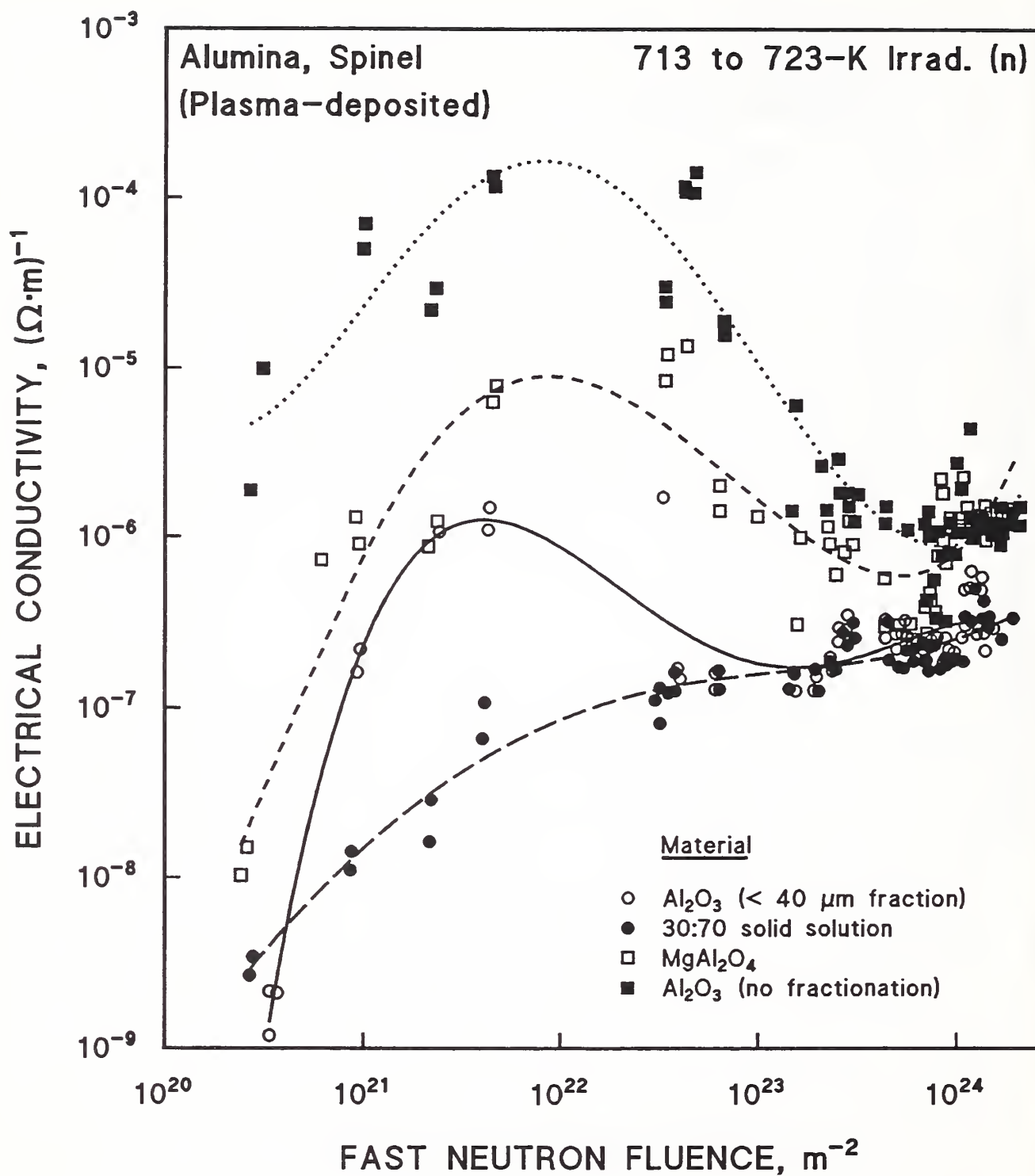


Figure 11.3.2. Increase of electrical conductivity of Al_2O_3 and MgAl_2O_4 under neutron irradiation and electric field. Data from Ivanov et al. [1981].

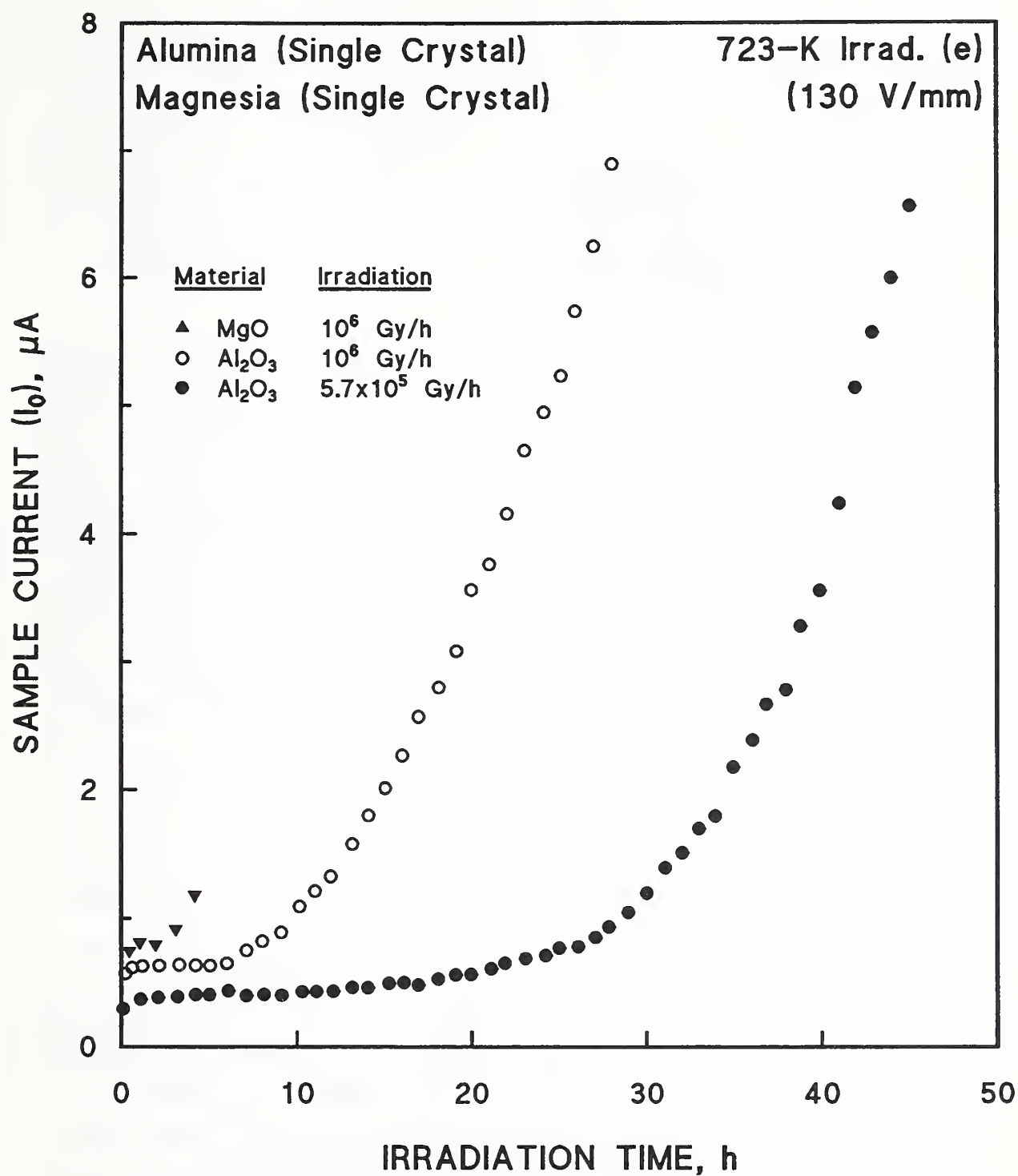


Figure 11.3.3. The RIC and onset of electrical breakdown for Al_2O_3 and MgO at 723 K. Data from Hodgson [1989].

Hodgson [1991] has related the dose rate and temperature dependence of his results to the growth of colloids in alkali halides. Impurities also play a role in the degradation, since radiation enhances their diffusion, and the less pure MgO showed a different value of δ (Figure 11.3.4). The use of highly pure materials may not provide a solution, however, owing to the increasing impurity content from transmutation products during neutron irradiation. For example, Na is an important transmutation product of Al that enhances the electrical conductivity of Al_2O_3 .

At first it was thought that electric-field dependent breakdown occurred only under highly ionizing irradiation. However, Shikama et al. [1992b] reported radiation-induced electrical degradation (RIED) in Al_2O_3 at temperatures of 600 to 800 K, under fission-reactor, rather than electron, irradiation. Figure 11.3.5 shows the effect of a dc field of 500 V/mm on the conductivity at 700 to 800 K. Since two identical specimens were irradiated (one without an applied field), it was hoped that spurious effects were largely eliminated. Precautions were taken to improve the vacuum and electrical insulation of the specimens. This work corroborated that of Hodgson, who claimed that the application of a voltage was necessary for the observation of RIED. It also indicated that the effect does not require electron irradiation, but will take place in a fission-reactor irradiation environment. (This was indicated earlier by the work of Ivanov et al. [1981], but was not recognized until later.) There were quantitative disagreements between the work of Shikama et al. and of Hodgson in the total doses at which the phenomenon occurred and in the dependence upon irradiation time. If the electrical conductivity, σ , was expressed as $\sigma \propto t^n$, where t represents irradiation time, Shikama et al. observed $n \sim 0.5$ to 0.8 , whereas Hodgson observed $n \sim 4$ to 5 . The latter values agree with the growth rate of colloids in alkali halides, but the lower values agree with the power dependence of colloid growth observed with HVEM irradiation on Al_2O_3 (§2.1). The ratio of ionization dose rate to displacement damage rate is much larger for electron irradiation than for neutron irradiation (Table 1.2.7), which may explain some of the differences in observations between the two groups. The differences are related to the mechanism and temperature dependence of the effect: if colloid formation is necessary, and if Al_2O_3 is similar in this respect to alkali halides, where temperatures in the range of 700 to 1000 K may be necessary for the effect, then RIED should not

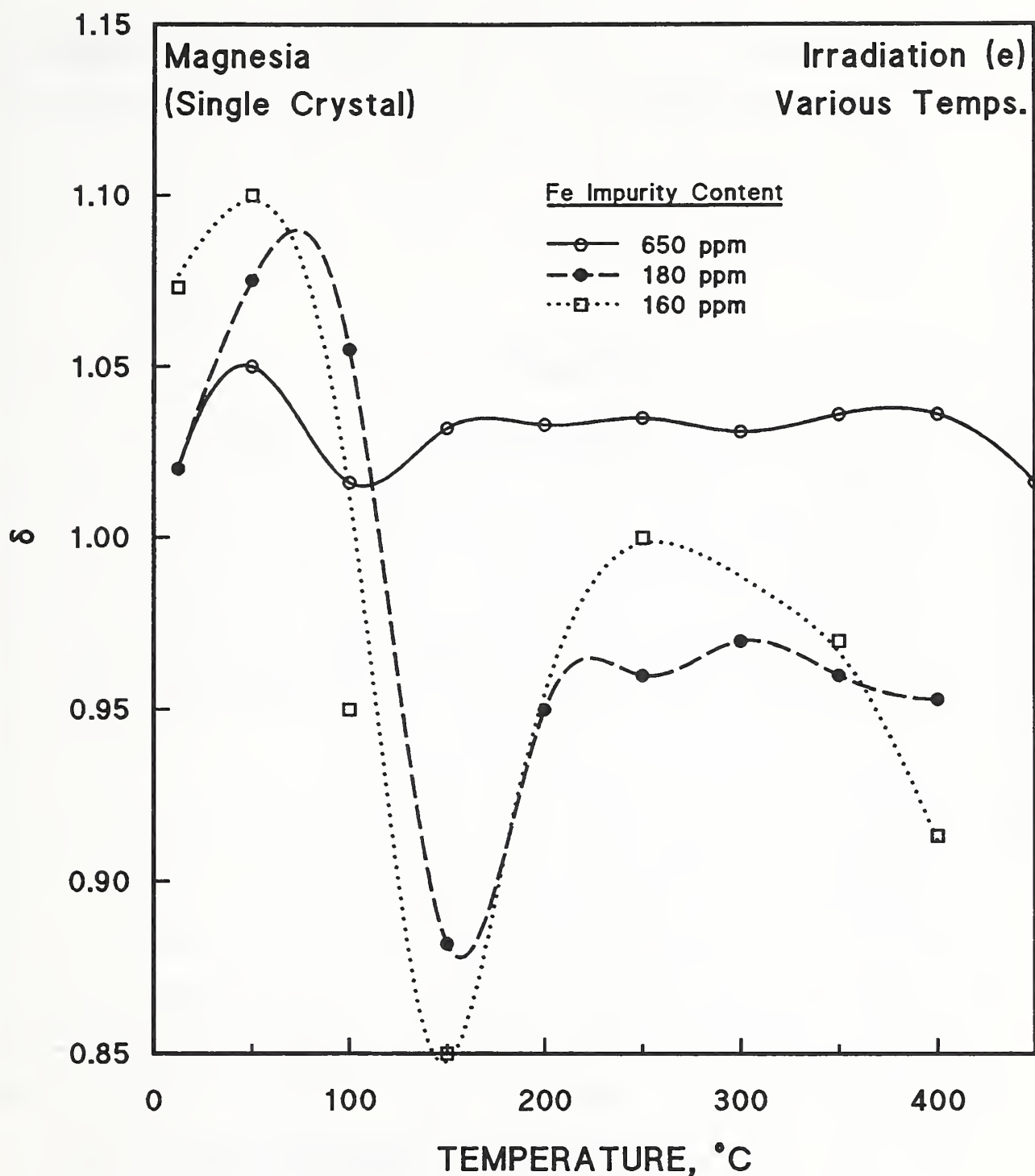


Figure 11.3.4. Change of δ with temperature and impurity level in MgO. Data from Hodgson and Clement [1988].

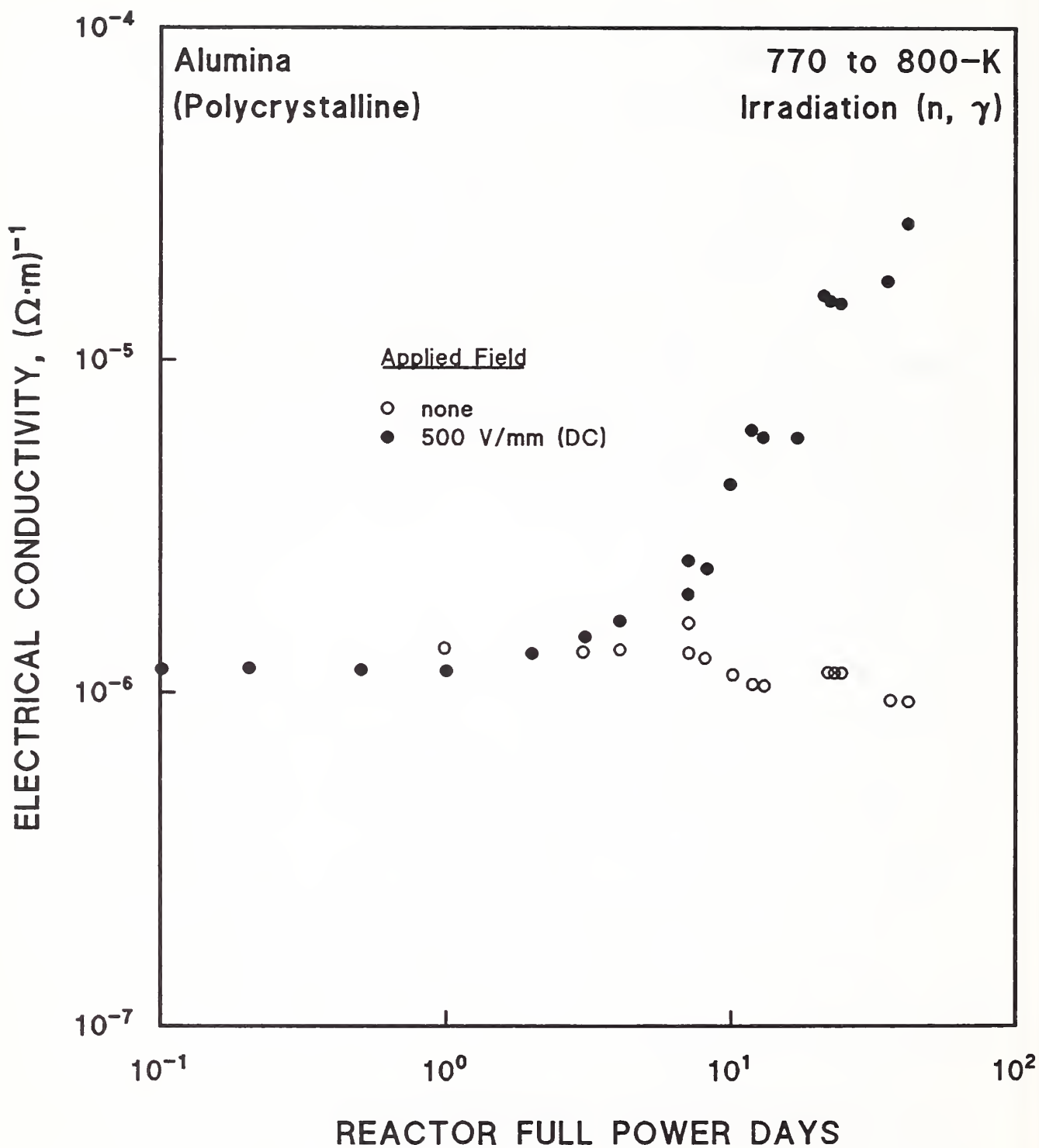


Figure 11.3.5. Electrical conductivity of Al_2O_3 vs. reactor time, with and without an electric field (500 V/mm). Data from Shikama et al. [1992b].

be expected at lower temperatures. However, Hodgson also showed that displacement damage was necessary to RIED, and this should be more severe at 4 K for a given fluence. A field-enhanced increase in the vacancy-interstitial production rate or decrease in the recombination rate was hypothesized to facilitate the nucleation and growth of colloids and to explain the field effect. Both an increase in vacancy production and a decrease in recombination rate would occur at 4 K, even without the presence of an electric field.

Pells [1991] reviewed references showing that at temperatures above 1000°C, a number of refractory oxides exhibited increases in conductivity and eventual breakdown when exposed to fields ~100 V/mm. However, in contrast to the data shown above in Figure 11.3.1, the activation energy did not change, even near breakdown, and if the field was removed before breakdown, the samples completely recovered their original dc conductivity. This process is known as solid-state electrolysis. But, the addition of radiation to this process lowers the temperature of breakdown significantly, and the increase in conductivity is permanent and cannot be reduced by annealing to temperatures up to 650°C. Furthermore, as discussed below, a new conductivity mechanism is introduced, that of electronic conductivity.

In a review of various RIED observations, Zinkle and Hodgson [1992] stated that the effect has been reported at temperatures as low as 573 K to somewhat below the 700 to 1000 K range, and that it occurs for damage levels of only 10^{-5} to 10^{-2} dpa. They noted that Pells [1991] also found a greatly reduced activation energy for the conductivity, in some cases, <0.1 eV, which implies that the mechanism involves electronic, rather than ionic, conductivity. The mobility of ions affects the ionic conductivity and decreases at lower temperatures, but electron mobility would not be as temperature-dependent. Figure 11.3.6 from Hodgson and Clement [1988] shows the RIC in single-crystal MgO at a relatively low temperature of 287 K. Zinkle and Hodgson [1992] also reviewed degradation of the dielectric loss tangent and thermal conductivity in ceramics at low temperatures and at a damage levels of $\sim 10^{-5}$ to 10^{-3} dpa. On page 64 they state "There does not appear to be a strong incentive for operating ceramics at cryogenic temperatures for damage levels $>10^{-3}$ dpa unless in situ anneals can be performed, due to the higher degradation rates in the thermal conductivity and loss tangent at low temperatures." Klaffky [1980]

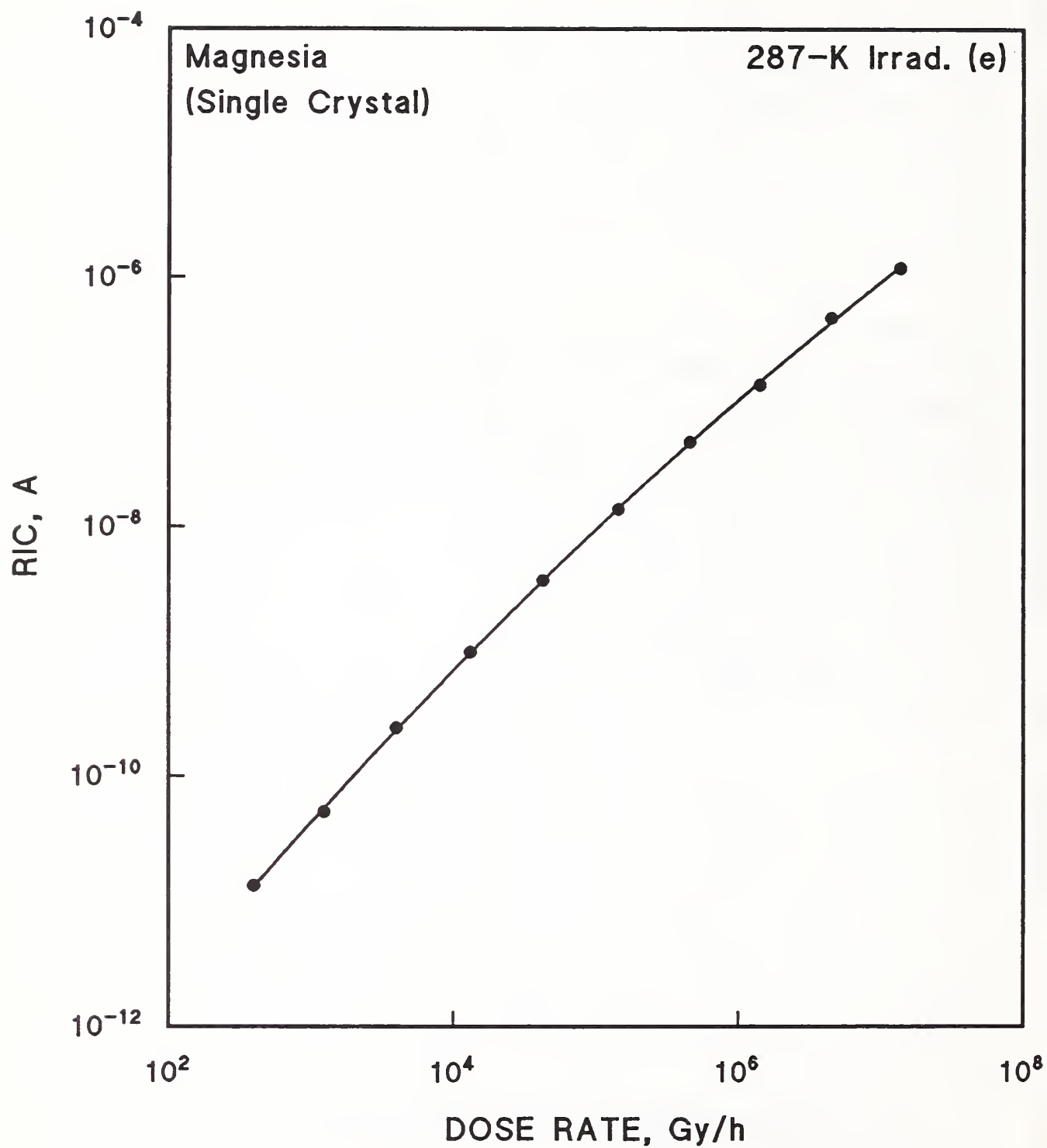


Figure 11.3.6. The RIC at 287 K in single-crystal MgO. Data from Hodgson and Clement [1988].

cited observations of a decrease in the electrical breakdown strength of Al_2O_3 below 450 K at an ionizing dose rate of only 5 Gy/s.

Figure 11.3.7 from Hodgson [1992b] shows a voltage threshold effect for RIED of about 50 V/mm in Al_2O_3 . The field threshold for the RIED effect has been shown to be as low as 19 V/mm, but longer irradiation times before breakdown were required for lower fields, as Figure 11.3.8 indicates [Hodgson, 1992a,b]. The process occurs from dc to at least 126 MHz.

Pells [1990, 1991] compared the response of polycrystalline MgAl_2O_4 and Al_2O_3 to 18-MeV proton irradiation at temperatures from 200 to 500°C in an electric field of 0.5 kV/mm. This field is about half that expected at the ITER TF magnet (Table 1.1.1). The ionization dose rate was 5×10^4 Gy/s and the displacement damage rate was $\sim 10^{-8}$ dpa/s. The total irradiation time for each sample was ~ 100 h, giving an ionization dose of about 1.8×10^{10} Gy and 3.6×10^{-3} dpa. Figure 11.3.9 for polycrystalline MgAl_2O_4 indicates that the phenomenon of increased conductivity occurs for an irradiation temperature as low as 200°C (however, the measurements were complicated by annealing at a higher temperature); Figure 11.3.10 for polycrystalline Al_2O_3 indicates the existence of a threshold temperature for REID of between 400 and 500°C. The figures also indicate that ionization doses of $\sim 10^9$ Gy are required for conductivity increases. These thresholds have not yet been reproduced with other irradiation sources. Thresholds for oxides having different impurity levels and other sources of material variability have also not been established. Investigations of RIED have been limited to ceramic oxides, at present [Zinkle and Hodgson, 1992]. The data in Figures 11.3.9 and 11.3.10 indicate that the threshold temperature for an effect measured with 18-MeV protons is higher for Al_2O_3 than it is for MgAl_2O_4 . In studies performed at high temperatures, but without irradiation, Al_2O_3 also showed superior resistance to electrical field breakdown when compared with MgO and MgAl_2O_4 [citation, Pells, 1991].

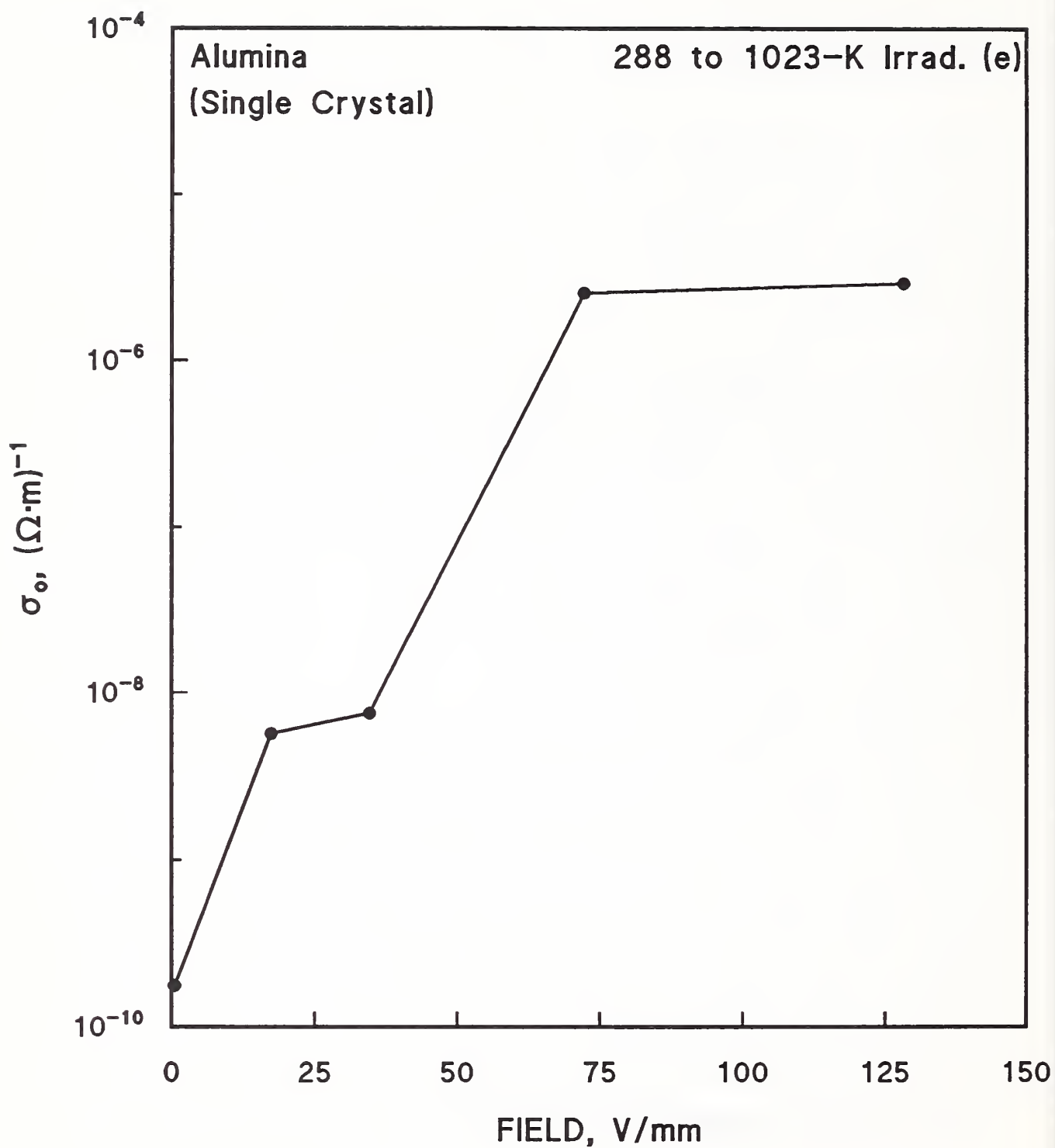


Figure 11.3.7. DC base conductivity after electron irradiation of 2×10^7 Gy at 723 K, vs. field. Data from Hodgson [1992b].

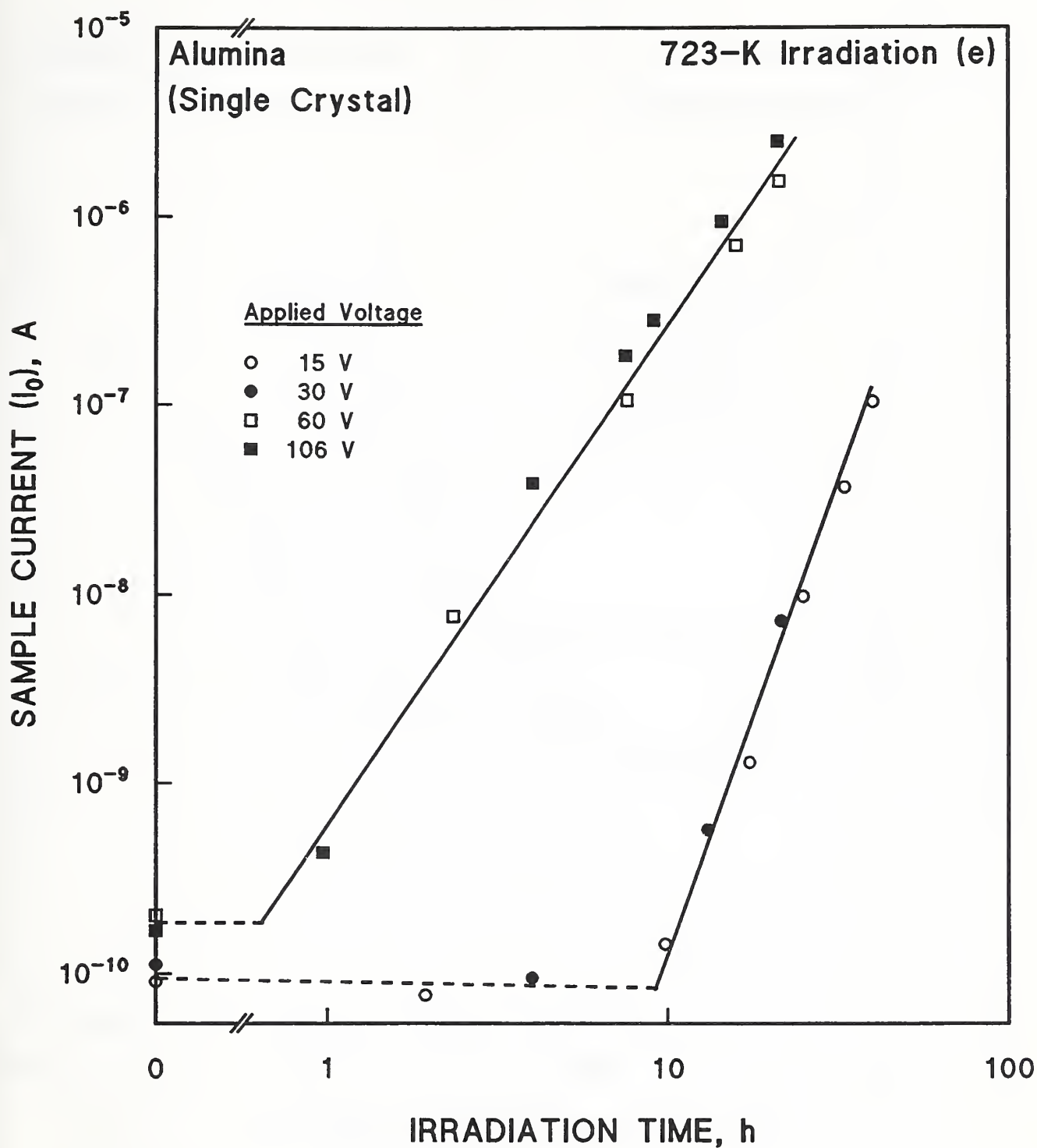


Figure 11.3.8. Electrical degradation of Al_2O_3 , as indicated by sample current, following electron irradiation for times and voltages indicated. The highest field corresponds to 133 V/mm. Data from Hodgson [1992a].

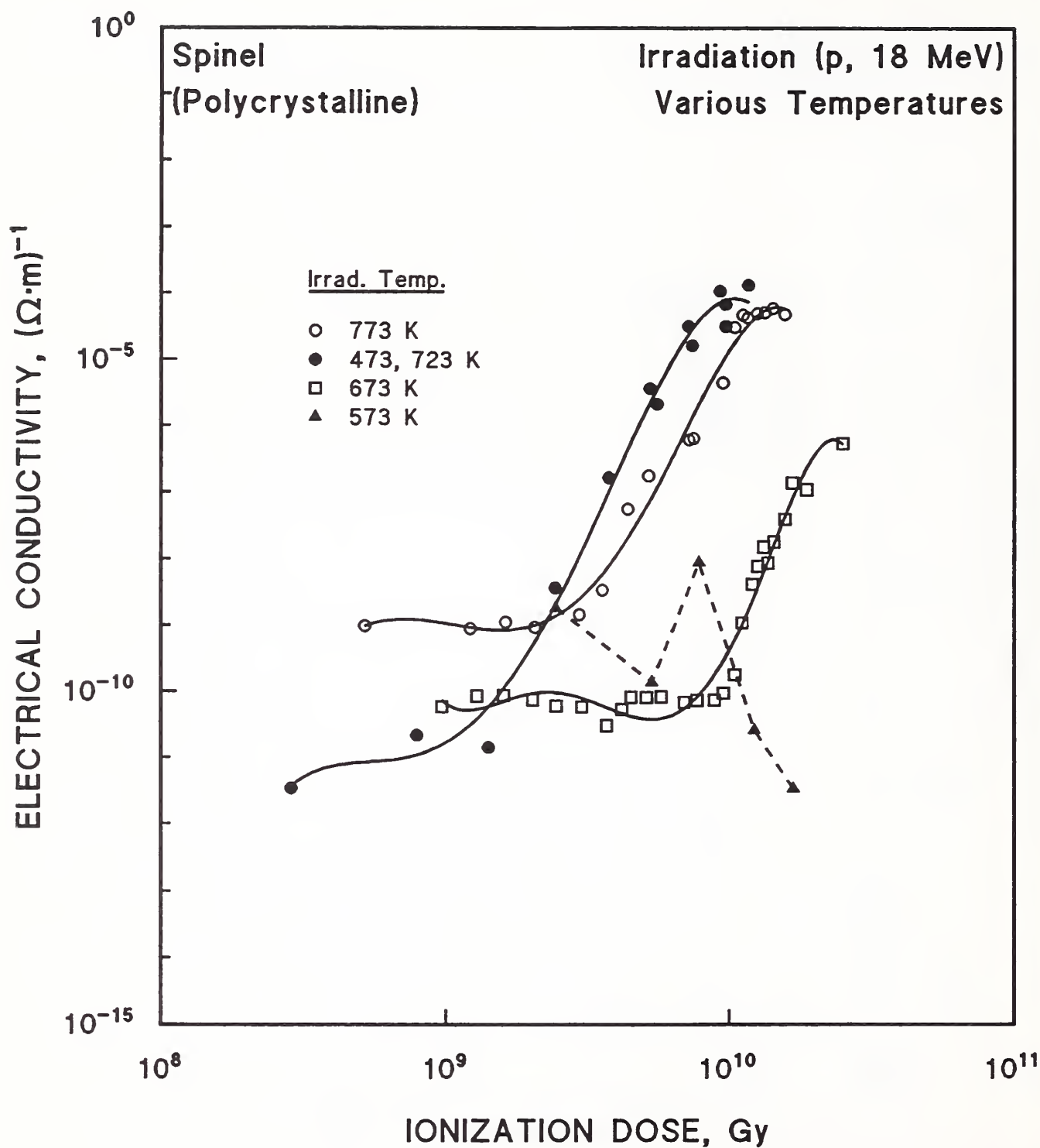


Figure 11.3.9. The intrinsic electrical conductivity of MgAl_2O_4 vs. ionization dose from 18-MeV protons, after irradiation at indicated temperatures. Data from Pells [1990].

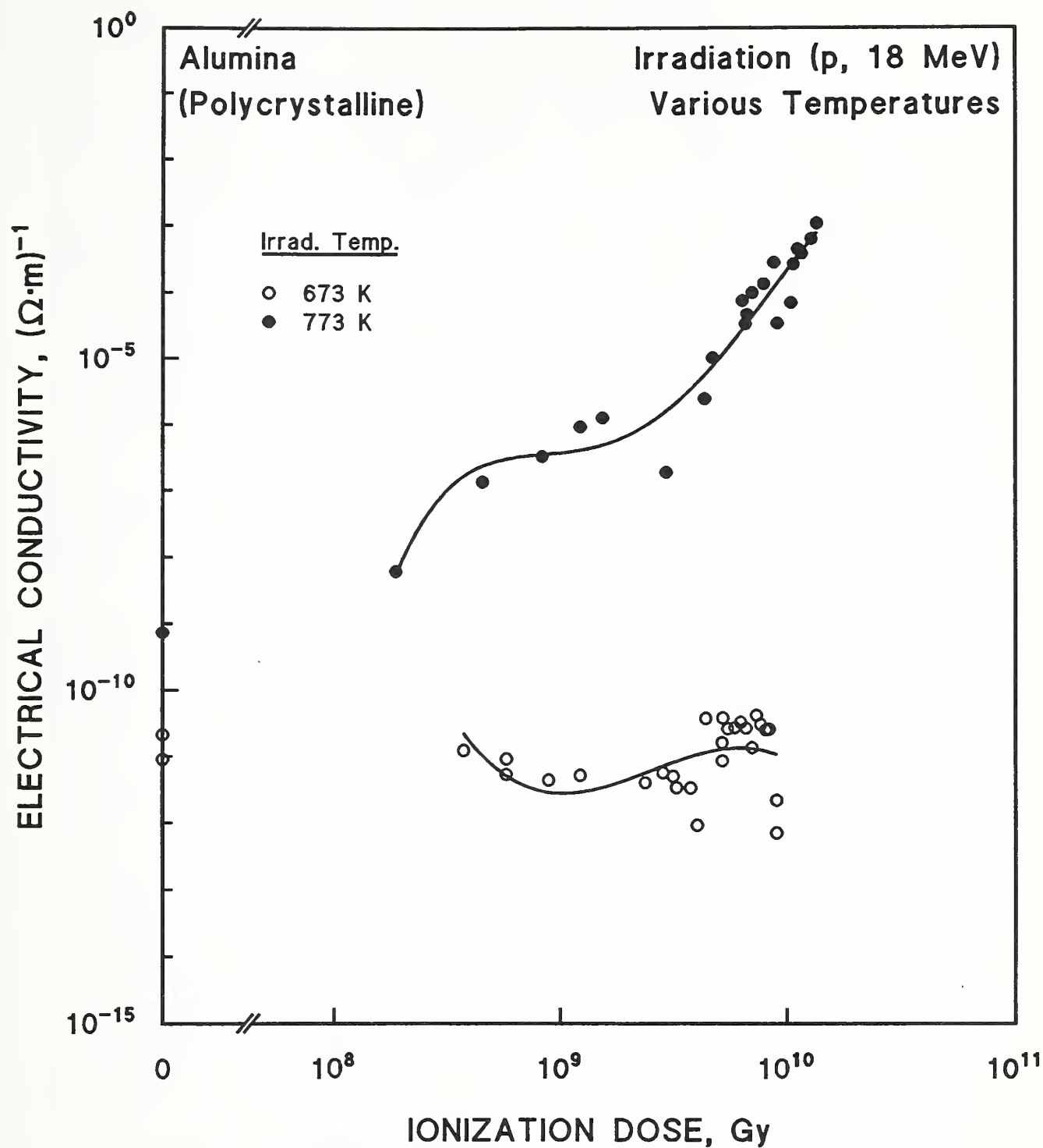


Figure 11.3.10. The intrinsic electrical conductivity of Al_2O_3 vs. ionization dose from 18-MeV protons, after irradiation at indicated temperatures. Data from Pells [1990].

12. COMPARATIVE EVALUATION OF INSULATORS; CONCLUSIONS

Data on the in situ compressive strength and electrical breakdown strength of insulators after a fusion fast neutron fluence of $10^{22}/\text{m}^2$ at 4 K are needed for the design of the ITER TF magnets; however, such data were not found in an extensive literature search on the inorganic insulators Al_2O_3 , AlN , MgO , porcelain, SiO_2 , MgAl_2O_4 , ZrO_2 , mica, and Macor. The existing cryogenic irradiation data, though very sketchy, indicate that considerable thermal recovery of displacement defects occurs at 300 K, so that 4-K irradiation damage can be indicated to a first approximation by results from an ambient-temperature fluence about a factor of 100 higher. There is evidence, however, that the predominant type of defect created at 4 K in a ceramic oxide may differ from that created at ambient temperature ([Atobe and Nakagawa, 1987], §2.1) and that host ion or neutron amorphization of ceramic oxides, while nearly impossible at 300 K, occurs readily at 77 K ([McHargue et al., 1986], §§1.3, 2.3). Therefore, a factor of 100 may not be sufficiently conservative. Also, usually only properties measured at ambient temperature are available for comparison, rather than 4-K properties, which may differ significantly. Nevertheless, to provide guidance for downselection of the materials reviewed, the following four sections, 12.1, 12.2, 12.3, and 12.4, summarize their ambient-temperature defect densities, changes in volume, degrees of amorphization, and retained mechanical strengths after an ambient fast neutron fluence of $\sim 10^{24}/\text{m}^2$. Section 12.5 applies these results to material downselection, and §12.6 presents the case for using ion simulation for further 4-K research, given that 4-K neutron irradiation sources are scarce, and difficult to access. Section 12.7 briefly reviews the few results on the radiation resistance of hybrid insulations and §12.8 summarizes evidence for the degradation of the electrical breakdown strength when an electric field, and both ionizing and displacive radiation, are simultaneously present.

12.1. COMPARISON OF DEFECT DENSITIES

Most of the data on defect density were generated from indirect optical measurements that chiefly detect anion (O) vacancies, but require the trapping of electrons at the vacancy site. Although Equation (2.1) can be used to calculate the volume concentration of defects from optical absorption data,

comparison of defects in different insulators by this technique cannot be done with complete accuracy, because of the requirement for electron trapping, which may not occur with equal probability in different materials. Impurity levels are also influential in stabilizing some types of defects. Furthermore, although in situ optical absorption measurements are relatively easy to perform at cryogenic temperatures, compared to mechanical and electrical property measurements, systematic studies have not been carried out for most materials of interest. However, the creation of defects in Al_2O_3 at 77 and 300 K has been investigated; before saturation, about 30 times more defects were created at 77 K for the same N-ion fluence [Pells and Murphy, 1992]. (See also §§1.3 and 2.1 for related investigations.)

For ambient temperature irradiation and measurement, Table 12.1.1 compares the information retrieved in the literature search. An attempt was made to extrapolate the results to a fast neutron fluence of $10^{24}/\text{m}^2$, since the data are at ambient temperature, and this may predict, very roughly, the number of such (detectable) defects that would remain after a fusion fast neutron fluence of $10^{22}/\text{m}^2$ at 4 K. The data for quartz were obtained with EPR techniques.

Table 12.1.1. Comparison of Defect Densities after Ambient Fast Neutron Fluence of $10^{24}/\text{m}^2$.

INSULATOR	DEFECTS/ cm^3	BASIS; COMMENTS
Al_2O_3	$\sim 7 \times 10^{20}$	Atobe and Nakagawa [1987], ambient-temperature, surviving defects from 15-K irradiation, extrapolation from $10^{21}/\text{m}^2$
AlN	—	—
MgO	$\sim 2 \times 10^{19}$	Henderson and Bowen [1971], Figure 4.1.1 Extrapolation, Chen et al. [1975], Figure 4.1.4
Porcelain	—	—
Vitreous SiO_2	—	—
Quartz	3×10^{19}	Extrapolation from $3 \times 10^{23}/\text{m}^2$; Shamfarov and Smirnova [1963], Shamfarov [1967]
MgAl_2O_4	—	—
ZrO_2	$\sim 10^{19}$	Estimate, Harrop et al. [1967]
Mica	—	—

Only three of the materials under consideration can be quantitatively compared: Al_2O_3 , MgO , and quartz. Although Al_2O_3 has the largest number of defects, this number may be inaccurate, because it was obtained from linear extrapolation to the target fluence of defects created at 15 K by a fluence 3 orders of magnitude smaller. The smaller defect densities in MgO and quartz were obtained by other methods. Therefore, the available data on defect density at present do not furnish a basis for material downselection. Such measurements have chiefly been useful in indicating that a greater number of defects survive irradiation at cryogenic, rather than ambient temperatures. Measurements of the defect density have also quantified the difference in numbers of defects created by fission neutrons and 14-MeV neutrons (§2.1), although recovery processes probably obliterated part of this difference, and the experiments should be repeated with 4-K irradiation and in situ measurements.

Note also that compressive strength measurements were made and correlated with defect density only for MgO , and only at ambient temperature, where considerable recovery is expected. Yet, the onset of brittle behavior occurred at a defect density of only $\sim 3 \times 10^{18}/\text{cm}^3$ [McGowan and Sibley, 1969]. This is an order of magnitude below the defect densities of ~ 2 or $3 \times 10^{19}/\text{cm}^3$ expected at the ITER TF magnet, based on Table 12.1.1. The brittle behavior corresponds to a dpa of only about 2.8×10^{-5} , since there are about 1.07×10^{23} atoms/ cm^3 in MgO . [$N(\text{atoms}/\text{cm}^3) = N(\text{Avogadro}) \cdot (\rho/M) \cdot (\text{No. of atoms/molecule})$, where M is the molecular mass]. The dpa at the TF magnets has been estimated above as between 10^{-3} to 10^{-4} , based on published σ_{dis} for Al_2O_3 (Table 1.2.3, §1.2.1).

12.2. COMPARISON OF VOLUME CHANGES

Volume change, or swelling after irradiation, has not been measured at cryogenic temperatures. Pells and Murphy [1992] compared swelling after Ne-ion irradiation at 200 K with that at higher temperatures, and found a considerable increase (Figure 1.3.8). However, the swelling measurements on the specimens were made at ambient temperature, and the lowest irradiation temperature was still far above 4 K. The large number of volume and density measurements at ambient temperature, after ambient irradiation, do permit a comparison of

the radiation resistances of the insulators in this survey. To obtain the values for volume changes in Table 12.2.1, measurements were extrapolated or interpolated to a fast neutron fluence of $10^{24}/\text{m}^2$. On the basis of the data in this table, either MgAl_2O_4 or Al_2O_3 would be preferred, because of their lower amount of volume change. Data at 14 MeV, but at lower fluences (Figure 2.2.2), indicate a lower swelling of MgAl_2O_4 than of Al_2O_3 for the same fluence. Also, the swelling in MgAl_2O_4 is isotropic, eliminating the possibility of grain boundary decohesion in the polycrystalline form, as may occur in Al_2O_3 . However, Figure 2.2.7 indicates that decohesion should not be a problem until fairly high fluences are reached, at least for material of low porosity.

Table 12.2.1. Comparison of Volume Changes after Ambient Irradiation to a Fast Neutron Fluence of $10^{24}/\text{m}^2$.

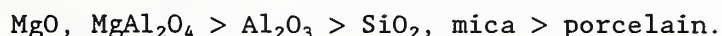
INSULATOR	$\Delta V/V$, %	BASIS; COMMENTS
Al_2O_3	0.35	Figure 2.8.8, lowest irradiation temperature (70 to 90°C)
AlN	0.7	Figure 3.2.2, lowest irradiation temperature (75 to 100°C), summation of lattice expansion
MgO	0.75 ± 0.2	Figures 4.2.1, 4.2.2, lowest irradiation temperature (45°C), extrapolated. Figure 4.2.5 (summary plot)
Porcelain	0.6 ± 0.3	$4 \times 10^{24}/\text{m}^2$ ($E > 100$ eV) (Table 5.1.1)*
Vitreous SiO_2	3	Figures 6.2.2, 6.2.4
Quartz	11	Figures 6.2.3, 6.2.4
MgAl_2O_4	0.04 ($2 \times 10^{22}\text{n}/\text{m}^2$) 0.8 ($2 \times 10^{26}\text{n}/\text{m}^2$)	§7.2
ZrO_2	0.28, a axis	stabilized? Klein [1955]
Mica	≥ 7	Figure 9.2.2 (interpolation; epithermal fluence)

* Comparable expansions from this table were 1% for single-crystal Al_2O_3 (50% higher fluence); -1.2% for vitreous SiO_2 ; 0 for MgAl_2O_4 ; 14% for mica.

12.3. COMPARISON OF FLUENCES REQUIRED FOR AMORPHIZATION

As Table 12.3.1 indicates, it is difficult to make comparisons on the basis of existing information, or to obtain absolute values of the neutron fluences required for amorphization, even at ambient temperature. Much of the data were obtained by ion irradiation, at ambient temperature, but the investigations of McHargue et al. [1986] on Al_2O_3 (§§1.3, 3.2) showed that achievement of amorphization at 300 K was difficult, owing to recovery, and depended upon ion chemical and size effects to stabilize the damage. McHargue et al. were apparently unable to amorphize Al_2O_3 at 300 K with Al ions, although both Al and O were effective at 77 K, where recovery was less pronounced. (Ion fluences of 4 and $6 \times 10^{20}/\text{m}^2$ amorphized Al_2O_3 at 77 K; the threshold fluence was apparently not determined.) In the case of Cr-ion irradiation, where 300-K amorphization has been reported, McHargue et al. found that the fluence required at 77 K was about 200 times smaller than that needed at 300 K. Therefore, the data in Table 12.3.1 must be treated with caution, in regard to predicting the 4-K fluence necessary for amorphization. Attempting to amorphize a ceramic oxide with a neutron fluence at ambient temperatures (or, above) is similar to attempting to amorphize it with host atom ions, since it is the PKAs produced by the incident neutrons that do the actual damage.

At ambient temperature, the apparent relative order of stability against irradiation-induced amorphization is:



This ordering is based upon relative comparisons given in Table 12.3.1. See §§4.3 and 9.4 for more details of the investigations. The covalently bonded AlN is evidently more resistant to neutron amorphization than quartz, but its relative stability with regard to the other ceramic oxides is unclear. Highly pure, single-crystal ZrO_2 (monoclinic) is apparently more stable than quartz, but natural and Y_2O_3 -stabilized ZrO_2 have been shown to transform readily (§8.4). The highly pure form of ZrO_2 is probably very costly and may have poor mechanical properties, since it is in the monoclinic form, rather than the cubic, stabilized form usually preferred for applications. Presumably, the ionically-bonded ceramic oxides MgO , MgAl_2O_4 , and Al_2O_3 would recover more completely upon warm-up to 300 K, from damage incurred at 4 K, than

covalently-bonded silicates such as SiO₂, porcelain, and mica. The covalently-bonded AlN may be intermediate in recovery between these two groups.

Table 12.3.1. Comparison of Fluences Required for Amorphization (Ambient Temperature).

INSULATOR	AMORPHIZATION FLUENCE	REFERENCE
Al ₂ O ₃	4 × 10 ¹⁷ /m ² (40-keV Kr, Xe ions) onset, 3 × 10 ¹⁷ /m ² (10-keV Kr ions)	Matzke and Whittton [1966] Jech [1967]
AlN	crystalline, 2.8 × 10 ²⁴ n/m ² (E > 1 MeV) onset, ~3.7 × 10 ²⁴ n/m ² (E > 1 MeV) (75 to 100°C)	Hickman and Jostsons [1969]
MgO	4 × 10 ¹⁸ /m ² (40-keV Kr, Xe ions) crystalline, 3 × 10 ²³ n/m ² (150°C) line broadening, 4 × 10 ²⁴ n/m ² (150°C) onset, 4.2 × 10 ²³ n/m ² (100°C)	Matzke and Whitton [1966] Wilks [1968]
Porcelain	onset, 8.4 × 10 ¹⁴ n/m ² (E > 14 MeV) complete, 2.1 × 10 ¹⁵ n/m ² (E > 14 MeV) crystalline, 2 × 10 ²⁴ n/m ² (E > 100 eV)	Abdel-Fattah et al. [1981] Klein [1955]
Quartz	≥5 × 10 ¹⁷ /m ² (150-keV Ar ions) onset, ~2 × 10 ²³ n/m ² (E not specified) complete, 1.2 × 10 ²⁴ n/m ² (E not specified)	Fischer et al. [1983b] Wittels and Sherrill [1954]
MgAl ₂ O ₄	10 ²¹ /m ² (3-keV Ar ions) plasma-sprayed only crystalline, 10 ²¹ /m ² (3-keV Ar ions) crystalline, 3 × 10 ²¹ /m ² (2.4-MeV Mg ions) crystalline, 1.6 × 10 ²¹ /m ² (2-MeV Al ions)	Iwamoto et al. [1986] Zinkle and Kojima [1990]
ZrO ₂	synthetic, pure ZrO ₂ untransformed at 3.6 × 10 ²⁴ n/m ² (fast neutrons) onset, ~1.3 × 10 ¹⁸ /m ² N ions, 10 mol% Y ₂ O ₃	Wittels and Sherrill [1954] Hasegawa et al. [1986]
Mica	onset, 5 × 10 ¹⁶ /m ² (10-keV Kr ions) complete, 5 × 10 ¹⁷ /m ² (10-keV Kr ions) observable mottling, mica phase, Macor, onset ~10 ²² n/m ² (E = 14 MeV)	Jech [1967] Fowler et al. [1981]

Review in §§4.3, 7.3 gives evidence for relative stability:

MgO, MgAl₂O₄ > Al₂O₃ > SiO₂, mica (see §§9.4, 9.6)

McHargue et al. [1986] demonstrated that host ion irradiation may not induce amorphization at 300 K, but will at 77 K, owing to recovery of damage without chemical, size effects, etc. of foreign ions that stabilize damage at ~300 K.

12.4. COMPARISON OF MECHANICAL PROPERTIES; COMPRESSIVE FAILURE

12.4.1. Mechanical-Property Measurements

Recent data obtained by Dienst and Zimmermann [1994], kindly supplied by the authors as a preprint, furnishes the best comparative evidence of the effect of ambient-temperature neutron irradiation on ambient-temperature mechanical properties. Although the measurements were of the three-point bending strength, and 4-K compressive strength after irradiation is needed for the design of TF magnets, the authors compared their results at fast neutron fluences of 1.5 to $2.0 \times 10^{25}/\text{m}^2$ ($E > 0.1$ MeV) at $\sim 100^\circ\text{C}$ with previous measurements at fluences $5 \times 10^{25}/\text{m}^2$ (at 400 to 500°C), and concluded that the fluence threshold for a significant decrease of strength in Al_2O_3 was in the range of about 3 to $5 \times 10^{24}/\text{m}^2$ ($E > 0.1$ MeV). Since this conclusion is valid for irradiation temperatures at least 100 K above 300 K, the implications for a fusion fast neutron fluence of $10^{22}/\text{m}^2$ at 4 K are somewhat disconcerting, because the sketchy data available, reviewed in §1.3, indicated that the defects retained from this fluence at 4 K may correspond to a fluence about 100 times higher at ~ 300 K. Therefore, the threshold for significant mechanical property damage may be exceeded by the predicted TF magnet fluence. (The low fluence required for brittle behavior in MgO near ambient temperature reinforces this supposition.) Dienst and Zimmermann suggested that the strength reduction that they observed was probably due to large defect aggregates that formed spontaneously, independent of considerable thermal diffusion. Although the calculated dpa (e.g., from Table 1.2.3) of this threshold is about 0.5 and the corresponding calculated TF magnet dpa would be $\sim 5 \times 10^{-4}$, the amount of retained damage at the two widely different temperatures from fluences differing by several orders of magnitude could be similar.

The three materials compared in these tests consisted of several grades of Al_2O_3 , including fine-grained Al_2O_3 -Vitox and Al_2O_3 -10% ZrO_2 , MgAl_2O_4 , and sintered AlN . Table 12.4.1 shows that all of the grades of Al_2O_3 exhibited a similar reduction in strength of 20 to 25% and that the strength of the AlN fell drastically to only about 37% of its initial value. However, the mean flexural strength of MgAl_2O_4 actually increased in value, although the change was within the calculated statistical standard deviation. This result is in

accord with previous high-temperature results of Clinard et al. [1984]. The flexural strength of the irradiated MgAl_2O_4 is still below that of the irradiated Al_2O_3 , however. With regard to retention of mechanical properties under irradiation, the order of resistance, according to the data presented in Table 12.4.1 is:

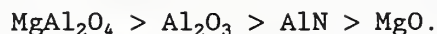
$$\text{MgAl}_2\text{O}_4 > \text{Al}_2\text{O}_3 > \text{AlN}.$$

Table 12.4.1. The Change in the Mean Ultimate Bending Strength (with statistical standard deviation for 13 specimens, each value) of Several Ceramic Insulators after a Fast Neutron Fluence of $2.0 \pm 0.2 \times 10^{25}/\text{m}^2$ ($E > 0.1$ MeV) at 110 to 115°C. Data from Dienst and Zimmermann [1994].

MATERIAL	MEAN ULTIMATE BENDING STRENGTH, UNIRRADIATED, MPa	MEAN ULTIMATE BENDING STRENGTH, IRRADIATED, MPa
Al_2O_3 -SC	372 ± 48	273 ± 39
Al_2O_3 -10% ZrO_2	503 ± 46	427 ± 59
Al_2O_3 -Vitox	418 ± 35	352 ± 46
Al_2O_3 -Bio	322 ± 35	255 ± 36
Al_2O_3 -AL23	208 ± 24	150 ± 30
MgAl_2O_4	148 ± 53	168 ± 49
AlN-Shapal	301 ± 21	112 ± 12

Diametral compressive tests by Hurley et al. [1981] after a fast neutron fluence of $2.1 \times 10^{26}/\text{m}^2$ at 430 ± 5 K indicated a higher initial tensile strength for polycrystalline MgAl_2O_4 than for MgO , and, on average, slightly better strengthening after irradiation for MgAl_2O_4 . Compressive strength data on single-crystal MgO indicated a severe deterioration at an ambient fluence just below $2 \times 10^{22}/\text{m}^2$ ($E > 1$ MeV). Most specimens broke before testing could be completed. The irradiation temperature was 40 to 60°C. Since all three ceramics tested by Dienst and Zimmermann survived irradiation at 100°C and were tested in tension, which may be a more sensitive test of irradiation

damage than compression, the order of retention of mechanical properties can be expanded to:



However, polycrystalline MgO might have fared better under comparable irradiation at somewhat higher temperatures of 100°C and above that allow more defect recombination. The compressive flow strength of the MgO was increasing very rapidly with fluence until the sudden onset of brittle failure that made specimens very difficult to handle (§4.4). The problem occurred at a defect concentration of only $\sim 3 \times 10^{18}/\text{cm}^3$ ($\approx 3 \times 10^{-5}$ dpa).

Comparable measurements of mechanical strength after irradiation have not been made on porcelain, quartz, pure and stabilized ZrO_2 , and mica. The onset of mechanical degradation in pure ZrO_2 may occur at a fast neutron fluence as low as $5 \times 10^{23}/\text{m}^2$ ($E > 1$ MeV) [Harrop et al., 1967], but this observation was obtained on a bending test of an oxide-metal sandwich (§8.4). The results may have been affected by radiation damage in the metal, or by the characteristics of the film of ZrO_2 tested. The unirradiated, ambient-temperature compressive strengths of some of these materials are given in Table 12.4.2. The comparative values from Rice [1971] were the highest available at the time. The compressive strength of quartz is comparable to that of the ceramic oxides. However, its fluence of amorphization is much lower.

12.4.2. Critical Strain for Compressive Failure

The critical strain at which compressive failure would occur in insulation is given by the ratio of the compressive strength to the compressive modulus. Using the 295-K values for these quantities, given in Tables 12.4.2 and 12.4.3 for several insulators, the critical strains, ϵ_{crit} , are calculated and given in the second table. For comparison with the experimental volume swelling given in Table 12.2.1, the critical strains are multiplied by 3 to give a value for $(\Delta V/V)_{\text{crit}}$. This simple calculation assumes that all of the force from the radiation expansion is applied to the polycrystalline material as a compressive stress. This is not necessarily the worst case, since additional compressive forces could be exerted by other metallic components, which generally contract more than the ceramics between 295 and 4 K, and which may also

Table 12.4.2. The Compressive Strength at 295 K of Several Polycrystalline Oxides and a Nitride, and Quartz, Porcelain, Mica, and Glass-Mica Composites.

INSULATOR	COMPRESSIVE STRENGTH, GPa	REFERENCE
Al ₂ O ₃	4.48*	Rice [1971]
MgO	1.38	Rice [1971]
MgAl ₂ O ₄	2.76	Rice [1971]
SiO ₂ (crystal)	2.48	Rice [1971]
SiO ₂ (vitreous)	1.38	Rice [1971]
CaO ₄ -stab.ZrO ₂	2.00	Rice [1971]
AlN	2.48	Rice [1971]
Porcelains (experimental electrical)	0.66 to ≤1.38	Schroeder and Guertin [1978]
Mica (multiple- ply paper)	~0.138 (550°C)	Ketterer [1964]
Macor (various flake sizes)	0.104 to 0.276	Chyung [1974]
Glass-mica com- posite	>0.053	Low [1980]

* Highest observed for Al₂O₃; grain size 2 μ m.

swell somewhat under irradiation. The last two columns of Table 12.4.3 compare $(\Delta V/V)_{crit}$ with the expected swelling for an ambient neutron fluence of $\sim 10^{24}/m^2$ from Table 12.2.1. Spinel appears to have the best resistance to swelling-induced compressive failure, and among the ceramic oxides, MgO is closest to this type of failure. Owing to the lack of reliable modulus values and comparative compressive strength measurements, this calculation was not carried out for mica. Note, however, the large expansion and low compressive strength of the mica paper compared to the other ceramics. A mica-glass material, identified by the authors as a type of mica paper, failed in compression at less than 10 000 cycles before irradiation; consequently, it was not included in a radiation fatigue program [Erez and Becker, 1982]. The volume expansion of quartz is far above the critical strain.

Table 12.4.3. Comparison of $(\Delta V/V)_{\text{crit}}$ with Experimental Swelling.

INSULATOR	E, GPa	ϵ_{crit}	$(\Delta V/V)_{\text{crit}}, \%$	$(\Delta V/V)_{\text{expt}}, \%$
Al ₂ O ₃	380*	0.0118	3.54	0.35
MgO	283	0.00488	1.46	0.75
MgAl ₂ O ₄	270*	0.0102	3.06	<0.35
AlN	320*	0.00647	1.94	0.7
Quartz	476	0.0028	0.82	11

* Dienst et al. [1990]

12.5. CONCLUSIONS: MATERIAL SELECTION

On the basis of the data on volume change, fluence of amorphization, and retention of mechanical properties, MgAl₂O₄ appears to have the best resistance to irradiation of the materials surveyed for this report. However, its compressive strength is lower than that of Al₂O₃, and in plasma-sprayed form, MgAl₂O₄ may be considerably less radiation-resistant than it is in polycrystalline form (§7.3). Data on its resistance to host-atom amorphization at cryogenic temperatures are lacking, in comparison to the 77-K data on Al₂O₃ obtained by McHargue et al.

In situ measurements after 4-K fast neutron irradiation of the most promising inorganic insulation candidates, MgAl₂O₄, Al₂O₃, AlN, and MgO are urgently needed. Mica is not a promising candidate, in view of its possible delamination, existing porosity, tracking from ²³⁵U fission, and, perhaps, additional 4-K tracking from α particles produced by very high energy neutrons. However, mica could perform an essential role in averting electrical breaking and permitting less costly fabrication procedures. Therefore, it should also be tested in situ. Compressive strength, shear strength (if needed in the design), electrical breakdown, and any other critical properties must be measured in situ. Testing after warm-up will not correctly simulate operating conditions, owing to recovery of nearly all 4-K defects by 300 K. In fact, many 4-K defects may recover by 77 K. (Atobe and Nakagawa [1987] claimed that there was no further recovery, between 77 and 300 K, of defects generated at

15 K.) Therefore, storage at 77 K before testing may give misleading results, and any such storage procedures should be first validated by in situ, 4-K testing after 4-K irradiation. The simulation of "operating conditions" for electrical breakdown strength measurements includes the provision of an electrical field of maximum strength, because electrical fields present during neutron irradiation may adversely and permanently alter electrical characteristics of ceramic oxides (§11).

12.6. CONCLUSIONS: FURTHER RESEARCH

Owing to recovery processes, the absence of 4-K irradiation and in situ testing of inorganic insulation is a severe limitation in material downselection, and in setting realistic radiation limits for the ITER TF magnets. No meaningful design data are available at present, so it is not known whether a magnet can be constructed with insulation that will withstand the projected fast neutron fluence of $10^{22}/\text{m}^2$ at 4 K. The most conservative course is to remove silicate-bonded materials from consideration, since they are known to amorphize at ~ 300 K at an onset fast neutron fluence of $\sim 10^{23}/\text{m}^2$. This eliminates quartz, vitreous SiO_2 , porcelain, and mica. Both highly pure and stabilized ZrO_2 should be eliminated also, because of the difficulty of maintaining high purity during fabrication and high energy irradiation, and the probable transformation of cubic-stabilized phases to other phases during irradiation. This leaves AlN , MgAl_2O_4 , MgO , and Al_2O_3 . AlN can be eliminated because it is covalent and of lower strength, and MgO can be eliminated because of poor post-irradiation compressive strength. Although the remaining two ceramic oxides appear to resist neutron or host atom amorphization at ~ 300 K, which the silicates do not, host ion amorphization has been demonstrated for Al_2O_3 at 77 K, and has apparently not been attempted in MgAl_2O_4 at 77 K (§§2.3, 7.3). (Host ion amorphization is roughly equivalent to neutron amorphization since it is the host PKAs that do the damage in neutron irradiation. The ion fluences used for Al_2O_3 were high, but apparently, a threshold fluence was not established.) The observation, by McHargue et al. [1986] of a pronounced temperature dependence of amorphization, raises a cautionary signal against proceeding with the design of ITER TF magnets under the present assumptions, without 4-K irradiation and in situ test measurements of critical properties, such as the electrical breakdown and compressive strengths.

If 4-K neutron irradiation sources are not available, ion irradiation simulation is the next best alternative in most cases, although the short range of ions severely limits specimen size and the properties that can be measured.

If warm-up to ~300 K is contemplated to allow recovery and permit a higher total fluence before serious radiation damage occurs, note that there is no data base at present to thoroughly validate and quantify such procedures. However, it is likely that the ceramic oxides would be amenable to such procedures, whereas damage to the silicate bonds in vitreous SiO_2 , quartz, mica, and porcelain might be harder to repair. Note that at least two observations indicate that porous ceramic oxides may be more subject to microcracking and amorphization: see §2.2 for microcracking in Al_2O_3 of 7% porosity and §7.3 for amorphization of plasma-sprayed, rather than sintered MgAl_2O_4 . This indicates that the good radiation resistance of the dense, polycrystalline ceramic oxides cannot be extrapolated to plasma-sprayed forms.

12.7. HYBRID INSULATION SUMMARY

Coghlan and Clinard [1991] presented evidence of an unusual dependence of the volume swelling of Macor upon fluence, which they traced to the extensive swelling of the mica constituent coupled with compaction of the glassy matrix (§10.1.2). Such differential swelling in composites may lead to severe interfacial stresses in irradiated hybrid insulation, culminating in severe loss of strength [Clinard et al., 1984]. In an early survey of radiation damage to insulators [Sisman et al., 1957], the break-up of glass-bonded mica specimens was reported at an epithermal fluence of 2 to $6 \times 10^{24}/\text{m}^2$, which other materials in the survey, such as Al_2O_3 , MgAl_2O_4 , porcelain, and non-bonded forms of mica and SiO_2 , evidently survived. Theoretical studies of interfacial stresses in irradiated, bonded materials have also been carried out (§10.3), but only for metals.

12.8. ELECTRICAL DEGRADATION BY RADIATION AND FIELD: SUMMARY

Both ionizing and displacive radiation are necessary for RIC. Therefore, electrical degradation from a neutron fluence cannot be simulated by γ or electron radiation. The presence of an electric field during radiation

appears to cause permanent damage to the insulator that probably cannot be repaired by annealing, even at temperatures far above ambient. Electron, rather than ion, conduction appears to be the chief contributor to RIED. This conclusion is based upon the permanent diminution of the activation energy that is observed after radiation accompanied by an electric field. The threshold field for an effect is as low as 19 V/mm; longer irradiations are required at lower fields before the onset of electrical breakdown. At present, only a few ceramic oxides, such as MgO , Al_2O_3 , and MgAl_2O_4 , have been investigated for RIED, but there are data on RIC from ionization sources for SiO_2 , ZrO_2 and mica.

Since displacive radiation is required for the effect, and the displacive component of radiation does more damage at 4 K than at ambient temperature, a cryogenic effect cannot be ruled out, although no testing below 300 K has been done, and there are some indications of higher-temperature thresholds. Furthermore, since electron conduction, rather than ion conduction, is predominantly involved in the process, the decrease of ionic conductivity that occurs in insulators at low temperatures, owing to reduced ion mobility, may be irrelevant to the dependence of the effect upon temperature. At present, a temperature threshold has not been established with certainty for all conditions, including exposure to electric fields and radiation for extended time periods. However, under certain conditions, some data indicate a shorter time period before onset in MgO than in Al_2O_3 (Figure 11.3.3), and a lower temperature threshold in MgAl_2O_4 than in Al_2O_3 (Figures 11.3.9 and 11.3.10). These results, indicating superior resistance of Al_2O_3 to electrical breakdown under irradiation, are supported by the high resistance of single-crystal Al_2O_3 to high-temperature electrical breakdown. Because the electrical breakdown phenomena are not well understood, 4-K, in situ tests of insulators under operating conditions are recommended. Goland [1978] described an experimental chamber for dielectric breakdown measurements to be used in an electron accelerator. More recent information on instrumentation for use in a fission reactor is available [Shikama et al., 1992a,b, and citations therein].

13. REFERENCES

- Abdel-Fattah, W.I.; Abou-Saif, E.A.; El-Alousi, D.S. 1981. Structural Damage of Porcelain by Fast Neutron Bombardment. *Sprechsaal* 114. pp. 753-757.
- Abe, K.; Logan, C.M.; Saneyoshi, K.; Clinard, F.W., Jr. 1987. Irradiation Effects in KAPTON Polyimide Film from 14-MeV Neutrons and Cobalt-60 Gamma Rays. In: *Influence of Radiation on Material Properties: 13th International Symposium (Part II)*, ASTM STP 956. F.A. Garner, C.H. Henager, Jr., and N. Igata, eds. American Society for Testing and Materials, Philadelphia, PA. pp. 668-681.
- Abou Sekkina, M.M.; Ewaida, M.A.; Ibrahim, E.M.H.; Al-Adawy, A.A. 1987. Novel Investigations on the Effects of Temperature and Gamma Radiation Damage on the Electro-Mechanical Properties of Double Doped Zirconia Refractories. *Isotopenpraxis* 23. pp. 391-395.
- Abramishvili, M.G.; Altukhov, V.I.; Kalabegishvili, T.L.; Kvachadze, V.G. 1981. Low-Temperature Heat Conduction of γ -Irradiated MgO Crystals. *Physica Status Solidi (b)* 104. pp. 49-55.
- Agranovich, V.M.; Kirsanov, V.V. 1986. Production of Radiation Defects by Collision Cascades in Metals. In: *Physics of Radiation Effects in Crystals*, R.A. Johnson and A.N. Arlov, eds. Elsevier Science Publishers B.V., North-Holland Physics Publishing Division, North-Holland, Amsterdam, The Netherlands. pp. 117-187.
- Ahn, J.H.; Peacor, D.R.; Essene, E.J. 1986. Cation-Diffusion-Induced Characteristic Beam Damage in Transmission Electron Microscope Images of Micas. *Ultramicroscopy* 19. pp. 375-382.
- Aki, F.; Matsunobu, K.; Kadotani, K. 1983. Developments in Coil Insulation Technology for Nuclear Fusion Equipment. *Hitachi Review* 32. pp. 153-158.
- Albrecht, D.; Armbruster, P.; Spohr, R.; Roth, M.; Schaupt, K.; Stuhmann, H. 1985. Investigation of Heavy Ion Produced Defect Structures in Insulators by Small Angle Scattering. *Applied Physics A* 37. pp. 37-46.
- Antal, J.J.; Goland, A.N. 1958. Study of Ractor-Irradiated α -Al₂O₃. *Physical Review* 112. pp. 103-111.
- Arnold, G.W.; Compton, W.D. 1959. Radiation Effects in Silica at Low Temperatures. *Physical Review* 116. pp. 802-811.
- Arnold, G.W.; Compton, W.D. 1960. Threshold Energy for Lattice Displacements in α -Al₂O₃. *Physical Review Letters* 4. pp. 66-68.
- Arnold, G.W.; Krefft, G.B.; Norris, C.B. 1974. Atomic Displacement and Ionization Effects on the Optical Absorption and Structural Properties of Ion-implanted Al₂O₃. *Applied Physics Letters* 25. pp. 540-542.

- Atobe, K.; Nakagawa, M. 1987. Production Rate and Thermal Stability of F Center in α -Al₂O₃ with Irradiation Temperature. *Crystal Lattice Defects and Amorphous Materials* 17. pp. 229-233.
- Atobe, K.; Nishimoto, N.; Nakagawa, M. 1985. Irradiation-Induced Aggregate Centers in Single Crystal Al₂O₃. *Physica Status Solidi (a)* 89. pp. 155-162.
- Baëta, R.D.; Ashbee, K.H.G. 1973. Transmission Electron Microscopy Studies of Plastically Deformed Quartz. *Physica Status Solidi (a)* 18. pp. 155-170.
- Baeta, R.D.; Ashbee, K.H.G. 1975. Electron Irradiation Damage in Synthetic Quartz. In: *Proceedings of EMAG '75*. pp. 307-310.
- Bahadur, H.; Parshad, R. 1980 Radiation Induced Damage on Quartz Crystal Surfaces Detected by Scanning Electron Microscope. *Physica Status Solidi (a)* 59. pp. K13-K16.
- Banford, H.M. 1984. Electrical Insulation and Fusion Reactors. In: *Advances in Nuclear Science and Technology*, Vol. 16. J. Lewins, M. Becker, eds. Plenum Press, New York, NY. pp. 1-73.
- Barber, D.J.; Tighe, N.J. 1968. Neutron Damage in Single Crystal Aluminum Oxide. *Journal of The American Ceramic Society* 51. pp. 611-617.
- Barr, H.N.; Hittman, F.; Brown, R.D.; Clinard, F.W., Jr.; Lopez, M.R.; Martinez, H.; Romero, T.J.; Cook, J.H. 1990. Testing of Neutron-Irradiated Ceramic-to-Metal Seals. *Fusion Technology* 17. pp. 385-390.
- Bean, C.P.; Doyle, M.V.; Entine, G. 1970. Etching of Submicron Pores in Irradiated Mica. *Journal of Applied Physics* 41. pp. 1454-1459.
- Beeler, J.R., Jr. 1966. Displacement Spikes in Cubic Metals. I. α -Iron, Copper, and Tungsten. *Physical Review* 150. pp. 470-487.
- Berger, M.J.; Seltzer, S.M. 1982. Stopping Powers and Ranges of Electrons and Positrons (2nd Ed.). NBSIR 82-2550-A. National Bureau of Standards (U.S.). 169 pp.
- Berman, R. 1951. The Thermal Conductivities of Some Dielectric Solids at Low Temperatures. *Proceedings of the Royal Society A* 208. pp. 90-107.
- 1952. The Thermal Conductivity of Disordered Solids at Low Temperatures. *Bulletin de l'Institut International du Froid*, Annexe 1952-1. pp. 13-20.
- Berman, R.; Klemens, P.G.; Simon, F.E. 1950. Effect of Neutron Irradiation on the Thermal Conductivity of a Quartz Crystal at Low Temperature. *Nature* 166. pp. 864-866.

- Berman, R.; Foster, E.L.; Rosenberg, H.M. 1955. The Thermal Conductivity of Irradiated Dielectric Crystals at Low Temperatures. In: *Defects in Crystalline Solids*. The Physical Society, London, U.K. pp. 321-327.
- Berman, R.M.; Bleiberg, M.L.; Yeniscavich, W. 1960a. Fission Fragment Damage to Crystal Structures. *Journal of Nuclear Materials* 2. pp. 129-140.
- Berman, R.; Foster, E.L.; Schneidmesser, B.; Tirmizi, S.M.A. 1960b. Effects of Irradiation on the Thermal Conductivity of Synthetic Sapphire. *Journal of Applied Physics* 31. pp. 2156-2159.
- Billington, D.S.; Crawford, J.H., Jr. 1961. *Radiation Damage in Solids*. Princeton University Press, Princeton, NJ.
- Billy, J.; Labbe, J.C.; Lee, Y.M.; Roult, G. 1984. Résistance du Nitrure d'Aluminium à l'Irradiation Par Neutrons Rapides. *Review Internationale des Hautes Temperatures et des Refractaires*, 21. pp. 19-25.
- Bøgh, E.; Høgild, P.; Stensgaard, I. 1969. An Experimental Study of the Spatial Distribution of Defects in Ion-Bombarded Solids. In: *Radiation Damage in Reactor Materials*, Vol. 1. International Atomic Energy Agency, Vienna, Austria. pp. 77-87.
- Blanchard, J.P. 1988. Analysis of Singular Stress Fields in Duplex Fusion Components. Dissertation. University of California, Los Angeles, CA.
- Blanchard, J.P.; Ghoniem, N.M. 1990. Analysis of Singular Stress Fields in Duplex Fusion Components. *Journal of Nuclear Materials* 172. pp. 54-70.
- Bonfiglioli, G.; Ferro, A.; Mojoni, A. 1961. Electron Microscope Investigation on the Nature of Tracks of Fission Products in Mica. *Journal of Applied Physics* 32. pp. 2499-2503.
- Bopp, C.D.; Sisman, O.; Towns, R.L. 1960. The Effect of Irradiation on the Thermal Stability of Muscovite Mica. In: *Solid State Division Annual Progress Report for Period Ending August 31, 1960*. ORNL-3017. Oak Ridge National Laboratory, Oak Ridge, TN. pp. 98-100.
- Bowen, D.H.; Clarke, F.J.P. 1964. The Growth of Neutron Irradiated Magnesium Oxide. *Philosophical Magazine* 9. pp. 413-421.
- Bradley, A.; Pinkerton, A.P.; Grand, S. 1959. Induced Conductivity in Pre-irradiated Insulating Materials. In: *Fourth Radiation Effects Symposium*, vol. 1, paper #3. The Aircraft Nuclear Propulsion Department, General Electric Co. unpagd.
- Brindley, G.W. 1981. Phyllosilicates. *Encyclopedia of Earth Sciences*, Vol. IVB. In: *The Encyclopedia of Mineralogy*, K. Frye, ed. Hutchinson Ross Publishing Co., Stroudsburg, PA. pp. 369-376.
- Brown, I.J.; Brown, M.A. 1981. Low-Temperature Thermal Expansion of γ -Irradiated Ruby. *Physical Review Letters* 46, 13. pp. 835-837.

- Buckley, S.N. 1984. High Dose Electron Irradiation Damage in MgAl_2O_4 Spinel. In: *Proceedings of the 13th Symposium on Fusion Technology*, Vol. 2. Commission of the European Communities. pp. 1011-1015.
- 1986. Structural Damage in MgAl_2O_4 Spinel after High Dose Electron Irradiation at Elevated Temperatures. *Journal of Nuclear Materials* 141-143. pp. 387-391.
- Buckley, S.N.; Shaibani, S.J. 1987. The Variable Resistance of Magnesium Aluminate Spinel to Point-Defect Aggregation During Irradiation. *Philosophical Magazine Letters* 55. pp. 15-20.
- Bunch, J.M. 1977a. Mollwo-Ivey Relation between Peak Color-Center Absorption Energy and Average Oxygen Ion Spacing in Several Oxides of Group-II and -III Metals. *Physical Review B* 16. pp. 724-725.
- 1977b. LASL Controlled Thermonuclear Research Program Progress Report. LA-7474. Los Alamos Scientific Laboratory, Los Alamos, NM. pp. 204.
- Bunch, J.M.; Clinard, F.W., Jr. 1974. Damage of Single-Crystal Al_2O_3 by 14-MeV Neutrons. *Journal of the American Ceramic Society* 57. pp. 279-280.
- Burnett, P.J.; Page, T.F. 1986. Criteria for Mechanical Property Modifications of Ceramic Surfaces by Ion Implantation. *Radiation Effects* 97. pp. 283-296.
- Bushnell, C.W. 1994. Private communication (presentation, ITER Magnet Discussions, NIST, Boulder, CO, February 4, 1994). ITER EDA, Naka Co-Center, Naka-gun, Ibaraki-ken, Japan.
- Cain, L.S.; Pogatshnik, G.J.; Chen, Y. 1988. Optical Transitions in Neutron-Irradiated MgAl_2O_4 Spinel Crystals. *Physical Review B* 37. pp. 2645-2652.
- Cannon, C.P. 1982. Comparative Gamma Radiation and Temperature Effects on SiO_2 and MgO Insulated Nuclear Instrument Cable. *IEEE Transactions on Nuclear Science* 29. pp. 705-708.
- Caulfield, K.J.; Cooper, R.; Boas, J.F. 1990. A Temperature Effect in the Luminescence Emission from Electron-Irradiated MgO . *Journal of Chemical Physics* 92. pp. 6441-6446.
- Chadderton, L.T. 1965. *Radiation Damage in Crystals*. Methuen & Co., Ltd., London, U.K.
- Chaussy, J.; Gilchrist, J. Le G.; Lasjaunias, J.C.; Saint-Paul, M. 1979. Thermal Properties of Smoky Quartz at Very Low Temperatures. *Journal of Physics and Chemistry of Solids* 40. pp. 1073-1078.
- Chen, Y.; Sibley, W.A. 1967. Study of Ionization-Induced Radiation Damage in MgO . *Physical Review* 154. pp. 842-850.

- Chen, Y.; Williams, R.T.; Sibley, W.A. 1969. Defect Cluster Enters in MgO. *Physical Review* 182. pp. 960-964.
- Chen, Y.; Abraham, M.M.; Robinson, M.T. 1975. Production of Point Defects in 14.8 MeV Neutron-Irradiated MgO. *Proceedings, International Conference on Radiation Effects and Tritium Technology of Fusion Reactors* 11. pp. 492-497.
- Chyung, K. 1974. Fracture Energy and Thermal Shock Resistance of Mica Glass-Ceramics. In: *Fracture Mechanics of Ceramics* 2. Bradt, R.C.; Hasselman, D.P.H.; Lange, F.F. eds. Plenum Press, New York, NY. pp. 495-508.
- Clark, W.G., Jr.; Logsdon, W.A. 1974. The Applicability of Fracture Mechanics Technology to Porcelain Ceramics. In: *Fracture Mechanics of Ceramics*, Vol. 2. Bradt, R.C.; Hasselman, D.P.H.; Lange, F.F. eds. Plenum Press, New York, NY. pp. 843-861.
- Clinard, F.W., Jr. 1979. Ceramics for Applications in Fusion Systems. *Journal of Nuclear Materials* 85 & 86. pp. 393-404.
- Clinard, F.W., Jr; Hobbs, L.W. 1986. Radiation Effects in Non-Metals. In: *Physics of Radiation Effects in Crystals*. Johnson R.A.; Orlor, A.N. eds. Elsevier Science Publishers B.V. pp. 388-471.
- Clinard, F.W., Jr.; Rohr, D.L.; Ranken, W.A. 1977. Neutron-Irradiation Damage in Stabilized ZrO₂. *Journal of the American Ceramic Society* 60. pp. 287-288.
- Clinard, F.W., Jr.; Hurley, G.F.; Klaffky, R.W. 1983. Ceramics for Fusion Reactor Applications. *Res Mechanica* 8. pp. 207-234.
- Clinard, R.W., Jr; Hurley, G.F.; Hobbs, L.W.; Rohr, D.L.; Youngman, R.A. 1984. Structural Performance of Ceramics in a High-Fluence Fusion Environment. *Journal of Nuclear Materials* 122 & 123. pp. 1386-1392.
- Coghlan, W.A.; Clinard, F.W., Jr. 1991. Damage to Macor Glass-Ceramic from High-Dose 14 MeV Neutrons. *Journal of Nuclear Materials* 179-181. pp. 391-394.
- Coghlan, W.A.; Clinard, F.W., Jr.; Itoh, N.; Greenwood, L.R. 1986. Swelling of Spinel after Low-Dose Neutron Irradiation. *Journal of Nuclear Materials* 141-143. pp. 382-386.
- Cohen, A.F. 1958. Low-Temperature Thermal Conductivity in Neutron Irradiated Vitreous Silica. *Journal of Applied Physics* 29. pp. 591-593.
- Comer, J.J. 1972. Electron Microscope Study of Dauphiné Microtwins Formed in Synthetic Quartz. *Journal of Crystal Growth* 15. pp. 179-187.
- Compton, W.D.; Arnold, G.W. 1961. Radiation Effects in Fused Silica and α -Al₂O₃. *Discussions Faraday Society* 31. pp. 130-139.

- Coulter, C.A.; Parkin, D.M. 1980. Damage Energy Functions in Polyatomic Materials. *Journal of Nuclear Materials* 88. pp. 249-260.
- Crannell, C.J.; Crannell, H.; O'Sullivan, C.; May, T.H. 1970. Enhancement of Alpha Particle Tracks in Cellulose Nitrate Using Electric Fields. *IEEE Transactions on Nuclear Science* 17. pp. 337-339.
- Crawford, J.H., Jr. 1984. Defects and Defect Processes in Ionic Oxides: Where Do We Stand Today? *Nuclear Instruments and Methods in Physics Research B1*. pp. 159-165.
- Crawford, J.H.; Wittels, M.C. 1958. Radiation Stability of Nonmetals and Ceramics. In: *Second United Nations International Conference on the Peaceful Uses of Atomic Energy, Geneva, Switzerland, vol. 5*. pp. 300-309.
- Crawford, J.H.; Lee, K.H.; White, G.S. 1978. Displacement Energy for Stable Defect Creation in MgAl_2O_4 . *Bulletin of the American Physical Society* 23. pp. 253-254.
- Dartyge, E.; Lambert, M.; Maurette, M. 1976. Structure et Enregistrement des Traces Latentes d'Ions Argon et Fer dans L'Olivine et le Mica Muscovite. *Le Journal de Physique* 37. pp. 939-943.
- Das, G.; Mitchell, T.E. 1974. Electron Irradiation Damage in Quartz. *Radiation Effects* 23. pp. 49-52.
- Davidge, R.W. 1968. Irradiation Damage and Irradiation Hardening in Single Crystal MgO After Low Neutron Doses $< 10^{18}$ nvt (> 1 MeV). *Journal of Nuclear Materials* 25. pp. 75-86.
- Davidson, A.T.; Yoffe, A.D. 1965. Dielectric Breakdown in Thin Mica Crystals. *Nature* 206. pp. 1247-1248.
- Dell, G.F.; Goland, A.N. 1981. Radiation Damage Parameters in Multicomponent Nonmetals. *Journal of Nuclear Materials* 102. pp. 246-258.
- Dell, G.F.; Berry, H.C.; Goland, A.N.; Lazareth, O.W. 1979. Calculation of Radiation Damage in Insulators for Fusion Reactors. *Journal of Nuclear Materials* 85 & 86. pp. 373-377.
- Dellin, T.A.; Tichenor, D.A.; Barsis, E.H. 1977. Volume, Index-of-Refractive, and Stress Changes in Electron-Irradiated Vitreous Silica. *Journal of Applied Physics* 48. pp. 1131-1138.
- DePino, A., Jr.; Dahl, R.E. 1967. Fission Track Dosimetry. In: *Irradiation Effects on Reactor Structural Materials, Quarterly Progress Report, Nov., Dec. 1966 - Jan. 1967*. BNWL-CC-1053. Battelle-Northwest, Richland, WA. Pacific Northwest Laboratory. 203 pp.
- Desport, J.A.; Smith, J.A.G. 1964. Irradiation-Induced Growth in Oxides of Beryllium, Magnesium and Aluminium. *Journal of Nuclear Materials* 14. pp. 135-140.

- Devine, R.A.B. 1990. Radiation Damage and the Role of Structure in Amorphous SiO_2 . *Nuclear Instruments and Methods in Physics Research B* 46. pp. 244-251.
- Dienst, W. 1992. Reduction of the Mechanical Strength of Al_2O_3 , AlN and SiC under Neutron Irradiation. *Journal of Nuclear Materials* 191-194. pp. 555-559.
- Dienst, W.; Zimmermann, H. 1994. Fracture Toughness and Strength Change of Neutron-Irradiated Ceramic Materials. *Journal of Nuclear Materials* (in press).
- Dienst, W.; Fett, T.; Heidinger, R.; Rohrig, H.D.; Schulz, B. 1990. Investigations on Ceramic Materials for Fusion Technology. *Journal of Nuclear Materials* 174. pp. 102-109.
- Dierckx, R. 1987. The Importance of the PKA-Energy Spectrum for Radiation Damage Simulation. *Journal of Nuclear Materials* 144. pp. 214-227.
- Egusa, S.; Kirk, M.A.; Birtcher, R.C. 1984. Neutron Irradiation Effects on the Mechanical Properties of Organic Composite Materials. *Journal of Nuclear Materials* 126. pp. 152-159.
- Erez, E.A.; Becker, H. 1982. Radiation Damage in Thin Sheet Fiberglass Insulators. In: *Nonmetallic Materials and Composites at Cryogenic Temperatures*, Hartwig, G.; Evans, D., eds. Plenum Press, New York, NY. pp. 59-71.
- Evans, A.G.; Davidge, R.W. 1969. The Strength and Fracture of Fully Dense Polycrystalline Magnesium Oxide. *Philosophical Magazine* 20. pp. 373-388.
- Evans, B.D. 1974. Influence of Temperature and Particle Fluence on F-Type Center Production in MgO . Department of Physics, Tohoku University, Japan. International Conference on Color Centers in Ionic Crystals, Sendai, Japan, 18-23 August, 1974. Abstract 62.
- Evans, B.D.; Stapelbroek, M. 1979. Fusion/Fission Neutron Damage Ratio for Alumina. *Journal of Nuclear Materials* 85 & 86. pp. 497-502.
- Evans, B.D.; Comas, J.; Malmberg, P.R. 1972. Coloration Induced in MgO by MeV $^{20}\text{Ne}^+$ Bombardment. *Physical Review B* 6. 2453-2462.
- Fassò, A.; Goebel, K.; Höfert, M.; Rau, G.; Schönbacher, H.; Stevenson, G.R.; Sullivan, A.H.; Swanson, W.P.; Tuyn, J.W.N. 1984. Radiation Problems in the Design of the Large Electron-Positron Collider (LEP). CERN 84-02. European Organization for Nuclear Research, Geneva, Switzerland. 93 pp.
- Fischer, H.; Götz, G.; Karge, H. 1983a. Radiation Damage in Ion-Implanted Quartz Crystals, Part I: Nuclear and Electronic Energy Deposition. *Physica Status Solidi (a)* 76. pp. 249-256.

- Fischer, H.; Götz, G.; Karge, H. 1983b. Radiation Damage in Ion-Implanted Quartz Crystals, Part II: Annealing Behavior. *Physica Status Solidi (a)* 76. pp. 493-498.
- Fleischer, R.L.; Price, P.B. 1964. Decay Constant for Spontaneous Fission of U^{238} . *Physical Review* 133. pp. B63-B64.
- Fleischer, R.L.; Price, P.B.; Walker, R.M.; Hubbard, E.L. 1964. Track Registration in Various Solid-State Nuclear Track Detectors. *Physical Review* 133. pp. A1443-A1449.
- Fleischer, R.L.; Price, P.B.; Walker, R.M. 1965a. Effects of Temperature, Pressure, and Ionization of the Formation and Stability of Fission Tracks in Minerals and Glasses. *Journal of Geophysical Research* 70. pp. 1497-1502.
- 1965b. Ion Explosion Spike Mechanism for Formation of Charged-Particle Tracks in Solids. *Journal of Applied Physics* 36. pp. 3645-3652.
- 1975. *Nuclear Tracks in Solids*. University of California Press, Berkeley, CA.
- Fowler, J.D., Jr.; Hurley, G.F.; Kennedy, J.C.; Clinard, F.W., Jr. 1981. 14 MeV Neutron Irradiation Effects in Macor Glass-Ceramic. *Journal of Nuclear Materials* 103 & 104. pp. 755-760.
- Fukushima, Y.; Yano, T.; Maruyama, T. 1990. Swelling, Thermal Diffusivity and Microstructural Investigation of Neutron-Irradiated Single Crystals of Nonstoichiometric Spinel. *Journal of Nuclear Materials* 175. pp. 203-208.
- Gardner, J.W.; Anderson, A.C. 1981a. Low-Temperature Specific Heat and Thermal Conductivity of Neutron-Irradiated Crystalline Quartz. *Physical Review B* 23. pp. 474-482.
- 1981b. Effect of Neutron Irradiation on the Low-Temperature Specific Heat and Thermal Conductivity of Magnesium Oxide. *Physical Review B* 23. pp. 1988-1991.
- Garner, F.A.; Heinisch, H.L.; Simons, R.L.; Mann, F.M. 1990. Implications of Neutron Spectrum and Flux Differences on Fission-Fusion Correlations at High Neutron Fluence. *Radiation Effects and Defects in Solids* 113. pp. 229-255.
- Ghoniem, N.M.; Chou, S.P. 1988. Binary Collision Monte Carlo Simulations of Cascades in Polyatomic Ceramics. *Journal of Nuclear Materials* 155-157. pp. 1263-1267.
- Glasgow, B.B.; Wolfer, W.G. 1985. Stress Analysis of a Duplex Structure in a High Heat Flux Fusion Environment. *Fusion Technology* 8. pp. 596-601.

- Goland, A. 1978. Insulation Irradiation Studies at Brookhaven National Laboratory. In: *Proceedings of the Meeting on CTR Electrical Insulation*. pp. 199-212.
- Golding, B.; Graebner, J.E. 1980. Echo Phenomena in Disordered Solids. In: *Phonon Scattering in Condensed Matter (Proceedings of the 3rd International Conference)*. H.J. Maris, ed. Plenum Press, New York, NY. pp. 11-20.
- Grant, J.L.; Cooper, R.; Zeglinski, P.; Boas, J.F. 1989. Time Resolved Luminescence Spectroscopy of Alkaline Earth Oxides After Pulsed Electron Beam Irradiation. II. Spectra and Thresholds of MgO. *Journal of Chemical Physics* 90. pp. 807-812.
- Greenwood, L.R. 1990. Radiation Damage Calculations for Compound Materials. In: *Effects of Radiation on Materials: 14th International Symposium (Vol. II)*, ASTM STP 1046. N.H. Packan, R.E. Stoller, A.S. Kumar, eds. American Society for Testing and Materials, Philadelphia, PA. pp. 633-641.
- Griscom, D.L. 1979. Point Defects and Radiation Damage Processes in α -Quartz. In: *Proceedings of the Annual Frequency Control Symposium*, Vol 33. pp. 98-109.
- Gulden, T.D. 1967. On the Nature of Dislocation Loops in Neutron Irradiated Sapphire. *Materials Research Bulletin* 2. pp. 49-53.
- Harrop, P.J.; Wilkins, N.J.M.; Wanklyn, J.N. 1967. Radiation Damage in Zirconia. In: *Proceedings of the British Ceramic Society* 9. pp. 279-286.
- Hasegawa, H.; Hioki, T.; Kamigaito, O. 1986. Ion Implantation Induced Phase Transformation in Fully Stabilized Zirconia. *Journal of the Japan Institute of Metals* 50. pp. 515-520.
- Hashemi-Nezhad, S.R.; Bull, R.K.; Durrani, S.A. 1982. Electron and Alpha Particle Damage in Biotite Mica: Implications for Track Formation Mechanisms. In: *Proceeding of the 11th International Conference on Solid State Nuclear Track Detectors*. Pergamon Press, Oxford, U.K. pp. 23-26.
- Heidinger, R. 1991. Design Parameters of Ceramic Insulator Materials for Fusion Reactors. *Journal of Nuclear Materials* 179-181. pp. 64-69.
- Heinisch, H.L. 1993. Defect Production in Irradiated Metals. In: *Fusion Reactor Materials, Semiannual Progress Report for the Period Ending March 31, 1993*. DOE/ER-0313/14. DOE Office of Fusion Energy. pp. 145-149.
- Henderson, B.; Bowen, D.H. 1971. Radiation Damage in Magnesium Oxide I. Dose Dependence of Reactor Damage. *Journal of Physics C: Solid State Physics* 4. pp. 1487-1495.

- Hickman, B.S.; Jostsons, A. 1969. Anisotropic Growth of Aluminium Nitride Under Neutron Irradiation. *Journal of Nuclear Materials* 29. pp. 121-122.
- Hines, R.L.; Arndt, R. 1960. Radiation Effects of Bombardment of Quartz and Vitreous Silica by 7.5-keV to 59-keV Positive Ions. *Physical Review* 119. pp. 623-633.
- Hodgson, E.R. 1989. High Temperature Electron Irradiation of Fusion Materials. *Crystal Lattice Defects and Amorphous Materials* 18. pp. 169-180.
- 1991. Radiation-Enhanced Electrical Breakdown in Fusion Insulators. *Journal of Nuclear Materials* 179-181. pp. 383-386.
- 1992a. Radiation Enhanced Electrical Breakdown in Fusion Insulators from dc to 126 MHz. *Journal of Nuclear Materials* 191-194. pp. 552-554.
- 1992b. Radiation Enhanced Electrical Breakdown in Al_2O_3 : Field Effect. *Nuclear Instruments and Methods in Physics Research B* 65. pp. 298-300.
- Hodgson, E.R.; Clement, S. 1988. Dose Rate Dependence of the Radiation-Induced Electrical Conductivity in MgO . *Journal of Nuclear Materials* 155-157. pp. 357-360.
- Hofacker, M.; Löhneysen, H.v. 1981. Low Temperature Thermal Properties of Crystalline Quartz after Electron Irradiation. *Zeitschrift für Physik B-Condensed Matter* 42. pp. 291-296.
- Howitt, D.G.; Mitchell, T.E. 1981. Electron irradiation damage in $\alpha\text{-Al}_2\text{O}_3$. *Philosophical Magazine A* 44. pp. 229-238.
- Hughes, A.E. 1986. Radiation Damage in Insulators at High Doses. *Radiation Effects* 97. pp. 161-173.
- Hurley, G.F.; Clinard, F.W., Jr. 1980. Neutron Irradiation Testing of Mica-Containing Ceramics. In: *Special Purpose Materials. Annual Progress Report, October 2, 1979*. DoE/ER - 0048/1 (Department of Energy, Washington, DC). 1980. 106 pp.
- Hurley, G.F.; Kennedy, J.C.; Clinard, F.W., Jr.; Youngman, R.A.; McDonnell, W.R. 1981. Structural Properties of MgO and MgAl_2O_4 After Fission Neutron Irradiation Near Room Temperature. *Journal of Nuclear Materials* 103 & 104. pp. 761-766.
- Hurley, P.; Fairbairn, H.W. 1952. Alpha-Radiation Damage in Zircon. *Journal of Applied Physics* 23. p. 1408.
- Ibarra, A.; Mariani, D.F.; Jiménez de Castro, M. 1991a. Thermoluminescent Processes of MgAl_2O_4 Irradiated at Room Temperature. *Physical Review B* 44. pp. 12158-12165.
- Ibarra, A.; López, F.J.; Jiménez de Castro, M. 1991b. V Centers in MgAl_2O_4 Spinels. *Physical Review B* 44. pp. 7256-7262.

- Iida, T.; Sumita, K.; Yamanaka, T. 1991. Effects of 14-MeV Neutron Irradiation on Some Components for Fusion Diagnostics. In: *Proceedings of the 16th Symposium on Fusion Technology, Vol 1*. Keen, B.E.; Huguet, M.; Hemsworth, R., eds. Elsevier Science Publishers B.V., London, U.K. pp. 557-561.
- Iijima, S.; Zhu, J. 1982. Electron Microscopy of a Muscovite-Biotite Interface. *American Mineralogist* 67. pp. 1195-1205.
- Itoh, N.; Tanimura, K. 1986. Radiation Effects in Ionic Solids. *Radiation Effects* 98. pp. 269-287.
- Ivanov, V.M.; Kalinin, G.M.; Kuzovitskin, V.F.; Sklizkov, S.P.; Markina, N.V.; Sarksyian, V.V.; Skobeleva, V.A. 1981. Electrophysical Properties of Plasma-Deposited Refractory Oxides Under Reactor Irradiation. *Inorganic Materials* 17. pp. 1203-1207.
- Iwamoto, N.; Makino, Y.; Endo, S.; Itoh, N.; Matsunami, N. 1985a. Characterization of Ar⁺-Ion Irradiated Alumina Coatings. *Journal of Nuclear Materials* 133 and 134. pp. 736-740.
- Iwamoto, N.; Makino, Y.; Endo, S.; Yamamoto, T.; Matsunami, N. 1985b. TSEE from Aluminas and Spinelns Subjected to Ar⁺-Ion Irradiation. *Japanese Journal of Applied Physics* 24. pp. 212-215.
- Iwamoto, N.; Endo, S.; Makino, Y. 1986. Characterization of Ar⁺-Ion Irradiated Spinelns. *Radiation Effects* 97. pp. 243-250.
- Jech, C. 1967. Ion-Bombardment Enhanced Solubility in Solids. *Physica Status Solidi* 21. pp. 481-486.
- Jones, P.L.; Schaffer, J.P.; Cocks, F.H.; Clinard, F.W., Jr.; Hurley, G.F. 1985. A Comparison of the Doppler-Broadened Positron Annihilation Spectra of Neutron Irradiated Al₂O₃ and MgAl₂O₄. *Journal of Nuclear Materials* 127. pp. 221-224.
- Katz, R.; Kobetich, E.J. 1968. Formation of Etchable Tracks in Dielectrics. *Physical Review B* 170. pp. 401-405.
- Kawanishi, M. 1985. The Progress of Research on Exoelectron Emission and Applications in Japan. *Japanese Journal of Applied Physics* 24. pp. 1-5.
- Keilholtz, G.W.; Lee, J.E., Jr.; Moore, R.E. 1964. The Effect of Fast-Neutron Irradiation on Beryllium Oxide Compacts at High Temperatures. *Journal of Nuclear Materials* 11. pp. 253-264.
- Keilholtz, G.W.; Moore, R.E.; Robertson, H.E. 1971. Effects of Fast Neutrons on Polycrystalline Alumina and Other Electrical Insulators at Temperatures from 60° to 1230° C. ORNL-4678. Oak Ridge National Laboratory, TN. 109 pp.
- Ketterer, R.J. 1964. Mica Paper Insulations—State of the Art. *Insulation* 10. pp. 24-32.

- Khan, H.A.; Khan, N.A. 1983. Radiation Damage Studies in Muscovite and Biotite Mica-Track Detectors. *International Journal of Applied Radiation and Isotopes* 34. pp. 1497-1500.
- Khan, H.A.; Khan, N.A.; Jamil, K.; Brandt, R. 1984. Annealing of Heavy Ion Latent Damage Trails in Muscovite Mica and CR-39 Plastic Track Detectors. *Nuclear Tracks and Radiation Measurements* 8. pp. 377-380.
- Kinchin, G.H.; Pease, R.S. 1955. The Displacement of Atoms in Solids by Radiation. *Reports on Progress in Physics* 18. pp. 1-51.
- Kircher, J.F. 1964. Basic Concepts of Radiation Effects. In: *Effects of Radiation on Materials and Components*. Kircher, J.F.; Bowman, R.E., eds. Reinhold Publishing Corp., New York, NY. pp. 11-48.
- Klaffky, R.W. 1980. Technique for Measuring High-Field Resistivity and Dielectric Breakdown Strength of Insulators Under Ionizing Radiation. In: *Special Purpose Materials. Annual Progress Report, October 1, 1979*. DoE/ER - 0048/1. Department of Energy, Washington, DC. 106 pp.
- Klein, G.E. 1955. X-Ray Examination of Ceramic Samples. In: *Solid State Division Semiannual Progress Report, for Period Ending February 28, 1955*. ORNL-1852. Oak Ridge National Laboratory, TN. pp. 35-36.
- Klein, H.H. 1981. Influence of Mica Paper Parameters on the Quality of Electrical Insulation. In: *Proceedings of the 15th Electrical/Electronics Insulation Conference*. pp. 172-173.
- Klemens, P.G. 1958. Imperfections Induced in Solids by Fast Particle Irradiation. In: *Australian Atomic Energy Symposium*. Melbourne University Press, Melbourne, Australia. pp. 555-561.
- Kostyukov, N.S.; Antonova, N.P.; Bogdanova, O.N.; Dubinin, G.V.; Yatskovich, I.I. 1981. Effect of Structure on the Radiation Resistance of Electrical Ceramics. In: *Thirteenth Conference on Silicate Industry and Silicate Science*. OMKDK, Budapest, Hungary. pp. 195-200.
- Krefft, G.B.; EerNisse, E.P. 1978. Volume Expansion and Annealing Compaction of Ion-Bombarded Single-Crystal and Polycrystalline α -Al₂O₃. *Journal of Applied Physics* 49. pp. 2725-2730.
- Kulcinski, G.L. 1979. Fusion Reactors: Their Challenge to Materials Scientists. *Contemporary Physics* 20. pp. 417-447.
- Kupperman, D.S., Kurz, G.; Weinstock, H. 1973. Thermal Conductivity of Neutron-Irradiated MgO. *Journal of Low Temperature Physics* 10. pp. 193-201.
- Labauve, R.J.; Livak, R.J.; Clinard, F.W., Jr. 1988. Calculations for Isotopically Tailored Ceramics in Fission and Fusion Reactors. *Advanced Ceramic Materials* 3. pp. 353-356.

- Laermans, C. 1979. Saturation of the 9.4-GHz Hypersonic Attenuation in Fast-Neutron-Irradiated Crystalline Quartz. *Physical Review Letters* 42. pp. 250-254.
- Laermans, C.; Daudin, B. 1980. Further Study of the "Glassy" Low Temperature Properties of Irradiated Crystalline Quartz. In: *Phonon Scattering in Condensed Matter (Proceedings of the 3rd International Conference)*. Maris, H.J., ed. Plenum Press, New York, NY. pp. 21-24.
- Laermans, C.; de Goër, A.M.; Locatelli, M. 1980. Evidence for the Presence of Two Level Systems Related to Point Defects in Electron Irradiated Crystalline Quartz. *Physics Letters* 80A. pp. 331-336.
- Lapp, R.E.; Andrews, H.L. 1954. *Nuclear Radiation Physics*. Prentice-Hall, Inc., New York, NY.
- Lee, W.E.; Jenkins, M.L.; Pells, G.P. 1985. The Influence of Helium Doping on the Damage Microstructure of Heavy-Ion Irradiated α -Al₂O₃. *Philosophical Magazine A* 51. pp. 639-659.
- Leighton, R.B. 1959. *Principles of Modern Physics*. McGraw-Hill Book Co., Inc., New York, NY.
- Lell, E.; Kreidl, N.J.; Hensler, J.R. 1966. Radiation Effects in Quartz, Silica and Glasses. In: *Progress in Ceramic Science* 4. J.E. Benke, ed. Pergamon, Oxford, U.K. pp. 1-93.
- Levy, P.W. 1960. Reactor and Gamma-Ray Induced Coloring of Corning Fused Silica. *Journal of Physics and Chemistry of Solids* 13. pp. 287-295
- Levy, P.W. 1961. Color Centers and Radiation-Induced Defects in Al₂O₃. *Physical Review* 123. pp. 1226-1233.
- Lindhard, J.; Scharff, M.; Schiøtt, H.E. 1963. Range Concepts and Heavy Ion Ranges. *Matematisk-fysiske Meddelelser Det Kongelige Danske Videnskabernes Selskab* 33. pp. 1-42.
- Löhneysen, H.v.; Platte, M. 1979. Low Temperature Thermal Properties and Intrinsic Defects in Vitreous Silica. *Zeitschrift für Physik B* 36. pp. 113-120.
- Low, N.L.P. 1980. Formation and Properties of Glass-Mica Composite Materials. *Ceramurgia International* 6. pp. 85-90.
- Macauley-Newcombe, R.G.; Thompson, D.A. 1984. Ion Bombardment Damage in α -Quartz at 50-295 K. *Nuclear Instruments and Methods in Physics Research B1*. pp. 176-182.
- Macauley-Newcombe, R.G.; Thompson, D.A.; Davies, J.A.; Stevanovic, D.V. 1990. Ion-Beam Damage to Quartz Crystals. *Nuclear Instruments and Methods in Physics Research B46*. pp. 180-184.

- Martin, D.G. 1959. Dimensional Changes in Single Crystals of Synthetic Sapphire after Irradiation. *The Physics and Chemistry of Solids* 10. pp. 64-65.
- Matzke, Hj. 1982. Radiation Damage in Crystalline Insulators, Oxides and Ceramic Nuclear Fuels. *Radiation Effects* 64. pp. 3-33.
- Matzke, Hj.; Whitton, J.L. 1966. Ion-Bombardment-Induced Radiation Damage in Some Ceramics and Ionic Crystals. *Canadian Journal of Physics* 44. pp. 995-1010.
- Maurette, P.M. 1966. Étude de l'Enregistrement des Trajectoires de Fragments de Fission dans Quelques Substances Solides Isolantes. *Le Journal de Physique* 27. pp. 505-512.
- Mazey, D.J. 1990. Fundamental Aspects of High-Energy Ion-Beam Simulation Techniques and Their Relevance to Fusion Materials Studies. *Journal of Nuclear Materials* 174. pp. 196-209.
- McDonald, D.L. 1963. Low-Temperature Irradiation of Beryllium Oxide. *Applied Physics Letters* 2. pp. 175-176.
- McGowan, W.C.; Sibley, W.A. 1969. Hardening of MgO Single Crystals by Electron and Neutron Irradiation. *Philosophical Magazine* 19. pp. 967-976.
- McHargue, C.J.; Farlow, G.C.; Begun, G.M.; Williams, J.M.; White, C.W.; Appleton, B.R.; Sklad, P.S.; Angelini, P. 1986. Damage Accumulation in Ceramics During Ion Implantation. *Nuclear Instruments and Methods in Physics Research B* 16. pp. 212-220.
- McLane, V.; Dunford, C.L.; Rose, P.F. 1988. *Neutron Cross Sections, Vol. 2, Neutron Cross Section Curves*. Academic Press, Inc., Boston, MA.
- Merkle, K.L. 1974. TEM Investigation of 14-MeV Neutron Damage. *Nuclear Technology* 22. pp. 66-78.
- Mike, T.M.; Steierman, B.L.; Degering, E. F. 1960. Effects of Electron Bombardment on Properties of Various Glasses. *Journal of the American Ceramic Society* 43. pp. 405-407.
- Naguib, H.M.; Kelly, R. 1975. Criteria for Bombardment-Induced Structural Changes in Non-Metallic Solids. *Radiation Effects* 25. pp. 1-12.
- Nelson, C.M. 1957. Optical Absorption Studies of Irradiated Solids. In: *Solid State Division Annual Progress Report, for Period Ending August 31, 1957*. ORNL-2413. Oak Ridge National Laboratory, Oak Ridge, TN. pp. 58-63.
- Noda, S.; Doi, H.; Hioki, T.; Kamigaito, O. 1985. Deformation and Cracking of Metal-Deposited Single Crystal Alumina and the Effects of Ion-Irradiation. *Journal of Materials Science Letters* 4. pp. 523-525.

- Noren, J.R.; Ball, J.H. 1969. New Insulation from Large Mica Flakes. In: *Proceedings of the 9th Electrical Insulation Conference*. pp. 1-3.
- Norgett, M.J.; Robinson, M.T.; Torrens, I.M. 1975. A Proposed Method of Calculating Displacement Dose Rates. *Nuclear Engineering and Design* 33. pp. 50-54.
- Norris, C.B.; EerNisse, E.P. 1974. Ionization Dilatation Effects in Fused Silica from 2 to 18-keV Electron Irradiation. *Journal of Applied Physics* 45. pp. 3876-3882.
- Oen, O.S.; Holmes, D.K. 1959. Cross Sections for Atomic Displacements in Solids by Gamma Rays. *Journal of Applied Physics* 30. pp. 1289-1295.
- Parker, C.A.; Hobbs, L.W.; Russell, K.C.; Clinard, F.W., Jr. 1985. Damage Structures in Fast Neutron Irradiated Magnesium Aluminate and Electron Irradiated Aluminum Oxynitride Spinels. *Journal of Nuclear Materials* 133 & 134. pp. 741-744.
- Parkin, D.M. 1990. The Displacement Cascade in Ceramic Oxides. *Nuclear Instruments and Methods in Physics Research B46*. pp. 26-35.
- Pascucci, M.R.; Hutchison, J.L.; Hobbs, L.W. 1983. The Metamict Transformation in Alpha-Quartz. *Radiation Effects* 74. pp. 219-226.
- Patrick, A.J. 1965. Irradiation Damage to Ceramics, Metallic-Ceramic Bonds, and Brazing Alloys. LA-3285-MS. Los Alamos Scientific Laboratory, NM. 47 pp.
- Pauling, L. 1930. The Structure of the Micas and Related Materials. In: *Proceedings of the National Academy of Science* 16. pp. 123-129.
- Paymal, A.J.; LeClerc, P. 1964. Elastic Properties of Some Glasses After Neutron Irradiation. *Journal of the American Ceramic Society* 47. pp. 548-554.
- Pells, G.P. 1982. The Temperature Dependence of the Threshold Displacement Energy in MgO. *Radiation Effects* 64. pp. 71-75.
- 1986. Electrical Conductivity of Alumina in a Radiation Field at Temperatures up to 700°C. *Radiation Effects* 97. pp. 199-207.
- 1988. Radiation Effects and Damage Mechanisms in Ceramic Insulators and Window Materials. *Journal of Nuclear Materials* 155 & 157. pp. 67-76.
- 1990. Radiation-Induced Degradation of the Electrical Conductivity of $MgAl_2O_4$ and Al_2O_3 . AEA FUS 86. Euratom/UKAEA Fusion Association. 19 pp.
- 1991. Radiation-Induced Degradation of the Intrinsic Electrical Conductivity of $MgAl_2O_4$ and Al_2O_3 . *Journal of Nuclear Materials* 184. pp. 177-182.

- Pells, G.P.; Murphy, M.J. 1991. The Effects of Transmutation Products on the Radiation-Induced Swelling of Al_2O_3 and MgAl_2O_4 . *Journal of Nuclear Materials* 183. pp. 137-144.
- 1992. Radiation-Induced Swelling of Polycrystalline Alumina Over the Temperature Range 200-890K. *Journal of Nuclear Materials* 191-194. pp. 621-624.
- Pells, G.P.; Phillips, D.C. 1979a. Radiation Damage of $\alpha\text{-Al}_2\text{O}_3$ in the HVEM. I. Temperature Dependence of the Displacement Threshold. *Journal of Nuclear Materials* 80. pp. 207-214.
- 1979b. Radiation Damage of $\alpha\text{-Al}_2\text{O}_3$ in the HVEM. II. Radiation Damage at High Temperature and High Dose. *Journal of Nuclear Materials* 80. pp. 215-222.
- Penkovskii, V.V. 1964. *Effect of Radiation on Metals and Other High-Melting Materials*. Elsevier Publishing Co., Amsterdam, The Netherlands.
- Perkins, L.J. 1984. Materials Considerations for Highly Irradiated Normal-Conducting Magnets in Fusion Reactor Applications. *Journal of Nuclear Materials* 122 & 123. pp. 1371-1375.
- Porter, D.L.; Pascucci, M.R.; Olbert, B.H. 1981. Neutron Irradiation Effects on SiO_2 and SiO_2 -Based Glass Ceramics. *Journal of Nuclear Materials* 103 & 104. pp. 767-772.
- Povarennykh, A.S. 1972. *Crystal Chemical Classification of Minerals, Vol. 1*. Plenum Press, New York, NY.
- Price, P.B.; Walker, R.M. 1962a. Observations of Charged-Particle Tracks in Solids. *Journal of Applied Physics* 33. pp. 3400-3406.
- 1962b. Chemical Etching of Charged-Particle Tracks in Solids. *Journal of Applied Physics* 33. pp. 3407-3412.
- 1963. Fossil Tracks of Charged Particles in Mica and the Age of Minerals. *Journal of Geophysical Research* 68. pp. 4847-4862.
- Primak, W. 1954. The Metamict State. *Physical Review* 95. p. 837.
- 1956. Fast-Neutron Damaging in Nuclear Reactors: Its Kinetics and the Carbon Atom Displacement Rate. *Physical Review* 103. pp. 1681-1692.
- 1958. Fast-Neutron-Induced Changes in Quartz and Vitreous Silica. *Physical Review* 110. pp. 1240-1253.
- 1964. Radiation-Induced Stress Relaxation in Quartz and Vitreous Silica. *Journal of Applied Physics* 35. pp. 1342-1347.
- 1972. Threshold for Radiation Effects in Silica. *Physical Review B* 6. pp. 4846-4851.

- 1975. *The Compacted States of Vitreous Silica*. Gordon and Breach Science Publisher, Inc., New York, NY.
- 1980. Radiation Damage by High-Energy Neutrons. *Nuclear Science and Engineering* 73. pp. 29-34.
- Primak, W.; Szymanski, H. 1956. Radiation Damage in Vitreous Silica: Annealing of the Density Changes. *Physical Review* 101. pp. 1268-1271.
- Primak, W.; Fuchs, L.H.; Day, P. 1953. Radiation Damage in Insulators. *Physical Review* 92. pp. 1064-1065.
- 1955. Effects of Nuclear Reactor Exposure on Some Properties of Vitreous Silica and Quartz. *Journal of the American Ceramic Society* 38. pp. 135-139.
- Pryor, A.W.; Tainsh, R.J.; White, G.K. 1964. Thermal Conductivity at Low Temperature of Neutron-Irradiated BeO. *Journal of Nuclear Materials* 14. pp. 208-219.
- Raychaudhuri, A.K.; Pohl, R.O. 1982. Thermal Conductivity of Neutron-Irradiated Silica. *Solid State Communications* 44. pp. 711-714.
- Rechtin, M.D. 1979. A Transmission Electron Microscopy Study of the Defect Microstructure of Al₂O₃ Subjected to Ion Bombardment. *Radiation Effects* 42. pp. 129-144.
- Reed, R.P. 1993. Private communication. (Transmission from ITER EDA Naka Co-Center, July and December, 1993) Cryogenic Materials, Inc., Boulder, CO.
- Rice, R.W. 1971. The Compressive Strength of Ceramics. In: *Ceramics in Severe Environments*, Vol. 5. W.W. Kriegel, H. Palmour III, eds. Plenum Press, New York, NY. pp. 195-229.
- Ritchie, R.H.; Claussen, C. 1982. A Core Plasma Model of Charged Particle Track. *Nuclear Instruments and Methods* 198. pp. 133-138.
- Rohde, M. 1991. Reduction of the Thermal Conductivity of SiC by Radiation Damage. *Journal of Nuclear Materials* 182. pp. 87-92.
- Rohde, M.; Schulz, B. 1992. Radiation Damage in Fusion Window Materials Studied by Thermal Conductivity. In: *Effects of Radiation on Materials: 15th International Symposium, ASTM STP 1125*. R.E. Stoller, A.S. Kumar, D.S. Gelles, eds. American Society for Testing and Materials, Philadelphia, PA. pp. 764-755.
- Saint-Paul, M.; Lasjaunias, J.C. 1981. Low-Temperature Specific Heat of Neutron-Irradiated Crystalline Quartz. *Journal of Physics C: Solid State Physics* 14. pp. 365-370.

- Saint-Paul, M.; Lasjaunias, J.C.; Locatelli, M. 1982. Low-Temperature Thermal Properties of Neutron-Irradiated Crystalline Quartz. *Journal of Physics C: Solid State Physics* 15. pp. 2375-2385.
- Sawan, M. 1993. Private communication. Memorandum dated March 4, to N. Simon, D. Reed, B. Montgomery, J. Schultz, J. Doggett, B. Hassenzahl and presentation to Task Group on Tentative Radiation Standards for ITER TF Coil Insulation, March 22, 1993. Fusion Technology Institute, University of Wisconsin, Madison, WI.
- Schroeder, J.E.; Dieselman, H.D. 1969. Ellipsometric Analysis of Radiation Damage in Dielectrics. *Journal of Applied Physics* 40. pp. 2559-2564.
- Schroeder, J.E.; Guertin, J.P. 1978. Extremely High Strength Porcelain. EL-722. Electric Power Research Institute, Palo Alto, CA.
- Shamfarov, Y.L. 1967. Electron Spin-Lattice Relaxation in Neutron-Irradiated Quartz at 37 GHz and Liquid-Helium Temperatures. *Soviet Physics-Solid State* 8. pp. 2083-2086.
- Shamfarov, Y.L.; Smirnova, T.A. 1963. Investigation of Spin-Lattice Relaxation in Neutron-Irradiated Quartz. *Soviet Physics-Solid State* 5. pp. 761-763.
- Shelby, J.E. 1980. Effect of Radiation on the Physical Properties of Borosilicate Glasses. *Journal of Applied Physics* 51. pp. 2561-2565.
- Sherman, N.K. 1962. Superconducting Nuclear Particle Detector. *Physical Review Letters* 8. pp. 438-439.
- Shikama, T.; Narui, M.; Endo, Y.; Ochiai, A.; Kayano, H. 1992a. Study of Radiation Induced Conductivity by AC-Method in a Fission Reactor. *Journal of Nuclear Materials* 191-194. pp. 544-547.
- Shikama, T.; Narui, M.; Endo, Y.; Sagawa, T.; Kayano, H. 1992b. Radiation Induced Conductivity of Ceramic Insulators Measured in a Fission Reactor. *Journal of Nuclear Materials* 191-194. pp. 575-578.
- Sibley, W.A. 1971. Radiation Damage in Oxides and Other Materials. *IEEE Transactiona on Nuclear Science* 18. pp. 273-280.
- Sibley, W.A.; Chen, Y. 1967. Radiation Damage in MgO. *Physical Review* 160. pp. 712-716.
- Sigrist, A.; Balzer, R. 1977. Untersuchungen zur Bildung von Tracks in Kristallen. *Helvetica Physica Acta* 50. pp. 49-61.
- Simmons, R.O.; Balluffi, R.W. 1958. X-Ray Study of Deuteron-Irradiated Copper near 10°K. *Physical Review* 109. pp. 335-344.
- Simon, I. 1957. Structure of Neutron-Irradiated Quartz and Vitreous Silica. *Journal of the American Ceramic Society* 40. pp. 150-153.

- Simon, I. 1958. Note on Thermal Expansion of Neutron-Irradiated Silica. *Journal of the American Ceramic Society* 41. p. 116.
- Simon, N.J. 1993. A Review of Irradiation Effects on Organic-Matrix Insulation. NISTIR 3999. National Institute of Standards and Technology, Boulder, CO. 500 pp.
- Simon, N.J. 1994. A Review of Cryogenic Properties of Inorganic Insulation Materials for ITER Magnets. NISTIR (in press) National Institute of Standards and Technology, Boulder, CO.
- Singh, N.P.; Singh, M.; Singh, S.; Virk, H.S. 1984. Etching Studies of Fission Damage in Quartz. *Indian Journal of Pure and Applied Physics* 22. pp 496-497.
- Sisman, O.; Bopp, C.D.; Towns, R.L.. 1955. Radiation Effects on the Thermal Conductivity of Ceramics. In: *Solid State Division Semiannual Progress Report, for Period Ending February 28, 1955*. ORNL-1852. Oak Ridge National Laboratory, Oak Ridge, TN. pp. 33-35.
- 1957. Radiation Stability of Ceramic Materials. In: *Solid State Division Annual Progress Report, for Period Ending August 31, 1957*. ORNL-2413. Oak Ridge National Laboratory, Oak Ridge, TN. pp. 80-82.
- Smith, T.L.; Anthony, P.J.; Anderson, A.C. 1978. Effect of Neutron Irradiation on the Density of Low-Energy Excitations in Vitreous Silica. *Physical Review B* 17. pp. 4997-5008.
- Spitzer, H.J. 1970. Preparation of Mica Specimen Support Films for Electron Microscopy and Radiation Damage Induced by High Energy Electron Bombardment. AD717037. Report 1982. NTIS/U.S. Army Mobility Equipment Research and Development Center, Fort Belvoir, VA. 3 pp.
- Stevanovic, M.; Elston, J. 1967. Effect of Fast Neutron Irradiation in Sintered Alumina and Magnesia. *Proceedings of the British Ceramic Society* 7. pp. 423-437.
- Strakna, R.E.; Clark, A.E.; Bradley, D.L.; Slie, W.M. 1963. Effect of Fast-Neutron Irradiation on the Pressure and Temperature Dependence of the Elastic Moduli of SiO₂ Glass. *Journal of Applied Physics* 34. pp. 1439-1443.
- Summers, G.P. 1980. Radiation Damage in MgAl₂O₄. *Physical Review B* 21. pp. 2578-2584.
- Tanaka, H.; Hirashima, T.; Shintani, T. 1982. Pure-Silica Core Optical Fiber and Fiber Cable for Radiation Fields. In: *International Wire & Cable Symposium Proceedings 1982*. pp. 452-458.
- Tanimura, K.; Itoh, N.; Clinard, F.W. 1987. Volume Change of Al₂O₃ and MgAl₂O₄ Induced by 14-MeV Neutron Irradiation. *Journal of Nuclear Materials* 150. pp. 182-185.

- Tawfik, A.; Abd El-Ati, M.I.; El-Ashry, F.M.; Abou Sekkina, M.M. 1985. Further Investigation on the Effects of Temperature and Energetic Ionizing Radiation on Monoclinic Zirconia Refractory. *Journal of the Physical Society of Japan* 54. pp. 3012-3017.
- Thompson, M.W. 1957. The Strength of Silica Glass after Pile Irradiation at 100 C and -196 C. AERE-MIR-2305. Atomic Energy Research Establishment, Harwell, U.K. 3 pp.
- Thorne, R.P.; Howard, V.C. 1967. Changes Induced in Polycrystalline Alumina by Fast Neutron Irradiation. *Proceedings of the British Ceramic Society* 7. pp. 439-441.
- To, K.; Stoneham, A.M.; Henderson, B. 1969. Electron Spin Resonance from a Vacancy-Pair Center in Magnesium Oxide. *Physical Review* 181. pp. 1237-1240.
- Toulemonde, M.; Fuchs, G.; Nguyen, N.; Studer, F.; Groult, D. 1987. Damage Processes and Magnetic Field Orientation in Ferrimagnetic Oxides $\text{Y}_3\text{Fe}_5\text{O}_{12}$ and $\text{BaFe}_{12}\text{O}_{19}$ Irradiated by High-Energy Heavy Ions: A Mössbauer Study. *Physical Review B* 35. pp. 6560-6569.
- Toulemonde, M.; Balanzat, E.; Bouffard, S.; Jousset, J.C. 1989. Structural Modifications Induced by Electronic Energy Deposition During the Slowing Down of Heavy Ions in Matter. *Nuclear Instruments and Methods in Physics Research B* 39. pp. 1-6.
- Toulemonde, M.; Balanzat, E.; Bouffard, S.; Grob, J.J.; Hage-Ali, M.; Stoquert, J.P. 1990. Damage Induced by High Electronic Stopping Power in SiO_2 Quartz. *Nuclear Instruments and Methods in Physics Research B* 46. pp. 64-68.
- Toulemonde, M.; Dufour, C.; Paumier, E. 1992. Transient Thermal Process After a High-Energy Heavy-Ion Irradiation of Amorphous Metals and Semiconductors. *Physical Review B* 46. pp. 14362-14369.
- Tsumbu, M.; Segers, D.; Van Brabander, F.; Dorikens-Vanpraet, L.; Dorikens, M. 1982. Positron Annihilation Measurements in Neutron Irradiated Crystalline Quartz. *Radiation Effects* 62. pp. 19-24.
- Tucker, D.S.; Zocco, T.; Kise, C.D.; Kennedy, J.C. 1986. Effects of Neutron-Irradiation on MgAl_2O_4 and Al_2O_3 . *Journal of Nuclear Materials* 141-143. pp. 401-404.
- Tuller, H.L. 1986. Highly Conductive Ceramics. In: *Ceramic Materials for Electronics*. R.C. Buchanan, ed. Marcel Dekker, Inc., New York, NY. pp. 425-473.
- Turner, T.J.; Crawford, J.H., Jr. 1976. Nature of the 6.1-eV band in Neutron-Irradiated Al_2O_3 Single Crystals. *Physical Review B* 13. pp. 1735-1740.

- van den Bosch, A.; Segers, D.; Tsumbu, M.; Dorikens-Vanpraet, L.; Dorikens, M. 1983. Neutron-Radiation Damage in Alpha-Quartz Crystals Studied by Positron Annihilation. *Radiation Effects* 74. pp. 161-166.
- Van der Pluijm, B.; Lee, J.H.; Peacor, D.R. 1988. Analytical Electron Microscopy and the Problem of Potassium Diffusion. *Clays and Clay Minerals* 36. pp. 498-504.
- Vance, E.R.; Gowda, K.A.; Cartz, L.; Karioris, F.G. 1983. Irradiation of Pollucite, Spinel and $\text{CaAl}_{12}\text{O}_{19}$ by 3 MeV Argon Ions. *Radiation Effects* 79. pp. 245-249.
- Veitch, S.; Marmach, M.; Swain, M.V. 1987. Strength and Toughness of Mg-PSZ and Y-TZP Materials at Cryogenic Temperatures. In: *Advanced Structural Ceramics, MRS Symposium Proceedings*. P.F. Becher, M.V. Swain, S. Sömiya, eds. Materials Research Society, Pittsburgh, PA. pp. 97-106.
- Vook, R.; Wert, C. 1958. Expansion of Copper upon Low-Temperature Deuteron Irradiation. *Physical Review* 109. pp. 1529-1537.
- Weeks, R.A. 1963. Paramagnetic Spectra of E_2' Centers in Crystalline Quartz. *Physical Review* 130. pp. 570-576.
- Weeks, R.A.; Sonder, E.; Narayan, J. 1978. Thermal Electric Breakdown Processes in Oxide Single Crystals. *American Ceramic Society Bulletin* 57. p. 316.
- Weissmann, S.; Nakajima, K. 1963. Defect Structure and Density Decrease in Neutron-Irradiated Quartz. *Journal of Applied Physics* 34. pp. 611-618.
- White, G.K.; Birch, J.A. 1965. Thermal Properties of Silica at Low Temperatures. *Physics and Chemistry of Glasses* 6. pp. 85-89.
- Wilks, R.S. 1968. Neutron-Induced Damage in BeO , Al_2O_3 and MgO —A Review. *Journal of Nuclear Materials* 26. pp. 137-173.
- Wilks, R.S.; Desport, J.A.; Smith, J.A.G. 1967. The Irradiation-Induced Macroscopic Growth of $\alpha\text{-Al}_2\text{O}_3$ Single Crystals. *Journal of Nuclear Materials* 24. pp. 80-86.
- Wittels, M.; Sherrill, F.A. 1954. Radiation Damage in SiO_2 Structures. *Physical Review* 93. pp. 1117-1118.
- 1956. Irradiation-Induced Phase Transformation in Zirconia. *Journal of Applied Physics* 27. pp. 643-644.
- 1959. Fission Fragment Damage in Zirconia. *Physical Review Letters* 3. pp. 176-177.
- Wullaert, R.A.; Burian, R.J.; Melehan, J.B.; Kangilaski, M.; Gates, J.E. 1964. Effects of Radiation on Ceramic Materials. In: *Effects of Radiation on Materials and Components*. J.F. Kircher, R.E. Bowman, eds. Reinhold Publishing Corp., New York, NY. pp. 277-402.

- Yamada, R.; Zinkle, S.J.; Pells, G.P. 1992. Defect Formation in Ion-Irradiated Al_2O_3 and MgAl_2O_4 : Effects of Grain Boundaries and Fusion Transmutation Products. *Journal of Nuclear Materials* 191-194. pp. 640-644.
- Yano, T.; Iseki, T. 1991. Thermal and Mechanical Properties of Neutron-Irradiated Aluminum Nitride. *Journal of Nuclear Materials* 179-181. pp. 387-390.
- Yau, Y.; Anovitz, L.M.; Essene, E.J.; Peacor, D.R. 1984. Phlogopite-Chlorite Reaction Mechanisms and Physical Conditions During Retrograde Reactions in the Marble Formation, Franklin, New Jersey. *Contributions to Mineralogy and Petrology* 88. pp. 299-306.
- Ziegler, J.F.; Biersack, J.P.; Littmark, U. 1985. *The Stopping and Range of Ions in Solids*. Pergamon Press, New York, NY.
- Zinkle, S.J. 1989. Hardness and Depth-Dependent Microstructure of Ion-Irradiated Magnesium Aluminate Spinel. *Journal of the American Ceramic Society* 72. pp. 1343-1351.
- 1991. Microstructural Changes in Oxide Ceramics Following Light Ion Irradiation. In: *Fusion Reactor Materials, Semiannual Progress Report, for the Period Ending March 31, 1991*. DOE/ER-0313/10. DOE Office of Fusion Energy. pp. 302-309.
- 1993a. Ceramics Radiation Effects Issues for ITER. In: *Fusion Reactor Materials, Semiannual Progress Report, for the Period Ending March 31, 1993*. DOE/ER-0313/14. DOE Office of Fusion Energy. pp. 415-425.
- 1993b. Effect of Irradiation Spectrum on the Microstructural Evolution in Oxide Ceramics. In: *Fusion Reactor Materials, Semiannual Progress Report, for the Period Ending March 31, 1993*. DOE/ER-0313/14. DOE Office of Fusion Energy. pp. 426-436.
- Zinkle, S.J.; Kojima, S. 1990. Microstructural Changes in MgAl_2O_4 Induced by Ion Irradiation. *Nuclear Instruments and Methods in Physics Research B* 46. pp. 165-170.
- 1991. Helium-Assisted Cavity Formation in Ion-Irradiated Ceramics. *Journal of Nuclear Materials* 179-181. pp. 395-398.
- Zinkle, S.J.; Hodgson, E.R. 1992. Radiation-Induced Changes in the Physical Properties of Ceramic Materials. *Journal of Nuclear Materials* 191-194. pp. 58-66.
- Zinkle, S.J.; Greenwood, L.R. 1993. Summary of Ionizing and Displacive Irradiation Fields in Various Facilities. In: *Fusion Reactor Materials, Semiannual Progress Report, for the Period Ending March 31, 1993*. DOE/ER-0313/14. DOE Office of Fusion Energy. pp. 74-78.

